# DYNAMIC ANALYSIS OF OFFSHORE FLOATING WIND TURBINE COMBINED WITH WAVE ENERGY CONVERTER

Thesis
submitted in partial fulfillment of the requirements for the degree of

**DOCTOR OF PHILOSOPHY**

by

**RONY J. S.**
(197AM018)


**DEPARTMENT OF WATER RESOURCES & OCEAN ENGINEERING**
**NATIONAL INSTITUTE OF TECHNOLOGY KARNATAKA**
**SURATHKAL, MANGALORE - 575 025, INDIA**

**MAY 2024**

# DYNAMIC ANALYSIS OF OFFSHORE FLOATING WIND TURBINE COMBINED WITH WAVE ENERGY CONVERTER

Thesis
submitted in partial fulfillment of the requirements for the degree of

**DOCTOR OF PHILOSOPHY**

by

**RONY J. S.**
(197AM018)

Under the guidance of

**Dr. DEBABRATA KARMAKAR**

**DEPARTMENT OF WATER RESOURCES & OCEAN ENGINEERING**
**NATIONAL INSTITUTE OF TECHNOLOGY KARNATAKA**
**SURATHKAL, MANGALORE - 575 025, INDIA**

**MAY 2024**

# DECLARATION

I hereby declare that the Ph.D. Thesis entitled **"Dynamic analysis of offshore floating wind turbine combined with wave energy converter"** which is being submitted to **National Institute of Technology Karnataka, Surathkal,** for the partial fulfillment of the requirement for the award of degree of **Doctor of Philosophy** in the **Department of Water Resources and Ocean Engineering.** is a bonafide report of the work carried out by me. The material contained in this Ph.D. Thesis has not been submitted to any university or Institution for the award of any degree.

07/05/24

.....

**RONY J. S. (197AM018)**

Department of Water Resources and Ocean Engineering

National Institute of Technology Karnataka, Surathkal

Place: NITK, SURATHKAL.

Date: 07TH MAY 2024

# CERTIFICATE

This is to certify that the Ph.D. Thesis entitled **"Dynamic analysis of offshore floating wind turbine combined with wave energy converter"** submitted by **RONY J. S. (197AM018),** as the record of the work carried out by him, is accepted as the Ph.D. Thesis submission in partial fulfillment of the requirements for the award of the degree of **Doctor of Philosophy** in the **Department of Water Resources and Ocean Engineering, National Institute of Technology Karnataka, Surathkal**, is a bonafide work carried out by him under my supervision and guidance.

Dkarmakar 07/05/2024

.....

**Dr. DEBABRATA KARMAKAR**

Associate Professor

Department of Water Resources and Ocean Engineering

National Institute of Technology Karnataka, Surathkal

Dept. of Water Resources & Ocean Engineering ★ NITK Surathkal

Vaija K 13.5.24

.....

**Chairman - DRPC**

Department of Water Resources and Ocean Engineering

National Institute of Technology Karnataka, Surathkal

**Chairman (DRPC)**
**Dept. of Water Resources & Ocean Engineering**

# ACKNOWLEDGEMENT

Writing this Ph.D. thesis in Marine Structures has been an extraordinary voyage of discovery and academic growth, and I am deeply grateful to the numerous individuals and institutions whose support and guidance have made this accomplishment possible.

I am immensely thankful to my guide **Dr. D. Karmakar**, Assistant Professor, Department of Water Resources and Ocean Engineering, National Institute of Technology Karnataka for his exceptional mentorship, expert guidance, and unwavering belief in my capabilities. His profound knowledge in the field of Ocean Engineering and his willingness to invest time and effort in nurturing my research skills has been instrumental in shaping the trajectory of this thesis.

I extend my gratitude to the members of my Research Progress Assessment Committee members **Dr. Manu,** Professor, Department of Water Resources and Ocean Engineering, and **Dr. A.S. Balu**, Associate Professor, Department of Civil Engineering, for dedicating their time and expertise to evaluate and provide valuable feedback on this thesis. Their critical input has significantly improved the quality and rigour of my research.

I am thankful to **Prof. Amba Shetty** and **Prof. B.M. Dodamani**, former Heads of the Department of Water Resources and Ocean Engineering, and **Dr. Varija K**., Head of the Department of Water Resources and Ocean Engineering, National Institute of Technology Karnataka, Surathkal for providing access to state-of-the-art facilities and resources, which were instrumental in conducting experiments and simulations central to this thesis. I am grateful to **Prof. Carlos Guedes Soares**, President, Centre for Marine Technology and Ocean Engineering (CENTEC), IST Lisbon, Portugal, for the valuable advice and suggestions on the research work.

My special thanks to Mr. Shrikanth F. Bhojgar, Ms. Sweekritha and Mr. Vishwanath Poojary, Asst. Executive Engineer and Mr. Seetharam, Department of Water Resources and Ocean Engineering for their help in all the departmental works. I would also like to thank all the non-teaching staff of the Department of Water Resources and Ocean Engineering, National Institute of Technology Karnataka, Surathkal for their co-operation and help during the project work.

I want to acknowledge my co-researcher Binoy and fellow researchers and colleagues Athul, Aparna, Hemanth and Ronit for their stimulating discussions, sharing of ideas, and collaborative efforts. Their support and camaraderie have been a constant source of motivation during this academic pursuit. I extend my heartfelt appreciation to my friends Ashwitha, Parthasarathy, Tom, Alka, Harikrishnan, Varun, Manu, Basil, Arjun, David, Namitha, Sarah,

Arun, Sharook, Vani, Aswathy, Bincy, Amalu, Manju, Neeraj, Akhil, Mansoor, Badira, Anju, Aswathy, KP, Sujay, Abhi, Dinesh, Justin, Amala, Therese, Shruthi and Tejeswani for their support, understanding, and encouragement throughout this academic journey. Their love and belief in me have been the driving force behind my determination to achieve my goals.

I am grateful to DST and MHRD for providing financial support that enabled me to pursue research and contribute to the advancement of Ocean Engineering knowledge.

My deepest gratitude goes to my parents, N.J. Jayaraj and T.V. Sujatha, whose boundless love and unwavering belief in my abilities have been the driving force behind my academic pursuits. Their constant encouragement, sacrifices, and emotional support have inspired me to persevere through challenges and aim for excellence in all my endeavours. I want to express my heartfelt thanks to my brother, Reji J.S., for his unyielding support and companionship. His willingness to lend a helping hand whenever needed has been a tremendous source of strength and relief throughout this journey.

I am deeply grateful to my loving partner, Dr Sandra A., for being my pillar of strength and my constant source of encouragement. Her unwavering belief in my potential and her patience, and understanding during the demanding periods of research have been pivotal in my ability to focus and excel in my studies. I also extend my heartfelt gratitude to all my extended family members and relatives, especially my mother-in-law, Dr Aju N V, who have shown support and encouragement throughout this journey.

In conclusion, I deeply appreciate all those who have supported me during this academic journey. Their collective impact has left an indelible mark on my academic journey, and I hope that the outcomes of this research make a meaningful contribution to the field of Ocean Engineering and Sustainable Management of ocean resources.

Above all, I thank Lord, the almighty, for his grace throughout the research work.

**RONY J. S. (197AM018)**

# ABSTRACT

The combined offshore wind and wave energy on an integrated platform is an economical solution for the offshore energy industry as they share the infrastructure and ocean space. The study presents the dynamic analysis of the Submerged Tension-Leg Platform (STLP) and Frustum Tension-Leg Platform (FTLP) combined with a heaving-type point absorber wave energy converter (WEC). The feasibility study of the hybrid concept is performed using the aero-servo-hydro-elastic simulation. The study analyses the responses of the combined system to understand the influence of the WECs on the STLP and FTLP platforms for various operating conditions of the wind turbine under regular and irregular waves. The platform responses are analysed for the North Atlantic wave region. A positive synergy is observed between the platform and the WECs, and the study focuses on the forces and moments developed at the interface of the tower and platform to understand the effect of wind energy on the turbine tower and the importance of motion amplitudes on the performance of the combined platform system. Further, the hydrodynamic performance of circular and concentric arrangements of cone-cylinder-type heaving WECs around STLP and FTLP is analysed. The influence of the hydrodynamic coefficients is analysed by determining the ratio of the hydrodynamic coefficients for a single WEC system to those for a hybrid system. The study analyses the instantaneous wave power absorbed and the wave power under the influence of PTO for the WECs arranged around the TLP floaters. The rigid body analysis observed reduced motion response for the STLP+6WECs and FTLP+8WECs configurations.

The dynamic responses of the hybrid platforms for different mooring layouts are studied for different met ocean conditions. The time history and spectrum of the generator power are analysed to observe the effect of second-order wave load and turbulent wind loads on the power production of the hybrid floater under different mooring configurations. Further, the most probable values of the motion amplitudes are calculated using long-term response analysis for the hybrid wave and wind energy system. The long-term distribution is performed using the short-term responses based on Rayleigh distribution and North Atlantic wave data. The transfer function for the long-term analysis of the floater is obtained using the numerical simulation tool FAST. The analysis is performed for zero-degree wave heading angle and different operational conditions of the wind turbine. Thereafter, the reliability of hybrid floating wind turbine platforms against extreme loads is established using the Inverse First Order Reliability Method (IFORM) which includes the randomness in the gross wind environment and the extreme response given wind conditions. The maximum values of the responses for both 1-D and 2-D models are studied and compared. The probability of the exceedance of the responses (Surge, sway, and yaw) for the platforms is studied for different return periods. The study suggests the best possible arrangement pattern for wave power absorption and power uniformity among the floaters in the array. The study performed will be helpful in the design and analysis of the combined wave and wind energy device for wave power absorption.

*Keywords: Submerged Tension-Leg Platform (STLP); Frustum Tension-Leg Platform (FTLP); Wave energy converter (WEC); Aero-servo-hydro-elastic simulation; Long-term response; Environmental Contour Method.*

# ABBREVIATIONS AND NOMENCLATURE

| | |
|---|---|
| DOF | Degree of Freedom |
| FAST | Fatigue Aerodynamic Structure Turbulence |
| FEA | Finite Element Analysis |
| FOWT | Floating offshore wind turbine |
| FPSO | Floating Production Storage and Offloading |
| HAWC2 | Horizontal Axis Wind turbine simulation Code 2nd generation |
| HOBEM | Higher-Order Boundary Element Method |
| JONSWAP | Joint North Sea Wave Project |
| NREL | National Renewable Energy Laboratory |
| OC3 | Offshore Code Comparison Collaboration |
| OWC | Oscillating Water Column |
| PTO | Power Take-Off |
| STC | Spar Torus Combination |
| STLP | Submerged Tension Leg Platform |
| TLP | Tension Leg-Platform |
| TWWC | Tension-leg platform with a heaving-type wave energy converter |
| W2P | W2Power |
| WAMIT | Wave Analysis MIT |
| WEC | Wave energy converter |
| $A$ | Added Mass |
| $A_w$ | Water Line Area |
| $B$ | Damping coefficient |
| $b_{ext}$ | external damping coefficient |
| $b_{hyd}$ | Hydrodynamic damping |
| $CoV$ | Coefficient of Variation |
| $C_L$ | Lift coefficient |
| $C_D$ | Drag coefficient |
| $c$ | Chord length |
| $\Delta r$ | Radial length of the blade section |

| | |
|---|---|
| $F_B$ | Buoyancy force |
| $F_{damp}$ | Damping force |
| $F_g$ | Gravity force |
| $F_{res}$ | Restoring Force |
| $F_{tun}$ | Tuning force |
| $F_T$ | Total tether force |
| $f_p$ | Peak frequency |
| $f_r(r)$ | Probability density function for response variance |
| $f_{H_s,T_p}(h,t)$ | Probability density function for the significant wave height |
| $g$ | Acceleration due to gravity |
| $\gamma$ | Peak enhancement factor |
| $H_s$ | Significant wave height |
| $H(\omega)$ | Transfer function |
| $h_{ij}(\tau)$ | Retardation function |
| $K$ | Impulse Function |
| $k$ | Linear spring constant |
| $L_{tether}$ | Unstretched length of the tethers |
| $m$ | Mass |
| $m_{\text{sup}}$ | Supplementary mass |
| $N$ | Number of WECs |
| $n_i$ | Unit vector normal to wetted surface |
| $P_{abs}$ | Absorbed power |
| $P_{isolated}$ | Wave power absorbed by an isolated WEC |
| $P_{Total}$ | Total wave power absorbed by the array of WECs |
| $\varphi_j$ | Velocity Potential |

| | |
|---|---|
| $Q_L(x)$ | Probability of exceeding amplitude |
| $Q_s$ | Probability of Exceedance |
| $q_{mean}$ | Mean Interaction factor |
| $R$ | Variance |
| $RAO(\omega)$ | Response amplitude operator |
| $R_d$ | Radial distance to the tether fairled |
| $R_{ij}$ | Restoring coefficient |
| $\rho_{air}$ | Air density |
| $\rho$ | Density of water |
| $S_b$ | Body Structure |
| $S_\zeta(\omega)$ | Wave Amplitude spectra |
| $S_H(\omega)$ | Input wave spectrum |
| $T_s$ | Significant wave period |
| $T_p$ | peak wave period |
| $T_0$ | Peak period |
| $T_{ps}$ | Peak spectral period |
| $\tau_{PTO}$ | PTO Torque |
| $U_w$ | Wind speed |
| $V$ | Wind Velocity |
| $V_{rel}$ | Relative velocity |
| $V(t)$ | Instantaneous submerged floater volume |
| $w(T_p)$ | Weighing factor |
| $\omega$ | Wave frequency |
| $\omega_0$ | Peak frequency |
| $\omega_{arm}$ | Rotational velocity of WEC arm |
| $X_i$ | Hydrodynamic pressure |

| | |
|---|---|
| $X$ | Displacement |
| $\dot{X}$ | Velocity |
| $\ddot{X}$ | Acceleration |
| $x$ | Wave Elevation |
| $\ddot{z}$ | Floater acceleration |
| $z_A$ | Heave Amplitude |
| $\zeta_A$ | Wave Amplitude |

# LIST OF FIGURES

# LIST OF TABLES

# TABLE OF CONTENTS

# CHAPTER 1

# GENERAL INTRODUCTION

## 1.1 PREAMBLE

The demand for clean, renewable energy resources has increased due to the limited availability of fossil fuels and increased global warming. Many researchers have devoted their studies towards the potential renewable resources like wind, wave, tidal, solar, biomass, geothermal and hydropower. Wind energy has been used for many years for generating power on land. With the maximum impregnation of wind power on land, the impact of noise, destruction of the ecological environment and radiation on residents has increased the demand to shift the wind turbines to the sea. The shift of the wind turbines towards the sea has helped reduce the impacts of visual and noise pollution. In offshore regions, the water depth rapidly increases with the distance from the land. So the cost of traditional jacket type or gravity-based foundation increases with the increase in water depth. So, the initiative has been carried out to derive wind energy from offshore wind farms having larger sea areas with steadier and stronger winds with the aid of floating offshore wind turbines (Berlo et al., 2010). The Hywind, equipped with a 2.3 MW wind turbine installed on the west coast of Norway, has been quite promising with success in its power production and has inspired the development of floating offshore wind turbines (Goupee et al., 2014).

The concept of combining a wind turbine with WECs has come into existence, allowing for a reduced cost by sharing mooring systems and electrical cables and making better use of the ocean area. In addition to the reduced cost, the combined concept also allows for increased power production. The offshore renewable energy industry is still in its initial stage of development. Still, a significant study explores hybrid renewable energy concepts such as wind-wave, wind-current, wind-solar and wind-aquamarine. The offshore hybrid concepts are very useful in reducing the overall project and logistic costs, further allowing for increased renewable energy yield per unit square kilometre of ocean space (Wang et al., 2010). Roddier et al. (2010) developed the semisubmersible WindFloat hull fitted with heave plates, which provides acceptable static and dynamic motions for the operation of large wind turbines while limiting expensive offshore installation and maintenance procedures. López et al. (2013) categorised hybrid devices based on the installed location, the principle on which they operate

and the directional characteristics of the devices. To have sufficient energy production, the best facilities are required to be provided for the wind turbine. Myhr et al. (2014) showed that, with the depletion of shallow water resources, the study on exploration and production of offshore energy is shifted towards the deep and ultra-deep water region. Karimirad et al. (2015) suggested that compared to other renewable energy resources, the resources in the ocean, such as waves and tides, wind energy and its associated technology, are considered as matured and rather well established for offshore FWTs.

### 1.1.1 Offshore Floating Wind Turbine Platforms

The increasing number of fixed-type wind turbines on land and in shallow water regions makes the requirement of space harder to fulfil. Further, as the water depth increases, the resources obtained are uneconomical. Butterfield et al. (2007) classified floating offshore platforms into three general categories based on the physical principle or strategy for achieving static stability. The study addressed that some floating platforms achieve stability by using ballast weights that hang below a central buoyancy by creating a righting moment, high inertial resistance to pitch and roll and usually enough draft to offset heave motion. On the other hand, some platforms achieve stability through mooring line tension, and some platforms achieve stability through distributed buoyancy, taking advantage of the weighted water plane area for the righting moment. Jonkman and Matha (2009) studied the three primary concepts of offshore platforms, which includes the Tension-Leg platform (TLP), Spar buoy configuration and Barge configuration.

In the case of TLP platforms, the restoring moments are provided primarily through the mooring system combined with excess buoyancy in the platform. Whereas, a deep draft combined with ballast and a shallow draft combined with water plane area is considered for the other two concepts of the spar and barge-type platforms. The power performance is greatly influenced by the selection of offshore platforms, as explained by Bagbanci et al. (2012). The floating platforms should be capable of satisfying the increasing needs for energy and securing global needs. Myhr et al. (2014) suggested that every possible site for installing offshore wind turbines depends on the wave and wind characteristics, sea bed properties and social conditions. Further, the usage of floating wind turbines at some water depth is most important due to the cost-related issues. Karimirad and Michailides (2016) briefed the issues related to the design configuration of these support structures, installation, grid connection, operation and maintenance, significantly affecting the cost of electricity production. Hence, the feasibility of

different floating concepts needs to be addressed, and innovative support structures for mature offshore wind technology need to be developed.

The disadvantage of all TLP designs is the expensive tension leg mooring system and expensive anchors needed. Matha (2010) observed that TLP has a large amount of ballast and a very high volume of the platform. The big cross-section at mean sea level also poses a significant obstacle for incident-waves and adds to drag. The long spokes are a source of failure; to build them with the necessary strength requires additional costly material and manufacturing work. Installation also is the most difficult because the design is fairly deep drafted, the tension leg anchors are difficult to install, and without adding additional ballast the design is quite unstable without a mooring system (which makes the towing-out process challenging). Chandrasakeran and Koshti (2013) suggested that TLPs may experience increased dynamic response and motion in deeper waters due to longer tether lengths and greater water depths. This could lead to higher fatigue loads on the structure and mooring system, potentially affecting the platform's structural integrity and long-term reliability. Wang et al. (2014) observed that as water depth increases, the length of the tension legs also needs to increase to maintain adequate tension and stability. This poses engineering challenges and cost implications. Beyond a certain depth, the length and weight of the tension legs become impractical, making TLPs unsuitable for ultra-deep water environments.

### 1.1.2 Offshore Wave Energy Converters

Wave energy converters (WECs) are devices that can generate electricity from ocean wave energy. There are various technologies developed to capture wave energy to generate electricity. However, these technologies are at a very early stage of development to analyse or combine but it will be useful in future commercial marketing. Compared to other renewable energy resources, the wave energy conversion concepts are large in number. WECs are classified by location, type and mode of operation (Falnes, 2007). Wave energy conversion based on location is divided into shoreline devices, nearshore devices and offshore devices. The shoreline devices are near the utility network, making them easy to maintain and repair. As the waves travel from the deepwater region towards the shoreline, the speed of waves will be reduced, resulting in less damage to the shoreline-mounted WEC devices. The devices which are located in shallow water depth regions are called nearshore devices. Devices in such locations are usually attached to the sea bed, which gives space against which the oscillating device works. The devices located in deep water regions are called offshore devices.

The main advantage of offshore devices is that wave power extraction from waves exceeds the above two types of devices. As the waves in deep water zones exhibit greater velocity, hence resulting in a higher magnitude of kinetic energy. Depending upon the orientation of devices among the waves, the WEC is broadly classified as Attenuator, Point absorber and Terminator (Beherens et al., 2012). These are WECs, and the orientation of these devices is parallel to the propagating wave direction. The point absorber WEC possesses a small dimension compared to its incident wavelength. As these devices are small, the wave direction is unimportant, and they can absorb wave energy from all directions (Ozkop and Altas, 2017). These devices are, in general, floating types moving up and down on the free surface of the ocean and absorbing the wave energy. Terminators are similar to attenuators, but the orientation of the device is kept perpendicular to the direction of the propagating wave and physically intercepts the wave to absorb the wave power (Zhang et al., 2021).

### 1.1.3 Hybrid Offshore Floating Wind Turbine Platforms

The power generation mostly comes from the wind turbine, and WEC is still auxiliary. The floating support structures have been well thought out and considered more suitable to be integrated with auxiliary devices like WEC. However, until now, for the specific hybrid design, there is no guideline for selecting floating support structures and WECs. Even for existing hybrid systems, no device performs superior to others. Some concepts for combining wind and wave are Spar-tours combination (STC), Semi-submersible with flap type WEC, TLP with heaving WEC, TLP with torus WEC and Windfloat (Roddier, 2010, Muliawan, 2012, Wan, 2015). The hybrid STC system integrates the spar-type FWT with the torus (doughnut-shaped WEC). In the STC hybrid system, the torus WEC will move up and down in the heave direction along with the Spar platform to capture energy from the incident waves, while wind turbines generate energy from the wind. So the point absorber will benefit not only from using a floating wind turbine mooring system but also from power cable for power transmission (Muliawan, 2013). TLP with heaving WEC consist of TLP combined with a heave buoy-type WEC. The TLP has a very high pretension per pontoon. Due to this, at each pontoon, a single large tendon is used (Zhou, 2016). The TLP with torus WEC combines a TLP type FWT and a heaving type WEC (TWWC) (Ren, 2020). In this concept, WEC slips along TLP to extract energy by relative heave motions through the PTO system from the incident waves, while the wind turbine produces electrical energy from the wind. The semi-submersible type wind turbine with flap-type WEC is an integrated concept that combines a semi-submersible type wind turbine and a

flap-type WEC (Lee et al., 2023). The measured responses examined included semi-submersible motions, flap-type WECs rotation, mooring line tension, internal loads of WECs arms, and the energy produced by WECs. Structural responses for the mooring lines and the tower bending moment are affected by wind load, while structural responses related to WEC are not affected by wind load.

## 1.2 MOTIVATION

In recent years there has been a significant increase in the interest in floating offshore wind turbines from the wind energy industry, governments and academia. Partially driven by the higher consumption of fossil fuels and warnings for global warming, also by the lack or complete absence of shallow waters in various countries around the globe, making fixed offshore wind turbines infeasible, different types of floating offshore wind turbines have been proposed. The most well-known of these is Hywind by Statoil, which has been operational off the coast of Norway since the end of 2009. The offshore wind industry has now achieved notable achievements in emerging offshore markets. The GWEC and IRENA have signed a UN Energy compact pledging to work together to deploy 2000 GW of offshore wind needed by 2050, which requires a huge upsurge in the annual installation of 35 GW offshore wind turbines globally (GWEC, 2023). The operating offshore wind capacity in China has reached 31.4 GW and accounts for approximately 10% of the country's wind capacity (Zhou et al., 2022). With an active development in wind energy, researchers found a new concept of combining the wind and WEC on a single platform, utilising the ocean space and the resources more effectively, thus ensuring the sustainable development of renewable resources. The first practical solution for the combined extraction of wind and wave energy is W2Power in Norway, which supports two 3.6 MW wind turbines and hydraulic pump-type WECs to produce 10 MW power. Further, studies have shown that combining wind and wave energy can make the system cost-effective with shared survey and maintenance charges, subsea cables, mooring and anchor systems, reducing the cost of produced power.

The first Offshore Wind Project of India (FOWPI) part of the "Clean Energy Cooperation with India" (CECI), funded by the European Union (EU), aims at enhancing India's capacity to improve energy efficiency by deploying an offshore wind farm near the coast of Gujarat, 25 km off Jafarabad. Recent studies by researchers have observed that the west coast of India has a maximum of 9 m/s wind speed during the monsoon season and a wave height of 0.4 to 1.0 m in deep water areas. Further, combining the WECs with the wind turbine platform might

improve the response behaviour of the floating platform, improving the wind energy absorption. Hence, the study focuses on floating-type combined wind and wave extraction platforms installed in deep waters to utilise wind and wave energy.

## 1.3 AIM AND OBJECTIVES

The proposed work focuses on the brief description of combined concepts of TLP-type floating wind turbines combined with an array of WECs. The coupled dynamic analysis of the combined floating system for a set of environmental conditions will be discussed and calculates the power absorbed by WECs for multiple body interactions. The study examines the influence of the WECs on platform behaviour. Further, the study analyses the importance of mooring lines for the hybrid floating system changing the number of mooring lines. The study will also predict the most probable values of motion amplitudes for the hybrid floating system. The following objectives are framed to achieve the proposed work:

- Coupled dynamic analysis is performed for the TLP-type floating wind turbine combined with the array of WECs.
  - ✓ Hydrodynamic and coupled dynamic analysis of the different configurations is performed to understand the responses of the system under wave load for zero-degree wave heading angle to understand the responses, platform forces and moments at the tower base and the mooring line tension under the wind and wave load for 5 MW wind turbine.
- Multibody analysis is performed for the TLP-type floating wind turbine combined with the array of WECs.
  - ✓ Multibody analysis of the combined wave and wind energy platform is performed to understand the interaction between the floating platform and the attached WECs by analysing the hydrodynamic coefficients.
  - ✓ Power absorbed by the WECs in the circular and concentric pattern is performed under regular and irregular waves for the TLP Platforms.
  - ✓ Design of PTO control is performed to improve the wave power absorption of the WECs when arranged in circular and concentric patterns.
- The numerical simulation of the TLP platforms with the different number of mooring lines is analysed. The motion responses of the hybrid system, tower base forces and moments and the tension developed on the mooring lines are discussed.

- Long-term analysis and reliability analysis using the Environmental Contour Method are performed to predict the most probable maximum values of motion amplitudes for the TLP Platforms for the North Atlantic wave data.

### 1.3.1 Scope of the Work

The offshore wind sector is rapidly developing with intense research and technological advancements to attain a low-carbon economy and sustainable development. The wind turbines have moved to deeper waters by installing three floating wind farms in the North Baltic and Iberian seas. The wave energy sector, however remains relatively immature, and there are over 1000 reported patents which show the diversity of the concepts available. Unlike the wind industry, the wave energy sector does not have a converged technology. The cost of energy from waves is still far higher than most renewable energy sources, including offshore wind. Combining offshore wind with wave energy offers a solution to many of the hurdles faced by both sectors. The symbiosis of the systems is mutually beneficial, reducing the need for separate substructures, mooring systems, power grids, logistics, maintenance, etc. The combination of suitable WECs with a wind platform has been reported to reduce the platform motions improving the hydrodynamic performance of both systems, thus increasing the overall energy yield. The waves are more predictable compared to offshore wind, and the downtime of the combined system can also be reduced, which is advantageous. The EU has funded several research programmes to develop hybrid systems like MARINA, TROPOS, POSEIDON, etc. The optimisation and implementation of hybrid systems require characterisation of the dynamics of various combination options of the available concepts. In addition, experience has shown that the sector presents unique technical challenges that must be addressed through research and development.

The present study combines a TLP-type floating platform supporting 5 MW with a point absorber-type WEC. The addition of WEC to the platform ensures a continuous supply of energy. The study analyses the motion amplitudes of the system to observe the inertia load acting on the structure. The response analysis forms the basis for the preliminary design of the combined system, as the orientation of the wind turbine is dependent on the system's motion. The influence of the wind and wave load on the system is analysed by investigating the forces and moments developed on the base of the turbine tower. Further, the tension developed on the mooring cables is examined to understand the influence of the WEC on the floating system and the structural integrity of the combined system. The study further calculates the maximum

probable value of motion amplitude to be developed on the system for the lifetime of the structure. The present work will give an insight into the power performance, structural integrity and dynamic motions of the hybrid floating wind turbine platforms under different operational conditions, which will help the designers to develop better design standards.

## 1.4 COMBINED WIND-WAVE ENERGY CONCEPTS

Sustainable utilisation of natural marine resources, together with the need for reduction in the cost of the energy derived, enhances the need to combine the exploitation of offshore wind and wave energy. The researchers have shown two main groups of synergies between the wind and wave energy technologies, namely the legislative synergies and the technological synergies (Pérez-Collazo et al., 2015). The synergies define the advantages of combining both offshore wind and wave energy. The individual cost of WECs and floating offshore wind turbines are also very high. So, to reduce the initial investment and maintenance cost, there is a need for a hybrid concept. As wind and waves are closely related to the ocean, the hybrid concept for extracting offshore renewable energy will be beneficial.

### 1.4.1 Rigid Body Analysis of Hybrid Wind-Wave Concepts

There are a lot of scopes in exploring the hybrid concepts of renewable energy, such as wind-wave, wind-current, wind-solar, and wind-aquamarine. Hence, utilising the offshore hybrid concepts to extract offshore energy is very useful to reduce the overall project cost and logistics cost, increasing the renewable energy yield per unit square kilometre of ocean space. Bachynski and Moan (2012) studied the dynamic responses of a single-column TLP supporting a 5 MW wind turbine. The floating platform is integrated with three-point absorber WECs in the time domain using Simo-Riflex-Aerodyn. Muliawan et al. (2012) studied the spar torus combination (STC) and concluded that STC produces 6% higher power than a spar-type FWT. It can increase up to 15% more than spar-type FWT when combined with the WEC. Further, Muliawan et al. (2013) observed that the torus WEC is subjected to severe loads in case of extreme conditions. Three survival modes are proposed for the STC, and two modes are numerically simulated to estimate forces on the structure and its motion. Jeon et al. (2013) showed that the dynamic response of a spar-type offshore wind turbine to wind and wave excitations is usually evaluated in terms of the rigid body degrees of freedom of the floating substructure. Naess and Moan (2013) established a hybrid frequency and time domain model to predict the dynamic responses of STC. The STC consists of a spar-floater with a permanent

ballast, a doughnut-shaped torus ballasted with water, a WEC Power Take-Off system (PTO), a wind turbine, a bearing system, end stops, and three main mooring lines. Bachynski and Moan (2013) investigated the heave-type point absorber WEC combined with a TLP. The effect of WEC on the wind turbine PTO is studied, and the platform motions are discussed. Several benefits, such as reduced surge and pitch motions, minimal tendon tension, and reduced bending moment, are observed when compared to TLP-type wind turbines. Boo et al. (2016) discussed the design challenges of the combined platform utilising multiple energy. The study presents the motion response analysis, power cable analysis, mooring analysis and structural analysis of the hybrid system. The comparative study between numerical motion responses and experimental data is performed to validate the numerical model. Gao et al. (2016) compared two combined concepts of wind and wave energy converters. Numerical analysis of the Spar torus combination and semi-submersible flap combination indicates that the SIMO-RIFLEX-AeroDyn numerical model can predict responses very well. Crudu et al. (2016) evaluated the forces in the mooring lines for a moored offshore structure to analyse the mooring forces acting on the structure and also to predict the motions of the floating offshore structure under different environmental conditions. The analysis of the moored structure and the dynamic behaviour of the mooring chain is considered for five different scales.

Further, Chen et al. (2016) established a W2P of single row wind-wave power plant layout method with one large floating platform, one wind turbine generator, 3-DOF mechanism hemispherical shaped oscillating body along with the accumulators, hydraulic motors and the electrical generators to extract both wind and wave power effectively. The wind turbines are designed with retractable blades to capture maximum wind energy with minimum wind load on the wind turbine by adjusting the diameter of the turbine and the velocity. The power performance of the WECs was tested by calculating the q-factor to understand the wave effect on the WEC device. Pan et al. (2016) numerically modelled the responses of mooring lines for large floating structures. The study considered a water depth of 100m and used the Deep-C module of SESAM to forecast the motions on large platforms with the impact of mooring systems. The study proved that the responses are sensitive to the length of the mooring line, and the dynamic responses of the platform are observed to increase with the decrease in the responses of the mooring system. Karimirad and Koushan (2016) performed feasibility studies for operational conditions of a combined spar-type floating offshore wind turbine with a WEC using numerical simulations. The power production and motion responses are investigated for PTO systems of wave energy devices and wind turbines showed a positive synergy for hybrid

systems. Zhou et al. (2017) presented a novel concept by combining a TLP and heaving-type wave energy converter (TWWC). Time domain simulations were performed to understand the feasibility of the system. Hydrodynamic analysis was conducted using AQWA code, where multibody modelling, including the hydrodynamic and mechanical coupling between the TLP and WEC is evaluated. The study investigated the effect of wave period and different power take of systems on the performance of the proposed system carrying an NREL 5 MW wind turbine. Tabeshpour et al. (2018) investigated the influence of the TLP's damaged tendon state on tendon tensions and behaviour in the range of wave frequencies. The equilibrium of TLP is examined, and its stiffness matrix is generated under conditions of tendon injury using the boundary element method to calculate wave loads and hydrodynamic coefficients. The study demonstrated that, despite having a relatively minor impact on response amplitude magnification, the condition of damaged tendons significantly affects the tension of tendons that are close to failing.

A simulation model is developed by Yang et al. (2020) to calculate the motion responses and forces of WEC to ensure the reliability and long-term performance of a floating-point absorber WEC moored using a three-legged mooring system. The study is performed for the 1:20 scale model to validate the numerical model in the deepwater basin. The study also observed the axial force developed at the top of the mooring system. Le et al. (2020) studied a submerged FOWT for an intermediate water depth. The coupled dynamic response of the FOWT under different mooring conditions is analysed using a numerical aero-servo-hydro-elastic-mooring tool for irregular wave environments. The study observed the significance of tether length on the motion responses of the surge, heave, pitch and yaw. Zhang et al. (2020) conducted the hydrodynamic analysis of V-shaped semi-submersible, braceless semi-submersible and OC4-DeepCwind semi-submersible supporting 5 MW reference wind turbine. The hydrodynamic responses of the platform for two different water depths are observed to influence the second-order wave loads on the platform motions and mooring tensions using the Newmans approximation and Quadratic transfer function. Wan et al. (2020) studied three integrated concepts of column-type wind turbines and heaving wave energy converters (WEC) for deep, shallow, and intermediate water conditions. Spar-type wind turbines with long and short floaters are proposed for deep and intermediate water depth conditions. The study analysed and compared the dynamic motion responses, forces, and moments for the three different configurations and observed the significant influence of environmental conditions on the responses of the hybrid system. Jin et al. (2020) developed a full-time 2-D numerical model

for the coupled dynamic response analysis of tension-leg submerged floating tunnel structures. The equation of motion of the hull and the dynamic equations of the mooring lines is solved simultaneously to determine the tension on the mooring lines and the influence of viscous damping and mooring stiffness on first and second-order motion responses.

The semi-submersible platform consisting of four different mooring arrangements is modelled by Tabeshpour and Abbasian (2021). The impact of the failure on the platform responses is examined after one of the four mooring lines is damaged during the storm. The six degrees of freedom responses are compared, and the ideal mooring configuration is selected to minimise structural vibrations following the mooring failure. Gaspar et al. (2021) proposed a hybrid floating concept combining a wind turbine with WECs. The study is performed on the synergies for utilising the WECs to assist the platform water ballast system in compensation for variations of five different sea state conditions. The study concluded that the WECs on the downwind and upwind sides of the platform have different roles in the dynamics of the floating system. Zhao et al. (2021) analysed the intact stability of a semi-submersible floating platform supporting a 10 MW wind turbine using the aero-servo-hydro-elastic simulation. The study examined the dynamic responses of the floating platform under different operational and fault conditions of the wind turbine. The study also observed the effect of mooring line damping on the dynamic behaviour of the floating system. Li and Liu (2021) illustrated the effect of wave directionality on the dynamic response of an offshore floating wind turbine. The study observed the longitudinal response, tower base fore-aft bending moment and mooring line tension force developed under the short-crested wave.

The damage diagnosis problem of damage detection, identification of damaged tendons and quantification of precise damage is studied by Sakaris et al. (2021) under various operating conditions for a 10 MW multibody FOWT supported on a platform having two rigid bodies supported by 12 tendons. Dynamic responses of the WT under different damage states are obtained based on the stimulated FOWT. Niranjan et al. (2022) carried out the ultimate load analysis and coupled dynamic analysis for a 15 MW wind turbine mounted on UMaine VolturnUS-S semi-submersible floating platform. Time-domain coupled dynamic simulation uses OpenFAST to determine the power production under parked and fault conditions. The study presented the mean, minimum and maximum values of characteristic loads and platform motions for different environmental conditions. Further, the impact of yaw misalignment, wind-wave misalignment, and wave forces on the dynamic motions of the floating system is

discussed. Amaechi et al. (2022) studied the mooring dynamics, mooring line tensions, and the global performance of a paired semi-submersible column using a dynamic coupled approach. The numerical simulation tool ANSYS-AQWA and Orcaflex is used for the hydrodynamic study to observe the behaviour of mooring lines. The study followed the importance of the mooring line tension and the increase in mooring line tension when the cables are damaged. Hu et al. (2022) integrated a 10 MW wind turbine on a fully submerged TLP and studied the dynamic responses of the floating system. The study concluded the closeness of results obtained from the potential flow theory and the Morrison equation with tuned added mass coefficient.

### 1.4.2 Coupled Dynamic Analysis using FAST

Coupled and uncoupled modelling approaches are used to study FOWTs, though the actual system exhibits highly coupled physical behaviour. The most studied coupled model for the floating structure includes the FAST (Fatigue, Aerodynamics, Structures, and Turbulence) code developed by NREL, now named openFAST. Ramachandran et al. (2013) examined the consistency between the RAOs computed using WAMIT, a linear frequency domain tool, to RAOs derived using FAST code, a nonlinear aero-servo-hydro-elastic tool. The study is further extended to examine the changes in RAOs for flexible and operational wind turbine conditions. The result showed that the RAOs computed from FAST and WAMIT are similar for the rigid turbine configuration subjected to only waves. Coulling et al. (2013) validated the FAST model using a DeepCwind semi-submersible platform supporting a 5 MW wind turbine. Experiment investigation of the dynamic responses of the system under combined wind and wave loading was conducted on a 1:50 scale model in the MARIN'soffshore basin. The DeepCwind semi-submersible FWT's coupled aero-hydro-elastic response performed as estimated in the validation study, according to FAST. Karimi et al. (2017) present a frequency domain approach for the numerical analysis of coupled wind turbines, floating platforms and mooring systems. FAST and WAMIT are used to generate frequency domain aerodynamic and hydrodynamic characteristics for OC3 hywind spar, TLP and OC4 DeepCwind floaters. Han et al. (2017) proposed the concept of a STLP for the offshore wind turbine. The platform is self-stable during the transportation phase due to the large water plane area and is stable during the operation phase due to the submergence. The stability during the transportation and installation phase is studied and observed to have safe wet towing during the transportation phase. The dynamic response study was conducted to analyse the effect of second-order wave loads, water depths

and wind wave misalignment. The analysis showed that the effect of second-order wave loads on the dynamics of STLP is slightly higher in the parked conditions than that in the normal operation condition.The platform stability during the operation phase is observed to depend on the surge, sway, roll and pitch motions. Oguz et al. (2018) examined the Iberdrola TLP wind turbine concept, TLPWIND, experimentally and numerically under real-world wind and wave conditions. The free oscillation, tests in regular and irregular waves, and simulations of wind conditions were all examined numerically using the simulation tool FAST. Comparing the results of physical and numerical simulations shows that, while in some cases, the numerical predictions made by FAST were extremely near to the results of the experiments, in another case, the numerical model could not effectively anticipate the platform response.

The dynamic responses of the spar platform is analysed by Wang et al. (2018) under different wind and wave conditions using fully coupled FAST code, and the results were validated using the model test. Minor discrepancies are observed as the FAST code underestimates the impact of low frequency on the heave and mooring tension. The study concluded that the wind and current induce low-frequency average responses though wave induces the fluctuation range of responses. Yang et al. (2021) investigated the dynamic response of a 10MW offshore wind turbine supported by a multibody floating platform consisting of a cylindrical platform supported by six tendons to observe the different tendon breakage scenarios. Numerical simulation tool F2A based on AQWA and FAST is used to perform coupled analysis of FOWT. The study observed the influence of platform response on the health of tendons. Guo et al. (2022) conducted the dynamic response analysis for the IEA 10-MW Spar Floating Offshore platform supporting a 10-MW reference wind turbine. The numerical simulation FAST tool builds a nonlinear aero-hydro-servo-elastic numerical model. The study examines the natural periods by free-decay experiments. Further, the wind turbine's accuracy and controller's sensitivity are studied. The platform's natural periods in its six degrees of freedom are within the permitted range. Zhang et al. (2023) conducted the dynamic response analysis of a hybrid semi-submersible floating wind turbine and two types of WECs DBSC (DeepCwind-Wavebob-Wavestar Combination) system. The study examines the dynamic responses, power generation and pitch performance of the hybrid systems using the simulation tool FAST and AQWA.

### 1.4.3 Multibody Analysis of Hybrid Wind-Wave Concepts

Hydrodynamic study of multiple bodies is generally carried out for a WEC farm and for an array of WECs combined with the floating platform to analyse the responses of each system

under the action of waves. The study is essential to understand the influence of one device on other devices, further investigating the overall performance of the array. Child and Venugopal (2010) studied the optimal configurations of wave energy device arrays using parabolic intersection and a genetic algorithm. Hydrodynamic interactions occurring in an array of WECs are determined considering radiation and scattering from the WEC devices moving independently incorporating energy extraction. Sinha et al. (2015) studied the power absorption of different arrangements of point absorbers. Three different shaped floaters are considered to study the effect of change of shape in power absorption, and WAMIT (Lee et al., 1995) is used for the analysis of hydrodynamic forces and coefficients. Konispoliatis and Mavrakos (2016) performed the hydrodynamic analysis of an array of interacting free oscillating water column (OWC) devices exposed to finite water depths and regular surface waves. The interaction phenomenon with neighbouring bodies is observed, and the added mass, damping coefficient, air flow rate, and wave power efficiency for each device are evaluated. Zheng and Zhang (2018) performed a theoretical study of a hybrid wave energy system consisting of oscillating water columns and several oscillating floats hinged around the device. The hydrodynamic analysis is performed to assess the dynamic response and power absorption of a hybrid WEC in the frequency domain.

A simulation model of floating WECs to calculate the responses, forces and moments, and mooring forces are developed by Yang et al. (2020). The study examined the reliability and long-term performance of floating WECs. A 1:20 scaled model is tested in the deepwater offshore basin to compare the numerically simulated coupled hydrodynamic responses. Ren et al. (2020) studied a novel concept combining a TLP type FOWT and a heaving type wave energy converter termed TWWC. The study analysed the dynamic responses of the combined system numerically in time-domain and by using a 1:50 scaled model under operational conditions of the 5MW reference wind turbine. The hydrodynamic numerical code AQWA is used to model the mechanical and hydrodynamic coupling of the TLP and the WEC. Kamarlouei et al. (2020) experimentally studied the responses of the floating platform with WECs arranged in circular and concentric patterns. The heave and pitch response of the floating platform is observed to reduce with the addition of WECs. Different floater shapes are studied and better hydrodynamic performance is observed for the cone-cylinder-shaped WEC, where minimum variation in average power absorption is noted. Howey et al. (2021) experimentally examined the power production performance of different configurations of a five-device array of IST spar-buoy OWC WECs in a wave basin. The study compared the performance of a

single isolated WEC, an array of independently moored WECs and three arrays with interbody connections, with mooring arranged at different levels. The power performance is observed to be better for the array of WECs with interconnected moorings, though the mooring load was on the higher side. Silva et al. (2022) examined the motion suppression characteristics and wave power absorption of hybrid floating platforms. A semisubmersible floater with three-point absorbers in the floating and submerged conditions under turbulent wind and wave loads is used to observe the dynamic non-linear characteristics of the hybrid system. Kamarlouei et al. (2022) proposed an axisymmetric concentric two-body WEC by combining a torus-shaped WEC with a floater whose energy extraction is through the relative heave motion. The study analysed the hydrodynamic properties of the system in the frequency domain, and further, a coupled hydrodynamic model was developed in the hybrid time-frequency domain. The optimization maximises the pressure and power in the hydraulic power take-off system while considering the hydrodynamic efficiency of various torus forms.

The power take-off (PTO) system is one of the components of WEC with significant room for optimization, and many researchers are working to create and improve power absorption through the PTO system. Wave power extraction uses different wave energy conversion systems based on working principles (Mayrakos, 1991). Kofoed et al. (2006) documented the prototype testing of Wave Dragon placed at Nissum Bredning, Denmark. The prototype efficiency in terms of power production and stability is examined. Drew et al. (2009) identified the possible power take-off systems and considered control strategies to increase the efficiency of point absorber WECs. Hals et al. (2011) discussed the comparison strategies to control WECs. The comparative study is performed for the absorbed energy, reactive energy flow, peak-to-average power ratios, and the complexity of execution. Cho et al. (2012) suggested a PTO through an inner dynamic system inside a floating buoy. The study investigated the optimal condition of the dynamic system for maximum PTO and observed that maximum power could be derived at optimal spring and damper conditions. The study suggested that the bandwidth of high-performance regions need not be higher at the maximum PTO condition. Luan et al. (2014) explored the possibility of combining the wind and wave energy on the semi-submersible platform and presented the concept of combining 5 MW semi-submersible wind turbines and three rotating flap-type WECs. Numerical simulation is conducted using the time domain simulation model Simo/Riflex/Aerodyn. The system is made nonlinear with the introduction of PTO system. The study observed that the selection of PTO and the mass of the WECs have a significant effect on power generation. Lee et al. (2016) simulated the one-way

coupled dynamics of offshore floating platforms with WECs. The study concentrated on the PTO damping of static WECs on the platform and concluded that the WECs might develop significant damping of the platform motions in heave, roll and pitch. Negahdari et al. (2018) developed a two-body wave power transformer by incorporating the effect of hydraulic PTO parameters. Experimental studies on the motion properties of the WEC are performed by Kim et al. (2019). The study analysed the rotation, speed, and acceleration of the wave energy system. Si et al. (2021) proposed a combined floating wind and WECs by integrating a semi-submersible floating platform and three-point absorber WECs. The study also observed the dynamics of different power take off (PTO) control strategies which showed considerable influence on the motions of the combined system. Chandrasekaran and Sricharan (2021) performed the numerical analysis of a new, bean-shaped, multibody floating wave energy converter (BFWEC) using WEC-Sim. Multiple bodies produce more power due to the increased net excitation force. The novel device extracted a more significant excitation force, which better radiates capabilities. Ghafari et al. (2021) investigated the effect of Wavestar WECs on the wave power production and the platform motions of an OC3- Hywind spar platform. The study observed increased surge, heave and pitch RAO for the floating platform under regular waves of 1.2 m height and wave period varying from 4 s to 16 s.

A numerical model of WEC using the open-source CFD platform, OpenFOAM, is developed by Katsidoniotaki et al. (2022) to study the wave interaction of the Humboldt Bay site in California. The study used the overset method to evaluate the body motions and compared them with the morphing method. The study observed the importance of wave steepness that tends to develop wave loads on the WEC. Further, Katsidoniotaki et al. (2022) assessed the viability of a point-absorber WEC using CFD models for a chosen site in the North Sea. The extreme waves are modelled by focused wave groups, and the analytical breaking criterion shows that the numerical breaking waves precisely estimate the breaking state. Windt et al. (2022) examined the significance of high-fidelity numerical modelling of WECs under controlled conditions using two separate test scenarios for two different WECs. The study observed that high-fidelity hydrodynamic models must be used to evaluate the performance of the aggressive energy maximum control (EMCS) for WEC control, which pushes the system further away from the assumptions in the linear hydrodynamic model. Sun and Zhang (2022) investigated the optimal parameter and the performance of an inverter-based point absorber WEC. The analytical expression for the optimal parameters is derived for regular wave conditions, and further performance under irregular waves is conducted for optimised

parameters with constraints on system modal frequencies. Amini et al. (2022) observed that adjusting PTO parameters is a difficult optimization challenge as there is a complex and nonlinear relationship between various parameters of the PTO systems used for the WEC and the absorbed power output. The study seeks to improve the PTO system parameters of a point absorber WEC using several optimisation approaches to analyse the optimal parameters by solving non-linear problems. Liu et al. (2022) discussed a novel discrete control strategy to improve the power-capture performance of WECs with a hydraulic PTO system. A high-pressure gas accumulator or a low-pressure gas accumulator can be actively and independently connected to each chamber of hydraulic cylinders using this unique discrete control technique, which introduces separate switching valves. The switching action of the switching valves is controlled, which boosts the PTO system's flexibility and improves its controllability.

### 1.4.4 Long-Term Analysis of Hybrid Floating Wind-Wave Concepts

In order to have sufficient energy production, the best facilities should be provided for the wind turbine. The performance is greatly influenced by the selection of offshore floaters. Hence, the assessment of the performance of the floater is an important phenomenon for the design of the floater. Prediction of the most probable maximum values of accelerations, displacements or relative motions which are likely to occur during the lifetime of the floater is necessary to have reference values for design targets. The long-term formulation for predicting the wave-induced response of offshore floating structures was initially proposed by Fukuda (1967) and further adopted and developed by Guedes Soares and Moan (1991). The study observed the importance of the long-term probability distribution of wave-induced load effects on the design of fatigue loads on ships by studying the long-term distribution of the wave-induced wave-bending moments in ships. Guedes Soares (1993) further explained the importance of considering the non-linearity of wave-induced load effects in long-term predictions. The study observed that the long-term prediction of nonlinear wave-induced vertical bending moments depends on ship characteristics. Guedes Soares et al. (2004) developed a long-term linear prediction method that generates from summing the short-range distribution of the maximum estimated probability of occurrence is used to predict the vertical bending moments during the operating life of the Floating Production Storage and Offloading (FPSO) acted upon by abnormal waves. Saha et al. (2014) investigated the long-term extreme responses of the spar-torus type system. The investigation considers the largest peak values that follow the Gumbel distribution in short-term cases. The estimation of a 50-year extreme response is conducted based on a simplified

contour line method. Karmakar et al. (2016) discussed the inverse reliability technique to predict the extreme loads on the offshore floating wind turbine. The study estimates long-term joint probability distribution of the extreme loads using the environmental contour method for spar and semi-submersible floating wind turbines holding 5 MW wind turbines. The study observed that the out-of-plane bending moment at the blade root and tower base of the wind turbine is less for the spar-type floating wind turbine platform. Wandji et al. (2016) developed a semi-floater concept of a floating offshore wind turbine support structure for installation under moderate water depth. The reliability analysis and fatigue load calculations are performed to ensure the desired life expectancy of the structure. Low and Huang (2017) studied the long-term extreme response analysis of offshore structures considering all possible sea states, where each sea state involves a stochastic dynamic analysis. The environmental contour lines approach appeared as a practical method for drawing the extreme responses of the floating system.

A reliability assessment framework by combining finite element analysis (FEA) modelling, is developed by Kolios et al. (2018) to analyse the response surface modelling and reliability assessment for point absorber WEC. The study developed an analytical model to analyse the wave load and validate the FEA model. The study observed that the floater is prone to fatigue failure during the nominal service life. Li et al. (2018) compared different methods to forecast the long-term extreme responses of semi-submersible platforms combined with flap-type wave energy devices. Numerical as well as experimental studies are carried out for the integrated concept. In adverse conditions, the wind and wave power converters are converted in a safety mode that minimizes dynamic forces and motions. Different methods for predicting the long-term responses considering the wind and wave conditions at two European sites are carried out. Further, the structural response quantities are analysed and compared. The response quantities analysed are the axial forces and bending moments of the semisubmersible wind energy and flap-type WEC, including those of the wind turbine, arms of the flap-type WECs and mooring lines, also the six degrees of freedom platform motions. The study shows that the environmental contour method gives an under-prediction of the long-term extreme responses of quantities related to the wind turbine. Vijay et al. (2018) investigated the long-term response analysis of various configurations of TLP-type offshore wind turbines. The long-term distribution is obtained for the transfer functions. Preliminary analysis of the performance of wave-induced response of floaters is performed using long-term analysis. The long-term analysis is also performed for the vertical motions along with tower base bending moments to

ensure safety against overturning in high waves and wind speed. Xu et al. (2020) analysed the extreme responses of a semi-submersible platform using efficient Monte Carlo computational simulations. The study adopts averaged conditional exceedance rate (ACER) method for the efficient use of measured data.

### 1.4.5 Reliability Analysis using Environmental Contour Method

Extreme responses of offshore wind turbines are of major importance, and efforts are made to design the structure so that it can withstand such extreme conditions of loading during its service life. Using probabilistic design approaches for obtaining extreme limit states is a method that has been used by researchers over time but involves a considerable number of simulations of wind turbines. Long-term extreme response for any offshore structure needs to be estimated for a given return period. Offshore structures use this design methodology, of which the full long-term analysis yields correct results but is very time-consuming and tedious. For the structural analysis and design, the probabilistic approach is beneficial by using only limited environmental conditions to ensure sufficient capacity. The Inverse First Order Reliability Method (IFORM) is suggested by Winterstein et al. (1993), which involves finding contours of environmental parameters that are independent of the structure with the variables decoupled with the response. Extreme sea states can be determined by this method, and IFORM is introduced over the FORM method, which proves to be beneficial. Winterstein (1998) presented the reliability-based prediction of design loads and responses for floating structures, including the Tension-Leg-platform and Spar buoy, which can be an alternative to the full long-term analysis. The environmental contour method is used by Christensen and Arnbjerg-Nielsen (2000) to obtain the design shear force and overturning moment at the seabed for an active stall-regulated wind turbine at two sites. Fitzwater et al. (2003) presented the background of the development of the EC applied to wind energy systems. The theory is applied to develop contours based on design code descriptions of environmental conditions or measured data for a site-specific application. The study observed that the ECM provides reasonable estimates of the expected extreme load compared with the full integration method. Saranyasoontorn and Manuel (2004, 2005) demonstrated how the environmental contour method could be applied to establish ultimate wind turbine blade bending design loads for various wind turbines. The values thus obtained are compared with the solution by full integration over the failure domain, and its accuracy is tested. A full random characterisation of both wind conditions and short-term maximum response, given the wind conditions, will yield extreme design loads that might

be approximated reasonably well by models that include the randomness in the wind environment. Alternative modelling assumptions for randomness in the gross environment and in the extreme response given wind conditions to establish nominal design loads are studied. The study examined the accuracy of the derived design loads by comparing full integration over the random variables and by accurately describing the failure domain.

The reliability analysis of DeepCWind semi-submersible offshore floating wind turbine using 1-D model and 2-D model for 10-min mean wind speed is discussed in Karmakar et al. (2014). The out-of-the-plane bending moment loads at the blade root and tower base moment loads for the DeepCwind FWT was analysed. The inverse reliability techniques are used to estimate the joint wind and wave design loads for the wind turbine. Karmakar et al. (2015) compared the design loads of the floating wind turbine for I-D, 2-D and 3-D environmental contour methods by performing reliability analysis on spar-type, DeepCWind and WindFloat semi-submersible floater. The estimation of the long-term joint probability distribution of extreme loads for different types of offshore floating wind turbines is studied using the environmental contour (EC) method. The out-of-plane bending moment loads at the blade root and tower base moment loads for the offshore floating wind turbine of different floater configuration like spar-type, DeepCWind and WindFloat semi-submersible floater is presented. The dynamic behaviour of a coupled platform turbine system and the statistics of tower and rotor loads and platform motions is studied by Sultania et al. (2018) using time domain analysis. The 2-D and 3-D IFORM method is used considering wind speed and wave height for the environmental parameters for extreme loading. This helps understand the comparison of the different methods used and their accuracy. The environmental contour method is used to obtain the extreme responses under certain misalignment conditions adopted, and the uncertainties in response are studied by correcting the two-dimensional EC method. Further, different mooring patterns are studied to know the characteristics under different aligned wind-wave conditions and the structural properties.

The short-term response of an integrated system using the EC method is obtained by Liu et al. (2019), and the long-term response is extrapolated based on these loads. The 3D approach is used considering the uncertainties and is noted to give more accurate long-term analysis responses. Raed et al. (2019) obtained the 1D and 2D environmental contours for employing the inverse first-order reliability method to derive the extreme responses on a semi-submersible floating wind turbine. The environmental random variables, significant wave height and peak period, are used to estimate the contour. The results thus obtained by 1D and 2D environmental

contour methods are compared by performing a full long-term analysis. This study gives a broader view and comparison of the full long-term analysis compared to the approximate methods used. Recently, Konispoliatis et al. (2021) studied a multi-purpose floating TLP concept suitable for the combined offshore wind and wave energy resources exploitation, considering the prevailing environmental conditions. The environmental contours are developed by computing the joint distribution of environmental parameters using the statistical characteristics of wind and wave time series at the examined location. Zhao et al. (2022) studied extreme tension developed on the mooring cables of semi-submersible platforms using the Environmental Contour (EC) method. In addition to the traditional EC method, the study considered the short-term uncertainties and developed a parametric model based on numerical simulations combined with a linear interpolation technique.

### 1.4.6 Physical Model Studies of Offshore Floating Wind-Wave Platforms

Model tests under controlled environmental conditions in laboratories are important steps to study the dynamic behaviour of offshore wind turbines and WECs. In recent years, significant model tests have been conducted for floating wind turbines with different types of floaters. The hydrodynamic responses of the Spar-Torus combination are analysed by Wan et al. (2015) using both numerical and experimental studies. The numerical study observed a positive synergy with the combination of spar with torus wave energy converter though it was challenging to maintain structural integrity between the platform and the WEC. The study is performed for a 1:50 scale model for two survival modes, torus locked to spar and kept at mean water level (MWL) and torus locked to spar and submerged below MWL. The model test analysed the six degrees of freedom (DOF) motions, mooring line tension and force between spar and torus for three directions and compared them with the numerical simulations. The test was conducted under regular wave conditions, irregular wave conditions and also with combined wind and wave conditions to understand the importance of wind wave misalignment for the motions of the platform. Perez-Collazo et al. (2018) conducted an experimental study to define a simplified version of the WEC-sub-system hybrid converter. The hydrodynamic response of the 1:37.5 scaled model is studied for both regular and irregular waves. The responses are characterised by incident and reflected waves through RAOs of the free surface elevation to understand the influence of incident waves on the device response. The point absorbers are WECs with dimensions smaller than the wavelength and are capable of deriving energy from the wavefront much greater than the physical dimensions of the device. Zabihi et

al. (2019) studied a 1:15 scaled fixed offshore OWC model in a large towing tank to observe the effect of wave spectrum shape on the efficiency of the model. The study examines how geometric and hydrodynamic parameters affect the effectiveness of the OWC device and identifies novel locations where nonlinear interaction, or sloshing, takes place inside the chamber. The type of incident wave spectrum was observed to have an impact on the form of the spectrum inside the chamber, particularly for long waves. Further, for longer incident wave periods, the Pierson-Moskowitz spectrum led to higher device efficiency compared to the JONSWAP spectrum.

The dynamic responses of the TLP structure is studied by Riefolo et al. (2019) using experimental investigation. The structure was modelled using Froude's scale to test the structure under regular waves for steady wind. Free vibration and hammer test was conducted to study the natural frequency of the system. Further, displacements, rotations and the forces developed at the mooring lines were investigated for rated and parked condition of the wind turbine. The study observed that the responses for the parked conditions are higher compared to the operation condition due to the aerodynamic effect of the turbine. The responses of the combined system of TLP and a series of buoys around the structure together named SerBouys-TLP are analysed by Ma et al. (2019). Numerical and experimental studies are conducted to investigate the motion amplitudes of the system. The numerical simulations are conducted using a time domain simulation (DUTMST) based on MATLAB. The model test was conducted on wave flume for a 1:50 scaled model, and the scaling down was done using Froude's law. The study observed that the addition of buoys on the TLP significantly reduces the horizontal motions of the system. Further, the responses of the combined system are investigated for different wave factors and buoy parameters.

The performance of a semi-submersible platform combined with WECs is experimentally analysed by Sarmiento et al. (2019). The global responses and the performance of the OWC WEC are studied using the wave tank test. The model was subject to regular waves under wind and no wind conditions for survival and operational conditions of the wind turbine. The dynamic response of a moored floating oscillating water column under realistic wave states is experimentally investigated by Singh et al. (2020). The experimental setup was modelled with wave trains developed using a piston-type wave maker. Global response motions, dynamic tendon response, wave elevation, and air chamber pressure were measured using the experimental setup. The study observed to have stiff heave and pitch motion and significant

surge motions. Ruehl et al. (2020) analysed the 1:33 scaled model of the floating oscillating wave surge converter (FOSWEC). The WEC system was tested for a different range of conditions like static offset, forced oscillation, free decay, wave excitation and the responses for four different configurations of the converter system. The numerical simulations are conducted using open-source WEC-sim code, and the simulation results are validated using experimental data. Kim and Shin (2020) examined a 750 kW semi-submersible FOWT model numerically and with experimental data set to understand the stability and motion performance of the system. The dynamic response simulation was conducted using FAST, developed by NREL, to validate the experimental study under regular and irregular waves with the rotation effect of the blades of the turbine. The comparison of result showed that the model tests agreed with the numerical study for the regular wave condition. Ren et al. (2020) studied a novel combined concept of TLP with heaving WEC. Coupled dynamic responses of the combined system was analysed numerically using the simulation tool AQWA and was experimentally validated using 1:50 scale model. Two non-linear air dampers were used to simulate the PTOs and a rotating wind turbine was used to develop the mean thrust effect. Zhou et al. (2021) conducted a numerical and experimental study on semi-submersible FWT. The study compared the dynamic responses developed by both the structures mounting 5MW wind turbines as well as the tower base loads and nacelle acceleration for the two structures.

## 1.5 CRITICAL REVIEW AND RESEARCH GAP

Sustainable offshore wind and ocean development requires efficient use of natural resources, which could optimise their exploitation. The challenge thus arises for both the wind and wave industries that incentive the integration of wind and wave energy converters. The exploitation of the combined wave and wind energy device is a very recent research topic with a limited number of studies on the combination of wave and offshore wind energy focussing mainly on the combined electricity production, proposing new alternatives to combine the exploitation of wave-wind energies. Most of the work on the combined wind and wave energy concepts is performed by EU-funded projects trying to enhance industrial and scientific collaboration to develop sustainable energy. As a result, many concepts of combined exploration of wind and wave energy were explained. The present literature study highlighted the concept of hybrid platforms for exploring wind and wave energy resources.

The researchers showed the importance of response analysis of the hybrid platform to compute the load developing onto the combined system for the preliminary design of the platform. The

researchers have developed different numerical simulation tools in both the time and frequency domains for the response analysis of the combined concept of wind and wave energy. The researchers have also highlighted the importance of hybrid frequency and time domain simulations for global response analysis. The researchers examined the performance of point absorbers in capturing the wave energy for the heaving point absorbers combined with a floating wind turbine platform. The researchers showed the importance of site selection for the substantial availability of wind and waves. The system must be designed in the ultimate limit state based on load effects corresponding to 50-year wind and wave conditions. Hence extreme response analysis of the offshore structures was performed with full long-term analysis using short-term responses for all environmental conditions. Further extreme responses are also analysed using the contour surface method when two environmental variables are present. Different floating hybrid concepts, namely spar-torus combination (combining spar platform with torus-shaped heaving WEC), semi-submersible flap combination (providing three rotating flaps at three pontoons), oscillating water column array with a wind turbine, W2Power, Wind wave Float and Poseidon floating plant is studied intensively by previous researchers.

With limited research on the combined wind and WEC concept, the hybrid platform of wind and wave energy converter is a less exploited area. Most of the hybrid concepts are based on the combination of a spar platform with WECs and also on the semi-submersible platform with additional attachments for extraction of wave energy. The studies are limited to the combined concept of a TLP with WECs. Further, the TLP being stabilised by tensioned tendons, the addition of WECs will develop only minimum variation of the responses of the system but can improve the power production, also ensuring a continuous supply of energy. Hence, point absorber-type heaving WECs can be attached to a TLP-type floating platform supporting a 5 MW wind turbine for smooth conversion of wind and wave energy. The present study numerically analyses a Submerged Tension Leg Platform (STLP) integrated with cone-cylinder-shaped WECs. The researchers observed better stability for the STLP floating system in both the transportation phase and the installation phase. Further, the cone-cylinder-shaped WECs in the array were observed to have maximum energy extraction. The study further models a new concept of the Frustum Tension Leg Platform (FTLP) system and examines the performance of the system under different environmental conditions. The STLP and FTLP are combined with cone-cylinder WECs to study the influence of the WECs on the floating system and observe the efficiency of the wind and wave power extraction.

## 1.6 BRIEF OVERVIEW OF THE THESIS

The thesis is structured into seven chapters, each focusing on a specific aspect of the physical problem investigated and the approach taken to formulate a solution. The detailed description of each chapter are as follows:

In Chapter 1, the introduction and motivation for the present study are discussed along with the detailed literature review on the dynamic analysis of the hybrid floating wind-wave system, the performance of the WECs in array with the floating wind turbine platform and also on the long-term response and reliability analysis of the combined floating systems are presented. The numerical and experimental findings relating to the response behaviour of the combined wind-wave system are examined. The chapter discusses the aim and objectives derived from the literature along with the scope of the research work. In addition, the research gap and a critical review based on the literature review is described.

In Chapter 2, the coupled dynamic analysis of the STLP and FTLP combined with WECs most suitable for deep water conditions is analysed. The natural frequency and rigid body motions of the STLP and FTLP supporting the 5 MW wind turbine are studied and compared. A circular array of cone-cylinder-shaped point absorber WECs is provided around STLP and FTLP to absorb wind and wave energy. Further, the study observed the forces and moments developed at the base of the turbine tower and the tension developed on the mooring cables to understand the performance of the floating hybrid TLP concepts against wind and wave.

In Chapter 3, the hydrodynamic performance of six different arrays of cone-cylinder point absorber WECs placed around an STLP and FTLP supporting a 5 MW wind turbine platform is examined. The heaving point absorber-type WEC in concentric and circular arrays are studied to observe the influence of the TLP and other WECs on the platform's stability and wave power absorption. instantaneous power absorbed by the wave energy device in the circular and concentric pattern is then calculated for several specified ocean conditions of the North Sea. The study then examines the influence of a hydraulic PTO system by analysing the power absorbed by the WEC using two different control strategies of the PTO system. In addition, the mean interaction factor (q-factor) and the capture width ratio (CWR) are studied to observe the efficiency of the hybrid system and also the utilization of the incident wave.

In Chapter 4, the STLP+6WECs and FTLP+8WECs hybrid floating wind turbine platforms are studied for different mooring layouts. The combined TLP-WEC is supported with tensioned mooring cables to stabilize the system against wind and waves. The study identifies a novel hybrid TLP-WEC concept with the optimum number of mooring lines for stabilizing the

combined system by studying the responses, forces and moments and tension developed on the mooring cables of the hybrid system. The forces and moments developed on the base of the floating wind turbine are further examined to analyse the impact of wind and wave loading on the responses of the hybrid floater.

In Chapter 5, the most probable values of motion amplitude of a hybrid wind-wave energy converter system are studied using long-term analysis. The long-term response analysis is obtained using short-term responses represented using Rayleigh distribution. The aero-servo-hydro-elastic simulation is performed for the combined concept of STLP and FTLP with a heaving cone-cylinder point absorber WEC. The performance of the combined system is based on the transfer functions and the choice of wave spectrum model. The study preferred the JONSWAP spectrum to predict the most probable values as it follows the Rayleigh distribution and incorporates wave refraction for partially developed sea states.

In Chapter 6, the reliability of hybrid floating wind turbine platforms against extreme loads is established using the IFORM that includes the randomness in the gross wind environment and the extreme response given wind conditions. The extreme responses on different configurations of hybrid STLP and FTLP-type floating offshore wind turbines are analysed using the Environmental Contour Method. The maximum values of the responses for both 1-D and 2-D models are studied and compared. The probability of the exceedance of the responses (Surge, sway, and yaw) for the platforms is studied for different return periods. The study further analyses the maximum values of tower base bending moment load at the platform-tower junction to observe the influence of the wind load on the floating wind turbine.

Finally, Chapter 7 summarizes the major findings of the thesis and restates the research objectives and contributions. It emphasizes the main conclusions drawn from the study and their implications. The chapter discusses the research's importance in a wider context and suggests potential directions for future studies. The brief outline of the thesis is presented as a flow chart in Figure. 1.1.

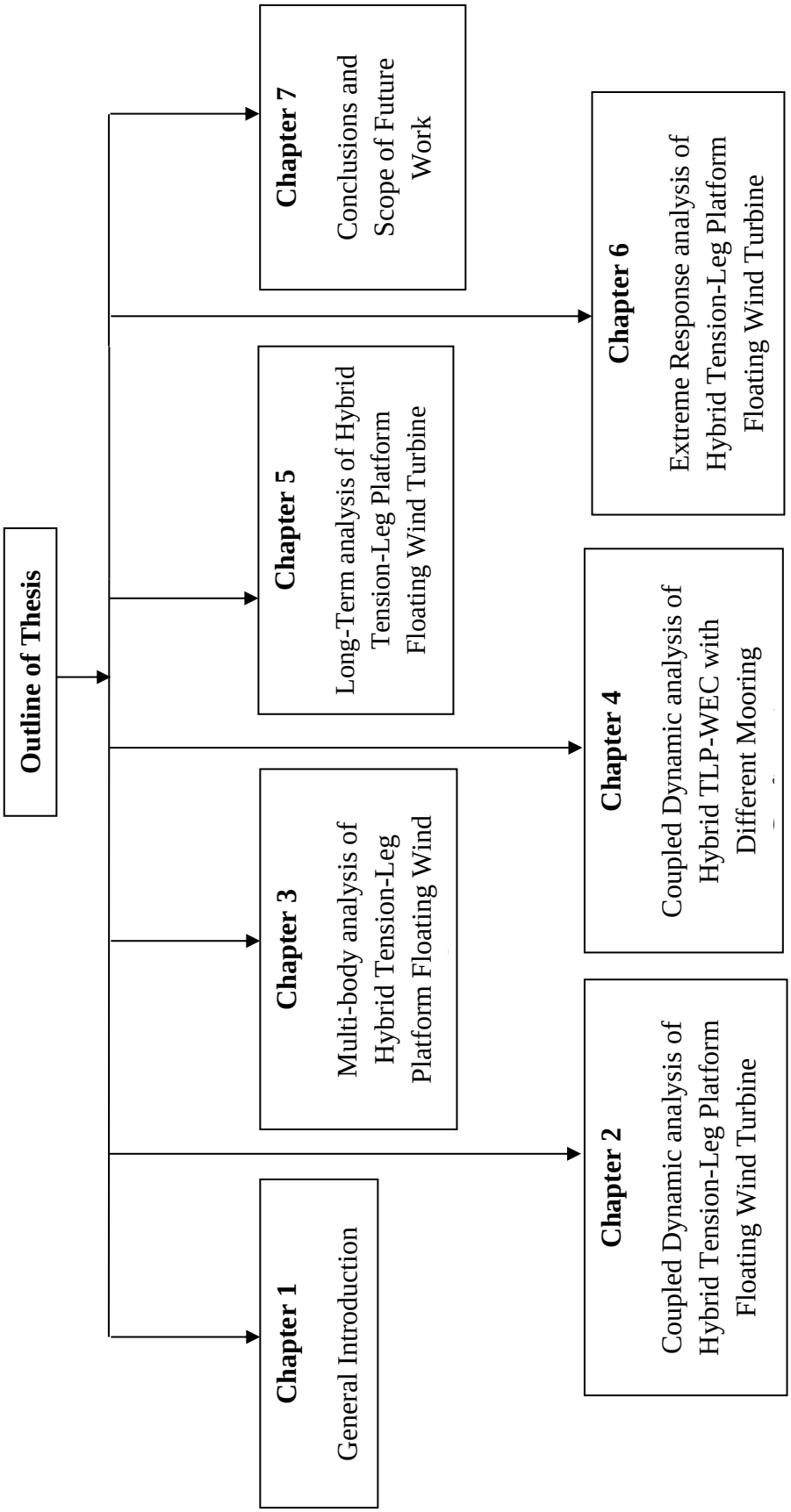


Fig. 1.1: Flow chart of the outline of the thesis.

### 1.6.1 List of Publications in Journals:

1. Rony, J.S., Karmakar, D. and C. Guedes Soares. (2021). Coupled dynamic analysis of spar-type floating wind turbine under different wind and wave loading. *Marine Systems and Ocean Technology*, 16, 169-198. DOI: 10.1007/s40868-021-00106-7.

2. Rony, J.S. and Karmakar, D. (2022). Coupled dynamic analysis of hybrid offshore wind turbine and wave energy converter. *Journal of Offshore Mechanics and Artic Engineering*, 144, 1-13. DOI: 10.1115/1.4052936.

3. Rony, J. S., and Karmakar, D. (2023). Performance of a hybrid TLP floating wind turbine combined with arrays of heaving point absorbers. *Ocean Engineering*, 282, 1-17. DOI: 10.1177/147509022211127.

4. Rony, J. S., and Karmakar, D. (2023). Dynamic analysis of frustum TLP-type wind turbine multi-purpose floating platform. *Ships and Offshore Structures*, 1-15. DOI: 10.1016/j.oceaneng.2023.114939.

5. Rony, J. S., and Karmakar, D. (2023). Coupled dynamic analysis of hybrid STLP-WEC offshore floating wind turbine with different mooring configurations. *Journal of Ocean Engineering and Marine Energy*, 1-29. DOI: 10.1007/s40722-023-00287-w.

6. Rony, J.S., Chaitanya Sai, K., and Karmakar, D. (2023). Numerical investigation of offshore wind turbine combined with Wave Energy Converter. *Marine Systems and Ocean Technology*, 18, 14-44. DOI: 10.1007/s40868-023-00127-4

7. Rony, J.S. and Karmakar, D. (2023). Hydrodynamic response analysis of a hybrid TLP and heaving-buoy wave energy converter with PTO damping. *Renewable Energy*. 226, 1-17. DOI: 10.1016/j.renene.2024.120380

8. Rony, J.S. and Karmakar, D. (2023). Long-term response analysis of hybrid STLP-WEC offshore floating wind turbine. *Ships and Offshore Structures*. (Under Review).

9. Rony, J.S. and Karmakar, D. (2023). Extreme response analysis of hybrid Tension Leg-type offshore wind turbine platform using inverse reliability method. *Wind Engineering*, (Submitted).

10. Rony, J.S. and Karmakar, D. (2023). Reliability based design loads of hybrid Submerged Tension Leg-type offshore wind turbine platform, *Journal of Ocean Engineering and Marine Energy*. (Submitted).

### 1.6.2 List of Publications in Book Chapters:

1. Rony, J.S., Karmakar, D. and C. Guedes Soares. (2021), Dynamic analysis of submerged Tension-Leg-Platform combined with heaving wave energy converter, *Developments in Marine Technology and Engineering, (Eds. C. Guedes Soares and T.A. Santos), CRC Press*, Vol-2, pp. 639-646. DOI: 10.1201/9781003216599

2. Rony, J.S., Karmakar, D. and C. Guedes Soares. (2021), Dynamic response analysis of a combined wave and wind energy platform under different mooring configuration, *Trends in Maritime Technology and Engineering, (Eds. C. Guedes Soares and T.A. Santos), CRC Press*, Vol-2, pp. 477-487. DOI: 10.1201/9781003320289

3. Sreebhadra, M.N., Rony, J.S., Karmakar, D. and C. Guedes Soares. (2021), Extreme response analysis for TLP-type floating wind turbine using Environmental Contour Method, *Trends in Maritime Technology and Engineering, (Eds. C. Guedes Soares and T.A. Santos), CRC Press*, Vol-2, pp. 315-324. DOI: 10.1201/9781003320289

4. Rony, J. S. and Karmakar, D. (2023). Dynamic analysis of submerged tension leg platform combined with wave energy converters for different mooring configuration. *AIP Conference Proceedings*, Vol. 2584, pp. 1-8. DOI: 10.1063/5.0127786

### 1.6.3 List of Publications in Conference Proceedings:

1. Rony J.S. and D. Karmakar. (2019). Long-term response analysis of different configurations of spar-type floating wind turbine. *International Conference on Trending Moments and Steer Forces – Civil Engineering Today (TMSF),* 20th October – 1st November, 2019, Fatorda, Goa.

2. Rony J.S. and D. Karmakar. (2019). Response analysis of combined wave and wind energy spar type platform, *International Conference on Hydraulics, Water Resource and Coastal Engineering (HYDRO),* $18^{th}$ – $20^{th}$ December, 2019, University College of Engineering, Osmania University, Hyderabad.

3. K. Kalyan Kumar, Rony J.S. and D. Karmakar. (2020). Response analysis of spar type platform with different mooring line configuration, *International Conference on Recent Advances on Renewable Energy (RARE-2020)* $7^{th}$ – $9^{th}$ February, 2020, NITK Surathkal, Mangalore, India.

4. Rony J. S. and D. Karmakar. (2020). Coupled dynamic analysis of Submerged Tension-Leg-Platform combined with heaving wave energy converter, *$1^{st}$ Online International Conference on Recent Advances in Computational and Experimental Mechanics*, $4^{th}$ – $6^{th}$ September 2020, Indian Institute of Technology Kharagpur, India.

5. Rony J. S. and D. Karmakar. (2021). Hydrodynamic performance of array of heaving point absorbers combined with STLP-type floating wind turbine, *International Conference on Hydraulics, Water Resource and Coastal Engineering (HYDRO),* $26^{th}$ – $28^{th}$ March, 2021, National Institute of Technology Rourkela, Odisha, India.

6. Rony J. S. and D. Karmakar. (2022). Dynamic Response of Combined Tension Leg-Platform Floating Wind Turbine and Point Absorber Wave Energy Converter, *International Conference on Hydraulics, Water Resource and Coastal Engineering (HYDRO),* $22^{nd}$ – $24^{th}$ December, 2022, Punjab Engineering College, Chandigarh, India.

### 1.6.4 List of Patent submitted:

1. Rony, J.S., and Karmakar, D. (2021). Frustum Tension-leg platform for floating wind turbine. Indian Patent No. 202141018525, Filed Application No. TEMP/E-1/19819/2021-CHE.

## 1.7 CLOSURE

The chapter briefly overviews the global wind energy scenario, offshore floating platforms, WECs and hybrid wind-wave platforms. Different concepts of hybrid floating wind-wave combined systems supporting the wind turbine and the WECs are discussed. The hybrid time and frequency domain simulation technique for the coupled dynamic analysis of the combined floating systems studied by the researchers is discussed in detail. The researchers discussed the importance of response analysis of the integrated system for the preliminary design of the system. The literature review also examined the interaction of WECs with the platform and discussed the power performance of the same. Further, the PTO system for optimising the power absorption of the WECs studied by the researchers is detailed. Different control parameters of the PTO are discussed. The studies presented the importance of the station-keeping system for the floating system, with analysis also being carried out to calculate the tension developed on the tether. The chapter also highlighted the importance of predicting maximum values of motion amplitude for the combined system using different techniques. With limited research on the combining wind and wave energy converter concept, the hybrid platform of wind and wave energy converter is a less exploited area.

# CHAPTER 2

# COUPLED DYNAMIC ANALYSIS OF HYBRID TENSION-LEG PLATFORM FLOATING WIND TURBINE

## 2.1 GENERAL INTRODUCTION

The studies on offshore floating foundations for generating wind power in the deep-sea gained interest in recent decades as the deep-water foundations proved more economical than conventional land-based and shallow-water fixed foundations. Further, the initial investment and maintenance cost for independent Wave Energy Converter (WEC) and floating offshore wind turbines are high (Weiss et al., 2018). As a result, the need for hybrid concepts came into existence. As winds and waves are closely related in the ocean, a hybrid concept for energy extraction is found to be beneficial. The hybrid structures are designed by combining WEC with Offshore Wind Turbines (OWT). They are observed to have less construction and maintenance costs when compared to independent OWT/WECs. The coupled dynamic analysis of a Tension-Leg Platform (TLP) combined with WECs, most suitable for deep-water conditions is examined. Two different forms of TLP combined with circular arrays of cone-cylinder-shaped point absorber WECs are analysed to understand the importance of hybrid systems. The influence of the WECs on the rigid body motions of the platform is studied in the time domain using the numerical simulation tool FAST. Further, the study observed the forces and moments developed at the base of the turbine tower and the tension developed on the mooring cables to understand the performance of the floating FTLP concept against wind and wave.

## 2.2 NUMERICAL MODELLING

The numerical model based on the aero-servo-hydro-elastic simulation is adopted to analyse the influence of WECs on the floating offshore wind turbine platforms under regular wave conditions. The complex system, including the floating wind turbine, the point absorber WEC and the mooring system for both hydrodynamic and aerodynamic analysis, is considered in the present study. An integrated aero-hydro-servo-elastic analysis is performed to predict the forces and the motion response. The hydrodynamic properties of the rigid body, including the six Degrees of Freedom (DOF), excitation force, potential damping, added mass and the

coupling terms of the body due to hydrodynamic interaction are simulated using WAMIT. The equation of motion is given by

$$-\omega^2\left(M+A(\omega)\right)X(\omega)+i\omega C(\omega)X(\omega)+RX(\omega)=F(\omega), \tag{2.1}$$

where $M$ gives the structural mass, $A(\omega)$ is the added mass, $X(\omega)$ is the displacement vector, $C(\omega)$ is the damping co-efficient, $R$ is the restoring co-efficient and $F(\omega)$ is the external force. The equation of motion, as in Eq. 2.1 is based on the linear potential flow theory, but to incorporate the non-linear effects, the time domain analysis is required. The equation of motion considering the quadratic viscous damping with six DOF for a rigid body is expressed as

$$\left\{M+A(\infty)\right\}\ddot{X}(t)+B\dot{X}\left|\dot{X}\right|+\int_0^t k(t-\tau)X(\tau)d\tau+RX(t)=f\left(t,X,\dot{X}\right), \tag{2.2}$$

where $A(\infty)$ is the added mass at infinite frequency, $X$, $\dot{X}$ and $\ddot{X}$ are the displacement, velocity and acceleration in the time domain, $B$ is the quadratic viscous damping co-efficient, $k(\tau)$ is the retardation function and $f\left(t,X,\dot{X}\right)$ is the external force vector which is the function of displacement and velocity in the time domain

### 2.2.1 General Equation of Motion

The equation of motion in FAST is derived using Kane's dynamics method. It is based on the principle that all generalised active and inertial forces acting on the complex system of the coupled RNA, the tower, and the support platform are balanced. The time-domain equation of motion (Jonkman, 2009) for the support platform and the coupled wind turbine is given by

$$M_{ij}(q,u,t)\ddot{q}_j=f_i(q,\dot{q},u,t), \tag{2.3}$$

where $M_{ij}$ represents the inertia mass matrix depending on degrees of freedom $q$, control input and time $t$. The expression in Eq. (2.3) considers the contributions from aerodynamics, platform mass and inertia, gravity, hydrodynamics and the reactional loads of the mooring system.

### 2.2.2 Aerodynamic Loading

The aerodynamic load on the wind turbine is based on the blade element momentum theory, which is based on the blade momentum theory and the blade element theory. The blade momentum theory finds the forces at the blade based on the conservation of linear and angular momentum. The blade element theory is based on the forces at the section of the blade at the

blade geometry. The relative velocity of the airflow (Jonkman, 2009) that moves the blade element is given by

$$V_{rel} = V\sqrt{\left(1-a\right)^2 + \left[\frac{r\Omega_r}{V}\left(1+a^{'}\right)\right]^2}, \tag{2.4}$$

where $V$ is the upstream wind velocity, $a$ and $a^{'}$ are the axial and angular induction factors, respectively, $\Omega_r$ is the angular velocity and $r$ is the distance of the airfoil section from the blade root. The angle of attack $\alpha$ and the relative angle of the wind $\phi$ is given by

$$\alpha = \phi - \beta \text{ and } \tan\phi = \frac{V}{r\Omega_r}\frac{1-a}{1+a^{'}}, \tag{2.5}$$

where $\beta$ is the section pitch angle. For maximum power to be developed, the axial and angular induction factors are related as

$$a^{'} = \frac{1-3a}{4a-1}. \tag{2.6}$$

The axial force developed on the rotor is the combination of lift force $F_L$ and drag force $F_D$ is given by

$$F_T = F_L\cos\phi + F_D\sin\phi. \tag{2.7}$$

The lift force expressed in terms of the lift coefficient $C_L$, air density $\rho_{air}$, airfoil chord length $c$, radial length of blade section $\Delta r$, and relative velocity $V_{rel}$ is given by

$$F_L = \frac{\rho_{air}c}{2}V_{rel}^2 C_L\left(\alpha\right)\Delta r. \tag{2.8}$$

The drag force expressed in terms of the drag co-efficient is given by

$$F_D = \frac{\rho_{air}c}{2}V_{rel}^2 C_D\left(\alpha\right)\Delta r. \tag{2.9}$$

### 2.2.3 Hydrodynamic Loading

The total external load acting on the platform other than the weight of the support platform and the load transmitted (Jonkman and Matha, 2011) from the wind turbine is given by

$$F_i^{Platfrom} = -A_{ij}\ddot{q}_j + F_i^{Hydrodynamic} + F_i^{Lines}, \tag{2.10}$$

Where $A_{ij}$ represents the contribution from added mass component, $F_i^{Hydrodynamic}$ is the hydrodynamic load on the support platform and $F_i^{Lines}$ is the load from the mooring lines. To obtain the equation of motion for the hydrodynamic load developed on the system, the

radiation, diffraction and hydrostatic loads are considered, and the hydrodynamic load is given by

$$F_i^{Hydrodynamic} = F_i^{Waves} + F_i^{Viscous} + F_i^{Hydrostatic}. \tag{2.11}$$

The hydrodynamic load equation considers the total excitation load on the support platform from the incident waves $F_i^{Waves}$ which is closely related to the wave elevation $\zeta$. The Airy's wave theory describes the kinematics of regular waves, whose periodic elevation is a sinusoidal wave propagating at a single amplitude and frequency (period) or wavelength. The contribution to the linear potential wave force on the support platform is expressed as

$$F_i^{Waves} = F_i^{Radiation} + F_i^{Diffraction}. \tag{2.12}$$

The force due to radiation $F_i^{Radiation}$ is due to the forced oscillations of the support platform in all DOF when no incident wave is present. The resulting radiation force includes contributions from added mass and force, which is proportional to accelerations and contributions from the radiation damping, which is proportional to platform velocity.

$$F_i^{Radiation} = -A_{ij}(\omega)\ddot{q}_j(t) - B_{ij}(\omega)\dot{q}_j(t). \tag{2.13}$$

The total radiation load can be obtained by the inverse transformation of the radiation loads in the frequency domain and is given by

$$F_i^{Radiation} = -A_{ij}(\infty)\ddot{q}_j(t) - \int_t^t h_{ij}(t-\tau)\dot{q}_j(t)d\tau, \tag{2.14}$$

where $A_{ij}(\infty)$ is the added mass coefficient at the infinite frequency and $h_{ij}(\tau)$ is the retardation function. The retardation function is given by

$$h_{ij}(\tau) = \frac{2}{\pi}\int_0^\infty B_{ij}(\omega)\cos(\omega\tau)d\omega. \tag{2.15}$$

The irregular or random waves representing various stochastic sea states are modelled as the summation or superposition of multiple wave components, as determined by an appropriate wave spectrum. The HydroDyn module includes the Pierson-Moskowitz spectrum for the fully developed sea state, the JONSWAP spectrum for the limited fetch conditions, and is also equipped with user prescribed site-specific wave spectrum. The excitation load to determine the diffraction force $F_i^{Diffraction}$ is given by

$$\zeta(t) = \frac{1}{2\pi}\int_{-\infty}^{\infty} W(\omega)\sqrt{2\pi S_\zeta^{2-sided}(\omega)}e^{j\omega t}d\omega, \tag{2.16}$$

$$F_i^{Diffraction} = \frac{1}{2\pi}\int_{-\infty}^{\infty} W(\omega)\sqrt{2\pi S_\zeta^{2-sided}(\omega)}X_i(\omega,\beta)e^{jwt}d\omega. \tag{2.17}$$

The relation as in Eq. (19) is an inverse transform depending on the 2-sided power spectral density of the wave per unit time $S_\zeta^{2-sided}$, Fourier transforms of a realisation of white Gaussian noise time series process with zero mean and unit variance $W(\omega)$ and the complex-valued array representing the wave excitation force on support platform normalised per unit wave amplitude $X_i(\omega,\beta)$ depending on frequency $\omega$ and direction $\beta$ of incident wave. To animate the wave surface around the floating platform, the wave elevation is given by

$$\zeta(t,X,Y) = \frac{1}{2\pi}\int_{-\infty}^{\infty} W(\omega)\sqrt{2\pi S_\zeta^{2-sided}(\omega)}e^{-jk(\omega)\left[X\cos(\beta)+Y\sin(\beta)\right]}e^{i\omega t}d\omega, \tag{2.18}$$

which is valid for any location along with the mean position. $(X,Y)$ represents the initial reference plane on the still water level, and $k(\omega)$ represents the wave number for any wave direction $\beta$. The wave number, water depth, incident wave frequency and the gravitational constant are co-related by the dispersion relation given by

$$\sigma^2 = gk(\omega)\tanh k(w)h. \tag{2.19}$$

The viscous drag load is modelled using the Morison equation and is expressed as

$$F_i^{Viscous} = \frac{1}{2}C_d\rho_w A\left[v_i(t)-\dot{\varsigma}_i(t)\right]\left|v_i(t)-\dot{\varsigma}_i(t)\right|, \tag{2.20}$$

where $\dot{\varsigma}_i(t)$ is the undisturbed flow velocity taken at the instantaneous position of the centre of gravity, $v_i(t)$ is the velocity of the support platform, $C_d$ is the viscous co-efficient having projection area $A$ and $\rho_w$ is the water density. The hydrostatic force includes the buoyancy force from the Archimedes principle and the linear hydrostatic restoring force from the water plane area, and the centre of buoyancy is given by

$$F_i^{Hydrostatic} = \rho g V_o \delta_{i3} - C_{ij}^{Hydrostatic} q_j. \tag{2.21}$$

The linear hydrostatic force $(\rho g V_o \delta_{i3})$ is acting directly upward and is equal to the weight of the displaced fluid when the support platform is un-displaced. This term is nonzero only for the vertical heave-displacement DOF of the support platform because the centre of buoyancy of the platform is assumed to lie on the centre line of the undeflected tower (or z-axis of the platform).

The change in the hydrostatic force and moment resulting from the effects of the water pane area and the centre of buoyancy, $C_{ij}^{Hydrostatic}$ is the same as in Jonkman (2007). The relation for the centre of buoyancy, $C_{ij}^{Hydrostatic}$ suggests that the hydrostatics provide restoring only for the heave pitch and roll motions, and the rest is restored by the mooring lines. The numerical convolution in time domain is also implemented in the hydrodynamic load to capture the memory effect directly. In general, the memory effect decays to zero after a certain amount of elapsed time. Hence HydroDyn is enabled to truncate the numerical convolution after a user-specified amount of time, thus allowing faster calculations of the memory effect. Thus, the HydroDyn module accounts for the linear hydrostatic restoring, non-linear viscous drag from incident-wave kinematics, sea currents, and platform motion. The added mass and damping contributions are from linear wave radiation, including free surface memory effects and incident-wave excitation from linear diffraction in regular or irregular seas.

### 2.2.4 Mooring Load

The mooring lines hold the platform against winds, waves, and currents. In the case of the TLP, the mooring cables are tensioned and hence provide extra stability. The total load on the support platform due to mooring lines (Hall and Goupee, 2015) is given by

$$F_i^{Lines} = F_i^{Lines,0} - C_{ij}^{Lines} q_j \tag{2.22}$$

where $F_i^{Lines,0}$ is the i$^{th}$ component of the total mooring system load acting on the support platform in its un-displaced position and $C_{ij}^{Lines}$ is the component of the linearised restoring matrix from all mooring lines. In the case of catenary mooring lines $F_i^{Lines,0}$ takes the pre-tension at the fairlead from the weight of the cable not resting on the sea floor. If the catenary mooring lines are neutrally buoyant, then the pre-tension developed is zero. In the case of taut mooring system, $F_i^{Lines,0}$ is calculated based on the excess buoyancy in the tank in an un-displaced position, including the weight of the cable in water. The component of the linearised restoring matrix $C_{ij}^{Lines}$ is calculated based on the elastic stiffness of the mooring lines and the effective geometric stiffness with the weight of the cable in water depending on the system layout. As the responses of the mooring system include non-linearities in force-displacement relationships, a quasi-static model is developed to model the non-linear restoring loads from the mooring system of the floating platforms. In FAST, tension mooring system is designed by using the MoorDyn module. The MoorDyn module can model the taut mooring (Jonkman,

2007) and the effects of interaction between the seabed and mooring lines. The coupled restoring stiffness matrix for the TLP platform is discussed by Zhao et al. (2016). The steady-state displacement of the floating platform (Wayman et al., 2006) is given by

$$\xi_1 = \frac{F_1}{C_{11}}. \tag{2.23}$$

The pretension of the mooring cable is thus reached by limiting the system's steady state displacement. The tension thus obtained for the tethers must satisfy the condition that it should not be more than the maximum allowable for the windward side tether and should not fall below the minimum value for the leeward side tether. Also, the position of the fairlead tension is an important factor to sustain the tension in the mooring lines. Moving the fairlead positions further from the centre line of the structure leads to reduced line tension oscillating amplitudes and therefore decreases the probability of the lines going slack under heavy wind and wave conditions.

### 2.2.5 Response Amplitude Operator

FAST code uses cross spectral-auto spectral method to compute the Response Amplitude Operator (RAO) for the floating structures. Squared RAO is expressed as an absolute value of ratio of the cross spectral density between the input wave spectrum and responses of the system, to the auto spectral density of the input wave spectrum is given by

$$RAO = \left|H(\omega)\right| = \left[\frac{S_{XY}(\omega)}{S_{XX}(\omega)}\right]^{1/2} \tag{2.24}$$

where the auto spectral density $S_{XX}$ is equal to the Fourier transform of the power-based auto-correlation function $S_{XX} = FT(R_{XX})$ and $S_{XY}$ is the cross power spectral density $S_{XY} = FT(R_{XY})$ expressed as the Fourier transform of the cross-correlation function $R_{XY}$. The cross-spectral method avoids the issue of spectral leakage leading to uncorrelated noise at the start and end of the spectrum, and has the added advantage of providing information on the phase relationship between the two signals.

## 2.3 GEOMETRIC MODELLING

Geometric modelling is a critical step in numerical simulation for creating a digital representation of the physical structure of the floating wind turbine system. Geometric modelling plays a crucial role in accurately predicting the dynamic behaviour and performance

of the floating wind turbine system under various environmental conditions. The study considers two types of TLP combined with heaving point absorber WECs.

### 2.3.1 Submerged Tension-Leg Platform Combined with Point Absorber WEC

The Submerged Tension-Leg Platform (STLP) combined with a different number of WECs in a circular pattern that supports the NREL 5-MW reference wind turbine is modelled. The STLP consists of four vertical pontoons at four square corners connected by horizontal pontoons. Each vertical pontoons are kept at a distance of 40 m. The wind turbine is placed on the central column connected to the vertical pontoon through cross braces. The diameter of the central column is 6.5 m, which ensures the better hydrodynamic performance of the platform during the operation phase due to the small water plane area (Han et al., 2017). To the central column, the point absorber-type WECs are connected. The study considers a cone-cylinder floater with a cone having an apex angle of 90° to be attached to the STLP platform. The cone-cylinder floater ensures maximum power extracted from waves when arranged in a circular pattern, as discussed in Sinha et al. (2015). The structural dimensions of the STLP platform and the cone-cylinder heaving point absorber shown in Fig. 2.1(a,b) are listed in Table 2.1 and Table 2.2, respectively, and the inertial properties are listed in Table 2.3 and Table 2.4.

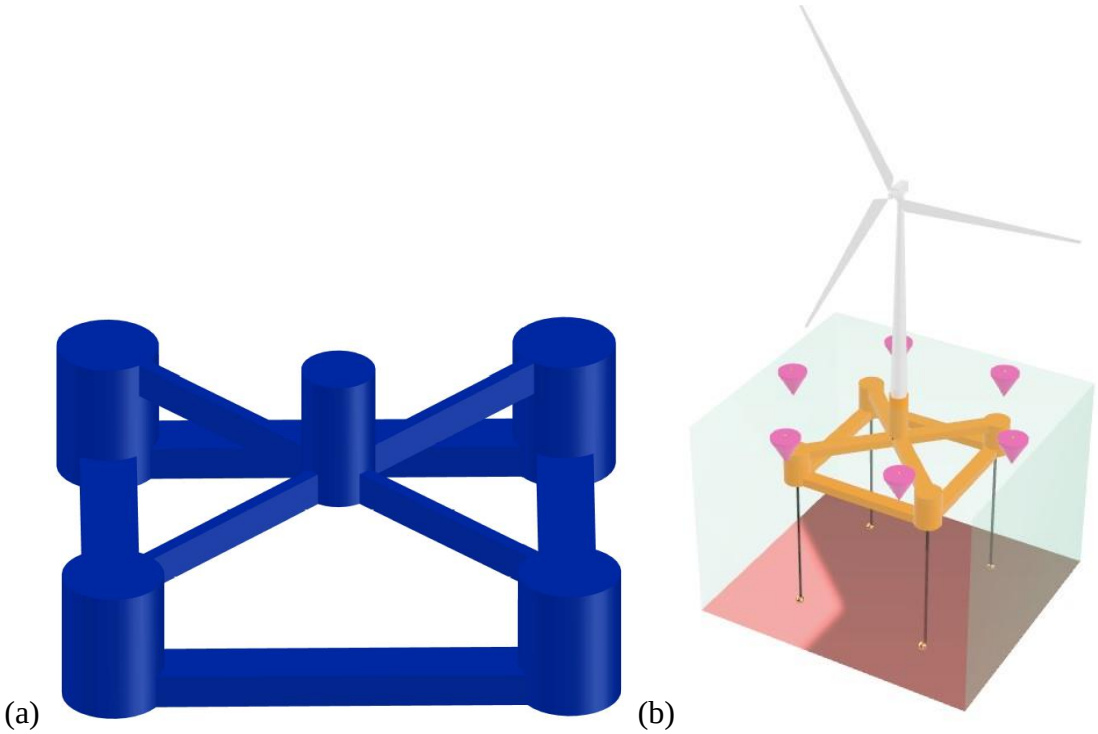

(a) (b)

Fig. 2.1: Schematic representation of (a) STLP and (b) STLP with 5MW wind turbine and WECs.

Table 2.1: Dimensions of the STLP floater (Han et al., 2017).

| Parameter | Dimensions |
|---|---|
| Column Diameter | 6.5 m |
| Diameter of vertical pontoon | 9.0 m |
| Height of vertical pontoon | 12.0 m |
| Distance between Vertical pontoons | 40.0 m |
| Width of horizontal pontoon | 5.0 m |
| Height of horizontal pontoon | 3.0 m |

Table 2.2: Dimensions of the cone-cylinder floater.

| Parameters | Dimensions |
|---|---|
| Base radius of the cone-cylinder floater | 5.0 m |
| Apex angle of the cone portion | 90° |
| Height of cylindrical portion | 1.0 m |

Table 2.3: Inertia properties of the Platform and WEC.

| Parameters | Platform | WEC |
|---|---|---|
| Mass | 7.721 x $10^6$ kg | 9.43 x $10^5$ kg |
| CM below MSL | -18.23 m | -1.47 m |
| Roll inertia about CM | 1.73E10 kg $m^2$ | 1.12 x $10^5$ kg $m^2$ |
| Pitch inertia about CM | 1.73E10 kg $m^2$ | 1.12 x $10^5$ kg $m^2$ |
| Yaw inertia about CM | 3.24E10 kg $m^2$ | 2.13 x $10^5$ kg $m^2$ |

Table 2.4: Inertia properties of the hybrid concept.

| Parameters | STLP+2WEC | STLP+4WEC | STLP+6WEC | STLP+8WEC |
|---|---|---|---|---|
| Mass | 8.099 x $10^6$ kg | 8.47 x $10^6$ kg | 7.854 x $10^6$ kg | 9.23 x $10^6$ kg |
| CM below MSL | -17.42 m | -16.68 m | -16.02 m | -15.43 m |
| Roll inertia about CM | 1.91E10 kg $m^2$ | 2.64E10 kg $m^2$ | 3.08E10 kg $m^2$ | 3.59E10 kg $m^2$ |
| Pitch inertia about CM | 2.46E10 kg $m^2$ | 2.65E10 kg $m^2$ | 3.08E10 kg $m^2$ | 3.59E10 kg $m^2$ |
| Yaw inertia about CM | 4.02E10 kg $m^2$ | 4.81E10 kg $m^2$ | 5.56E10 kg $m^2$ | 6.45E10 kg $m^2$ |

Mooring cables are paramount for TLPs, providing load transfer, dynamic response, station keeping, safety, reliability, redundancy, and risk reduction. They are critical components that ensure the stability, performance, and safety of TLPs during their operational lifespan in deep-water environments. The STLP-WEC hybrid system is kept in position with the help of

tensioned mooring cables, which ensures that the platform is placed at 150 m water depth with a negligible heave, pitch and roll motions. Four tensioned cables are used for the stability of the hybrid system, and the properties of the mooring system are presented in Table 2.5.

Table 2.5: Properties of mooring system.

| Parameters | Values |
|---|---|
| Number of mooring lines | 4 |
| Fairlead distance from centre | 25 m |
| Unstretched mooring-line length | 130.978 m |
| Line diameter | 0.12 m |
| Line mass per unit length | 115.9248 kg/m |
| Line extensional stiffness | 31.359E9 N |
| Average steel density | 7850 $kg/m^3$ |
| Average concrete density | 2562.5 $kg/m^3$ |

#### 2.3.1.1 Arrangement Pattern

The point absorbers WEC operate in arrays to produce a large amount of power from ocean waves. The study considers STLP with two, four, six and eight numbers of WECs arranged in a circular array. The WECs in line with the central column of the STLP are placed at 40 m in the x-direction such that there is no interaction between the platform and the WECs when arranged in a circular pattern. The floater and the WECs are considered a single body moving together in wind and wave. The circular arrangement pattern of the WECs around STLP is detailed in Table 2.6.

Table 2.6: Different configurations of hybrid STLP-WEC system.

| Configuration | Description | Schematic representation |
|---|---|---|
| STLP+2WECs | Two WECs around STLP in the direction of wave. | 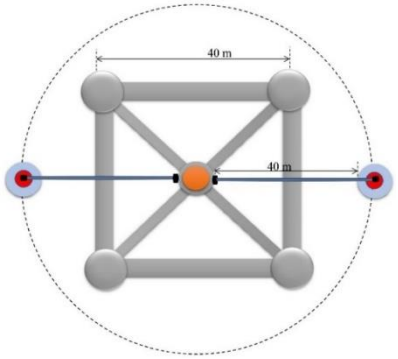  |

| | | |
|---|---|---|
| STLP+4WECs | Four WECs equally spaced around STLP. | 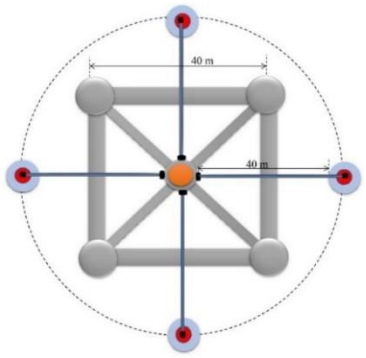 |
| STLP+6WECs | Six WECs equally spaced around STLP. | 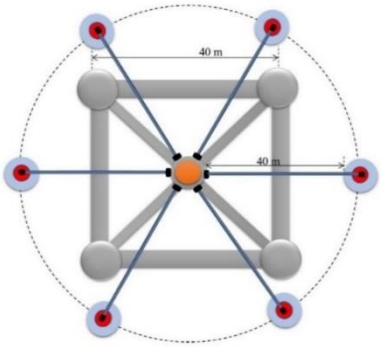 |
| STLP+8WECs | Eight WECs equally spaced around STLP. | 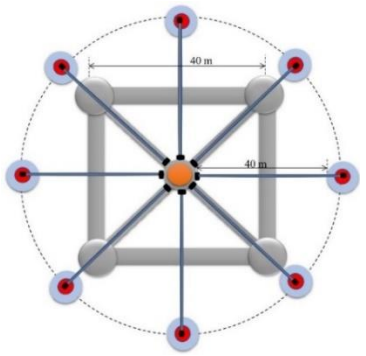 |

### 2.3.2 Frustum Tension-Leg Platform Combined with Point Absorber WEC

The Frustum Tension-Leg Platform (FTLP) concept for a moderate water depth of 70 – 150 m bounding the deep-water condition is designed to hold a 5 MW wind turbine. The hexagon-shaped structure consists of six vertical pontoons of frustum shape placed 50 m apart. The outer frustum-shaped vertical pontoons have a diameter of 10 m at the bottom and 6.5 m at the top, with a total height of 20 m. Horizontal pontoons connect these vertical pontoons. The central column supporting the 5 MW wind turbine is frustum-shaped and is having same dimensions. The central column and the vertical pontoons are further connected by rectangular-shaped supporting braces of 2.0 m x 1.0 m at the bottom and 1.0 m x 1.0 m at the top. The supporting braces are further stiffened with horizontal braces at the top and bottom to provide better stability. The FTLP floater of height 20 m is provided with a draft of 12.5 m below mean sea

level (MSL). The symmetry of the offshore floating platform helps in improving its stability. The geometric dimensions of the FTLP are detailed in Table 2.7, and the schematic representation of FTLP is shown in Fig. 2.2(a,b). The FTLP floating wind turbine floater is provided with different arrays of heaving point absorber WECs in a circular pattern to absorb wave energy. The study provides centro-symmetrically distributed WECs to ensure better power quality and smoothness when the waves pass through the system.

Table 2.7: Dimensions of the FTLP floater.

| Parameters | Dimensions |
|---|---|
| Diameter of the central column at the top | 6.5 m |
| Diameter of the central column at the bottom | 10.0 m |
| Diameter of the vertical pontoon at top | 6.5 m |
| Diameter of the vertical pontoon at bottom | 10.0 m |
| Height of vertical pontoon | 20.0 m |
| Draft of the platform | 12.5 m |
| Centre-to-centre distance between vertical pontoons | 50.0 m |
| Width and height of horizontal pontoons | 4.0 m |
| Width and height of supporting braces at the top | 1.0 m |
| Width and height of supporting braces at the bottom | 1.0 m |
| Width and Height of horizontal braces at the top | 1.0 m |
| Width of Inclined Braces at bottom | 1.0 m |
| Height of Inclined Braces at bottom | 2.0 m |

Table 2.8: Inertia properties of the FTLP floater and Cone-cylinder point absorber WEC**.**

| Parameters | FTLP floater | WEC |
|---|---|---|
| Mass | 5.121 x $10^6$ kg | 9.43 x $10^5$ kg |
| CM below MSL | -6.824 m | -1.47 m |
| Roll inertia about CM | 4.22E09 kg $m^2$ | 1.12 x $10^5$ kg $m^2$ |
| Pitch inertia about CM | 4.22E09 kg $m^2$ | 1.12 x $10^5$ kg $m^2$ |
| Yaw inertia about CM | 8.01E09 kg $m^2$ | 2.13 x $10^5$ kg $m^2$ |

The cone-cylinder-shaped point absorber with a cone having an apex angle of 90° is provided around the FTLP to examine the influence of WECs on the dynamic response of the FTLP, further to analyse the efficiency of the wind power absorption of the hybrid FTLP-WEC floating platform. The structural dimensions of the cone-cylinder heaving point absorber WEC

are detailed in Table 2.2, and the inertial properties of the FTLP and the cone-cylinder WEC are described in Table 2.8.

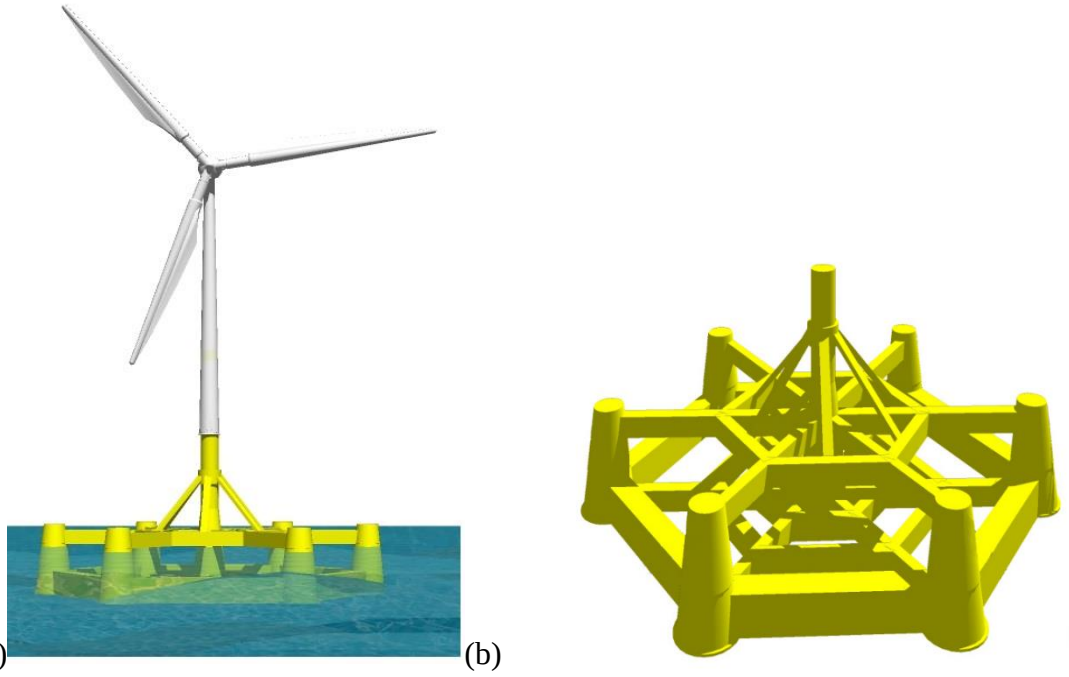

(a) (b)

Fig. 2.2: Pictorial representation of (a) Frustum-TLP supporting 5MW wind turbine (b) Frustum-TLP.

Table 2.9: Properties of mooring system

| Characteristics | Values |
|---|---|
| Number of mooring lines | 6 |
| Unstretched mooring-line length | 130.978 m |
| Line diameter | 0.12 m |
| Line mass per unit length | 115.9248 kg/m |
| Line extensional stiffness | 31.359E8 N |
| Average steel density | 7850 kg/m$^3$ |
| Average concrete density | 2562.5 kg/m$^3$ |

The submerged FTLP with excess buoyancy is vertically moored to the seabed using taut mooring lines called tendons or tethers. The submerged floating structure is vertically restrained, precluding the motions vertically (heave) and rotationally (pitch and roll). The FOWT is compliant in the horizontal direction permitting lateral surge and sway motions. The present study provides six mooring cables for the FTLP, each on the centre portion of the outer Frustum-shaped vertical pontoons. The properties of the mooring cables are detailed in Table 2.9.

#### 2.3.2.1 Arrangement Pattern

The heaving cone-cylinder point absorber WECs operate in arrays to absorb tremendous wave power from oceans. The study combines FTLP with two, four, six, and eight numbers of heaving WECs in a circular pattern at 65 m from the centre of the FTLP. The floater and the WECs are considered a single body moving together in the wind and wave. Table 2.10 describes different arrangement patterns of WEC around the FTLP.

Table 2.10: Different configurations of hybrid FTLP-WEC system.

| Configuration | Description | Schematic representation |
|---|---|---|
| FTLP+2WECsx | Two WECs around FTLP in the direction of wave | 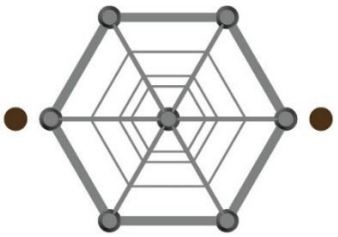 |
| FTLP+2WECsy | Two WECs around FTLP in the perpendicular direction of the wave | 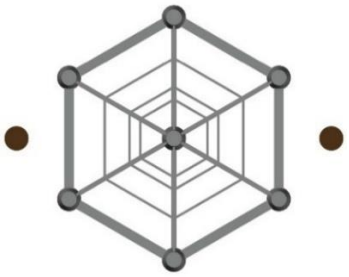 |
| FTLP+4WECs | Four WECs equally spaced around FTLP | 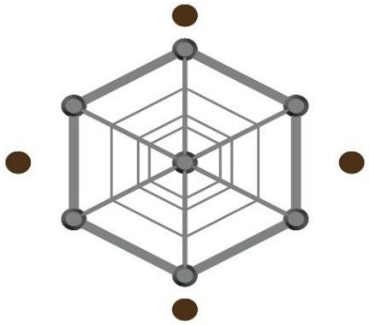 |
| FTLP+6WECs | Six WECs equally spaced around FTLP | 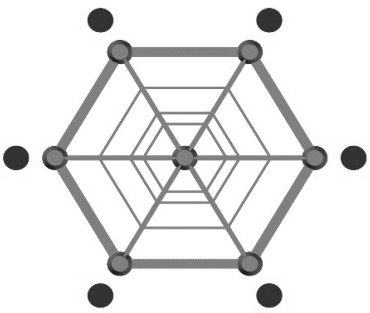 |

| | | |
|---|---|---|
| FTLP+8WECs | Eight WECs equally spaced around FTLP | 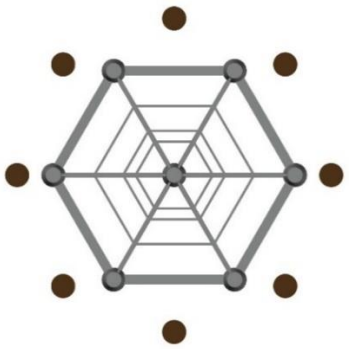 |

### 2.3.3 Integration of TLP-type Wind Turbine Platform with WEC

The study considers TLP with two, four, six and eight numbers of WECs in a circular array. The WECs are connected through connecting arms, as shown in Fig. 2.3(a,b). A hinged structure is provided between the connecting arm and the column, which limits the relative motion and allows rotation around the hinged shaft that drives the PTO to produce power. For STLP floating platform, the WECs are placed in line with the central column (Fig. 2.3a), and for the FTLP floating system, the cone-cylinder WECs are placed in line with the vertical outer pontoons as shown in Fig. 2.3(b).

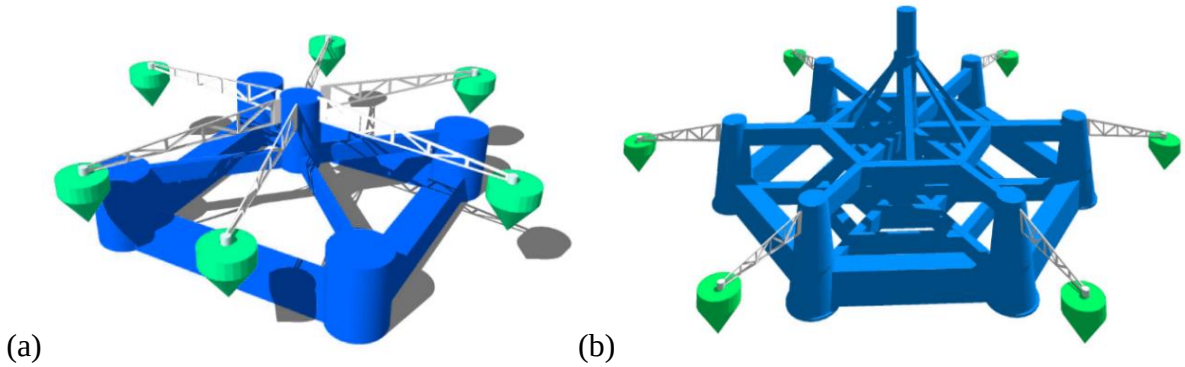

(a) (b)

Fig. 2.3: Schematic representation of the hybrid (a)STLP-WEC and (b) FTLP-WEC wind-wave system.

The PTO systems of the oscillating body WECs use mechanical or hydraulic transmissions to power conventional high-speed rotational generators or install specially designed linear generators for direct drive. The hydraulic PTO shown in Fig. 2.4 is used in the WECs of the hybrid concept. The absorbed power (Si et al., 2021) of the system with rotational velocity $\omega_{arm}$ is calculated using the relation

$$P_{WEC} = \tau_{PTO}\omega_{arm} \tag{25}$$

To derive maximum wave energy, the PTO applied load torque $\tau_{PTO}$ is controlled as a function of wave and body movement to keep the buoy in resonant motion in waves. Hansen (2013) stated that the success of WECs largely depends on advancement in PTO, thus becoming critical for wind and wave hybrid power generation. The study presents an aero-servo-hydro-elastic simulation of the hybrid platform using the numerical simulation tool FAST. The numerical simulation tools for FOWTs and WECs are quite different as they have distinct DOFs and environmental loadings, even though they have similar physical domains.

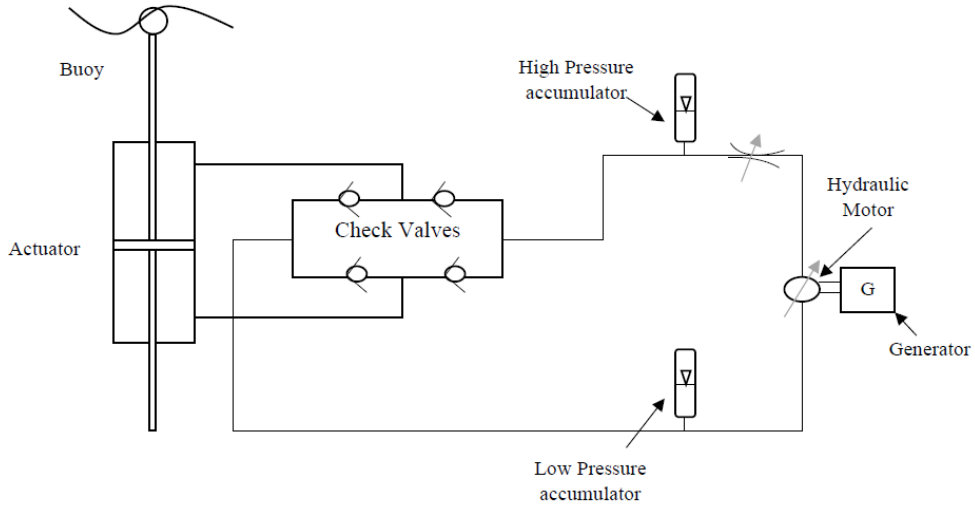


Fig. 2.4: Hydraulic PTO circuit for WEC.

### 2.3.4 NREL 5 MW Wind Turbine System

The coupled dynamic analysis considers the horizontal axis three-bladed 5 MW NREL reference wind turbine. The geometrical properties and mass properties of Rotor Nacelle Assembly (RNA), along with the tower mass and tower properties, are presented in Table 2.11.

Table 2.11: Properties of 5 MW NREL wind turbine (Jonkman, 2007).

| Characteristics | Value | |
|---|---|---|
| Power | 5 MW | |
| Rotor Orientation, Configuration | Upwind, 3 Blades | |
| Control Strategy | Variable speed collective pitch | |
| Cut-in, rated, cut-out wind speed | 3 m/s, 11.4 m/s, 25 m/s | |
| Cut-in, rated rotor speed | 6.9 rpm, 12.1 rpm | |
| Rotor Nacelle Assembly (RNA) | Hub height | 90 m |
| | Rotor hub dia | 126 m, 3 m |

| | | |
|---|---|---|
| | Rotor mass | 110,000 kg |
| | Nacelle mass | 240,000 kg |
| | C.G. location | (-0.414,0,89.57) |
| Tower | Mass | 347,460 kg |
| | Height | 87.6 m |
| | Top Diameter | 3.7 m |
| | Base diameter | 6 m |
| | C.G. location | (-0.2, 0, 64) m |

### 2.3.5 Methodology

The geometric modelling of the hybrid TLP and WEC system under the design water surface is achieved using Rhinoceros 3D version 6.0. Rhinoceros is a rich and versatile computer-aided design (CAD) package for the parametric design of 3D geometric objects, particularly objects free from curves and surfaces. The model surface is subdivided into meshes/panels, and all the panels represent the wetted surface.

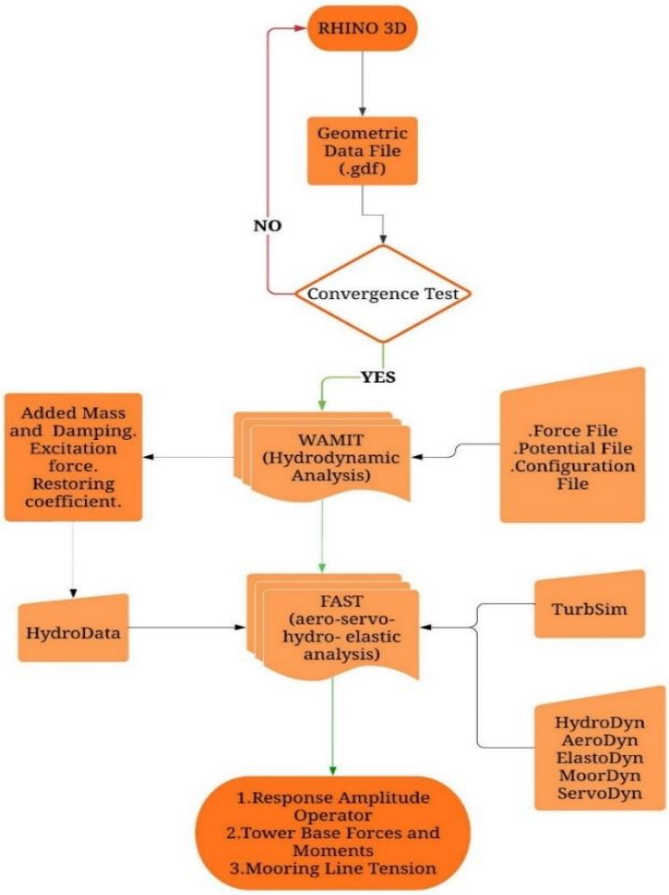


Fig. 2.5: Flow chart describing the methodology for coupled dynamic analysis.

The panel size is modified depending on the accuracy requirements by performing the convergence test. The convergence test examines the closeness of the hydrodynamic coefficients of the floating system for the different panel sizes. The convergence test considering the added mass concludes the minimum number of panels required to provide maximum efficiency. The geometric data file (gdf) obtained from Rhinoceros 3D represents the coordinates of the submerged portion of the structure that is used as an input for hydrodynamic analysis. Hydrodynamic analysis of the combined TLP-WEC system uses WAMIT V6.414 to calculate the added mass, excitation force, and restoring coefficient, considering only the wave load. The added mass, restoring co-efficient and the excitation force obtained from WAMIT are used as input for the aero-servo-hydro-elastic simulation tool FAST Version 7.0 to analyse the dynamic responses of the hybrid floating system. The study used 13$^{th}$ Gen Intel(R) core(TM) i7-13700 2.10 GHz processor and 16GB RAM for the hydrodynamic and coupled dynamic simulation of the FOWT platforms. FAST incorporates the HydroDyn, ElastoDyn, ServoDyn, AeroDyn and MoorDyn to optimise wind turbine responses and calculate the loads under real operational conditions. The wind data input for the North Atlantic Sea conditions is simulated using TurbSim. The wind speed conditions representing the operating conditions of the 5 MW wind turbine are chosen to observe the response amplitudes of the hybrid system. The study further analyses the tower base forces and moments developed at the turbine junction and the tension developed on the mooring cables for each hybrid configuration. The flow chart depicting the methodology is shown in Fig. 2.5.

### 2.3.6 Load Case Definition

The study considers northern North Sea environmental conditions, and the simulation measurements for the area have been taken for both wind and waves from 1973 to 1999. The data measured have been fitted to the analytical function by using 2-parameter Weibull distribution to calculate the expected value of significant wave height.

Table 2.12: Metocean conditions (Muliawan et al., 2013).

| Case no. | $V_{mean}\,(m/s)$ | $H_s\,(m)$ | $T_p\,(s)$ | Turbine status |
|---|---|---|---|---|
| SS-1 | 8 | 2.5 | 9.8 | Operating |
| SS-2 | 11.2 | 3 | 10 | Operating |
| SS-3 | 14 | 3.6 | 10.2 | Operating |
| SS-4 | 17 | 4.2 | 10.5 | Operating |

A log-normal distribution was introduced to fit the peak period distribution, and hence expected value for the peak period for a given wind speed and wave height is calculated (Johannessen et al., 2001). In the present study, different wind speeds representing the operational conditions of the wind turbine are chosen to analyse the motion amplitudes of the hybrid system. Table 2.12 lists the selected wind speeds and the correlated sea state conditions (expected values of $H_s$ and $T_p$) used for the investigation of the motion response of the system as well as the tower base forces and moments.

## 2.4 VERIFICATION OF NUMERICAL MODELLING

The dynamic responses simulated using FAST are verified using the numerical model developed by Vardaroglu et al. (2022). The study performed by Vardaroglu et al. (2022) is carried out for MIT/NREL TLP numerical model using NEMOH. The time domain analysis using FAST is performed to observe the motion response. Further, a physical model test is conducted in the 1:40 scale model to observe the 6-DOFs for parked and operating conditions of the 5 MW wind turbine. The validation of the numerical method is conducted with the numerical model of MIT/NREL TLP, as in Vardaroglu et al. (2022), to observe the motion responses of the system.

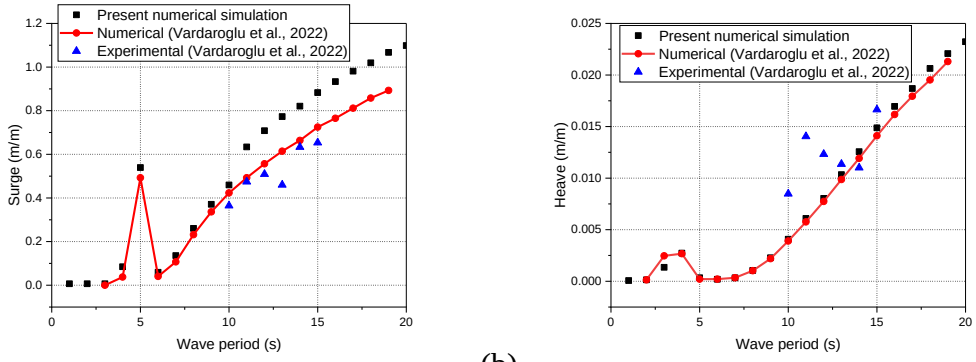


(a) (b)

Fig. 2.6: (a) Surge and (a) heave response of the MIT/NREL TLP floater.

The hydrodynamic analysis of the model in the frequency domain is simulated using the tool WAMIT to calculate the added mass, radiation damping and the hydrostatic restoring coefficient. Further, the time domain aero-hydro-servo-elastic simulation is carried out using FAST for the parked condition of a 5 MW wind turbine. The study compared the surge and heave motion response of the MIT/NREL model with the numerical and experimental results of Vardaroglu et al. (2022). In Fig. 2.6(a,b), the numerical results of the surge and heave response with Vardaroglu et al. (2022) for the MIT/NREL TLP matches the result obtained in

the present study for the MIT/NREL TLP. The experimental values for the surge motion response have good agreement with the present numerical model, shown in Fig. 2.6(a). But slight variation is observed for the heave motion response, may be because of the difference in the material stiffness and damping characteristics of the mooring cables. Calibration errors, sensor noise, and data processing techniques may contribute to discrepancies between the two sets of results. The surge response is observed to increase with the increase in wave period in both cases, with slight variation for higher wave periods. In the case of heave motion, the amplitudes are low due to the significant tendon stiffness, and the variation is observed to be minimal.

## 2.5 RESULTS AND DISCUSSION

The performance of the TLPs (STLP and FTLP) is investigated through the dynamic response analysis under regular and irregular wave and wind conditions. The study under the combined wind and wave concept provides the performance of the floater under real sea states under a wide range of operational conditions. The TLP-type floaters are observed to have maximum stability due to the unextendible mooring lines when installed in deep-sea conditions. Further, the axially rigid mooring lines ensure very small motions in heave, roll and pitch, and significant rigid body motion amplitudes are observed in the surge, sway, and yaw motion.

### 2.5.1 Natural Frequencies in the Installed Condition

The natural frequency is an essential factor that impacts how an offshore floating wind turbine platform responds to external loads like wind, waves, and currents. The frequency at which the platform will oscillate if disturbed by no external force is known as the natural frequency. It depends on the platform's stiffness, mass, and geometry. There are several methods to study the natural frequency of a system like the free decay test which involves measuring the platform's response to an initial disturbance and then analyzing the decay of the resulting motion. Also, analytical or numerical models that take the platform's hydrodynamic behaviour into account, such as its added mass and radiation damping can be used to determine the natural frequency of the system. In the present study, the natural frequency of rigid body motions of the FTLP and STLP (Han et al., 2017) wind turbine is calculated using the free decay test in FAST for still water level and the supported wind turbine in parked condition. In the case of each mode of rigid body motions, both the floating FTLP and STLP are released from a prescribed offset. The time history of this free decay is then used to compute the natural frequencies of rigid body motions of FTLP and STLP as in Table 2.13. Further, the natural

frequency of WindStar TLP is as in Zhao et al. (2012) is also compared with FTLP and STLP floater. The coupled floater and wind turbine avoids resonance with the environmental and turbine-induced excitations. The natural frequency in heave, roll and pitch motion for the WindStar TLP is chosen between 1-P and 3-P rotation frequency intervals. It is observed that the natural frequencies of both horizontal and vertical motions of the floating FTLP are very close compared to STLP and Windstar TLP. In addition, the resonance excited by the wave-frequency loads is higher for the FTLP floater compared to STLP and WindStar TLP.

Table 2.13: Natural Frequency (in Hz) of FTLP, STLP and WindStar TLP type FOWT platforms.

| FOWT Platforms | Surge | Sway | Heave | Roll | Pitch | Yaw |
|---|---|---|---|---|---|---|
| FTLP | 0.33 | 0.32 | 0.33 | 0.28 | 0.27 | 0.47 |
| STLP | 0.06 | 0.06 | 0.32 | 0.34 | 0.34 | 0.08 |
| WindStar TLP | 0.024 | 0.024 | 0.303 | 0.247 | 0.248 | 0.049 |

### 2.5.2 Comparison of Dynamic Responses of STLP and FTLP

The interaction of offshore floating wind turbine platforms with the wind and waves generates a range of dynamic motion responses. Hence it is important to understand the motion responses to design the platform to be flexible and able to respond to the changing environmental conditions. The maximum rigid body motions for the STLP and FTLP floaters under regular and irregular wave circumstances are derived in the case of combined wind and wave conditions, and they are compared as illustrated in Tables 2.14 and 2.15, respectively.

Table 2.14: Maximum values of rigid body motions for FTLP and STLP floater for regular wave conditions.

| Metocean Condition | Floater Model | Surge (m/m) | Sway (m/m) | Heave (m/m) | Roll (deg/m) | Pitch (deg/m) | Yaw (deg/m) |
|---|---|---|---|---|---|---|---|
| SS-1 | FTLP | 0.525 | 1.61 | 0.0562 | 0.000629 | 0.00251 | 0.05679 |
| | STLP | 0.8878 | 1.986 | 0.0672 | 0.00206 | 0.00337 | 3.67 |
| SS-2 | FTLP | 0.6803 | 1.229 | 0.2189 | 0.003183 | 0.001893 | 0.41267 |
| | STLP | 1.0949 | 5.0833 | 0.1904 | 0.00357 | 0.00234 | 5.24 |
| SS-3 | FTLP | 6.001 | 0.88424 | 0.05801 | 0.0006374 | 0.002459 | 0.056984 |
| | STLP | 1.4648 | 6.747 | 0.2947 | 0.004682 | 0.009343 | 6.82 |
| SS-4 | FTLP | 5.8858 | 0.7269 | 0.10589 | 0.0005219 | 0.002152 | 0.048924 |
| | STLP | 3.19 | 6.3939 | 0.1805 | 0.004848 | 0.007744 | 7.82 |

Table 2.15: Maximum values of rigid body motions for FTLP and STLP floater for irregular wave conditions.

| Metocean Condition | Floater Model | Surge (m/m) | Sway (m/m) | Heave (m/m) | Roll (deg/m) | Pitch (deg/m) | Yaw (deg/m) |
|---|---|---|---|---|---|---|---|
| SS-1 | FTLP | 0.5123 | 1.001 | 0.232 | 0.000945 | 0.0003577 | 0.2485 |
| | STLP | 1.129 | 0.77 | 0.346 | 0.0008611 | 0.00121 | 1.60 |
| SS-2 | FTLP | 3.194 | 0.2932 | 0.0238 | 0.00555 | 0.000958 | 0.7381 |
| | STLP | 1.269 | 1.215 | 0.0427 | 0.00124 | 0.00164 | 2.13 |
| SS-3 | FTLP | 1.631 | 0.325 | 0.0207 | 0.0002276 | 0.000777 | 0.01949 |
| | STLP | 1.529 | 1.075 | 0.0609 | 0.00255 | 0.001931 | 2.80 |
| SS-4 | FTLP | 1.838 | 0.376 | 0.0313 | 0.000264 | 0.000869 | 0.0255 |
| | STLP | 1.224 | 1.433 | 0.0718 | 0.002007 | 0.002001 | 4.22 |

For the regular sea wave conditions, the sway, heave, roll, pitch and yaw RAOs are minimal for the FTLP compared to the STLP for any wind speed conditions. But for surge RAOs, the values are observed to be minimum for FTLP for wind speed below 11.4 m/s (rated wind speed condition), and for wind speed conditions above the rated wind speed, the surge RAOs are higher for the FTLP compared to the STLP for regular sea waves. Further, the variation observed for yaw RAOs comparing FTLP and STLP concludes the better efficiency of the FTLP compared to the STLP for the wind power absorption. In the case of irregular sea wave conditions, the surge RAOs are higher for FTLP floater than STLP for 11.2 m/s, 14 m/s and 17 m/s wind speed conditions. The sway, heave, pitch, roll and yaw RAOs are observed to be lower for FTLP compared to STLP. Under real sea-state conditions, the variation in surge RAO is minimal for FTLP floater for higher wind speed conditions. The reduced RAOs for the FTLP floater are due to the additional two axially rigid mooring lines provided for the FTLP floater for seakeeping. In addition, the mass of the FTLP platform is observed to be doubled with the addition of two outer pontoons compared to the STLP floater resulting in reduced responses.

### 2.5.3 Dynamic Response Analysis of Hybrid Floating Systems

The dynamic motion response analysis aids in assessing the floating platform's structural integrity under various environmental factors, including waves, wind, and currents. It determines if the platform can bear extremely high loads and guarantees the structure will remain secure and safe for its operating life. Understanding the dynamic behaviour aids in designing robust and reliable platforms that withstand the forces developing on the floating system. The analysis is conducted for different operational wind speed conditions of 5 MW

wind turbines representing the northern North Sea condition. The rated wind speed at which a 5 MW floating wind turbine can produce its maximum power output is 11.4 m/s. The turbine begins to limit its power output when the wind speed surpasses this rated speed to protect its internal parts. The turbine and its support structure may experience large dynamic stresses at a wind speed of 14 m/s, which is high. To ensure the stability and safety of the platform under these circumstances, the floating wind turbine's design and mooring system must be able to handle these loads. The study thus presents the dynamic motion responses of the hybrid floating platform for 14 m/s wind speed and 3.6 m high gravity waves of wave period between 1 s and 25 s.

#### 2.5.3.1 Submerged Tension-Leg Platform Combined with Cone-cylinder WEC

The dynamic analysis of the STLP-type floating wind turbine combined with cone-cylinder WEC is investigated for different circular arrangements. The study is performed to analyse the Response Amplitude Operators (RAOs) for the translation and rotational motions of the hybrid floating wind-wave system. The RAOs are conventionally frequency response functions defined as the ratio of system responses to wave elevation. The RAOs give the idea of the motion amplitude of the system for unit wave elevation. RAOs are important in the preliminary design stage of offshore floating platforms for wind turbines, considering the hydrodynamic load, aerodynamic load, structural dynamics and control dynamics. In Fig. 2.7(a-c), the surge, sway and heave translational motions of the combined STLP-WEC system for 14 m/s wind speed and 3.6 m wave height are analysed for different numbers of WECs. The surge RAO for the different configurations of the combined system is discussed in Fig. 2.7(a). It is observed that the addition of WECs influences the surge motion amplitudes. The peak value for surge motion of the STLP floater increased with the addition of WECs. The surge motion amplitude is also observed to increase with the increase in wind speed and wave height.

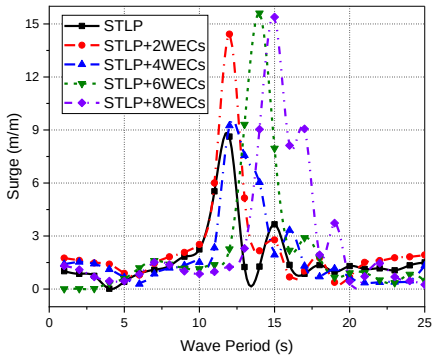


(a)

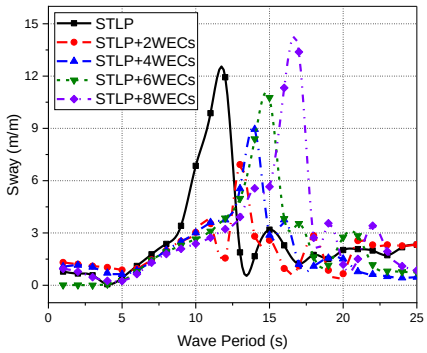


(b)

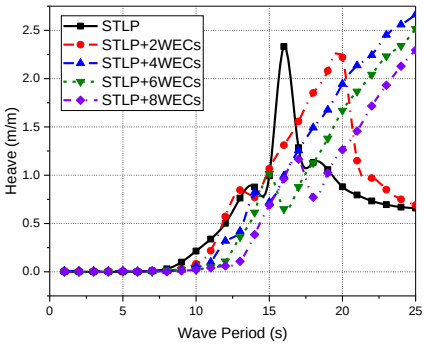


(c)

Fig. 2.7: RAOs for (a) Surge (b) Sway and (c) Heave for 14 m/s wind speed

Apart from the peak value, the surge motion amplitudes for STLP+6WECs and STLP+8WECs are minimal for waves of wave period less than 11.3 s. The wave period 11.3 s represents the waves generated by wind speed 25 m/s (cut-out wind speed for 5 MW reference wind turbine) for North Atlantic Sea. The sway motion (Fig. 2.7b) follows a similar trend as the surge response, and the sway motion amplitude tends to increase with the increase in wind speed and wave height. It is observed that the motion amplitudes of heave are having a very negligible impact on the wave and wind as the tensioned tendons have provided extra stability in that direction. Further, in Fig. 2.7(c), it is also observed that the heave motion amplitude slightly increases for the waves of a higher wave period. Also, it is evident from Fig. 2.7(a-c) that the motion amplitude is minimum for the STLP+6WECs for the gravity waves.

The Fig. 2.8(a-c) shows the rotational motion amplitudes for different configurations of the combined system for the 14 m/s wind speed metocean condition. The values of the motion amplitude tend to have only a very slight increase with the addition of WECs. The roll motion amplitude is observed to have higher peak values with the addition of WECs for the waves of higher wave periods as seen in Fig. 2.8(a). The variation in pitch motion with the addition of WECs is noted in Fig. 2.8(b), and the peak values slightly increased for waves of wave period higher than 16s. The yaw response (Fig. 2.8c) for this operational condition is very high when the wave period is more than 10 s, and the values of the yaw motion amplitude tend to increase with the increase in wave period. The yaw motion amplitude is very high compared to other responses of the hybrid STLP-WEC system. The reduced value of roll motion is due to the symmetry of the systems considered and is observed to be well below 0.4 deg/m, which indicates the stability of the hybrid system against wind and wave. For the different metocean conditions studied, the surge and pitch response for $V_{mean} = 8\ m/s$ is very minimal for the

STLP+6WECs configuration for the majority of the wave period conditions. Whereas for 11.2 m/s, 14 m/s, and 17 m/s wind speed conditions, the surge motion is observed to be minimum for both STLP+6WECs and STLP+8WECs configuration for waves of wave periods, $T_p < 11.3\ s$. But the pitch motion is observed to be higher for the STLP+8WECs configuration compared to the STLP+6WECs configuration and the pitch motion is observed to be minimum for the STLP+2WECs configuration. Comparing four different arrangements of WECs around STLP, STLP+6WECs configuration is observed to have optimum values for the surge and pitch motion.

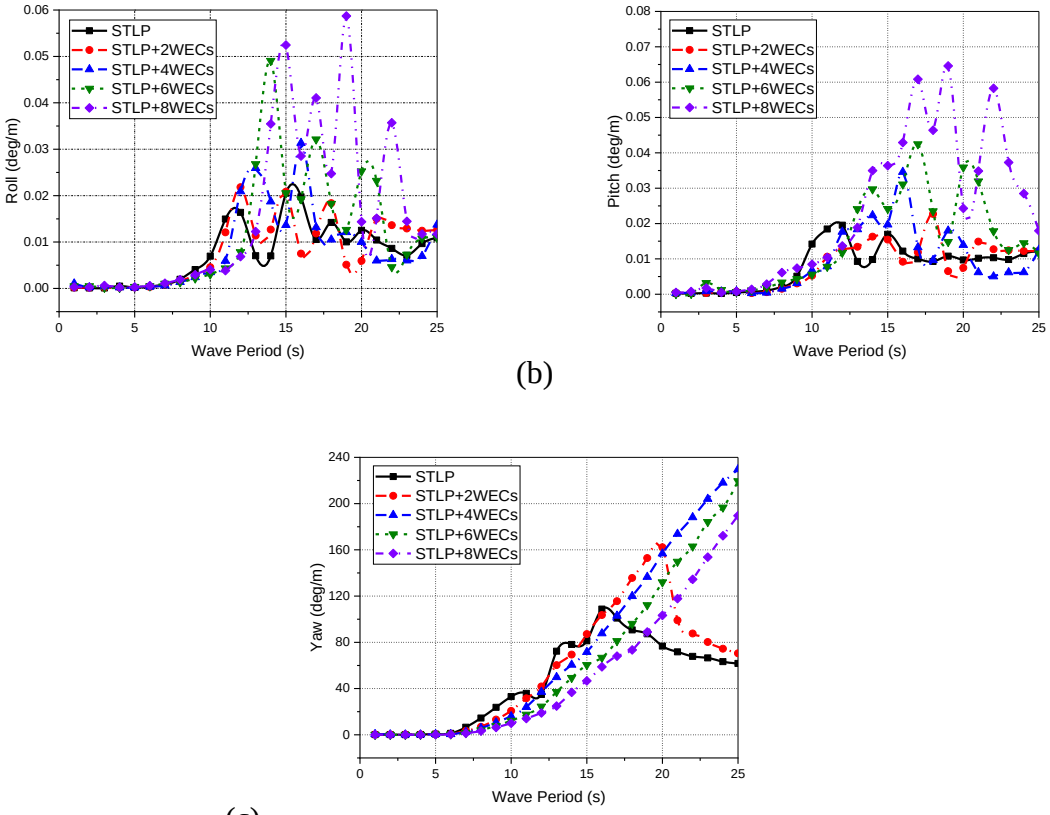


Fig. 2.8: RAOs for (a) Roll (b) Pitch and (c) Yaw for 14 m/s wind speed

The stability and control of a TLP are directly impacted by surge and pitch motions. Pitch motion is the rotation of the platform around the transverse axis, whereas surge motion is the linear movement of the platform along the horizontal axis. The platform's ability to retain stability and control in the face of various external factors, including wind and waves, can be evaluated by analysing these responses. Further, the surge and pitch motion determine the proper orientation of the wind turbine towards the wind direction for higher efficiency of the 5 MW reference wind turbine. Also, the dynamic loads that the wind turbine and the structural

elements of the platform are subjected to are closely correlated with the surge and pitch responses. Increased dynamic stresses on the turbine tower, blades, and other structural elements may result from excessive surge and pitch motions.

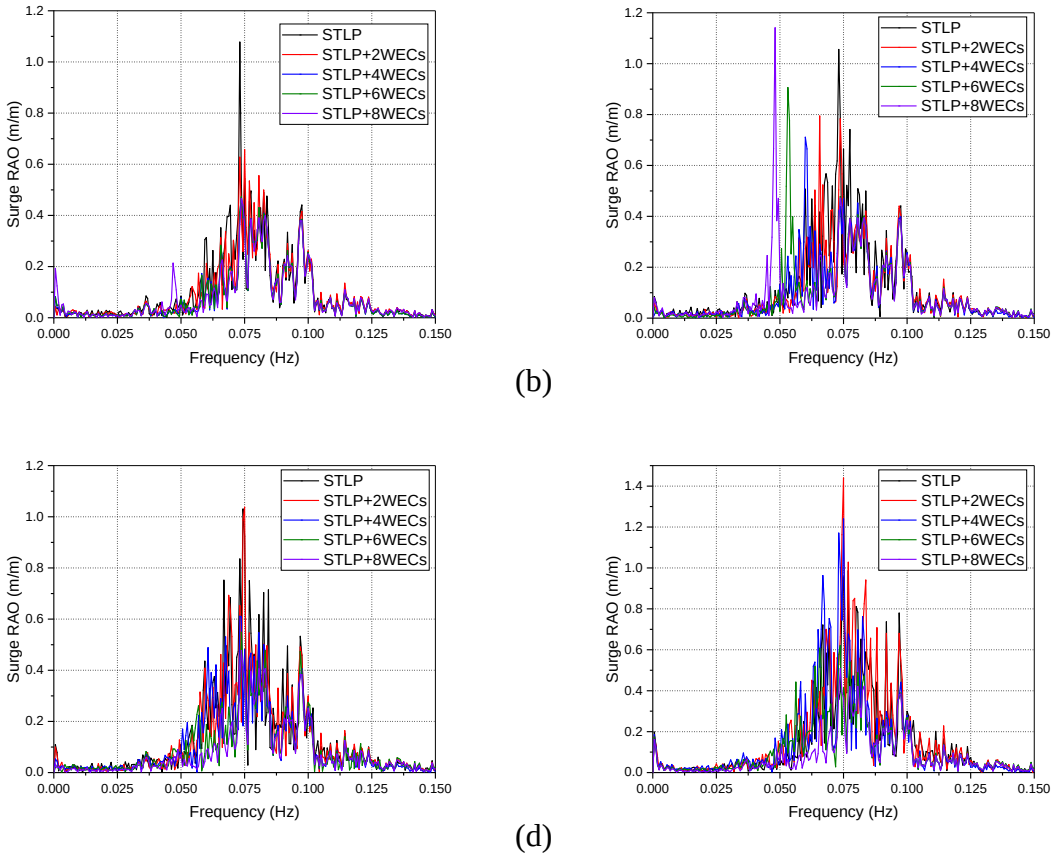


Fig. 2.9: Surge response spectra for different configurations of combined STLP floater for (a) SS-1 (b) SS-2 (c) SS-3 and (d) SS-4 under irregular sea waves.

Further, the study discusses the response spectra for the dominant rigid body motions surge, sway and yaw motions for five different configurations of the STLP combined with point absorber-type WECs under irregular wave conditions. Fig. 2.9(a-d) shows the surge response motion for different metocean condition. The motion amplitudes are higher for the $V_{mean} = 17\ m/s$ wind speed condition (SS-4) and are minimum for the $V_{mean} = 14\ m/s$ wind speed condition (SS-3). Fig. 2.9(a) shows the surge motion amplitude for SS-1 for different WEC configurations studied. The responses are observed to decrease with the addition of the WECs. The maximum surge motion amplitude is observed for the frequency range $0.06 < \omega < 0.12\ rad\ s^{-1}$. The natural frequency of the STLP is 0.06 rad/s, and hence proper design methods have to be provided to avoid resonance of the hybrid system as the wave frequency and natural frequency for the system are observed to be very closer. For the SS-1

condition, the wave frequency regions for the hybrid configurations are much closer, when compared to other metocean conditions. Fig. 2.9(b) shows the surge RAO comparing different arrangement patterns of STLP for the SS-2 condition. The wave frequency regions for the hybrid configurations are observed to be moving away from the wave frequency region of the STLP with the increase in the number of WECs. Thus, the possibility of the occurrence of the resonance decreases with the addition of the WECs for the $V_{mean} = 11.2\ m/s$ metocean condition. The maximum value of surge RAO is minimal for the STLP+4WECs configuration.

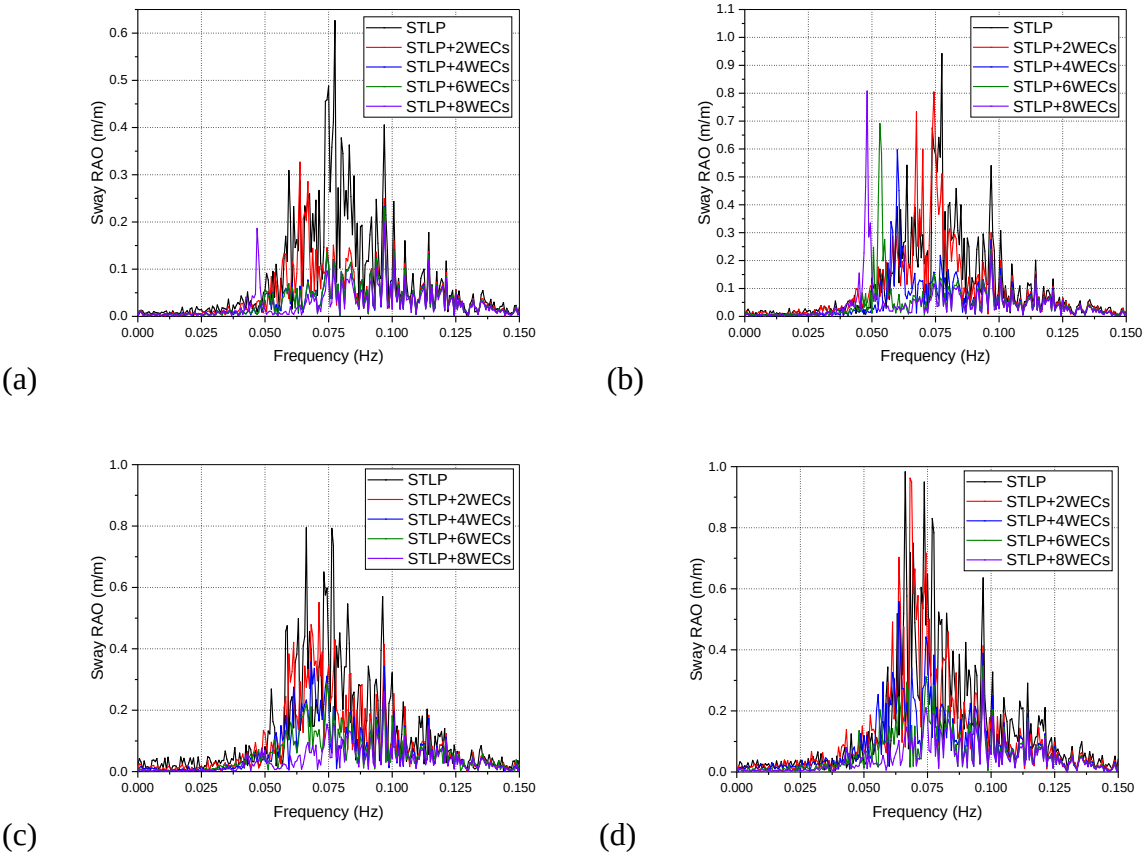


Fig. 2.10: Sway response spectra for different configurations of combined STLP floater for (a) SS-1 (b) SS-2 (c) SS-3 and (d) SS-4 under irregular sea waves.

Fig. 2.9(c) shows the surge RAO for $V_{mean} = 14\ m/s$ metocean condition (SS-3). Similar to the SS-1 condition, the wave frequency regions for the STLP and the hybrid STLP-WECs are much closer to the natural frequency region. Further, proper design methods should be adopted to avoid the resonance condition. Apart from the STLP+2WECs configuration, the responses are observed to decrease by adding WECs. Further, the responses are observed to increase with the increase in the wind speed condition (Fig. 2.9d). For most metocean conditions, the surge RAO is minimum for the STLP+6WECs configuration. The reduced surge RAO for the hybrid

configurations ensures better orientation of the wind turbine for better wind power absorption. Also, the dynamic loads on the turbine tower, blades, and other structural elements are minimum for the hybrid system, further reducing the tension developed on the mooring cables for the hybrid STLP-WECs system. The performance of the wind turbine can be impacted by lateral platform vibrations in the relative wind direction and velocity. To maximise the efficiency of power generation, the turbine layout, yaw control systems, and other operational characteristics can be improved by the analysis of sway response.

Fig. 2.10(a-d) shows the surge RAO for different metocean conditions comparing STLP and different hybrid STLP-WEC floating platforms. Similar to the surge motion, the natural sway frequency for the STLP is 0.06 rad/s. The wave frequency for the hybrid system for different metocean conditions is very close to 0.06 rad/s and has a higher possibility of occurrence of resonance as seen in Fig. 2.10(a-d). Fig. 2.10(a) shows the sway RAO for the metocean condition SS-1. The sway RAO is much higher for the single STLP floating system compared to the hybrid STLP-WEC.

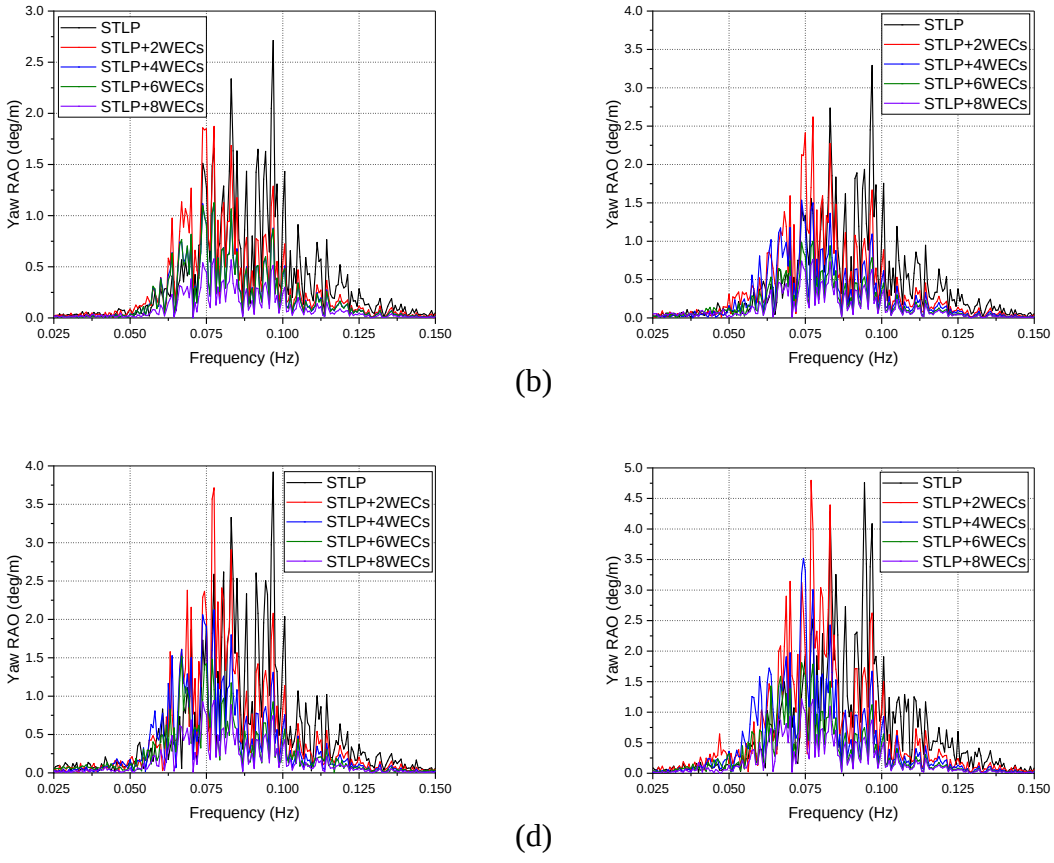


Fig. 2.11: Yaw response spectra for different configurations of combined STLP floater for (a) SS-1 (b) SS-2 (c) SS-3 and (d) SS-4 under irregular sea waves.

The minimum sway RAO is observed for STLP+8WECs configuration. The higher variation in sway RAO is observed for the frequency region $0.05 < \omega < 0.125\ rad\ s^{-1}$. For $V_{mean} = 11.2\ m/s$, a shift in wave frequencies (Fig. 2.10b) is observed with the addition of the WECs similar to that in the surge response. The maximum motion amplitudes for the hybrid systems are higher for SS-2 metocean conditions. The excessive sway platform motion causes underwater noises, disturbing marine life and may also cause sediment resuspension. Further, increased wind speed has minimum influence on the sway motion response (Fig. 2.10(c,d)). The maximum motion amplitudes are close to 0.9 m/m for the STLP and are observed to decrease with the addition of the WECs. The wave frequencies for the hybrid systems are observed to be much closer to the natural frequency region (0.06 rad/s).

Yaw motion describes how the wind turbine rotates around its vertical axis to face the direction of the predominant wind. In order to maintain the wind turbine's appropriate alignment with the wind and maximise power generation efficiency, it is essential to analyse the yaw reaction. The TLP's yaw control system must be designed and optimised using the yaw motion response analysis. The sensors, actuators, and control algorithms in the yaw control system make sure the wind turbine maintains the appropriate yaw angle. Yaw rate, response time, and angle limitations can all be improved with the help of analysing the yaw response. It guarantees precise and effective yaw motion control, maintaining turbine alignment and increasing power output. Fig. 2.11(a-d) shows the yaw motion response comparing the STLP and STLP-WEC hybrid concepts for different metocean conditions. The yaw motions are higher compared to the other rotational motions. Similar to the surge and sway translational motions, the wave frequency of the yaw motion is also much closer to the natural frequency region (0.08 rad/s). Minimum yaw motion is observed for the SS-1 metocean condition (Fig. 2.11a) and is observed to increase with the increase in the wind speed (Fig. 2.11 (b-d)). For any metocean condition, the variation in the yaw motions is much higher in the frequency region $0.06 < \omega < 0.125\ rad\ s^{-1}$. Also, the wave frequency region for the hybrid platforms is shifted away from the natural frequency region of STLP with the addition of WECs for the yaw motion response. Also, the higher magnitude of yaw RAO is observed for STLP+2WECs and the minimum value is observed for STLP+6WECs. The reduced yaw motion ensures a proper working platform for installation and maintenance purposes. Also, reduced yaw motion increases the life of the structural components as it is subjected to minimum fatigue load.

#### 2.5.3.2 Frustum Tension-Leg Platform Combined with Cone-cylinder WEC

The six degrees of freedom for the FTLP and hybrid FTLP-WEC are studied to understand the dynamic behaviour of the platforms under wind and wave conditions. Fig. 2.12(a-c) shows the translational motion of the floating system under 14 m/s wind speed and 3.6 m high gravity waves. Fig. 2.12(a) shows the surge RAO for the FTLP and hybrid FTLP-WEC system. Apart from the single FTLP, the variation of responses for the hybrid system is observed to be similar. The peak value of the surge response is observed to be higher for the hybrid platforms. But for most gravity waves, the surge responses are minimal for the hybrid platforms compared to single FTLP. The surge RAO is higher compared to other translation motions of the floating system. The TLP platforms are generally designed to restrain the vertical motions, hence having minimum resistance to lateral forces, further having higher surge RAO. The hybrid platforms with reduced surge RAO will have better wind power absorption efficiency than a single FTLP.

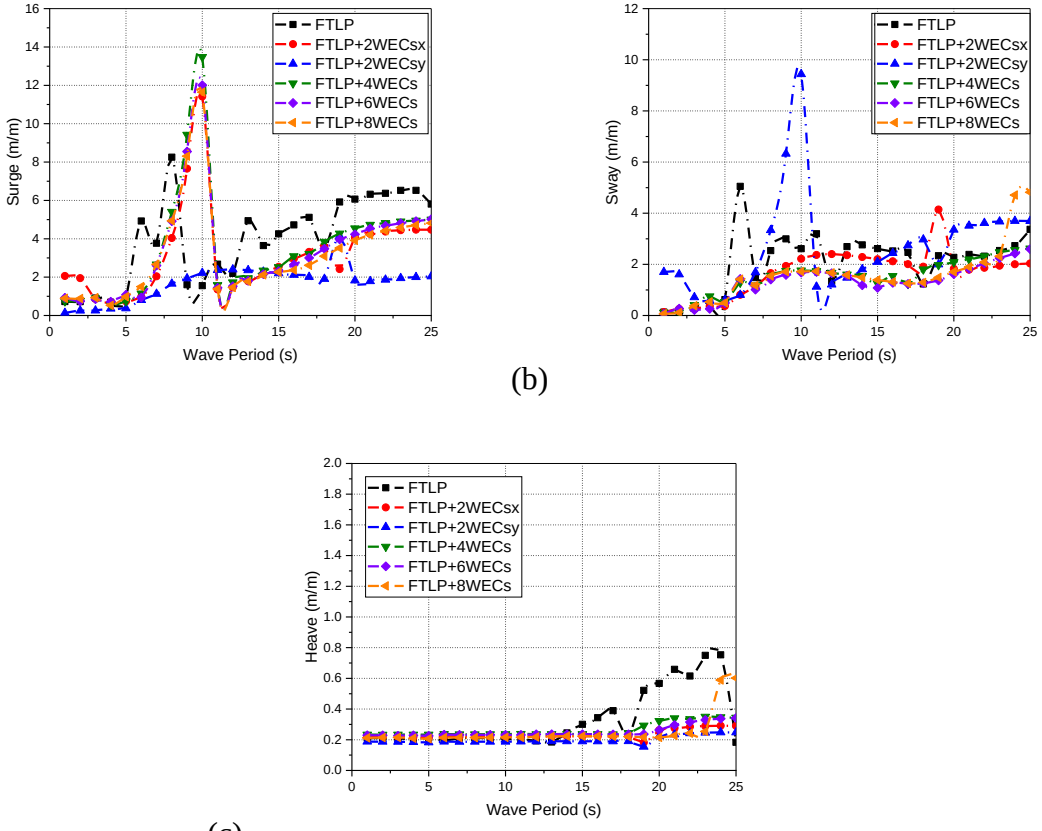


(a) (b)

(c)

Fig. 2.12: RAOs for (a) Surge (b) Sway and (c) Heave for 14 m/s wind speed.

FTLP+8WECs configuration has minimum surge RAO, possibly due to higher stiffness provided to the outer columns with the addition of the WECs. The FTLP+2WECsy has minimum surge RAO (Fig. 2.12a), which may be due to the position of the WECs, kept in the

direction perpendicular to the action of wind and wave. As seen in Fig. 2.12(b), the sway motion is very high for the FTLP+2WECsy configuration, though other hybrid platforms have reduced sway motion compared to a single FTLP. The sway motion is also observed to be minimum for the FTLP+8WECs configuration for any gravity waves. The environmental impact can be minimised by reducing the sway motion reaction. It supports environmental sustainability in offshore wind platform regions and reduces noise levels and disturbance to marine ecosystems. Fig. 2.12(c) shows the heave motion RAO for the different arrangements of WECs around FTLP. The variation of heave motion is minimal for the gravity waves of wave periods lower than 20 s. For waves of the period higher than 20 s, a slight increase in heave motion is observed. Further, the heave motion is observed to be reduced with the addition of the WECs. Similar to other translational motions, the heave response is also minimal for the FTLP+8WECs configuration.

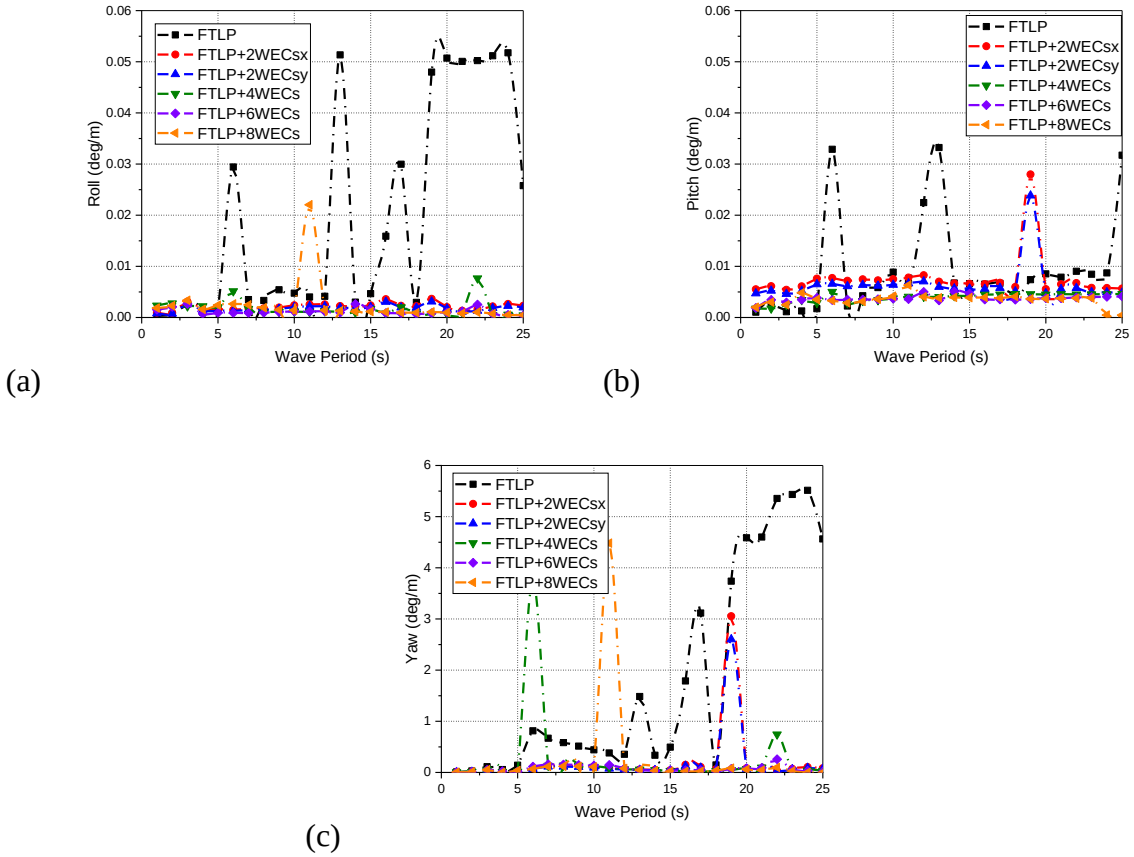


Fig. 2.13: RAOs for (a) Roll (b) Pitch and (c) Yaw for 14 m/s wind speed.

Fig. 2.13(a-c) shows the rotational motions of the FTLP and hybrid FTLP-WEC for the gravity waves of 3.6 m wave height under 14 m/s wind speed. The rotational motions are very small for the floating system. Fig. 2.13(a) shows the roll RAO of the system. The roll RAO is below

0.4 deg/m for any gravity waves, further having higher stability against overturning. The roll motion is further reduced with the addition of the WECs. The variation of the roll RAO is also observed to be minimum for the hybrid system. Fig. 2.13(b) shows that the pitch RAO is also reduced with the addition of the WECs. Minimum roll and pitch motion is observed for FTLP+8WECs configuration for any gravity waves. Fig. 2.13(c) shows the yaw RAO for FTLP and hybrid FTLP-WEC. The yaw motions are very higher for the floating system compared to roll and pitch rotational motions. The addition of the WECs has a higher impact on the yaw motion, as it is observed that the Yaw RAOs are decreased for the hybrid FTLP-WEC systems compared to single FTLP. The FTLP+8WECs configuration is observed to have minimum yaw motion, apart from a yaw value for wave period 11 s. The performance of the combined floating system under real sea states is investigated and presented for irregular wave conditions.

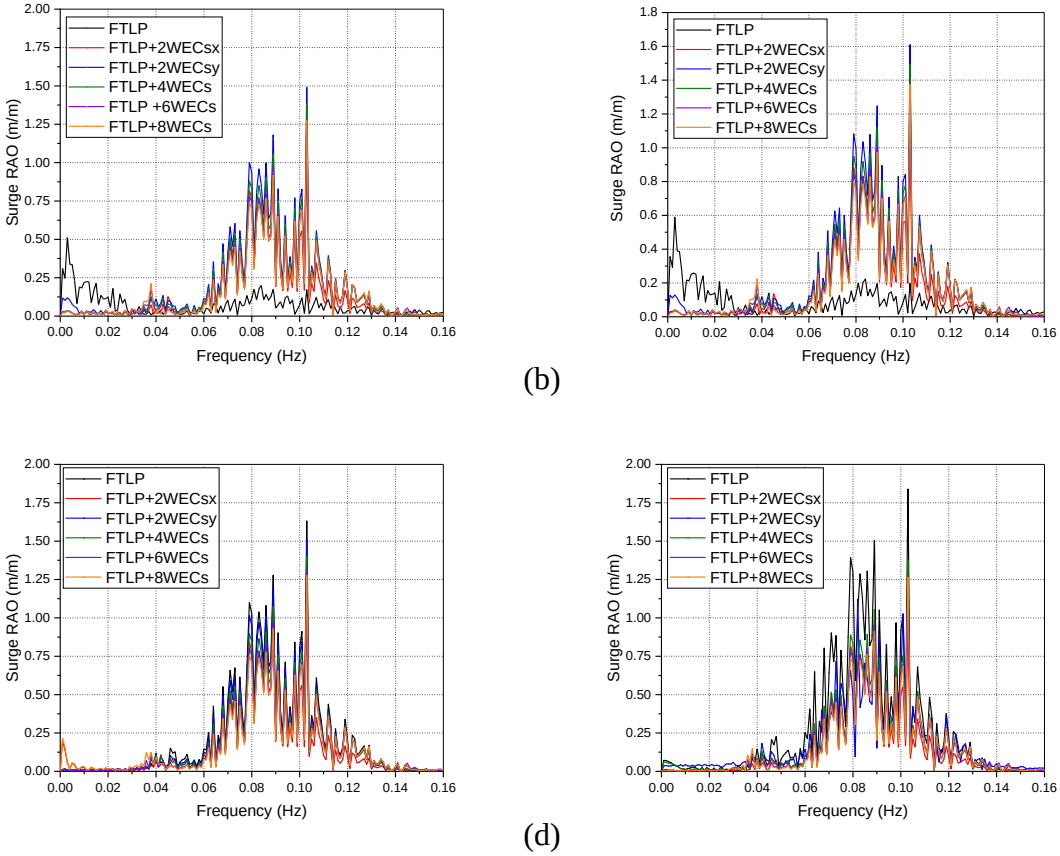


Fig. 2.14: Surge response spectra for different configurations of combined floater for (a) SS-1 (b) SS-2 (c) SS-3 and (d) SS-4 under irregular sea waves.

The RAOs are calculated for four different wind speed conditions corresponding to the operational conditions of the 5 MW wind turbine and for zero-degree wave heading angle. The zero-degree wave corresponds to the wave originating from the negative x-direction. The

axially rigid mooring cables for the FTLP ensure minimum vertical motion (heave), forward inclination (roll) and sideways inclination (pitch). Further, the study discusses the dominant rigid body motions surge, sway and yaw motions for six different configurations of FTLP combined with point absorber-type WECs. The response spectra of surge motion for four different wind speed conditions are presented in Fig. 2.14(a-d). Surge RAO for zero-degree wave heading angle is observed to be maximum for SS-4 condition as in Fig. 2.14(d) and minimum for SS-1 condition as in Fig. 2.14(a). For all wind speed conditions, the surge RAO is observed to have maximum amplitude for the frequency range $0.06 < \omega < 0.12\ rad\ s^{-1}$. In Fig. 2.14(a-d), it is observed that the wave frequency for any configuration of the hybrid platform is around the frequency range $0.08 < \omega < 0.10\ rad\ s^{-1}$, further allowing the platform to stay away from the resonance as the natural surge frequency for the FTLP and the hybrid FTLP-WEC is around the frequency range $0.31 < \omega < 0.33\ rad\ s^{-1}$. The surge response is also observed to be minimum for wind speed conditions closer to the rated wind speed of a 5 MW wind turbine, further showing the better orientation of the wind turbine towards wind direction for better power performance. In addition, the hybrid FTLP+8WECs is observed to have minimum values for surge responses compared to other hybrid configurations. The study observed the lowest value of Surge RAO for the FTLP in the case of wind speed conditions below the rated wind speed. With the addition of the WECs, the surge RAO is increasing for the FOWT system. This is due to the reduced aerodynamic forces on the tower and the nacelle system.

Sway response spectra for four different wind speed conditions are presented in Fig. 2.15(a-d). Similar to the surge response, the peak is observed around $0.10 < \omega < 0.11\ rad\ s^{-1}$ for FTLP and hybrid FTLP-WEC configurations.

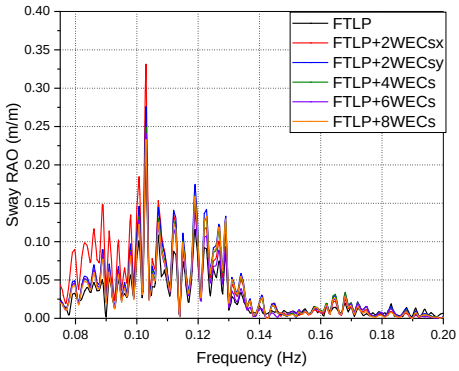


(a)

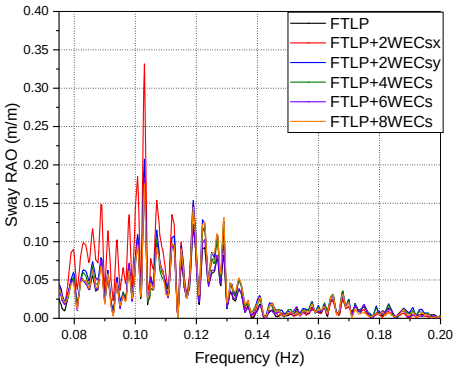


(b)

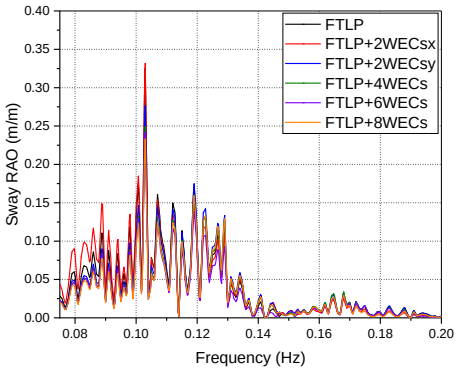


(c)

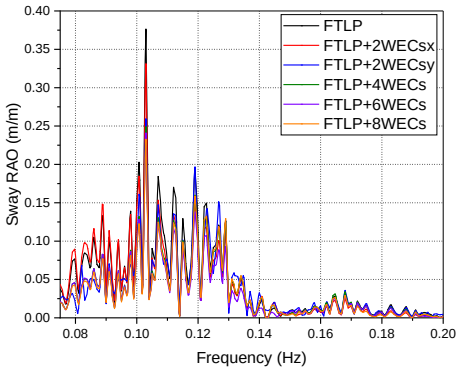


(d)

Fig. 2.15: Sway response spectra for different configurations of combined floater for (a) SS-1 (b) SS-2 (c) SS-3 and (d) SS-4 under irregular sea waves.

The sway response pattern for any wind speed condition is observed to be similar and the maximum sway response amplitude is observed for hybrid FTLP+2WECs in the direction of the wave for 8 m/s, 12 m/s and 14 m/s wind speeds as in Fig. 2.15(a-c), respectively. In the case of 17 m/s, wind speed, the FTLP is observed to have a higher sway value under wind and wave loading as in Fig. 2.15(d). Similar to surge motion, the addition of WECs has suppressed the sway response of the FTLP as in Fig. 2.15(a-d), further improving the stability of the platform against wind and waves. From Fig. 2.15(a-d), the wave frequency of the FTLP and the hybrid FTLP-WEC configurations are observed around the frequency range $0.10 < \omega < 0.11\ rad\ s^{-1}$, which is away from the natural frequency range $0.31 < \omega < 0.33\ rad\ s^{-1}$, further reducing the possibility of resonance in sway.

Yaw response spectra for four different wind speed conditions are presented in Fig. 2.16(a-d). The yaw response amplitude is observed to be lower for a zero-degree wave heading angle and for every wave direction. Further, with no excitation in yaw, the yaw motion response is due to the coupling with other degrees of freedom.

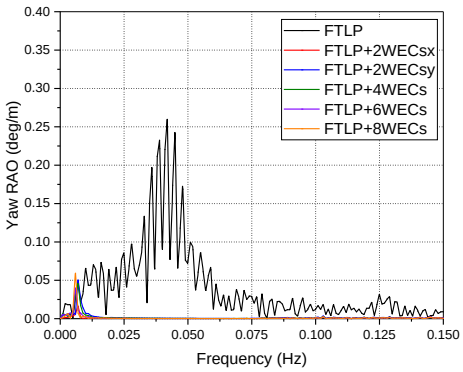


(a)

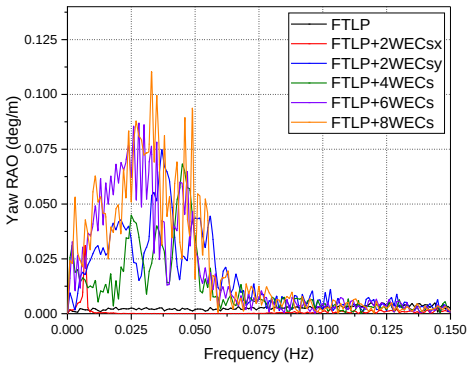


(b)

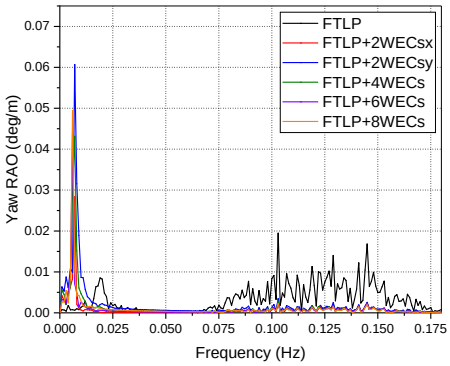


(c)

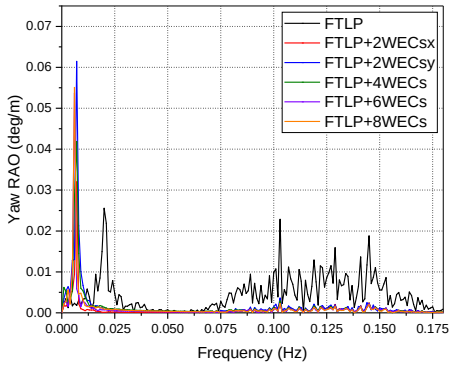


(d)

Fig. 2.16: Yaw response spectra for different configurations of combined floater for (a) SS-1 (b) SS-2 (c) SS-3 and (d) SS-4 under irregular sea waves.

Similar to other horizontal motions, the yaw motion response for FTLP is also suppressed with the addition of WECs as in Fig. 2.16(a,c,d). In the case of 11.2 m/s wind speed, the yaw response for the hybrid floater is observed to be higher compared to the single FTLP floater (Fig. 2.16b). The peak yaw motion amplitudes for the FTLP and hybrid FTLP-WEC are observed around the frequency range $0.025 < \omega < 0.05\ rad\ s^{-1}$, is much lower than the yaw natural frequency range $0.46 < \omega < 0.48\ rad\ s^{-1}$, reducing the chances of occurrences of resonance in yaw motion. For most operational conditions, minimum yaw motion amplitude is observed for hybrid FTLP+2WECsx configuration and maximum amplitude for hybrid FTLP+2WECsy as in Fig. 2.16(a-d). The study observed a higher yaw response value for the FTLP compared to the hybrid concepts. Further, the yaw response is observed to be reduced with the addition of WECs for the lowest wind speed condition of 8 m/s. In addition, the natural frequency of the FTLP is also shifted towards the lower frequency region with the addition of the WECs. The higher yaw response for the FTLP may be due to the coincidence of the natural period resonance region with the wave resonance region. A similar coincidence was not observed for other sea state conditions, as there is a shift in regions of natural frequency and wave excited frequency.

### 2.5.4 Tower Base Forces and Moments

The platform motions and the wind load acting on the turbine blades generate forces at the base of the wind turbine, namely, fore-aft shear force, side-to-side shear force and the vertical force in x, y and z directions, respectively. These forces at the base generate moments, namely, the side-to-side bending moment, fore-aft bending moment and the yaw moment in the x, y and z-

direction. The forces and moments developed at the tower-platform junction have contributions from gravity, aerodynamics, inertia, and hydrodynamic loads. The study gives insight to the influence of the wind and wave loading to the turbine tower and hence the performance of the combined system.

### 2.5.4.1 Submerged Tension-Leg Platform Combined with Cone-cylinder WEC

The shear forces developing on the base of the turbine tower have the influence of wind load, wave load and the platform motions. It is essential to properly analyse and take into account these shear forces when building a stable and structurally sound floating wind turbine platform. Fig. 2.17(a-c) shows the forces developed at the turbine's base for the combined STLP-WEC configurations for a wind velocity of 17 m/s and 4.2 m wave height representing the extreme operating conditions of the 5 MW wind turbine supported on STLP. The forces developed for the extreme operating conditions are almost equal to those generated for the rated wind speed conditions. As the study considers regular waves in the x-direction with a zero-degree wave heading angle, a higher fore-aft shear force is obtained (Fig. 2.17a).

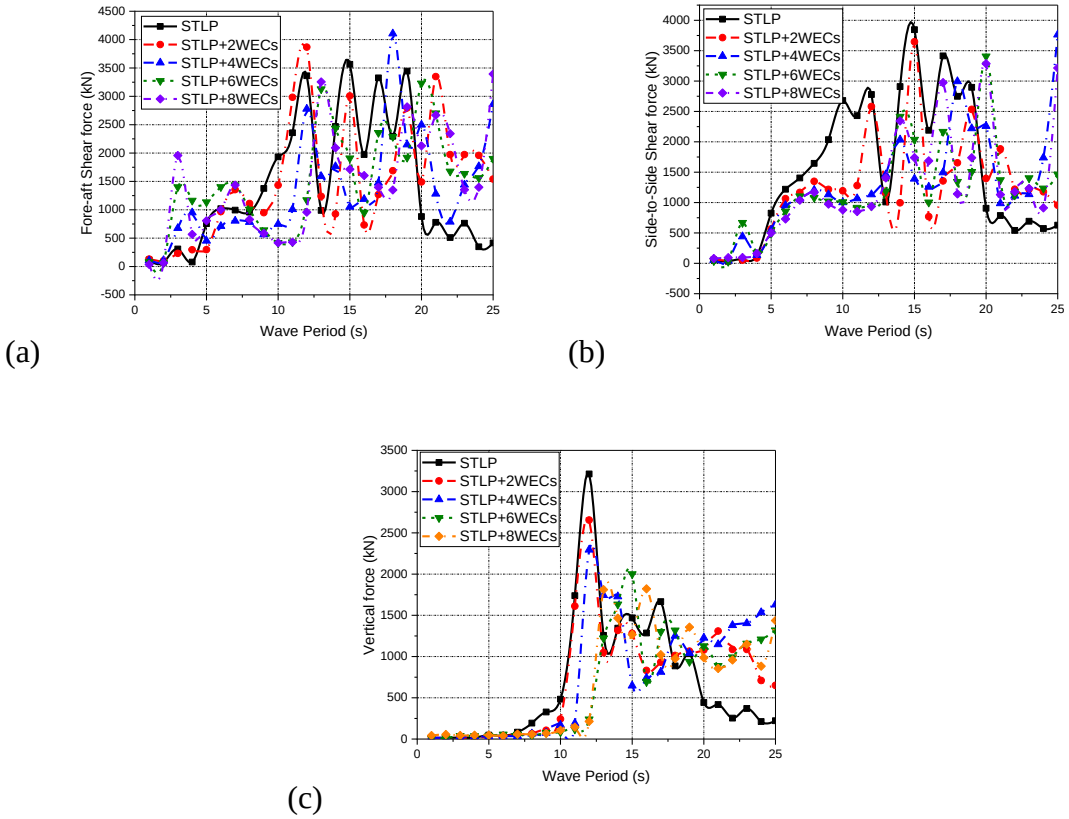


Fig. 2.17: Comparison of (a) for-aft shear force (b) side to side shear force and (c) vertical shear force for different arrangement of WECs.

Fig. 2.17(b,c) shows that the side-to-side shear force and the vertical shear force are minima for the STLP+6WECs, which can be attributed to the minimum inertial load developing on the wind turbine. Also, the variation of the shear force in the x-direction is minimal for the STLP+6WECs than STLP+8WECs, which have minimum fore-aft shear force.

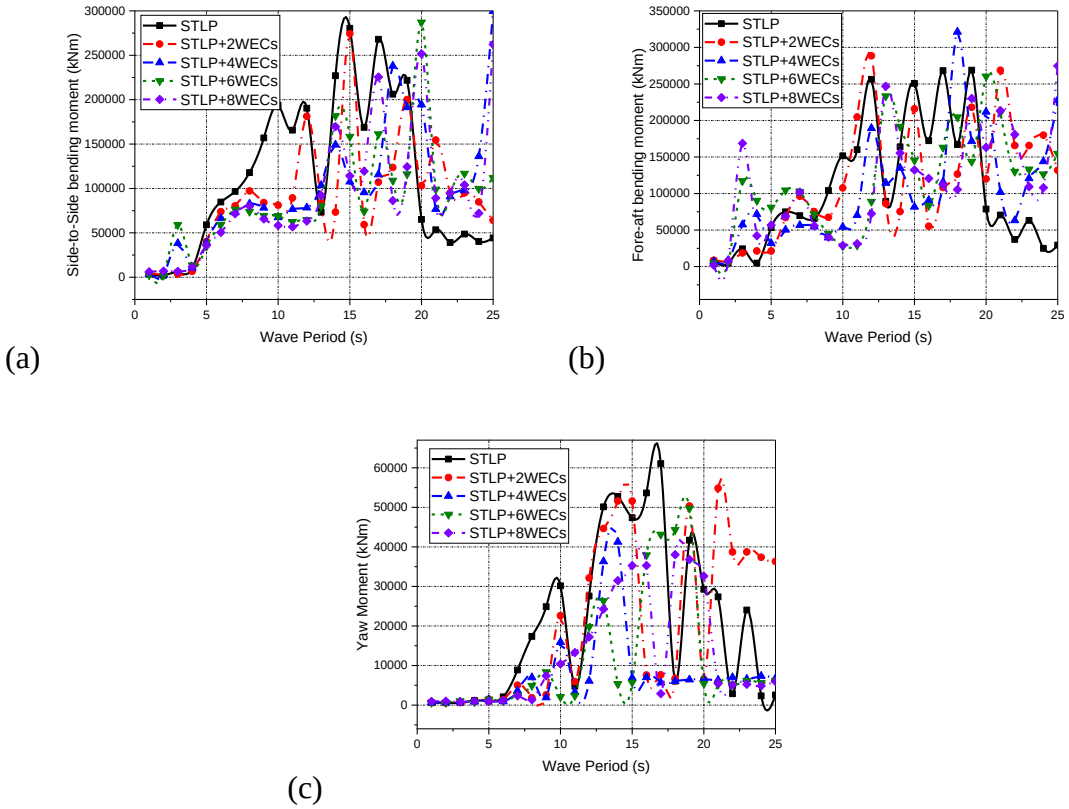


Fig. 2.18: Comparison of (a) side to side bending moment, (b) for-aft bending moment and (c) yaw moments for different arrangement of WECs.

Fig. 2.18(a-c) shows the moments generated at the turbine's base for the hybrid system for 17 m/s wind speed and 4.2 m wave height. From Fig. 2.18(a-c), the moments in all three directions developed for the STLP+6WECs configuration are minimal for most wave periods. Also, it is observed that the moments developed in the y-direction are higher when compared with those developed in the other two directions. The effect of wind and wave on the tower base bending moments is minimal, as the study shows a slight variation in the values of moments developed with an increase in wind speed. The minimum value of forces and moments for the STLP+6WECs configuration ensures better wind energy capture for the hybrid system.

The dynamic behaviour and load characteristics of a floating wind turbine can be better understood by looking at the power spectral density (PSD) of the fore-aft and side-to-side shear force developing at the base of the turbine tower. The PSD defines the distribution of the energy

in the frequency domain. Further, the PSD gives a clear idea about the dominant frequency ranges contributing to the shear forces developing at the turbine. Fig. 2.19(a-d) shows the power spectral density for the fore-aft shear force for four different operating conditions of the wind turbine. The study observes similar spectrum distribution for any operational condition. The dominant forces are closer to the natural frequency region of the floating system and hence proper damping mechanism has to be adopted to avoid resonance. For conditions below the rated wind speed (Fig. 2.19(a,b)), the wave frequency region of the hybrid platforms STLP+6WECs and STLP+8WECs are away from the natural frequency region (0.06 rad/s) compared to other configurations studied. Further, the fore-aft forces are observed to decrease with the increase in the wind speed. The load distribution is observed to be uniform (Fig. 2.19(c,d)) for the frequency range $0.1 < \omega < 0.4\ rad\ s^{-1}$ and is minimal for frequency regions below 0.05 rad/s.

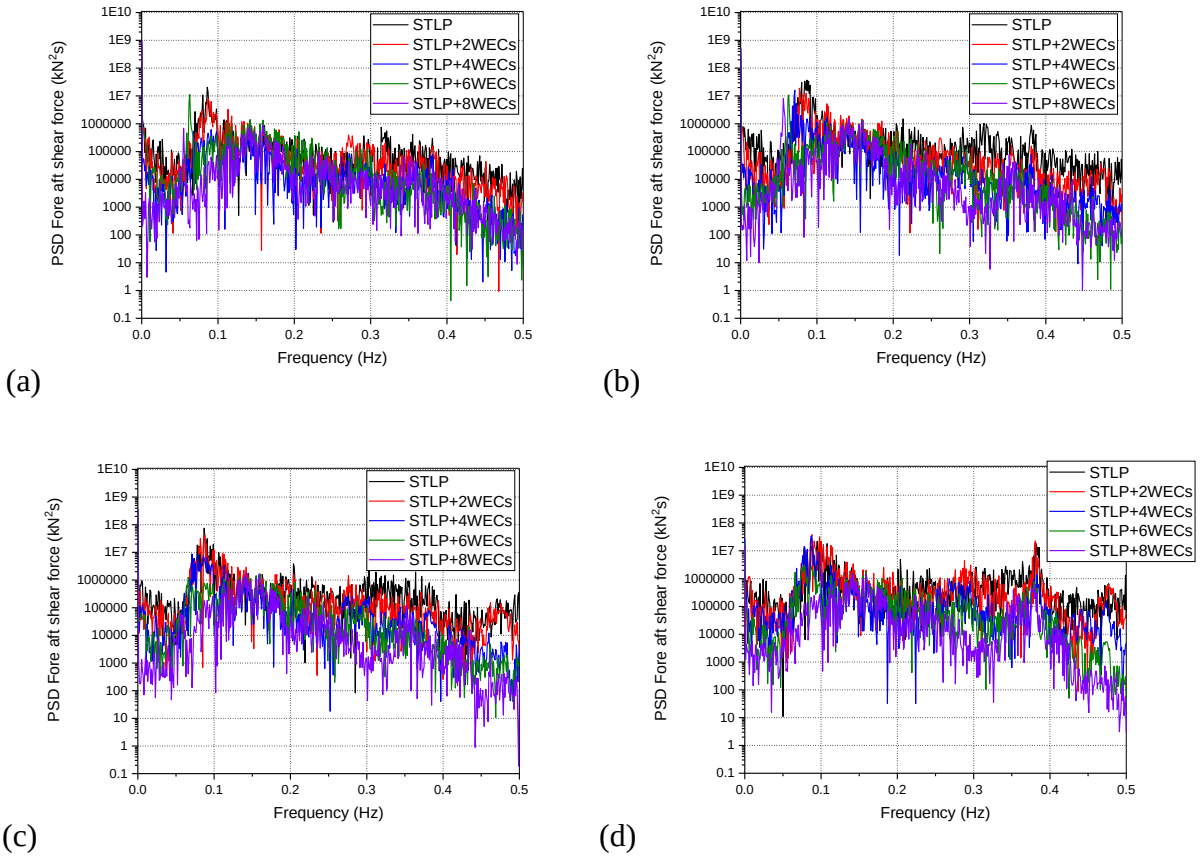


Fig. 2.19: Power spectral density for fore-aft shear force at (a) SS-1 (b) SS-2 (c) SS-3 and (d) SS-4 sea-state considering different configurations of combined floater for irregular waves.

Fig. 2.20(a-d) shows the PSD for the side-to-side shear force developing on the base of the floating wind turbine. The amplitude for the PSD shows that the side-to-side forces developed

are small compared to the fore-aft shear forces developed. Also, higher variation in load distribution is observed (Fig. 2.20(a,b)) for the side-to-side shear forces for wind speed conditions below 11.4 m/s. Also, the forces are minimum for the frequency ranges $\omega < 0.06\ rad\ s^{-1}$ and $\omega > 0.4\ rad\ s^{-1}$. The variation in forces developed for higher wind speed conditions (Fig. 2.20(c,d)) is minimum for $0.1 < \omega < 0.4\ rad\ s^{-1}$. The minimum variation in forces improves the fatigue life of the turbine components. Further, similar to the fore-aft shear forces, the wave frequency ranges for the side-to-side shear forces are also near the natural frequency and hence proper damping should be provided to prevent resonance.

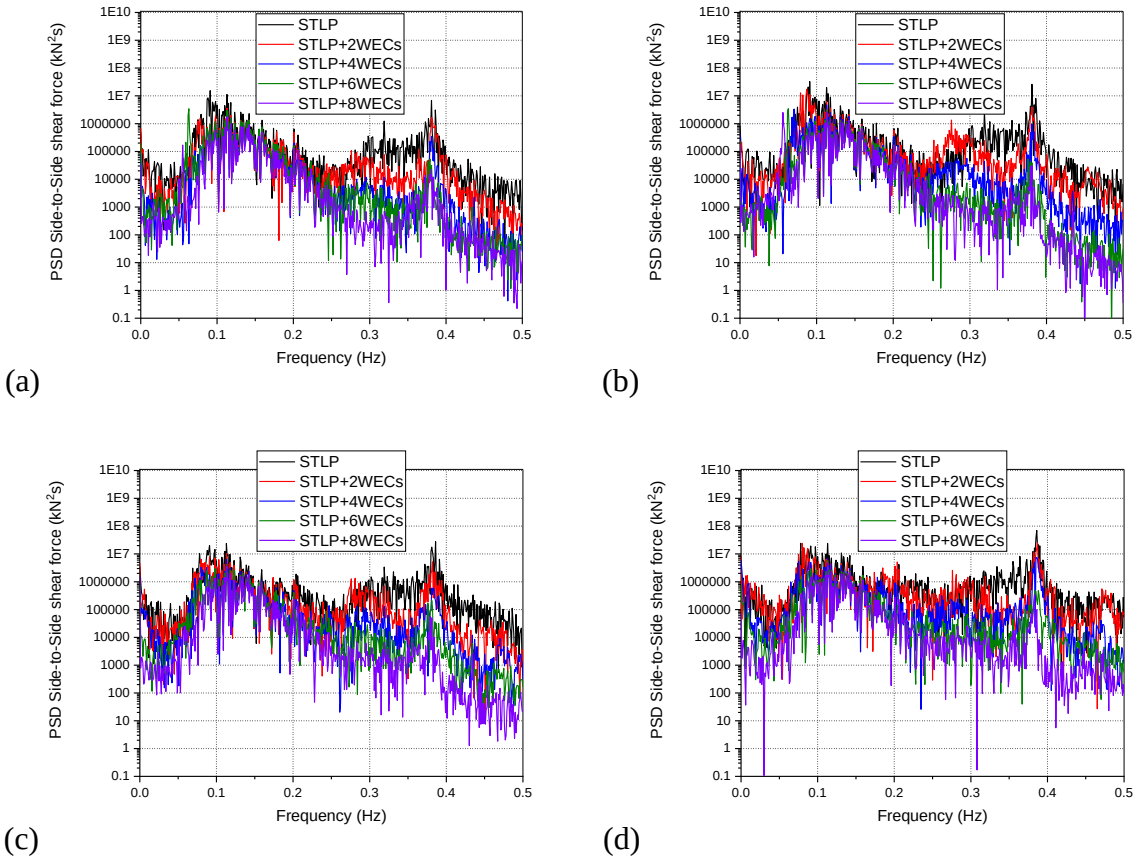


Fig. 2.20: Power spectral density for side-to-side shear force at (a) SS-1 (b) SS-2 (c) SS-3 and (d) SS-4 sea-state considering different configurations of combined floater for irregular waves.

Fig. 2.21(a-d) presents the PSD for the tower base side-to-side bending moments developed for different metocean conditions. The moments developed are mostly wind-induced moments for STLP and hybrid STLP-WEC systems. Also, it is observed that the wave-induced moments are minimum for any metocean condition considered. The amplitude of the moments has a minimum variation for $V_{mean} = 17\ m/s$ (Fig. 2.21d) for the frequency range $0.1 < \omega < 0.4\ rad\ s^{-1}$. An optimised variation in the moments developed is observed for other

wind speed conditions for the frequency range $0.01 < \omega < 0.3\ rad\ s^{-1}$. There is a further increase in moments (Fig. 2.21(a-c)) for the frequency range $0.3 < \omega < 0.4\ rad\ s^{-1}$. The variation in the moments for the lower wind speed conditions may influence the fatigue life of the turbine components. The minimum value of fore-aft shear force and side-to-side bending moments are observed for STLP+6WECs and STLP+8WECs hybrid platforms.

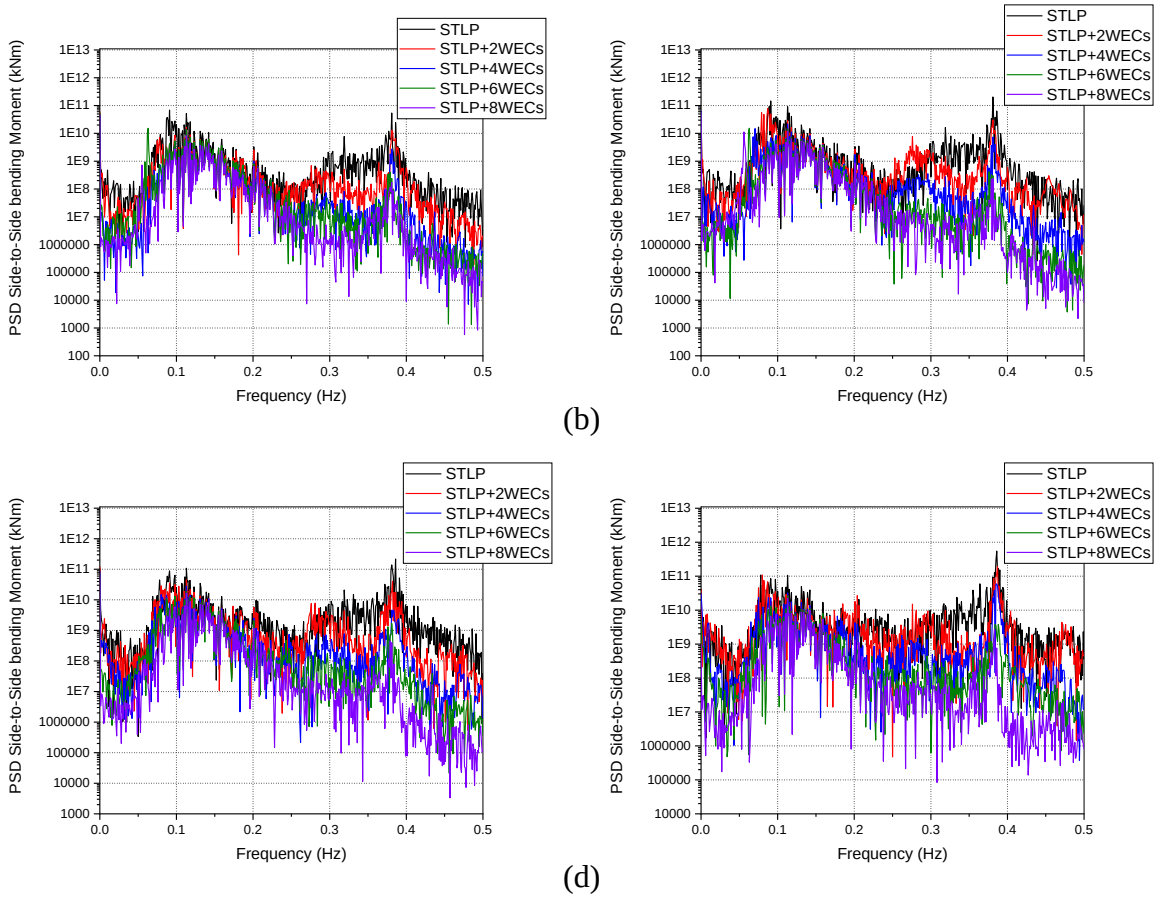


Fig. 2.21: Power spectral density for side-to-side bending moments at (a) SS-1 (b) SS-2 (c) SS-3 and (d) SS-4 sea-state considering different configurations of combined floater for irregular waves.

Fig. 2.22(a-d) presents the PSD for the fore-aft bending moment developing at the base of the floating turbine for four different operating conditions of the wind turbine. For all the metocean conditions considered, the fore-aft bending moments have minimum variations for the frequency region $0.1 < \omega < 0.4\ rad\ s^{-1}$. The side-to-side moments are slightly higher compared to the fore-aft moments developed at the base. This may be because the moments are mostly wind-induced and the wind direction is considered to be in positive x-direction. The STLP+6WECs and STLP+8WECs hybrid platforms are observed to have minimum values of the side-to-side shear force and fore-aft bending moments. The minimum shear forces ensure

higher fatigue strength, further improving the capacity of the components to withstand repetitive loading cycles and stress levels.

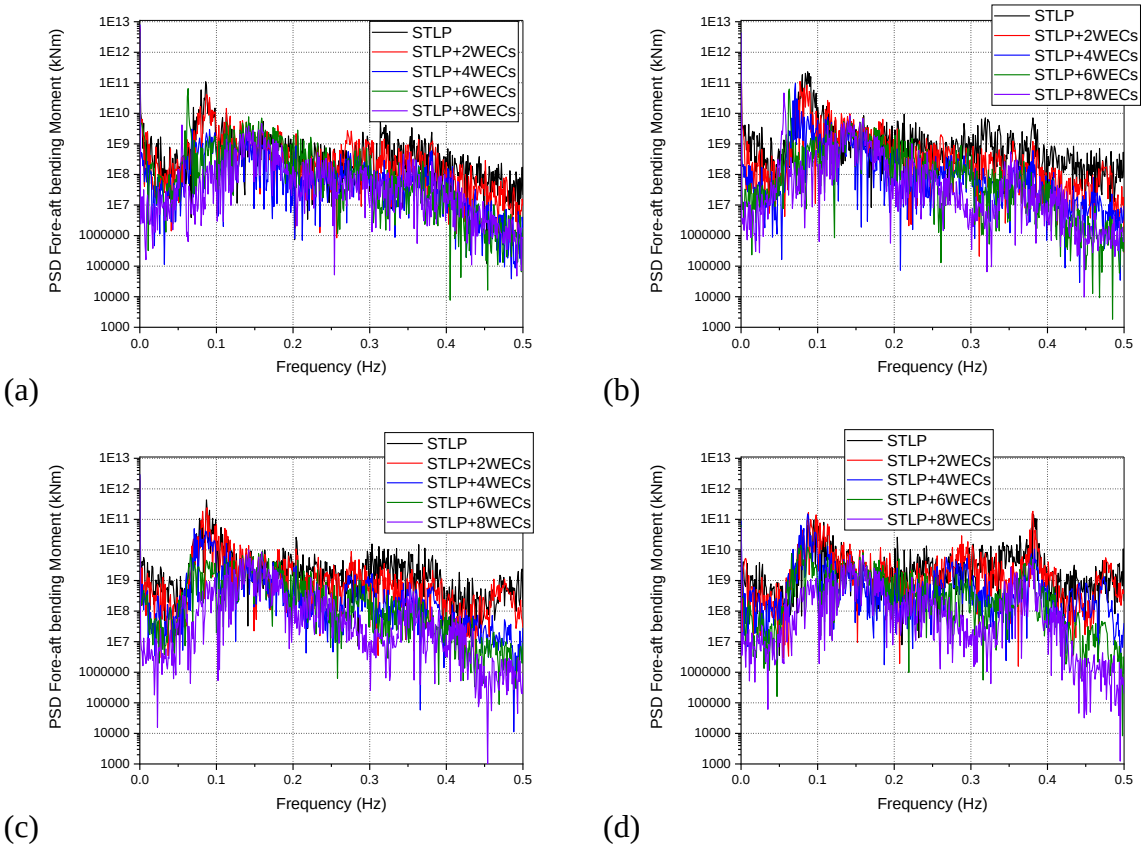


Fig. 2.22: Power spectral density for fore-aft bending moments at (a) SS-1 (b) SS-2 (c) SS-3 and (d) SS-4 sea-state considering different combined floater configuration for irregular waves.

### 2.5.4.2 Frustum Tension-Leg Platform Combined with Cone-cylinder WEC

Fig. 2.23(a-c) shows the shear forces developed at the base of the floating wind turbine. The fore-aft shear forces are observed to be higher (Fig. 2.23a) for any floating system compared to forces in the other two directions. Further, with the addition of the WECs, the forces are observed to reduce. This may be because, the WECs may absorb the waves coming onto the floating system, further reducing the wave-induced forces. The variation in the forces is minimum for the vertical force developed (Fig. 2.23c) and the variation is higher for the side-to-side shear force (Fig. 2.23b). Also, with the addition of the WECs, the wave period at which maximum values for the for-aft shear force occur is reduced. The FTLP+8WECs configuration has the highest value of the fore-aft shear force at the lower wave period region $\left(T_p = 4\ s\right)$ and is observed to decrease with the increase in wave period for the gravity waves. For the side-to-

side bending moment, there are several peaks for the gravity waves and is observed to be minimum for FTLP+8WECs.

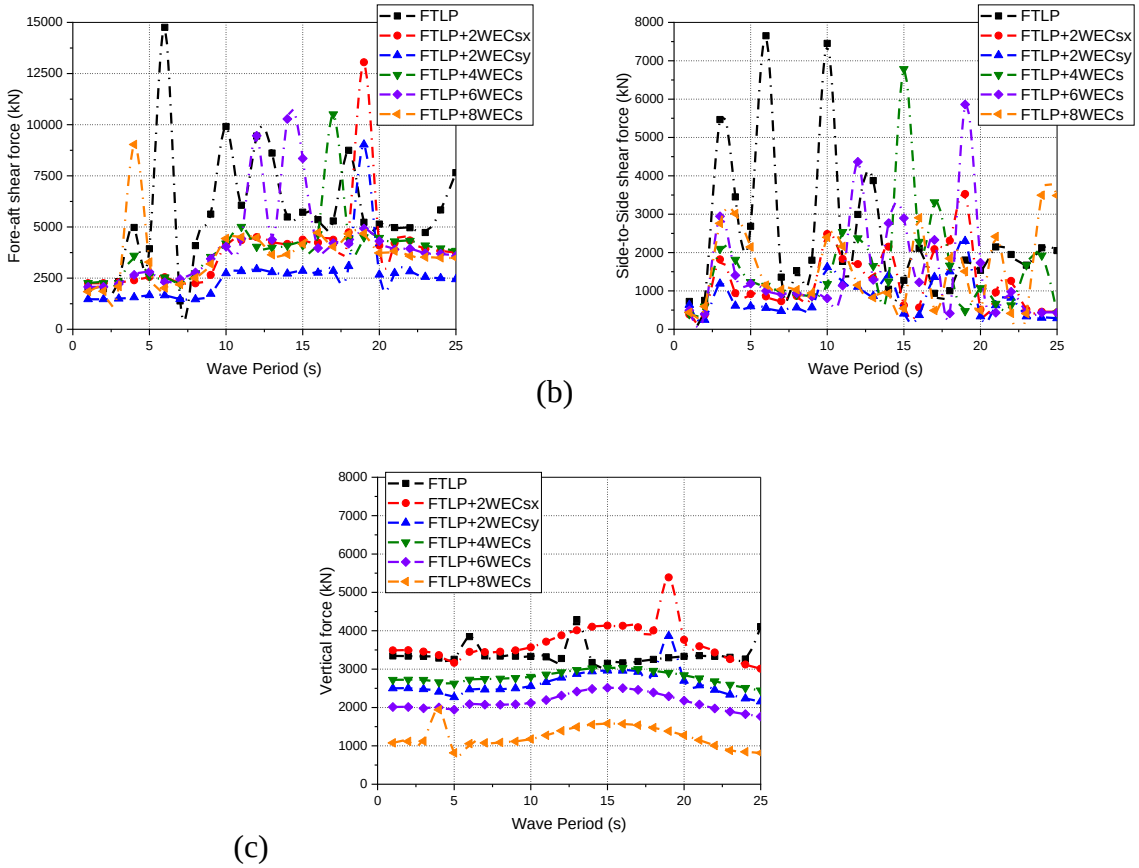


Fig. 2.23: Comparison of (a) fore-aft shear force (b) side to side shear force and (c) vertical shear force for different arrangement of WECs.

Fig. 2.24(a-c) studies the bending moments developed at the base of the turbine tower for different hybrid configurations of FTLP. Fig. 2.24(a) shows the side-to-side bending moments developed, are observed to be less compared to the fore-aft bending moment. The moments are reduced with the addition of the WECs.

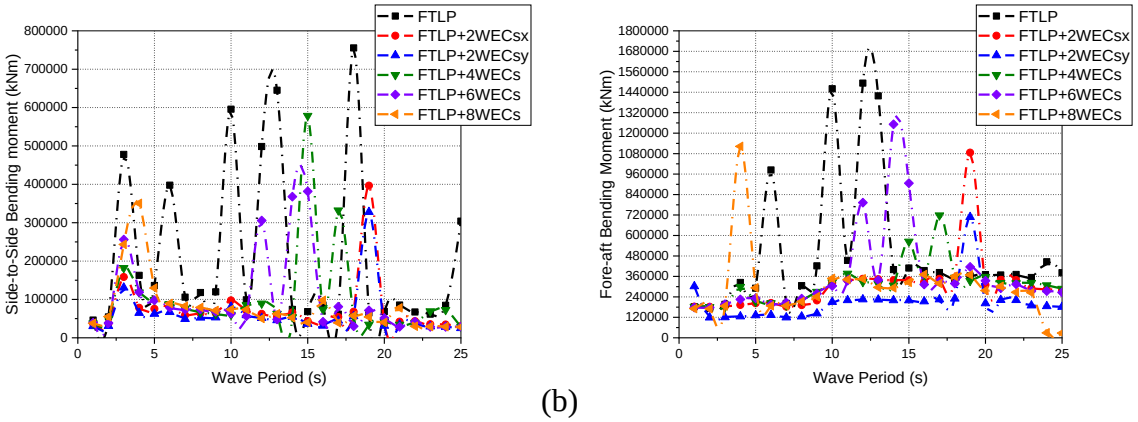

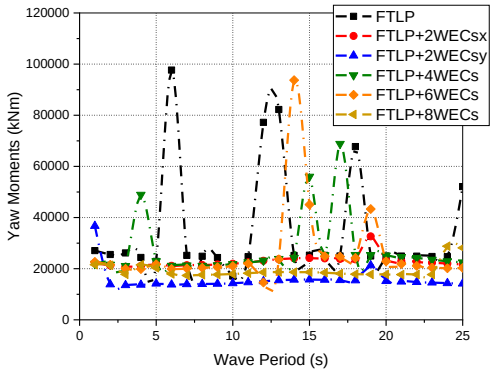


(c)

Fig. 2.24: Comparison of (a) side to side bending moment, (b) for-aft bending moment and (c) yaw moments for different arrangement of WECs.

The yaw moments are observed to be minimum (Fig. 2.24c), further having minimum fatigue load on the control systems of the wind turbine improving the wind power absorption and lifespan of the control systems. The FTLP+4WECs configuration is observed to have minimum fore-aft bending moments developed (Fig. 2.24b), even though the variation in the moments developed is higher compared to the FTLP+8WECs configuration. FTLP+8WECs configuration has a minimum value of the moments developed, ensuring minimum structural damage or failure for the hybrid system. Fig. 2.25(a-d) shows the power spectral density for fore-aft shear force for different operating conditions of wind turbines under irregular sea wave conditions. The study compares different configurations of hybrid floaters under operational wind speed conditions. Apart from 11.2 m/s wind speed, the spectrum variation is observed to be similar as in Fig. 2.25(a,c,d). The higher spectrum values are observed for a lower frequency range and are observed to decrease with increasing frequency. For surge and pitch motion, the response values are lower for lower frequency and hence show higher power absorption. The fore-aft forces are mainly wind-induced forces.

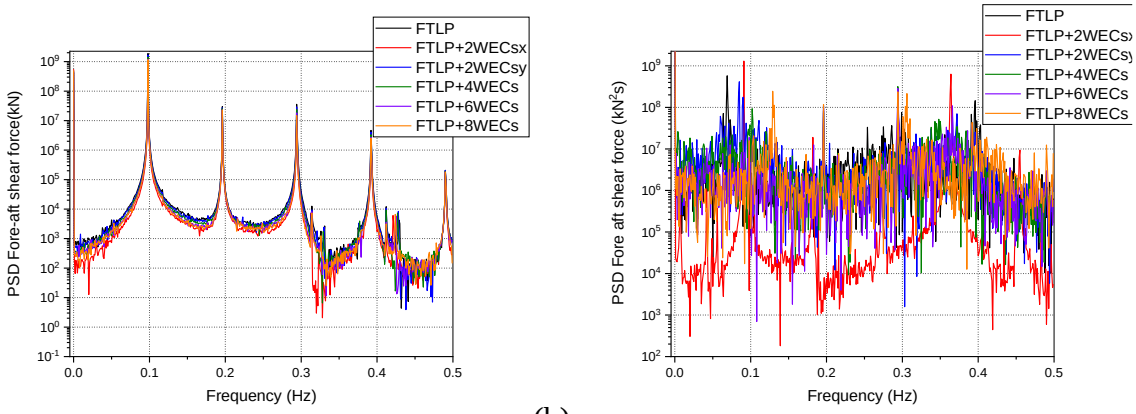


(a) (b)

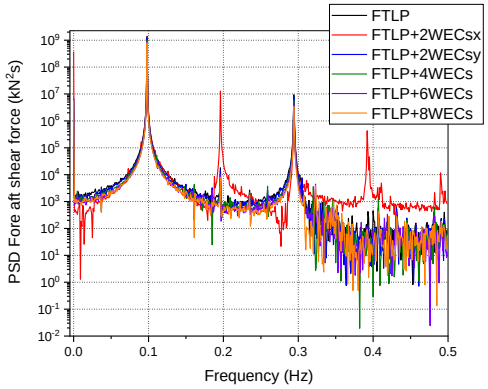


(c)

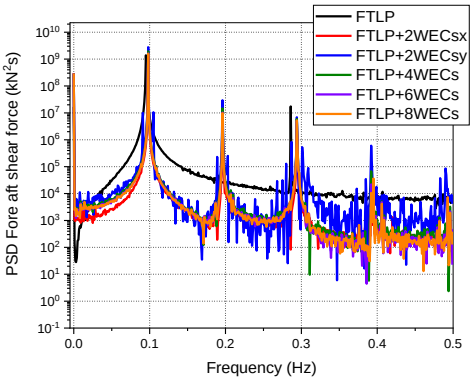


(d)

Fig. 2.25: Power spectral density for fore-aft shear force at (a) SS-1 (b) SS-2 (c) SS-3 and (d) SS-4 sea-state considering different configurations of combined floater for irregular waves.

Fig. 2.25(a-d) shows that the addition of WECs around FTLP has reduced the fore-aft forces developing on the platform, further improving the wind power absorption of the wind turbine. For 11.2 m/s wind speed FTLP+2WECx in the direction of the wave are observed to have lower spectrum values as in Fig. 2.25(b). But for wind speeds higher than 11.4 m/s (rated wind speed for 5 MW wind turbine), FTLP+8WECs are observed to have lower fore-aft values. Further, it is observed that the fore-aft shear forces are higher compared to side-to-side shear forces. For wind speed conditions lower than the rated wind speed, the fore-aft forces developed are higher for any configuration compared to higher wind speed conditions.

Fig. 2.26(a-d) presents the power spectral density for side-to-side shear force for different configurations of hybrid floaters for different operating conditions of wind turbines. The side-to-side forces are smaller compared to the fore-aft shear force developed on the turbine tower junction. The peak values for the forces are higher for the lower frequency range as in Fig. 2.26(a,c,d). But for 11.2 m/s wind speed, the peak value is observed to occur for a higher frequency range for any hybrid configuration.

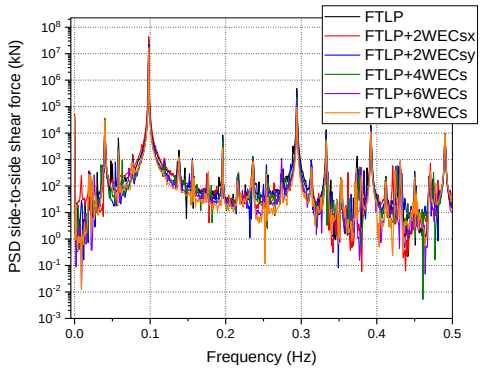


(a)

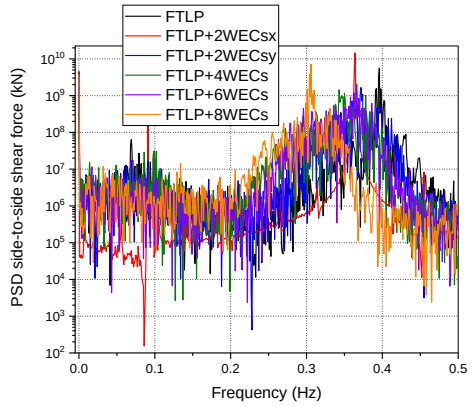


(b)

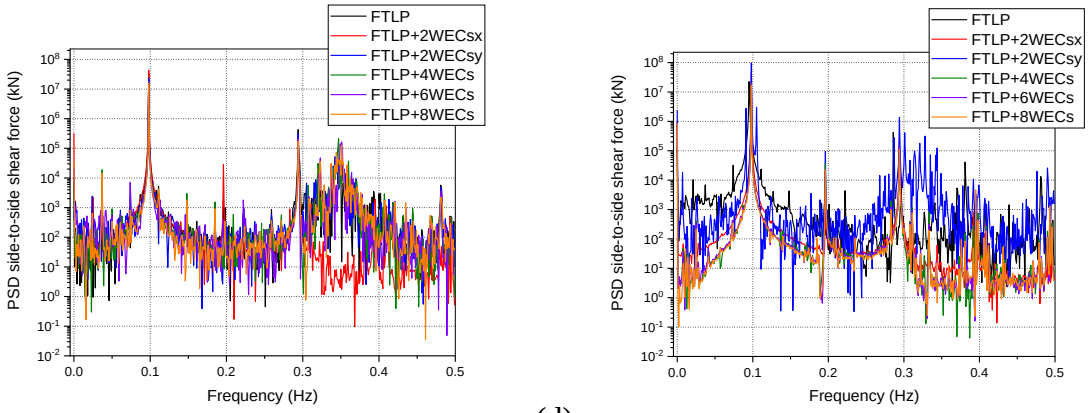


(c) (d)

Fig. 2.26: Power spectral density for side-to-side shear force at (a) SS-1 (b) SS-2 (c) SS-3 and (d) SS-4 sea-state considering different configurations of combined floater for irregular waves.

The addition of WECs has increased the side-to-side forces developed on the floater for the lower frequency range, further for the higher frequency range the force values decrease with the addition of WECs.

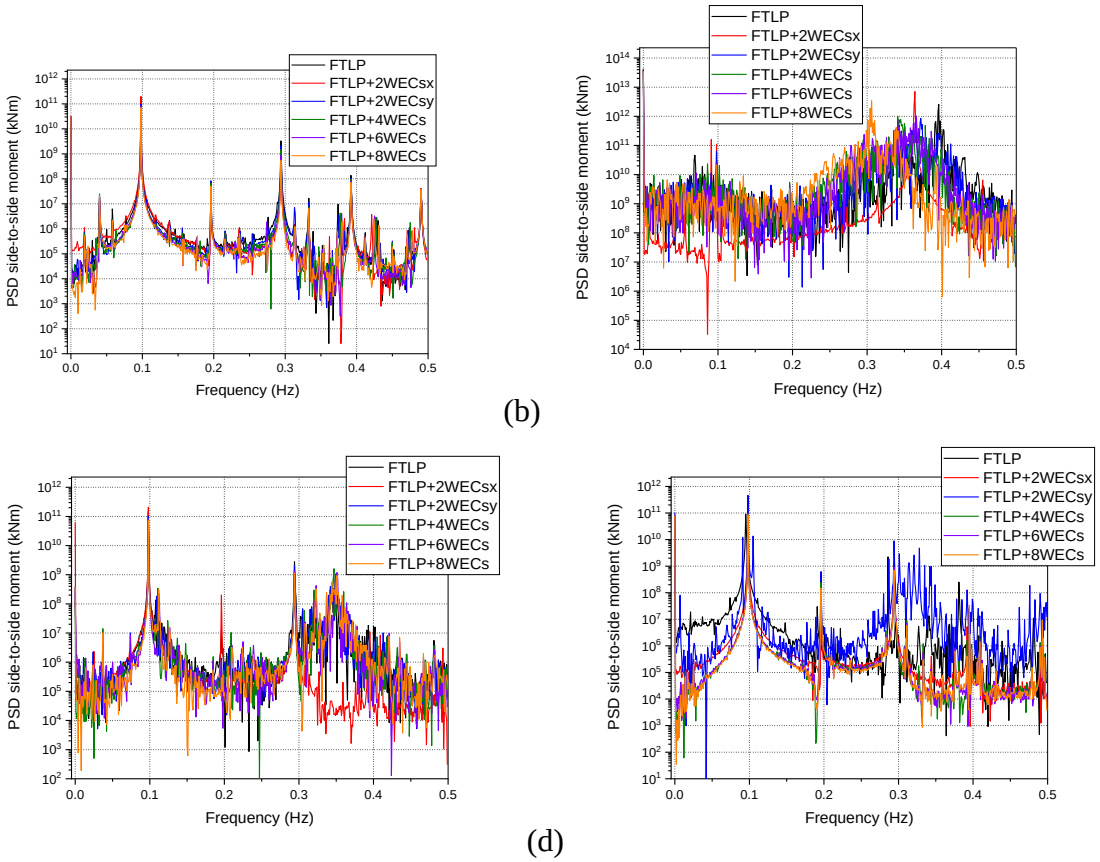


(a) (b)

(c) (d)

Fig. 2.27: Power spectral density for side-to-side bending moments at (a) SS-1 (b) SS-2 (c) SS-3 and (d) SS-4 sea-state considering different configurations of combined floater for irregular waves.

Fig. 2.27(a-d) presents the power spectral density for side-to-side bending moment for different configurations of hybrid floaters considering different operating conditions of wind turbines. The side-to-side bending moment values are higher compared to other moments which is due to the higher force developed in the direction of the wind. Further, Fig. 2.27(a-d) shows that the wave-induced moments are higher compared to the wind-induced moments for any wind speed condition. A higher variation in the side-to-side bending moments is observed for the FTLP+2WECsy for the 17 m/s wind speed condition (Fig. 2.27c). The higher variation may be due to the occurrence of the resonance for the extreme operational wind speed condition. Thus, proper damping mechanism have to be provided to the hybrid floating platform to dissipate the energy from the oscillations.

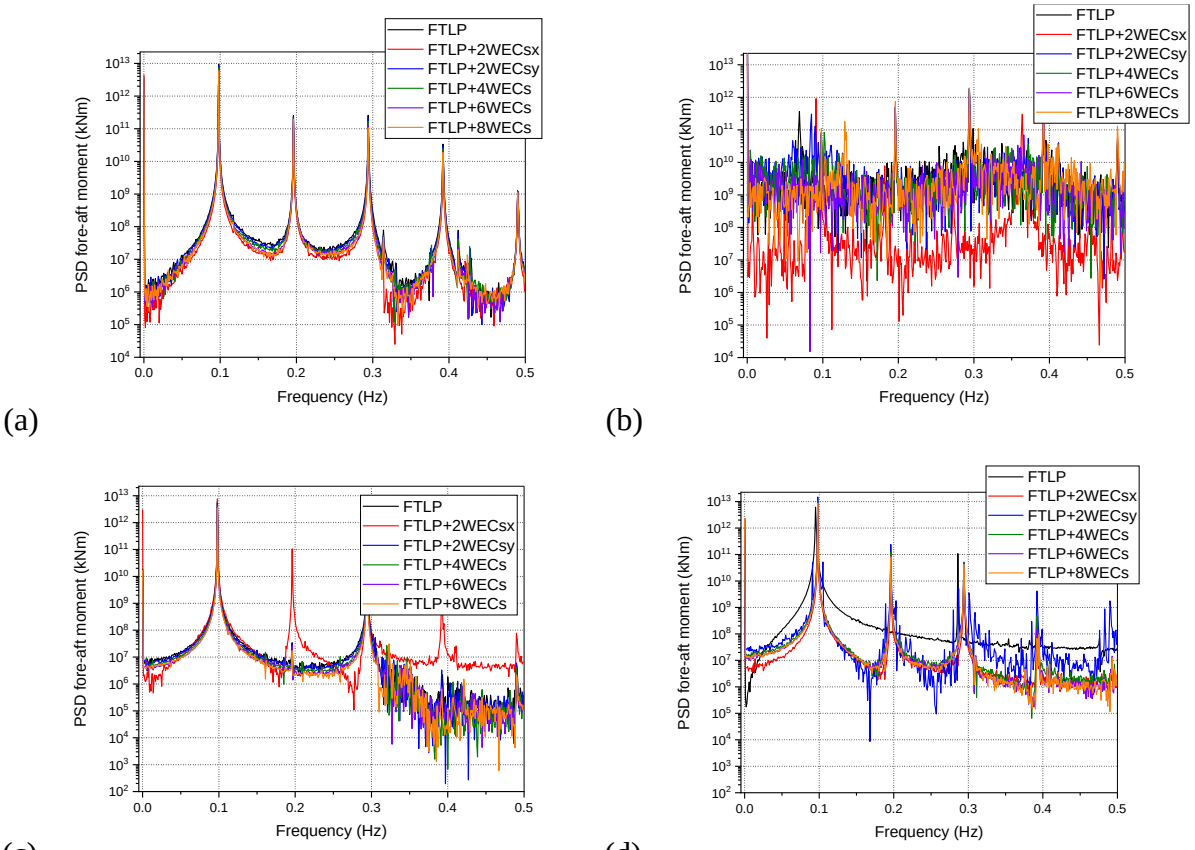


Fig. 2.28: Power spectral density for fore-aft bending moments at (a) SS-1 (b) SS-2 (c) SS-3 and (d) SS-4 sea-state considering different configurations of combined floater for irregular waves.

Fig. 2.28(a-d) presents the power spectral density for the fore-aft bending moment for different configurations of hybrid floaters for different operating conditions of wind turbines. For lower and higher wind speed conditions, the wind wave and rotor frequency peaks coincide for all configurations of FTLP as seen in Fig. 2.28(a,d). For 11.2 m/s and 14 m/s wind speed, the

wind, wave and rotor frequency peaks are at different locations as seen in Fig. 2.28(b,c) for FTLP+2WECsx configuration and also the wind-induced moments are higher compared to the wave-induced moments in the fore-aft direction. The study observed that the forces and moments are mainly induced by the wave forces compared to the wind and rotor force along with other resonating forces. For low and high wind speed conditions, the peaks for the wind, wave and rotor frequency are very much closer compared to the 11.2 m/s wind speed condition. At a wind speed of 11.2 m/s, it has been observed that the surge and pitch responses are reduced for all configurations. This reduction facilitates greater absorption of wind power, resulting in isolated peaks.

### 2.5.5 Mooring Line Tension

Tensioned mooring cables are an important factor in the design and operation of the TLPs. They give the platform with the stability, weight transmission, and positional control required for offshore support. The safe and dependable operation of the TLP depends on proper mooring cable design, monitoring, and maintenance. Typically, a TLP's mooring cables are organised in a radial arrangement all around the platform. Equitable load distribution and balanced strain across the cables are made possible by this arrangement. To prevent any individual cable from bearing an excessive load, the system ensures that the tension forces are uniformly distributed. The integrity of the tensioned mooring cables is critical for the overall safety and performance of the TLP. The tension developed on the cables on the seaward side (Mooring cable- 1) and the leeward side (Mooring cable- 4) for both the hybrid floating platforms are studied. Fig. 2.29(a,b) shows the Mooring cable- 1 and Mooring cable- 4 for the hybrid STLP and FTLP floating wind turbine platforms.

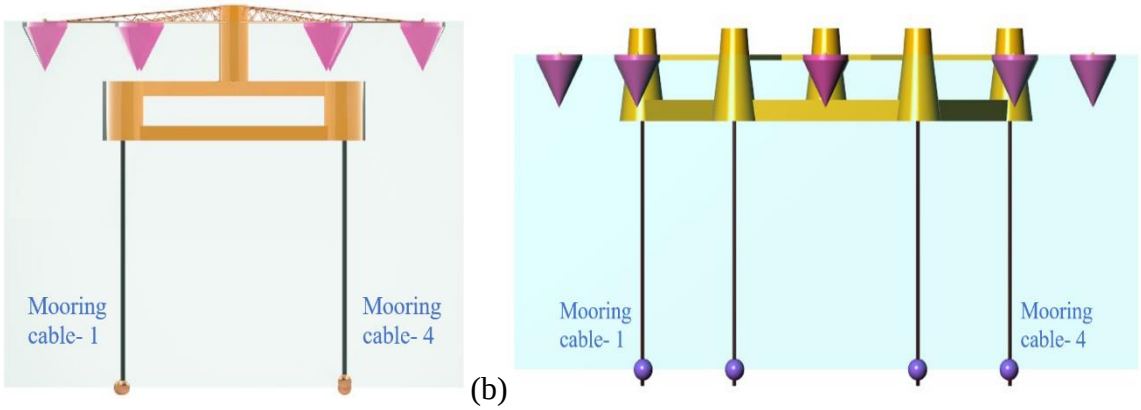


(a) (b)

Fig. 2.29: Mooring cable-1 and Mooring cable- 4 on the seaward and leeward side of (a) STLP and (b) FTLP floating wind turbine platforms.

### 2.5.5.1 Submerged Tension-Leg Platform Combined with Cone-cylinder WEC

The tension developed on the mooring cables on the seaward and leeward sides is shown in Fig. 2.30(a,b) for different metocean conditions. Fig. 2.30(a) shows the tension developed on the Mooring cable-1 on the leeward side. The addition of WECs has influenced the tension developed on the mooring cables. For the STLP+6WECs and STLP+8WECs configurations, the tension developed on the cables is reduced for any operational conditions of the wind turbine.

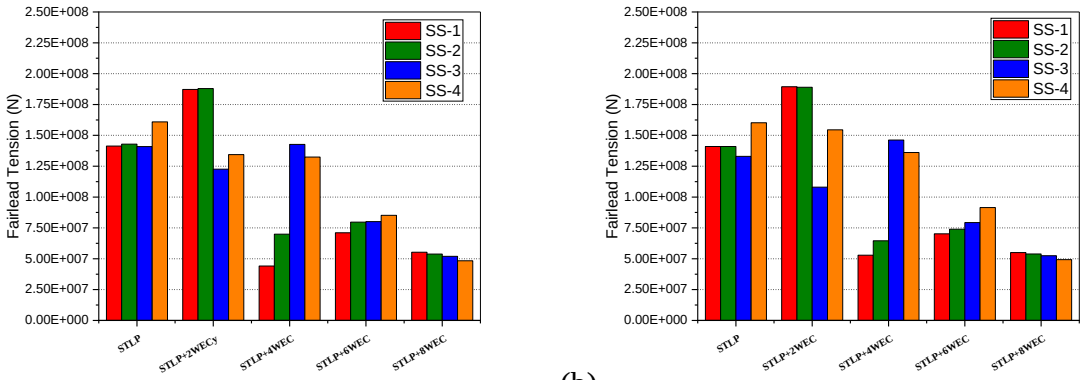


Fig. 2.30: Maximum fairlead tension for (a) Mooring cable-1 and (b) Mooring cable-4 for different environmental condition of several configurations considered.

For STLP+2WECs configuration, the tension developed on the mooring cables is reduced for wind speed conditions above the rated wind speed (11.4 m/s) of a 5 MW wind turbine. For the STLP+4WECs configuration, the reduced mooring line tension is observed for wind speed conditions below the rated wind speed condition. Fig. 2.30(b) shows the mooring line tension developed on the Mooring cable- 4 for different metocean conditions of the hybrid system. The variation of the maximum values of tension developed on the mooring cables is almost similar for both mooring cables. The reduced tension for the hybrid floating platforms ensures better orientation of the wind turbine and hence better wind power absorption. Also, the reduced tension of the mooring cables ensures a better life for the mooring system.

Table 2.16 shows the mean and standard deviation values for the tension developed on the Mooring cable- 1 and Mooring cable- 4 placed on the direction of the incident waves. The mean value of the tension developed on the Mooring cable- 1 and Mooring cable- 4 are almost equal. The equal value of tension for the mooring cables ensures equal sharing of loads avoiding the overstressing of the cables and reducing the risk of cable failure. Further, the platform is balanced and steady with equal strain across all wires, lowering the possibility of

tilting or capsizing. Also, the control system of the wind turbine is optimised more effectively with the equal distribution of the tension on the cables. For STLP+4WECs, STLP+6WECs and STLP+8WECs configurations, there is a higher variation between the mean and standard deviation values. The platform's response to external factors may be more uncertain and variable if there is a larger disparity between the mean and standard deviation values. The performance and dependability of the TLP are directly impacted by the tension created on the mooring lines. The platform's capacity to maintain stability, manage placement, and efficiently transfer loads may be impacted by this increased variability.

Table 2.16: Mean and Standard deviation of mooring line tension developed on Mooring cable-1 and Mooring cable-4 for 11.2 m/s wind speed (SS-2).

| Floater Configurations | Mooring cable- 1 | | Mooring cable- 4 | |
|---|---|---|---|---|
| | Mean (N) | Standard Deviation (N) | Mean (N) | Standard Deviation (N) |
| STLP | 4.84E+07 | 1.38E+07 | 4.29E+07 | 1.17E+07 |
| STLP+2WECs | 3.99E+07 | 1.05E+07 | 3.99E+07 | 1.01E+07 |
| STLP+4WECs | 3.34E+07 | 4.63E+06 | 3.43E+07 | 5.40E+06 |
| STLP+6WECs | 2.93E+07 | 2.96E+06 | 2.94E+07 | 3.01E+06 |
| STLP+8WECs | 2.53E+07 | 2.09E+06 | 2.53E+07 | 2.56E+06 |

#### 2.5.5.2 Frustum Tension-Leg Platform Combined with Cone-cylinder WEC

The study observed the tension developed on each mooring cable for a different arrangement of WECs in a circular array and presents the maximum values of fairlead tension developed on mooring cables for the different environmental conditions shown in Fig. 2.31(a,b) at two different fairlead points (Mooring cable- 1 and Mooring cable- 4). In the case of all configurations of FTLP with WEC, the tension developed on all six mooring lines is observed to be almost the same for different sea-state conditions. The reduction in tension developed on the cables is noted with the addition of WECs to the FTLP floater for SS-1, SS-3 and SS-4 conditions. The least values for the mooring line tension are observed for FTLP+8WECs and the maximum values of mooring line tension are observed for the single FTLP. Thus, showing the reduction in rigid body motions with the addition of WECs around FTLP. In addition, in the case of SS-2 metocean condition (wind speed of 11.2 m/s), the tension developed on the mooring cables is observed to increase with the increase in the number of WECs.

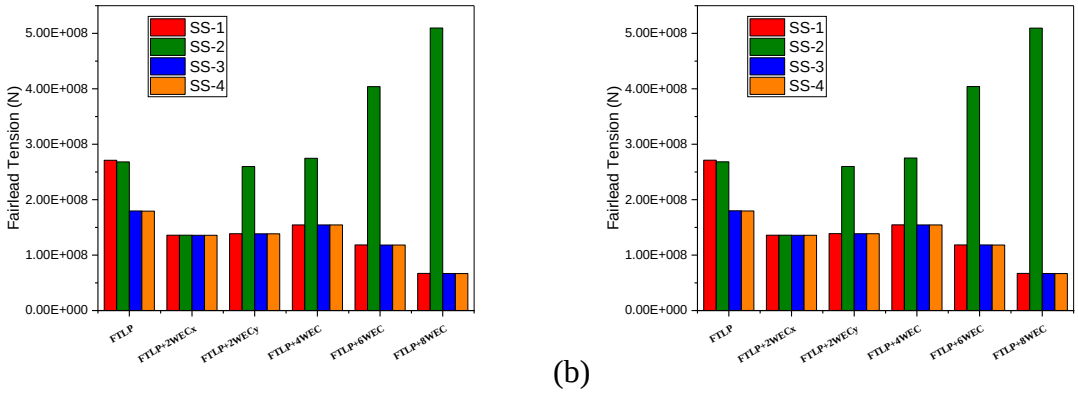


(a) (b)

Fig. 2.31: Maximum fairlead tension for (a) Mooring cable- 1 and (b) Mooring cable- 4 for different environmental condition of several configurations considered.

Table 2.17: Mean and Standard deviation of mooring line tension developed on mooring cable-1 and mooring cable-4 for 11.2 m/s wind speed (SS-2).

| Floater Configurations | Mooring cable- 1 | | Mooring cable- 4 | |
|---|---|---|---|---|
| | Mean (N) | Standard Deviation (N) | Mean (N) | Standard Deviation (N) |
| FTLP | 2.38E+08 | 5.63E+06 | 2.38E+08 | 5.65E+06 |
| FTLP+2WECsx | 2.20E+07 | 2.09E+06 | 2.21E+07 | 2.07E+06 |
| FTLP+2WECsy | 2.02E+08 | 5.06E+06 | 2.03E+08 | 5.07E+06 |
| FTLP+4WECs | 1.63E+08 | 3.68E+06 | 1.63E+08 | 3.69E+06 |
| FTLP+6WECs | 1.26E+08 | 5.48E+06 | 1.27E+08 | 5.48E+06 |
| FTLP+8WECs | 8.97E+07 | 7.43E+06 | 9.03E+07 | 7.43E+06 |

The mean and standard deviation values of the tension developed on the mooring cables for 11.2 m/s wind speed are presented in Table 2.17. It is observed that the mean values for the tension developed on the Mooring cable- 1 and Mooring cable- 4 reduce with the addition of WECs. Further, the least tension developed is observed for FTLP+2WECsx configuration in the direction of waves. The tension developed on mooring cables for FTLP+8WECs configuration is also observed to be minimum. The mean values for the tension developed are observed to be higher compared to the standard deviation values, further concluding that the tension developed on the cables is highly dependent on the wind load compared to wave loads. The variation in mean and the standard deviation is observed to be minimum for FTLP+2WECsx configuration and FTLP+8WECs configuration.

## 2.6 CLOSURE

In the present Chapter, the Submerged Tension-Leg Platform (STLP) and hexagon-shaped Frustum Tension-Leg Platform (FTLP) are proposed to support an offshore 5 MW wind turbine in moderate water depth. The dynamic response characteristics of the STLP and FTLP wind turbine floater are analysed using a numerical aero-servo-hydro-elastic simulation tool. The study considers different arrays of cone-cylinder shaped point absorber WEC around STLP and FTLP to understand the influence of the WECs on dynamic responses of the hybrid floating system, further examining the wind power absorption efficiency of the hybrid floating system. Fully coupled time-domain simulations using the numerical simulation tool FAST are carried out to investigate the platform motions, mooring line tensions and the forces and moments developed at the base of the turbine tower for regular and irregular wave conditions. The conclusions drawn from the study are as follows:

- The natural frequency for the surge, sway and yaw motions of the STLP is similar to a conventional TLP-type floating offshore platform $\left(0.06 < \omega_n < 0.08\ rad\ s^{-1}\right)$. But for the FTLP, the natural frequencies for the dominant motions are in the frequency range $0.3 < \omega_n < 0.5\ rad\ s^{-1}$, reducing the possibility of the resonance due to the wind and wave induced loads.
- The yaw motion response for the STLP floating platform is much higher than the yaw motion response of the FTLP for both regular and irregular wave conditions. An average 93% reduction is observed for the regular wave condition and 59% reduction is observed in random wave condition. The reduced yaw motion of the FTLP ensures minimum load on the control systems of the wind turbine, improving the wind power absorption efficiency and the life of the control systems.
- The STLP+6WECs and FTLP+8WECs hybrid floating offshore platforms are observed to have minimum surge, sway and yaw motion response for the operational conditions of the 5MW wind turbine.
- In the case of STLP and hybrid STLP-WEC floating platforms, the forces and moments developed at the turbine's base are wind-induced. This may be due to the higher wind power absorption of the supporting wind turbine. But for the FTLP and hybrid FTLP-WEC floating platforms, the forces and moments are wave induced. This may be because the WECs are placed closer to the FTLP.

# CHAPTER 3

# MULTI-BODY ANALYSIS OF A HYBRID TENSION-LEG PLATFORM FLOATING WIND TURBINE

## 3.1 GENERAL INTRODUCTION

Renewable energy sources are a good substitute for traditional energy sources as it is available in abundance and has no negative effects on the environment. Wind, waves, and currents in the ocean are abundant sources of renewable energy that can be converted into useful forms of energy. The offshore hybrid concepts for offshore energy extraction are highly helpful in lowering total project costs and logistics costs, further boosting the yield of renewable energy per unit square kilometre of ocean space (Perez-Collazo et al., 2019, Wan et al., 2020). The present section examines the hydrodynamic performance of six different arrays of cone-cylinder point absorber WEC around two TLPs supporting a 5 MW wind turbine platform. The heaving point absorber-type WEC in concentric and circular arrays is studied to observe the influence of the FTLP and other WECs on the platform's stability and wave power absorption. The hydrodynamic coefficients (added mass and damping coefficient) of the hybrid system under regular waves of unit amplitude are analysed using the numerical simulation programme WAMIT. The instantaneous power absorbed by the wave energy device and the influence of the Power take-off (PTO) for the wave energy absorption were calculated for several specified ocean conditions of the North Sea. Further, the mean interaction factor (q-factor) and the Capture Width Ratio (CWR) are studied to observe the efficiency of the hybrid system and the utilisation of the incident wave.

## 3.2 NUMERICAL FORMULATION

Multiple bodies interacting mechanically and hydrodynamically are analysed using the fully integrated hydrodynamic simulation programme WAMIT. Each body oscillates individually with six degress of freedom. The modelling tool WAMIT resolves the radiation and diffraction problem based on the panel technique and three-dimensional potential flow theory (Lee, 1995). The hydrodynamic simulation WAMIT tool assumes that there are no planes of hydrodynamic symmetry when there are several floating bodies. The equation of motion is discussed in this section for a single floating body before being expanded to include several floating WECs.

### 3.2.1 General Equation of Motion

The equation of motion for a floating WEC (Kim et al., 2019) with wave radiation force $F_R$, excitation force $F_{ex}$, restoring force $F_{static}$, and additional damping force $F_{loss}$, including a PTO system, $F_{PTO}$ is given by

$$m\ddot{x} = F_R + F_{ex} + F_{static} + F_{PTO} + F_{loss}. \tag{3.1}$$

The radiation and excitation force developed on the buoy can be obtained by solving the radiation and diffraction problem. The frequency-dependent radiation force in terms of added mass $m_{a33}$ and radiation damping $b_{33}$ is given by

$$F_R = -m_{a33}\ddot{z} - b_{33}\dot{z}. \tag{3.2}$$

Further, the excitation force developed on the buoy depends on the incident velocity potential $\varphi_I$ and diffraction velocity potential $\varphi_D$ over the body boundary $S_B$, which is given by

$$F_{ex} = -i\omega\rho\iint_{S_B}(\varphi_I + \varphi_D)\eta_3 dS. \tag{3.3}$$

The static force developing on the buoy with the vertical movement of the buoy is very much dependent on the buoyancy from the wetted volume of the body. The heaving restoring force with water plane area ($A_w$), vertical displacement ($z$), water density ($\rho$), and gravitational acceleration ($g$) can be expressed as

$$F_{static} = \rho g A_w z. \tag{3.4}$$

The viscous drag and the frictional force developed due to the interferences of the fixed platforms, buoys, and mechanical arms can be expressed as coulomb damping force. The total energy loss can be expressed as

$$F_{loss} = -\frac{1}{2}\rho C_d A_w(\dot{z} - \dot{\eta})|\dot{z} - \dot{\eta}| + -sign(\dot{z})F_{Mf0}, \tag{3.5}$$

where $F_{Mf0}$ is the magnitude of the mechanical friction force. The efficiency of the WEC is also dependent on the PTO system modelled. In the case of heaving WECs, the PTO systems use mechanical or hydraulic transmissions to drive high-speed rotational generators. The present study modelled a hydraulic PTO system with equivalent mass $M_{PTO}$, damping coefficient $C_{PTO}$, and spring coefficient $K_{PTO}$, as in the Wavestar model, which produces a large wave force. The power take-off force is given by

$$F_{PTO} = -M_{PTO}\ddot{z} - C_{PTO}sign(\dot{z}) - K_{PTO}z - F_f \tag{3.6}$$

### 3.2.2 Instantaneous Power Absorbed

The instantaneous wave power absorbed (Sinha et al., 2016) by a single floater for heave amplitude $z_A$ and external damping $b_{ext}$ in regular waves is given by

$$P_{abs} = \frac{1}{2} b_{ext} \omega^2 z_A^2 \tag{3.7}$$

In the case of irregular waves, the power absorbed is obtained by applying linear superposition of the floater responses given by

$$P_{abs} = \int_0^\infty b_{ext} \omega^2 \left( \frac{z_A}{\zeta_A} \right) S_\zeta(\omega) d\omega \tag{3.8}$$

where $\zeta_A$ is the wave amplitude and $S_\zeta(\omega)$ is the wave amplitude spectra. The wave amplitude spectra are based on the JONSWAP spectrum, which is given by

$$S_\zeta(f) = \alpha_s H_s^2 f_p^4 f^{-5} \gamma^{\beta_s} \exp\left( \frac{-5}{4} \left( \frac{f_p}{f} \right)^4 \right) \tag{3.9}$$

where the peal enhancement factor $\gamma = 3.3$, $f_p$ the peak frequency, and the factors $\alpha_s$ and $\beta_s$ are given by

$$\alpha_s = \frac{0.0624}{0.23 + 0.0336\gamma - \left( \frac{0.185}{1.9 + \gamma} \right)} \quad \text{and} \quad \beta_s = \exp\left( -\frac{(f - f_p)^2}{2\sigma_s^2 f_p^2} \right) \tag{3.10a}$$

The values of the spectral width parameter depend on the frequency given by

$$\sigma_s = 0.07 \text{ for } f < f_p \text{ and } \sigma_s = 0.09 \text{ for } f \geq f_p \tag{3.10b}$$

### 3.2.3 Power Take-off Mechanism

The WECs in a circular and concentric array around the TLP floating offshore platform are connected to the outer vertical columns using connecting arms, as shown in Fig. 3.1(a). For the STLP floating wind turbine platform, the WECs are connected to the central column, as in Fig. 3.1(a). The hinged structure between the connecting arm and the column limits the relative motion. It allows rotation around the hinged shaft, driving the power take-off (PTO) system to produce power (Hansen, 2013). For the FTLP floating platforms, the WECs are connected to the outer vertical pontoons, as in Fig. 3.1(b). The PTO for the point absorber requires a

cascaded conversion mechanism depending on the configuration. Mechanical or hydraulic transmissions to power conventional high-speed rotational generators are used mainly by PTO systems of the heaving point absorber type WECs. Also, specially designed linear generators are used for direct drive. The effective length is so assumed to restrict the maximum relative rotational angle $\theta_{arm}$ of the arm in the range $-20^{\circ} \le \theta_{arm} \le 20^{\circ}$ to abstract as much wave energy as possible. In the present study, the wave moves in a zero-degree direction towards the positive x-direction.

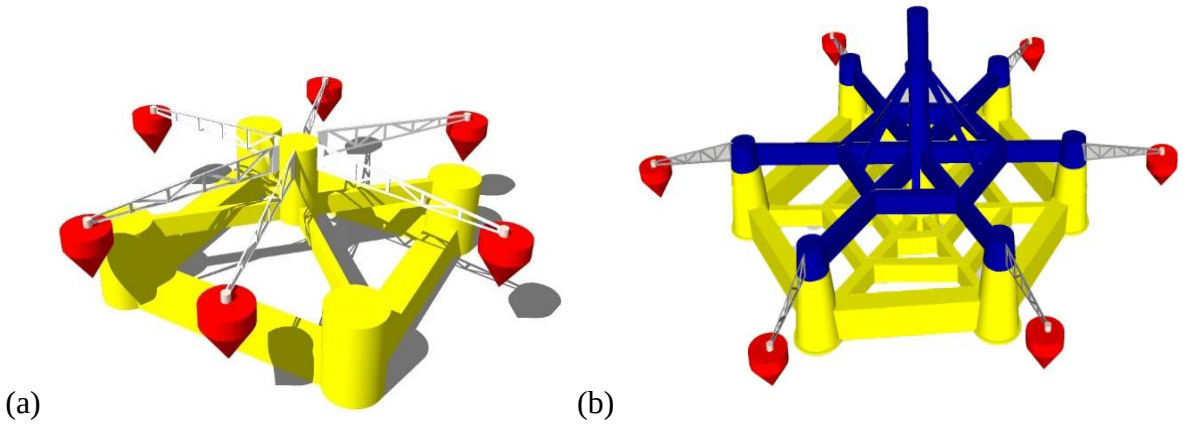

(a) (b)

Fig. 3.1:Heaving point absorber WEC connected to (a) STLP and (b) FTLP platform using hinges.

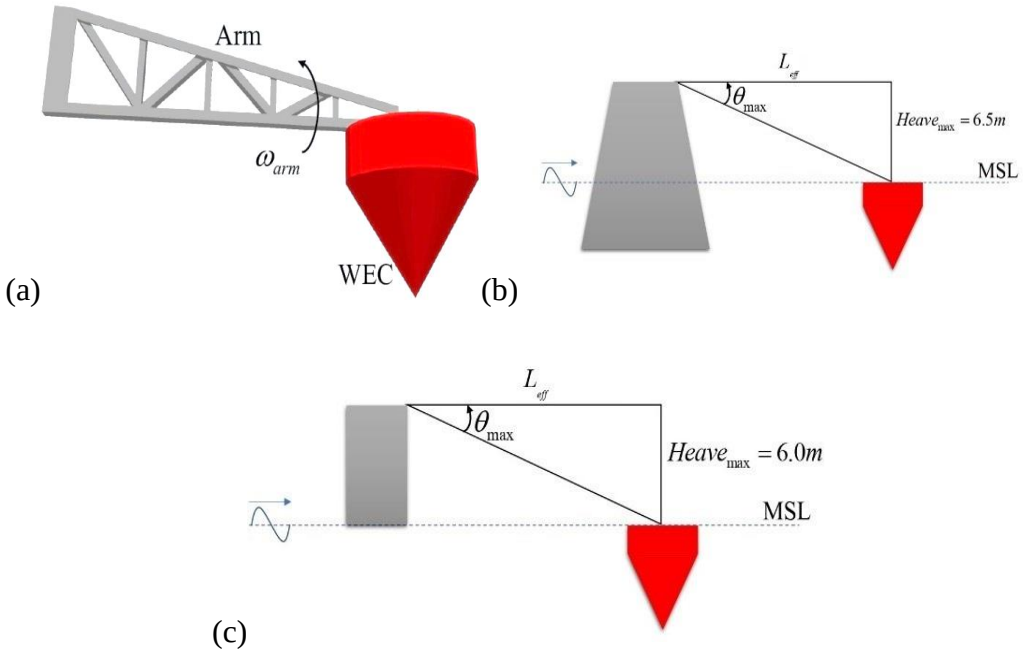


(a) (b)

(c)

Fig. 3.2: Schematic representation of (a) point absorber WEC connected using hinges, (b) WEC connected to an outer column of FTLP, and (c) WEC connected to the central column of STLP.

The study considers centro-symmetrically arranged heaving-type WECs to ensure better power quality and smoothness as the waves pass through the hybrid system. The absorbed power (Si et al., 2021) of the system with rotational velocity $\omega_{arm}$ is thus calculated by

$$P_{WEC} = \tau_{PTO}\omega_{arm}. \tag{3.11}$$

The point absorber WECs are narrow-banded with an under-damped resonant frequency. The power absorbed by the point absorber depends on the force or torque applied by the PTO. The present study uses a hydraulic PTO system as in the Wavestar model (Gaspar et al., 2021). With the geometry design of WEC, the study calculated the maximum rotational angle of the arm to understand the arm length $L_{arm}$. The effective length, $L_{eff}$ is calculated based on the position of the WECs around the TLP.

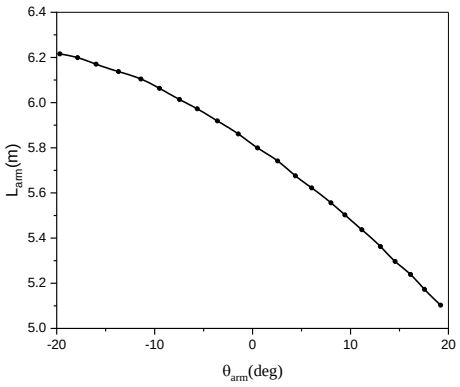


Fig. 3.3: Arm kinematics (Si et al. (2021)) to calculate the arm length based on the rotation angle of the arm.

The maximum heave value, $\mathrm{Heave}_{\max}$ and the effective length between the platform and the WEC, $L_{eff}$ are examined to understand the valuable working range for the arm movement, analysing the maximum rotation angle $\theta_{arm}$. Further, $\theta_{arm}$ is compared with the arm kinematics chart of the PTO torque shown in Fig. 3.3, as in Si et al. (2021), to understand the maximum arm length $L_{arm}$ that can be provided for the PTO mechanism. To derive maximum wave energy, the PTO applied load torque should be controlled as a function of wave and body movement to keep the WEC in resonant motion in waves. Linear damping, reactive control, latching control, and model predictive control are commonly used control strategies for the point absorber-type WECs. The linear damping allows the response to be attenuated without

moving the resonance frequency of the WECs to peak wave frequency. The Linear damping control reduces the response without shifting the WEC resonance frequency to the wave peak frequency. The Reactive control will inject additional control power to absorb a significantly higher quantity of wave energy, which often operates like a negative spring. The PTO torque for the linear damping $\tau_{LD}$ and the reactive control damping $\tau_{SD}$ (Si et al., 2021) is given by

$$\tau_{LD} = B_{PTO}\omega_{arm} \tag{3.12}$$

$$\tau_{SD} = B_{PTO}\omega_{arm} + K_{PTO}\theta_{arm} \tag{3.13}$$

where $B_{PTO}$ is the PTO damping coefficient, $K_{PTO}$ is the virtual spring term in reactive control, and $\theta_{arm}$ is the rotational angle of the WEC. The optimal values for $B_{PTO}$ and $K_{PTO}$ is given as

$$B_{PTO} = B_{hyd} \tag{3.14}$$

$$K_{PTO} = \left(J_{WEC} + J_{add}\right)\omega^2 - k_{res} \tag{3.15}$$

where $J_{add}$ is the added inertia of the WEC, $J_{WEC}$ is the inertia of the WEC, $k_{res}$ is the hydrostatic restoring stiffness coefficient, and $B_{hyd}$ is the hydrodynamic damping coefficient. These quantities are evaluated using the hydrodynamic simulation tool WAMIT based on the potential flow theory.

The vertical movements of the buoy with relative vertical $(dz)$ and angular displacement $(\theta_0)$ of the arm are translated into rotational movements of the arm (Kamarlouei et al., 2020) with

$$\theta = \theta_0 - \sin^{-1}\left(\frac{Z - dz}{L_{arm}}\right), \tag{3.16}$$

where $Z$ and $\theta$ are the initial vertical and angular displacements, respectively. The present study assumes the maximum heave value as the initial displacement of the arm connected.

### 3.2.4 Mean Interaction Factor $(q\text{-}factor)$

In order to quantify the effect of wave interactions on wave power in a WEC array, the mean interaction factor $(q\text{-}factor)$ defined as the ratio of the total wave power of the array to $N$ times wave power (Sinha et al., 2016) from a single isolated WEC, is examined and given by

$$q - factor(\omega) = \left( \frac{P_{Total}(\omega)}{N \times P_{isolated}(\omega)} \right), \tag{3.17}$$

where $P_{isolated}(\omega)$ is the total wave power of a single WEC at wave frequency $\omega$. The mean interaction factor, also known as the magnification factor, gives the idea of the constructive or destructive array interaction. The *q-factor* sums up the interactions as the results of the diffraction force experienced by each WEC and the reflection from the other WECs when the array is fixed in the direction of incident waves. The diffraction force is also developed by the movement of other WECs, i.e., with the movement of a single WEC in the still water level, the waves are generated and causes the movement of other WECs.

### 3.2.5 Capture Width Ratio (CWR)

The efficiency of the wave energy converters in the hybrid system can be expressed in terms of CWR. CWR is defined as the ratio of the total power absorbed by the hybrid system to the incident wave power. The study gives an indication of the width of the wave crest, which can be completely utilised by the WEC. The CWR (Ghafari et al., 2022) is given by

$$\text{CWR} = \frac{\text{Total absorbed power}[\text{W}]}{\text{Incident wave power}[W/m] * d[m]}, \tag{3.18}$$

where d is the diameter of the WEC. The incident wave power is given by

$$\text{Incident wave power} = \frac{\rho g^2 H^2 T b}{32\pi}, \tag{3.19}$$

where $\rho$ is the density of water, $g$ is the acceleration due to gravity, $H$ is the incident wave height, T is the wave period, and $b$ is the width of the wave crest. The width of the wave crest is considered as 1.0 m in the present study. The unit of the capture width is the length in metres.

## 3.3 GEOMETRIC MODELLING

The geometric modelling of the hybrid TLP floating wind turbine platform and cone-cylinder point absorber WEC beneath the design water surface is generated using Rhinoceros 3D. Panels representing the coordinates of the wetted surface are divided into the model surface. The ideal panel size is determined using a convergence test, optimising the simulation duration and increasing efficiency. Further, using the numerical simulation tool WAMIT, a hydrodynamic study for the TLP with a circular and concentric array of cone-cylinder WECs is carried out for regular waves of unit amplitude for four-wave heading directions.

### 3.3.1 Submerged Tension-Leg Platform with WEC

An STLP-type 5 MW floating wind turbine platform with arrays of WECs in circular and concentric patterns is modelled to analyse the hydrodynamic performance of the hybrid system, further analysing the power absorbed by the WECs in an array around the STLP. The schematic representation of the submerged platform, 5 MW wind turbine, and cone-cylinder WECs are shown in Fig. 3.4. The STLP-type floating offshore wind turbine floater and the cone-cylinder heaving point absorber WEC considered in the present study and the dimensions are detailed in Table 2.1 and Table 2.2, respectively, in Chapter 1. During the operation phase, the platform has improved hydrodynamic performance with a relatively small water plane area. Sinha et al. (2015) studied different-shaped heaving point absorber WECs and observed higher wave power absorption for cone-cylinder-shaped WECs.

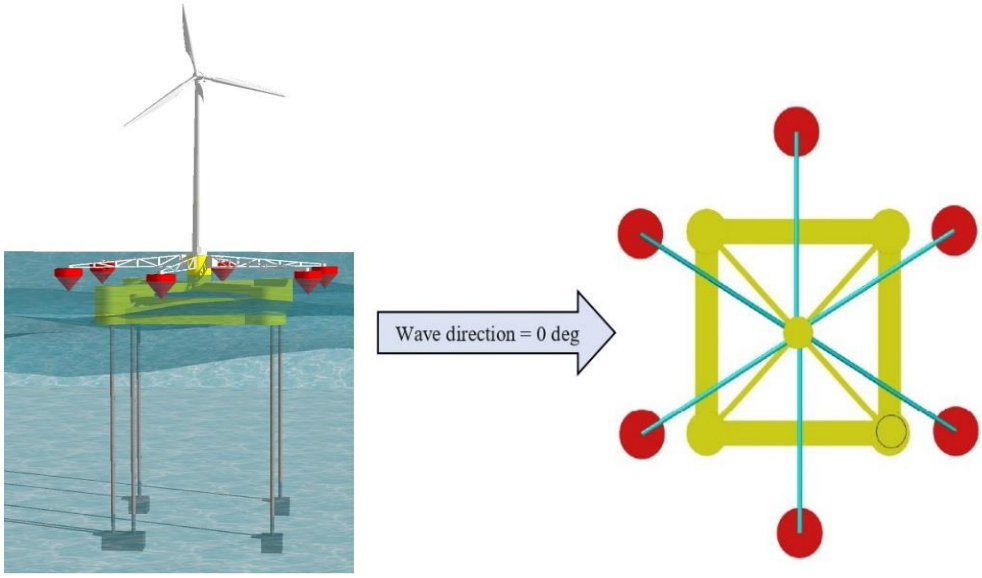


Fig. 3.4: STLP-type floating wind turbine floater with cone-cylinder heaving point absorber WEC in a circular array.

Table 3.1: Arrangement pattern of WECs around STLP.

| Configuration | Description | Remark |
|---|---|---|
| $C_1$ | 2WECs in a circular array around STLP | 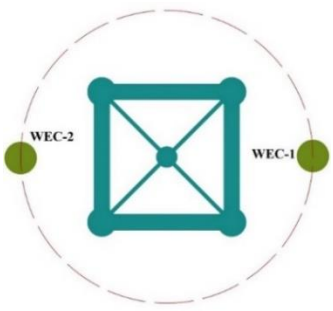  |

| | | |
|---|---|---|
| $C_2$ | 4WECs in a circular array around STLP | 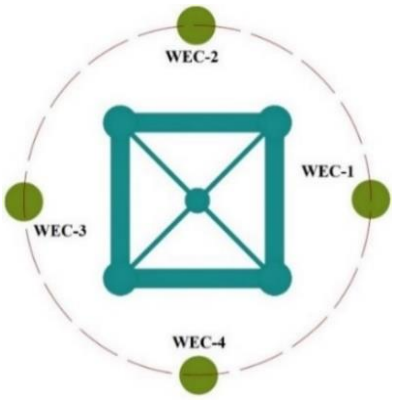 |
| $C_3$ | 6WECs in a circular array around STLP | 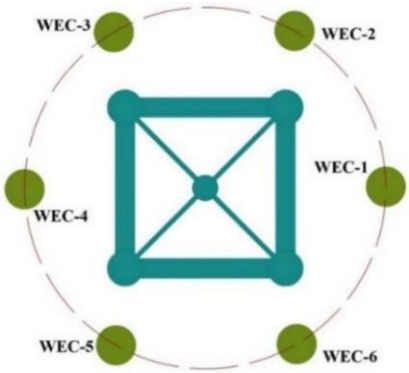 |
| $C_4$ | 8WECs in a circular array around STLP | 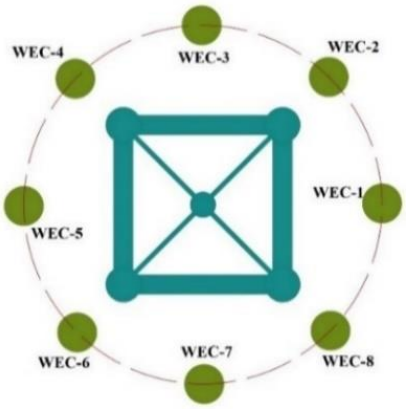 |
| $C_5$ | 8WECs in a concentric array around STLP | 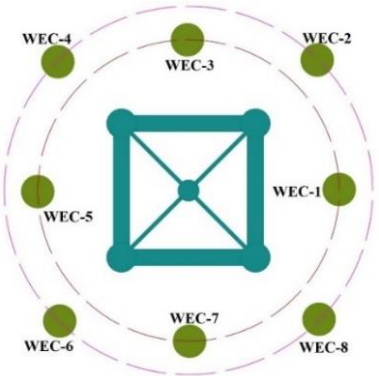 |

| | | |
|---|---|---|
| $C_6$ | 12WECs in a concentric array around STLP | 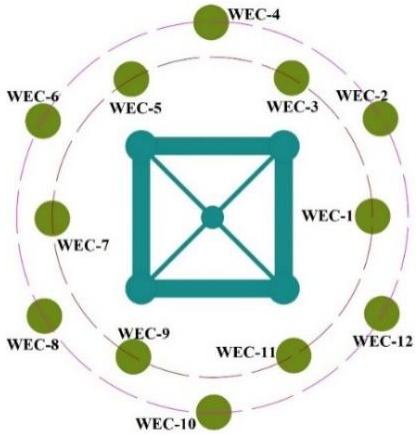 |

The study analysed different arrays of cone-cylinder-shaped heaving WECs around STLP-type FWT. The hybrid STLP-WEC configurations are observed to have minimum rigid body motions, further improving the wind power absorption of the wind turbine. Also, the addition of the WECs is observed to have minimum influence on the natural frequency of the STLP. In order to investigate the performance of hybrid STLP-WEC, six case studies of two, four, six, and eight cone-cylinder WECs with constant radius (45 m) and concentric pattern with radii 45 m and 55 m for eight and twelve WECs, as shown in Table 3.1 have been proposed. The wave is assumed to move towards the positive x-direction in zero degrees, as shown in Fig. 3.4.

### 3.3.2 Frustum Tension-Leg Platform with WEC

The hydrodynamic performance of the hybrid system is analysed using a hybrid model of an FTLP-type 5 MW floating wind turbine platform with arrays of WECs arranged in circular and concentric patterns (Fig. 3.4). The investigation also examines the power absorbed by the WECs arranged in an array surrounding the FTLP. The natural frequency of horizontal and vertical plane motions of the FTLP are outside the wave excitation frequency range, hence higher structural integrity. Further, the FTLP platform is observed to have lower surge motion and very minimum yaw motion. The lower values of the pitch and roll motion suggest the system's stability against overturning and the better orientation of the turbine towards the wind for higher wind power absorption. The dimensions of the FTLP supporting the wind turbine are detailed in Table 2.7 of the Chapter-1. Six case studies of the hybrid system are examined with two, four, six, and eight cone-cylinder WECs around FTLP with a constant radius of 70 m in a circular pattern and with radii 70 m and 80 m for eight and twelve WECs in a concentric pattern. Table 3.2 shows the different arrangement patterns of the WECs around FTLP.

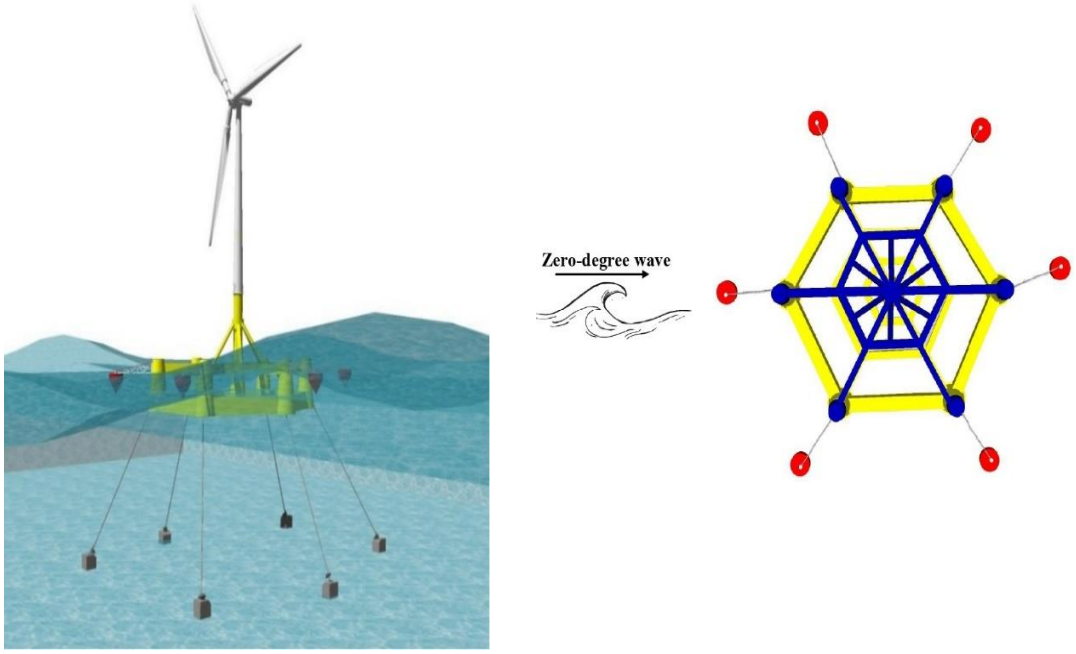


Fig. 3.5: Hybrid FTLP-WEC supporting 5 MW wind turbine.

Table 3.2: Arrangement pattern of WECs around FTLP.

| Configuration | Description | Remark |
|---|---|---|
| $FW_1$ | 2WECs in a circular array around FTLP. | 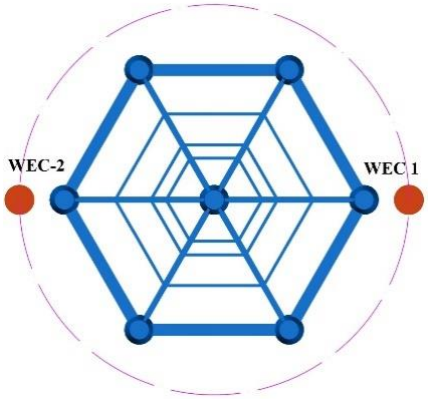  |
| $FW_2$ | 4WECs in a circular array around FTLP. | 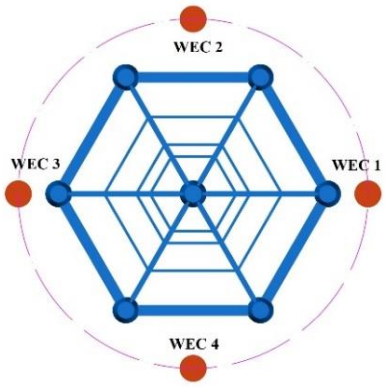  |

| | | |
|---|---|---|
| $FW_3$ | 6WECs in a circular array around FTLP. | 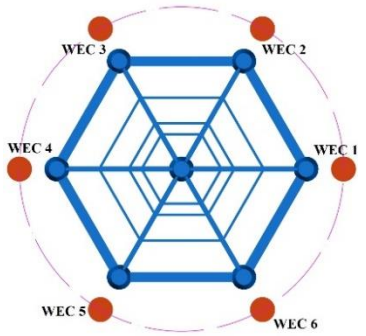 |
| $FW_4$ | 8WECs in a circular array around FTLP. | 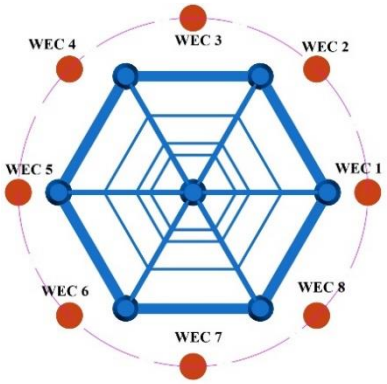 |
| $FW_5$ | 8WECs in a concentric array around FTLP. | 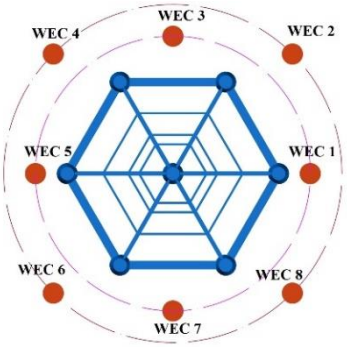 |
| $FW_6$ | 12WECs in a concentric array around FTLP. | 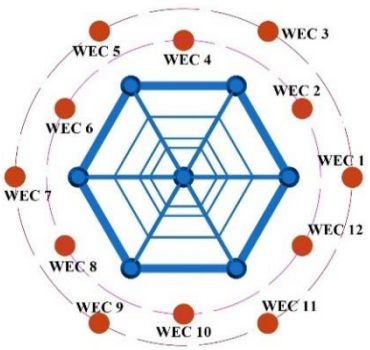 |

## 3.4 METHODOLOGY

The numerical modelling for the TLP-type floating wind turbine combined with arrays of WECs is performed using the hydrodynamic simulation tool WAMIT to analyse multiple

bodies interacting hydrodynamically. The simulation tool WAMIT is based on the panel method and solves the radiation and diffraction problem using three-dimensional potential flow theory (Lee, 1995). The WAMIT tool assumes that there are no planes of hydrodynamic symmetry when the number of bodies is more than one. The boundary element method for WAMIT discretises the structure's surface into panels and solves integral equations based on the linearised potential flow theory to compute the hydrodynamic response of the structure to incident waves.

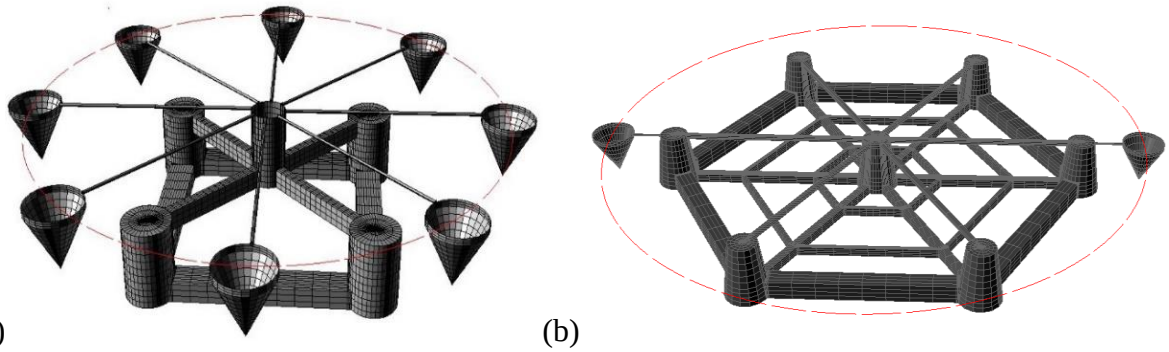

(a) (b)

Fig. 3.6: Mesh model for (a) STLP and (b) STLP with WECs in circular array.

It accounts for the interactions between panels and imposes boundary conditions to compute the surface elevation and velocity potential, which are used to compute various hydrodynamic quantities. The surface of the floating structure is divided into a set of panels. The panel size and distribution are determined using the convergence test. The mesh model used for the present study is shown in Fig. 3.6. The interactions between panels are computed using Green's function. These interactions are modelled as double-layer potentials, which relate the unknowns on one panel to those on neighbouring panels. The unknowns on each panel are solved simultaneously in a linear system of equations. The boundary conditions, which describe the interaction between the incoming waves and the structure, are imposed on the panels. These boundary conditions are typically expressed in terms of the surface elevation and the velocity potential. The incident waves interact with the structure through Green's function and are used to compute the structure's response. After considering the boundary conditions and interactions between the panels, the resulting linear system of equations is solved to determine the unknowns on the panels, which stand in for the structure's surface elevation and velocity potential. The unknowns are then used to compute various hydrodynamic quantities such as wave forces, wave loads, and structural response, which are analysed to understand the behaviour of the structure. The study observed the variation of added mass and damping ratio of the WECs to observe the influence of the WECs on the platform and other WECs.

Further, the time average power absorbed by the WECs are calculated for different hybrid configuration considered. Further, the study considered a hydraulic PTO model with two damping control models, Linear Damping control and Reactive Damping control. The power absorbed by the WECs under the influence of the PTO with two different control models is examined. Further, the mean interaction factor (q-factor) and the CWR for the wave power absorption of the two different hybrid concepts are studied to understand the efficiency of the hybrid system.

## 3.5 WAVE CLIMATE

The significant wave height $H_s$ and the peak spectral period $T_{ps}$ considered for the present study are representatives of the North Sea. Seven sea states, as in Sinha et al. (2016), shown in Table 5, are considered to analyse the wave power absorption. The sea states have been represented by using the JONSWAP spectrum for the North Sea. The spectrum is generated using a 2-parameter formula with significant wave height $H_s$ and peak spectral period $T_{ps}$.

Table 3.3: Reference Sea States (Sinha et al., 2016).

| Sea State | $H_s(m)$ | $T_{ps}(s)$ |
|---|---|---|
| 1 | 0.25 | 5.24 |
| 2 | 0.75 | 5.45 |
| 3 | 1.25 | 5.98 |
| 4 | 1.75 | 6.59 |
| 5 | 2.25 | 7.22 |
| 6 | 2.75 | 7.78 |
| 7 | 3.25 | 8.29 |

## 3.6 RESULTS AND DISCUSSION

The TLP-type floating wind turbine platform with various arrangements of cone-cylinder heaving WECs in circular and concentric patterns is examined under regular waves of unit amplitude using the numerical simulation tool WAMIT to study the effect of waves on the WECs when grouped in an array around the offshore floating wind turbine platform. The hydrodynamic coefficients (added mass and damping coefficient) of the WEC may change with the influence of the platform and other WECs. The ratio of the hydrodynamic coefficients for a single WEC to that for the hybrid system is evaluated, as by Hu et al. (2020), to analyse the

impact of the platform and other WECs. The added mass and damping represent the impedance to the system's motion. Further, the instantaneous wave power absorption of each hybrid configuration is compared for a zero-degree wave heading angle. The Influence of the PTO on wave power absorption is studied for two different damping control strategies of hydraulic PTO systems. The study then examines the efficiency of the hybrid system in wave power absorption.

### 3.6.1 Variation of Added Mass and Damping Coefficient

The virtual increase in mass that the WEC feels as a result of its interactions with the surrounding water is represented by the increased mass coefficient. It takes into account the water's inertia as it moves alongside the WEC as it oscillates in reaction to wave forces. A larger added mass coefficient might increase the absorption of wave energy because it denotes a greater mass impact. An increase in added mass increases the effective mass, improving the displacement of the WEC and further increasing the wave power absorption. The WEC's motion is dampened by dissipative forces, which are represented by the damping coefficient. It takes into consideration energy losses brought on by a number of different phenomena, including wave-induced drag, viscous effects, and power take-off system losses. The overall power absorption may be impacted by a higher damping coefficient, which denotes stronger dissipation. An optimal damping co-efficient can aid in maximising wave power absorption by balancing the extraction of energy from waves with the dissipation of excess energy.

#### 3.6.1.1 Submerged Tension-Leg Platform with WECs

The variation of the ratio of added mass for the circular arrangement of WECs around STLP is shown in Fig. 3.7(a-d). The most significant amplification factor of the ratio of added mass for $C_1$ (Fig. 3.7a) is close to 1.2, and the reduction factor is close to 0.3. Almost all the values are observed to be close to 1.0 for a wave period $T_p$ above 10s for both the WECs of the $C_1$ hybrid system, suggesting a negligible impact of the platform and other WECs on added mass. As the wave period increases, the interaction of the waves with the WEC gets reduced with a higher wavelength, further having a reduced impact on the added mass. The ratio of added mass is close to 1.0 for the $C_2$ configuration (Fig. 3.7b) for the wave period region, $T_p > 10s$ showing the negligible impact of the motion of STLP and WECs on the added mass. The most significant amplification factor is more than 1.4, and the reduction factor is close to 0.4 for

$T_p \leq 10s$ showing that the arrangement WECs around STLP in the $C_2$ configuration has an impact on added mass. The variation in the ratio of added mass for the circular $C_3$ patterns of six WECs is shown in Fig. 3.7c. The most significant amplification factor for the circular array $C_3$ is a little less than 1.2, as in Fig. 3.7(c). The variation may be because the wave has sufficient space to interact with the WECs in the $C_3$ configuration, nullifying the sheltering effect from other WECs. In addition, for the $C_4$ configuration, there is sufficient space for the reflection of waves from STLP and other WECs.

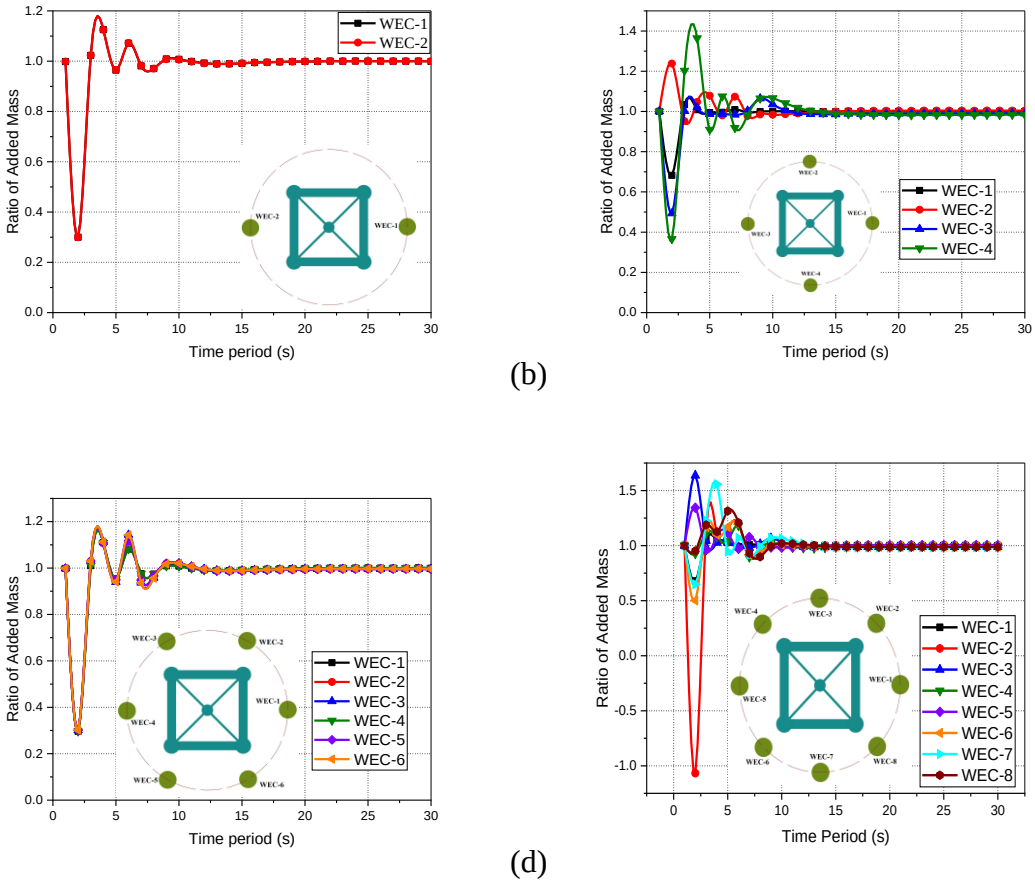


Fig. 3.7: Variation in ratio of added mass of (a) $C_1$, (b) $C_2$, (c) $C_3$, and (d) $C_4$ for the gravity waves.

Almost all the ratios of the added mass are close to 1.0 for both circular $C_4$ patterns of WECs for the wave period, indicating the influence of STLP and other WECs for both $C_4$ configurations is negligible on added mass. The most significant amplification factor of added mass for the circular pattern $C_4$ is close to 1.6 for the wave period within $2s \leq T_p \leq 4s$ for WEC-3, and the reduction factor is close to -1.0 for the wave period $2s \leq T_p \leq 4s$ for WEC-2, as in Fig. 3.7(d).

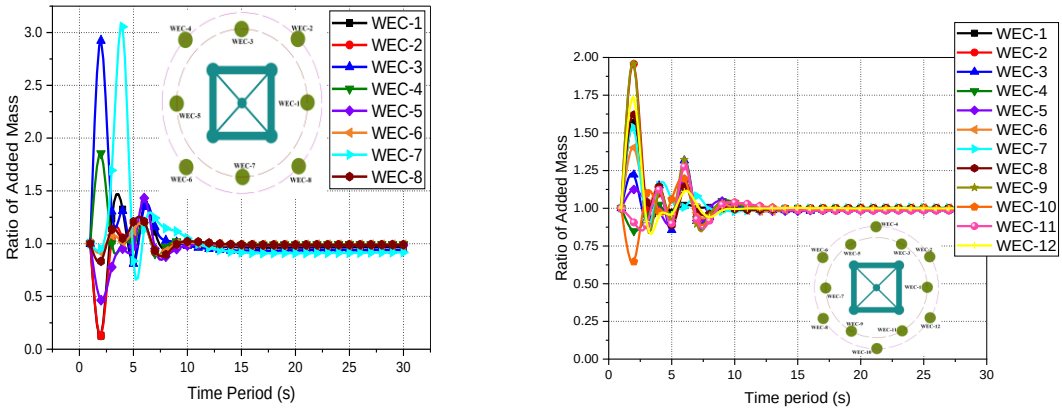


Fig. 3.8: Variation in ratio of added mass of (a) $C_5$ and (b) $C_6$ configurations for the gravity waves.

The variation in the ratio of added mass for the concentric arrangement of WECs around the STLP is shown in Fig. 3.8(a, b). The most significant amplification factor of added mass for the concentric pattern $C_5$ is just above 3.0 for the wave period $3s \leq T_p \leq 5s$ for WEC-7, and the reduction factor is close to 0.1 for the wave period $1s \leq T_p \leq 3s$ for WEC-2, as in Fig. 3.8(a). The impact of STLP and other WECs on the added mass is more significant for the $C_5$ configuration compared to the $C_4$ configuration. This may be because, for the $C_5$ configuration, the reflected waves from the STLP and other WECs may interact with the incident waves with more space between the STLP and the other WECs. Also, in the case of the $C_5$ configuration, the WEC-3 and WEC-7 are observed to have higher variation at 1.0. This may be due to the WECs being very close to the STLP floater and hence having a higher impact from the reflected waves and the effect of incident waves with minimum sheltering. Negative added mass is observed for $C_4$ configuration for wave period 1.0 s. The negative added mass shows the reduction in the actual mass of the WEC when oscillating, leading to the stability issues of the WEC-2 in the $C_4$ configuration. This may be due to the interaction of incident and reflected waves of the WECs. Also, with the reflected waves, the resonating pattern of the waves changes, leading to a sudden change in heave (Vijay et al., 2022). For the $C_6$ configuration, the most significant amplification factor for added mass is close to 2.0 for waves of the period $1s \leq T_p \leq 3s$ for WEC-6, and the reduction factor is close to 0.6 for the waves of the wave period $1s \leq T_p \leq 3s$ for WEC-10, as in Fig. 3.8(b). It is observed that the amplification factor is further increased with the addition of the WECs, suggesting the influence of the reflected waves from

the WECs and the STLP. Almost all the ratios are close to 1.0 for the $C_6$ hybrid system for the wave period $T_p > 8s$. This shows the negligible impact on added mass for the STLP and WECs for the $C_6$ configuration for higher wave periods. It has a minimum effect on the WECs and the STLP due to its considerable wavelength.

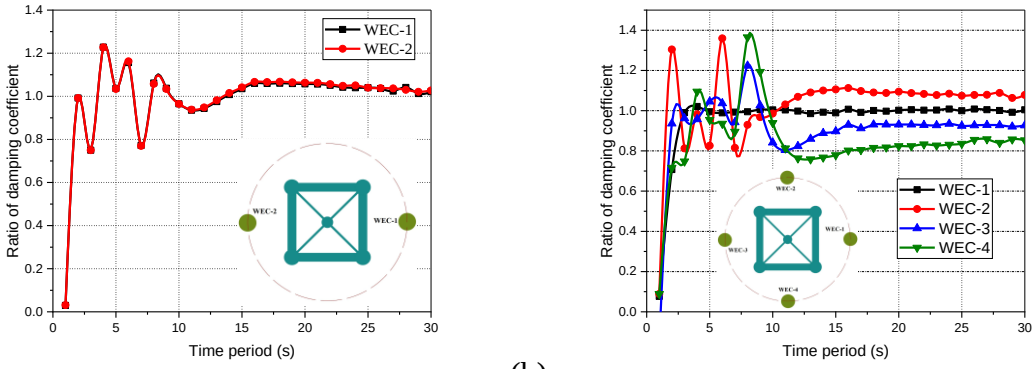


(a)




(b)

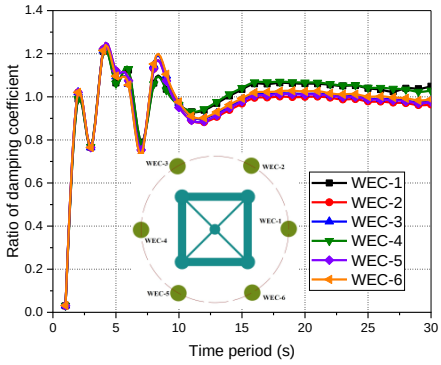


(c)

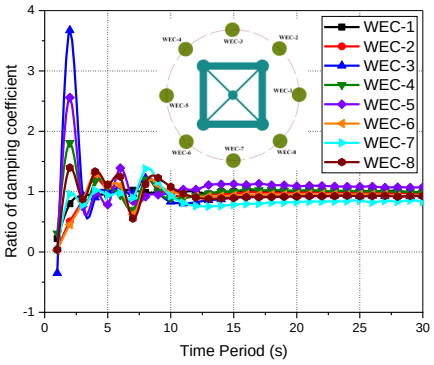


(d)

Fig. 3.9: Variation in ratio of the damping coefficient of (a) $C_1$, (b) $C_2$, (c) $C_3$, and (d) $C_4$ for the gravity waves.

The ratio of the damping coefficient (Fig. 3.9a) for the $C_1$ configuration is close to 1.0 for most gravity waves. Negligible variation in the ratio of the damping coefficient is observed for the wave period $T_p > 10s$. The wave period $T_p \leq 10s$ is observed to have the damping coefficient values fluctuating within 0.7-1.2, and it is observed that the impact of STLP and other WECs is more on the damping coefficient compared to added mass for the $C_1$ hybrid system. This may be due to the influence of the reflected waves from other bodies being minimum for $C_1$ configuration. The higher impact of the damping may increase the heave response amplitude and hence improve the power absorption of the system. Fig. 3.9(b) presents the ratio of the damping coefficient for the $C_2$ configuration. Apart from WEC-1 of the hybrid configuration

$C_2$, all other WECs have more deviations at 1.0, suggesting the significant influence of STLP and other WECs on the damping of WECs for $C_2$ configuration for the wave period region $T_p < 10s$. In the case of WEC-1, the STLP, and other WECs provide better shelter from the impact of waves, hence having the slightest variation.

Further, for the waves of wave period $T_p \leq 10s$, it is observed that the influence of STLP and other WECs on the damping of WECs is much more vital than on the added mass. Fig. 3.9(c) shows that the ratio is close to 1.0 for the $C_3$ configuration for $T_p > 13s$. The WEC-1 and WEC-4 have a ratio above 1.0 for $T_p > 13s$ showing the influence of the array of WECs on the motion of the WECs. The variation in the ratio of the damping coefficient for WEC-1 may be due to the direct impact of the waves without any sheltering, and in the case of WEC-4, the reflected waves may influence the added mass of the WEC. In addition, from the study of added mass and damping, it is observed that the influence of the STLP and other WECs on the damping coefficient is more significant than on the added mass. It is also observed that the variation in added mass and damping is minimum, with six WECs arranged in a circular pattern ($C_3$) compared to the $C_1$ configuration. The variation in the damping ratio for the $C_4$ configuration is less for $T_p \geq 10s$ as noted in Fig. 3.9(d), compared to the wave period $T_p < 10s$. The most significant amplification factor for the circular array $C_4$ is close to 3.6 for waves of wave period $1s \leq T_p \leq 3s$, and the reduction factor is close to -0.4 for waves of the period $0s \leq T_p \leq 2s$ for WEC-3. Negative damping is also observed for the $C_4$ configuration for wave period 1.0 s, confirming the influence of the entrapped fluid between the STLP and the WEC. The negative damping leads to higher heave response amplitude. Higher heave response for the WEC may lead to structural damage to the WEC in a short period, as discussed in Amere and Ayele (2018).

In the case of the concentric pattern $C_5$, the most significant amplification factor is above 4.5 for waves of period $2s \leq T_p \leq 4s$, and the reduction factor is around -0.5 at $0s \leq T_p \leq 2s$ as in Fig. 3.10(a). Further, the influence of STLP and WECs on damping for the concentric array $C_5$ is thus more substantial compared to the circular array of eight WECs ($C_4$). The maximum value for damping with eight WECs ($C_4$) is increased by 275% with the addition of WECs compared to the $C_1$ configuration. This is due to the more decisive influence of the reflected

waves from the STLP for the $C_5$ configuration. Also, the effect of the motion of STLP and WECs on damping is more substantial than on the system's added mass for both circular and concentric arrays of WECs, which can be due to the higher reflection of the waves from the WECs and the STLP.

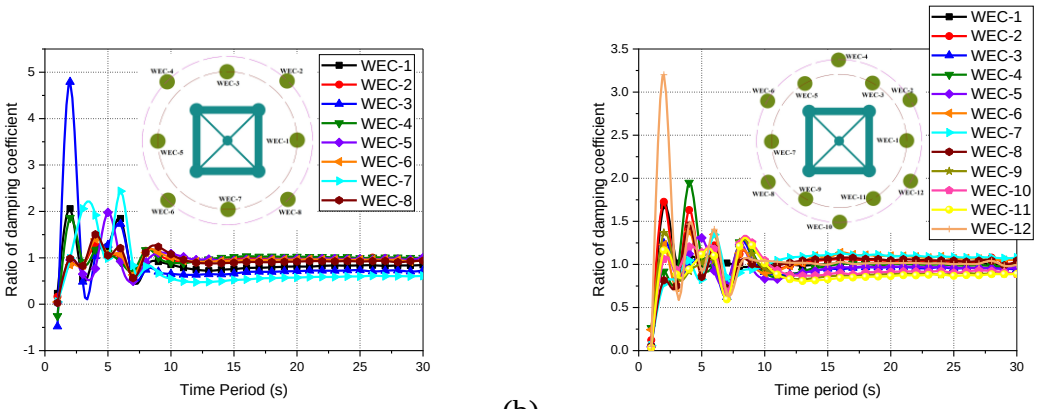


(a) (b)

Fig. 3.10: Variation in ratio of the damping coefficient of (a) $C_5$ and (b) $C_6$ for the gravity waves.

Fig. 3.10(b) presents the ratio of the damping coefficient for the $C_6$ hybrid floating platform. The ratio of the damping coefficient is close to 1.0 for waves of wave period $T_p > 8s$. The most significant amplification factor for the damping coefficient is above 3.0 for waves of the period $1s \le T_p \le 3s$ for WEC-12, and the reduction factor is close to 0.0 for the waves of the wave period within $0s \le T_p \le 2s$ for most of the WECs. The maximum amplification factor of the damping coefficient ratio for the $C_6$ configuration is also increased by 150% compared to the $C_1$ configuration confirming the influence of the reflected waves.

The WEC-4 and WEC-10 are observed to have higher variation from 1.0 for the damping coefficient, possibly due to the direct impact of the incident waves. Also, the WEC-4 and WEC-10 are away from the STLP and thus reduce the impact of the reflected waves. The comparative study on different configurations of WECs around STLP-type floating wind turbines indicates that for wave period $T_p > 10s$, the ratio of added mass and damping coefficient is close to 1.0 for all configurations, indicating that the size of wave energy converters is smaller than the wavelength of waves. For all configurations, the effect of the STLP and other WECs on the damping coefficient is more significant than added mass, especially at wave periods $T_p < 10s$. The deviation of added mass and damping coefficient ratios from 1.0 is more important at lower wave periods. The variation may be because, for lower wave periods, the wavelength will be

lower and may have more interaction with the single WEC compared to the hybrid system, as the wave acting on the WECs in front of the platform will be more compared to that at the back side due the sheltering effect of the platform and other WECs. In the case of a higher wave period, the wavelength will be larger and may have similar interactions with the WECs for both single and hybrid systems. Further, the study on the ratio of added mass and damping coefficient observed that the impact of waves on the WECs is minimum for the circular arrangement of eight WECs around the STLP ($C_4$). The deviation in the ratio of added mass for the circular arrangement of eight WECs ($C_4$) is observed only for the wave period below 4.0 s and is lowest compared to other arrangements. The deviation in the ratio of the damping coefficient for concentric arrangement $C_5$ is observed for a wave period below 5 s. This may be because, for concentric arrangement, the interaction of waves with the WECs will be more as it is widespread compared to other configurations. The reduced damping and minimum influence of the added mass on the motion of the WECs provide a higher ability for wave power absorption.

#### 3.6.1.2 Frustum Tension-Leg Platform with WECs

The variation observed in the hydrodynamic coefficients is related to the different positions of WECs. Fig. 3.11(a-d) shows the ratio of added mass for a single WEC to that for a WEC in the hybrid system for the different circular arrangements of the WECs around FTLP. Fig. 3.11(a) shows the ratio of added mass for the $FW_1$ configuration. It is observed that the variation of the ratio from 1.0 is minimal, showing the minimum influence of the FTLP and other WECs on the WEC. The variation from 1.0 is observed in the wave period region $T_p < 10s$, where the amplification factor is 1.005. The reduction factor is also observed very close to 0.99, confirming the negligible influence of the FTLP and other WECs on the WEC. Fig. 3.11(b) shows the ratio for $FW_2$ configuration with four WECs in a circular pattern around FTLP.

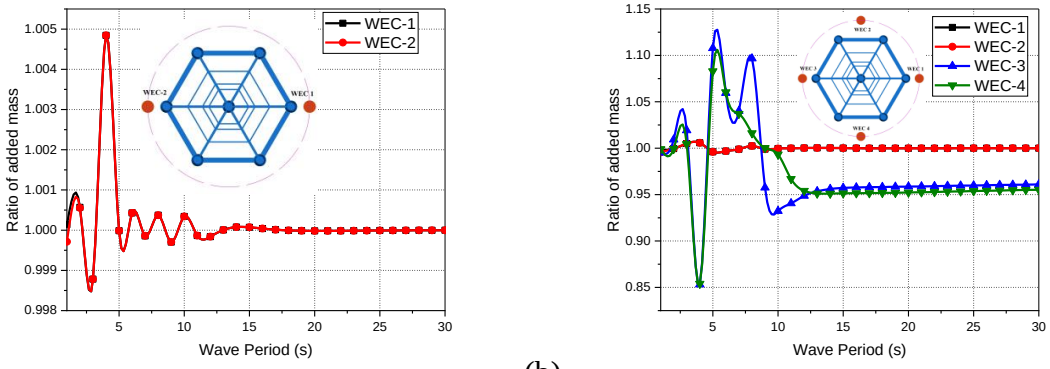


(a) (b)

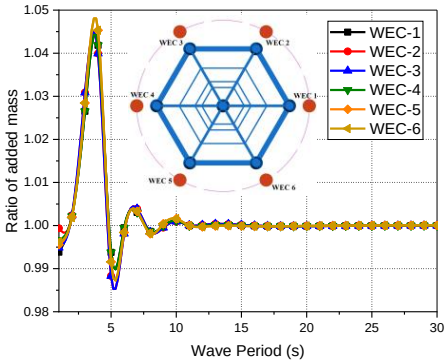


(c)

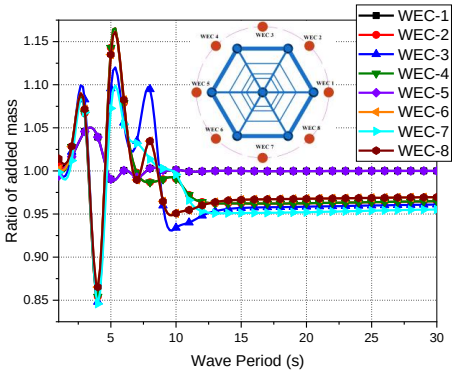


(d)

Fig. 3.11: Variation in ratio of added mass of (a) $FW_1$, (b) $FW_2$, (c) $FW_3$, and (d) $FW_4$ for the gravity waves.

The variation from 1.0 is observed to be higher for the region $T_p < 10s$ and is observed to be similar for other hybrid systems considered. The variation is negligible for WEC-1 and WEC-2, placed on the leeward side, maybe because of the minimum action of the reflected waves. For WEC-3 and WEC-4, the added mass increased by 12.5%, which may be due to sufficient room for the interaction of the incident and the reflected waves. Fig. 3.11(c) shows the ratio for $FW_3$, where the variation of the added mass is observed to be minimum.

Also, it is observed that the behaviour of all the WECs, placed around FTLP is similar, having an amplification factor close to 1.05 and a reduction factor close to 0.99 for $T_p < 10s$. This may be because the WECs are almost placed at a similar location, very close to the outer columns of the FTLP, further having similar behaviour. Also, a maximum increase of 5% in the added mass is only observed for the WECs in the FW3 configuration. The variation in the ratio of added mass for $FW_4$ is seen in Fig. 3.11(d). Similar to FW2, the variation in the ratio is higher for $FW_4$ than $FW_1$ and $FW_3$ for the wave period region $T_p < 10s$. The highest amplification factor is observed close to 1.15, and the reduction factor is close to 0.85 for the WEC-2, WEC-4, WEC-6, and WEC-8. It is seen from Fig. 3.11(d) that these WECs are placed at equal distances from FTLP and other WECs, further showing the negligible influence of wave sheltering. No variation is observed for the WEC-1 and WEC-5, placed on the seaward and leeward sides in the direction of the incident waves. This may be because of the sufficient restoring force developing on the WECs, with the influence of the reflected waves as the WECs are placed closer to FTLP. The ratio of added mass for the hybrid to those for a single WEC, for the concentric arrangement of WECs, is shown in Fig. 3.12(a,b). Similar variation is

observed for both circular and concentric arrangements of WECs ($FW_4$ and $FW_5$), as seen in Fig. 3.11(d) and Fig. 3.12(a).

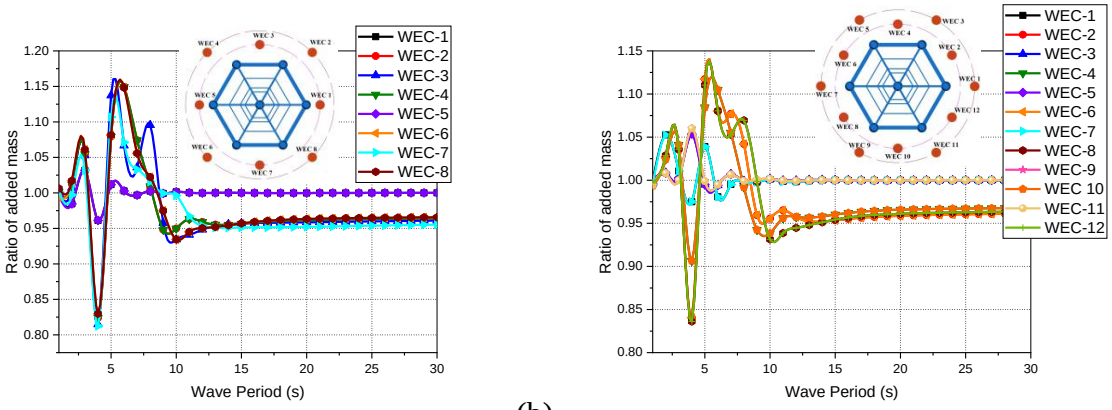


(a) (b)

Fig. 3.12: Variation in ratio of added mass of (a) $FW_5$ and (b) $FW_6$ configurations for the gravity waves.

The highest amplification factor and the reduction factor for the WECs in the $FW_5$ configuration are improved by 15% compared to isolated WECs for the wave period region $T_p < 10s$. The variation in the ratio of added mass for $FW_6$ is shown in Fig. 3.12(b). The highest amplification factor is close to 1.14, and the reduction factor close to 0.83 is observed for the WECs on the seaward side. With the increase in the WECs, the sheltering effect is improved, further reducing the added mass of the WECs on the leeward side. From the study, it is observed that the variation in the added mass is minimum for the waves of $T_p > 10s$. This may be because of the minimum interaction of the waves with the WECs due to the higher wavelength. Also, it is observed that the variation in added mass is minimum for the WECs closer to the outer pontoon for both circular and concentric patterns. This may be because there need to be more space for the action of reflected waves, further having minimum impact on the wave profile. When arranged in circular and concentric patterns, a higher influence on the added mass is observed for the eight WEC configurations ($FW_4$ and $FW_5$). The radiation resistance force is connected to the average power transferred between the water and the body. The waves that are produced with the movement of the body cause this force to exist. The radiation resistance coefficient estimates the size of the waves. The radiation resistance also indirectly indicates the amount of power that may be extracted from the incoming waves as these waves interfere with them.

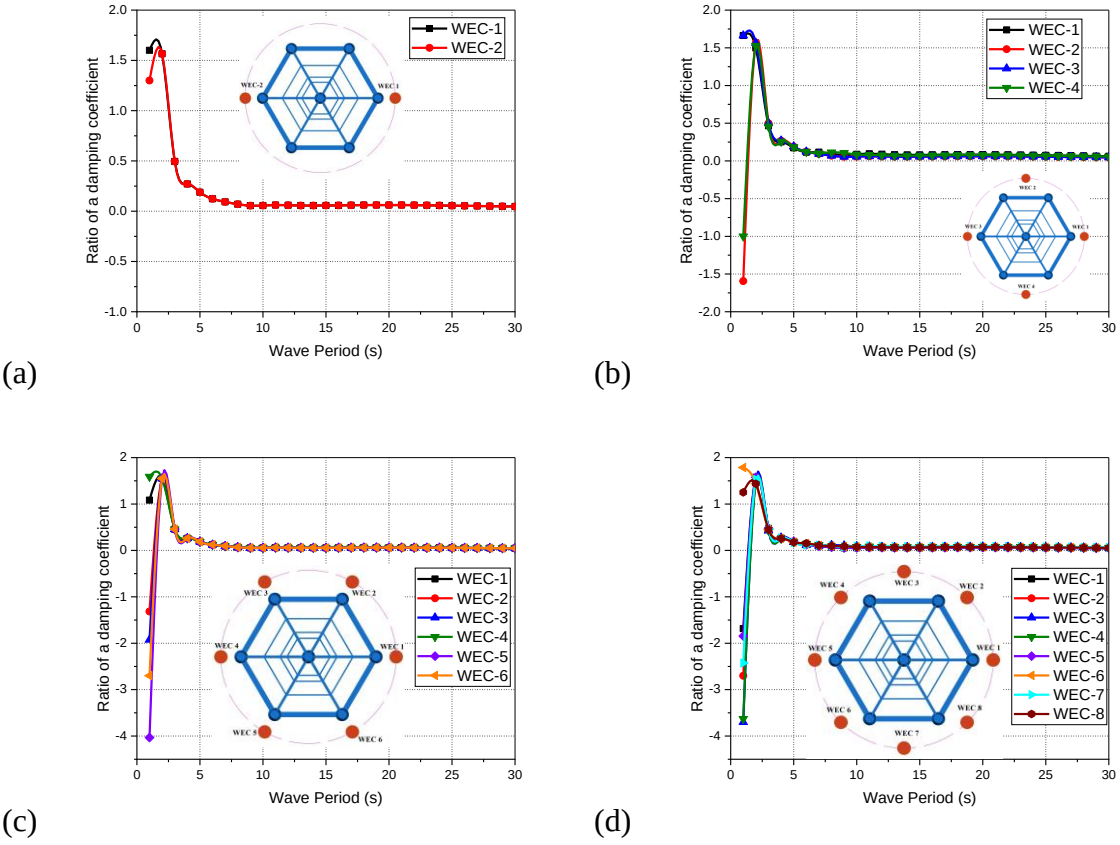


Fig. 3.13: Variation in ratio of the damping coefficient of (a) FW1, (b) FW2, (c) FW3, and (d) FW4 for the gravity waves.

Fig. 3.13(a-d) shows the variation in radiation damping for the circular arrangement of the WECs around FTLP. Fig. 3.13(a) shows that the impact on radiation damping is higher compared to added mass for the $FW_1$ configuration. The highest amplification factor for $_{FW1}$ is 1.7 for $T_p < 5s$ and the reduction factor is close to 0.0 for most gravity waves. The impact on damping for the WECs with the presence of FLTP and other WECs is higher than the isolated WEC. Fig. 3.13(b) shows that the variation in damping is not much disturbed with the addition of two WECs for the $FW_2$ configuration. The highest amplification is close to 1.7 for WEC-1 and WEC-3, similar to the $FW_1$ configuration. Negative damping is observed for the WEC-2 and WEC-4, placed in the transverse direction of the wave. This may be because of the sufficient space available for the reflected waves around the WEC and FTLP, causing additional damping. The variation in the radiation damping for $FW_3$ is shown in Fig. 3.13(c). The highest reduction factor is improved by around 300% for the wave period $T_p = 1s$ and has reduced drastically for other wave periods. Also, it is observed that the values are very close to zero, showing the considerable reduction in damping developed for the WECs when arranged

around STLP and other WECs. Similar to $FW_2$, negative damping is observed for the initial wave period for the WECs placed at some distance away from the direct impact of the waves. The reduction in damping may be because of the impact of the reflected waves formed in the clearance available between the FTLP and WEC. As seen in Fig. 3.13(d), the increase in the WECs around the FTLP has minimum influence on the radiation damping of the WECs. Negative damping is observed for the initial wave period and is coming close to zero to show the impact of the FTLP and other WECs in reducing the radiation damping. The negative damping may lead to a higher heave response of the WEC. Even though the power absorption of the system is improved with the higher heave response, there is every possibility of structural damage developing on the system in a short period.

The WECs are arranged in a concentric pattern around FTLP to observe the influence of the spacing around the WECs. The ratio of the damping coefficient for $FW_5$ and $FW_6$ is shown in Fig. 3.14(a,b). The variation in damping is observed to change with the arrangement pattern of the eight WECs, as seen in Fig. 3.14(a). The highest amplification factor is observed close to 4.0, and the reduction factor is observed close to -4.5 for the wave period $T_p = 1s.$ This may be because, with the concentric arrangement pattern, there is a further increase in the space between the FTLP and other WECs, having the more decisive influence of the reflected waves. Also, there will be sufficient space around the WECs to have a direct incidence of the WECs, producing more damping force. A negative damping ratio is observed for WEC-4, WEC-5, and WEC-6, possibly due to higher wave force with direct wave breaking on the WECs.

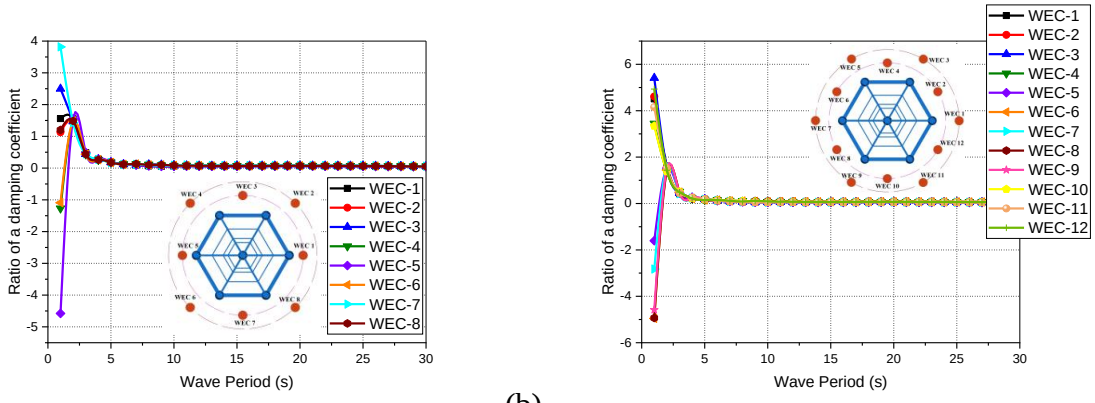


(a) (b)

Fig. 3.14: Variation in ratio of the damping coefficient of (a) FW5 and (b) FW6 for the gravity waves.

Fig. 3.14(b) shows the ratio of the damping coefficient for the $FW_6$ configuration. The highest amplification factor for the $FW_6$ is increased by 32.5% compared to the concentric arrangement

of the eight WECs ($FW_5$). This may be because, with the addition of the WECs in the similar constraint space around FTLP, there is more possibility of the reflection of the waves from the FTLP and other WECs, further increasing the damping force. The highest value for the reduction factor is almost similar to that of the $FW_5$ configuration. Fig.s 3.13(a-d) and 3.14(a,b) show that the impact of the FTLP and other WECs is more on the damping than the added mass. The damping ratio for most cases is very close to zero, depicting the higher value of the damping for the isolated WEC compared to the WEC in the array.

### 3.6.2 Instantaneous Power Absorbed

The total power absorption in irregular waves for each floater is determined for seven different sea states by applying the linear superposition of the floater responses in regular waves as in Sinha et al. (2016). The spectrum of the amplitude of the floater position for forty frequencies in the range between $0.22\ rad/s$ to $1.885\ rad/s$ with $\Delta\omega=0.0427\ rad/s$ is used in the present study. The floater heave response and the damping coefficient are calculated using the hydrodynamic tool WAMIT.

#### 3.6.2.1 Submerged Tension-Leg Platform with WEC

Fig. 3.15(a-d) shows the maximum instantaneous power absorbed for the different circular arrangements of WECs around the STLP for different sea state conditions. Fig. 3.15(a) presents the wave power absorption for STLP with two WECs in a circular pattern ($C_1$). The wave power absorption increases with the increase in the wave height. The wave power absorption is higher for the WEC-2, which is under the direct incidence of the waves. The maximum wave power absorption for WEC-2 is 10% higher compared to WEC-1, having the sheltering effect of the STLP. Fig. 3.15(b) shows the wave power absorption of WECs in the $C_2$ configuration. The wave power absorption is almost similar for the WEC-2, WEC-3, and WEC-4, having the direct wave incidence. The WEC-2 and WEC-4 is having slightly improved wave power absorption, possibly due to the influence of the reflected waves. The minimum wave power absorption of WEC-1 is due to the sheltering of the waves by the STLP and other WECs. Fig. 3.15(c) shows the wave power absorption for the $C_3$ configuration. The wave power absorption of the WECs is slightly less for the $C_3$ configuration compared to $C_2$. This may be because the WECs (other than WEC-1 and WEC-4) are kept much closer to the STLP, having the more scattering of waves. The wave power absorption by the WECs is almost similar to all six WECs arranged around STLP, though a slight higher absorption is observed for the WEC-2. Fig. 3.15(d) shows the wave power absorption for STLP with eight WECs in a circular pattern ($C_4$).

The WECs are observed to have higher wave power absorption compared to other circular patterns. An average 25% increase in wave power absorption is observed for the WECs in the $C_4$ configuration. This may be due to the influence of both incident and reflected waves, as the WECs are kept much closer compared to other arrangement patterns. The WEC-4, WEC-5, and WEC-6 having the direct wave incidence are observed to have higher wave power absorption.

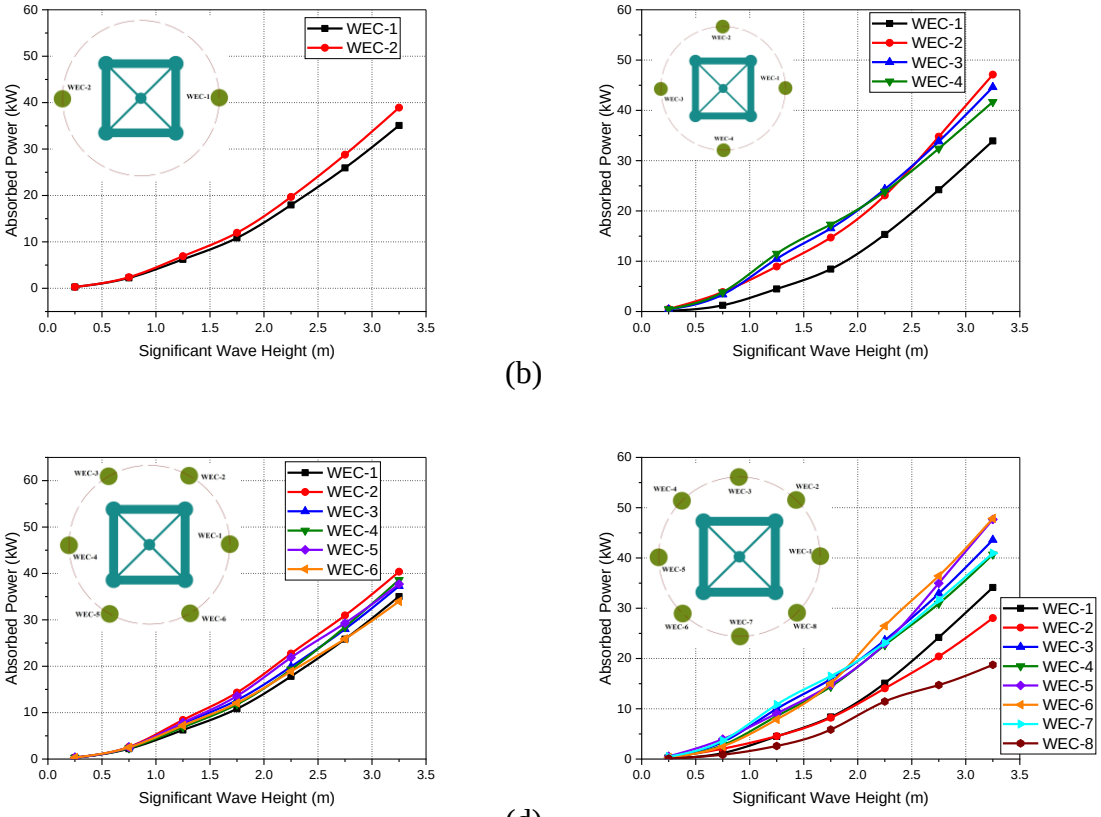


Fig. 3.15: Maximum power absorbed for (a) $C_1$, (b) $C_2$, (c) $C_3$, and (d) $C_4$ under zero-degree wave heading angle.

Fig. 3.16(a,b) shows the wave power absorption for the concentric arrangement of the WECs around the STLP. The highest wave power absorption is observed for the WECs in the $C_5$ configuration (Fig. 3.16a) having WECs in the concentric pattern. For the lower-height regions, the wave power absorption is higher for the circular arrangement of eight WECs ($C_4$). But for the regions with wave height above 2 m, the wave power absorption is higher for the concentric pattern ($C_5$). The WECs on the outer circle (WEC-2 and WEC-6) are observed to have higher wave power absorption for the lower wave height regions. WEC-7 placed in the inner circle

having the influence of both incident waves and reflected waves are observed to have the highest wave power absorption.

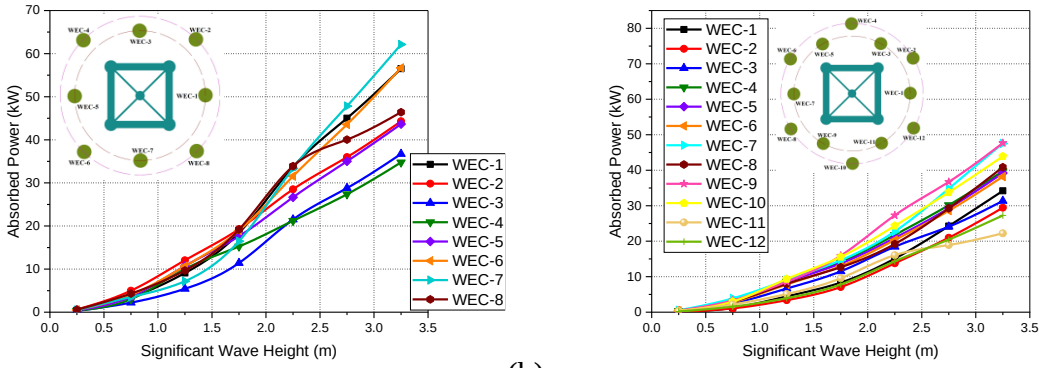


(a) (b)

Fig. 3.16: Maximum power absorbed for (a) $C_5$ and (b) $C_6$ under zero-degree wave heading angle.

A 30% increase in the wave power absorption is observed for the $C_5$ configuration in higher wave height regions. For the lower wave height regions, 11% increase in wave power absorption for the $C_4$ configuration is observed. Fig. 3.16(b) shows the wave power absorption for the concentric arrangement of twelve WECs ($C_6$). The wave power absorption for the $C_6$ configuration is less than $C_5$. This can be due to higher wave scattering with reduced space between the WECs and the STLP for the $C_6$ configuration. Higher wave power absorption is observed for WEC-7 and WEC-9 kept in front of the STLP, having the direct influence of the incident waves and a higher influence of the reflected waves. With reduced spacing between the WECs, even though the influence of the reflected waves is higher, the sheltering of the waves will also be higher. Further, it can be concluded that optimized spacing for wave power absorption by the WECs is observed for the concentric arrangement of eight WECs around STLP ($C_5$).

### 3.6.2.2 Frustum Tension-Leg Platform with WEC

The maximum power absorbed under irregular waves by each WEC for a zero-degree wave heading angle is studied and compared in Fig. 3.17(a-d). Fig. 3.17(a) shows the variation of the maximum power absorbed under different wave conditions for the $FW_1$ configuration. The wave power absorption is observed to increase with the increase in the wave height. Further, it is observed that the WEC on the seaward side has higher wave power absorption than that on the leeward side.

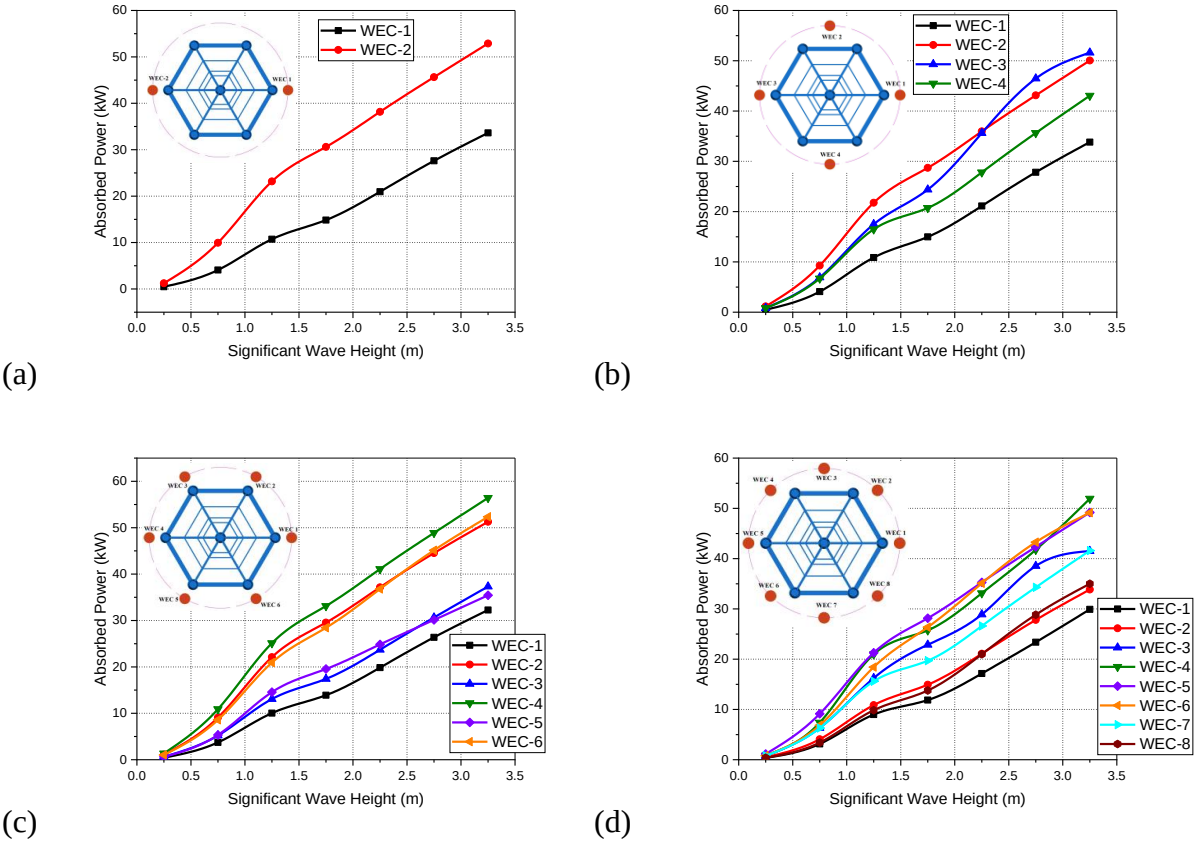


Fig. 3.17: Maximum power absorbed for (a) $FW_1$, (b) $FW_2$, (c) $FW_3$, and (d) $FW_4$ under zero-degree wave heading angle.

Approximately 130% increase in power absorption is observed for the WEC-2 for wave heights below 2.25 m, and around 90% increase in power is observed for the WEC-2 when kept at a region with wave heights above 2.25 m. This is due to higher wave force developing on the WEC-2 with the direct impact of the incident waves without any sheltering of FTLP and other WECs. Fig. 3.17(b) shows the maximum power absorption for the $FW_2$ configuration with four WECs in a circular pattern around FTLP. Similar to the $FW_1$ configuration, the WECs on the seaward side have higher wave power absorption than the other two WECs on the leeward side. An average 50% increase in power absorption is observed for the WECs on the seaward side compared to that on the leeward side. Further, it is observed that for wave heights above 2.25 m, the WEC-2 has higher power absorption compared to WEC-3, which may be due to the direct impact of waves without any sheltering. The WECs will also have the influence of the reflected waves from the FTLP and other WECs. Also, sufficient space for entrapping the fluid leads to the possibility of improving the heave response, further having higher wave power absorption. Also, it is observed that the power absorption of the WEC tends to decrease by 15%

(average) with the addition of the WECs around FTLP for $FW_2$ compared to $FW_1$. Fig. 3.17(c) shows the maximum power absorbed for the $FW_3$ configuration. The WEC-4 is observed to have the highest wave power absorption and is decreasing as the WECs are kept along the leeward side. WEC-2 and WEC-6 are also observed to have 60% (average) higher power absorption than WEC-3 and WEC-5 on the leeward side. This may be due to the influence of the reflected waves, as there is sufficient space available between the FTLP and the WECs for the interaction of the incident waves and the reflected waves, which may improve the heave response of the WEC. Also, there is an average 8% increase in the maximum power absorbed by the WECs for the $FW_3$ configuration. The maximum energy absorbed by the WECs in the FW4 configuration is shown in Fig. 3.17(d). Compared to the six WEC configurations in circular arrangement ($FW_3$), the $FW_4$ configuration is observed to have lower wave power absorption. There is an average reduction of about 30% compared to $FW_3$, which has the highest wave power absorption. Also, it is observed that the WEC-4, WEC-5, and WEC-6 have approximately similar wave power absorption for the waves of height more than 2.25 m, which may be due to the direct wave breaking on the WECs.

The power absorbed by the WECs is studied for the concentric arrangement of eight ($FW_5$) and twelve WECs ($FW_6$). Fig. 3.18(a,b) shows the total power absorbed for the FW5 and FW6 configurations. Fig. 3.18(a) shows that the wave power absorbed by the concentric arrangement of eight WECs ($FW_5$) configuration is more compared to the circular arrangement of eight WECs ($FW_4$). An average increase in wave power absorption of approximately 12% is observed for the $FW_5$ configuration compared to $FW_4$. Also, the highest wave power absorption is observed for WEC-6 and WEC-4, both having a direct incidence of the wave.

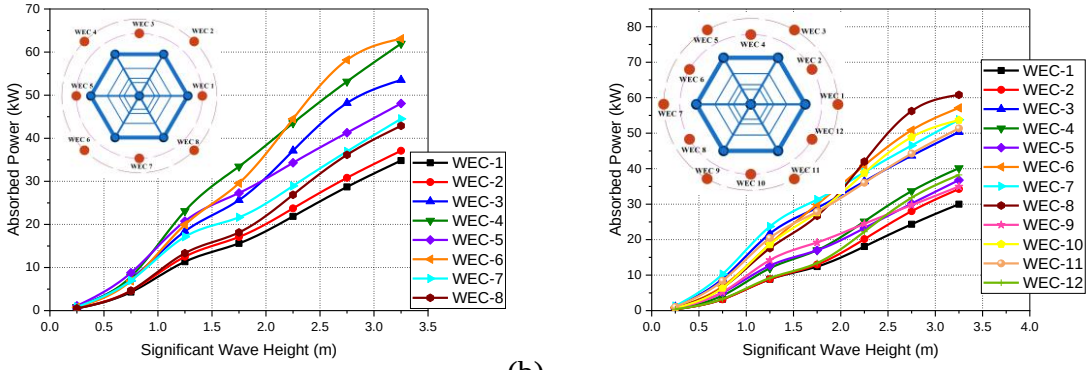


(a) (b)

Fig. 3.18: Maximum power absorbed for (a) $FW_5$ and (b) $FW_6$ under zero-degree wave heading angle.

Further, there is sufficient space around the FTLP and the WECs for the reflected waves to improve the heave response of WEC, leading to higher wave power absorption. It is observed that the wave power absorption is reduced by 8% (average) for the $FW_6$ configuration compared to $FW_5$, as seen in Fig. 3.18(b). This may be because the enclosed space between the FTLP and other WECs is reduced with the addition of the WECs, thereby reducing the influence of the reflected waves. Also, it is observed that the WEC-7 has the initial impact of the wave on the seaward side but lesser power absorption than WEC-6 and WEC-8, as the latter is placed closer to the FTLP. This confirms the influence of the reflected waves in the wave power absorption.

### 3.6.3 Influence of Wave Heading Angle on Wave Power Absorption

The direction from which the waves approach the platform is determined by the heading angle of the incoming waves. The alignment between the wave direction and the wave energy converter's orientation determines the wave power absorption. The vertical motion of the waves is converted into energy by the heaving point absorber wave energy converter. The efficiency of energy capture is maximised when the motion of the converter and the direction of the wave coincide. The power absorption may be diminished if the wave heading angle differs greatly from the converter's optimal direction.

#### 3.6.3.1 Submerged Tension-Leg Platform with WEC

The highest wave power absorption for the STLP-WEC hybrid system is observed for the concentric arrangement pattern of eight ($C_5$) and twelve ($C_6$) WECs. Further, the influence of the wave heading angle on the wave power absorption is studied for $C_5$ and $C_6$ configurations, as seen in Fig. 3.19(a,b). For both $C_5$ and $C_6$ configurations, the highest wave power absorption is observed for a 60° wave heading angle. For the $C_5$ configuration, the wave power absorption is higher for 0° wave heading angles for wave heights below 2.5 m and is slightly decreased for higher wave heights as seen in Fig. 3.19(a). Lower wave power absorption is observed for the 30° wave heading angle. This may be because, for the 30° wave heading angle, the waves have no direct incidence on the WECs, further having lower power absorption efficiency. For the $C_6$ configuration (Fig. 3.19b), the wave power absorption increases with the increase in the wave heading angle. This may be because of the reduced space between the WECs and the STLP, so that the waves have a direct incidence on the WECs, further improving the wave power absorption efficiency. The STLP with eight WECs in concentric pattern ($C_5$) under 60°

wave heading angles has maximum wave power absorption. The variation in wave power absorption with the change in the wave heading angle is minimum for the $C_6$ configuration.

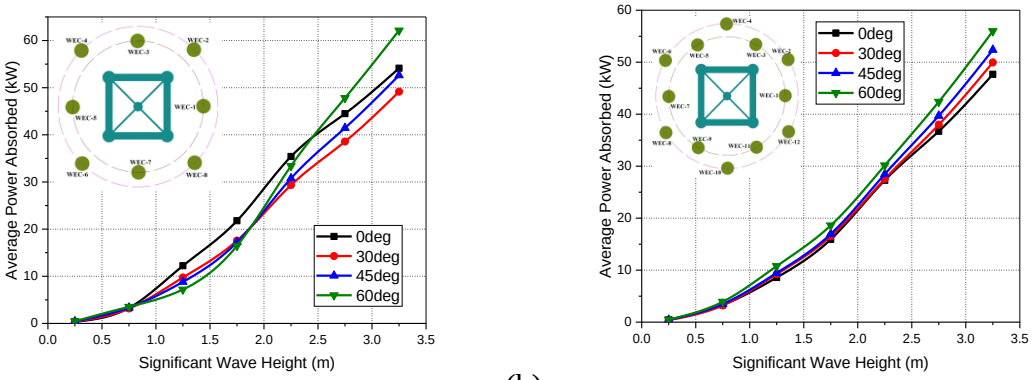


Fig. 3.19: Maximum power absorbed for (a) $C_5$ and (b) $C_6$ comparing different directions of wave incidence.

### 3.6.3.2 Frustum Tension-Leg Platform with WEC

It is observed that the highest absorption of wave power for the WECs is for the concentric arrangement pattern. The WECs of $FW_5$ and $FW_6$ are observed to have higher wave power capture. Further, average energy absorbed for different wave heading angles is studied for $FW_4$ and $FW_5$ configurations, as seen in Fig. 3.20(a,b), to observe the efficiency of the arrangement. Fig. 3.20(a) shows that variation in the wave power absorption is minimal for $FW_4$ with the change in the wave heading angle. The wave power absorption is higher for the 0° and 60°-wave heading angles. For the concentric arrangement of WECs, it is observed that the wave energy conversion increase with the change in the wave heading angle, as seen in Fig. 3.20(b).

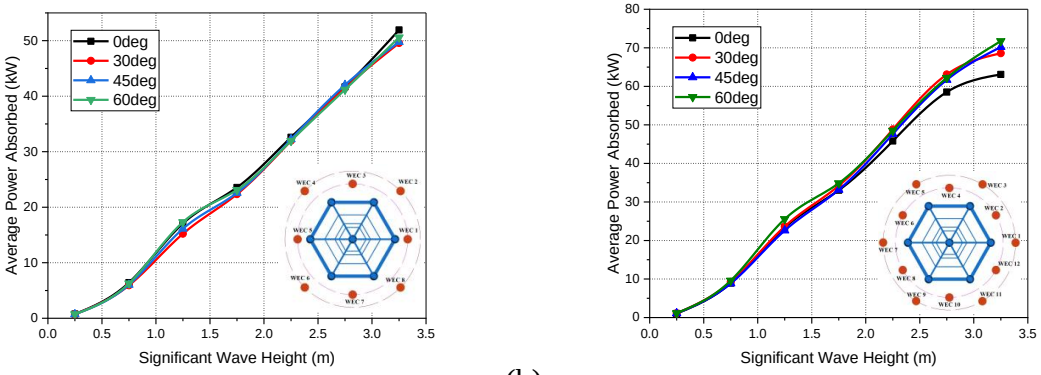


Fig. 3.20: Maximum power absorbed for (a) $FW_4$ and (b) $FW_5$ comparing different directions of wave incidence.

An average increase in 12% power absorption is observed for the $FW_5$ configuration as the wave direction changes from 0° to 60°. Also, it is observed that the wave power increases by 47% (average) for the $FW_5$ configuration compared to the FW4 configuration for irregular waves of different wave heading angles. The higher wave power absorption for the 0° and 60°-wave heading angles may be because of the direct wave incidence on the WECs, improving the heave response of the hybrid system.

### 3.6.4 Influence of PTO Damping

The maximum power absorbed by the WECs under the influence of PTO damping is studied for a zero-degree wave heading angle. The PTO systems of oscillating body WECs can install specially built linear generators for direct drive or employ mechanical or hydraulic gearboxes to power standard high-speed rotary generators. The present study deploys a hydraulic PTO system as in Si et al. (2021). Several feedback control strategies, such as linear damping, reactive control, latching control, and model predictive control, are proposed for the point absorber WECs. The present study adopts Linear damping (LD) control and Spring-damping (SD) or Reactive damping (RD) control for the different arrangements of the WECs around STLP and FTLP.

#### 3.6.4.1 Submerged Tension-Leg Platform with WEC

The wave power absorbed by six different hybrid STLP-WEC platforms for zero-degree wave heading angle using two different control strategies are studied. Fig. 3.21(a,b) shows the maximum wave power absorbed by the circular and concentric arrangement of WECs using the LD-control and RD-control for zero-degree wave heading angle. For both circular and concentric arrangements, the wave power absorption is observed to increase with the increase in the wave height for the LD-control. For the RD-control, the wave power tends to be higher for wave heights below 2.0 m and tends to decrease with the increase in the wave height. Further, the highest wave power absorption is observed for the RD-control. This may be because the PTO system react to the motion of the WEC by producing a reactive force that counteracts the motion caused by the waves. More wave energy can be efficiently absorbed by the WEC due to the reactive force's assistance in regulating and stabilising the WEC's motion. Reactive damping control allows the system to adjust according to the changing wave conditions and maximise power absorption by responding to the motion of the WECs. But for the LD-control, a fixed damping coefficient is used in linear damping control to consistently impede the motion of the WEC. While this strategy can also aid with WEC stabilisation, it

might not be as adaptable to various wave situations. Fig. 3.21(a) shows the wave power absorption for the circular arrangement of WECs for both LD-control and RD-control. For both LD-control and RD-control, the $C_4$ configuration is observed to have higher wave power absorption for any sea state conditions. The $C_2$ and $C_3$ configurations are observed to have almost similar wave power absorption for wave heights below 2.0 m using the RD-control, and the wave power absorption is observed to decrease for the $C_3$ configuration for higher wave heights. An average 15% higher wave power absorption is observed for the $C_4$ configuration compared to $C_1$.

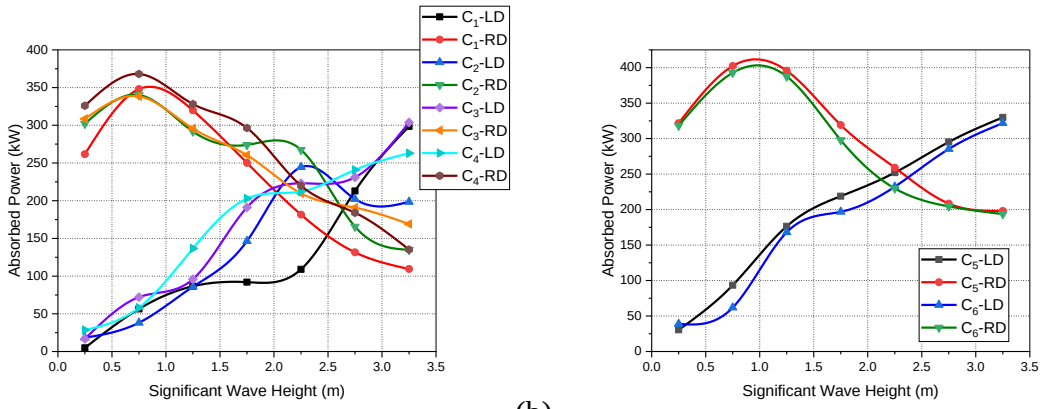


(a) (b)

Fig. 3.21: Maximum power absorbed for (a) Circular and (b) Concentric arrangement of WECs with RD and LD PTO strategies under 0°-wave heading angle.

The lowest wave power absorption is observed for the $C_1$ configuration using the LD-control. Fig. 3.21(b) shows the wave power absorption for the concentric arrangement using both LD-control and RD-control. Similar to the circular arrangement, the higher wave power absorption is higher for the RD-control for any configuration. The highest wave power absorption is observed for the concentric arrangement of 8 WECs around STLP($C_5$). An average of 10% higher wave power absorption is observed for the $C_5$ configuration with RD-control compared to $C_4$. The wave power absorption for $C_6$ is slightly lower than the $C_5$, as seen in Fig. 3.21(b). An average 2% decrease in wave power was only observed for the $C_6$ configuration compared to $C_5$. Further the wave power absorption is 6% (average) higher than the $C_4$ configuration.

#### 3.6.4.1.1 Power Absorption under RD-control for Circular and Concentric Pattern

The wave power absorption for gravity waves is studied for different arrangement patterns of WECs using a hydraulic PTO system with the RD-control. Fig. 3.22(a-d) presents the wave power absorption for the circular arrangement of WECs around STLP. The wave power absorption pattern for the WECs is almost similar to the circular arrangement of WECs. As the

WECs are symmetric, the study presents the wave power absorption of WECs placed on the positive x-axis. Fig. 3.22(a) shows the wave power absorption for the $C_1$ configuration.

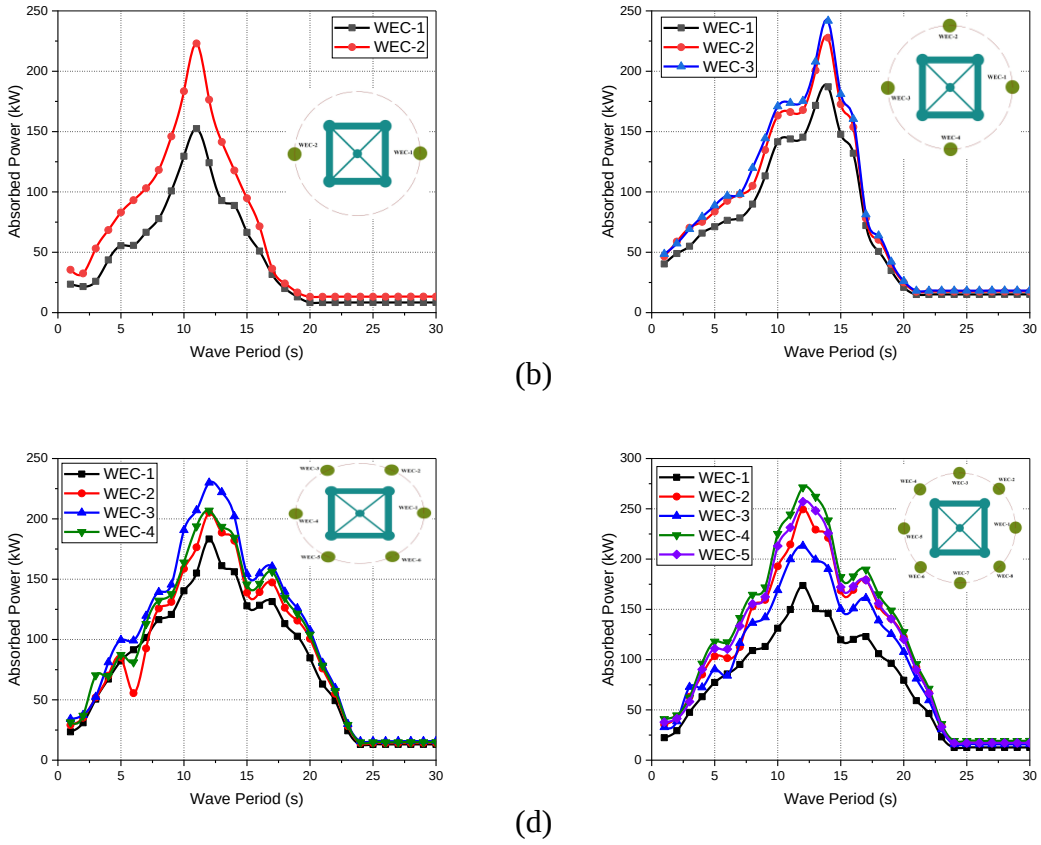


Fig. 3.22: Maximum power absorbed for (a) $C_1$, (b) $C_2$, (c) $C_3$, and (d) $C_4$ with RD-control PTO system under $0^{\circ}$-wave heading angle.

The WEC-2 on the seaward side has higher wave power absorption for waves of wave periods less than 15 s and is almost similar for waves of higher wave periods. This may be because, for higher wave periods, the motion of the WECs may be restricted, hence having lower wave power absorption. An average 24% increased wave power absorption is observed for WEC-2 compared to WEC-1 (Fig. 3.22a). Fig. 3.22(b) shows the wave power absorption for the $C_2$ configuration using RD-control. The wave power absorption is almost similar for the WEC-2 and WEC-3 compared to WEC-1 for wave periods below 15 s, and the power absorption decreases and is almost similar for all three WECs. Fig. 3.22(c) shows the wave power absorption for the $C_3$ configuration. The wave power absorption is almost similar for all the WECs for wave periods below 25 s. The wave power absorption is better for the six WEC configurations ($C_3$) compared to $C_1$ and $C_2$ as there is slightly higher wave power absorption for waves of higher wave periods (15 s < $T_p$ <25 s). WEC-3 is observed to have higher wave

power absorption due to the direct incidence of the waves and might also have the influence of the reflected waves, as the WEC-3 is kept much closer to the STLP compared to WEC-2 and WEC-4. The WEC-2 and WEC-4 have similar wave power absorption, though the absorption is slightly higher for the WEC-4, which has the highest impact on incident waves. Fig. 3.22(d) shows the wave power absorption for the eight WEC arrangements in a circular pattern around STLP ($C_4$). The highest wave power absorption is observed in the case of $C_4$ configuration with RD-control. The WEC-4 of the $C_4$ configuration is observed to have the highest wave power absorption compared to other circular arrangement patterns. This may be because the WECs are placed much closer to each other, so they will have a higher impact on the reflected waves along with the direct impact of the incident waves. An average 18% increase in wave power absorption is observed for WEC-4 of the $C_4$ configuration compared to WEC-3 of the $C_2$ configuration. For both $C_3$ and $C_4$ configurations, the wave power absorption is minimum for higher wave period regions ($T_p \geq 25s$).

Fig. 3.23(a,b) shows the wave power absorption for the concentric arrangement of WECs around STLP under the influence of the hydraulic PTO system using RD-control. The wave power absorption is slightly better for the concentric arrangement of eight WECs ($C_5$) compared to the circular arrangement of eight WECs around STLP ($C_4$). The highest wave power absorption is observed for the WEC-5 of $C_5$, which is 8% (average) higher (Fig. 3.23a) than WEC-4 of $C_4$ for the gravity waves of the North Sea.

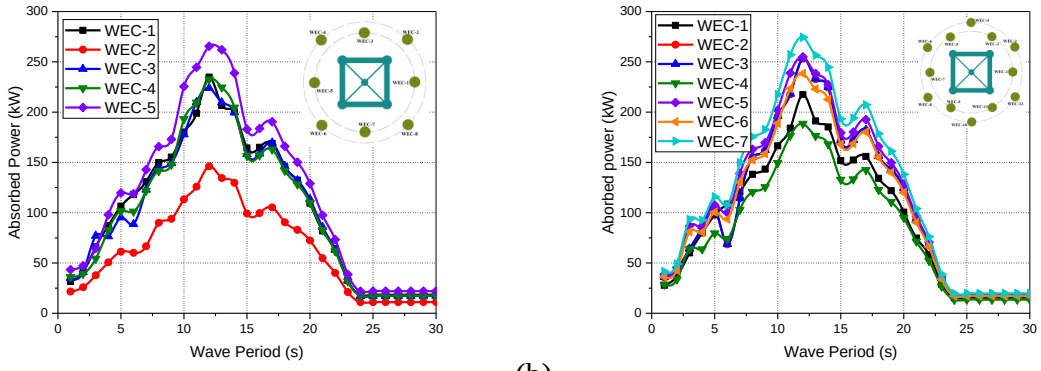


(a) (b)

Fig. 3.23: Maximum power absorbed for (a) $C_5$ and (b) $C_6$ with RD-control PTO system under $0^{\circ}$-wave heading angle.

Further, the wave power absorption is almost similar for WEC-1, WEC-3, and WEC-4, as seen in Fig. 3.23(a). Fig. 3.23(b) shows the wave power absorption for the $C_6$ configuration using RD-control. The wave power absorption is almost similar for most WECs in the $C_6$

configuration. The WEC-7 is observed to have the highest wave power absorption. The WEC-7 is in the direction of the WECs and has minimum sheltering of the WECs. Also, the WEC-7 has the higher influence on the reflected waves as the spacing between the WECs is lower compared to other configurations. The WEC-3, WEC-5, and WEC-6 are observed to have very similar wave power absorption due to the influence of the incident and reflected waves.

### 3.6.4.2 Frustum Tension-Leg Platform with WEC

The wave power absorbed by the WECs for Linear damping control and Spring-damping control is studied for the circular arrangement of the WECs. The maximum wave power absorbed for linear damping and the spring-damping is compared with the significant wave height, as seen in Fig. 3.24(a,b). The power absorption for the WECs is observed to increase with the addition of the PTO system for both control strategies. Fig. 3.24(a) shows the maximum wave power absorption for the circular configurations comparing two different control strategies. The Reactive damping control or the spring-damping control is observed to absorb higher wave power than the linear damping control, as seen in Fig. 3.24(a,b).

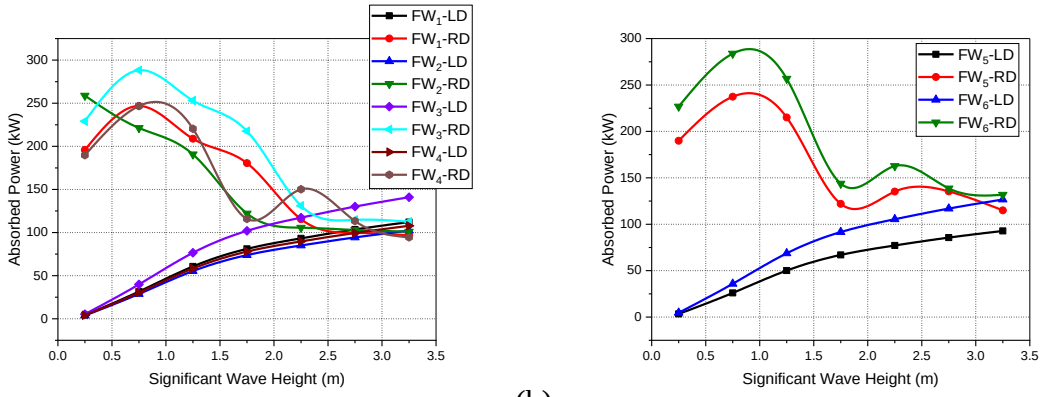


(a) (b)

Fig. 3.24: Maximum power absorbed for (a) Circular and (b) Concentric arrangements of WECs with RD and LD PTO strategies under the 0°-wave heading angle.

The higher wave power absorption is observed in the lower wave height region and is observed to decrease with the increase in wave height. For higher wave height regions, the wave power absorption is almost similar for the conditions. Fig. 3.24(a) shows the maximum wave power absorption for $FW_3$ configuration under two different control strategies. For the $FW_2$ configuration, the higher wave power absorption for the reactive damping control is observed for lower wave height and tends to decrease with the increase in wave height. For the $FW_2$ configuration, only a 3% (average) increase in wave power is observed for the reactive damping control strategy compared to the $FW_1$ configuration. An average 16% increase in wave power

for the FW3 configuration with reactive damping control is observed when compared to the four WECs configuration ($FW_2$). Further, wave power absorption for eight WECs in a circular pattern ($FW_4$) with two control strategies is observed to have reduced wave power absorption compared to the other arrangements. The maximum wave power absorbed by a WEC is almost similar for $FW_1$, $FW_2$, and $FW_4$. The higher wave power absorption is observed for the reactive damping control compared to the linear damping control. Also, for most case configurations, the highest wave power absorption for the reactive damping control is observed for the second sea state condition.

The wave power absorption for the concentric arrangement of eight and twelve WECs ($FW_5$ and $FW_6$) is shown in Fig. 3.24(b). Almost similar wave power absorption is observed for the $FW_4$ and $FW_5$ configurations with eight WECs in a circular and concentric arrangement. The maximum wave power absorbed by the circular arrangement is 3% higher for the reactive damping control strategy than the concentric arrangement, as seen in Fig. 3.24(a,b). This is because of the influence of the added mass, damping coefficient, and the restoring coefficient in the wave power absorption for the reactive damping control. A higher variation in the damping is observed for the concentric pattern ($FW_5$) compared to the circular pattern ($FW_4$). The wave power absorption for the FW6 configuration for linear and reactive damping control is shown in Fig. 3.24(b). The maximum wave power absorption is higher for $FW_6$ and is almost similar to the wave power absorption pattern of $FW_3$, having six WECs in a circular pattern. Also, improved variation in added mass and damping is observed for the $FW_3$ configuration, hence having higher wave power absorption.

#### 3.6.4.2.1 Power Absorption under RD-control for Circular and Concentric Pattern

The study observed that the higher wave power absorption of the RD control strategy is for the significant wave height of 0.75 m. The variation in power absorbed for the WEC under reactive damping control for the second sea state is studied for different configurations for zero-degree wave heading angles, as seen in Fig.s 3.25(a-d) and 3.26(a,b). Fig. 3.25(a) shows the wave power absorption for $FW_1$ configuration under RD-control for irregular waves. The wave power absorption is higher for the lower wave period region, which is the wave excitation region. The maximum wave power absorption is 40% (average) higher for WEC-2 than the WEC-1 placed on the leeward side. The wave power absorption is observed to reduce for a wave period above 10s. Fig. 3.25(b) shows the wave power absorption for $FW_2$ configuration with RD-control hydraulic PTO system. The wave power absorption is higher for the lower

wave period region, similar to the $FW_1$ configuration. The wave power absorption for the $FW_2$ configuration is higher than $FW_1$ for the waves of wave period up to 25 s. Also, the variation in wave power among the WECs is minimum, as seen in Fig. 3.25(b). The higher wave power absorption of the WECs may be due to the influence of the reflected waves, providing minimum variation in the added mass and damping. The wave power absorption for the $FW_3$ configuration is similar to the $FW_2$ configuration, as seen in Fig. 3.25(c).

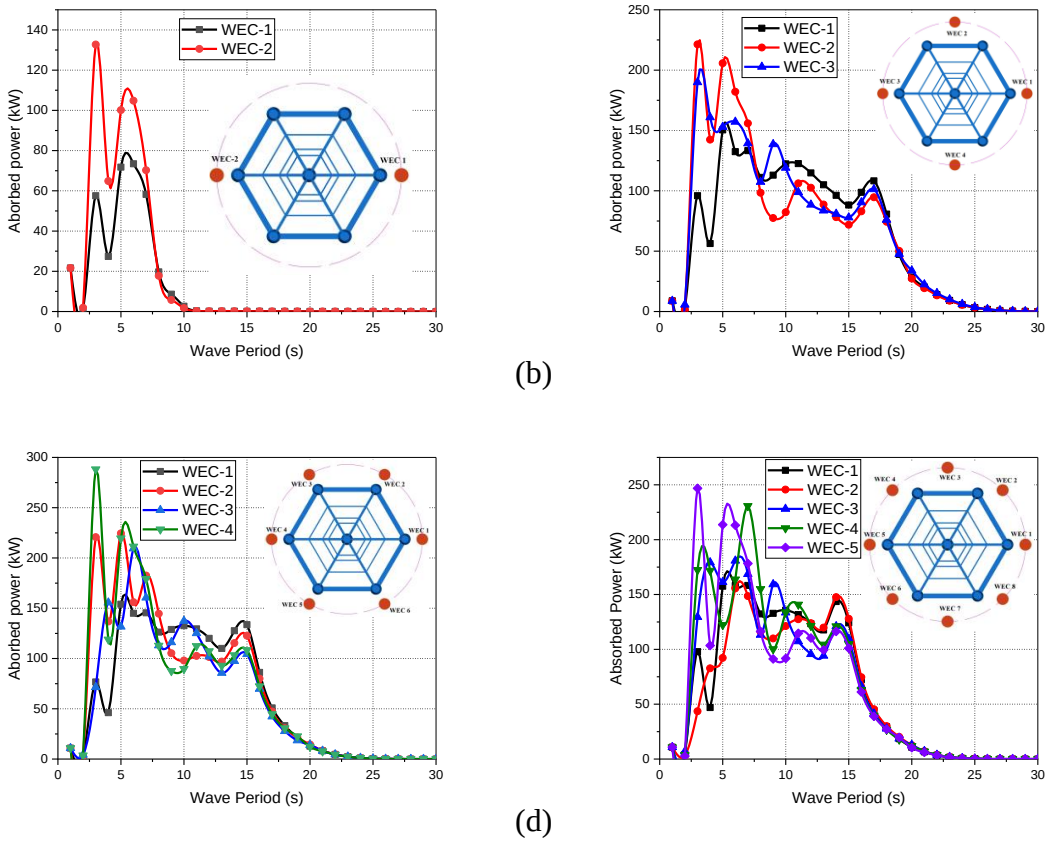


Fig. 3.25: Maximum power absorbed for (a) $FW_1$, (b) $FW_2$, (c) $FW_3$, and (d) $FW_4$ with RD-control PTO system under the 0°-wave heading angle.

The wave power absorption for the FW2 configuration is slightly better than the $FW_3$ configuration for the wave period region $20 \leq T_p \leq 25$, as seen in Fig. 3.25(b,c). An average 30% increase in wave power is observed for the $FW_3$ configuration compared to the four WECs configuration ($FW_2$). Fig. 3.25(d) shows the wave power absorption for the eight WECs configuration ($FW_4$) with RD-control system for the PTO. The power absorption is higher for the wave period region $T_p \leq 20$, which is the excited wave region. The maximum wave absorption is reduced by 18% (average) compared to the $FW_3$ configuration. The variation for the added mass and damping coefficient is minimum for the $FW_3$ configuration, hence the

higher wave power absorption by the WECs. The wave power absorption of WECs with RD control PTO is studied for the concentric arrangement of the WECs.

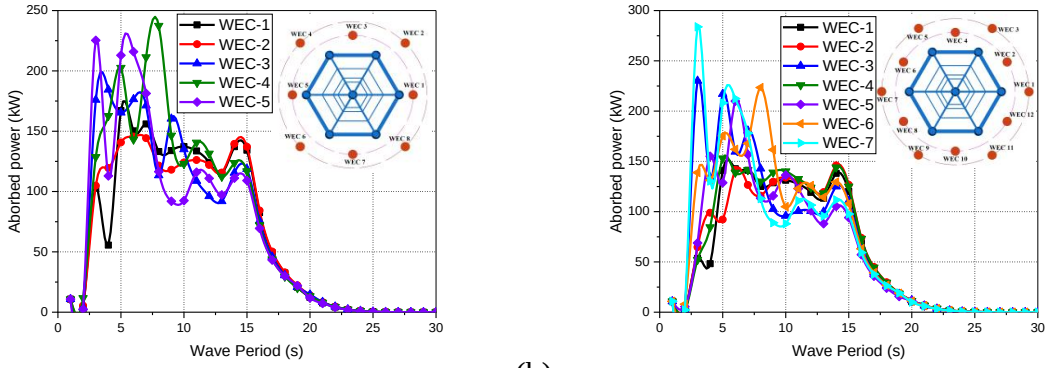


(a) (b)

Fig. 3.26: Maximum power absorbed for (a) $FW_5$ and (b) $FW_6$ with RD-control PTO system under the 0°-wave heading angle.

Fig. 3.26(a,b) shows the maximum wave power absorbed by the $FW_5$ and $FW_6$ configurations with the RD-control PTO system. Similar to the circular configuration, the higher wave power absorption for $FW_5$ is observed in the wave period region $T_p \leq 20$. The absorption in the wave power is almost similar for the WECs on the seaward side for the $FW_5$ configuration, as seen in Fig. 3.26(a). This may be due to the influence of the reflected waves with sufficient clearance between the FTLP and WECs. Fig. 3.26(b) shows the wave power absorption for the $FW_6$ configuration. The higher wave power absorption is observed for the WEC-7, kept on the seaward side away from the FTLP. This may be due to the direct incidence of the wave without sheltering. Further, only a 17% reduction in wave power is observed for the other WECs kept on the seaward side beyond WEC-7. The wave power absorption of those WECs may be due to the presence of reflected waves.

### 3.6.5 Mean Interaction Factor

The mean interaction factor $(q - factor)$ is the measure of how effectively the devise interacts with the waves and absorbs the wave power. The mean interaction factor is studied for the WECs with RD-control to investigate the effect of wave interactions on the power absorption for different arrangements of WECs (Sinha et al., 2016). The interaction caused by the diffraction force that each float will experience and the reflections from the other floats, if the array is held constant in the incoming waves, is summarised by the $q\text{-}factor$. The constructive

and destructive interference of the array of WECs around the TLP platform may be termed as the park effect. The park effect is said to be positive if $q-factor \geq 1$ and is negative otherwise.

### 3.6.5.1 Submerged Tension-Leg Platform with WEC

The $q-factor$ describes the average power absorbed by the different arrays of WECs compared to the wave power absorption of an isolated WEC. The effect of wave heading angle on the wave power absorption is also measured in terms of $q-factor$ as presented in Fig. 3.27(a-d). The $q-factor$ is highest for 60°-wave heading for lower wave height condition. For any wave heading direction, the power absorption is more efficient for the lower wave height condition ($H_s \leq 0.5\ m$), where the $q-factor > 1$.

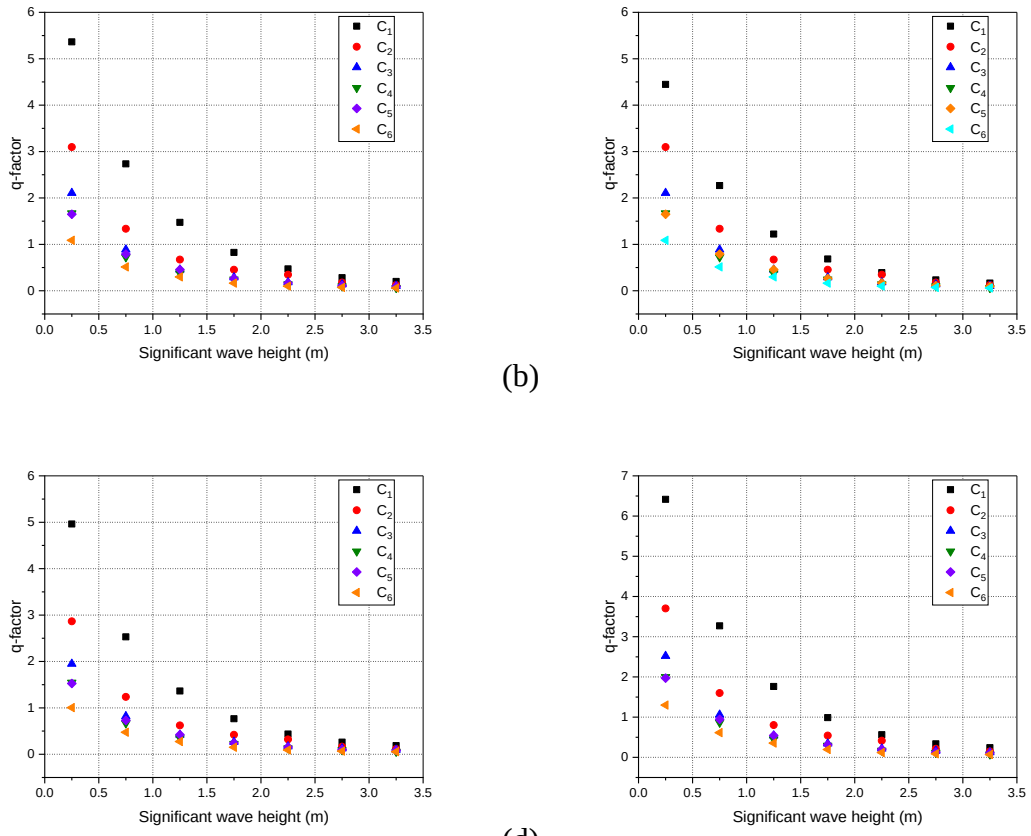


(a) (b)

(c) (d)

Fig. 3.27: Variation of q-factor with the different configurations for RD-control PTO system under (a) 0°, (b) 30°, (c) 45°, and (d) 60°-wave heading angle.

Fig. 3.27(a) shows the mean interaction factor for the 0°-wave heading angle. For the $C_1$ configuration, the park effect is positive for $H_s \leq 1.5\ m$ and is observed to fall below 1.0 for higher wave height. With the addition of the WECs, the average wave power absorption is observed to decrease compared to a single isolated float. Similar variation is observed for 30°

(Fig. 3.27b) and 45°- wave heading angles (Fig. 3.27c). The average wave power absorption is better for 60°-wave heading incidence (Fig. 3.27d). The park effect is positive for waves of wave height up to 2.0m ($H_s \leq 2.0\ m$). For any wave angle incidence, the addition of WECs have a higher impact on the average power absorbed. The variation in $q-factor$ is observed to decrease for the $C_4$, $C_5$ and $C_6$ configurations compared to other configurations. Also, it is observed that the variation in $q-factor$ is much similar for both the circular and concentric arrangements of eight WECs ($C_4$ and $C_5$).

### 3.6.5.2 Frustum Tension-Leg Platform with WEC

The variation in wave power absorbed using the mean interaction factor with various wave directions from 0° to 60°-wave heading angle is shown in Fig. 3.28(a-d). Fig. 3.28(a) shows the wave power absorption variation at the 0°-wave heading angle. It is observed that apart from the $FW_1$ configuration, smooth wave power absorption is observed only for the waves of height more than 1.5 m. The variation in the wave power absorption is higher for the lower wave heights. The higher wave power absorption at the lower period region may be because of the resonance condition. Also, it is observed that the variation in the wave power absorption with the increase in wave height is almost similar for $FW_3$, $FW_4$, $FW_5$, and $FW_6$ at different wave directions. The variation in power absorption is minimal with the change in the wave direction, as seen in Fig. 3.28(a,b,c). The wave power absorption is slightly higher for $FW_4$ and $FW_5$ at a 60°-wave heading angle, as seen in Fig. 3.28(d). Further, for higher wave heights $(H_s > 1.5m)$, the park effect is negative $(q\text{-}factor<1)$, i.e., the wave power absorbed by isolated WECs is higher than the same number of WECs placed in the array. For lower wave height regions, the wave is much more varied from 1.0, hence having higher efficiency for the array.

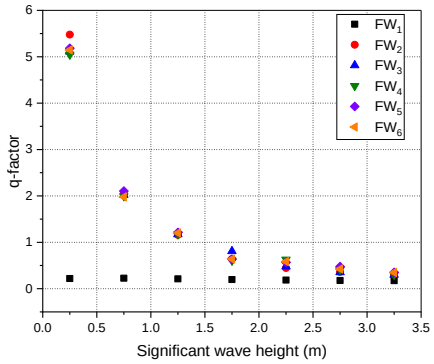


(a)

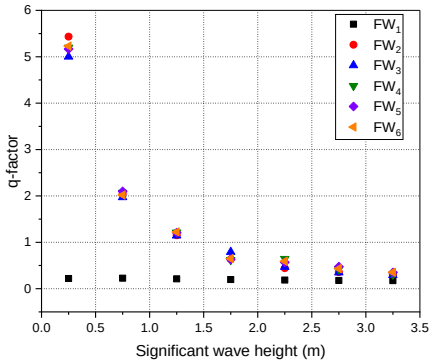


(b)

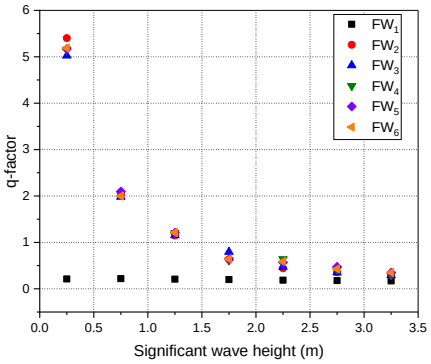


(c)

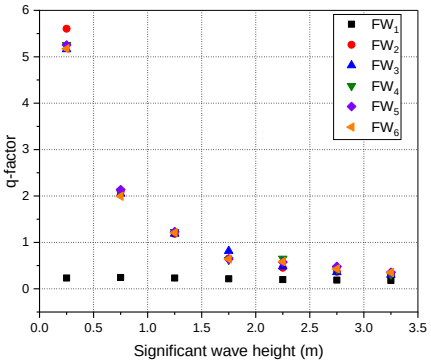


(d)

Fig. 3.28: Variation of q-factor with the different configurations for RD-control PTO system under (a) 0°, (b) 30°, (c) 45°, and (d) 60°-wave heading angle.

For any wave direction, the performance is higher for $FW_3$ and $FW_5$ hybrid systems compared to the same number of isolated WECs. Much better performance of the arrays is observed for the FTLP-WEC hybrid system compared to the STLP-WEC hybrid system. The array of WECs around the FTLP has better average power absorption $(q\text{-}factor \geq 1)$ compared to the array of WECs around the STLP for any wave heading incidence.

### 3.6.6 Capture Width Ratio (CWR)

The CWR is calculated as the ratio of the individual capture widths of each WEC in the array to the entire width of the WEC array (including the gaps between the devices). The effective width of each WEC that interacts with and absorbs energy from the incident waves is represented by the capture width. The spacing and configuration of WECs in an array are disclosed by the CWR. It aids in optimising the array configuration to increase energy extraction while minimising inter-device interference.

#### 3.6.6.1 Submerged Tension-Leg Platform with WEC

The effect of wave heading on wave power absorption is discussed in terms of CWR. Fig. 3.29(a-d) shows the CWR for different arrangement patterns of WECs around STLP for different wave heading incidences. The ratio is observed to be higher for the 60°-wave heading angle, hence the higher wave power absorption efficiency in terms of the space occupied by the hybrid floating system. Fig. 3.29(a) shows the CWR for different arrangement patterns of WECs having the influence of the 0°-wave heading angle. The CWR is higher for the concentric arrangement of eight WECs around the STLP ($C_5$). The variation in the CWR for $C_5$ and $C_4$ is minimum. The CWR is observed to improve with the addition of the WECs for

the 0° wave incidence. The CWR is efficient for waves $1 \leq H_s \leq 2.0\ m$ and is less efficient for the lower wave height condition $\left(H_s \leq 0.5\ m\right)$. A similar variation is observed for 30°, 45°, and 60°- wave heading angles (Fig. 3.29(b-d)). A better CWR is observed for the $C_4$ and $C_5$ configurations. An average 2% variation in CWR is only observed for the $C_4$ and $C_5$ configurations. An average 18% increase in CWR is observed for the $C_5$ configuration compared to the $C_1$ configuration, depicting the improvement of space utilisation with the addition of the WECs around the STLP. Further, it is observed that the variation in wave power absorption with the addition of the WECs in terms of CWR is also minimum (Fig. 3.29(a-d)).

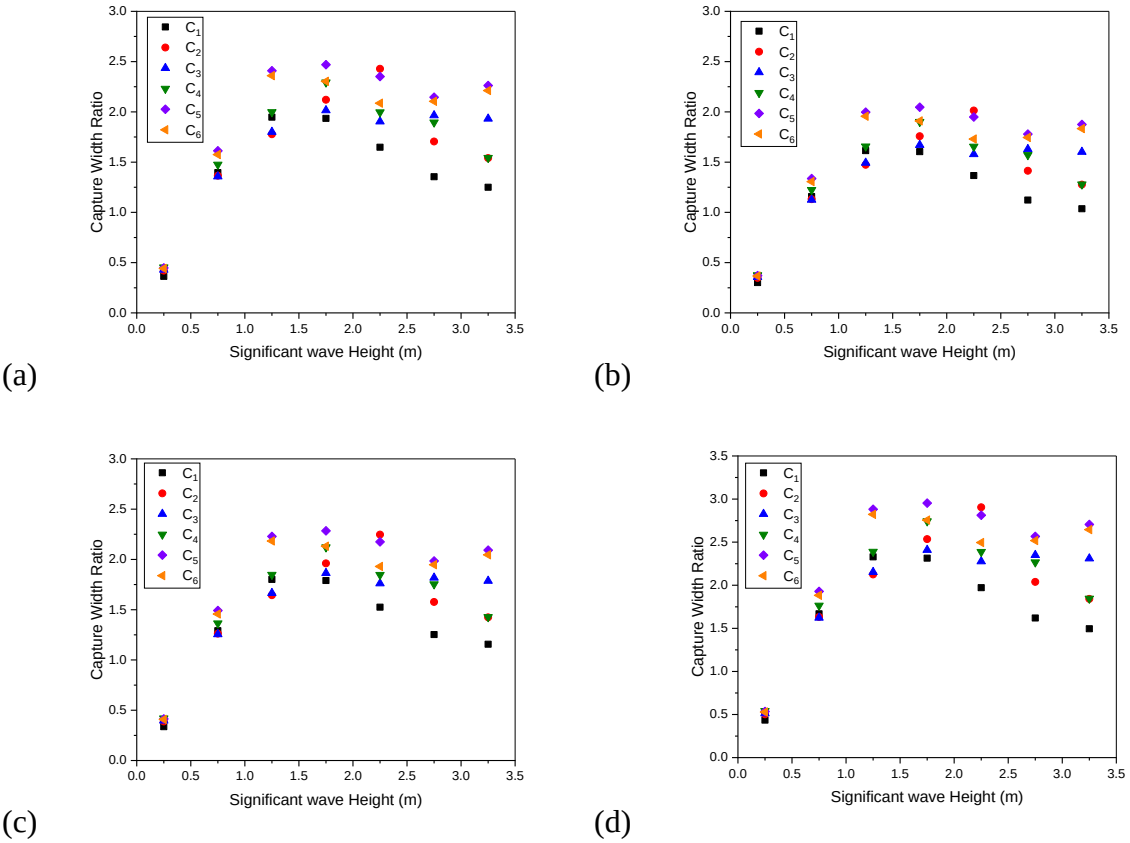


Fig. 3.29: CWR for RD-control PTO system under (a)0°, (b)30°, (c)45°, and (d)60°-wave heading angle.

### 3.6.6.2 Frustum Tension-Leg Platform with WEC

The efficiency of the WECs in the hybrid system is studied in terms of the CWR, as seen in Fig. 3.30(a-d) for four different wave directions. CWR gives the idea of the amount of wave crest utilised as the wave energy. Fig. 3.30(a) shows the CWR for all configurations at a 0°-wave heading angle. CWR is observed to increase with the increase in wave height. Also, it is

observed to increase with the increase in the number of WECs around the FTLP. This may be due to the influence of the reflected waves from the FTLP and other WECs. For the wave height region less than 2 m, the CWR variation is minimum for both circular and concentric arrangements of eight WECs ($FW_4$ and $FW_5$), as seen in Fig. 3.30(a). For wave height higher than 2.5 m, the concentric arrangement of eight WECs ($FW_5$) is higher than the circular arrangement ($FW_4$). For the most occurring wave height of 2.25 m, 1.10 times increase in wave crest utilisation is observed for the $FW_4$ configuration compared to $FW_5$.

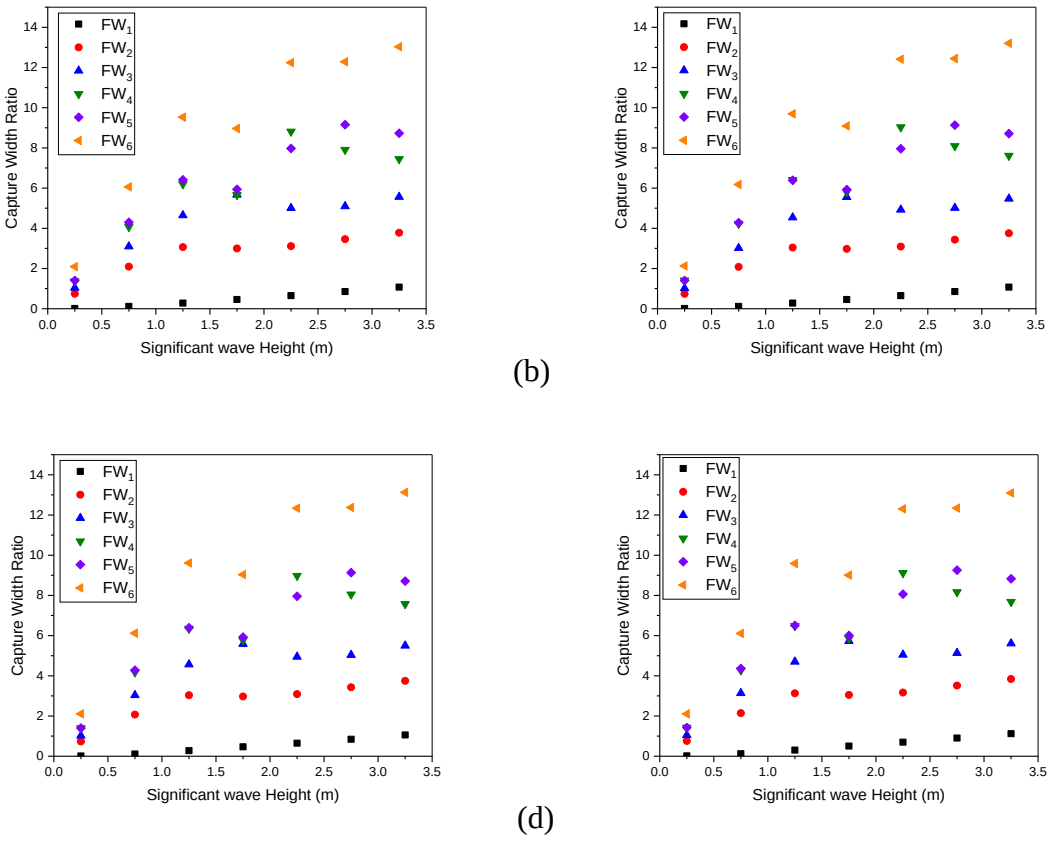


Fig. 3.30: CWR for RD-control PTO system under (a) 0°, (b) 30°, (c) 45°, and (d) 60°-wave heading angle.

The variation in CWR for $FW_1$, $FW_2$, and $FW_3$ is minimum for wave heights considered in the present study. For $FW_4$, $FW_5$, and $FW_6$ configurations, the variation in CWR with the wave heights is observed to be higher. Similar variation in CWR is observed for other wave directions, as seen in Fig. 3.30(b,c,d). The CWR for the 30°-wave heading angle is shown in Fig. 3.30(b). An average 5% increase in wave crest utilisation is observed for the $FW_5$ configuration compared to $FW_4$ for any wave height. Better utilisation of the wave crest is observed for the concentric arrangement of twelve WECs ($FW_6$). For the 45°-wave heading

angle, the average increase in wave power absorption for $FW_5$ is only 3% compared to $FW_4$, as seen in Fig. 3.30(c). This may be because the waves will be directed to WECs, with the sheltering of the FTLP. Similarly, for the 60-wave heading angle, the average increase in wave power absorption is only 3% for $FW_4$ compared to $FW_5$ (Fig. 3.30d). For any wave heading angle, an average 25% increase in wave crest utilisation is observed for $FW_4$ and $FW_5$ configurations, compared to $FW_3$. Similarly, a 35% increase in wave crest utilisation is observed for $FW_6$ compared to $FW_5$.

## 3.7 CLOSURE

The hydrodynamic performance of various arrays of heaving cone-cylinder point absorber-type WECs around both STLP and FTLP floating wind turbines in circular and concentric patterns are examined in the present work based on potential flow theory in the frequency domain. North Sea wave data is considered to analyse the power absorption for the various configurations of WECs surrounding the floating wind turbine platform. The study examined the influence of hydraulic PTO on wave power absorption for two different hybrid concepts. For various circular and concentric arrays of WECs, the hydrodynamic coefficient, time average wave power, the mean interaction factor, and the CWR are studied. The study observed the following conclusions:

- The effect of STLP and WEC on added mass and damping is more significant in the lower wave period region for all the arrangements of wave energy converters, as the variation of the ratio from 1.0 is higher. The higher variation can be due to the influence of the incident and the reflected waves from the STLP and WEC.
- The total time average wave power absorbed is highest for a concentric pattern of twelve WECs around the STLP floating hybrid system ($C_7$ configuration). The maximum power is absorbed by a single WEC when the point absorber-type WECs of eight numbers are arranged in a concentric pattern around the STLP ($C_6$ configuration). For the WECs around the FTLP, the highest wave power absorption is observed for the WEC in the $FW_5$ configuration.
- Similar to the STLP-WEC hybrid system, the variation of the added mass and damping for the hybrid FTLP-WEC system is more significant for the lower wave period region. The influence of the WECs on the FTLP and other WECs is minimal in the case of the FTLP-WEC system compared to the STLP-WEC system. This may be due to the higher

wave sheltering of the waves by the FTLP floating platform compared to the STLP floating platform.

- An average 78% increase in wave power is observed for the RD-control compared to LD-Control. Further, for most configurations, the highest wave power absorption for the reactive damping control is observed for the second sea state condition.
- For both the STLP-WEC hybrid system and FTLP-WEC hybrid system, the concentric arrangement of the wave energy converters under 60°-wave heading incidence is observed to have efficient wave power conversion.

# CHAPTER 4

# COUPLED DYNAMIC ANALYSIS OF HYBRID TLP-WEC WITH DIFFERENT MOORING CONFIGURATIONS

## 4.1 GENERAL INTRODUCTION

The Tension-Leg Platform (TLP) concept is a better solution for intermediate water depth, as the taut mooring system may be better suited for shallow water depth. Further, the TLP provides reduced platform motions compared to other offshore floating concepts, thus improving the power generation of the platform. A significant study on the dynamic response of TLP-type floating wind turbines under different wave and wind load conditions has been performed by various researchers. In recent years, studies on the dynamic response of a multi-column WindStar TLP-type FWT under operational and parked conditions (Zhao et al., 2016), dynamic motion response of TLP-type FOWT (Shen et al., 2016), submerged TLP-type offshore floating wind turbine (Han et al., 2017), stability of STLP-type FWT (Ding et al., 2017), combined tension leg platform type FOWT and a heaving wave energy converter (Ren et al., 2020) and dynamic responses of Windstar TLP (Han et al., 2022) is reported in the literature.

## 4.2 NUMERICAL FORMULATION

Simulating the platform's behaviour under various operational and extreme situations is an integral component of dynamic response analysis. The platform's response to wind, waves, and other dynamic loads is evaluated using frequency-domain and time-domain simulations with integrated numerical models. This research supports design optimisation and performance assessment by identifying the structural loads, motion amplitudes, and system behaviour. Optimisation algorithms are frequently combined with numerical simulations to find the optimal design configurations. To maximise energy output, reduce structural loads, and enhance overall performance, variables such as platform design, mooring system arrangement, turbine positioning, and control system settings can be optimised.

The frequency-domain analysis of the hybrid floating system is based on dynamic and modal analysis. The dynamic analysis resolves the RAOs (Response Amplitude Operator) of the

hybrid floating wind turbine system under different wind and wave loads. The dynamic analysis includes estimating loads on the hybrid system with the contributions from wind and waves acting along the platform, mooring system and the wind turbine. The modal analysis completes the dynamic part and provides access to natural frequencies, natural modes and the modal damping coefficient of the hybrid wind turbine system. The study analyses the coupling between the DOFs of the floater system and the forced motions of the floating system. The hybrid system is considered as a rigid body, and the equation of motion (Philippe et al., 2011) is given as

$$M_p \ddot{q} = F_{aero} + F_{achorage} + F_{hydro} \tag{4.1}$$

where $M_p$ is the platform inertia matrix, $\ddot{q}$ is the vector of degrees of freedom, $F_{aero}$ is the load transmitted from the wind turbine, $F_{hydro}$ is the hydrodynamic load and $F_{lines}$ is the mooring load. The hydrodynamic wave loads on the platform are calculated using WAMIT, which is based on linear potential flow theory. Using WAMIT simulation, the added mass and damping coefficient, restoring co-efficient and the excitation force developed on the floater system alone are obtained, which is used as the input for the coupled dynamic analysis. In addition, FAST, developed by NREL, is an aero-servo-hydro-elastic simulation tool that can linearise floating platform models about an operating point. The linearisation of the model is about the steady-state operating point found in static analysis. The outputs of FAST include the mass, damping and stiffness matrices of the complete hybrid system, which depends on the incident wave frequency $\omega$, vector of system displacement $\Delta q$ and the external force $F_{ex}$ . The equation of motion in the frequency domain under periodic wave load is given by

$$\left\{-\omega^2 M_{res}(\omega) + i\omega L_{res}(\omega) + K_{res}(\omega)\right\} \Delta q = F_{ex}. \tag{4.2}$$

The floating hybrid platform under the wave, wind, mooring line and the current forces are analysed using the aero-hydro-servo-elastic simulation tool FAST (Fatigue, Aerodynamics, Structures and Turbulence). The generalised equation of motion (Jonkman, 2007) for the hybrid platform is given by

$$M(q,u,t)\ddot{q} + f(q,\dot{q},\ddot{q},u,u_d,t) = 0 \tag{4.3}$$

where $M$ is the mass matrix, $f$ is the non-linear forcing function, $q$ is the vector of the DOF displacements, $\dot{q}$ is the vector of the DOF velocities, $\ddot{q}$ is the vector of the DOF accelerations, $u$ is the vector of the control points and $u_d$ is the vector of the wind input disturbances. The

total external load $F_i^{Platfrom}$ developing on the hybrid floater other than the weight of the support platform and the load transmitted (Jonkman, 2007) from the wind turbine is given by

$$F_i^{Platfrom} = -A_{ij}\ddot{q}_j + F_i^{Hydro} + F_i^{Lines}, \tag{4.4}$$

where $A_{ij}$ is the component of added mass, $F_i^{Hydro}$ is the hydrodynamic load on the support platform and $F_i^{Lines}$ is the load from the mooring lines. The hydrodynamic load developed on the system with the contribution from radiation, diffraction and hydrostatic loads are given by

$$F_i^{Hydro} = F_i^{Waves} + F_i^{Viscous} + F_i^{Hydrostatic}. \tag{4.5}$$

The hydrodynamic load equation considers the total excitation load on the support platform from the incident waves $F_i^{Waves}$, closely related to the wave elevation $\zeta$. Airy's wave theory describes the kinematics of regular waves whose periodic elevation is represented as a sinusoidal wave propagating at a single amplitude, and frequency (period) or wavelength expresses the linear potential wave force on the support platform as

$$F_i^{Waves} = F_i^{Radiation} + F_i^{Diffraction}. \tag{4.6}$$

The forced oscillations of the support platform develop the radiation force $F_i^{Radiation}$ in all DOF when no incident wave is present. The resulting radiation force is given by

$$F_i^{Radiation} = -A_{ij}(\omega)\ddot{q}_j(t) - B_{ij}(\omega)\dot{q}_j(t). \tag{4.7}$$

Thus, the contributions from added mass and force is proportional to accelerations and contributions from the radiation damping is proportional to platform velocity. The inverse transformation of the radiation loads gives the total radiational load as

$$F_i^{Radiation} = -A_{ij}(\infty)\ddot{q}_j(t) - \int_t^t h_{ij}(t-\tau)\dot{q}_j(t)d\tau, \tag{4.8}$$

where $A_{ij}(\infty)$ is the added mass coefficient at infinite frequency and $h_{ij}(\tau)$ is the retardation function. Hydrodynamic added mass, and damping are factors of the wave radiation loads (Eq. 4.7,4.8). The wave radiation loads are independent of the incident waves since the radiation problem and the diffraction problem are separated. The force mechanism proportional to the acceleration of the support platform is represented in Eq. 4.4 by the impulsive hydrodynamic-added-mass components $A_{ij}$, which are part of the time-domain radiation problem. The component $(i, j)$ specifically represents the hydrodynamic force in the direction of DOF $i$, which results from the integration of the component of the outgoing-wave pressure

field that is caused by and proportional to a unit acceleration of the $j^{th}$ DOF of the support platform over the wetted surface of the support platform. The impulsive hydrodynamic-added-mass matrix is symmetric, much like the body (inertia) mass matrix. The impulsive hydrodynamic-added-mass matrix, in contrast to the inertia mass matrix, may contain off-diagonal components that relate modes of motion that cannot be coupled with body inertia, depending on the configuration of the support platform. The convolution integral term in Eq. 4.8 represents the load contribution from wave-radiation damping and also represents an additional contribution from the added mass that is not accounted for in $A_{ij}$. The HydroDyn module of the FAST includes the Pierson-Moskowitz spectrum for the fully developed sea state, the JONSWAP spectrum for the limited fetch conditions and is also equipped with user prescribed site-specific wave spectrums representing various stochastic sea states, modelled as the summation or superposition of multiple wave components for irregular wave simulation. The excitation load (Jonkman, 2009) for the determination of diffraction force $F_i^{Diffraction}$ is given by

$$\zeta(t) = \frac{1}{2\pi}\int_{-\infty}^{\infty} W(\omega)\sqrt{2\pi S_{\zeta}^{2-sided}(\omega)}e^{j\omega t}d\omega, \tag{4.9}$$

$$F_i^{Diffraction} = \frac{1}{2\pi}\int_{-\infty}^{\infty} W(\omega)\sqrt{2\pi S_{\zeta}^{2-sided}(\omega)}X_i(\omega,\beta)e^{jwt}d\omega. \tag{4.10}$$

Due to the contributions from 2-sided power spectral density of the wave per unit time $S_{\zeta}^{2-sided}$, unit variance $W(\omega)$ and the complex-valued array representing the wave excitation force on the support platform normalised per unit wave amplitude $X_i(\omega,\beta)$ depending on frequency $\omega$ and direction $\beta$ of the incident wave. The viscous drag load is modelled using the Morison equation and is expressed as

$$F_i^{Viscous} = \frac{1}{2}C_d\rho_w A\left[v_i(t) - \dot{\varsigma}_i(t)\right]\left|v_i(t) - \dot{\varsigma}_i(t)\right|, \tag{4.11}$$

where $\dot{\varsigma}_i(t)$ is the undisturbed flow velocity taken at the instantaneous position of the centre of gravity, $v_i(t)$ is the velocity of the support platform, $C_d$ is the viscous co-efficient having projection area $A$ and $\rho_w$ is the water density. The hydrostatic force has contributions from the buoyancy force, and the linear hydrostatic restoring force from the water plane area is given by

$$F_i^{Hydrostatic} = \rho g V_o \delta_{i3} - C_{ij}^{Hydrostatic} q_j . \quad (4.12)$$

In the case of the un-displaced position of the support platform, the linear hydrostatic force $(\rho g V_o \delta_{i3})$ is acting directly upward and is equal to the weight of the displaced fluid. Further, for the vertical heave-displacement DOF of the support platform, this term is non-zero because the centre of buoyancy of the platform is assumed to lie on the centre line of the undeflected tower (or z-axis of the platform). The change in the hydrostatic force and moment resulting from the effects of the water pane area and the centre of buoyancy, $C_{ij}^{Hydrostatic}$ is the same as in Jonkman (2009).

### 4.2.1 Mooring Dynamics

The stability of a TLP-type floating platform is established using a mooring system. This is achieved by means of tensioned cables of chains, synthetic fibre or steel, which anchor the platform to the sea bed. The tension developed on the mooring lines depends on the buoyancy of the floater, viscous-separation effects, the elasticity of the cables, the weight of the cable in water and the geometric layout of the mooring system, which acts as the restraining forces at the fairlead points. In the case of the linear mooring system, ignoring the mooring inertia and damping, the total load (Matha, 2009) developing on the support platform is given by

$$F_i^{Lines} = F_i^{Lines,0} - C_{ij}^{Lines} q_j \quad (4.13)$$

where $F_i^{Lines,0}$ is the i$^{th}$ component of the total mooring system load acting on the support platform in its un-displaced position and $C_{ij}^{Lines}$ component of the linearised restoring matrix from all mooring lines. In the case of the catenary mooring system, $F_i^{Lines,0}$ takes the pretension at the fairlead from the weight of the cable not resting on the sea floor. If the catenary mooring lines are neutrally buoyant, then the pretension developed is zero. In the case of a taut mooring system, $F_i^{Lines,0}$ is calculated based on the excess buoyancy in the tank in an un-displaced position including the weight of the cable in water. $C_{ij}^{Lines}$ is the combination of elastic stiffness of the mooring lines and the effective geometric stiffness considering the weight of cables in water. The mooring system dynamics are not linear in nature. The non-linearities in mooring dynamics result from non-linearities in force-displacement relationships and non-linear hysteresis effect due to the loss of energy as the lines oscillate with floater about a mean position. The non-linear restoring loads are simulated using the quasi-static mooring module of FAST. Taut mooring lines are modelled considering the apparent weight in fluid, elastic

stretching and the sea bed friction of each line, not taking into account the individual line bending stiffness. Under the assumption that each cable is in static equilibrium at that instant, the mooring module calculates tensions within and configuration of each mooring line as the fairlead points for given platform displacement at any instant of time is known. With the knowledge of additional tension and loading on the platform from aerodynamics and hydrodynamics, the dynamic equation of motion for acceleration for the hybrid system is analysed. FAST then integrates in the time-domain to obtain new platforms and fairlead positions at the next time step, repeating the process. For any mooring system, individual analysis of every mooring line is deployed.

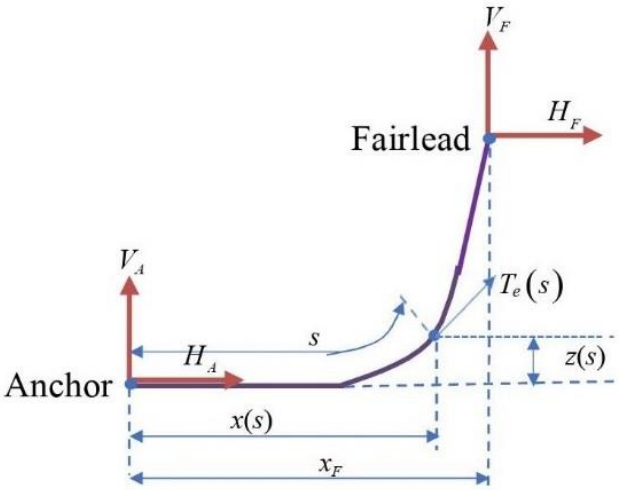


Fig. 4.1: Illustration of a mooring line in the local coordinate system.

For specifying the fairlead locations of each mooring line relative to the support platform, the anchor locations of each mooring line relative to the inertial frame, total unstretched length $L$, extensional stiffness $EA$, coefficient of sea bed friction drag $C_B$, the apparent weight in the fluid per unit length $\omega$, is all related to the mass of the line per unit length $\mu_c$ (Fig. 4.1). The relation is given by

$$\omega = \left( \mu_c - \rho \frac{\pi D_c^2}{4} \right) g. \tag{4.14}$$

The vertical anchor force (Jonkman, 2007 ) is given by

$$V_A = V - \omega L, \tag{4.15}$$

where $V$ is the vertical force applied at the fairlead point, which is less than the total weight of the cable and $L$ is the unstretched line length. The horizontal anchor force $H_F$ is the same as the horizontal force $H$ applied at the fairlead point. The vertical anchor force is zero when no

portion of the cable rests on the sea bed, the $V_A$ have minimum influence on the dynamic response of the floating system. The unstretched length of the cable lying on the sea bed is given by

$$L_B = L - \frac{V}{\omega}. \tag{4.16}$$

The equation for the horizontal and vertical distance from the anchor point to the given point on the line when no portion of the mooring line is resting on the sea bed follows the relation

$$x(s) = \frac{H_F}{\omega}\left\{\ln\left[\frac{V_A+\omega s}{H_F}+\sqrt{1+\left(\frac{V_A+\omega s}{H_F}\right)^2}\right]-\ln\left[\frac{V_A}{H_F}+\sqrt{1+\left(\frac{V_A}{H_F}\right)^2}\right]\right\}+\frac{H_F s}{EA}, \tag{4.17}$$

$$z(s) = \frac{H_F}{\omega}\left[\sqrt{1+\left(\frac{V_A+\omega s}{H_F}\right)^2}-\sqrt{1+\left(\frac{V_A}{H_F}\right)^2}\right]+\frac{1}{EA}\left(V_A s+\frac{\omega s^2}{2}\right). \tag{4.18}$$

The effective tension is calculated with the unstretched arc distance along the mooring line from a given point $s$, is given by

$$T_e(s) = \sqrt{H_F^2+(V_A+\omega s)^2}. \tag{4.19}$$

### 4.2.2 Environmental Conditions

The viability of designing a cost-effective hybrid wind-wave platform for an offshore wind turbine depends heavily on site-specific metocean conditions. Based on the metocean data of the north coast of the North Atlantic region, four load cases are defined for the operating state of the reference 5 MW wind turbine. The cases illustrate the mean wind speed, significant wave height and the spectral peak period, as shown in Table 2.12 of Chapter 1. The 3D turbulent wind fields are generated using NREL's TURBSIM based on the Kaimal turbulence model for IEC class C. The kinematics of the irregular waves are simulated based on the JONSWAP spectrum in FAST. In the present study, waves and winds are unidirectional and aligned with the x-axis for the hybrid floater.

## 4.3 METHODOLOGY

The hybrid TLP-WEC in the present study is modelled as a rigid body, two different TLP's combined with cone-cylinder-shaped point absorber WECs. The study arranges the WECs around the TLP in a circular pattern and is stabilised using different numbers of tensioned mooring cables. The wave is assumed to travel towards the positive x-direction. The WECs in

a circular array around the TLP floater are connected to the columns using connecting arms. The hinged structure between the connecting arm and the column limits the relative motion. It allows rotation around the hinged shaft, driving the power take-off (PTO) system to produce power (Hansen, 2013). The centro-symmetrically arranged heaving-type WECs ensure better power quality and smoothness as the waves pass through the hybrid system. The hybrid system is considered as a single rigid body with 6-DOF, and the analysis of the responses (surge, sway, heave, roll, pitch and yaw) of the hybrid STLP-WEC is performed to examine the wind power absorption by the hybrid system under wind and wave loading. The hybrid floating system is used to support a 5 MW wind turbine having properties as detailed in Chapter 1. The geometrical modelling of the combined wind-wave floater is performed using the Rhino-3D platform. The geometric data file (.gdf) is used as the input for WAMIT for the hydrodynamic analysis to obtain the hydrodynamic co-efficient and the restoring co-efficient, the pre-processor for the coupled dynamic tool FAST. The FAST developed by NREL considers the coupled interactions between the floating system and the wind turbine under regular and irregular wave conditions. The numerical simulation tool includes the gyroscopic loads of the turbine rotor, hydrodynamic damping during wave-body interaction, the forces caused by wave interactions and the aerodynamic damping by the wind turbine rotor. The study compares the responses of the hybrid system for four different mooring configurations in both frequency and time domains under different wind and wave load conditions. Both time and frequency-domain models are based on radiation or diffraction hydrodynamic theory. Further, the fairlead tension (FT) developed on each mooring cable is compared for different mooring configurations to understand the importance of the position of mooring cables. Further, the statistical analysis of the tower base forces and moments are conducted to observe the influence of wind and wave loads.

### 4.3.1 Submerged Tension-Leg Platform with Six WECs

The different arrangement pattern of cone-cylinder WECs around the STLP is detailed in Chapter 1. The study observed higher wind power absorption efficiency for the hybrid STLP+6WECs (STLP combined with six cone-cylinder WECs) stabilised using four tensioned mooring cables. The properties of the floating STLP combined with six WECs in a circular pattern are detailed in Chapter 1. In the present chapter, the hybrid STLP+6WECs is provided with a different number of mooring cables to analyse the motion response and the wind power absorption efficiency with changes in mooring cables. Fig. 4.2 shows the schematic

representation of hybrid STLP+6WECs stabilised using four tensioned mooring cables. Table 4.1 details the properties of the mooring lines studied, and Table 4.2 details the arrangement pattern of the mooring cables for different mooring layouts.

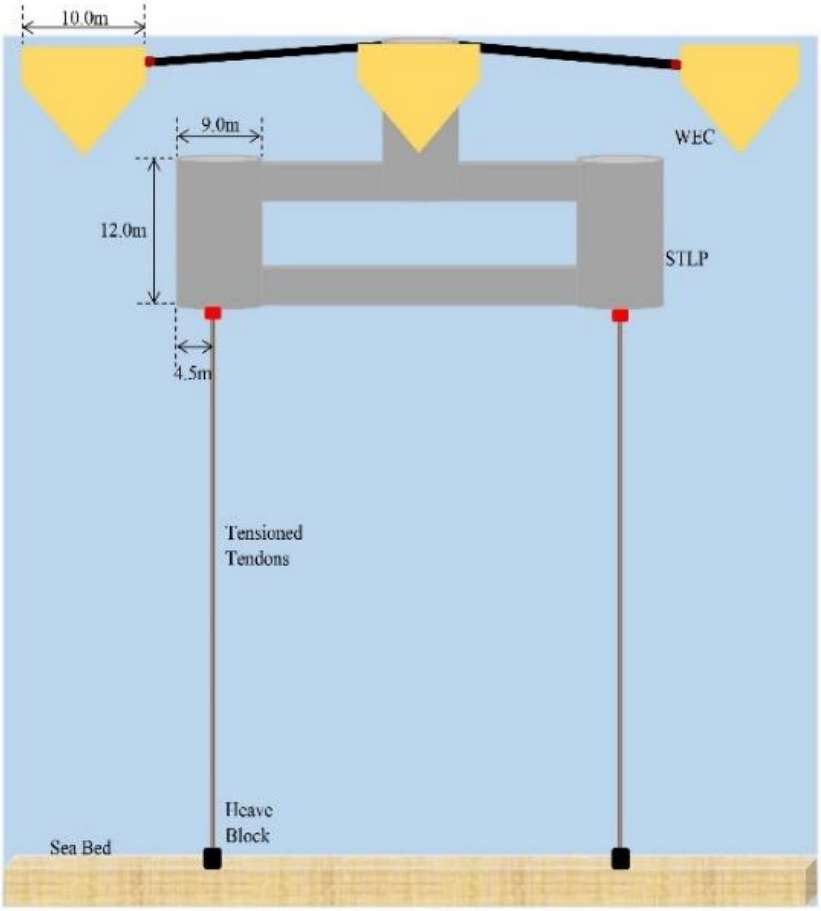


Fig. 4.2: Schematic diagram of submerged TLP connected to six WEC in a circular pattern stabilised by 4-Mooring tendons.

Table 4.1: Properties of different mooring layouts of hybrid STLP+6WECs (Matha, 2010).

| Characteristics/ Configuration | 4-Mooring | 5-Mooring | 8-Mooring | 9-Mooring |
|---|---|---|---|---|
| Number of mooring lines | 4 | 5 | 8 | 9 |
| Unstretched mooring-line length (m) | 130.978 | 130.978 | 120.978 | 120.978 |
| Line diameter (m) | 0.12 | 0.12 | 0.12 | 0.12 |
| Line mass per unit length (kg/m) | 115.9248 | 115.9248 | 115.9248 | 115.9248 |
| Line extensional stiffness (N) | 31.359E9 | 31.359E9 | 31.359E9 | 31.359E9 |
| Average steel density (kg/m$^3$) | 7850 | 7850 | 7850 | 7850 |
| Average concrete density (kg/m$^3$) | 2562.5 | 2562.5 | 2562.5 | 2562.5 |

Table 4.2: Different Mooring layouts for hybrid STLP+6WECs.

| | | |
|---|---|---|
| 4-Mooring | 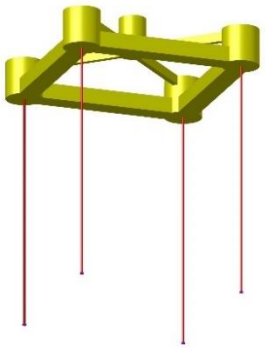 | Four tensioned mooring cables are provided at the centre of each outer pontoon. |
| 5-Mooring | 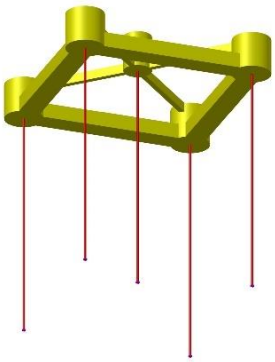 | Four tensioned mooring cables at the centre of each outer pontoon and one cable at the centre of the central column. |
| 8-Mooring | 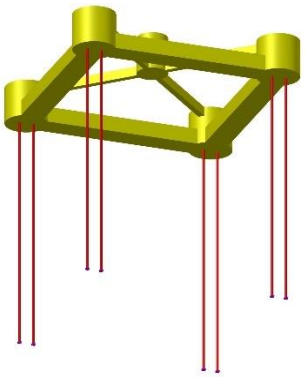 | Four outer pontoons are provided with two mooring cables, each spaced equally from the centre of the outer pontoon. |
| 9-Mooring | 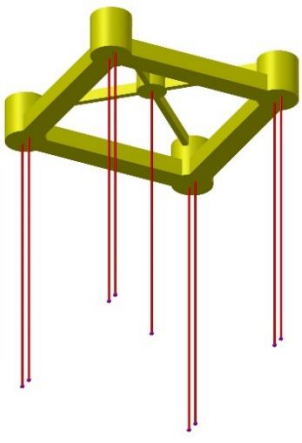 | Four outer pontoons are provided with two mooring cables, each spaced equally from the centre of the outer pontoon, and the central column is provided with a single mooring cable. |

### 4.3.2 Frustum Tension-Leg Platform with Eight WECs

The rigid body analysis of the FTLP combined with a different circular arrangement of WECs is studied in Chapter 1. The hybrid FTLP+8WECs (FTLP combined with eight WEC in a circular pattern) stabilised using six mooring cables (Fig. 4.3) is observed to have higher wind power absorption. In the present chapter, hybrid FTLP+8WECs is studied for different mooring layouts detailed in Table 4.4. The properties of the mooring cables used to stabilise the hybrid system are detailed in Table 4.3.

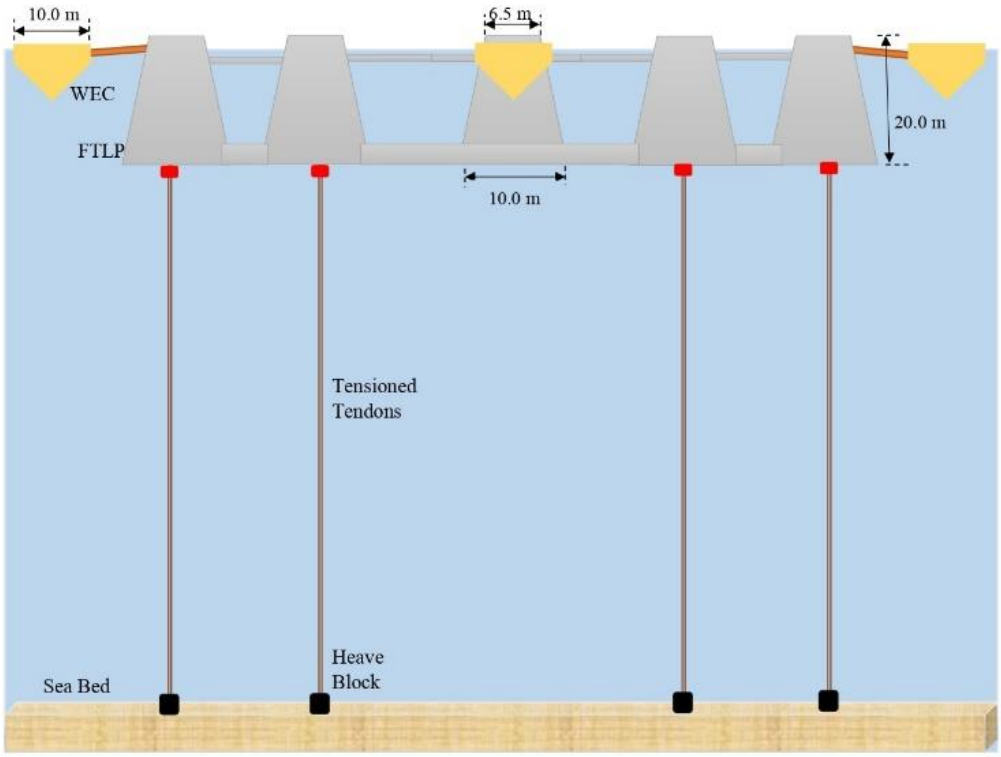


Fig. 4.3: Schematic diagram of the hybrid FTLP+8WECs stabilised by 6-Mooring tendons.

Table 4.3: Properties of different mooring layouts of hybrid FTLP+8WECs.

| Characteristics/ Configuration | 6-Mooring | 7-Mooring | 12-Mooring | 13-Mooring |
|---|---|---|---|---|
| Number of mooring lines | 6 | 7 | 12 | 13 |
| Unstretched mooring length (m) | 140.5 | 140.5 | 135.5 | 135.5 |
| Line diameter (m) | 0.12 | 0.12 | 0.12 | 0.12 |
| Line mass per unit length (kg/m) | 115.9248 | 115.9248 | 115.9248 | 115.9248 |
| Line extensional stiffness (N) | 31.359E9 | 31.359E9 | 31.359E9 | 31.359E9 |
| Average steel density (kg/m$^3$) | 7850 | 7850 | 7850 | 7850 |
| Average concrete density (kg/m$^3$) | 2562.5 | 2562.5 | 2562.5 | 2562.5 |

Table 4.4: Different Mooring layouts for hybrid FTLP+8WECs.

| | | |
|---|---|---|
| 6-Mooring | 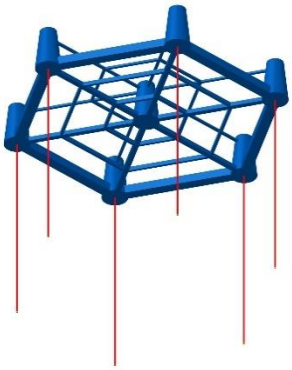 | Six tensioned mooring cables are provided at the centre of each outer pontoon. |
| 7-Mooring | 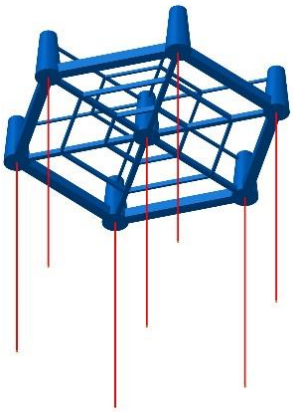 | Six tensioned mooring cables at the centre of each outer pontoon and one cable at the centre of the central column. |
| 12-Mooring | 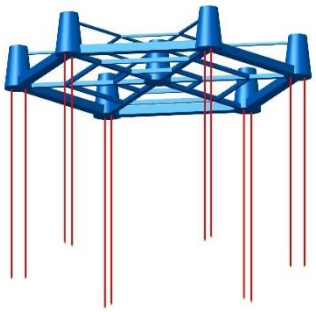 | Six outer pontoons are provided with two mooring cables, each spaced equally from the centre of the outer pontoon. |
| 13-Mooring | 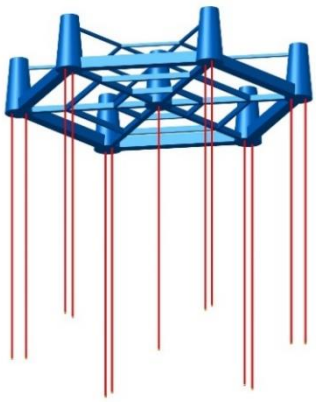 | Six outer pontoons are provided with two mooring cables, each spaced equally from the centre of the outer pontoon, and the central column is provided with a single mooring cable. |

## 4.4 RESULTS AND DISCUSSION

The dynamic motion responses of the TLP platform combined with wave energy converters for different mooring lines are analysed in the time and frequency-domain. The natural frequency for different configurations of hybrid floater is compared to observe the influence of WECs on the natural frequency of TLP. The system's responses in both the time and frequency-domains are studied to examine the performance of the wind turbine and the stability of the floating system. Further, the tower base forces and moments developed at the turbine base are analysed to study the effect of wind on the supporting hybrid platform. The tension developed on each mooring line for different hybrid configurations is analysed. The variation in the wind power generated is also analysed for the hybrid system under regular and irregular sea states.

### 4.4.1 Natural Frequency of Hybrid TLP-WEC Platforms

The natural frequency impacts the TLP's dynamic behaviour, particularly how it reacts to wind and wave stresses. Engineers can enhance the overall performance of the floating wind turbine system by analysing and optimising the natural frequency. To increase the TLP's stability and lower structural loads, this optimisation may entail changing the design specifications or the mooring and tensioning systems. The study employs free decay test to observe the natural frequency of the TLP's. The numerical simulations are carried out using the tool FAST. In FAST, the TLP configurations are released from a specific offset for each degree of freedom (DOF) in calm water with the wind turbine in parked condition.

Table 4.5: The natural frequency of STLP and hybrid STLP+6WECs configurations.

| Mode | STLP | STLP+6WECs |
|---|---|---|
| Surge | 0.06 | 0.06 |
| Sway | 0.06 | 0.06 |
| heave | 0.32 | 0.29 |
| Roll | 0.34 | 0.34 |
| Pitch | 0.34 | 0.34 |
| Yaw | 0.08 | 0.07 |

Table 4.5 shows the natural frequency of the STLP and the hybrid STLP+6WECs. Table 4.5 shows that the natural frequencies of horizontal plane motions (surge, sway and yaw) are lower than those in the vertical plane motions (heave, pitch and roll), which concludes that the stiffness for the submerged TLP is higher in the vertical plane. It is also observed that the

natural frequency of the submerged TLP is not much disturbed by the arrangement of the WECs around the floater. Table 4.6 shows the natural frequency of the FTLP and hybrid FTLP+8WECs configurations. The natural frequency of horizontal and vertical plane motions of the Frustum-TLP are outside the wave excitation frequency range (0.04–0.25 Hz) and hence provide higher structural integrity. Similar to the hybrid STLP-WEC, adding the WECs to the FTLP minimally influence the natural frequencies of the rigid body motions.

Table 4.6: The natural frequency of FTLP and hybrid FTLP+8WECs configurations.

| Mode | FTLP | FTLP+8WECs |
|---|---|---|
| Surge | 0.33 | 0.32 |
| Sway | 0.32 | 0.32 |
| heave | 0.33 | 0.32 |
| Roll | 0.28 | 0.27 |
| Pitch | 0.27 | 0.27 |
| Yaw | 0.47 | 0.47 |

### 4.4.2 Response Analysis of Hybrid STLP and FTLP Platforms

The dynamic motion responses of the hybrid STLP+6WECs and FTLP+8WECs are studied under regular and irregular waves for a zero-degree wave heading angle in the frequency-domain. The study is conducted for four mooring configurations to analyse the importance of the mooring lines in determining the stability of the combined floater. The results obtained in the time domain are converted to the frequency-domain using Fast Fourier Transform (FFT).

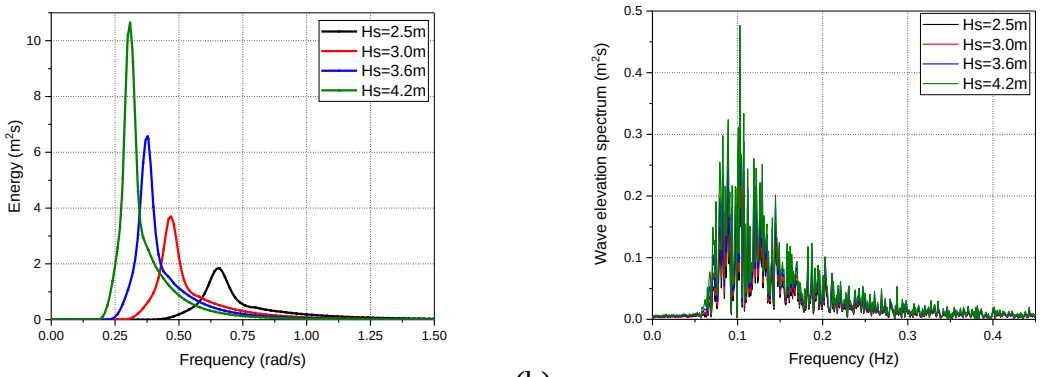


(a) (b)

Fig. 4.4: The energy spectrum for (a) JONSWAP and (b) Incident wave elevation.

The FFT is a function that decomposes a time series signal to its corresponding individual frequency components. The JONSWAP wave spectra are used to simulate the incident irregular waves. The JONSWAP and wave elevation spectra for the considered significant wave heights

and peak wave periods are depicted in Fig. 4.4(a,b). Fig. 4.4(a) shows the JONSWAP spectrum used for the simulation of the incident irregular waves based on empirical data collected from the North Sea and takes into account factors such as wind speed and duration, wave height, and fetch length (the distance over which the wind has blown without significant obstructions). Fig. 4.4(b) shows the wave elevation spectrum, and the graphical representation of the distribution of the wave heights. The waves are observed to be dominant over the wave frequency region of 0.05 Hz to 0.2 Hz for any wave height condition. The higher wave energy is observed for the wave height of 4.2 m.

#### 4.4.2.1 Submerged Tension-Leg Platform with Six WECs

Fig. 4.5(a-d) presents the surge motion response of the combined floater under irregular waves for four mooring arrangements. The variation in surge response is observed to be almost similar for each wind speed condition. The responses are observed to be minimum for wind speeds below the rated wind speed condition (Fig. 4.5(a, b)), and the responses are observed to be higher for 17 m/s wind speed (Fig. 4.5d). The higher surge response may be due to the higher wave energy (Fig. 4.3b) for the 17 m/s wind speed. It is observed that the surge response is higher for the frequency region 0.05 Hz to 0.15 Hz, as the incident wave energy is higher for the same frequency region. The higher surge motion results in lower power absorption of the combined floater as the wind turbine will be moved away from the direction of the wind. The surge response of the combined floater under irregular waves is observed to be minimum as compared to the response of the combined floater under regular waves. Also, it is observed that the 9-Mooring configuration has higher values for surge response, and the 4-mooring configurations have lower surge response, especially for wind speed above the rated wind speed.

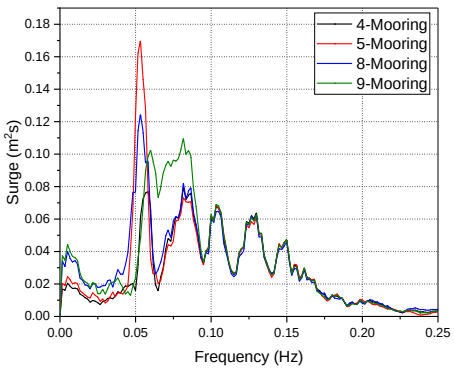


(a)

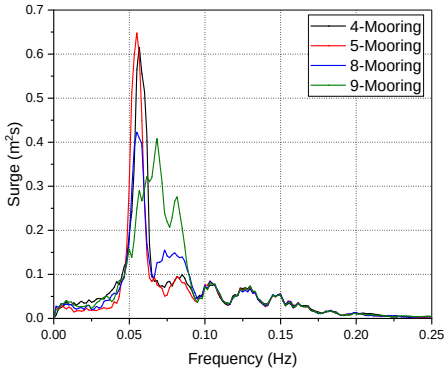


(b)

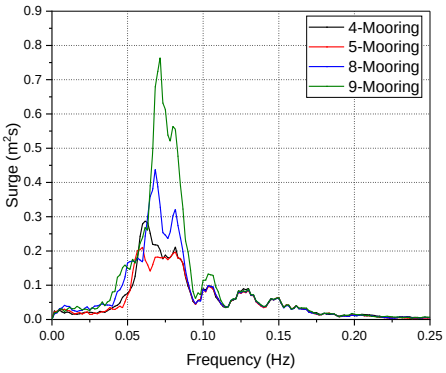


(c)

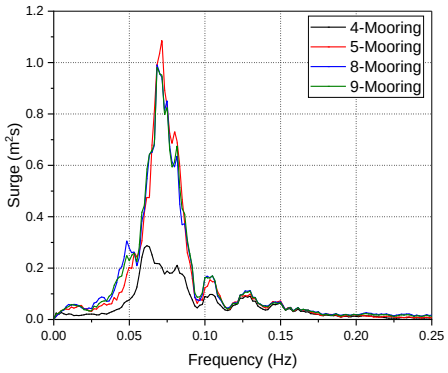


(d)

Fig. 4.5: Surge response of hybrid STLP+6WECs under irregular waves for (a) SS-1, (b) SS-2, (c) SS-3, and (d) SS-4 for different mooring configurations.

The peak value of the surge response for the combined floater is closer to the natural frequency of the floater, thus having the possibility of occurrence of resonance. The closeness of the peak value is observed to be higher for the lower wind speed conditions.

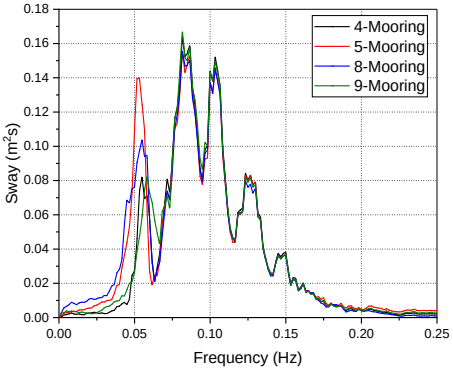


(a)

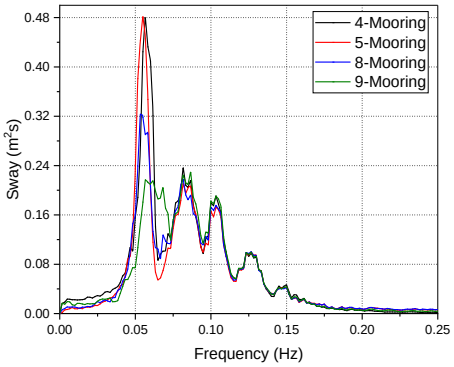


(b)

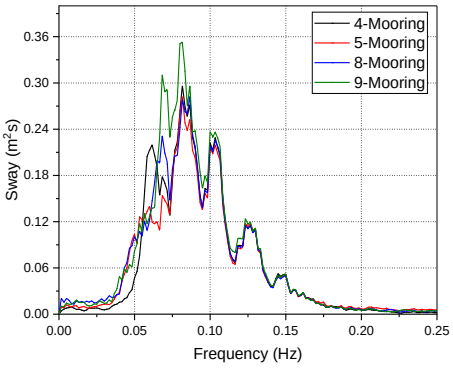


(c)

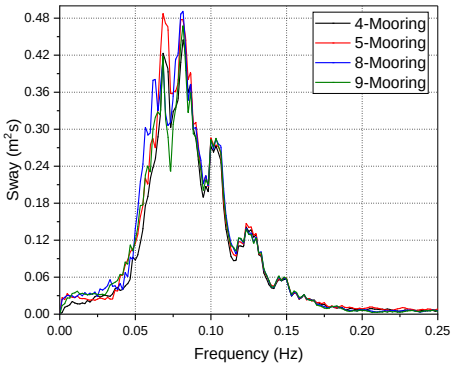


(d)

Fig. 4.6: Sway response of the hybrid STLP+6WECs under irregular waves for (a) SS-1, (b) SS-2, (c) SS-3, and (d) SS-4 for different mooring configurations.

Fig. 4.6(a-d) presents the sway motion response of the combined floater under irregular waves for four mooring arrangements. The sway motion for the combined floater tends to increase with the increase in wind speed, similar to the case of surge motion. It is also observed that the variation in responses is minimum with the increase in the mooring cables for all four wind speed conditions suggesting that the increase in the number of mooring lines has a negligible impact on sway, apart from the lower wind speed condition (Fig. 4.6a). For lower wind speed conditions, the 8-Mooring and 9-Mooring are observed to have lower sway motion (Fig. 4.6(a,b)). The Fig. shows different peaks for each wind speed condition within $0.5 \leq \omega \leq 0.15$ frequency range. This may be due to the higher variation of wave energy distribution for that frequency range of $0.05 \leq \omega \leq 0.2$, as seen in Fig. 4.3(b). The possibility of resonance in sway is higher for the combined floater for all four mooring conditions. The sway response for the combined floater is lower under irregular wave conditions than under regular wave conditions. Higher surge and sway response is observed when an additional mooring line is provided to the central column, reducing the platform's displacement.

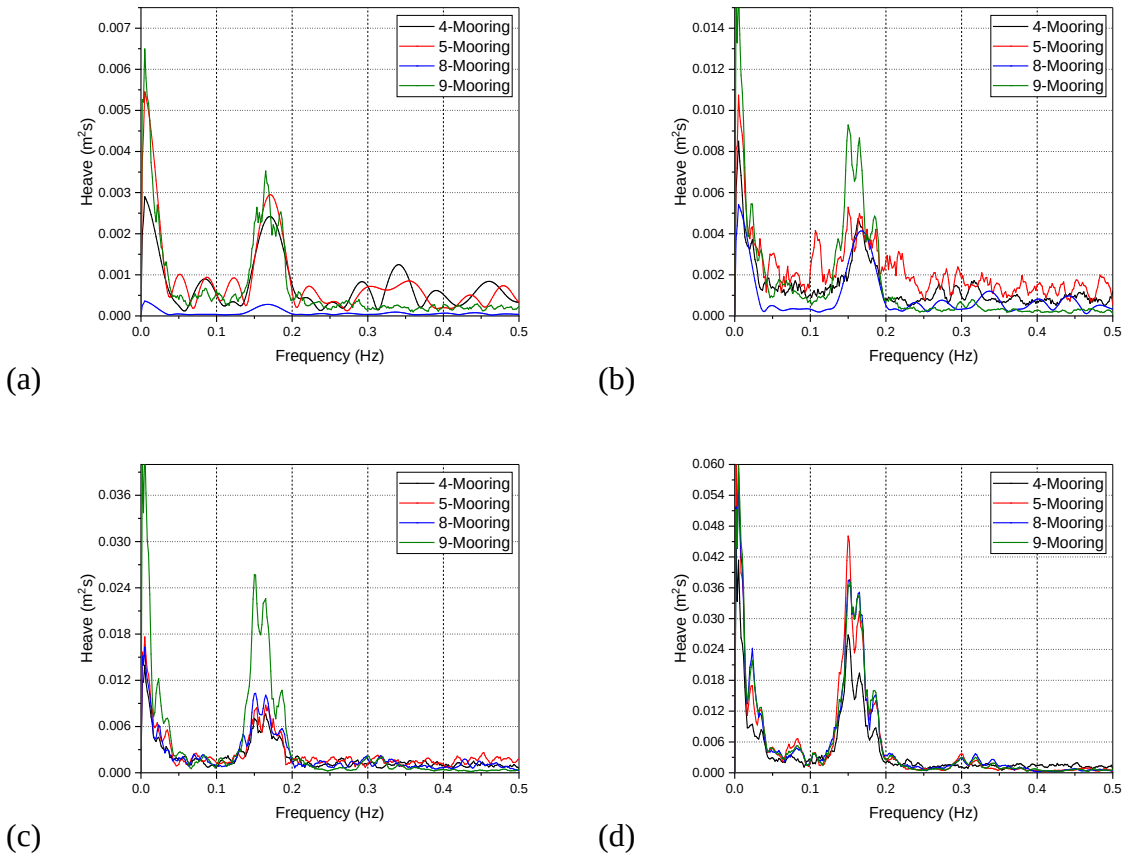


Fig. 4.7: Heave response of the hybrid STLP+6WECs under irregular waves for (a) SS-1, (b) SS-2, (c) SS-3, and (d) SS-4 for different mooring configurations.

Fig. 4.7(a-d) presents the heave motion response of the combined floater under irregular waves for four mooring arrangements. The heave response amplitude is small compared to other translational motions. The reduced heave motion is due to tensioned tendons stabilising the floater. The heave motion amplitude tends to increase with the increase in wind speed and wave height. In the case of wind speed below the rated wind speed of 11.4 m/s, the heave response is minimal for the 8-Mooring configuration, as seen in Fig. 4.7(a,b). But for higher wind speed conditions, the responses are observed to be minimum for the 4-Mooring configuration, as in Fig. 4.7(c,d). For any wind speed conditions, the heave motion amplitude of the hybrid floater with a 9-Mooring configuration is observed to be higher. It is also observed that, apart from the peak value of heave motion for frequency range $0.1 \leq \omega \leq 0.2$, the motion amplitude is observed to be very small. The wave frequency for the heave motion is observed to be away from the natural frequency of 0.29 Hz, further ensuring that the probability of occurrence of resonance is minimal.

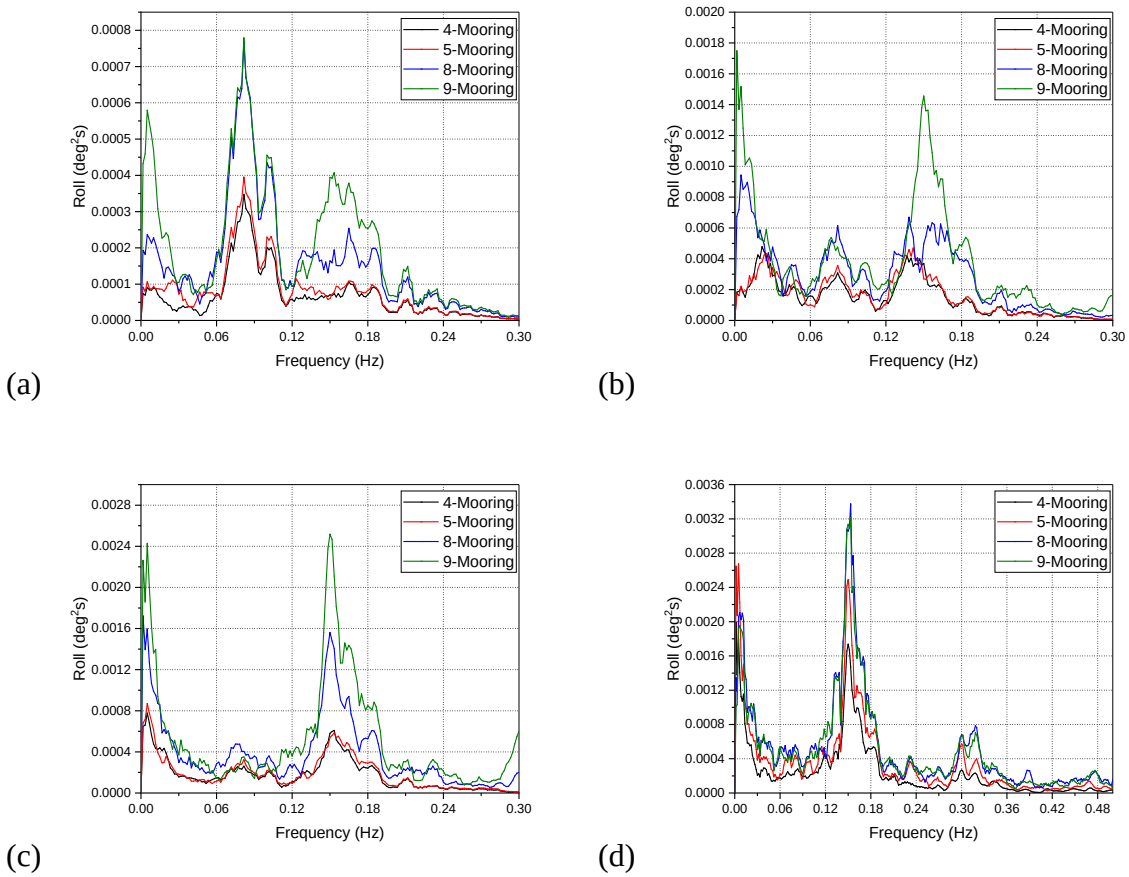


Fig. 4.8: Roll response of the hybrid STLP+6WECs under irregular waves for (a) SS-1, (b) SS-2, (c) SS-3, and (d) SS-4 for different mooring configurations.

Fig. 4.8(a-d) shows the roll motion spectrum for different mooring configurations of six WEC configurations under different operating wind speed conditions and irregular wave loads. From Fig. 4.8(b-d), it is observed that the peak frequency for the three operating conditions for the roll motion is close to 0.16 Hz, and the peak response value is minimal, thus showing higher stability of the combined system against overturning. For lower wind speed conditions (Fig. 4.8a), the dominant peak is observed near to 0.08 Hz frequency range. Both peaks are observed away from the natural frequency, further suggesting that there is no possibility of the occurrence of resonance. Higher roll motion response is observed for 9-Mooring lines for all wind speed conditions. Minimum variation in roll motion is observed for the four and five mooring configurations for all wind speed conditions. The minimum variation in roll response with the increase in mooring lines is due to the assumption that the tethers are infinitely stiff. In the case of higher wind speed conditions (Fig. 4.8d), the roll response variation is minimal with the increase in the mooring lines.

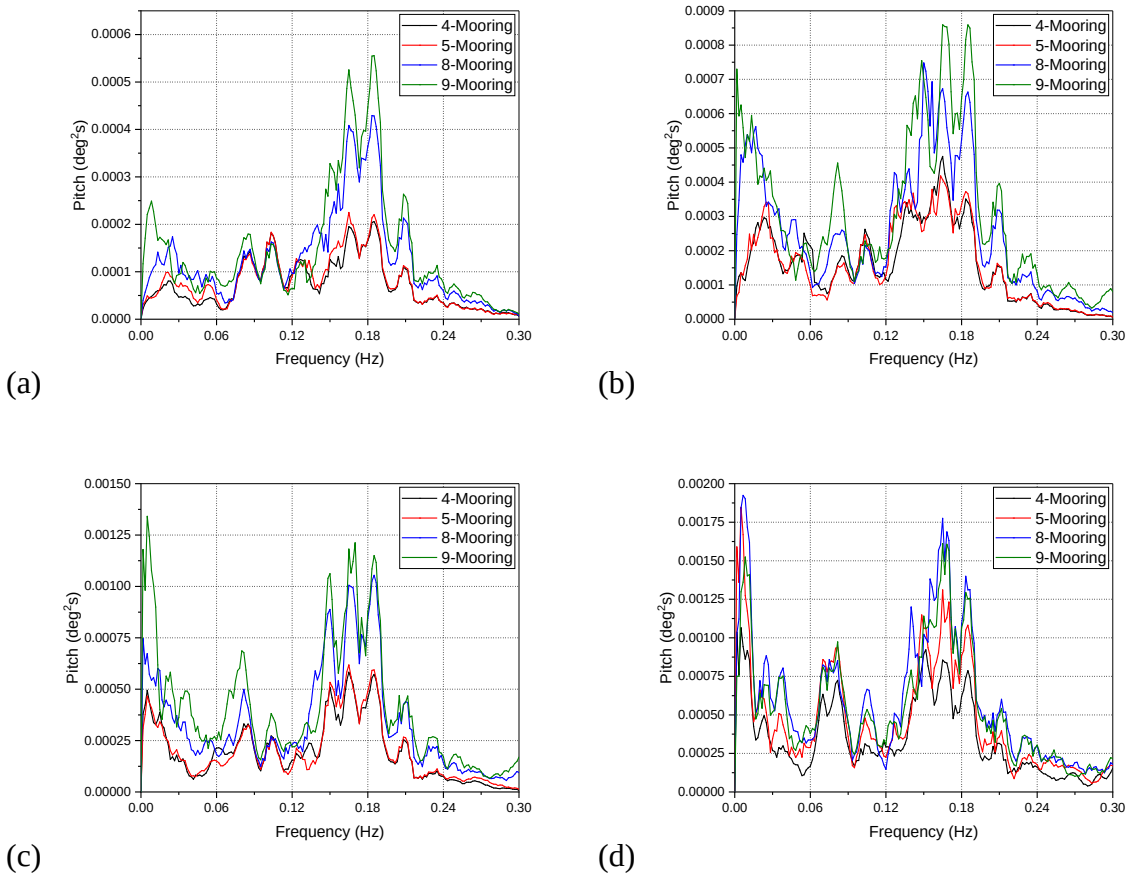


Fig. 4.9: Pitch response of the hybrid STLP+6WECs under irregular waves for (a) SS-1, (b) SS-2, (c) SS-3, and (d) SS-4 for different mooring configurations.

Fig. 4.9(a-d) shows the pitch response for the hybrid floater under different wind and wave loading conditions. The responses tend to increase with the increase in wind speed and wave height. Two dominant peaks are observed (Fig. 4.9(a,b)) for the load case having a wind speed less than the rated wind speed (11.4 m/s) for the 5 MW wind turbine. Both peaks are observed to be away from the natural frequency region, reducing the possibility of a significant pitch motion response. The peaks for the pitch response for any wind speed condition are observed in the region ( $0.15 \leq \omega \leq 0.22$ Hz) where the incident wave energy tends to reduce, as in Fig. 4.3(b). Three dominant peaks are observed for wind speeds greater than 11.4 m/s, as seen in Fig. 4.9(c, d). The peaks are observed to be closer and are well away from the natural frequency region, ensuring reduced pitch motions. The different peaks observed for surge and pitch motion show the coupling effect between the surge and pitch motion.

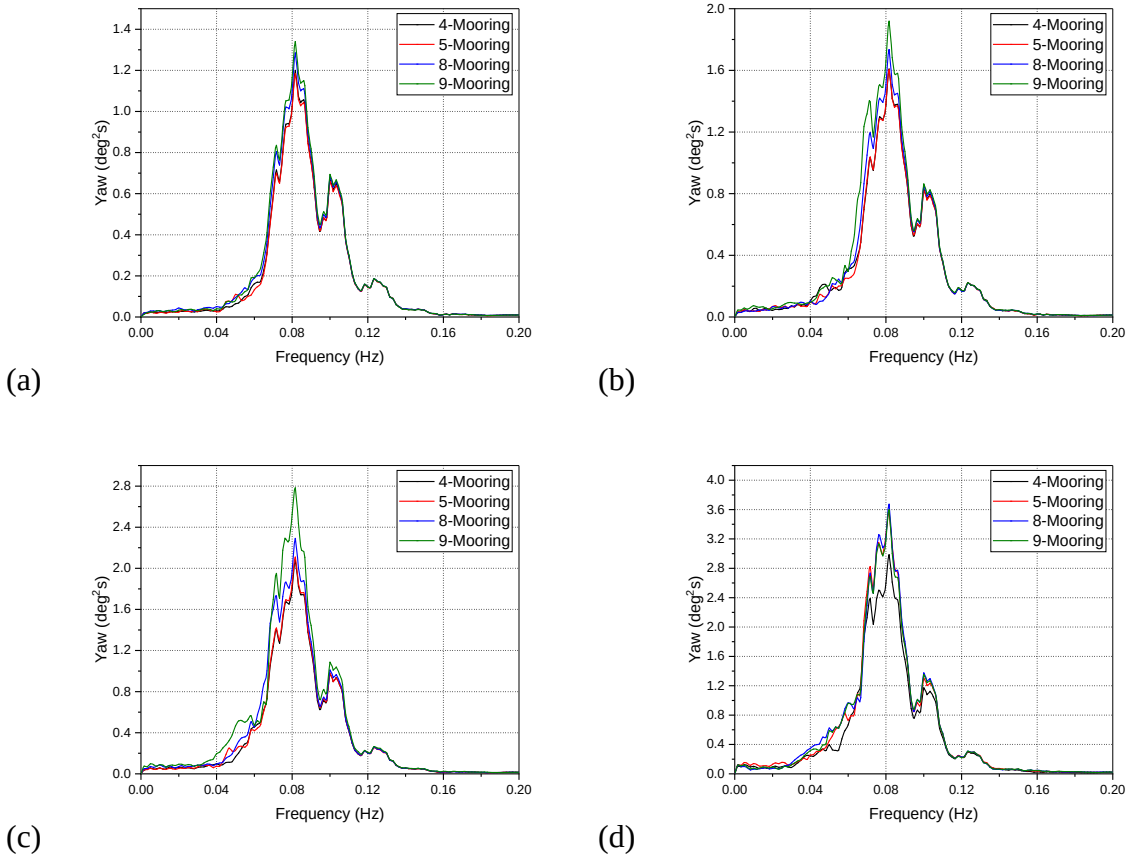


Fig. 4.10: Yaw response of the hybrid STLP+6WECs floater under irregular waves for (a) SS-1, (b) SS-2, (c) SS-3, and (d) SS-4 for different mooring configurations.

The yaw response motion is higher than all other vertical and horizontal plane motions, as in Fig. 4.10(a-d). The peak response values for the yaw motion are also observed to increase with the increase in wind speed. The peak value for the yaw motion is observed within the frequency

range $0.08 \leq \omega \leq 0.10$ Hz for all four operating conditions considered. The frequency corresponding to the peak value for the yaw motion is observed to be closer to the natural frequency of the floater. Hence, proper floater damping must be provided to prevent the floater from resonance. The yaw response for all mooring conditions is closer for wind and wave loading. Higher yaw responses for all mooring layouts are observed in the initial phase of the incident wave energy region ( $0.05 \leq \omega \leq 0.08$ Hz). From Fig. 4.5 - Fig. 4.10, it is observed that the responses for the floater are higher for the 8-Mooring and 9-Mooring configurations. The higher responses ensure minimum placement of the hybrid floater. The peak response for the surge and pitch motion is moved closer to the natural frequency region in the case of the 9-Mooring configuration, suggesting that the position of the taut mooring for the 9-Mooring configuration needs to be shifted towards the centre of gravity (CG) of the outer pontoon of the floater. The minimum values for the horizontal and vertical plane motions are observed for 4-Mooring configurations under irregular waves for all four load cases. Further, suggesting that the position of the mooring lines also significantly influences the responses of the hybrid offshore floating platforms.

#### 4.4.2.2 Frustum Tension-Leg Platform with Eight WECs

Fig. 4.11(a-d) shows the surge response motion for the hybrid FTLP+8WECs stabilised using different mooring layouts under irregular wave conditions. The surge response is higher for the lower wind speed condition and is observed to decrease with the increase in the wind speed condition. Fig. 4.11(a) shows the surge motion response for 8 m/s wind speed conditions. The surge motion is observed to be slightly higher for the 6-Mooring configuration and is reduced with an increase in the mooring cables. Further, minimum surge response motion is observed for the 7-Mooring configuration compared to 12-Mooring and 13-Mooring, though the variation in the surge motion response is minimum with the increase in the mooring cables. Thus, the study shows that the position of the mooring cables is one significant factor in improving the performance of the floating platform. Fig. 4.11(b) shows the surge motion response for 11.2 m/s wind speed conditions. Higher surge motion response is observed for the 11.2 m/s wind speed condition. Further, the surge motion response for the 11.2 m/s wind speed condition is higher for the 12-Mooring configuration and is minimum for the 7-Mooring configuration. Also, the variation in the surge motion response for the 7-Mooring and 13-Mooring layouts is minimal, depicting the importance of providing the mooring cables on the central column supporting the wind turbine.

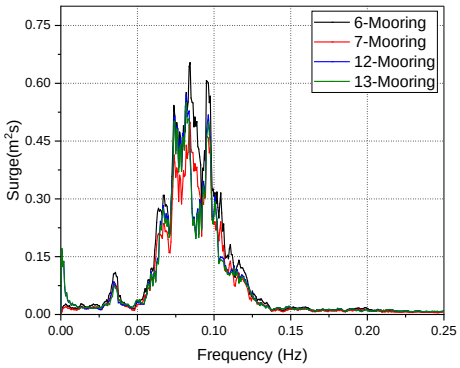


(a)

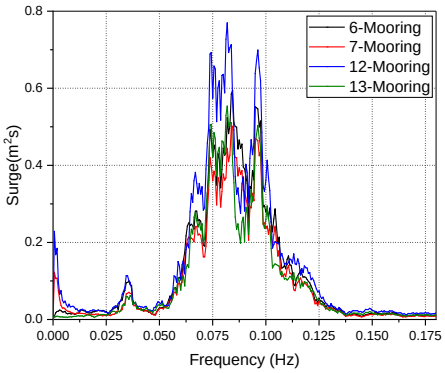


(b)

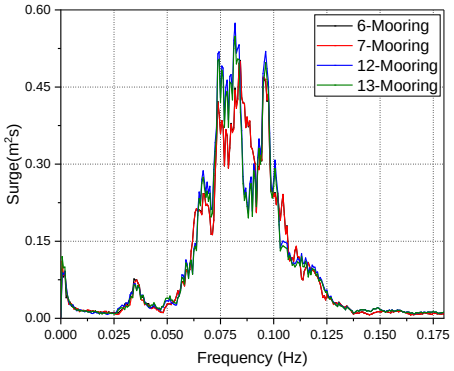


(c)

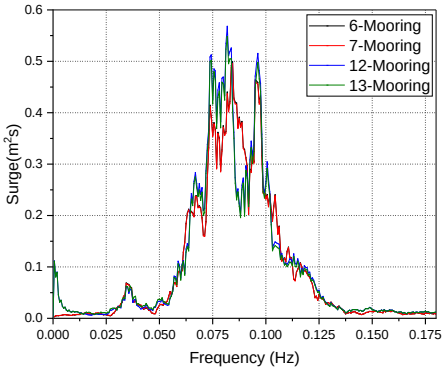


(d)

Fig. 4.11: Surge response of the hybrid FTLP+8WECs floater under irregular waves for (a) SS-1, (b) SS-2, (c) SS-3, and (d) SS-4 for different mooring configurations.

The surge motion response is observed to decrease for 14 m/s (Fig. 4.11c) and 17 m/s (Fig. 4.11d). For any load case condition, the wave frequency of the surge motion is observed in the frequency range of 0.075 to 0.10 Hz, which is away from the natural surge frequency of the floating system. Hence the floating system is safe against resonance for any mooring layouts.

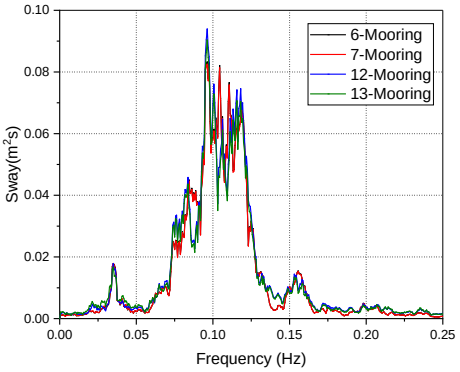


(a)

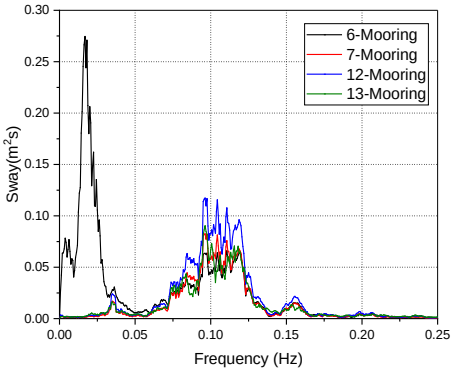


(b)

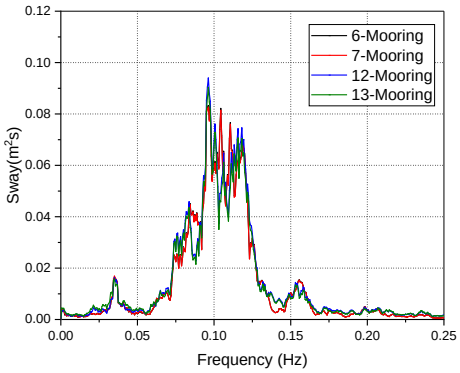


(c)

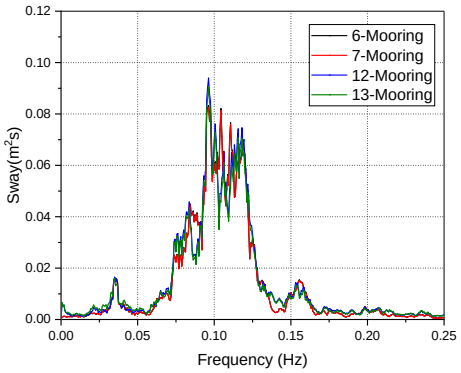


(d)

Fig. 4.12: Sway response of the hybrid FTLP+8WECs floater under irregular waves for (a) SS-1, (b) SS-2, (c) SS-3, and (d) SS-4 for different mooring configurations.

Fig. 4.12(a-d) shows the sway motion response for the different mooring configurations of hybrid FTLP+8WECs. The sway responses of the hybrid FTLP+8WECs are less compared to surge motion responses. Fig. 4.12(a) shows the sway motion response of the hybrid system for 8 m/s operational wind speed conditions. The peak sway motion response is observed for the 12-Mooring configuration for the frequency range $0.08 \le \omega \le 0.10$ Hz and is observed to be the minimum for the 7-Mooring configuration. For the 11.2 m/s wind speed condition, the variation of sway motion is higher for the 6-Mooring configuration (Fig. 4.12b) for the frequency range $0.01 \le \omega \le 0.03$Hz and the sway motion is reduced with the change in mooring layout. The wave frequency range for the other three layouts for the 11.2 m/s condition is in the range of $0.08 \le \omega \le 0.13$ Hz. With the increase in the wind speed, the variation of the sway motion for different mooring layouts is minimum (Fig. 4.12(c,d)). The minimum variation in sway motion provides a better platform for the maintenance operation of the floating system. Further, the minimum sway motion allows for better power transmission through the electrical cables as the stain developed on the cables will be minimum for minimum variation in sway.

Fig. 4.13(a-d) shows the heave motion response of the hybrid FTLP+8WECs offshore floating wind turbine platform for different mooring layouts under irregular wave conditions. The variation in heave motion with the increase in the wind speed condition is minimal. For any wind speed and mooring layout conditions, the wave frequency region of the heave motion for the hybrid FTLP+8WECs is in the range of $0.15 \le \omega \le 0.20$ Hz, is below the natural frequency region, and provides higher stability for the floating system. The variation of the heave motion for the frequency range $0.05 \le \omega \le 0.10$ Hz is slightly higher for the 8 m/s wind speed condition

(Fig. 4.13a) and is minimum for the 11.2 m/s wind speed (Fig. 4.13b). The minimum variation in heave motion is due to the tensioned mooring cables provided for the hybrid system.

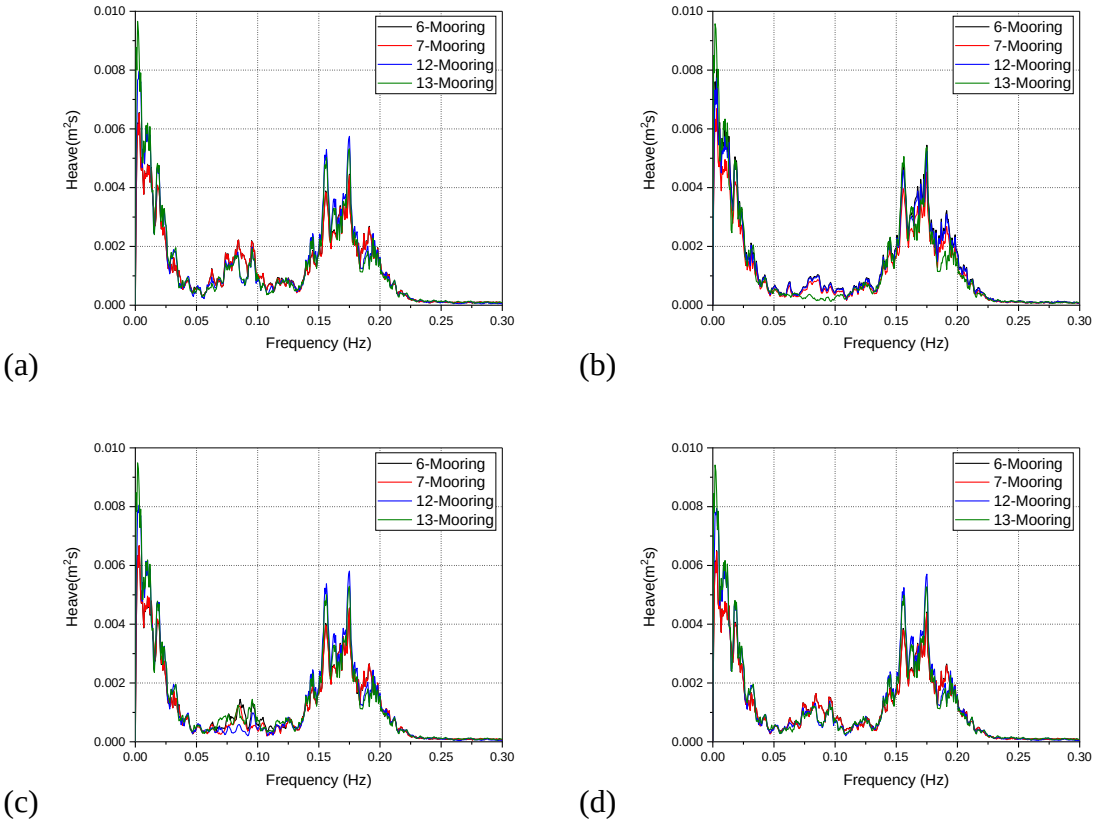


Fig. 4.13: Heave response of the hybrid FTLP+8WECs floater under irregular waves for (a) SS-1, (b) SS-2, (c) SS-3, and (d) SS-4 for different mooring configurations.

Fig. 4.14(a-d) shows the roll motion spectra for the hybrid FTLP+8WECs floating system under irregular wave conditions of the North Atlantic. For any wind speed condition, the responses are very small and hence have higher stability against overturning. For any wind speed conditions, the dominant wave frequency is in the range $0.05 \le \omega \le 0.125$ Hz, and is also away from the natural frequency region, avoiding the possibility of resonance.

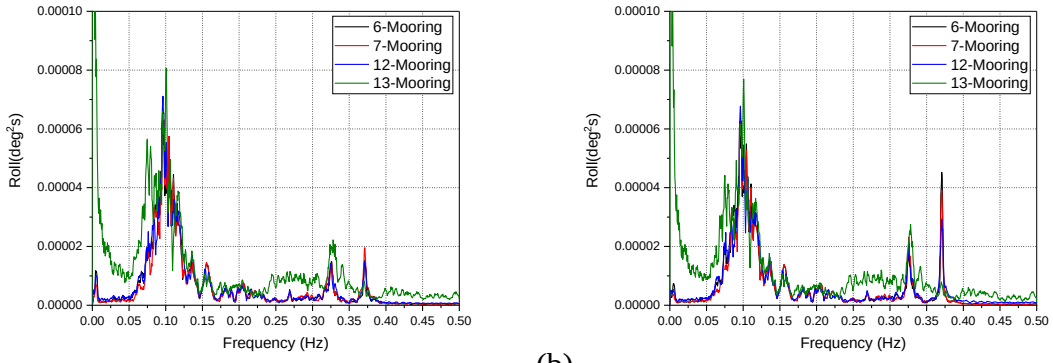

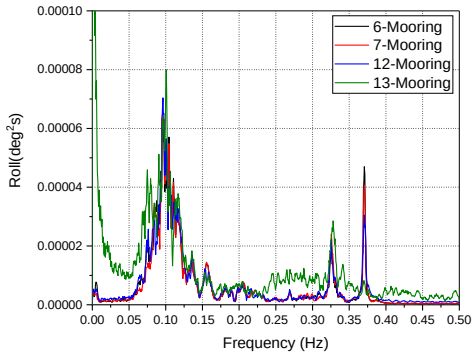


(c)

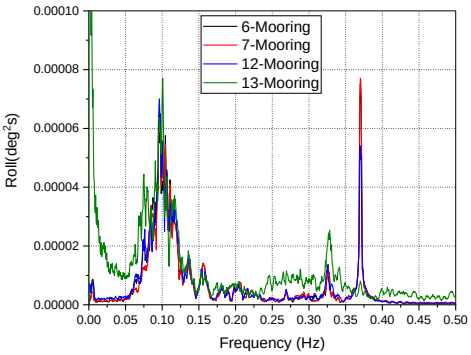


(d)

Fig. 4.14: Roll response of the hybrid FTLP+8WECs floater under irregular waves for (a) SS-1, (b) SS-2, (c) SS-3, and (d) SS-4 for different mooring configurations.

The excitations outside the frequency range of 0.2 Hz are due to second-order wave excitations (Robertson et al., 2013). Minimum roll excitation with the transient effect is observed for the 8 m/s wind speed condition (Fig. 4.14a). Higher excitations are observed for 17 m/s wind speed conditions (Fig. 4.14d) and are reduced with the decrease in the wind speed. For any wind speed condition, the roll motion is higher for the 13-Mooring configurations and is the minimum for the 7-Mooring configuration.

Fig. 4.15(a-d) shows the pitch motion spectra for the hybrid FTLP+8WECs configuration stabilised using different mooring layouts. Like the roll motion spectra, the pitch motion is similar for 8 m/s, 14 m/s and 17 m/s wind speed conditions. The highest pitch motion response is observed for the 12-Mooring configuration for the wave frequency range $0.05 \le \omega \le 0.18$ Hz. Further, a lower pitch motion response is observed for the 7-Mooring configuration, and the peak motion response is shifted further away from the natural frequency region for the 7-Mooring configuration. The wave frequency for the 7-Mooring configuration is in the range of $0.05 \le \omega \le 0.09$ Hz, having lower chances of developing resonance.

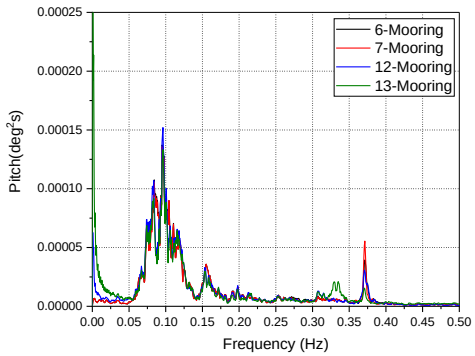


(a)

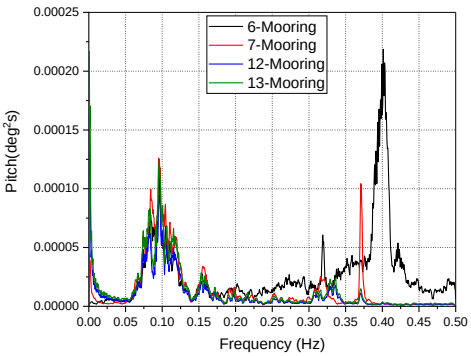


(b)

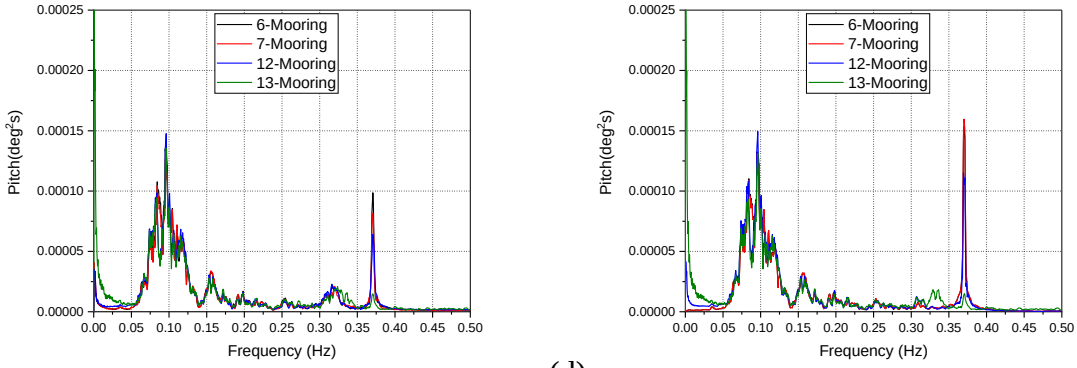


(c) (d)

Fig. 4.15: Pitch response of the hybrid FTLP+8WECs floater under irregular waves for (a) SS-1, (b) SS-2, (c) SS-3, and (d) SS-4 for different mooring configurations.

A second-order wave excitation in pitch motion is also observed for the load cases studied. Minimum second-order excitation is observed for the 8 m/s load case (Fig. 4.15a) and is observed to increase with the increase in the wind speed (Fig. 4.15(b,d)). For the 11.2 m/s wind speed condition (Fig. 4.15b), the 6-Mooring configuration has a higher transient effect of the waves for the pitch motion. This may be because the wind conditions are not synchronising with the dominant wave frequencies. Also, the frequencies of the wind-induced vibrations may not necessarily align with the natural frequencies or the dominant wave frequencies.

Fig. 4.16(a-d) shows the yaw motion response spectra for the FTLP+8WECs hybrid floating platform for different load case conditions. The peak values for the yaw motion occur at very low-frequency regions, and also the variation of the motion is observed to be minimum. Minimum yaw motion response is observed for the 8 m/s wind speed condition (Fig. 4.16d) and increases with the increase in wind speed. Further, the variation in the yaw motion is minimum for wind speed conditions above 8 m/s (Fig. 4.16(b-d)). The wave frequency region for any mooring layout is in the range of $0.004 \leq \omega \leq 0.008$ Hz for different load cases considered. Further, minimum yaw motion response is observed for the 7-Mooring configuration and is higher for the 13-Mooring configuration. The yaw motion response for the hybrid FTLP+8WECs are minimal compared to that of the hybrid STLP+6WECs for any mooring configurations. This may be because of the higher stiffens of the floating FTLP compared to the STLP. The minimum yaw motion of the hybrid system ensures better wind power absorption and higher efficiency of the generator system, as the lateral load developing on the control system is minimum for the reduced yaw motion of the floating system.

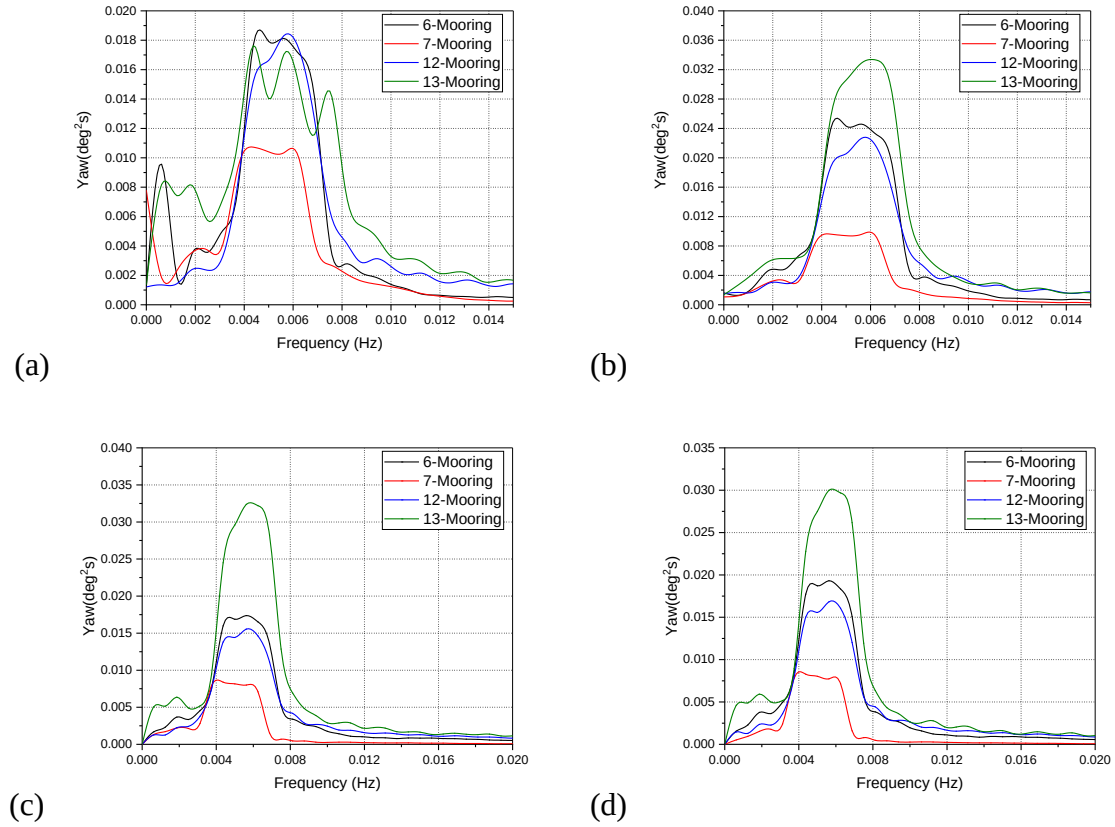


Fig. 4.16: Yaw response of the hybrid FTLP+8WECs floater under irregular waves for (a) SS-1, (b) SS-2, (c) SS-3, and (d) SS-4 for different mooring configurations.

### 4.4.3 Time Series Analysis

The time-domain response analysis of the hybrid floater is performed for 150 m water depth. To focus on the most critical conditions, surge, sway, and yaw motion of the combined floater configuration for four operational conditions of a 5 MW wind turbine with the different numbers of mooring lines are studied to understand the influence of mooring lines and the position of the tendons.

#### 4.4.3.1 Submerged Tension-Leg Platform with Six WECs

The total simulation time for the hybrid floater is 3600 s, and the initial 2600 s are neglected to remove the transient effect. In Fig. 4.17(a-d), it is observed that the surge responses are higher for wind speed condition above the rated wind speed of 5 MW wind turbine (11.4 m/s). Maximum surge value is noted within $10 \leq \xi \leq 12$ for 11.2 m/s wind speed (Fig. 4.17b), which is close to the rated wind speed condition of the 5 MW wind turbine. The responses are observed to be minimum for wind speed close to the rated wind speed condition, thus showing the improved wind power generation of the hybrid floater. Also, it is observed that the variation

of surge responses with a change in the number of mooring lines is observed to be minimum for lower wind velocities compared to higher wind velocities. Further, the surge responses are observed to increase with the increase in the mooring lines.

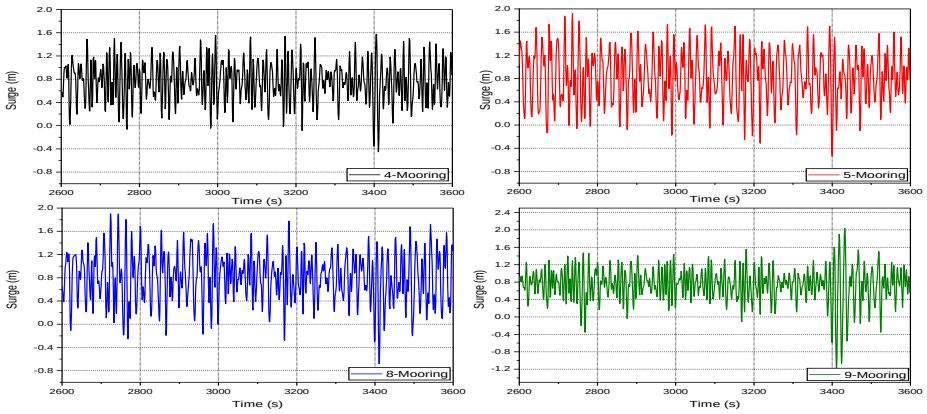


(a)

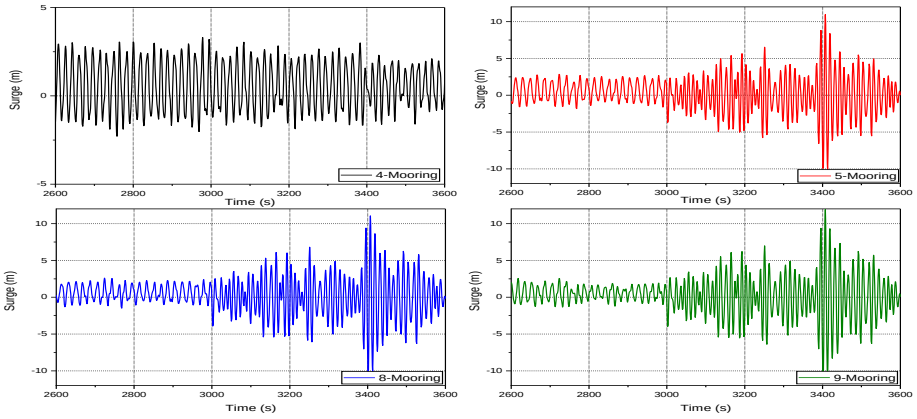


(b)

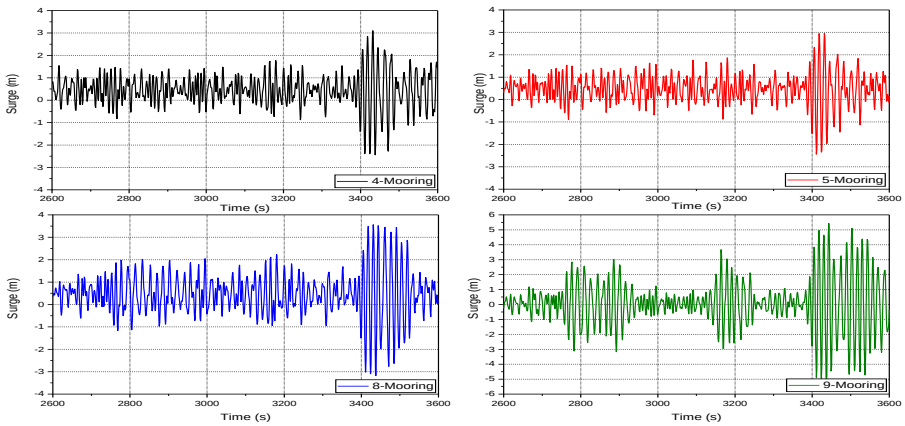


(c)

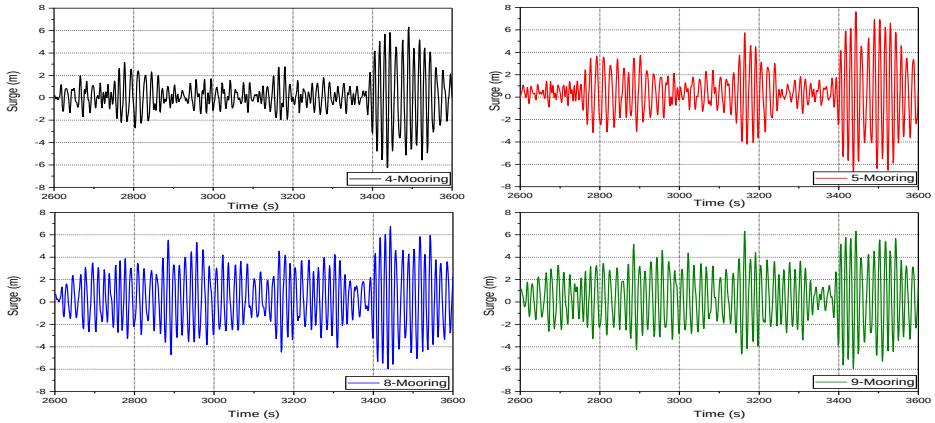


(d)

Fig. 4.17: Time series surge motion of hybrid STLP+6WECs for (a) SS-1, (b) SS-2, (c) SS-3, and (d) SS-4 for different mooring configurations under irregular waves.

Fig. 4.18(a-d) shows the motion time-domain response of sway motion for the hybrid floater. Minimum variation in sway response is observed with the increase in wind speed and wave height. The maximum value of sway motion is noted within $3.5 \leq \xi \leq 4.5$ for 17 m/s wind speed conditions, and the minimum value is observed for 8 m/s wind speed conditions. The time-domain variation of the sway motion with the increase in the mooring lines is also negligible for any wind speed condition. The sway motion amplitude is reduced when an additional mooring cable is provided for the central column (Fig. 4.18a). The 9-mooring configuration is having the least sway motion amplitude for any operational sea state condition of the 5 MW wind turbine.

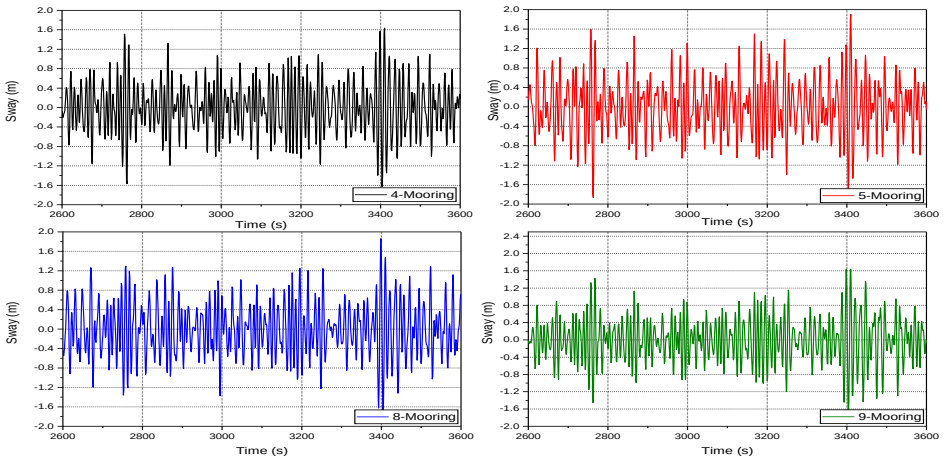


(a)

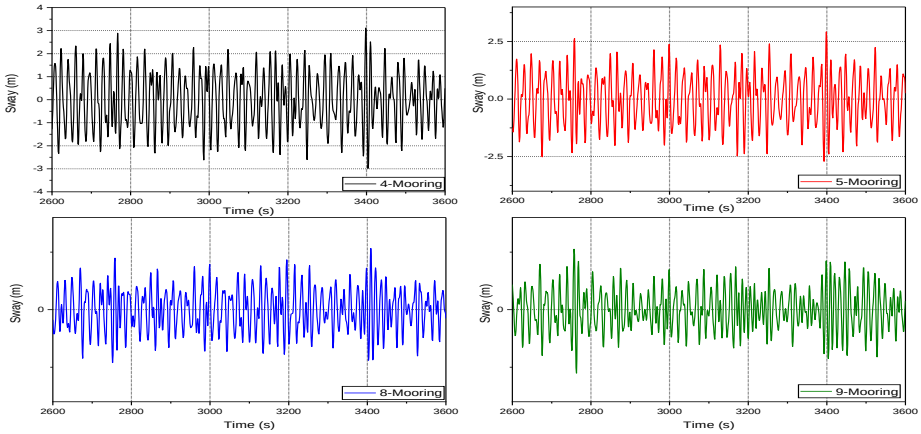


(b)

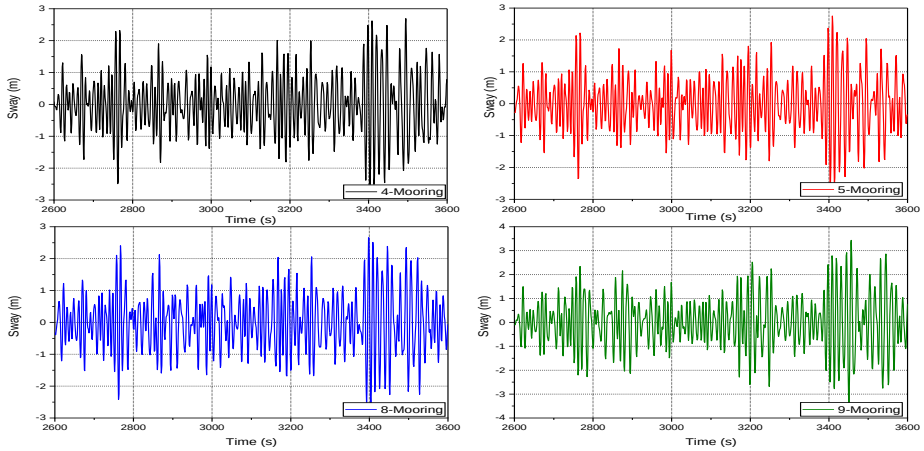


(c)

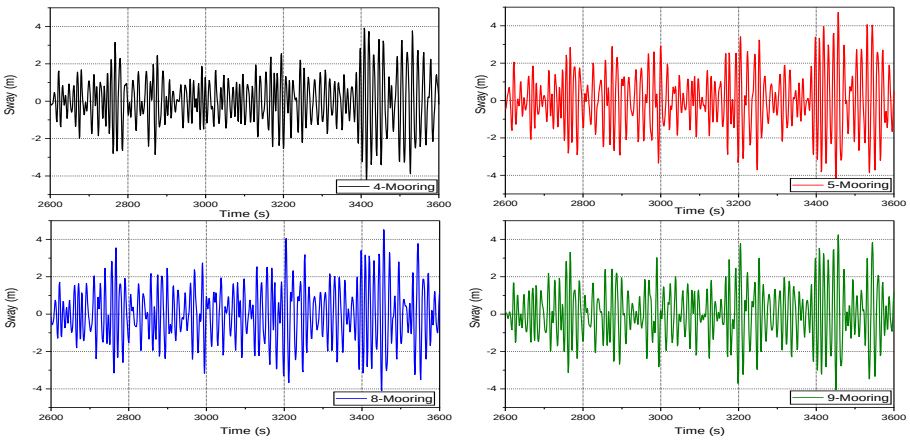


(d)

Fig. 4.18: Time series sway motion of hybrid STLP+6WECs for (a) SS-1, (b) SS-2, (c) SS-3, and (d) SS-4 for different mooring configurations of combined floater under irregular waves.

Time-domain response of yaw motion for the hybrid floater under different loading conditions is shown in Fig. 4.19(a-d). The yaw motion response is observed to be higher compared to the other two horizontal plane motions. The yaw motions response is also observed to increase with the increase in wind speed. The maximum value of yaw motion is observed for the wind speed condition close to the parked state of the 5 MW wind turbine ($V_{mean}$= 17 m/s). The time-domain simulation shows that proper restoring force is observed for all horizontal and vertical plane motions, thus ensuring higher stability of the hybrid system. The additional mooring cable provided for the central column have minimum influence for the yaw motion amplitude of the hybrid system. Similar variation in yaw motion amplitude is observed for any mooring configurations for the different operational wind speed conditions of the 5 MW wind turbine. This shows the minimal influence of the number of mooring cables on the yaw motion amplitudes of the hybrid STLP+6WECs.

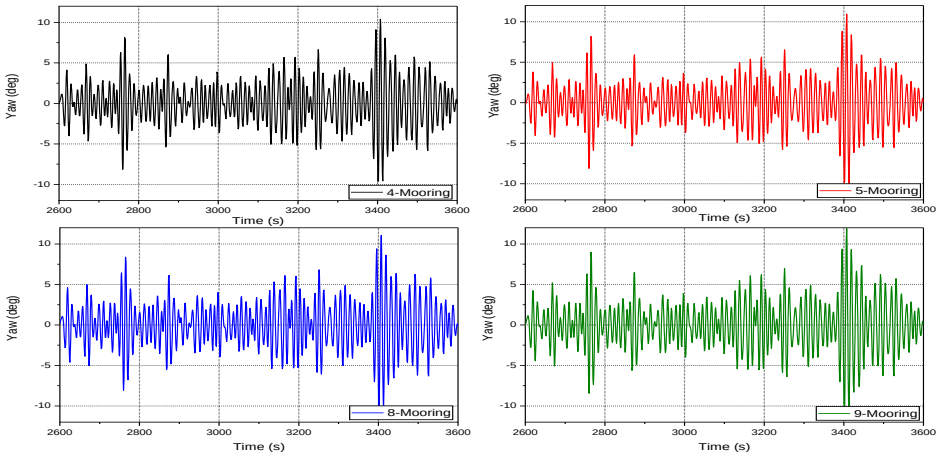


(a)

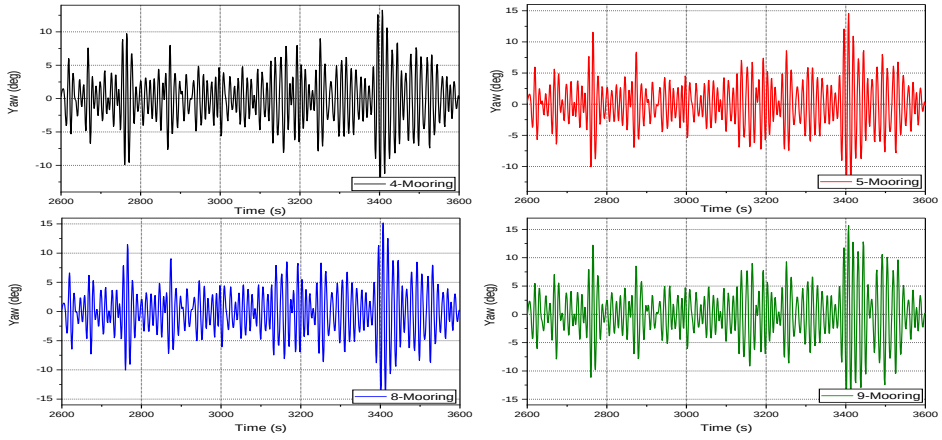


(b)

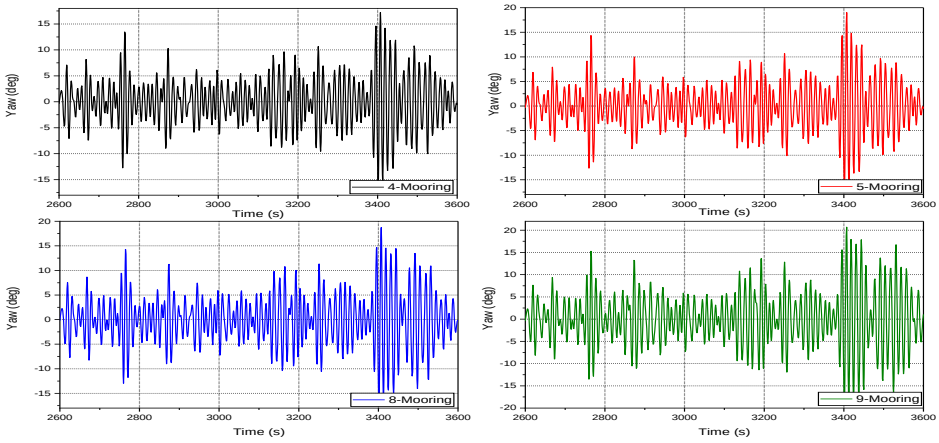


(c)

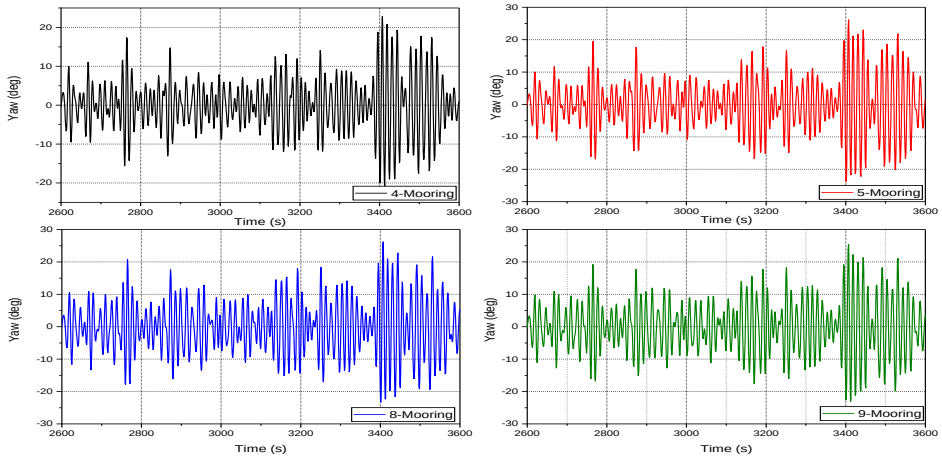


(d)

Fig. 4.19: Time series yaw motion of hybrid STLP+6WECs for (a) SS-1, (b) SS-2, (c) SS-3, and (d) SS-4 for different mooring configurations under irregular waves.

#### 4.4.3.2 Frustum Tension-Leg Platform with Eight WEC

The time series data of surge motion for different mooring layouts of hybrid FTLP+8WECs configuration is shown in Fig. 4.20(a-d). Fig. 4.20(a) shows the surge motion response of the FTLP+8WECs platform for the SS-1 load case. Higher surge motion in the range of $4.5 \leq \xi \leq 5.0\ m$ is observed for the 6-Mooring configuration and decreases with the increase in the number of mooring lines. Minimum variation in the surge motion response is observed with the change in the mooring layouts. This may be because, with the increase in the mooring cables, the location of the mooring cables may also influence the surge response of the floating platform. Similar to the surge motion of the 8 m/s wind speed condition, SS-2 (Fig. 4.20b), SS-3 (Fig. 4.20c), and SS-4 (Fig. 4.20d) conditions have similar response motion. From the

comparison of four different mooring layouts 12-Mooring and 13-Mooring are observed to have minimum surge motion amplitudes. An additional mooring cable on the central column have minimal influence on the surge motion of the hybrid system.

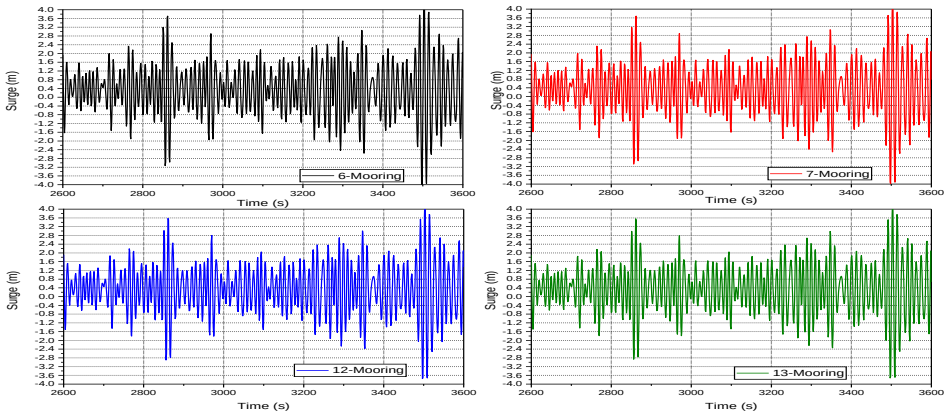


(a)

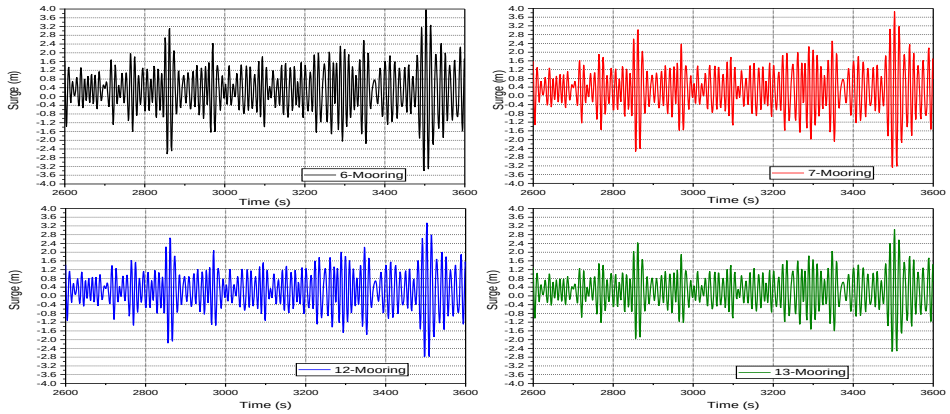


(b)

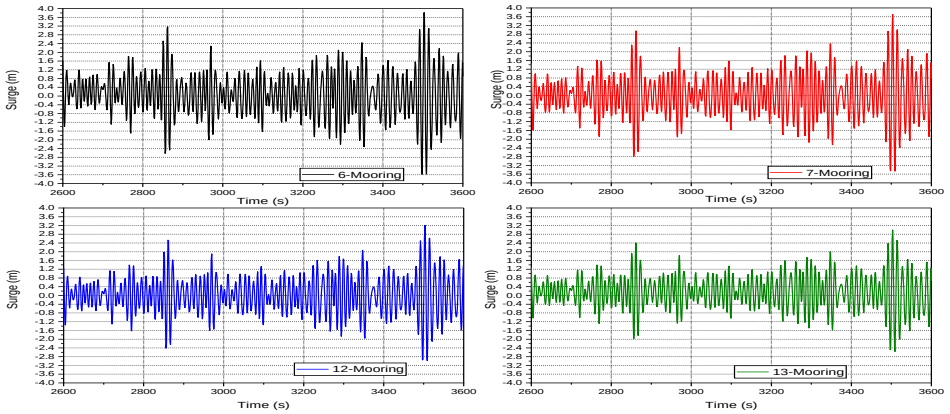


(c)

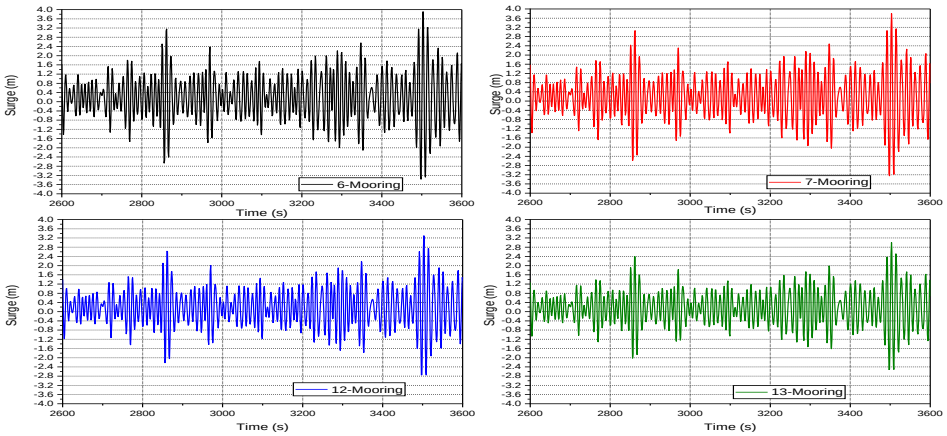


(d)

Fig. 4.20: Time series surge motion of hybrid FTLP+8WECs for (a) SS-1, (b) SS-2, (c) SS-3, and (d) SS-4 for different mooring configurations under irregular waves.

Fig. 4.21(a-d) shows the sway motion amplitudes of the FTLP+8WECs for different mooring layouts of the North Atlantic wave conditions. Higher sway motion amplitudes of the range $1.0 \le \xi \le 1.3\ m$ are observed for the SS-1 load case condition (Fig. 4.21a) and are observed to reduce with the increase in the mooring cables. Further, lower sway motion amplitude of the range $0.8 \le \xi \le 1.0\ m$ is observed for the SS-2 condition (Fig. 4.21d). The minimum sway motion of the platform ensures minimum dynamic loads on the platform's structural components, including the tower, mooring system, and floating structure. Further, the minimum sway motion of the platform ensures minimum lateral forces developing on the mooring cables, improving the life of the mooring systems. Further, minimum sway motion ensures reduced fatigue load on the mooring cables of the hybrid system.

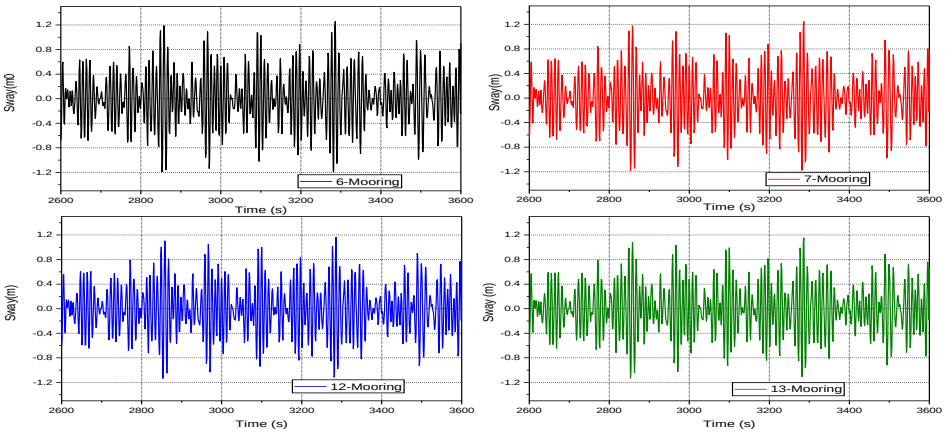


(a)

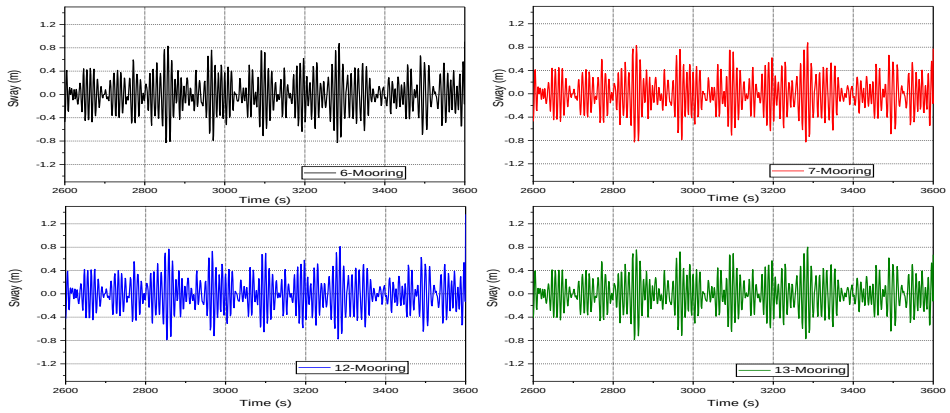


(b)

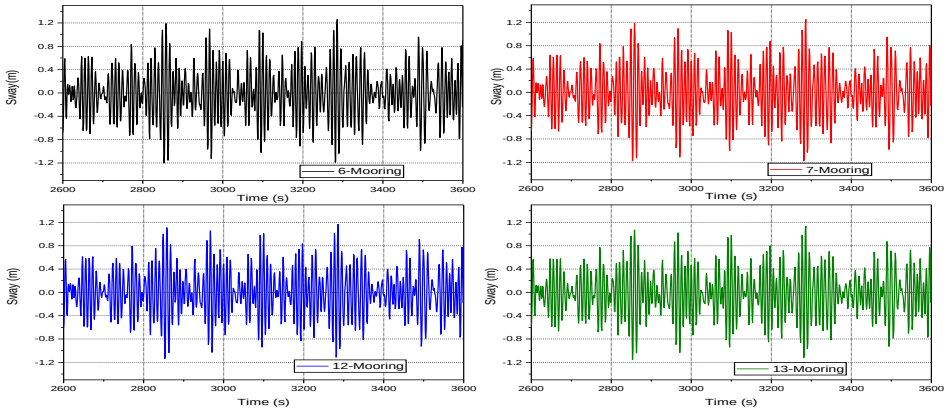


(c)

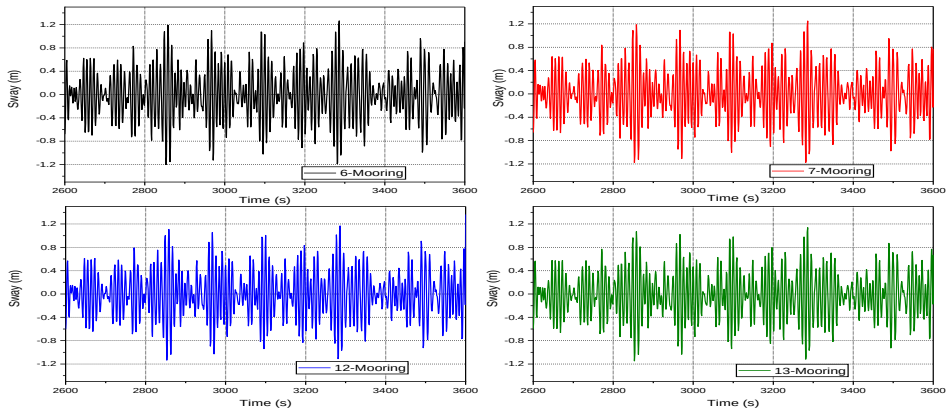


(d)

Fig. 4.21: Time series sway motion of hybrid FTLP+8WECs for (a) SS-1, (b) SS-2, (c) SS-3, and (d) SS-4 for different mooring configurations under irregular waves.

Fig. 4.22(a-d) shows the yaw motion response of the hybrid FTLP+8WEC under irregular waves of the North Atlantic region for different mooring layouts. The variation in yaw motion

with time is minimal for any load case condition. Further, for any wind speed condition, the yaw motion response is minimum for the 7-Mooring configuration (Fig. 4.22(a-d)). The highest yaw motion amplitude of the floating FTLP+8WECs is of the range $0.06 \le \xi \le 0.08$ *deg* for the 12-Mooring configuration for the waves of SS-1 load case condition (Fig. 4.22(a)). Further, the yaw motion amplitude is observed with the time for the SS-3 (Fig. 4.22c) and SS-4 (Fig. 4.22d) load conditions. The minimum yaw amplitude of the platform ensures better orientation of the turbine towards the wind, improving the turbine's power output. Also, fine-tuning the yaw motion amplitude helps to maximise the energy capture and improves the turbine's overall efficiency. The 13-Mooring configuration is observed to have higher yaw motion amplitude for the FTLP+8WECs. The addition of the mooring cable to the central pontoon of the hybrid system have significant influence on the yaw motion amplitude of the FTLP+8WECs, the yaw motion increases for the 13-Mooring and the yaw motion decrease for the 7-Mooring configuration.

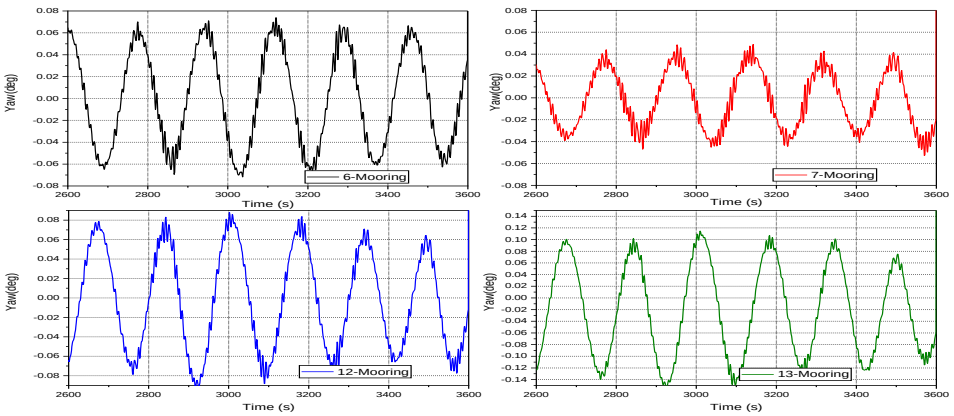


(a)

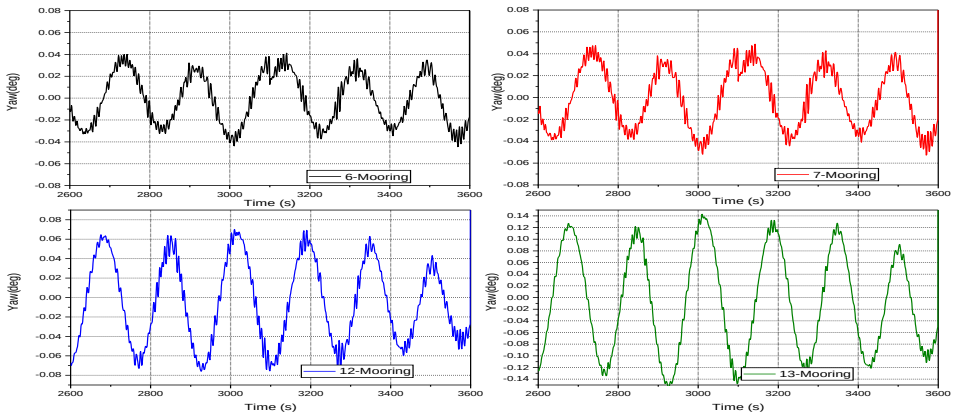


(b)

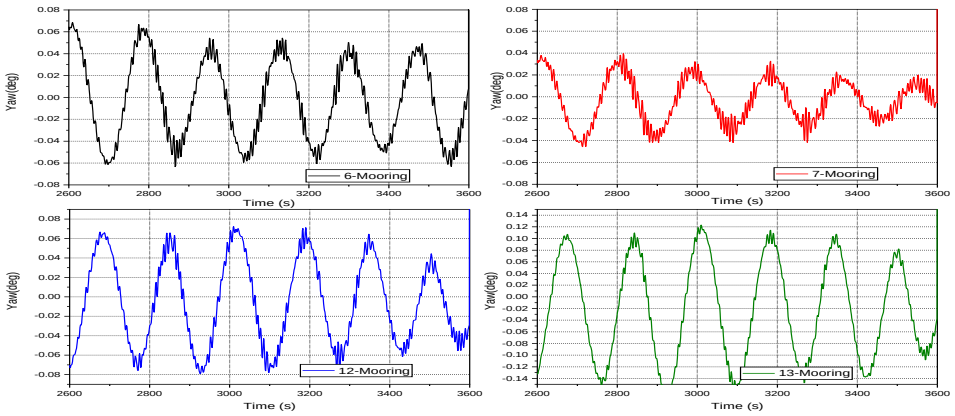


(c)

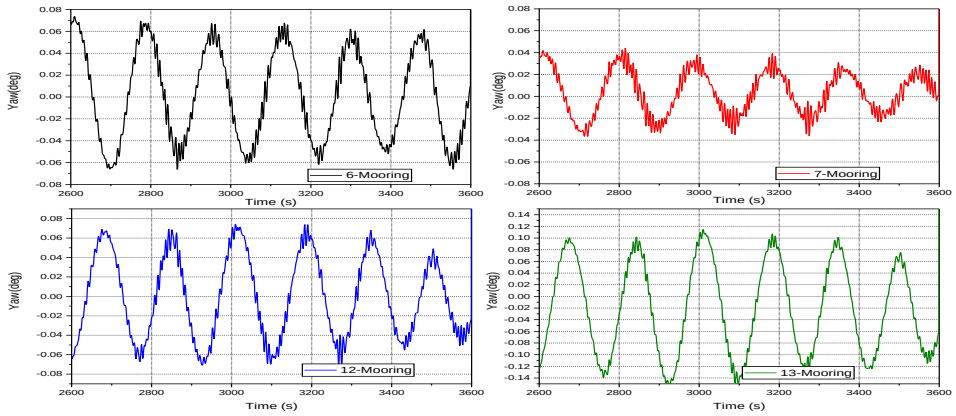


(d)

Fig. 4.22: Time series Yaw motion of hybrid FTLP+8WECs for (a) SS-1, (b) SS-2, (c) SS-3, and (d) SS-4 for different mooring configurations under irregular waves.

### 4.4.4 Fairlead Tension

The motions of the platform through the fairleads are what primarily cause the mooring loading of floating offshore wind turbines. The mooring dynamics are insignificant and have little impact on the general behaviour of the floating wind turbine from the perspective of the loads over the platform dynamics. However, for the TLPs, the dynamic impacts in mooring analysis design are essential and can increase the design Fairlead Tensions (FT). The principal loads in the dynamic analysis of the mooring lines are gravity load, hydrodynamic load and the inertial effects of the platform. In the present section, the maximum tension developed on each mooring cable for different mooring layouts of the hybrid STLP+6WECs and FTLP+8WECs platforms are studied to analyse the importance of the addition of the mooring cables and the position of the mooring cables.

#### 4.4.4.1 Submerged Tension-Leg Platform with Six WECs

The maximum value of tension developed on each mooring cable of the hybrid floater is studied for different load case conditions, as seen in Fig. 4.23(a-d). The tension developed on each cable is considerably reduced with the increasing number of mooring cables. From Fig. 4.23(a), it is observed that under the operational conditions of the 5 MW wind turbine, the 4-Mooring system cables have almost equal tension developed on each mooring cable for different wind load conditions. But for the 5-Mooring configuration (Fig. 4.23b), the tension developed on the cable provided on the central column is minimum compared to other cables provided for the outer pontoons. Further, in the case of the 8-Mooring configuration (Fig. 4.23c), a significant variation in motion response is observed for wind speed conditions close to the parked state. The tension developed on each cable is almost equal for all other wind speed conditions. In the case of the 9-Mooring configuration (Fig. 4.23d), the tendons on the leeward side are observed to have higher tension for wind speeds, more significant than the rated wind speed for the 5 MW wind turbine. The study also observed that adding wave energy converters around the STLP floater has helped reduce the tension developed on the mooring cable.

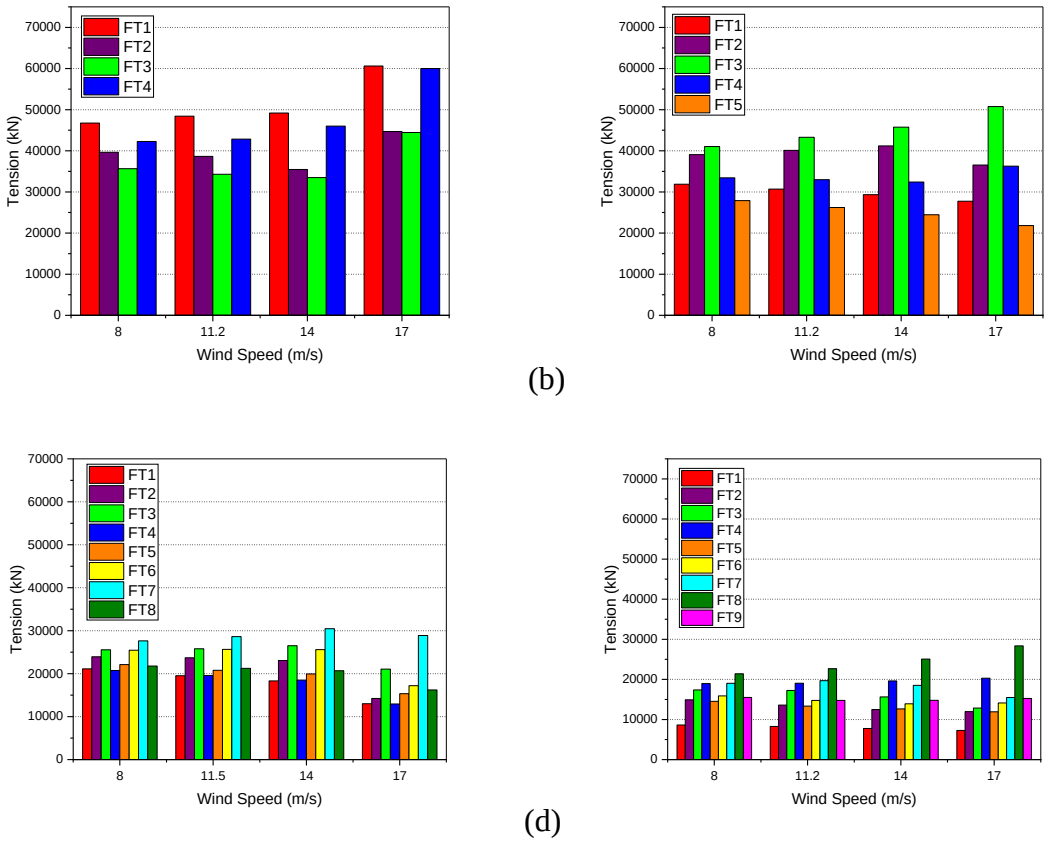


Fig. 4.23: Maximum tension developed on the tendons for (a) 4-Mooring, (b) 5-Mooring, (c) 8-Mooring, and (d) 9-Mooring for the hybrid STLP+6WECs.

Also, a higher tension value is observed to be developed for the cable provided for the central column compared to the outer pontoons. This shows that the restoration of the hybrid system is higher for lower wind speed conditions, and it is more until the rated wind speed of the reference wind turbine. Once the wind speed is above the rated wind speed, the restoration of the floater system is reduced, and thus higher tension is observed for the floating system.

#### 4.4.4.2 Frustum Tension-Leg Platform with Eight WECs

The maximum value of tension developed on the mooring cables for different mooring layouts of hybrid FTLP+8WECs is studied in Fig. 4.24(a-d). The tension developed on the mooring cables is reduced with the increase in the number of mooring cables provided to stabilise the floating system. Fig. 4.24(a) shows the mooring cable tension developed for the 6-Mooring layout of the hybrid FTLP+8WECs for the different operational conditions of the wind turbine. Higher tension for the cables is observed for the 11.2 m/s wind speed condition and is observed to be less for the 8, 14 and 17 m/s wind speed conditions. Further, the tension developed on the mooring cables is almost similar for any cables for different operational conditions.

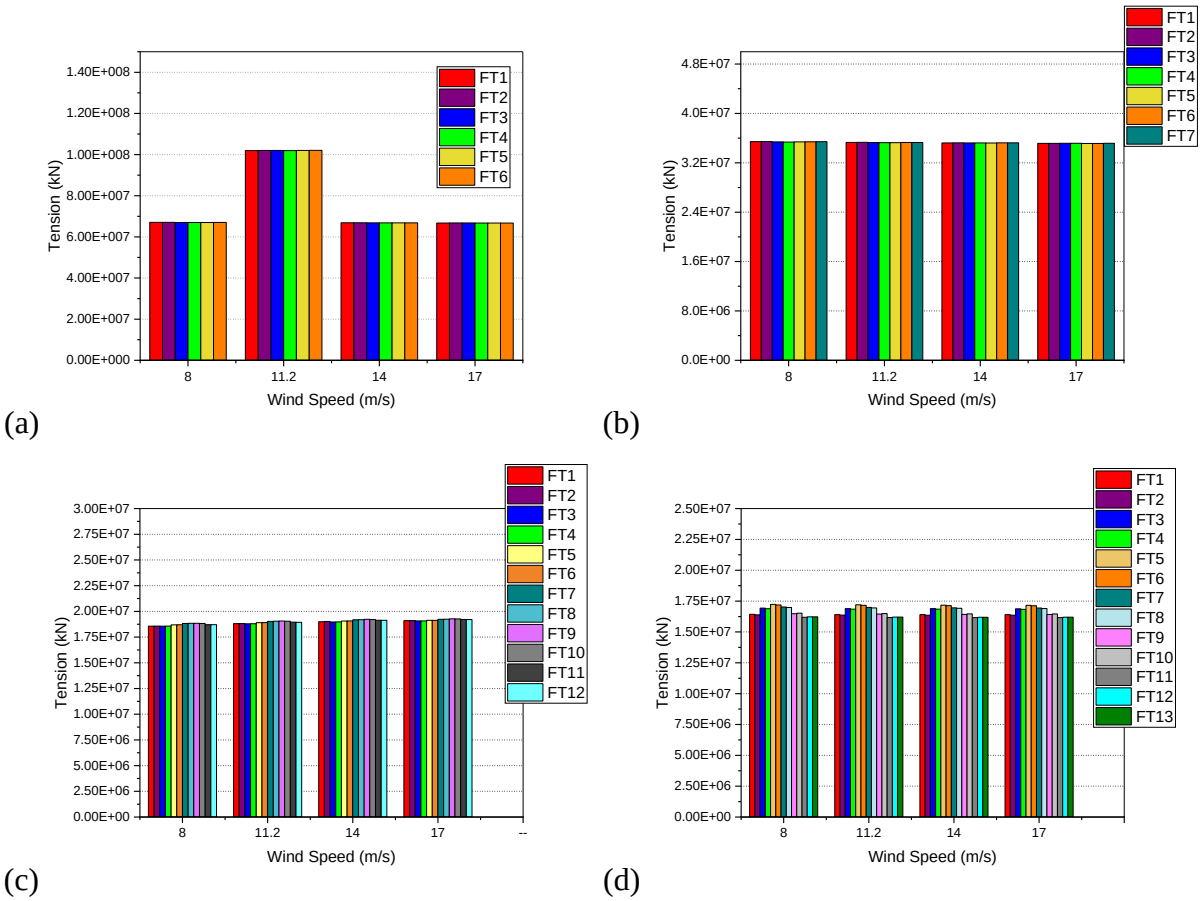


Fig. 4.24: Maximum tension developed on the tendons for (a) 6-Mooring, (b) 7-Mooring, (c) 12-Mooring, and (d) 13-Mooring for the hybrid FTLP+8WECs.

Slightly higher tension values are observed for the cables on the seaward side, which may be due to the direct impact of the waves. Fig. 4.24(b) shows the tension developed for the 7-Mooring layout of the hybrid FTLP+8WECs. Tension developed on the mooring cables is similar to any wind speed conditions. Slightly higher values are observed for 8 and 11.2 m/s wind speed conditions and are observed to decrease with the increase in the wind speed. Further, the tension developed on the cables is almost equal for any wind speed condition. Similar variation in tension developed is observed for both 12-Mooring (Fig. 4.24c) and 13-Mooring (Fig. 4.24d) layout supporting the hybrid system. For all four mooring layout conditions, the higher tension developed is for the 11.2 m/s wind speed condition. This may be because the rated wind speed (11.4 m/s) yields the highest wind power absorption, further having a higher wind load on the platform, increasing the tension developing on the mooring cables. Also, it is observed that the tension developed on the cables for any mooring layout is evenly distributed. This prevents the overloading of the individual cables, reducing the risk of failure or excessive stress on an individual cable. Compared to hybrid STLP+6WECs with different mooring layouts, hybrid FTLP+8WECs floating wind turbines have better performance and higher stability in terms of tension developed on the mooring cables.

### 4.4.5 Generator Power

A 5 MW wind turbine is typically built to produce 5 MW (or 5,000 kW) of nominal power output. A wind turbine's power production changes according to wind speed and is not constant. In order to prevent damage, wind turbines have rated or cut-in wind speeds at which they begin to generate power and cut-out wind speeds at which they must shut down. The power output rises with wind speed within the rated wind speed range, following a power curve unique to the turbine model. The correlation between wind speed and the related power output is depicted by the power curve of a wind turbine. A wind turbine typically operates at its maximum capacity (rated power) at a specific wind speed, typically between 10 and 15 m/s. Until the cut-out wind speed is achieved, the power output remains steady above this wind speed. The generator power for the hybrid STLP+6WECs and hybrid FTLP+8WECs is studied to understand the influence of the floating platforms on wind power generation.

#### 4.4.5.1 Submerged Tension-Leg Platform with Six WECs

The time-domain characteristics of generator power for irregular waves for the hybrid floating platform are shown in Fig. 4.25(a-d). The study shows that the hybrid system has approximately the same mean generator power output during operation and can generate the

power of 5 MW at any wind speed between the cut-in and cut-out wind speed of the 5 MW reference wind turbine.

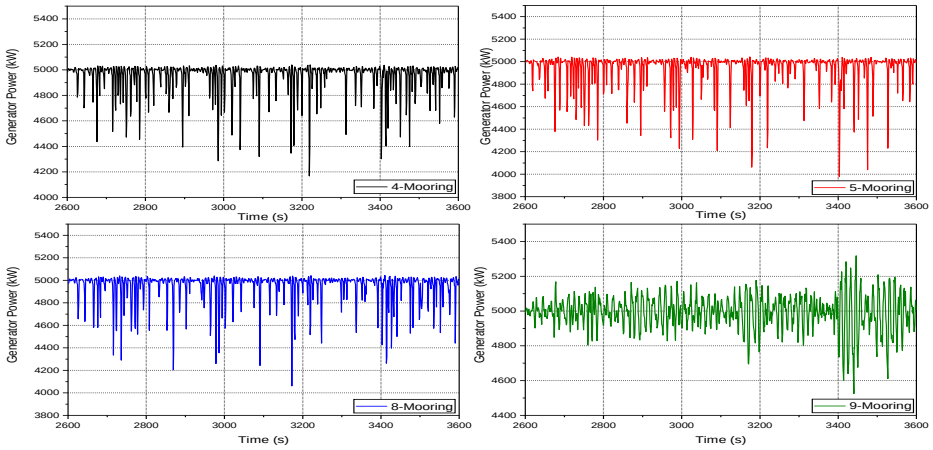


(a)

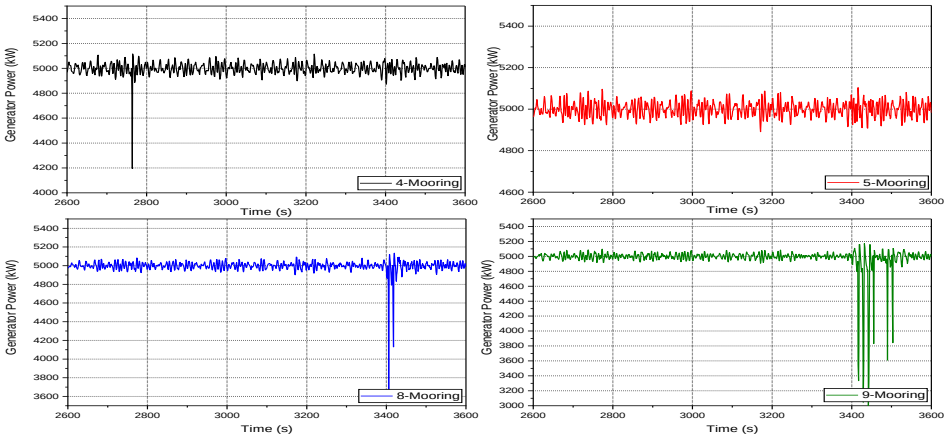


(b)

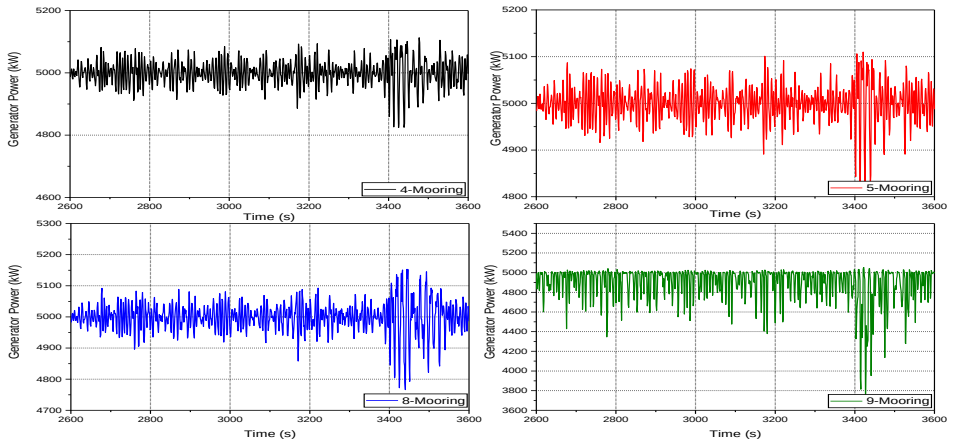


(c)

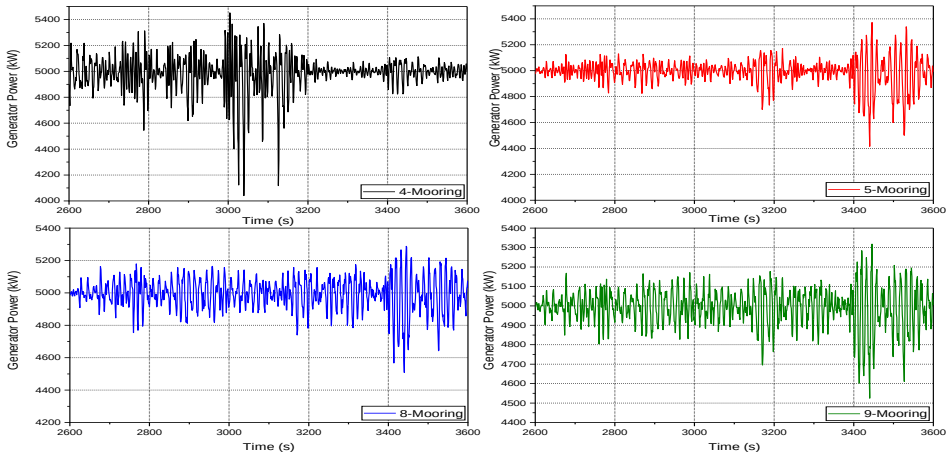


(d)

Fig. 4.25: Generator power for (a) SS-1, (b) SS-2, (c) SS-3, and (d) SS-4 for different mooring configurations of hybrid STLP+6WECs under irregular waves.

The variations in the generator power conclude the influence of wind gusts and control action on the power generation. For a wind speed of 11.2 m/s, the study observes to have very minimum variation in power generation for all four different mooring configurations of the hybrid floater under irregular waves, as seen in Fig. 4.25(b). The minimum variation in the power generator concludes the minimum value of pitch for the hybrid system, further ensuring that the load developed at the base of the turbine under the action of wind will be minimum. From Fig. 4.25(d), a higher variation in power generation for the hybrid floater is observed for the wind speed of 17 m/s, which is close to the parked condition of the 5 MW reference wind turbine.

### 4.4.5.2 Frustum Tension-Leg Platform with Eight WECs

The generator power of the 5 MW wind turbine supported on the hybrid FTLP+8WECs floating platform stabilised using different mooring layouts for different operational wind speed conditions is discussed in Fig. 4.26(a-d). The higher variation in power generation is observed for the 8 m/s (Fig. 4.26a) and 11.2 m/s (Fig. 4.26b) wind speed conditions. This may be because, for lower wind speed conditions, the variations of the platform motions may be higher, leading to higher variations in power generation. Generator power may fluctuate as the control system adjusts to the changing environment in response to variations in wind conditions and platform motion. Further, the variation in power generation is minimum with the change in the number of mooring cables for any wind speed condition. For wind speed conditions above 11.4 m/s, variation in power generation is minimum. Fig. 4.26(c) shows the variation in power

generation for 14 m/s wind speed conditions. The variation is minimal for the 14 m/s wind load condition.

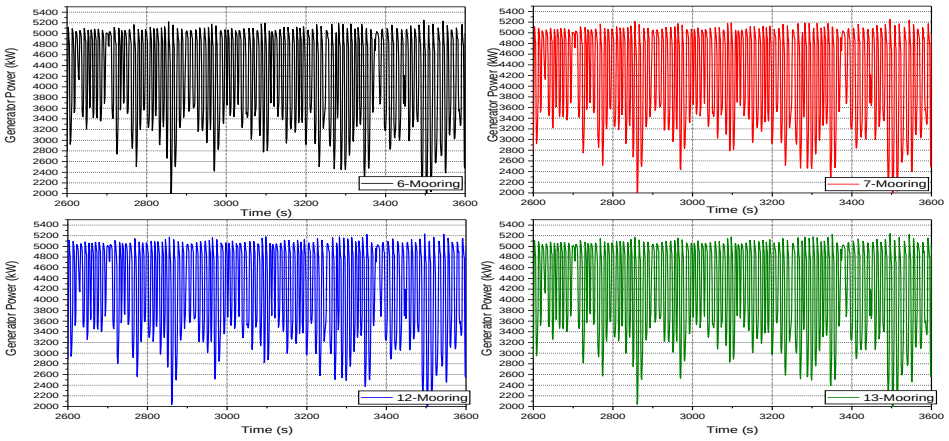


(a)

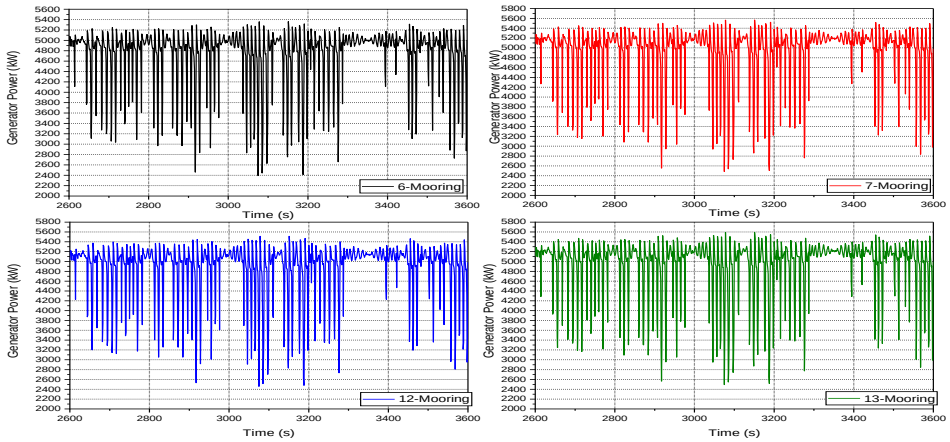


(b)

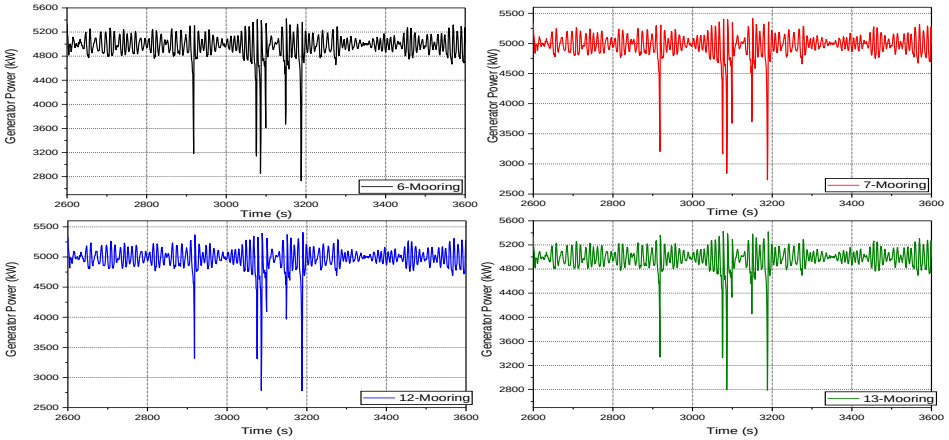


(c)

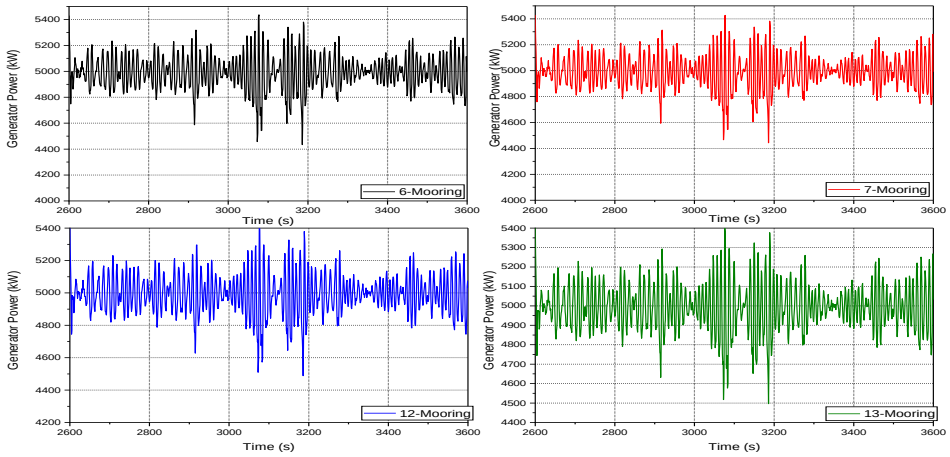


(d)

Fig. 4.26: Generator power for (a) SS-1, (b) SS-2, (c) SS-3, and (d) SS-4 for different mooring configurations of hybrid FTLP+8WECs under irregular waves.

Further, the variation is observed to increase for the 17 m/s wind speed condition (Fig. 4.26d). For both STLP+6WECs and FTLP+8WECs hybrid floating systems, the variation in power generation is minimum for the 11.2 and 14 m/s wind speed conditions. Also, it has minimum influence on the change in number of mooring cables.

### 4.4.6 Tower Base Forces and Moments

The forces and moments developed at the base of the wind turbine are studied for wind speeds below and above the rated wind speed of the reference wind turbine for the North Atlantic region. The forces and moments developed on the turbine's base explain the impact of wind and waves on the turbine. The side-to-side shear force developed on the longitudinal axis is mainly due to the aerodynamic drag of the blades. The aerodynamic drag developed on the blades is more sensitive to the local angle of attack than the aerodynamic lift. Further, for both the wind speed conditions, it is observed that the magnitude of the side-to-side shear force developed is less than the fore-aft shear force, further highlighting that the discrepancy of the side-to-side force is insignificant to the resulting force developed.

#### 4.4.6.1 Submerged Tension-Leg Platform with Six WECs

The variation in the fore-aft shear forces generated at the base of the turbine with the increase in the number of mooring lines is insignificant, as seen in Table 4.7. The maximum value of the fore-aft shear force developed is for the 8-Mooring configuration for the mean wind speed of 11.2 m/s. Further, it is observed that the mean and standard deviation for the force in the 8-

Mooring configuration system is minimal compared to the other three configurations. For the 9-Mooring configuration, it is observed that the mean and standard deviation of the forces is more compared to the other three configurations. Further, the lowest magnitude for the maximum fore-aft force is observed for the 9-Mooring configuration.

Table 4.7: Statistics of the fore-aft shear force for $V_{mean}$ = 11.2 m/s.

| | Parameters | 4-Mooring | 5-Mooring | 8-Mooring | 9-Mooring |
|---|---|---|---|---|---|
| Regular Waves | Mean (kN) | 513.36 | 511.74 | 382.94 | 518.45 |
| | Standard Deviation (kN) | 153.72 | 143.83 | 206.03 | 142.40 |
| | Max (kN) | 798.4 | 752.3 | 638.6 | 707.0 |
| | Min (kN) | 153.72 | 143.83 | 114.4 | 142.4 |
| Irregular Waves | Mean (kN) | 520.62 | 515.47 | 517.96 | 535.26 |
| | Standard Deviation (kN) | 251.01 | 231.97 | 222.88 | 250.84 |
| | Max (kN) | 1349 | 1163 | 1430 | 1603 |
| | Min (kN) | 2.553 | 0.9816 | 0.0578 | 0.520 |

Table 4.8: Statistics of the side-to-side shear force for $V_{mean}$ = 11.2 m/s.

| | Parameters | 4-Mooring | 5-Mooring | 8-Mooring | 9-Mooring |
|---|---|---|---|---|---|
| Regular Waves | Mean (kN) | 228.56 | 220.48 | 221.38 | 228.807 |
| | Standard Deviation (kN) | 100.72 | 95.01 | 84.17 | 86.44 |
| | Max (kN) | 396.23 | 369.45 | 323.56 | 336.98 |
| | Min (kN) | 31.01 | 44.44 | 82.56 | 93.25 |
| Irregular Waves | Mean (kN) | 181.88 | 175.88 | 179.21 | 191.54 |
| | Standard Deviation (kN) | 139.38 | 132.57 | 137.64 | 147.08 |
| | Max (kN) | 729.4 | 674.3 | 876.9 | 850.3 |
| | Min (kN) | 0.1083 | 0.023 | 0.075 | 0.0458 |

Table 4.8 presents the side-to-side shear force developed at the base of the floating wind turbine platform. The variation observed for side-to-side shear force is similar to that for the fore-aft force. With the increase in the mooring lines, the mean and standard deviation of the forces developing at the base are minimal showing the importance of the mooring line for stabilising the platform. The highest magnitude for maximum side-to-side shear force developed is

observed for the 8-mooring configuration, and the lowest magnitude is observed for the 9-Mooring configuration.

Table 4.9: Statistics of the side-to-side bending moment for $V_{mean}$ = 11.2 m/s.

| | Parameters | 4-Mooring | 5-Mooring | 8-Mooring | 9-Mooring |
|---|---|---|---|---|---|
| Regular Waves | Mean (kN-m) | 1.55E+4 | 1.5E+4 | 1.505E+4 | 1.55E+4 |
| | Standard Deviation (kN-m) | 8511.45 | 8259.95 | 7786.24 | 7970.97 |
| | Max (kN-m) | 3.13E+4 | 2.96E+4 | 2.63E+4 | 2.72E+4 |
| | Min (kN-m) | 8.737 | 27.94 | 96.65 | 175.4 |
| Irregular Waves | Mean (kN-m) | 1.31E+4 | 1.27E+4 | 1.32E+4 | 1.43E+4 |
| | Standard Deviation (kN-m) | 9878.45 | 9597.37 | 10347.4 | 11150.81 |
| | Max (kN-m) | 4.76E+4 | 5.05E+4 | 6.89E+4 | 6.77E+4 |
| | Min (kN-m) | 27.78 | 35.38 | 50.83 | 49.16 |

Table 4.10: Statistics of the fore-aft bending moment for $V_{mean}$ = 11.2 m/s.

| | Parameters | 4-Mooring | 5-Mooring | 8-Mooring | 9-Mooring |
|---|---|---|---|---|---|
| Regular Waves | Mean (kN-m) | 4.64E+4 | 4.62E+4 | 4.61E+4 | 4.71E+4 |
| | Standard Deviation (kN-m) | 10891.04 | 10122.34 | 9620.77 | 10001.21 |
| | Max (kN-m) | 6.68E+4 | 6.36E+4 | 5.83E+4 | 6.01E+4 |
| | Min (kN-m) | 2.52E+4 | 2.81E+4 | 3.15E+4 | 3.09E+4 |
| Irregular Waves | Mean (kN-m) | 4.68E+4 | 4.64E+4 | 4.65E+4 | 4.80E+4 |
| | Standard Deviation (kN-m) | 19073.5 | 17326.28 | 16735.99 | 19171.6 |
| | Max (kN-m) | 1.08E+5 | 9.26E+4 | 1.17E+5 | 1.32E+5 |
| | Min (kN-m) | 662.28 | 936.4 | 792.5 | 1027 |

Table 4.9 and 4.10 shows the moments developed at the turbine's base for a mean wind speed of 11.2 m/s. The mean value of the fore-aft bending moment developed at the turbine tower is mainly wind-induced. Further, the standard deviation of the moment is primarily induced by wind and wave loads. Table 4.9 and Table 4.10 shows that the standard deviation values for the moments developed are higher compared to the mean values for all four mooring configurations. Thus, it is concluded that the moments developed on the hybrid floater are induced by both wind and wave loads. Both the mean and standard deviation for the bending

moment developed is minimum for the 8-Mooring configuration, concluding that the impact of both wind and waves on the hybrid floater supported by 8-Mooring lines will be minimum. It is also observed that the maximum values for the forces and moments developed are observed for the 4-Mooring configuration.

#### 4.4.6.2 Frustum Tension-Leg Platform with Eight WECs

The forces and moments developed at the base of the turbine tower are studied for the hybrid FTLP+8WECs platform for different mooring layouts. The mean and standard deviation of the fore-aft shear force and side-to-side shear force developing at the base of the turbine tower are studied (Table 4.11 and Table 4.12) for both regular and irregular wave conditions.

Table 4.11: Statistics of the fore-aft shear force for $V_{mean}$ = 11.2 m/s.

| | Parameters | 6-Mooring | 7-Mooring | 12-Mooring | 13-Mooring |
|---|---|---|---|---|---|
| Regular Waves | Mean (kN) | 987.625 | 951.717 | 482.904 | 478.448 |
| | Standard Deviation (kN) | 87.38 | 99.017 | 79.01 | 85.46 |
| | Max (kN) | 2.83E+03 | 2.41E+03 | 1.55E+03 | 1.55E+03 |
| | Min (kN) | 8.01E+02 | 8.89E+02 | 2.28E+02 | 2.28E+02 |
| Irregular Waves | Mean (kN) | 1.85E+03 | 1.65E+03 | 595.87 | 496.21 |
| | Standard Deviation (kN) | 86.61 | 71.96 | 55.17 | 52.03 |
| | Max (kN) | 2.84E+03 | 2.61E+03 | 1.52E+03 | 1.51E+03 |
| | Min (kN) | 7.69E+02 | 8.38E+02 | 1.16E+02 | 1.09E+02 |

Table 4.12: Statistics of the side-to-side shear force for $V_{mean}$ = 11.2 m/s.

| | Parameters | 6-Mooring | 7-Mooring | 12-Mooring | 13-Mooring |
|---|---|---|---|---|---|
| Regular Waves | Mean (kN) | 581.38 | 577.80 | 225.26 | 209.52 |
| | Standard Deviation (kN) | 52.37 | 36.69 | 31.36 | 30.61 |
| | Max (kN) | 856.69 | 839.52 | 446.82 | 445.73 |
| | Min (kN) | 168.63 | 152.93 | 86.04 | 79.27 |
| Irregular Waves | Mean (kN) | 682.95 | 698.28 | 320.32 | 319.83 |
| | Standard Deviation (kN) | 66.07 | 68.67 | 75.13 | 73.40 |
| | Max (kN) | 1.14E+03 | 1.01E+03 | 570.13 | 561.02 |
| | Min (kN) | 674.83 | 529.37 | 68.02 | 65.47 |

Also the maximum and minimum values of the moments are studied. The forces for the platform are observed to be higher under irregular wave conditions. The fore-aft shear force is observed to be higher for both regular and irregular wave conditions, as seen in Table 4.11. This may be because of the zero-degree wave direction considered in the study. Further, the forces are observed to reduce with the increase in the number of mooring cables. With the addition of the mooring cable to the central column, the standard deviation of the fore-aft shear forces increases, showing random fluctuations in shear force, which may be due to turbulence or wind gusts.

Table 4.13: Statistics of the side-to-side bending moment for $V_{mean}$ = 11.2 m/s.

| | Parameters | 6-Mooring | 7-Mooring | 12-Mooring | 13-Mooring |
|---|---|---|---|---|---|
| Regular Waves | Mean (kN-m) | 1.30E+05 | 1.22E+05 | 9.52E+04 | 9.52E+04 |
| | Standard Deviation (kN-m) | 439.05 | 418.023 | 305.287 | 303.287 |
| | Max (kN-m) | 7.24E+05 | 6.97E+05 | 4.97E+05 | 4.97E+05 |
| | Min (kN-m) | 8.14E+04 | 7.26E+04 | 2.30E+04 | 2.30E+04 |
| Irregular Waves | Mean (kN-m) | 1.78E+05 | 1.56E+05 | 8.93E+04 | 8.72E+04 |
| | Standard Deviation (kN-m) | 453.46 | 438.38 | 329.75 | 330.34 |
| | Max (kN-m) | 6.99E+05 | 6.76E+05 | 3.58E+05 | 3.61E+05 |
| | Min (kN-m) | 4.43E+04 | 3.82E+04 | 2.30E+04 | 2.25E+04 |

Table 4.14: Statistics of the fore-aft bending moment for $V_{mean}$ = 11.2 m/s.

| | Parameters | 6-Mooring | 7-Mooring | 12-Mooring | 13-Mooring |
|---|---|---|---|---|---|
| Regular Waves | Mean (kN-m) | 1.36E+06 | 1.30E+06 | 4.68E+05 | 4.68E+05 |
| | Standard Deviation (kN-m) | 743.48 | 696.34 | 400.31 | 400.31 |
| | Max (kN-m) | 2.39E+06 | 1.92E+06 | 8.43E+05 | 8.36E+05 |
| | Min (kN-m) | 1.76E+05 | 1.50E+05 | 1.63E+04 | 1.43E+04 |
| Irregular Waves | Mean (kN-m) | 2.35E+06 | 2.14E+06 | 7.40E+05 | 7.40E+05 |
| | Standard Deviation (kN-m) | 841.34 | 768.86 | 416.33 | 414.67 |
| | Max (kN-m) | 4.27E+06 | 3.93E+06 | 1.91E+06 | 1.90E+06 |
| | Min (kN-m) | 8.97E+05 | 7.32E+05 | 2.06E+05 | 2.15E+05 |

Table 4.13 and Table 4.14 shows the side-to-side bending moment and the for-aft bending moment developed at the base of the turbine tower. Similar to the forces developed, the moments are influenced by the change in the mooring layout. The moments are observed to reduce with the increase in the mooring cables, though the variation is not much higher. The mean value of the tower base fore-aft bending moment is mainly wind-induced, while its standard deviation is induced by both wind loads and wave loads (Han et al., 2017). Higher variations in the standard deviation values for different mooring layouts are observed for the fore-aft bending moments. The standard deviation values for the moments are reduced significantly for the 12-Mooring and 13-Mooring configurations, further showing the reduced influence of the wind and wave loads.

## 4.5 CLOSURE

This chapter investigates the dynamic behaviour of a 5 MW wind turbine supported by two-hybrid concepts, STLP+6WECs and FTLP+8WECs, both stabilised by different mooring line layouts. A fully coupled aero-servo-hydro-elastic simulation of the hybrid floater with different mooring layouts is conducted using FAST for regular and irregular wave conditions. The responses of the floating platform in the frequency-domain are analysed to examine the wave frequency region of the hybrid system for different mooring layouts. Further, the study analyses the time series data of the responses in six degrees of freedom, forces and moments at the base of the turbine tower, generator power and the mooring tension developed on each mooring cable of the different mooring layouts considered. The conclusions drawn from the study are as follows:

- The stiffness of the hybrid platform is observed to be higher in the vertical plane than in the horizontal plane. Minimum variation in the natural frequency of STLP and FTLP is observed with the addition of WECs around the TLP floaters in a circular pattern.
- The 4-Mooring layout of STLP+6WECs and 7-Mooring layout of FTLP+8WECs configurations are observed to have the lower surge, sway and heave energy for the wave frequency region. An average 18% reduction in surge, 13 % reduction in heave and 3% reduction in yaw motion response is observed for the 4-Mooring layout of STLP+6WECs converters compared to the 9-Mooring layout. An average 7% reduction in surge, 5% reduction in heave and 11% reduction in yaw motion response is observed for the 7-Mooring layout of STLP+6WECs converters compared to the 13-Mooring layout.

- The addition of the WECs around the STLP and FTLP has helped to reduce the tension developing on the mooring cables, which may be due to the additional stiffness provided by the WEC. An average 36% reduction in tension is observed for the 9-Mooring layout of STLP compared to 4-Mooring Layout for different operational conditions. An average 55% reduction in tension is observed for the 13-Mooring layout of FTLP compared to 6-Mooring Layout for 8 m/s, 14 m/s and 17m/s operational conditions. For 11.2 m/s wind speed condition, 82% reduction in the tension id observed for the 13-Mooring layout.
- The variation in the generator power for the STLP+6WECs hybrid system is minimal compared to FTLP+8WEC for SS-1 and SS-2 load case conditions for any mooring layouts. Hence the efficiency in the wind power absorption is higher for the 5 MW wind turbine supported on STLP+6WECs for wind speed conditions below 11.4 m/s.
- The fore-aft shear force and fore-aft bending moments are minimum for the STLP+6WECs configuration supported with an 8-Mooring layout and FTLP+8WECs supported with 13-Mooring, with a minimum impact of wind and wave-induced loads.

# CHAPTER 5

# LONG-TERM ANALYSIS OF HYBRID TLP-WEC

## 5.1 GENERAL INTRODUCTION

The immense availability of ocean waves and wind has turned the world's attention towards new renewable energy alternatives. The capacity of the world's wind power generation is proliferating, with an annual increase of 30% over the last decade, which shows the potential of the available wind resource. The deep-water regions being a continuous source of wind and wave energy, have proved to be a promising ground for energy derivation using floating offshore wind turbines (FOWT). As the FOWT is set up and installed in deep waters, the assessment of the performance of the FOWT is essential to define the design targets of the floater. Thus, it becomes important to determine the maximum possible values of motion parameters such as displacements, forces, moments, accelerations and relative motions, which are probable to occur during the life period of the FOWT. The design parameters are defined by obtaining the long-term probability distributions, which depend on the wave amplitude, wave spectra and the wave climate descriptions. The knowledge of the probability distribution of the amplitudes during the lifetime of the wind turbine provides the percentage of time for which the operating conditions of the turbine would prevail (Li et al., 2015). Though probability-based studies are developed for the design and analysis of structures, they have equal importance for other design variables.

## 5.2 NUMERICAL MODELLING

In the present study, a complex system that includes a floating wind turbine, a point absorber WEC, and a mooring system is considered for the integrated aero-hydro-servo-elastic simulation to predict the dynamic responses of the rigid system. The equation of motion (Eq. 2.3) for the wind turbine and the coupled support platform in the time domain for the FAST developed by NREL is derived from Kane's dynamics. The expression in Eq. (2.3) balances all the generalised active and inertia forces of the complex coupled Rotor Nacelle Assembly (RNA). The total axial force developing on the rotor takes the contributions of lift

force and drag force, depending on the air density, airfoil chord length, relative velocity and the radial length of the blade section.

The total external load (Eq. 2.7) other than the weight of the support platform has contributed from the component of added mass, the hydrodynamic load and the load developed by the mooring lines. The hydrodynamic load (Eq. 2.11) acting on the support platform depends on the hydrostatic loads, the radiation force and the diffraction force. The hydrodynamic load also has the contributions from the viscous drag force developing on the support platform, further modelled using the Morison equation. The total wave force (Eq. 2.12) action of the support platform has influences on the added mass coefficient at infinite frequency, the retardation function, the 2-sided power spectral density of the wave per unit time, the Fourier transform of a realisation of white Gaussian noise time series process with zero mean and unit variance and the complex-valued array representing the wave excitation force on support platform normalised per unit wave amplitude depending on frequency and direction of the incident wave.

The TLP is intended to achieve structural stability through the tensioned mooring system that is stiff in pitch. The average tension developed on the mooring cables is analysed by assuming the balance of forces and moments for the cables with wind propagating in the positive x direction. The balance of forces (Wayman et al., 2006) representing the angle tethers make with the vertical is represented as

$$F_B + \rho g \pi R_d^2 \left( L_{tether} - L_{tether} \cos\theta \right) - M_{11} g = \cos\theta \sum F_{T,i}, \tag{5.1}$$

where $F_B$ is the buoyancy force, $R_d$ is the radial distance to the tether fairlead, $M_{11}$ is the total mass of the system, $F_T$ is the total tether force exerted and $L_{tether}$ is the unstretched length of the tethers. With the four tethers placed at $90^0$ interval, the average tether force $\left( F_{T,ave} \right)$ developed is given by

$$F_{T,ave} = \frac{F_B + \rho g \pi R_d{}^2 \left( L_{tether} - L_{tether} \cos\theta \right) - M_{11} g}{4 \cos\theta}. \tag{5.2}$$

The initial tether tension must be carefully chosen to prevent the tension value from going to zero or exceeding the maximum value of allowable tension. Further, the tether tension must be approximately equal to the water ballast weight to stabilise the structure during installation. In the case of the turbine at rest during the towing of the platform, the absence of the wind load on the platform ensures minimum operational thrust as the maximum value of wind loading

during towing. The system requires adequate hydrostatic and inertial restoring to limit the steady-state pitch values below $10^0$, which is achieved by adjusting the level of concrete ballast and also the height and radius of the cylinder.

### 5.2.1 Response Amplitude Operators (RAOs)

The linear dynamic motions of the hybrid system (Wayman et al. 2006) for mass $M$, added mass $A(\omega)$, and stiffness matrix $C$ are solved using the equation of motion given as

$$\left[-\omega^2\left\{M+A(\omega)\right\}+i\omega B(\omega)+C\right]\Xi(\omega)=X(\omega), \tag{5.3}$$

with the system's dimensional response in each mode of motion $\Xi(\omega)$. The added mass, damping matrix and exciting forces are evaluated using WAMIT. The RAO (Eq. 2.24) for the translational modes of motion for wave amplitude $A_{wave}$ is used as the transfer function for long-term analysis.

### 5.2.2 Long-Term Analysis

The long-term models are developed using the short-term situations expected to occur during the life period of the structure. In the study of floating offshore structures using long-term analysis, the probability density function of a response depending on the physical condition must be constructed. The short-term situation for a sea surface elevation is assumed to be modelled as a stationary Gaussian stochastic process. The probability $Q_s$ of exceeding the amplitude $x$ of wave elevation (Bagbanci et al., 2015) described by Rayleigh distribution in the short-term situation is given by

$$Q_s\left(x/R_v\right)=e\left(-x^2/2R_v\right), \tag{5.4}$$

where $R_v$ is the variance, and for the narrow band process, the variance $R$ is determined by

$$R_v=\int_0^\infty S_H(\omega)\partial\omega. \tag{5.5}$$

where $S_H(\omega)$ is the input wave spectrum dependent on the sea state condition. The concept of probability of exceedance, also known as "return period," refers to the likelihood that a certain event or value will be exceeded in a given period. It is commonly expressed as a percentage or reciprocal of the number of years an event is expected to occur. The probability of exceedance is calculated using historical data and statistical models such as the Gumbel distribution, the

Weibull distribution, or the Extreme Value Distribution. These models are used to estimate the probability that a certain event will occur, given a set of data. The study considers the North Atlantic offshore region, and the wave data is taken from International Association for Classification Societies (IACS). The probabilistic approach method is presented for determining the largest response that the structure may experience throughout the span of its service life. However, the response values are significantly determined by the distribution being considered. As with wave heights, it is expected that responses generally follow the Rayleigh distribution. The average wave period is calculated to be 8.5 seconds using long-term data, and the long-term probability of exceeding it once per 20 years is found to be $1.35\times10^{8}$. This is based on the assumption that the structure's service life is 20 years.

The present study observes different wave spectrum models to compare spectrum models. The Pierson-Moskowitz (PM) spectra model describes a fully developed sea determined by one parameter, wind speed. The fetch and duration of wind speed are considered to be infinite. So, for the PM model, the wind moves over a larger area for a closely constant speed for many hours before the wave record is obtained, and the wind direction does not vary more than a certain defined amount. The PM model is useful in representing a severe storm wave in the design of offshore structures. The Pierson-Moskowitz (PM) spectrum model (Setiyawan et al., 2013) is described as

$$S(\omega)=\alpha g^{2}\omega^{-5}\exp\left[-0.74\left(\frac{\omega U_{w}}{g}\right)^{-4}\right], \tag{5.6a}$$

where α = 0.0081. Alternatively, in terms of the frequency of the spectral peak, the PM model is given by

$$S(\omega)=\alpha g^{2}\omega^{-5}\exp\left[-1.25\left(\frac{\omega}{\omega_{0}}\right)^{-4}\right]. \tag{5.6b}$$

Thus, the peak frequency is related to $\omega_z$ as $\omega_0$ = 0.710 $\omega_z$. In the case of the sea state being still in the development stage, the study uses the JONSWAP spectrum given by

$$S_{J}(\omega)=\alpha g^{2}(2\pi)^{-4}\left(\frac{\omega}{2\pi}\right)^{-5}e^{\left\{-1.25\left(\frac{\omega}{\omega_{p}}\right)^{-4}\right\}}x\gamma e^{\left\{\frac{(\omega-\omega_{p})^{2}}{2\sigma^{2}\omega_{p}^{2}}\right\}}, \tag{5.7}$$

Where $\gamma$ is the peak enhancement factor. Assuming the spectrum to be narrow-banded, the individual wave period and wave height follow the Rayleigh distribution. Bretschneider (1959, 1969) derived the spectral model which is given by

$$S(\omega) = 0.1687 H_s{}^2 \frac{\omega_s^4}{\omega^5} e^{-0.675\left(\frac{\omega_s}{\omega}\right)^4} \tag{5.8}$$

where $\omega_s = 2\pi/T_s$, $H_s$ is the significant wave height and $T_s$ is the significant wave period defined as the average period of the significant waves. Thus, from the Bretschneider spectral model, it can be shown that $T_s = 0.946T_0$ with $T_0$ is the peak period. The relationship between the significant wave period and peak wave period makes the Bretschneider and the PM models equivalent. The International Ship Structures Congress (1964) suggested a slight modification in the Bretschneider spectrum to define the ISSC spectrum model of the form

$$S(\omega) = 0.1107 H_s{}^2 \frac{\varpi^4}{\omega^5} e^{-0.4427\left(\frac{\varpi}{\omega}\right)^4} \tag{5.9}$$

The relationship between the peak frequency $\omega_0$ and $\varpi$ for ISSC spectrum is of the form $\bar{\omega} = 1.296\omega_0$. The ITTC Spectrum is given by

$$S(\omega) = \alpha g^2 \omega^{-5} \exp\left[-\frac{4\alpha g^2 \omega^{-4}}{H_s^2}\right] \tag{5.10}$$

where $\alpha = \frac{0.081}{k^4}$ and $k = \sqrt{\frac{g}{\sigma}} / 3.54\omega_z$. In which $\sigma = \sqrt{m_0} = \frac{H_s}{4}$ is the standard deviation (r.m.s value) of the water surface elevation. The response spectrum obtained from the input wave spectrum $S_H(\omega)$ (Vijay et al., 2020) is given by

$$S_R(\omega) = |H(\omega)|^2 S_H(\omega), \tag{5.11}$$

where $H(\omega)$ is the transfer function. In the long-term analysis considering the lifetime of the structure, the probability density function describing the variance of response at a random point is given by

$$f_r(r) = f_{H_s,T_p}(h,t). \tag{5.12}$$

where $f_{H_s,T_p}(h,t)$ is the joint probability density function of significant wave height and average period. Thus, the probability of exceeding amplitude $x$ during the structure's lifetime at a random point in time can be achieved by unconditioning the short-term probability of exceedance, which is given by

$$Q_L(x) = \int_0^\infty w(T_p).Q_s(x/R_v).f_R(r)\,dr, \tag{5.13}$$

where $w\left(T_p\right)$ is a weighing factor which is a function of the average period of sea state and accounts for different numbers of amplitude that occur in sea states of different periods. Thus, to design a structure against collapse or extreme load conditions, researchers are interested in predicting a large enough value to be met not more than once during the lifetime of the structure. The short-term description for the study is presented with a wave height spectrum, and the long-term model indicates the variations of spectral parameters on a larger time scale.

## 5.3 GEOMETRIC MODELLING

The TLP is a FOWT platform that tethers the platform tightly to the sea bed using tension cables, eliminating the vertical movements usually used for a water depth of 70-150 m. The present study discusses an STLP and an FTLP floater combined with different numbers of heaving cone-cylinder-shaped point absorber WECs in a circular pattern around the floater, as shown in Fig. 5.1(a,b). Compared to other shapes of heaving point absorber WECs, the cone-cylinder shape has higher hydrodynamic added mass, damping coefficient, and excitation force.

(a) 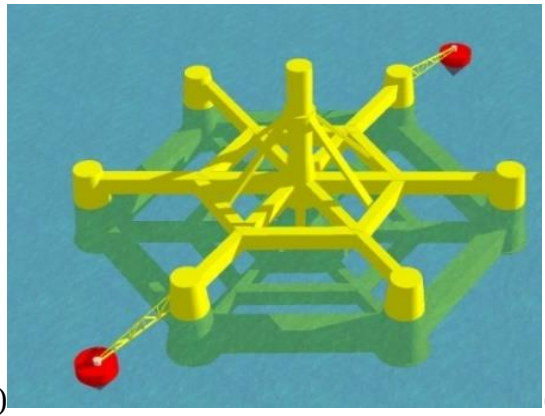 (b) 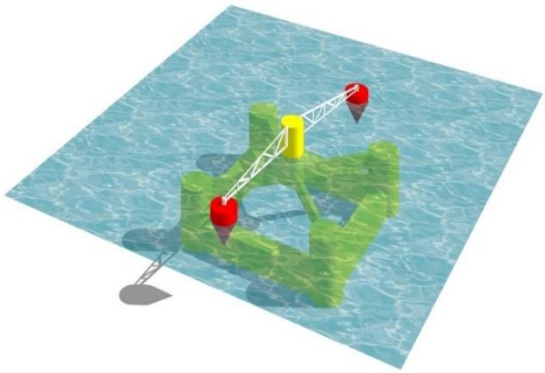

Fig. 5.1: (a) FTLP and (b) STLP floating wind turbine platform combined with two cone-cylinder heaving point absorber WECs.

Higher wave power absorption than the other two floater designs was achieved by the cone-cylinder-shaped point absorber WEC due to its better hydrodynamic coefficients (Sinha et al., 2016). The additional WECs should provide more power and enhance the floating platform's motion dynamics. The geometric modelling of the wetted surfaces of the hybrid system below the design water level is achieved using Rhinoceros 3D modelling software. The model surface is subdivided into meshes, and all the meshes represent the wetted surface of the combined system. Further, to perform a better continuation of the body surface discretised by these meshes, a set of small elements called panels are defined with these meshes. The optimum

number of panels required for the analysis is determined using the convergence test of hydrodynamic coefficients. The optimum number of panels ensures the accuracy of the transfer functions and also provides optimal simulation time. The modelling and meshing done for five different circular arrays of the WECs around the STLP and FTLP floating 5 MW wind turbine platform are detailed in Chapter 1.

## 5.4 METHODOLOGY

The hydrodynamic analysis and coupled dynamic analysis for different configurations of the hybrid platform are conducted for different wind and wave load conditions (Table 2.12) of the Northern North Sea. The hydrodynamic analysis is conducted using WAMIT, based on a 3-D numerical panel method in the frequency domain, solving the linearised hydrodynamic radiation and diffraction problems for the FOWT interacting with the surface waves.

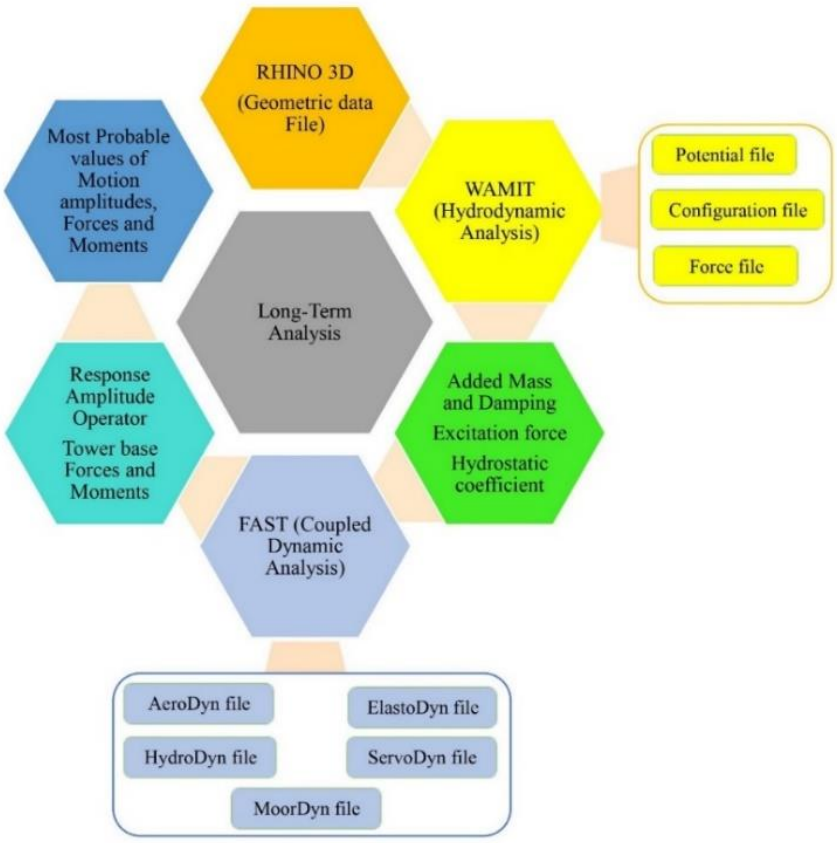


Fig. 5.2: Flow chart depicting methodology for the long-term response analysis.

The time domain analysis is performed for the combined platform through a fully coupled aero-hydro-servo-elastic simulation tool FAST. The FAST code stimulates stochastic time-domain turbine response and computes hydrodynamic loads using Morison's equation. The wind and

waves are the most important meteorological and oceanographic data for analysing an offshore floating wind turbine and WEC system. The load data cases are subsequently used to calculate the coupled dynamic responses through aero-hydro-servo-elastic simulation for the TLP-type wind turbine combined with a circular array of heaving cone-cylinder WECs. The study also observes the forces and moments developed at the base of the turbine tower to analyse the performance of the hybrid system under severe wind loading. A flow chart detailing the methodology adopted is shown in Fig. 5.2.

## 5.5 RESULTS AND DISCUSSION

The most probable values of motion amplitude of a hybrid wind-wave energy converter system are studied using long-term analysis. The long-term response analysis is obtained using short-term responses represented using Rayleigh distribution and further calculated the extreme responses for North Atlantic wave data. The WECs are arranged around the STLP and FTLP floating system in different numbers (two, four, six and eight) in a circular pattern. The transfer functions for the responses (surge, sway, heave, roll, pitch and yaw) and the tower base forces and moments of the hybrid system are obtained using the aero-servo-hydro-elastic simulation tool FAST developed by NREL. The performance of the combined system is based on the transfer functions and the choice of wave spectrum model.

### 5.5.1 Comparison of Wave Spectra Models

The long-term analysis is conducted for different wave spectra models, which closely represent the sea state conditions. The spectral models are generally based on one or more parameters like significant wave height, wave period, shape factor etc. The Pierson-Moskowitz (PM) spectrum model is the most used single-parameter model based on significant wave height or wind speed, representing fully developed sea state conditions. Bretschneider, ISSC, and ITTC spectrum models are two spectral parameter models. Developing seas usually have a more peaked spectrum. i.e., the JONSWAP spectra with five parameters where three are held constant. The JONSWAP spectrum follows Rayleigh distribution and incorporates the effect of wave refraction.

#### 5.5.1.1 Hybrid STLP-WEC FOWT Platforms

The long-term probabilistic approach is compared for different wave spectra and is tabulated for different configurations for the hybrid STLP platform. Table 5.1 and Table 5.2 shows the long-term surge and pitch response for 14 m/s wind speed condition (wind speed condition

above the rated wind speed condition of 5 MW wind turbine) at the characteristic level of $10^{-8}$ comparing different spectrums. The long-term response is observed to be higher for the JONSWAP spectrum with considerable variation as the wind is assumed to blow steadily over the large area for a more extended period as the waves come in equilibrium with the wind.

Table 5.1: Maximum values of long-term surge response (m/m) for 14.0 m/s wind speed.

| Configurations | JONSWAP Spectra | PM Spectra | Bretschneider Spectra | ISSC Spectra | ITTC Spectra |
|---|---|---|---|---|---|
| STLP | 90.7 | 21.3 | 21.9 | 21.9 | 21.9 |
| STLP+2WECs | 115.6 | 10.8 | 11.3 | 11.3 | 11.3 |
| STLP+4WECs | 78.2 | 11.3 | 10.7 | 10.7 | 10.7 |
| STLP+6WECs | 28.2 | 15.9 | 15.1 | 15.1 | 15.1 |
| STLP+8WECs | 13.5 | 7.1 | 7.3 | 7.3 | 7.3 |

Table 5.2: Maximum values of long-term pitch response (deg/m) for 14.0 m/s wind speed.

| Configurations | JONSWAP Spectra | PM Spectra | Bretschneider Spectra | ISSC Spectra | ITTC Spectra |
|---|---|---|---|---|---|
| STLP | 0.72 | 0.16 | 0.16 | 0.16 | 0.16 |
| STLP+2WECs | 0.73 | 0.12 | 0.13 | 0.13 | 0.13 |
| STLP+4WECs | 0.75 | 0.22 | 0.22 | 0.22 | 0.22 |
| STLP+6WECs | 0.69 | 0.60 | 0.60 | 0.60 | 0.60 |
| STLP+8WECs | 1.08 | 0.40 | 0.40 | 0.40 | 0.40 |

The PM, Bretschneider, ISSC, and ITTC spectrums are observed to have comparatively similar energy levels. The minimum surge and pitch response is observed for STLP+6WECs configuration, with higher wind power absorption. The minimum surge and pitch response of the hybrid system ensures better platform orientation towards the wind direction, having higher wind power absorption.

#### 5.5.1.2 Hybrid FTLP-WEC FOWT Platforms

Tables 5.3 and 5.4 study the long-term surge and pitch response for the single FTLP and hybrid FTLP-WEC configurations for five wave spectra models. The JONSWAP wave spectra model is observed to have a higher long-term response wave compared to other wave models. This may be because the peak enhancement factor, which denotes the peak wave's increased energy compared to a typical sea condition, is incorporated into the spectral shape parameter. The

JONSWAP model assumes that there is a greater probability of encountering larger waves with more energy in the peak under specific wind conditions. As a result, compared to other models, the JONSWAP model generates greater values for the peak wave energy.

Table 5.3: Maximum values of long-term surge response (m/m) for 14.0 m/s wind speed.

| Configurations | JONSWAP Spectra | PM Spectra | Bretschneider Spectra | ISSC Spectra | ITTC Spectra |
|---|---|---|---|---|---|
| FTLP | 347.4 | 91.4 | 100.2 | 101.6 | 101.6 |
| FTLP+2WECsx | 268.2 | 52.5 | 63.3 | 66.7 | 66.7 |
| FTLP+4WECs | 298.2 | 58.3 | 68.6 | 69.6 | 69.6 |
| FTLP+6WECs | 298.8 | 54.5 | 63.6 | 66.6 | 66.6 |
| FTLP+8WECs | 288.2 | 50.2 | 58.7 | 61.3 | 61.3 |

Table 5.4: Maximum values of long-term pitch response (deg/m) for 14.0 m/s wind speed.

| Configurations | JONSWAP Spectra | PM Spectra | Bretschneider Spectra | ISSC Spectra | ITTC Spectra |
|---|---|---|---|---|---|
| FTLP | 0.431 | 0.11 | 0.135 | 0.138 | 0.138 |
| FTLP+2WECsx | 0.328 | 0.063 | 0.089 | 0.091 | 0.091 |
| FTLP+4WECs | 0.223 | 0.058 | 0.073 | 0.077 | 0.077 |
| FTLP+6WECs | 0.214 | 0.049 | 0.068 | 0.071 | 0.071 |
| FTLP+8WECs | 0.197 | 0.046 | 0.061 | 0.064 | 0.064 |

Comparing the long-term surge and pitch response for the different hybrid models studied, the FTLP+2WECsx and FTLP+8WECs configurations are observed to have the minimum long-term values. Comparing both hybrid configurations of STLP and FTLP, the long-term surge response values are observed to be higher for the STLP and hybrid STLP-WEC configurations, and the long-term pitch responses are minimum for the hybrid FTLP-WEC configurations. The minimum surge response may be due to the complete submergence of the platform, reducing the wave load impact and reducing the chances of fatigue and potential damage caused by the wave load. The reduced pitch motion of the FTLP and hybrid FTLP-WEC may be due to the additional mass of the platform compared to STLP. The reduced pitch motion minimises the tension load developing on the floating system. The present study examines the long-term response of the combined system for the JONSWAP spectrum model for different operational wind speed conditions of a 5 MW wind turbine, which can be used to improve the design loads or motions of the floating offshore structures.

### 5.5.2 Translation and Rotational Motions

The unextendible mooring lines of TLP make it the most stable platform class in the installed position. The axially rigid mooring lines ensure no significant heave, roll, or pitch motion. There will be surge and sway translational motion along with yaw rotational motion. Further, the long-term responses for surge, sway and yaw motion of the hybrid TLP-WEC for different operational conditions of the wind turbine are analysed and presented.

#### 5.5.2.1 Hybrid STLP-WEC FOWT Platforms

The long-term responses for surge, sway and yaw motion (Fig. 5.3(a-c)) using the JONSWAP spectrum are plotted for 8 m/s wind speed comparing different circular arrays of cone-cylinder point absorber WECs around STLP. The response pattern remains the same for different arrays of WECs around STLP.

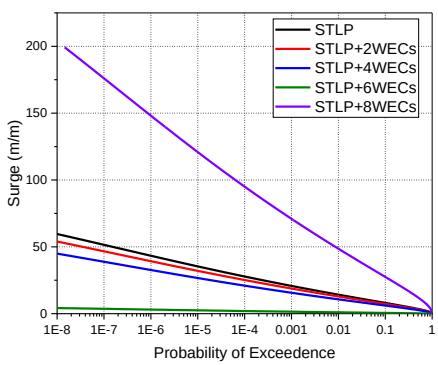


(a)

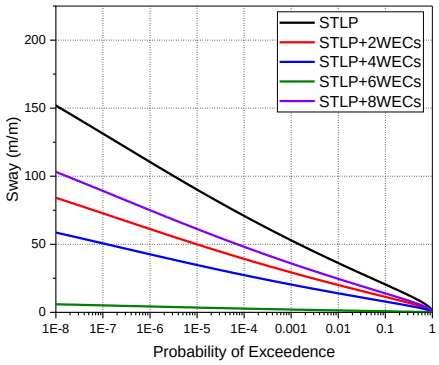


(b)

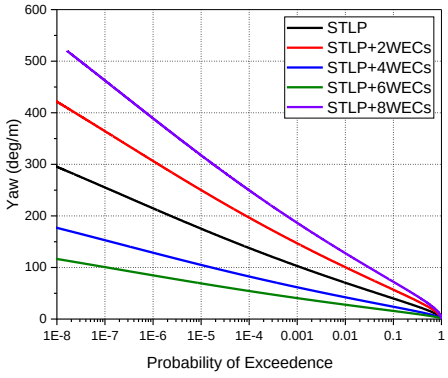


(c)

Fig. 5.3: Long-term responses for (a) surge, (b) sway, and (c) yaw for 8 m/s wind speed.

The long-term probabilistic value is higher for the surge motion (Fig. 5.3a) in the case of translational motions. For the rotational motion, yaw is higher than other translational values at the characteristic level of $10^{-8}$. The higher surge value may be due to the large diameter of

the hybrid system resulting in lower values of added mass and moment of inertia, further ensuring the least displacement for the hybrid system. The study observes that the long-term response value for the STLP+6WECs configuration is minimal at the characteristic level of $10^{-8}$, thus ensuring higher stability for the system. The higher yaw (Fig. 5.3c) value may be due to the higher wind load developing on the nacelle.

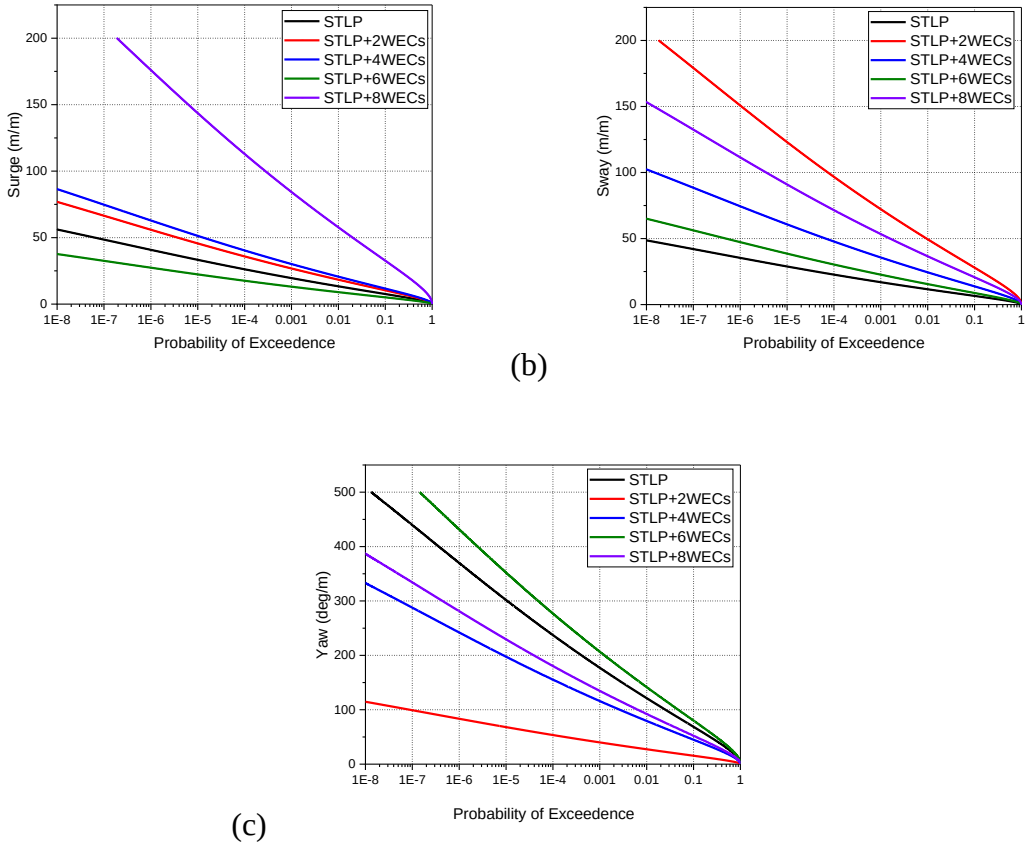


Fig. 5.4: Long-term responses for (a) surge, (b) sway, and (c) yaw for 11.2 m/s wind speed.

In Fig. 5.4(a-c), the long-term responses for surge, sway and yaw motion using the JONSWAP spectrum are plotted for 11.2 m/s wind speed, comparing different circular arrays of cone-cylinder WECs around STLP. The study observes that the long-term response for the sway motion (Fig. 5.4b) is higher for 11.2 m/s wind speed conditions for all circular arrays of WECs apart from the STLP+8WECs configuration. For the STLP+8WECs, the surge motion is on the higher side at the $10^{-8}$ characteristic level. The higher surge motion (Fig. 5.4a) of the platform ensures the least displacement of the STLP+8WECs hybrid system. For the rotational motions, the long-term response for the yaw motion (Fig. 5.4c) is very high at a $10^{-8}$ characteristic level. The yaw response values were higher for the longer period waves, hence the larger yaw values during the structure's lifetime.

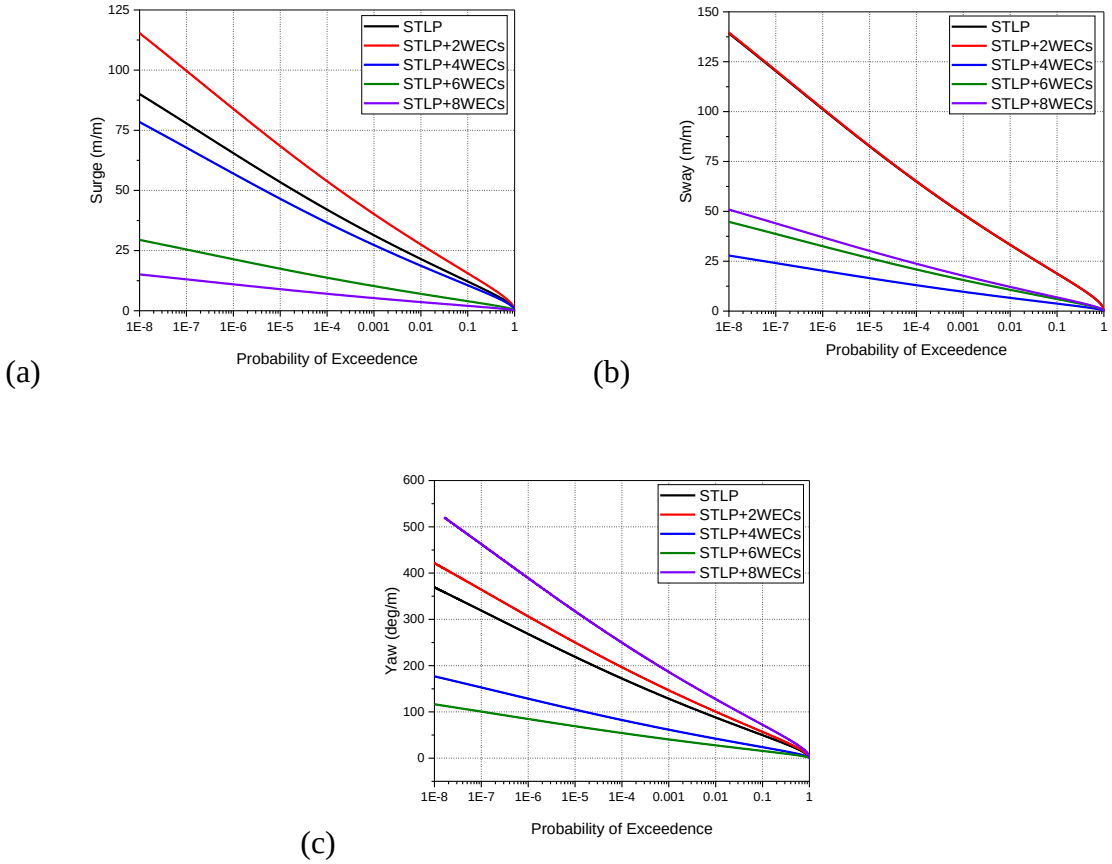


Fig. 5.5: Long-term responses for (a) surge, (b) sway, and (c) yaw for 14 m/s wind speed.

The long-term responses for surge, sway and yaw are analysed for 14 m/s wind speed, comparing different circular arrays of wave energy converters around STLP is shown in Fig. 5.5(a-c). The study observed that surge motion is higher than sway at a $10^{-8}$ characteristic level. The higher surge value is due to the least displacement of the hybrid STLP-WEC for all circular arrays of WECs around STLP. Higher variation is observed for the surge motion for different arrangements of WECs compared to sway motion, as seen in Fig. 5.5(a,b). Further, the long-term yaw response is on the higher side (Fig. 5.5c), which demands additional stiffness for the hybrid system to reduce the response value. The long-term surge responses at a $10^{-8}$ characteristic level are minimal for the STLP+6WECs configuration for both translational and rotational motions. The long-term surge responses at a $10^{-8}$ characteristic level are very high for STLP+8WECs at 14 m/s wind speed conditions (Fig. 5.5a). The higher long-term surge response may reduce the system's efficiency. The variation of the long-term surge and sway motion for the STLP+6WECs and STLP+8WECs is minimal compared to the yaw motion responses of the hybrid floating platforms for 14 m/s wind speed.(Fig. 5.5(a-c)).

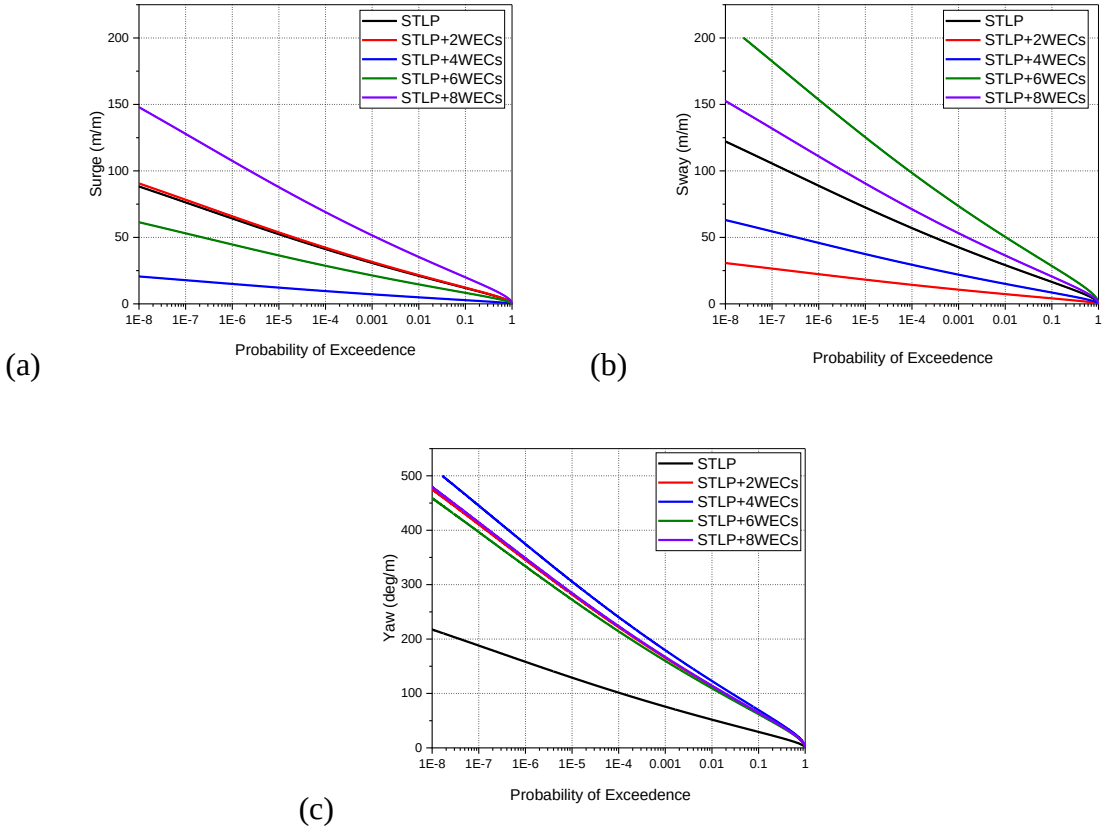


Fig. 5.6: Long-term responses for (a) surge, (b) sway, and (c) yaw for 17 m/s wind speed.

In Fig. 5.6(a-c), the long-term responses for (a) surge, (b) sway and (e) yaw motion of the hybrid system are analysed for 17 m/s wind speed. The variation in values of long-term response for different arrangements of wave energy converters is minimum for surge motion compared to sway motion (Fig. 5.6(a,b)). The long-term response value is higher for sway motion at a $10^{-8}$ characteristic level than the surge response. The value of long-term surge response is observed to be minimum for STLP+4WECs configuration and higher for STLP+8WECs. In the case of rotational motions, the long-term yaw response motion is higher at a $10^{-8}$ characteristic level. The long-term response of the yaw motion (Fig. 5.6c) is observed to increase by adding an array of WECs around the STLP. For 11.2 m/s and 17 m/s wind speed conditions, the long-term yaw response is higher for STLP+6WECs, though the surge and sway motions are lower.

The study of the long-term surge response motion is important for the knowledge of the displacement of the hybrid system and the initial pretension. The maximum long-term response value for surge motion is tabulated for different operational wind speed conditions, as seen in Table 5.5. The minimum long-term surge response is observed for STLP+6WECs

configuration at 8 m/s wind speed, further observed to be minimal compared to other circular arrays of WECs. Apart from the STLP+8WECs configuration, all different arrays of WECs have higher long-term surge response at wind speed than the rated wind speed of a 5 MW wind turbine. The long-term surge responses for STLP+8WECs configuration are minimum at 14 m/s wind speed, and the maximum value is observed for 11.2 m/s wind speed.

Table 5.5: Maximum long-term response value for surge motion for STLP and hybrid STLP.

| Configurations | V=8 m/s | V=11.2 m/s | V=14 m/s | V=17 m/s |
|---|---|---|---|---|
| STLP | 60.4 | 56.3 | 90.7 | 87.8 |
| STLP+2WECs | 51.1 | 76.2 | 115.6 | 89.1 |
| STLP+4WECs | 46.8 | 87.2 | 78.2 | 21.9 |
| STLP+6WECs | 6.2 | 37.4 | 28.2 | 57.8 |
| STLP+8WECs | 201.3 | 225.6 | 13.5 | 149.5 |

Table 5.6: Maximum long-term response value for pitch motion for STLP and hybrid STLP.

| Configurations | V=8 m/s | V=11.2 m/s | V=14 m/s | V=17 m/s |
|---|---|---|---|---|
| STLP | 0.48 | 0.53 | 0.72 | 0.52 |
| STLP+2WECs | 0.17 | 1.38 | 0.73 | 0.50 |
| STLP+4WECs | 0.26 | 1.1 | 0.75 | 0.52 |
| STLP+6WECs | 0.26 | 0.79 | 0.69 | 2.45 |
| STLP+8WECs | 0.81 | 2.75 | 1.08 | 1.74 |

Table 5.7: Maximum long-term response value for roll motion for STLP and hybrid STLP.

| Configurations | V=8 m/s | V=11.2 m/s | V=14 m/s | V=17 m/s |
|---|---|---|---|---|
| STLP | 0.75 | 0.48 | 0.65 | 0.55 |
| STLP+2WECs | 0.55 | 1.2 | 0.77 | 0.6 |
| STLP+4WECs | 0.53 | 0.9 | 0.82 | 0.5 |
| STLP+6WECs | 0.2 | 0.75 | 0.65 | 1.6 |
| STLP+8WECs | 3 | 3.51 | 0.7 | 3.4 |

The maximum long-term response values of pitch motion at different operational conditions of the wind turbine are also shown in Table 5.6. The values for pitch motion are minimal, further ensuring better orientation of the wind turbine towards the wind. The minimum value of the long-term surge response for an array of two, four and six WECs at 8 m/s wind speed ensures

better hybrid system efficiency. Further, it is observed that the array of WECs has influenced the STLP, as the long-term responses are reduced with the addition of WECs to STLP. The roll motion of less than 0.4 deg/m ensures higher system stability against the wind and waves. The maximum long-term response value for roll motion at a $10^{-8}$ characteristic level is shown in Table 5.7. The values are close to 0.4 deg/m for the single STLP, and the long-term roll response values at a $10^{-8}$ characteristic level are observed to increase with the addition of the WECs. Apart from the STLP+8WECs configuration, all other configurations have a long-term roll value of around 0.4 deg/m during the structure's lifetime.

#### 5.5.2.2 Hybrid FTLP-WEC FOWT Platforms

The long-term surge, sway and yaw motion responses for different wind speed conditions of the gravity waves are studied for FTLP and hybrid FTLP-WEC configurations. Fig. 5.7(a-c) shows the long-term surge, sway and yaw motions responses for 8 m/s wind speed conditions. The long-term surge response (Fig. 5.7a) is observed to be higher compared to the sway and yaw motion response throughout the design life of the structure. It can be observed that the integration of WECs to the FTLP has helped in mitigating the platform surge and yaw motions. The hybrid FTLP+4WECs exhibit the least motion responses relative to incident waves for the design period, while the FTLP platform has the highest motion amplitudes. The variation in surge motion throughout the probabilistic range is minimal compared to the sway and yaw responses. This may be attributed to the incident wave direction oriented in the positive x-direction. Fig. 5.7(b) shows the long-term sway response motion for different floating configurations. The long-term response is observed to be minimum for FTLP+4WECs, which is the same as the observation for the surge. The long-term sway motion is maximum for FTLP+8WEC configuration at the characteristic level of $10^{-8}$. Fig. 5.7(c) represents the long-term yaw response of different hybrid configurations of FTLP. The variation in yaw responses with different WEC numbers is higher than in other cases. The FTLP+8WECs configuration exhibits minor responses during the structure's lifetime, whereas the FTLP+6WECs configuration shows the maximum responses among the hybrid systems. The minimum yaw motion reduces the fatigue load developed on the control system, improving wind power absorption. For the hybrid systems considered, the FTLP+6WECs configuration is observed to have the highest surge, sway and yaw responses at the characteristic level of $10^{-8}$. This may be due to higher excitation loads attracted by the platform having six WEC connected to the outer pontoon of the platform.

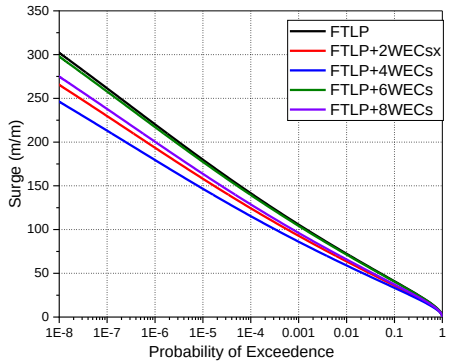


(a)

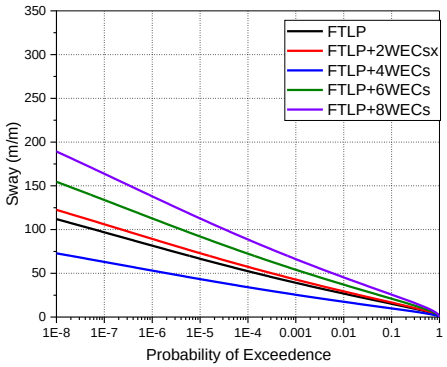


(b)

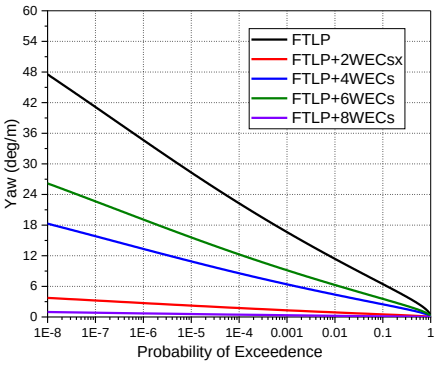


(c)

Fig. 5.7: Long-term responses for (a) surge, (b) sway, and (c) yaw for 8 m/s wind speed.

Fig. 5.8(a-c) shows the long-term surge, sway and yaw motions responses for 14 m/s wind speed conditions. The addition of the WECs on the FTLP is observed to have a minimum variation in the surge response during the lifetime of the hybrid configurations. The FTLP+2WECs is observed to have a higher variation in surge response (Fig. 5.8a) at the characteristic level of $10^{-8}$. This may be due to the minimum wave load developing on the platform with minimum water plane area. Like the surge response, the long-term sway response (Fig. 5.8b) motion is also observed to have minimal variation in the sway motion with the addition of the WECs apart from the FTLP+8WECs configuration. The long-term surge and sway response motion is observed to have similar values at the characteristic level of $10^{-8}$. This may be due to the symmetric arrangement pattern of the WECs around the FTLP. The long-term yaw response motion is observed to have higher variation with the addition of the WECs. This may be due to the increased moment of inertia of the hybrid system with the addition of the WECs. The long-term yaw response for the FTLP+8WECs is observed to be higher than the FTLP, similar to both the long-term surge and sway response.

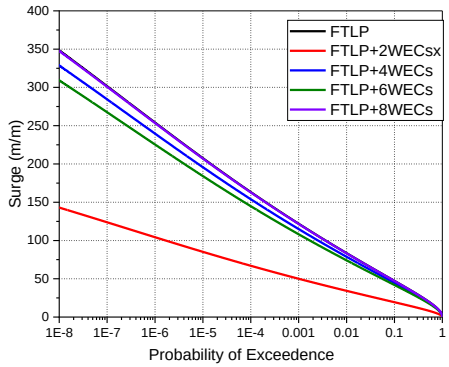


(a)

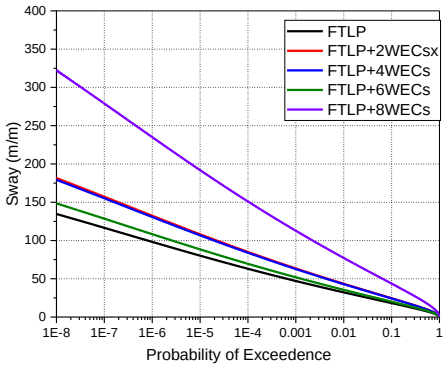


(b)

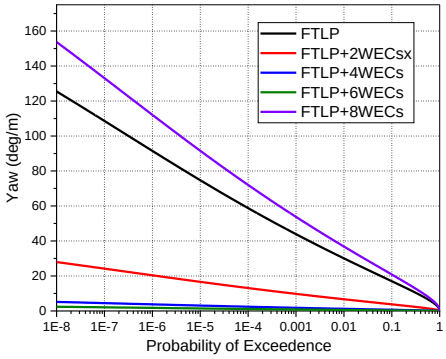


(c)

Fig. 5.8: Long-term responses for (a) surge, (b) sway, and (c) yaw for 11.2 m/s wind speed.

Fig. 5.9(a-c) shows the long-term surge, sway and yaw response motion of the FTLP and hybrid FTLP-WEC configuration for 14 m/s wind speed. Similar to other wind speed conditions below 11.4 m/s, the long-term surge motion (Fig. 5.9a) response is observed to have a smaller reduction in response amplitude at the characteristic level of $10^{-8}$. The FTLP+2WECs configuration is observed to have minimal surge response, and the FTLP+6WECs has a higher surge response at the characteristic level of $10^{-8}$. But for the long-term sway response motion, unlike 8 m/s and 11.2 m/s wind speed conditions, the long-term sway response motion is observed to reduce for the hybrid configuration (apart from FTLP+4WECs) compared to a single FTLP. Similar to the long-term surge response, the FTLP+2WECs configuration is observed to have minimal long-term sway response. The minimal sway motion reduces the later load developing on the platform, reducing the tension load developing on the mooring cables of the floating system. Fig. 5.9(c) shows the long-term yaw response motion for the 14 m/s wind speed. Adding the WECs has a higher influence on the long-term yaw motion. The hybrid FTLP-WEC configuration has minimal long-term yaw response compared to a single FTLP. The FTLP+6WECs hybrid configuration is observed to have minimum yaw response.

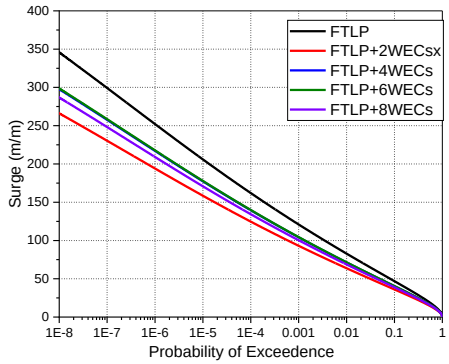


(a)

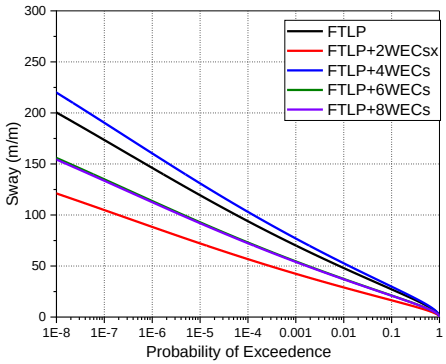


(b)

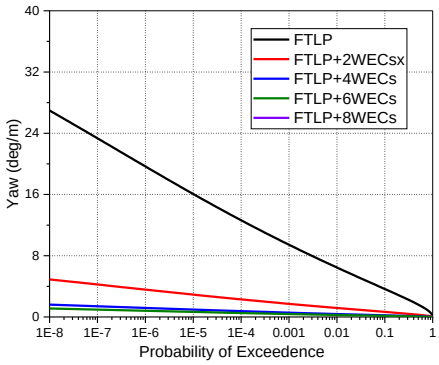


(c)

Fig. 5.9: Long-term responses for (a) surge, (b) sway, and (c) yaw for 14 m/s wind speed.

Fig. 5.10(a-c) shows the long-term surge, sway and yaw response motion for the extreme 17 m/s wind speed condition. Compared to other wind speed conditions, the responses are observed to be higher at the characteristic level of $10^{-8}$. This may be due to the higher wind load developing on the turbine tower as the wind speed condition is much closer to the parked wind speed condition of the 5 MW wind turbine. Adding the WECs has reduced the long-term surge response (Fig. 5.10a) for 17 m/s wind speed. Higher surge motion is observed for the FTLP+4WECs configuration, and the lowest surge response is observed for the FTLP+2WECs configuration. Unlike the surge response motion, the long-term sway response motion has a stronger influence with the addition of the WECs. The long-term sway response is observed to increase for the FTLP+6WECs and FTLP+8WECs configurations and is observed to decrease for FTLP+2WECs and FTLP+4WECs. The variation in long-term sway response is minimal for fewer WECs. The long-term yaw response for the 17 m/s wind speed condition is observed to have higher variation for two, six and eight WEC configurations. The FTLP+4WECs is observed to have minimal variation in yaw response for 17 m/s wind speed.

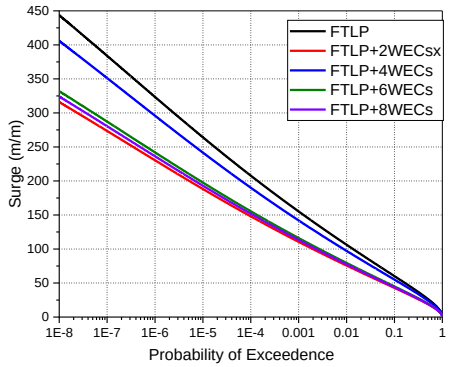


(a)

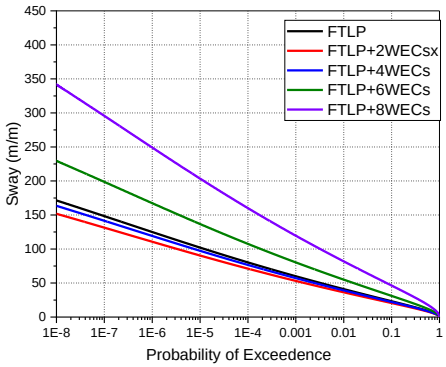


(b)

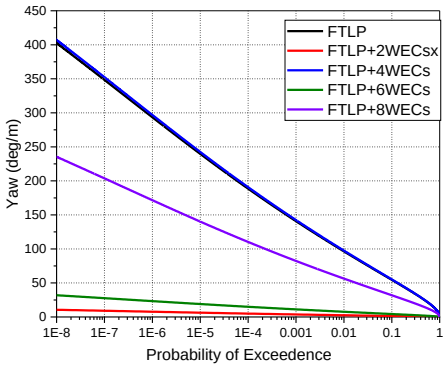


(c)

Fig. 5.10: Long-term responses for (a) surge, (b) sway, and (c) yaw for 17 m/s wind speed.

Table 5.8: Maximum long-term response value for surge motion for FTLP and hybrid FTLP.

| Configurations | V=8 m/s | V=11.2 m/s | V=14 m/s | V=17 m/s |
|---|---|---|---|---|
| FTLP | 301.4 | 327.8 | 347.4 | 448.2 |
| FTLP + 2WECsx | 223.4 | 140.2 | 268.2 | 319.6 |
| FTLP + 4WECs | 242.2 | 349.2 | 298.2 | 402.2 |
| FTLP + 6WECs | 298.6 | 310.6 | 298.8 | 328.6 |
| FTLP + 8WECs | 276.2 | 348.6 | 288.2 | 324.8 |

Table 5.8 shows the maximum values of long-term surge response at the characteristic level of $10^{-8}$ for gravity waves generated with different wind speeds. Adding the WECs has reduced the surge motion by about 16% (approx) for any wind speed conditions. A minimum surge response was observed for the FTLP+2WECx configuration, and a maximum surge response was observed for the FTLP+6WEC configuration. A higher surge response is observed for the FTLP+8WECs configuration of 11.2 m/s wind speed condition, which may be due to higher wave excitation due to the wave loads. Table 5.9 shows the maximum values of long-term pitch response for FTLP and hybrid FTLP-WEC under wind-generated gravity waves. The long-

term pitch motion response is observed to be minimal for any hybrid configurations of the FTLP. The long-term pitch response at the characteristic level of $10^{-8}$ is higher for 8 m/s wind speed conditions and reduces for higher wind speed conditions. Minimum long-term pitch response is observed for the FTLP+6WECs configuration, though the variation in the pitch response is minimal for any hybrid configurations.

Table 5.9: Maximum long-term response value for pitch motion for FTLP and hybrid FTLP.

| Configurations | V=8 m/s | V=11.2 m/s | V=14 m/s | V=17 m/s |
|---|---|---|---|---|
| FTLP | 0.422 | 0.446 | 1.431 | 0.623 |
| FTLP + 2WECsx | 0.223 | 1.416 | 0.328 | 0.6 |
| FTLP + 4WECs | 1.642 | 0.224 | 0.223 | 1.262 |
| FTLP + 6WECs | 0.262 | 0.232 | 0.214 | 0.228 |
| FTLP + 8WECs | 1.862 | 0.632 | 0.197 | 0.232 |

Table 5.10: Maximum long-term response value for roll motion for FTLP and hybrid FTLP.

| Configurations | V=8 m/s | V=11.2 m/s | V=14 m/s | V=17 m/s |
|---|---|---|---|---|
| FTLP | 1.832 | 1.026 | 0.646 | 0.896 |
| FTLP + 2WECx | 0.433 | 1.242 | 0.632 | 0.824 |
| FTLP + 4WEC | 1.252 | 0.442 | 0.682 | 1.242 |
| FTLP + 6WEC | 0.653 | 0.676 | 0.298 | 0.283 |
| FTLP + 8WEC | 1.665 | 1.262 | 0.286 | 1.264 |

Table 5.10 shows the long-term roll motion response for different wind speed conditions of FTLP and hybrid FTLP-WEC. Similar to the long-term pitch response, the long-term roll motion response is also observed to have minimum variation with the addition of the WECs. Minimum roll motion response is observed for the 14 m/s wind speed condition for any hybrid configurations. The minimum roll motion response for the FTLP and hybrid FTLP-WEC may be due to the orientation of the wave towards the positive x-direction. The minimum roll motion response ensures better stability of the platform against overturning. The hybrid FTLP+6WEC configuration is observed to have minimal long-term roll response.

### 5.5.3 Tower Base Shear Force and Bending Moment

Long-term distribution for the tower base forces are moments studied for the North Atlantic wave data using the JONSWAP spectrum. The study helps to understand the impact of wind

and waves on the floating STLP platform. Also, the analysis helps to study the impact of the addition of WECs on the STLP floater.

#### 5.5.3.1 Hybrid STLP-WEC FOWT Platforms

Fig. 5.11(a-c) shows the tower base forces developed on the hybrid system for 8 m/s wind speed and 2.5 m wave height. Fig. 5.11(a,b) shows that the addition of WECs has helped to reduce the forces in the x- and y- directions. The impact of wind and waves will be lower for the hybrid floater. The forces developed in the z-direction are observed to be minimum at $10^{-8}$ characteristic levels, as observed in Fig. 5.11(c). The fore-aft shear force and the side-to-side shear force are observed to be the same for all four hybrid platforms. The maximum force developed is observed to be $11.8\times10^{4}$ kN in the y-direction.

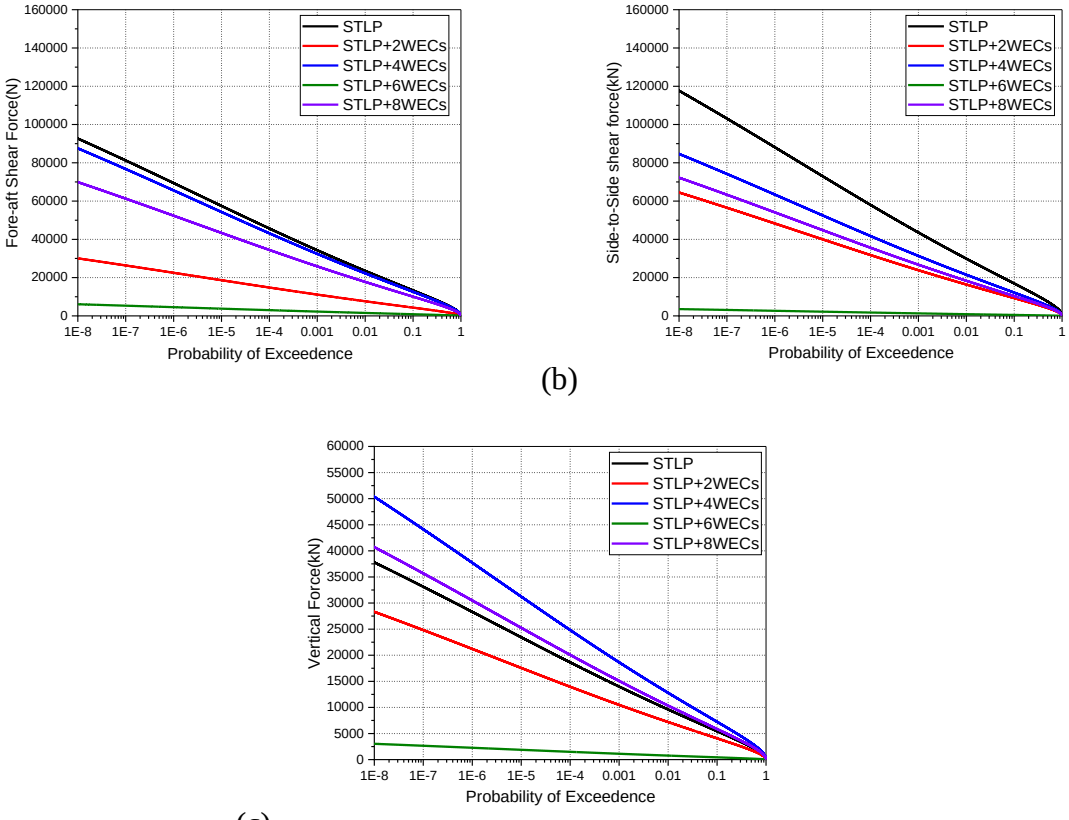


(a) (b)

(c)

Fig. 5.11: Long-term responses for (a) Fore-aft Shear force, (b) Side-to-Side Shear force, and (c) Vertical force for 8 m/s wind speed.

Fig. 5.12(a-c) shows the tower base moments developed on the hybrid system for 8 m/s wind speed and 2.5 m wave height. The addition of WECs helped to reduce the moments developed at the base of the turbine. The moment at $10^{-8}$ characteristic level is observed to be the minimum for the yaw moment. But for the STLP+8WECs configuration, the long-term yaw moment is

observed to be higher. The long-term forces and moment developed on the turbine's base are observed to be minimum for the STLP+6WECs configuration, further showing the minimum impact of wind and wave on the hybrid system. The maximum moment developed for the STLP+6WECs is observed to be $4.7\times10^5$ kN-m for 8 m/s wind speed.

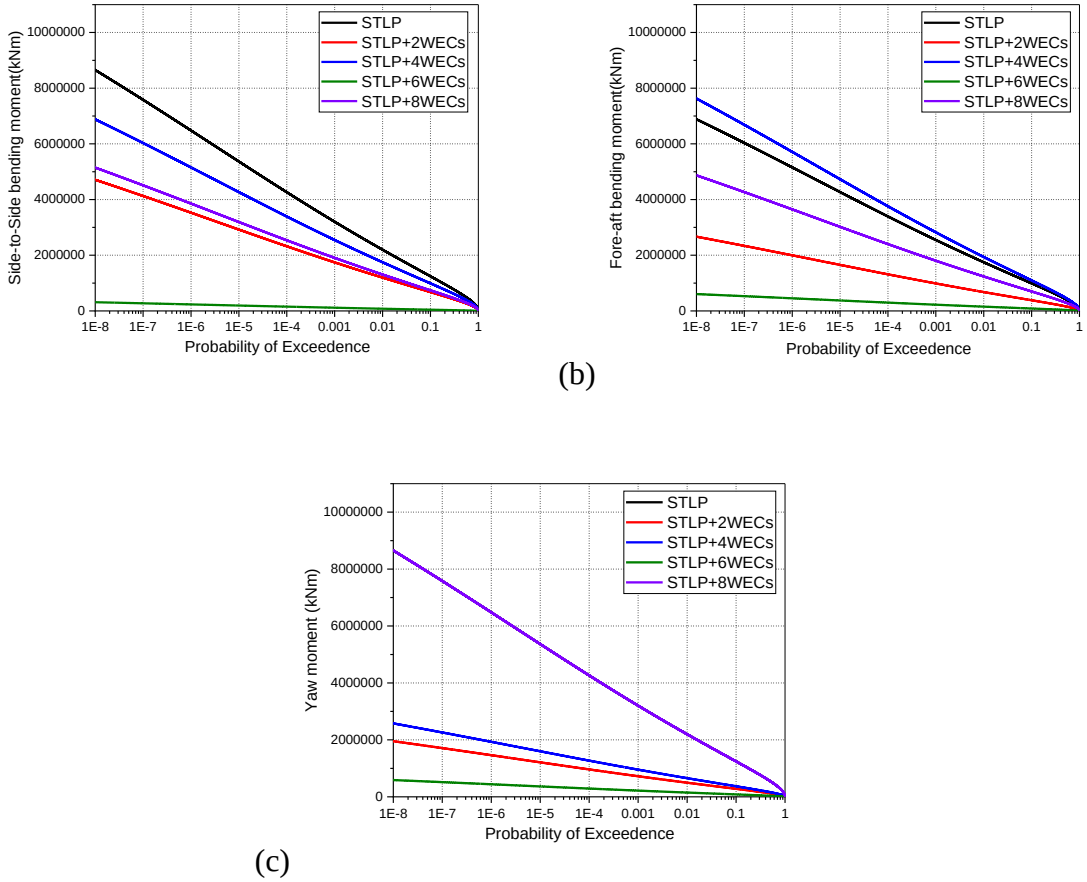


Fig. 5.12: Long-term responses for (a) Side-to-Side Bending Moment, (b) Fore-aft Bending Moment, and (c) Yaw Moment for 8 m/s wind speed.

Fig. 5.13(a-c) shows the tower base forces developed on the hybrid system for 11.2 m/s wind speed and 3.0 m wave height. The forces developed at the base of the tower tend to increase with the increase in wind speed. For the 14 m/s wind speed, the addition of WECs has a higher impact as the forces developed at the base is observed to increase. But for the STLP+6WECs configuration, the addition of WECs is observed to have reduced the impact of wind and waves. The maximum force developed observed for the STLP+2WECs configuration is close to $17\times10^4$ kN in both the fore-aft and side-to-side directions. Also, it is observed that the forces are minimum in the z-direction. The maximum force in the z-direction is observed to be

$7.5\times10^4$ kN. For the six WEC configurations (STLP+6WECs), the maximum force is observed to be $7\times10^4$ kN in both x-and y-directions.

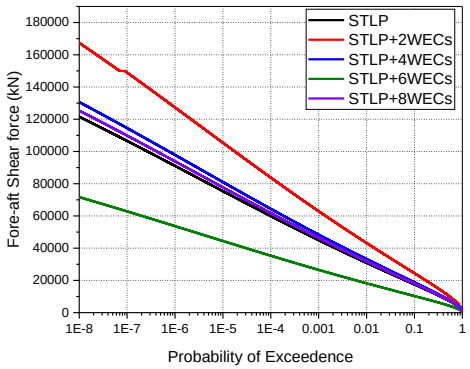


(a)

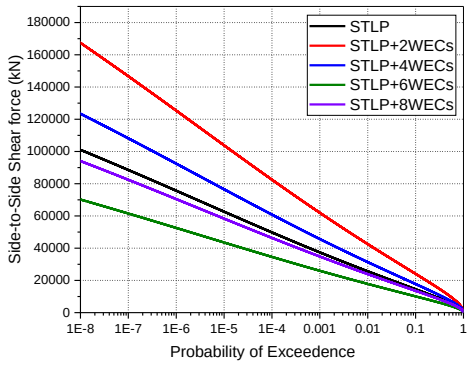


(b)

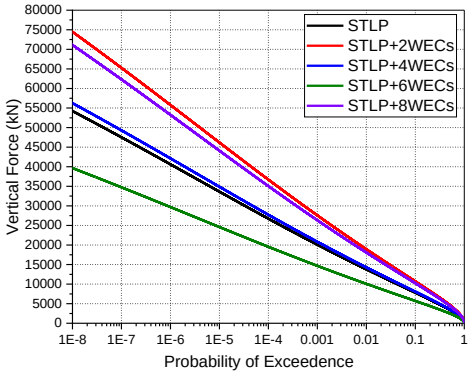


(c)

Fig. 5.13: Long-term responses for (a) Fore-aft Shear force, (b) Side-to-Side Shear force, and (c) Vertical force for 11.2m/s wind speed.

Fig. 5.14(a-c) shows the tower base moments developed on the hybrid system for 11.2 m/s wind speed and 3.0 m wave height. The moments are also observed to increase with the increase in wind speed and wave height. The moments are observed to reduce for the STLP+6WECs and STLP+8WECs configurations compared to a single STLP floater. Maximum moments are observed to be developed for the STLP+2WEC configuration as in Fig. 5.14(a,b) for both x- and y-directions. Fore-aft bending moment is observed to be slightly higher for the STLP+2WECs configuration, which is around $12.08\times10^6$ kN-m. The minimum moment of $5.94\times10^6$ kN-m is observed to be developed for STLP+6WECs configuration in the x-direction, as in Fig. 5.14(a). The long-term yaw moments are minimum for any configurations compared to the bending moments in the x- and y-directions (Fig. 5.14c), ensuring reduced load on the turbines, further improving the wind power absorption.

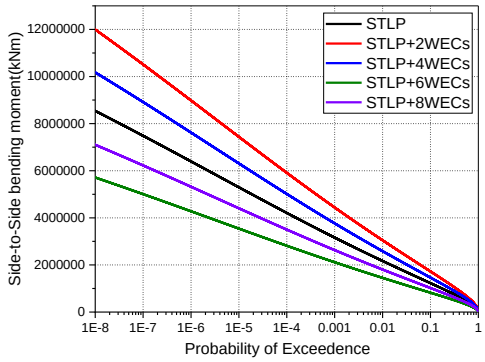


(a)

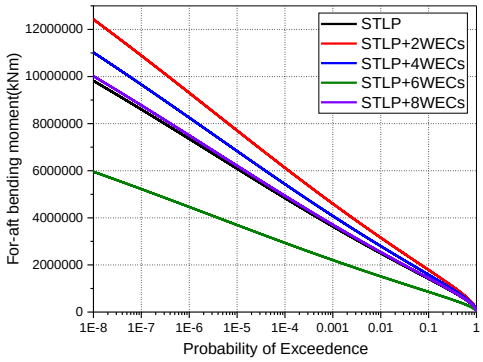


(b)

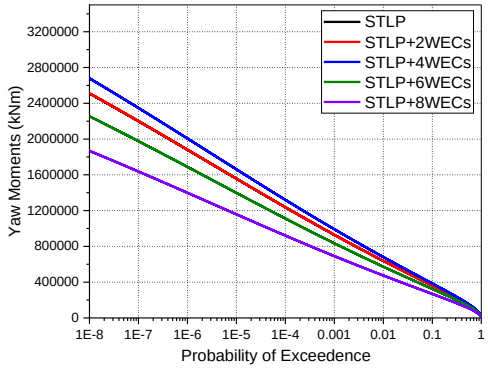


(c)

Fig. 5.14: Long-term responses for (a) Side-to-Side Bending Moment, (b) Fore-aft Bending Moment, and (c) Yaw Moment for 11.2 m/s wind speed.

Fig. 5.15(a-c) shows the tower base forces developed on the hybrid system for 14 m/s wind speed and 3.6 m wave height. 11.4 m/s is observed to be the rated wind speed for the 5 MW reference wind turbine, and a further increase in wind speed is observed to have a minimum impact on the efficiency of the wind turbine. The forces developed on the base of the tower are observed to decrease for the 14 m/s wind speed compared to the 11.2 m/s wind speed. This shows that the wind turbine is more oriented towards the wind for 11.2 m/s compared to the 14 m/s, as the forces are induced by the action of the wind. For the 14 m/s wind speed, the force developed is observed to be higher in the side-to-side direction and the vertical force is observed to be minimum, as seen in Fig. 5.15(b,c). The maximum force is observed for the STLP+6WECs configuration, which is close to $16.1\times10^4$ kN in y-direction. Minimum side-to-side shear force is observed to be developed for the STLP+8WECs configuration. Also, it is observed that the long-term vertical forces are minimal for the STLP+8WECs (Fig. 5.15c). The minimum side-to-side and vertical force for STLP+8WECs ensures reduced load on turbines.

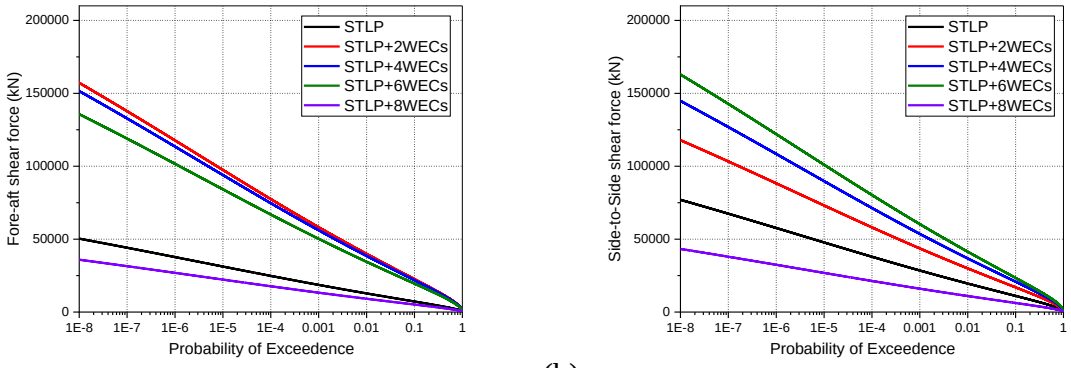


Fig. 5.15: Long-term responses for (a) Fore-aft Shear force, (b) Side-to-Side Shear force, and (c) Vertical force for 14 m/s wind speed.

Fig. 5.16(a-c) shows the tower base moments developed on the hybrid system for 14 m/s wind speed and 3.6 m wave height. The moments observed to have minimal impact with the increase in wind speed and wave height as the variations observed in moments are minimum. Higher force in the x-direction for the STLP+6WECs configuration has increased the fore-aft bending moment, as in Fig. 5.16(a). The maximum value for the fore-aft bending moment is observed to be $12.86\times10^{6}$ kN-m for the STLP+6WECs configuration. Side-to-Side bending moment is observed to be higher compared to moments developed in the other two directions. Fig. 5.16(c) shows that the yaw moments are minimal for the hybrid system other than the STLP+2WECs configuration. The minimal yaw moments ensure minimal wind and wave load developing on the hybrid floating platforms. It is observed that the STLP+2WECs configuration is having a higher impact from waves and winds as the forces and moments are observed to be higher. Minimal moments are observed for the STLP+8WECs hybrid floating system. The variation in the long-term yaw moments (Fig. 5.16c) are minimum for the hybrid concepts apart for the STLP+2WECs.

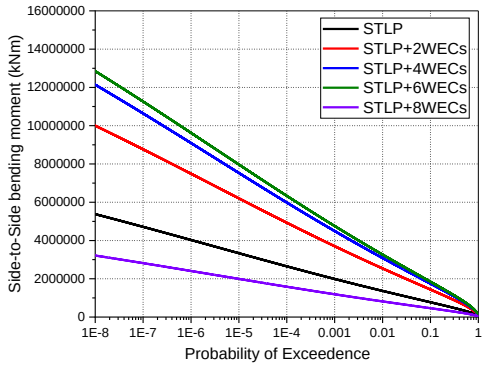


(a)

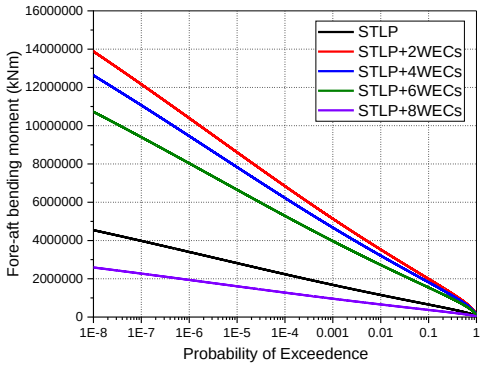


(b)

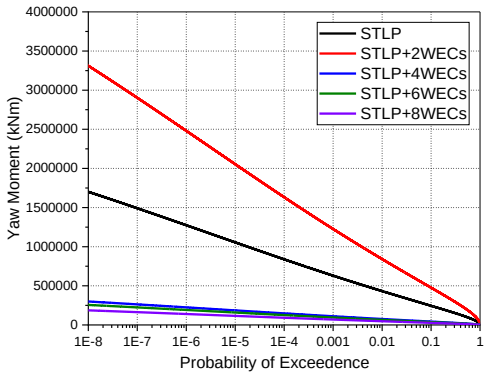


(c)

Fig. 5.16: Long-term responses for (a) Side-to-Side Bending Moment, (b) Fore-aft Bending Moment, and (c) Yaw Moment for 14 m/s wind speed.

Fig. 5.17(a-c) shows the tower base forces developed on the hybrid system for 17 m/s wind speed and 4.2 m wave height. The 17 m/s wind speed represents the extreme operating wind speed for 5 MW wind speed in Northern Atlantic Sea. The forces are observed to be higher for 17 m/s wind speed conditions compared to other operating wind speed conditions. Side-to-side shear force is observed to be maximum, as in Fig. 5.17(b), which is $19.1\times10^4$ kN for the STLP+6WECs configuration. For 17 m/s wind speed conditions, the hybrid configurations are observed to have higher shear force developed compared to the single STLP floater, showing that the influence of wind and wave will be more on the hybrid systems for this operating condition of 5 MW wind turbine. Also, it is observed that the minimum force develops in the z-direction during the life period of the hybrid system, as in Fig. 5.17(c). The addition of the WECs have increased the long-term tower base forces for the 17 m/s wind speed condition. The STLP+2WECs are observed to have minimal long-term force in the x- and y- directions. The long-term vertical force is minimum for STLP+8WECs (Fig. 5.17c).

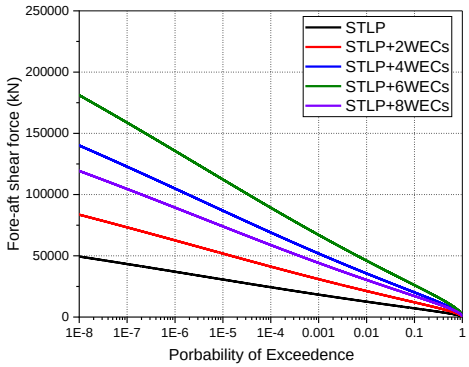


(a)

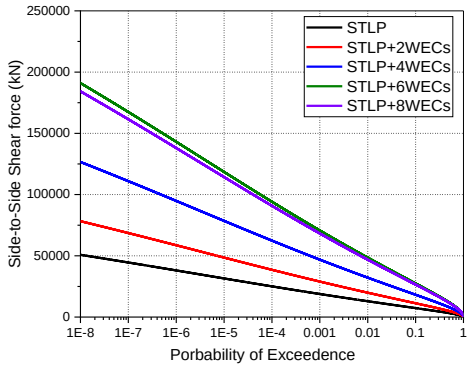


(b)

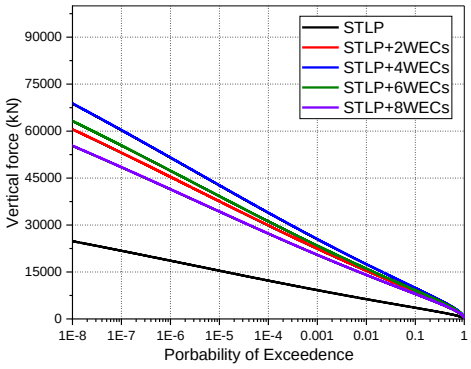


(c)

Fig. 5.17: Long-term responses for (a) Fore-aft Shear force, (b) Side-to-Side Shear force, and (c) Vertical force for 17 m/s wind speed.

Fig. 5.18(a-c) shows the tower base moments developed on the hybrid system for 17 m/s wind speed and 3.6 m wave height. Side -to-side bending moment is observed to be higher compared to other moments developed in y- and z- directions. The STLP+6WECs configuration is observed to have a higher value for both side-to-side and fore-aft bending moments. Yaw moments are higher for the STLP+8WECs configuration. From the study of long-term analysis of tower bases forces and moments, it is observed that the impact of wind and wave on the hybrid system is minimal for the wind speed less than the rated wind speed of the 5 MW wind turbine. This shows that the wind turbine efficiency of the hybrid system will be higher for lower wind speed conditions. Minimum forces and moments are observed for the STLP+6WECs configuration for wind speed conditions less than 11.4 m/s, and higher forces and moments are observed for the STLP+2WECs configuration. As the wind speed increases above the rated wind speed of 11.4 m/s, the forces and moments tend to increase for the STLP+6WECs configuration. For any wind speed conditions, the variation in the long-term forces and moments are minimum for hybrid STLP+8WECs.

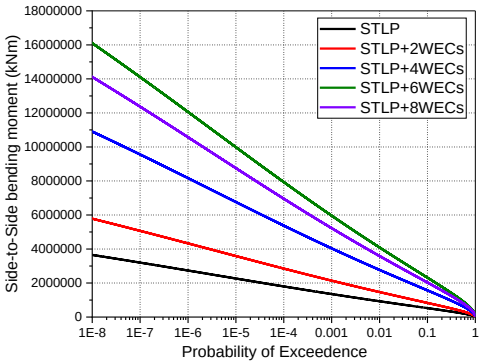


(a)

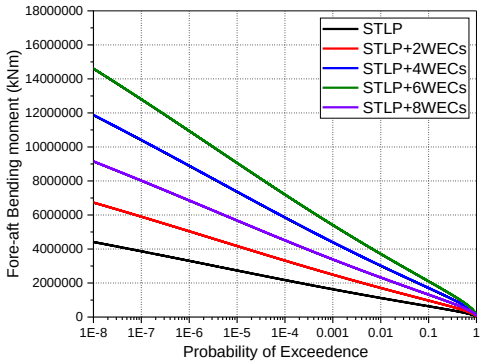


(b)

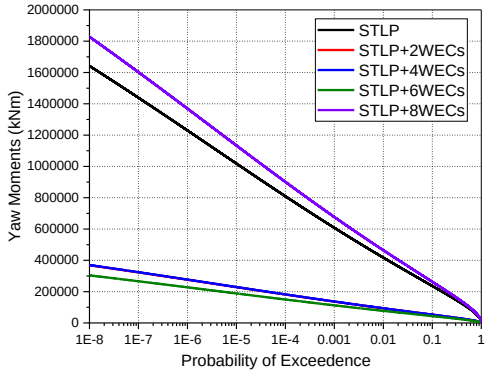


(c)

Fig. 5.18: Long-term responses for (a) Side-to-Side Bending Moment, (b) Fore-aft Bending Moment, and (c) Yaw Moment for 17 m/s wind speed.

### 5.5.3.2 Hybrid FTLP-WEC FOWT Platforms

The long-term forces and moments are studied for FTLP and hybrid FTLP-WEC floating wind turbine platforms. Fig. 5.19(a-c) shows the tower base forces for the 8 m/s wind speed conditions. The forces are observed to an influence by the addition of the WECs. Fig. 5.19(a) shows the long-term fore-aft shear force for different FTLP and hybrid FTLP-WEC configurations. The long-term forces tend to reduce for the FTLP+2WECsx, FTLP+6WECs and FTLP+8WECs, though the variation in the forces developed at the characteristic level of $10^{-8}$ is minimum. The FTLP+4WECs configuration is observed to have higher values of long-term fore-aft forces. Similar to the fore-aft forces, the long-term side-to-side forces (Fig. 5.19b) for the FTLP+2WECs, FTLP+6WECs and FTLP+8WECs are observed to reduce, though the FTLP+4WECs has higher variation in forces. The higher variation in forces for the four WEC configurations may be due to the higher wave load developing on the base of the turbine tower with a larger water plane area and minimum restoring forces developed. The long-term vertical

forces (Fig. 5.19c) are observed to reduce with the addition of the WECs. Minimum vertical forces are observed for FTLP+8WECs configurations.

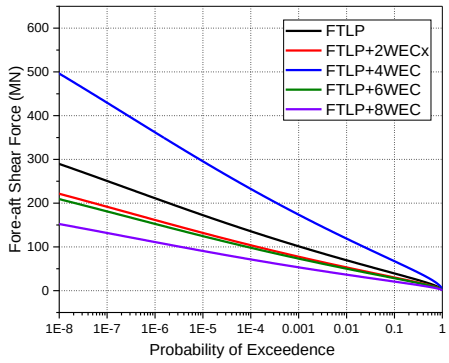


(a)

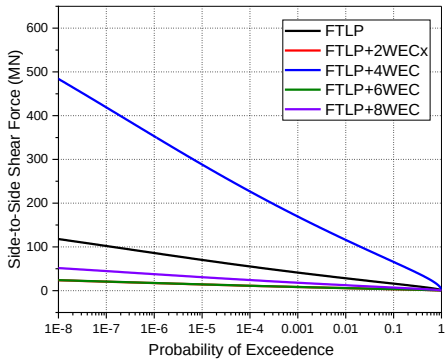


(b)

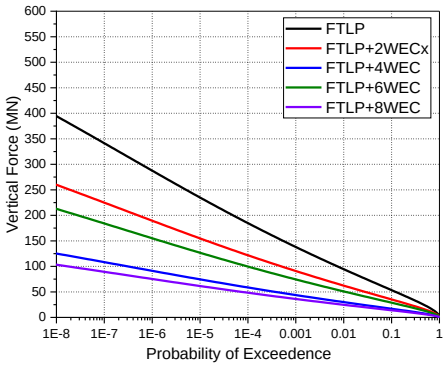


(c)

Fig. 5.19: Long-term responses for (a) Fore-aft Shear force, (b) Side-to-Side Shear force, and (c) Vertical force for 8 m/s wind speed.

Fig. 5.20(a-c) shows the long-term moments for different hybrid configurations for 8 m/s wind speed conditions. Similar to the long-term forces, the moments are also observed to be higher for the FTLP+4WECs configurations. For other hybrid systems, the moments are observed to reduce with the addition of the WECs. The higher variation in the long-term tower base moments for the FTLP+4WECs may be because of the resonance. A proper damping mechanism must be designed for STLP+4WECs to absorb the energy to prevent the failure of the hybrid floating system. Minimum long-term tower base moments are observed for FTLP+8WECs configurations. The minimum values of moments for the FTLP+8WECs configuration may be due to the higher restoring forces developed against the wave loads by the WECs. The minimum long-term moments ensure better wind power absorption of the hybrid systems. This is because the turbine supported on the platforms will be oriented towards the wind direction.

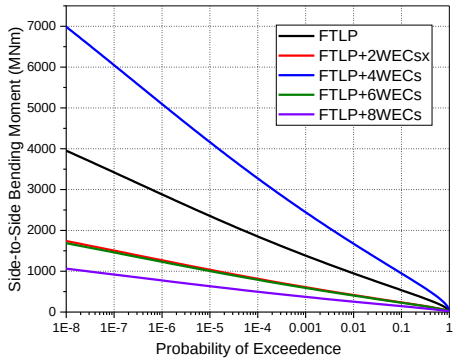


(a)

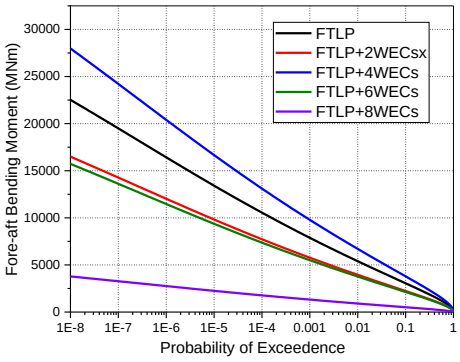


(b)

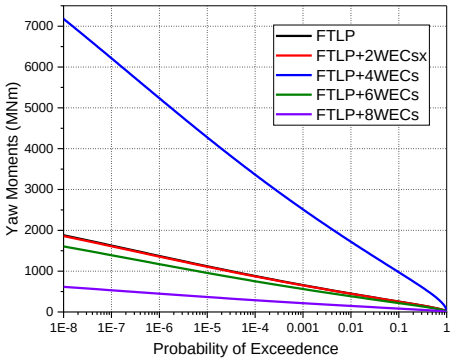


(c)

Fig. 5.20: Long-term responses for (a) Side-to-Side Bending Moment, (b) Fore-aft Bending Moment, and (c) Yaw Moment for 8 m/s wind speed.

Fig. 5.21(a-c) shows the long-term tower base forces for 11.2 m/s wind speed conditions. The addition of the WECs for the two and six WECs has reduced the forces developed at the base of the turbine tower in the x- and y-direction. The long-term vertical is observed to be higher for the hybrid floating system compared to the long-term fore-aft and side-to-side forces. Fig. 5.21(a) shows the long-term fore-aft shear forces for the FTLP and hybrid FTLP-WEC floating platforms. The long-term forces are observed to be higher for the FLTP+8WECs configuration and are minimum for the FTLP+6WECs configuration. Similarly, long-term side-to-side shear forces are observed to be higher for the FTLP+8WECs configuration and are minimum for the FTLP+2WECs configuration, as seen in Fig. 5.21(b). The vertical forces are observed to be higher for the FTLP+8WECs configuration, and for other hybrid configurations, the vertical forces are observed to decrease with the addition of the WECs. The vertical forces are dominant compared to the fore-aft shear forces, which may be due to the reduced inclining moments developed on the turbine tower for the wind speed conditions below 11.4 m/s.

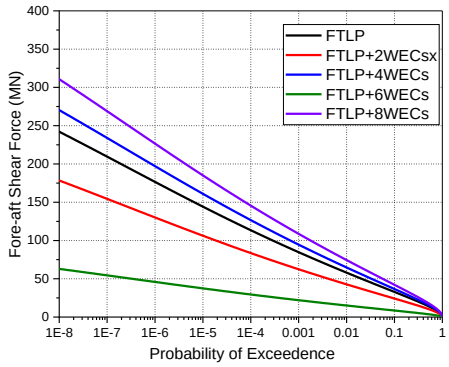


(a)

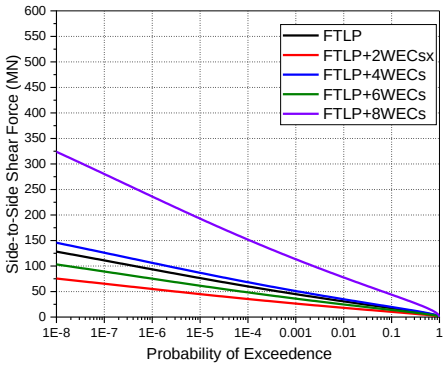


(b)

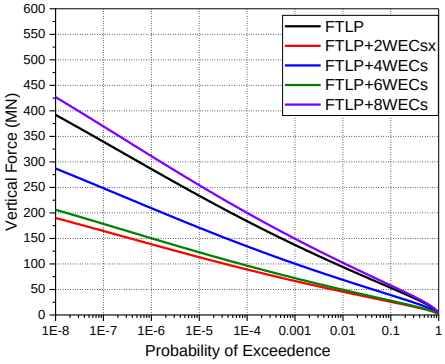


(c)

Fig. 5.21: Long-term responses for (a) Fore-aft Shear force, (b) Side-to-Side Shear force, and (c) Vertical force for 11.2 m/s wind speed.

Fig. 5.22(a-c) shows the long-term moments developed at the base of the turbine tower. The variation in the tower base side-to-side bending moments is minimum for the two, six and eight WEC configurations and the side-to-side moments are observed to increase with the addition of the WECs. Minimum fore-aft tower base bending moments (Fig. 5.22a) are observed for FTLP+4WECs configuration. Similar to the side-to-side bending moments, the fore-aft bending moments (Fig. 5.22b) for the hybrid FTLP+2WECs, FTLP+6WECs and FTLP+8WECs have minimum variation. Further, the FTLP+4WECs configuration is observed to have minimum long-term side-to-side bending moments. For any hybrid configurations, the long-term side-to-side bending moments are observed to be higher compared to the other tower base moments. This is because the wave direction is oriented towards the positive x-direction. The vertical moments are observed to increase with the addition of the WECs. Similar to other tower base moments, minimum vertical moments are observed for FTLP+4WECs. The STLP+4WECs are observed to have higher variations (Fig. 5.20(a-c) & Fig. 5.22(a-c)) in the forces and moments developed with the increase in the operational wind speed.

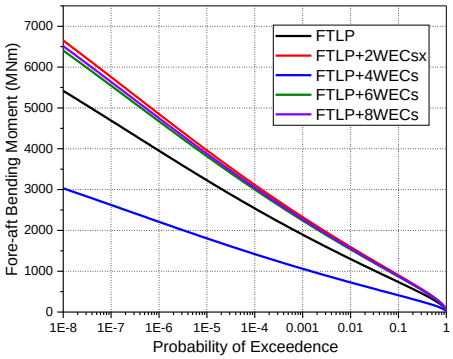


(a)

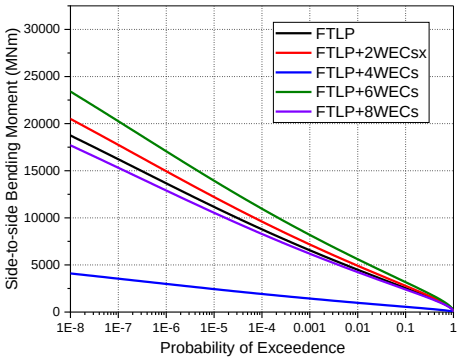


(b)

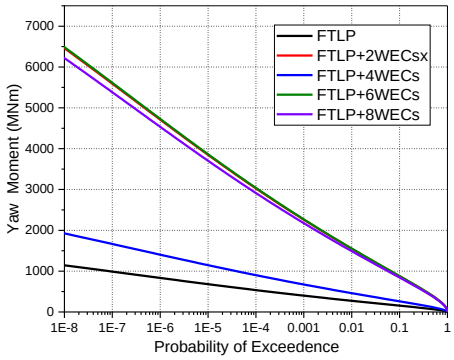


(c)

Fig. 5.22: Long-term responses for (a) Side-to-Side Bending Moment, (b) Fore-aft Bending Moment, and (c) Yaw Moment for 11.2 m/s wind speed.

Fig. 5.23(a-c) shows the tower base forces developed for the FTLP and hybrid FTLP-WEC for 14 m/s wind speed conditions. Forces are observed to be reduced with the addition of the WECs. The variation of fore-aft shear forces (Fig. 5.23a) for the hybrid platforms are minimal. Minimum fore-aft shear force is observed for the FTLP+8WECs configuration, and maximum fore-aft force is observed for the FTLP+4WECs configuration. For the side-to-side shear forces, the FTLP+8WECs is observed to have a higher force compared to other hybrid configurations, as seen in Fig. 5.23(b). FTLP+4WECs is observed to have minimum side-to-side shear force. The minimum side-to-side bending moment of the FTLP+4WECs ensure better efficiency of the supported wind turbine as the turbine is best oriented towards the wind direction. The Fig. 5.23(c) shows the vertical force developed at the base of the turbine tower. The vertical force is observed to be higher than the side-to-side shear force, causing higher loads to develop on the control system. Vertical force is the minimum for FTLP+8WECs configuration.

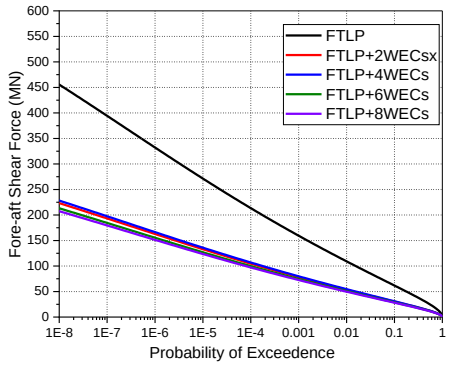


(a)

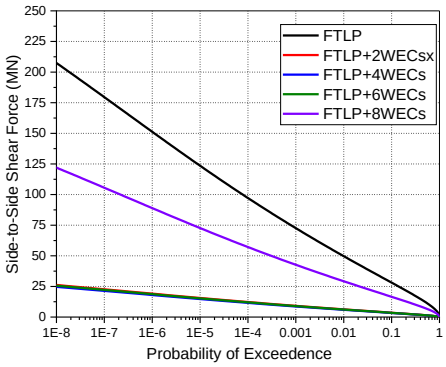


(b)

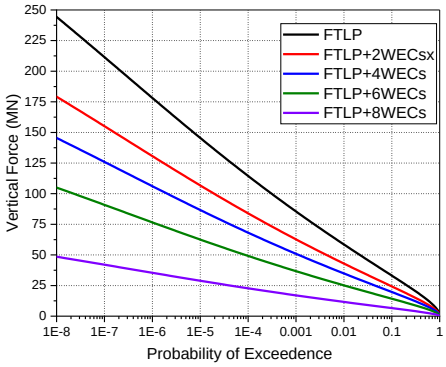


(c)

Fig. 5.23: Long-term responses for (a) Fore-aft Shear force, (b) Side-to-Side Shear force, and (c) Vertical force for 14 m/s wind speed.

Fig. 5.24(a-c) shows the moments developed at the base of the turbine tower for 14 m/s wind speed. Similar to the forces, the moments are reduced by adding the WECs. The fore-aft (Fig. 5.24a) and side-to-side moments are observed to be minimal for FTLP+8WECs configuration. The side-to-side moments are observed to be higher (Fig. 5.24b) compared to the moments developed in the other two directions. The variation of the yaw moments with the addition of the WECs is minimal, as seen in Fig. 5.24(c). The vertical moments are higher for FTLP+8WECs and minimum for FTLP+6WECs.

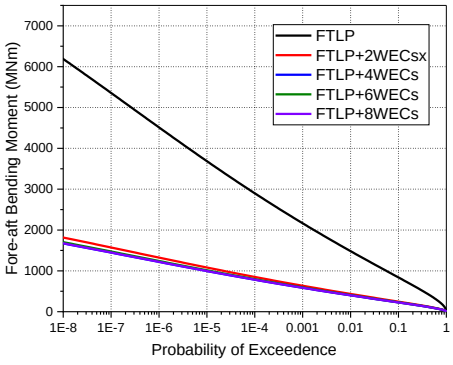


(a)

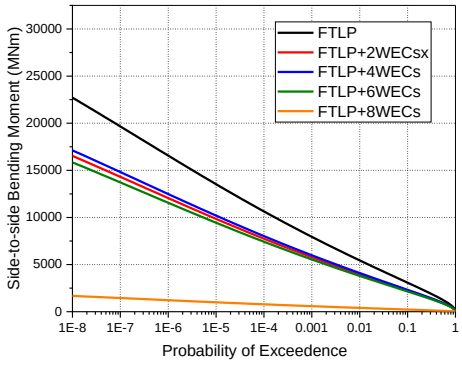


(b)

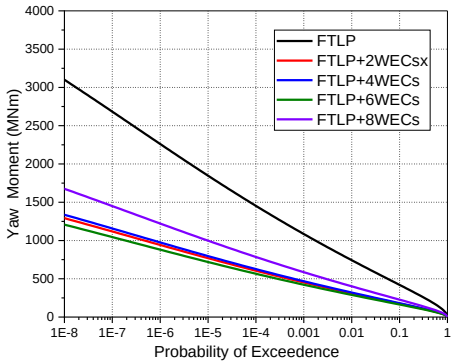


(c)

Fig. 5.24: Long-term responses for (a) Side-to-Side Bending Moment, (b) Fore-aft Bending Moment, and (c) Yaw Moment for 14 m/s wind speed.

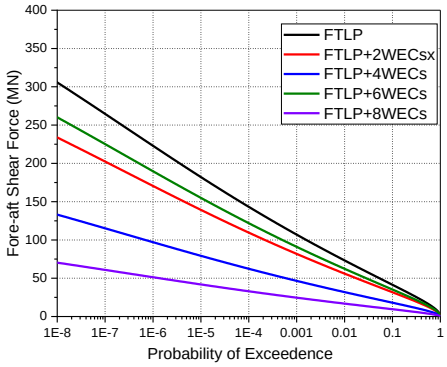


(a)

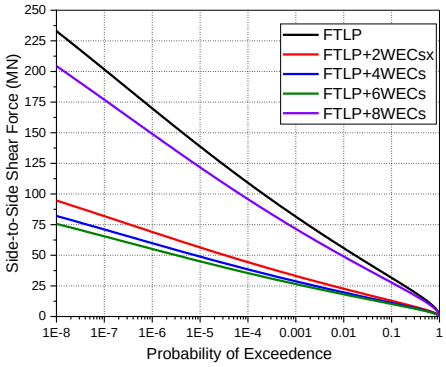


(b)

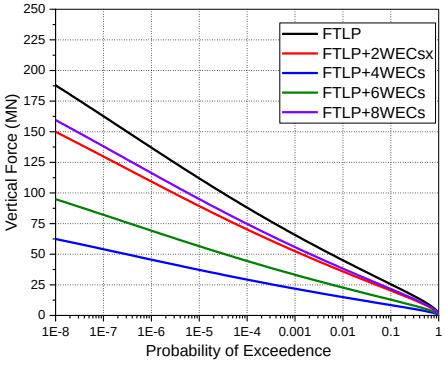


(c)

Fig. 5.25: Long-term responses for (a) Fore-aft Shear force, (b) Side-to-Side Shear force, and (c) Vertical force for 17 m/s wind speed.

Fig. 5.25(a-c) shows the tower base forces developed for 17 m/s wind speed at the base of the turbine tower for FTLP and hybrid FTLP-WEC. The forces are observed to reduce like for other wind speed conditions. The fore-aft shear forces are higher compared to side-to-side shear forces and vertical forces. The fore-aft shear forces are observed to be minimum for

FTLP+8WECs and maximum for FTLP+6WECs. For the side-to-side shear force, the shear force is higher for FTLP+8WECs and is minimal for FTLP+6WECs. The vertical forces are almost equal compared to the side-to-side shear force. The vertical forces are higher for FTLP+8WECs. The vertical forces are minimum for FTLP+4WECs.

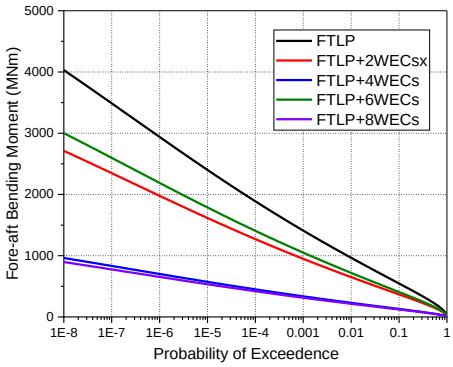


(a)

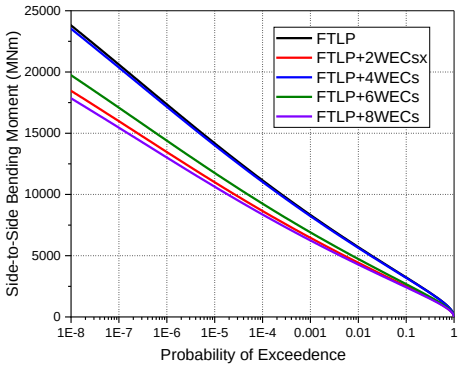


(b)

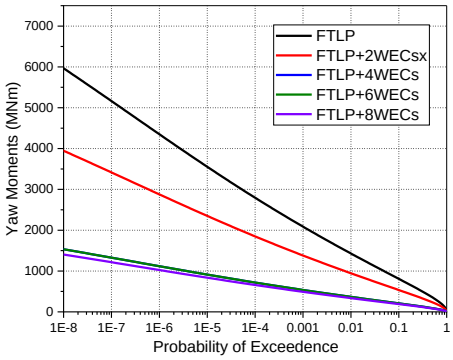


(c)

Fig. 5.26: Long-term responses for (a) Side-to-Side Bending Moment, (b) Fore-aft Bending Moment, and (c) Yaw Moment for 17 m/s wind speed.

Fig. 5.26(a-c) shows the moments developed at the base of the turbine tower for the FTLP and hybrid FTLP-WEC for 17 m/s wind-generated gravity waves. Similar to the shear forces developed, the moments at the base of the turbine tower are also reduced with the addition of the WECs. The fore-aft moments are minimal for FTLP+8WECs and maximum for FTLP+6WECs (Fig. 5.26a). The variation in the moments developed is minimal for the side-to-side bending moment at the base of the turbine tower. The moments are minimum for FTLP+8WECs and maximum for FTLP+6WECs. A higher reduction in yaw moments is observed for hybrid FTLP-WECs. FTLP+8WECs configuration is observed to have minimum vertical moment developed.

For the different wind speed conditions studied, the influence of the WECs on the forces and moments developed on the FTLP is higher for the wind speed conditions above the rated wind speed condition (11.4 m/s). The forces and moments are reduced by adding the WECs for 14 m/s and 17 m/s wind speed conditions. For wind speed conditions 8 m/s and 11.2 m/s, the forces and moments are observed to be higher for FTLP and FTLP-WEC hybrid systems compared to wind speed conditions above rated wind speed conditions. This may be due to the higher wind load developing on the turbine tower with higher wind absorption of the turbine blades. Apart from the 11.2 m/s wind speed condition, the FTP+8WECs configuration is observed to have the minimum forces and moments compared to other hybrid configurations. However, the variation of the forces and moments is minimal. This may be due to the symmetric arrangement pattern of the WECs around the FTLP offering sufficient restoring forces and moments to improve the stability of the hybrid system.

## 5.6 CLOSURE

The long-term response analysis is carried out for five different arrangements of WECs around the STLP and FTLP system for JONSWAP, Pierson Moskowitz, Bretschneider ISSC and ITTC wave spectra. The transfer functions for the long-term simulation are obtained from aero-servo-hydro-elastic simulation using the FAST tool developed by NREL. The comparative study is conducted for different environmental conditions representing the North Atlantic wave data for the structure's lifetime. The study observed higher surge motion for most wind case conditions compared to other translational motions. The higher surge motion of the hybrid system may be due to the coupling between the higher displacement and initial pretension. The long-term forces and moments are also discussed for different wind speed conditions.

- The long-term surge response is minimal (average 81% reduction) for the hybrid STLP-WEC compared to the hybrid FTLP-WEC for any wind speed conditions. The higher long-term surge response may be due to the higher water plane area of the FTLP FOWT, developing more wave load on the platform.
- The long-term response values of yaw response are observed to be higher (average 78%) for the hybrid STLP-WEC and minimal for the hybrid FTLP-WEC. The reduced long-term yaw response of hybrid FTLP-WEC may be due to the higher added mass and inertia of the floating system.

- The long-term pitch and roll response is almost similar for both hybrid configurations. The minimum roll response of the hybrid configurations ensures the stability of the systems against overturning.
- Long-term response of tower base forces and moments concluded that the impact of wind and wave on the hybrid STLP-WEC system is reduced for wind speeds less than the rated wind speed of the 5 MW wind turbine. But for the hybrid FTLP-WEC systems, the long-term forces and moments are minimal for 17 m/s wind speed.
- The long-term forces and moments are observed to be minimum (average 21% reduction) for the hybrid FTLP-WEC configurations compared to the STLP-WEC configurations for wind speed conditions above 11.2 m/s.

# CHAPTER 6

# EXTREME RESPONSE ANALYSIS OF HYBRID TLP-WEC USING ENVIRONMENTAL CONTOUR METHOD

## 6.1 GENERAL INTRODUCTION

The exploration of marine resources, such as the extraction of petroleum, the use of wave energy, and offshore wind energy, are active areas of research in ocean engineering. To support activities connected to the development of maritime resources, floating structures and mooring systems must be built to endure the complex marine environmental loads caused by wind, waves and currents. Non-linear time domain simulations are used to predict the extreme response levels during the design stage to ensure the survival and functioning of these floating structures in harsh environmental conditions. The joint distribution of the environmental parameters should be established to develop accurate design loads for the floating structures assigned with a particular target return period.

## 6.2 NUMERICAL MODELLING

The safety of the floating structure under consideration must be assured over the period of the planned operation. The wind or wave characteristics associated with a 50- or 100-Year return period are frequently used as the design basis for extreme conditions of the floating structures based on the statistical analysis of environmental factors (Lia et al., 2022). The most reliable and precise way to evaluate severe responses in marine structure design can be a full long-term analysis. However, the long-term analysis takes an extended period for massive complex systems. The Environmental Contour (EC) approach can be employed to simulate the extreme responses of maritime structures to minimise simulation time and enhance efficiency. The EC technique also has the advantage of decoupling structural reactions from their environment, which reduces the number of simulations that use non-linear time domain responses. The EC method can be based on Inverse First Order Reliability Method (IFORM), Inverse Second Order Reliability Method (ISORM), direct sampling contour and highest density contour methods (Ross et al., 2020, Chai and Leira, 2018). The present study adopts the EC method based on IFORM and can be employed to examine design loads with a specified return period.

The technique employs a reliability approach in which the environmental variables are transferred from the standard normal space to the point associated with the physical random variable based on the IFORM method, using the Rosenblatt transformation.

### 6.2.1 Reliability Based on Extreme Long-term Loads

The long-term extreme loads are computed by integrating the short-term distributions with the joint probability distribution function. The extreme design load is studied for a 10-min duration $L_{10-\min}$ and is considered to exceed the design load $L_T$ with a probability consistent with the service life of T-Years. The 10-min mean wind speed $V$ and the wave height $H_s$ are the physical parameters for the probabilistic distribution. Further, the design load of the turbine $L_T$ with an acceptable probability of exceedance can be formulated using the short-term conditional probability $P[L_{10-\min} > L_T \mid v, h_s]$ and the joint probability density function $f_{v,Hs}(v, h_s)$ of the environmental variables given by

$$P_f = P[L_{10-\min} > L_T] = \int_0^\infty \int_0^\infty P[L_{10-\min} > L_T \mid v, h_s] f_{v,H_s}(v, h_s) dv dh_s. \tag{6.1}$$

The mean wind speed and the significant wave height are modelled using the joint probability distribution function to account for the variability and the changes that occur for the variables for the offshore site HornsRev as in Saranyasoontorm and Manuel (2004). The mean wind speed of the model is assumed to follow the Weibull distribution, and the significant wave height is distributed like a Normal distribution. A transformation from the standard Gaussian U-space to the physical space is performed using Rosenblatt Transformation. The joint distribution function is given by

$$f_{V,H_s}(v, h_s) = f_{H_s/V}(h_s/v)\, f_V(v), \tag{6.2}$$

where the marginal mean wind speed distribution $f_V(v)$ is defined by the shape parameter $k$ and scale parameter, $a$. The relation for the marginal wind speed is expressed as

$$f_V(v) = 1 - \exp\left[ -\left( \frac{v}{a} \right)^k \right]. \tag{6.3}$$

The study assumes $k = 1.8$ and $a = 11$ m/s at a height of 60 m above the MSL. The wave height expressed as a normal distribution function can be defined as

$$f_{H_s/V}\left(h_s/v\right)=\Phi\left[\frac{h-\mu_H\left(v\right)}{\sigma_H}\right], \tag{6.4}$$

where $\mu_H\left(v\right)=0.13v$ and $\sigma_H=0.24$ m. Also, the wave period is not explicitly treated as a random variable.

### 6.2.2 Environmental Contour Based on IFORM

The EC method based on the IFORM is a traditional approach, where the environmental contours transform the original vector of Environmental variables $X$ into a vector $U$ of independent standard normally distributed variables. A set of desired properties in $U$ - space is obtained by developing an n-dimensional sphere centred around the origin with radius $\beta$, where $\phi\left(\beta\right)=1-P_f$, is the reliability and $P_f$ is the exceedance probability or the probability of the failure (Vanem, 2017). To obtain the response level for a particular return period $T_r$ and sea state duration for 10-min $T_s$, the probability of the failure is initially calculated using the relation given by

$$P_f=\frac{Ts}{365*24*Tr}. \tag{6.5}$$

The target return period for the environmental contour based on the reliability index $\beta$ and exceedance probability $P_f$ is given by

$$\beta=\phi^{-1}\left(r\right), \tag{6.6a}$$

$$\beta=\phi^{-1}\left(1-P_f\right), \tag{6.6b}$$

$$\beta=\phi^{-1}\left(1-\frac{Ts}{365*24*Tr}\right). \tag{6.7}$$

The transformation of the standard normal space to the physical standard space is required to calculate the nominal load, achieved using Rosenblatt Transformation. In the present study, we consider $n=1,2$, however the complete probabilistic representation of the random variables can only be achieved using the 3-D model, as only the 3-D model retains all random variables. The median value indicated in the definition of design load $L_T$ for the 2-D model forces one variable to zero, and for the 1-D model, two variables are forced to zero. Thus the 1-D EC model assumes that the mean wind speed for a 10-min duration $\left(V\right)$ is random, but it neglects the variability in the wave height, $H_s$ and the 10-min maximum response load, $L_T$. Hence in

the 1-D model, the n-dimensional sphere is a degenerate single point, $u_1 = \beta,\ u_2 = u_3 = 0.$ For the 2-D EC model, the variables V and $H_s$ are random, and the sphere is transformed into a circle, $u_1^2 + u_2^2 = \beta;\ u_3 = 0$. Further, for the 3-D model, all the environmental variables are considered random and hence it is transformed as a sphere $u_1^2 + u_2^2 + u_3^2 = \beta^2$. As the target reliability is expressed in terms of the return period, $T - \text{Years}$ associated with the design load $L_T$, and the $H_s$ is the extreme value for 10-min duration, the approximate value for $\beta$ need to be calculated using the Eq. (6.7).

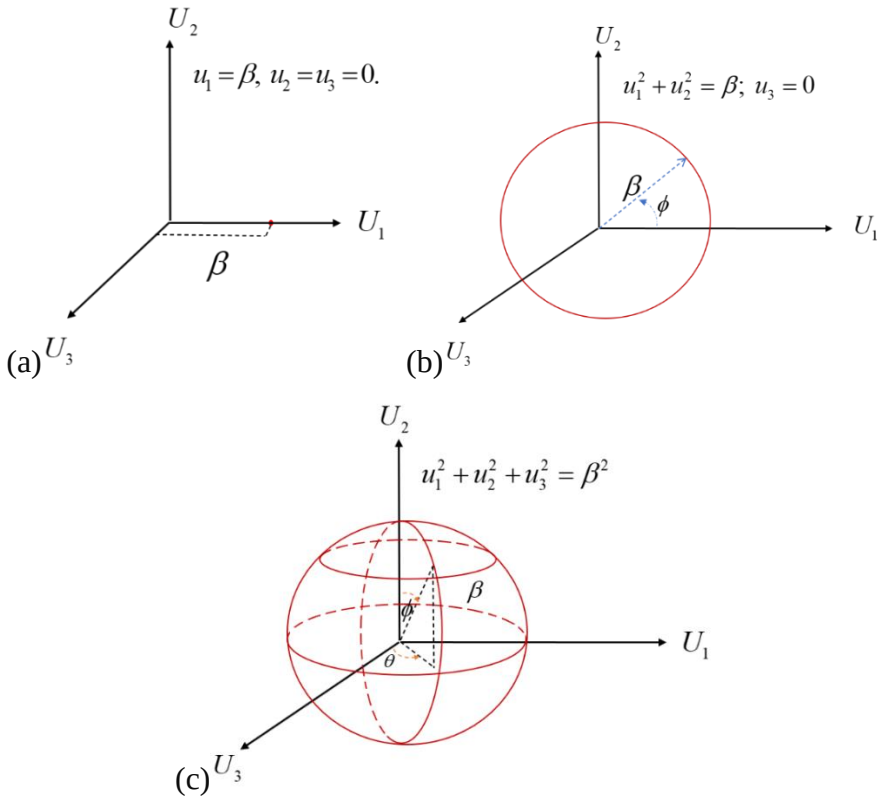


Fig. 6.1: Geometrical representation of the n-directional sphere in U-Space for (a) 1-D, (b) 2-D, and (c) 3-D EC models.

### 6.2.3 1-D Environmental Contour Model

In the 1-D EC model, the 10-min mean wind speed is modelled as random, whereas the standard deviation of the wind speed and the maximum response for the 10-min duration is kept at the median level. Considering the reliability index $\beta$ for a prescribed probability of exceedance and return period, the point corresponding to the failure probability in standard normal space can be obtained using the relation

$$u_1 = \beta,\ u_2 = u_3 = 0. \tag{6.8}$$

Further, the design point in relation to the nominal bending load in the physical random variable space is obtained using the Rosenblatt transformation given by

$$\phi(u_1) = F_V(v),\ \phi(u_2) = F_{H_s}(h_s),\ \phi(u_3) = F_{L_T}(l_T), \tag{6.9}$$

where $\phi$ is the standard normal cumulative distribution function and $F_v(v)$ is the standard normal cumulative distribution of mean wind speed $V$, which can be rewritten in the form

$$v = F_V^{-1}[\phi(\beta)],\ h_s = F_{H_s}^{-1}[\phi(0)],\ l_T = F_{L_T|V,H_s}^{-1}[\phi(0)]. \tag{6.10}$$

### 6.2.4 2-D Environmental Contour Model

The randomness for the environmental variables wind speed and the wind speed for the 10-min duration is modelled, and the maximum response is assumed deterministic at the median level. For the known reliability, a circle is generated in the standard normal space given by

$$u_1 = \beta\cos(\phi),\ u_2 = \beta\sin(\phi),\ u_3 = 0 \ \text{ for} - \pi \le \phi \le \pi. \tag{6.11}$$

As the circle lines in the plane, it is called the environmental contour as the circle is associated only with the random variables. To determine the design point on the circle, the Rosenblatt transformation is applied. The transformations are carried out for the environmental variables from u-space to the physical space using the relation

$$\phi(u_1) = F_V(v),\ \phi(u_2) = F_{H_s|V}(h_s),\ \phi(u_3) = F_{L_T|V,H_s}(l_T). \tag{6.12}$$

The standard normal cumulative distribution function of velocity $F_v(v)$ and the standard normal cumulative distribution function of wave height which is conditional on velocity $F_{H_s|V}(h_s)$, is rewritten in the form as

$$v = F_v^{-1}\left[\phi\left(\beta\cos(\phi)\right)\right], \tag{6.13}$$

$$h_s = F_{H_s}^{-1}\left[\phi\left(\beta\sin(\phi)\right)\right], \tag{6.14}$$

$$l_T = F_{l_T/v,H_s}^{-1}\left[\phi(0)\right]. \tag{6.15}$$

Every point on the transformed EC is such that the probability on the side of a tangent hyperplane at that point is the same, though each of those points is associated with a different median response.

### 6.2.5 3-D Environmental Contour Model

The 3-D model considers the randomness of all three environmental variables. So, for known reliability index $\beta$, a sphere can be constructed in the standard normal space using the relation

$$u_1 = \beta \sin(\phi)\sin(\theta),\ u_2 = \beta \cos(\phi),\ u_3 = \beta \sin(\phi)\cos(\theta) \quad \text{for} -\pi \le \phi \le \pi,\ -\pi \le \theta \le \pi. \quad (6.16)$$

Further, to calculate the design point, the complete sphere is examined for all values of $\theta$ and $\phi$. The Rosenblatt transformation yields the largest response value from the $U-$space using the relation

$$\phi(u_1) = F_v(v),\ \phi(u_2) = F_{H_s|V}(h_s),\ \phi(u_3) = F_{L_T|V,H_s}(l_T). \quad (6.17)$$

The standard normal cumulative distribution function of velocity $F_v(v)$ and the standard normal cumulative distribution function of wave height which is conditional on velocity $F_{H_s|V}(h_s)$, and the standard normal cumulative distribution of $l_T$ which is conditional on $v$ and $h_s$ is rewritten in the form as

$$v = F_v^{-1}\left[\phi\left(\beta \sin(\phi)\cos(\theta)\right)\right], \quad (6.18)$$

$$h_s = F_{H_s}^{-1}\left[\phi\left(\beta \cos(\phi)\right)\right], \quad (6.19)$$

$$l_T = F_{l_T/v,H_s}^{-1}\left[\phi\left(\sin(\phi)\cos(\theta)\right)\right]. \quad (6.20)$$

The three models discussed to calculate the extreme design points lead to different nominal loads. For any return period, for the 1-D and 2-D models, only slight variation can be observed because the standard deviation of the variable $V$ is unimportant compared to the mean wind speed $L_{10-\min}$. More differences can be observed for the 3-D model, as the short-term uncertainties are included in the model. The 2-D model is of much importance because the model uncouples the environment from the responses, which is more suitable when considering different wind turbines for specified environments.

### 6.2.6 Procedure to Develop 1-D and 2-D Models

A standard Gaussian Cumulative Distribution Function (CDF) is defined to develop the contour points using the IFORM. The exceedance probability is calculated using Eq. (5) to obtain the response level corresponding to a particular return period. The probability of exceedance is used to calculate the reliability, which is mapped on the standard Gaussian CDF to obtain the reliability index, $\beta$ as shown in Fig. 6.2(a). The reliability index $\beta$, considered for a probability of exceedance, is used in the EC method based on a particular target return period, given by the relation as in Eq. (6.6b) and Eq. (6.7). To generate the contour points, an inverse process is carried out to determine the radius of the circle (Fig. 6.2b), the reliability index $\beta$.

In the present study the model assumes mean wind speed to follow the Weibull distribution (Fig. 6.3a) and significant wave height is distributed like Normal distribution (Fig. 6.3b).

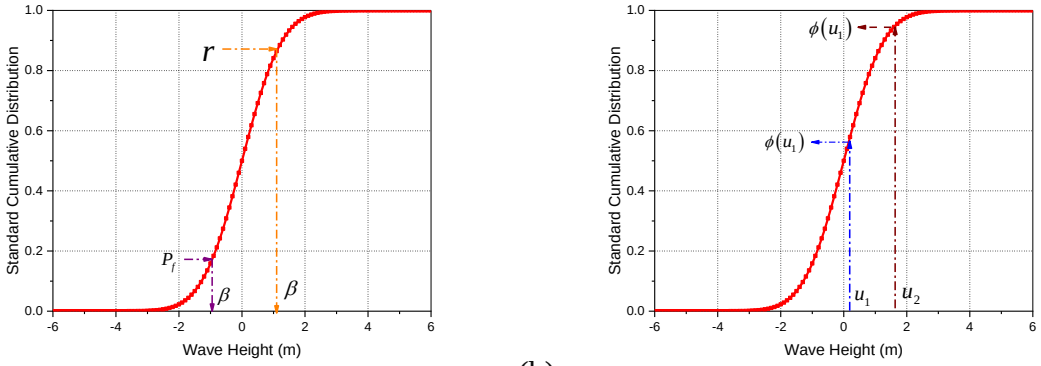


(a) (b)

Fig. 6.2: Cumulative distribution function of Standard Gaussian distribution to (a) Map the reliability index, and (b) Map the ordinates of the sphere.

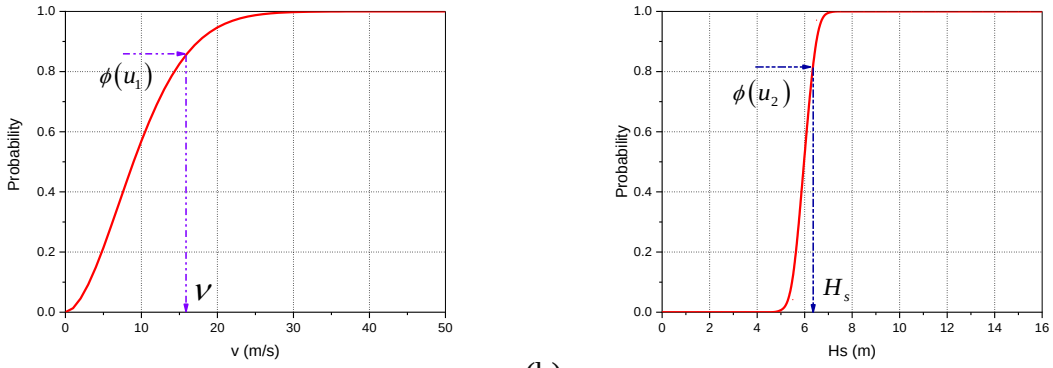


(a) (b)

Fig. 6.3: Transformation of Environmental variables using (a) Weibull distribution and (b) Normal Cumulative Distribution Function.

The present study considers five return periods 1-Year, 10-Year, 20-Year, 50-Year, and 100-Year, for the 1-D and 2-D models. The exceedance probability for the corresponding return periods considered are $1.9026\times10^{-5}$, $1.9026\times10^{-6}$, $9.5219\times10^{-7}$, $3.8052\times10^{-7}$, $1.9026\times10^{-7}$, for $\beta=4.1190$, $\beta=4.6217$, $\beta=4.7635$, $\beta=4.9451$, $\beta=5.0785$. The mean wave heights corresponding to different return periods for various 10-min mean wind speeds is obtained using the 1-D method as shown in Fig. 6.4 (a). Further, The EC based on the 2-D method (Fig. 6.4b) is developed using the five return periods, where the contour points are characterised by the combination of mean wind speed and significant wave height. The coupled aero-servo-hydro-elastic analysis for the hybrid platforms is carried out for various extreme environmental conditions (wind and wave) obtained from the 1-D and 2-D EC models.

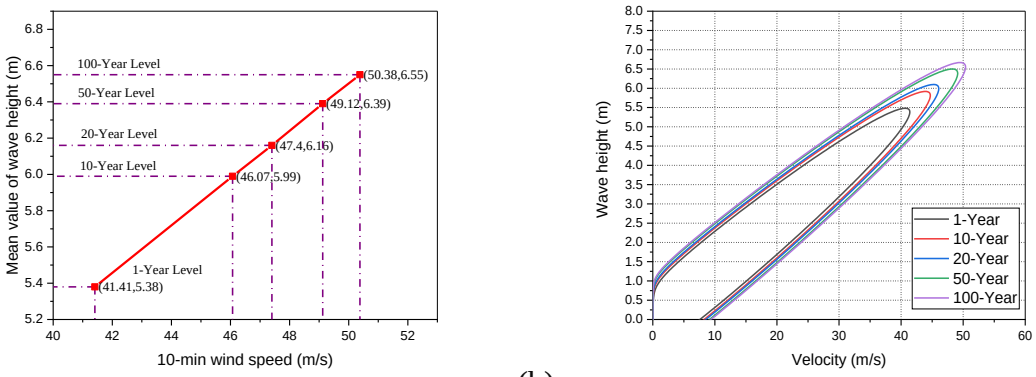


(a) (b)

Fig. 6.4: The (a) 1-D and (b) 2-D based EC for 1-Year, 10-Year, 20-Year, 50-Year, and 100-Year return period.

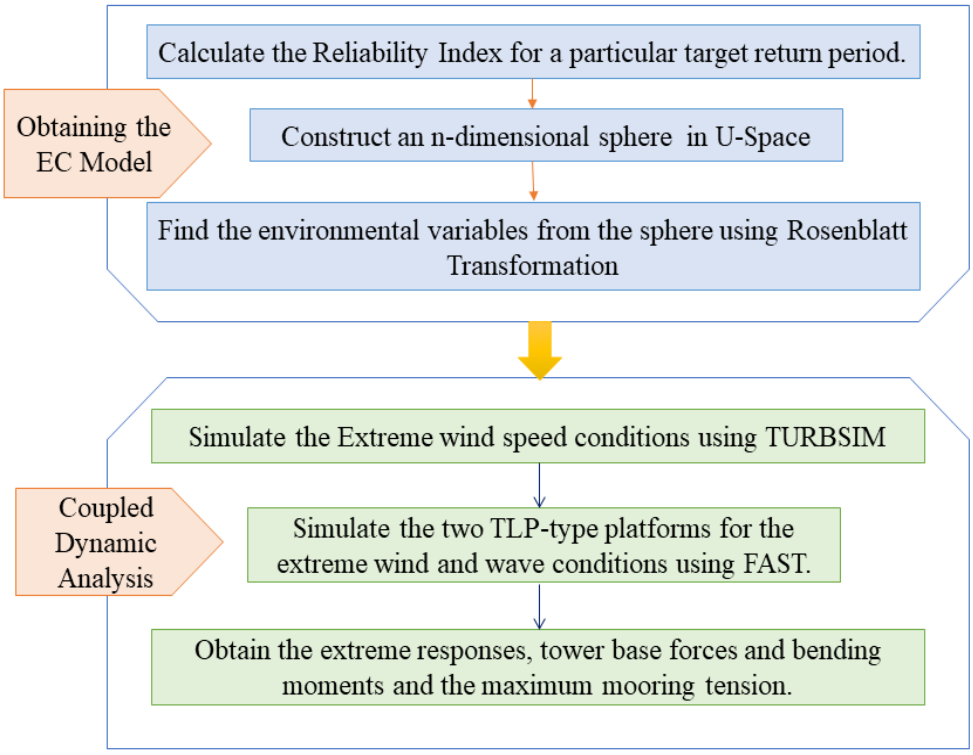


Fig. 6.5: Flow chart depicting methodology for the long-term response analysis.

The linearised hydrodynamic radiation and diffraction problems for the hybrid FOWT interacting with the surface waves are solved using WAMIT. Therafter, the fully coupled aero-hydro-servo-elastic simulation program FAST is employed to perform the time domain analysis for the hybrid FWT platforms. Morison's equation is used by the FAST to compute the hydrodynamic loads and trigger stochastic time-domain turbine response. The realistic wind data, including the turbulence intensity and the wind speed profiles for the FAST

program, are generated using the simulation tool TURBSIM. The study examines the dynamic responses of the hybrid floating platform to extreme wind speed conditions to study the stability of the floating system. Further, the forces and moments developed at the base of the turbine tower for different wind speed conditions of the 1-D and 2-D EC models are studied to observe the influence of the wind loading on the floating turbine system. The study also focuses on the extreme tension developed on each mooring cable for the hybrid platforms to observe the importance of the tensioned tendons providing for the stability of the floating system. The flow chart detailing the methodology adopted is shown in Fig. 6.5.

## 6.3 GEOMETRIC MODEL

The extreme responses of the hybrid STLP-WEC and hybrid FTLP-WEC for extreme wind and wave conditions are obtained from the 1-D and 2-D EC models. The hybrid floating platforms are studied for 150 m water depth. The dimension of the STLP and FTLP along with the heaving cone-cylinder point absorber WEC is discussed in Chapter 1. The rigid body analysis observed a reduction in the responses of the hybrid floating systems when the WECs were provided in a circular pattern around the WECs.

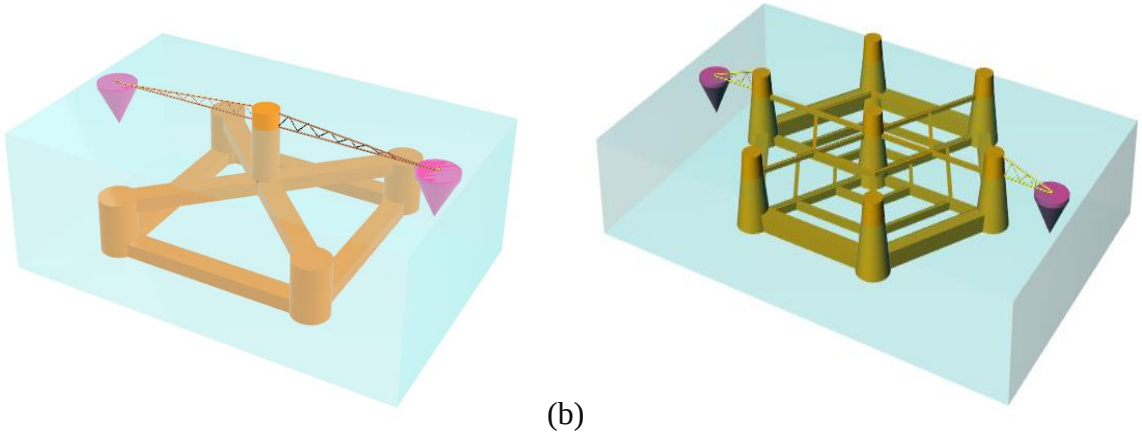

(a) (b)

Fig. 6.6: Geometric representation of (a) STLP and (b) FTLP combined with heaving cone-cylinder WECs.

The present study considers the single STLP, FTLP and the hybrid STLP+2WECs, STLP+4WECs, STLP+6WECs, STLP+8WECs, FTLP+2WECs (FTLP+2WECx), FTLP+4WECs, FTLP+6WECs and FTLP+8WECs for the extreme response analysis. The arrangement pattern of the WECs around the STLP and the FTLP is detailed in Chapter 1. The hybrid floating platforms are designed to support the NREL 5 MW wind turbine. The properties and the structural details of the 5 MW wind turbine are also detailed in Chapter 1. Fig. 6.6

shows a pictorial representation of the hybrid STLP-WEC (STLP+2WECs) and the hybrid FTLP-WEC (FTLP+2WECs).

## 6.4 RESULTS AND DISCUSSION

The reliability analysis of the hybrid offshore wind turbine is carried out using 1-D and 2-D EC models using IFORM. The study uses a 5 MW NREL wind turbine to observe the extreme loads. The significant wave height and the wind speed obtained from the environmental contours are used for the simulation of the 10-min wind speed. The different circular arrangements of cone-cylinder-shaped heaving point absorber WECs around both STLP and FTLP are used for the analysis, and contour points corresponding to 1-year, 10-year, 20-year, 50-year, and 100-year return periods are obtained.

### 6.4.1 Extreme Response Analysis using 1-D and 2-D EC Models

The design of the floating platform is improved with the help of extreme response analysis. It aids in the identification of crucial parts and weak spots to make the required design adjustments to increase performance and safety while lowering costs. The study proposes using the IFORM for the extreme response analysis. The first-order inverse reliability approach is a method for evaluating a structure's dependability by calculating the probability of failure under specific conditions of high loading. Assessing a structure's extreme reaction is the objective of this iterative approach, which considers the uncertainty in input parameters. Table 6.1 – Table 6.3 shows the extreme surge, sway and yaw response using 1-D and 2-D EC models for different return periods. The responses are observed to be slightly higher for the 1-D EC model compared to the 2-D model. This may be due to the fact that, the 1-D EC model uses single scalar environmental loads, significant wave height or wind speed, further not capturing the variability of the environmental conditions, leading to a simplified representation of loads. However the 2-D EC model considers different environmental variables like wave height and wave period, wind speed and wave height or wind speed and wind direction, thus providing a more comprehensive description of the environmental loads. Also, in the 1-D model, the marginal distribution of the individual variables is used to derive the extreme responses, whereas the 2-D model considers joint extreme value statistics. Further, the 1-D model underestimates the combined influence of extreme conditions. Table 6.1 shows the surge response motion of STLP and hybrid STLP-WEC floating platforms. The extreme responses are observed to decrease with the addition of the WECs. Also, the responses are observed to

decrease for the waves of the higher return period. For the 1-Year return period waves, the responses are minimal for the hybrid STLP+6WECs configuration. But for waves of higher return periods, the extreme surge response is minimal for STLP+8WECs. Table 6.2 shows the extreme sway response motion for waves of various return periods. Similar to the surge response, the sway response is observed to be minimised with the addition of the WECs. In addition, the sway response tends to reduce for the waves of higher return periods.

Table 6.1: Surge response for extreme wind speed conditions of 1-D and 2-D EC models.

| Configurations | 1-Yr Return Period | | 10-Yr Return Period | | 20-Yr Return Period | | 50-Yr Return Period | |
|---|---|---|---|---|---|---|---|---|
| | 1-D | 2-D | 1-D | 2-D | 1-D | 2-D | 1-D | 2-D |
| STLP | 7.98 | 7.78 | 7.38 | 7.20 | 7.40 | 7.22 | 7.53 | 7.35 |
| STLP+2WECs | 8.20 | 8.07 | 7.74 | 7.63 | 7.73 | 7.62 | 7.83 | 7.71 |
| STLP+4WECs | 7.98 | 7.73 | 8.76 | 8.49 | 8.77 | 8.51 | 8.80 | 8.54 |
| STLP+6WECs | 4.45 | 4.41 | 5.67 | 5.62 | 5.74 | 5.69 | 6.02 | 5.97 |
| STLP+8WECs | 4.72 | 4.61 | 3.26 | 3.18 | 3.28 | 3.21 | 3.60 | 3.52 |

Table 6.2: Sway response for extreme wind speed conditions of 1-D and 2-D EC models.

| Configurations | 1-Yr Return Period | | 10-Yr Return Period | | 20-Yr Return Period | | 50-Yr Return Period | |
|---|---|---|---|---|---|---|---|---|
| | 1-D | 2-D | 1-D | 2-D | 1-D | 2-D | 1-D | 2-D |
| STLP | 9.52 | 9.29 | 8.71 | 8.50 | 8.77 | 8.56 | 8.64 | 8.43 |
| STLP+2WECs | 5.18 | 5.10 | 4.91 | 4.84 | 5.04 | 4.97 | 5.20 | 5.13 |
| STLP+4WECs | 4.20 | 4.08 | 4.86 | 4.71 | 4.88 | 4.73 | 4.80 | 4.65 |
| STLP+6WECs | 4.45 | 4.42 | 4.60 | 4.56 | 4.68 | 4.63 | 5.00 | 4.95 |
| STLP+8WECs | 4.03 | 3.94 | 4.32 | 4.22 | 4.39 | 4.29 | 4.90 | 4.79 |

The hybrid STLP+8WECs configuration is observed to have minimum sway motion response for any environmental conditions. Reduced surge and sway motion on the floating platform ensures minimum chances of premature fatigue failure with the minimum dynamic load on the structural components of the wind turbine. Also, reduced lateral movements can reduce the stress concentration at the mooring connections and the structural joints. Environmental factors provide operational boundaries for floating platforms beyond which their ability to operate safely is affected. The reduced surge and sway motion allows the platform to operate within a wider operating perimeter and offers more flexibility in terms of operational circumstances.

Table 6.3: Yaw response for extreme wind speed conditions of 1-D and 2-D EC models.

| Configurations | 1-Yr Return Period | | 10-Yr Return Period | | 20-Yr Return Period | | 50-Yr Return Period | |
|---|---|---|---|---|---|---|---|---|
| | 1-D | 2-D | 1-D | 2-D | 1-D | 2-D | 1-D | 2-D |
| STLP | 45.31 | 44.20 | 50.85 | 49.61 | 51.40 | 50.15 | 53.35 | 52.05 |
| STLP+2WECs | 45.47 | 44.80 | 49.20 | 48.47 | 49.78 | 49.04 | 51.70 | 50.94 |
| STLP+4WECs | 35.65 | 34.58 | 40.63 | 39.41 | 41.11 | 39.87 | 42.61 | 41.33 |
| STLP+6WECs | 30.41 | 30.14 | 32.66 | 32.37 | 33.02 | 32.73 | 34.45 | 34.14 |
| STLP+8WECs | 25.39 | 24.82 | 26.17 | 25.58 | 26.57 | 25.97 | 27.36 | 26.74 |

Table 6.3 shows the extreme yaw motion response for the STLP and hybrid STLP-WEC floating platforms. The yaw motion responses are comparatively higher than the roll and pitch motion responses for an STLP-type floating platform. The STLP may have an increased tendency to yaw in response to environmental influences like waves and currents due to the unequal buoyancy distribution. A fully floating TLP, where buoyancy is distributed evenly, may not have any yawing moments since the submerged portion of the platform acts as a drag and generates yawing moments instead. Similar to the surge and sway responses, the yaw motion is also reduced by adding the WECs. Minimum yaw motion response is observed for the STLP+8WECs hybrid floating platform.

Table 6.4 – Table 6.6 shows the surge, sway and yaw motion responses for the FTLP and hybrid FTLP-WEC floating platforms for different return period waves. Similar to the STLP, the responses are slightly higher for the 1D EC model than for the 2D EC model. Table 6.4 shows the surge response motion for the FTLP and hybrid FTLP-WEC. With the addition of the WECs, the responses are observed to minimise.

Table 6.4: Surge response for extreme wind speed conditions of 1-D and 2-D EC models

| Configurations | 1-Yr Return Period | | 10-Yr Return Period | | 20-Yr Return Period | | 50-Yr Return Period | |
|---|---|---|---|---|---|---|---|---|
| | 1-D | 2-D | 1-D | 2-D | 1-D | 2-D | 1-D | 2-D |
| FTLP | 20.47 | 20.04 | 17.88 | 17.51 | 24.66 | 24.15 | 22.53 | 22.06 |
| FTLP+2WECs | 16.57 | 16.00 | 18.25 | 17.63 | 20.74 | 20.03 | 20.77 | 20.06 |
| FTLP+4WECs | 18.73 | 18.27 | 21.45 | 20.92 | 20.70 | 20.19 | 22.50 | 21.94 |
| FTLP+6WECs | 17.27 | 16.94 | 16.91 | 16.58 | 19.18 | 18.81 | 20.80 | 20.40 |
| FTLP+8WECs | 16.57 | 16.39 | 18.75 | 18.55 | 20.06 | 19.84 | 21.08 | 20.85 |

Table 6.5: Sway response for extreme wind speed conditions of 1-D and 2-D EC models.

| Configurations | 1-Yr Return Period | | 10-Yr Return Period | | 20-Yr Return Period | | 50-Yr Return Period | |
|---|---|---|---|---|---|---|---|---|
| | 1-D | 2-D | 1-D | 2-D | 1-D | 2-D | 1-D | 2-D |
| FTLP | 2.51 | 2.46 | 2.84 | 2.78 | 2.61 | 2.56 | 2.84 | 2.78 |
| FTLP+2WECs | 3.01 | 2.90 | 3.40 | 3.28 | 3.33 | 3.21 | 2.40 | 2.32 |
| FTLP+4WECs | 2.08 | 2.03 | 2.24 | 2.18 | 2.31 | 2.25 | 2.36 | 2.31 |
| FTLP+6WECs | 1.99 | 1.95 | 4.65 | 4.56 | 1.96 | 1.93 | 2.24 | 2.20 |
| FTLP+8WECs | 1.98 | 1.96 | 1.73 | 1.72 | 2.16 | 2.14 | 2.28 | 2.25 |

Also, for waves of higher return periods, the responses are observed to decrease for the FTLP and hybrid FTLP-WEC platforms. Like the surge response, the sway response (Table 6.5) is also reduced for the hybrid system, apart from the FTLP+2WECs configuration. This may be because, for the FTLP+2WECs platform, the WECs are placed in the direction of the waves. Further, having minimum chances of restoring forces from the lateral direction. For other hybrid platforms, the responses are observed to reduce. The surge responses are higher for the FTLP and FTLP-WEC hybrid systems than the STLP and STLP-WEC hybrid platforms.

Table 6.6: Yaw response for extreme wind speed conditions of 1-D and 2-D EC models.

| Configurations | 1-Yr Return Period | | 10-Yr Return Period | | 20-Yr Return Period | | 50-Yr Return Period | |
|---|---|---|---|---|---|---|---|---|
| | 1-D | 2-D | 1-D | 2-D | 1-D | 2-D | 1-D | 2-D |
| FTLP | 0.42 | 0.41 | 0.16 | 0.15 | 0.43 | 0.42 | 0.29 | 0.28 |
| FTLP+2WECs | 0.12 | 0.12 | 0.36 | 0.35 | 0.05 | 0.05 | 0.20 | 0.19 |
| FTLP+4WECs | 0.18 | 0.18 | 0.16 | 0.15 | 0.18 | 0.17 | 0.17 | 0.16 |
| FTLP+6WECs | 0.12 | 0.12 | 0.19 | 0.19 | 0.12 | 0.12 | 0.16 | 0.16 |
| FTLP+8WECs | 0.11 | 0.11 | 0.14 | 0.14 | 0.13 | 0.13 | 0.18 | 0.18 |

The higher surge motion of the FTLP may be because of the higher wave load developing on the portions of the outer pontons which lie above the MSL. But for the STLP, only a minimum portion of the system lies above MSL, leading to reduced wave influence, further resulting in reduced surge motion. Table 6.6 shows the yaw motion response for the FTLP and hybrid FTLP-WEC platforms. The yaw motion responses of the FTLP are minimal compared to the STLP platform (Table 6.3). The reduced yaw motion ensures minimal lateral load developing on the mooring cables of the floating system, further reducing the risk of fatigue failure of the

tensioned tendons. Also, minimum yaw response ensures a safer working environment for the maintenance of the system.

The variation in the surge and sway motion is not much significant while comparing the hybrid platforms for both STLP and FTLP. This may be because of the reduced mass of the point absorber WEC system compared to the single floating platform. Also, the addition of point absorber WECs to the STLP and FTLP may not significantly alter the overall mooring system design or layout. Hence the mooring system can efficiently accommodate the additional load developed by the WECs, resulting in the minimum variation in the surge and sway motion response. Further, the cone-cylinder point absorber WECs may act as stabilizing elements, dampening the surge and sway motion of the STLP and FTLP by absorbing energy from the waves. This stabilizing effect could counteract any additional motion induced by the presence of the WECs, resulting in only minor variations in surge and sway motion.

### 6.4.2 Extreme Motion Response using 2-D EC Model

The maximum loads that the platform can withstand under adverse environmental circumstances can be determined with the help of extreme motion responses. The maximum load capabilities can only be determined with the use of this data, which is also essential for designing components that can withstand these incredibly high loads without affecting the functionality or safety. Fig. 6.7(a-e) shows the maximum surge response motion for different wind speed conditions of 1-Year, 10-year, 20-Year, 50-Year, and 100-year return period waves. The surge responses are observed to increase with the increase in the wind speed condition. Further, apart from the higher wind speed condition, the STLP+2WECs are observed to have higher surge response motion. The STLP+4WECs, STLP+6WECs and STLP+8WECs have reduced surge response motion compared to the STLP. Fig. 6.7(a) shows the surge response motion for the waves of 1-year return period. The STLP+6WECs and STLP+8WECs configurations are observed to have minimum response motions compared to other hybrid platforms. Further, for waves of higher return periods, the surge response for the STLP+8WECs is minimal compared to other hybrid concepts. Fig. 6.7(b) shows the surge response motion for the 10-year return period waves. The STLP and STLP+4WEC configuration has a similar response pattern as compared to other hybrid STLP-WEC platforms. The STLP+6WECs and STLP+8WECs vary greatly in the surge response pattern for the 10-Year return period waves. Fig. 6.7(c) shows the surge response motion for the 20-Year return period of waves. The surge response is observed to reduce for the 20-Year return

period condition compared to the 1-Year and 10-Year return period conditions for STLP+2WECs and is observed to increase for STLP+6WECs.

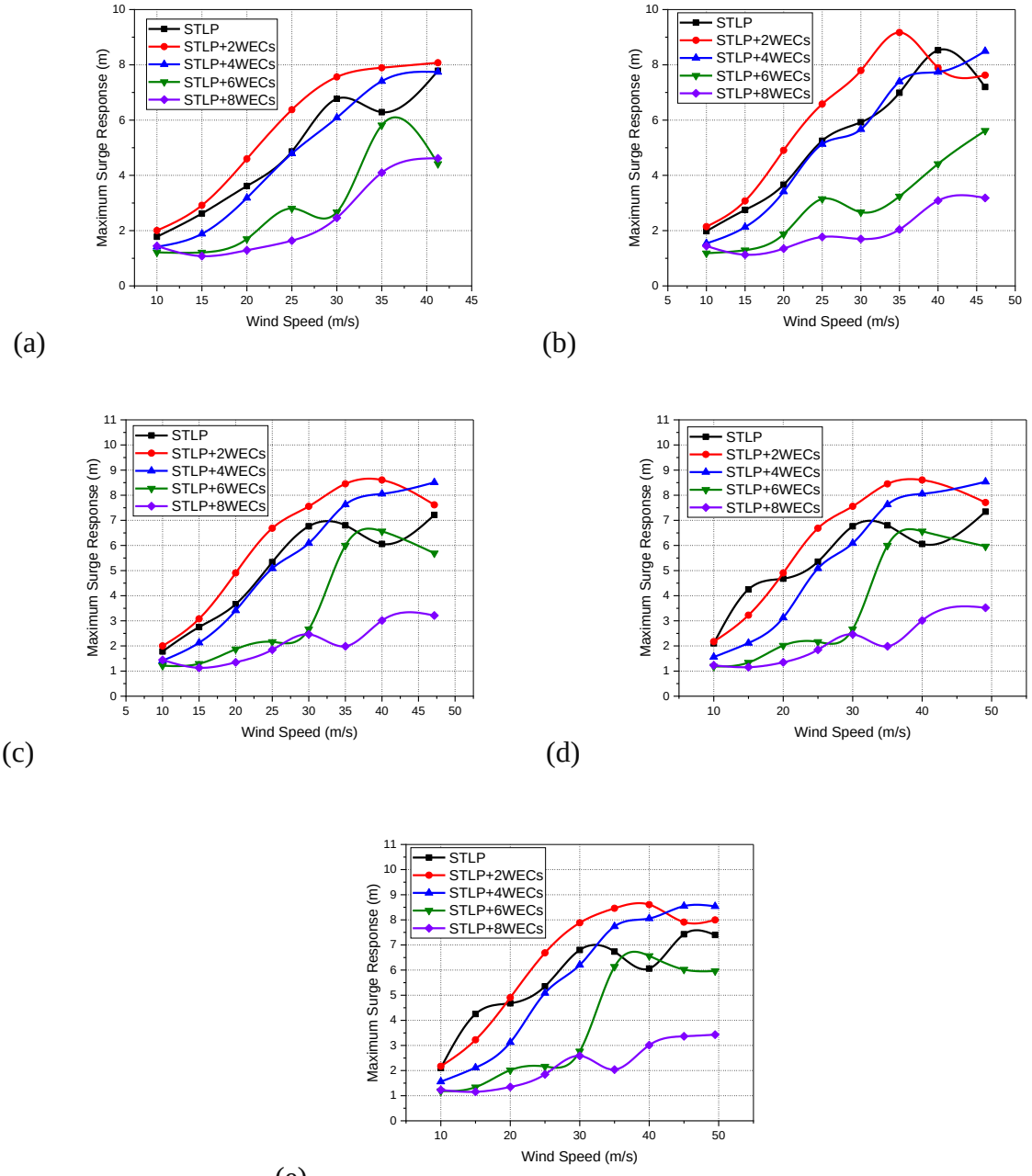


Fig. 6.7: Extreme surge response of STLP-WEC hybrid system for (a) 1-Year, (b) 10-Year, (c) 20-Year, (d) 50-year, and (e) 100-Year return period.

In the case of wind speed above 35 m/s, the surge responses of the STLP+4WECs are observed to be higher, though the variation in surge response for the STLP and STLP+4WECs is minimum for the operational wind speed conditions (3 to 25 m/s). The 50-Year (Fig. 6.7d) and 100-Year (Fig. 6.7e) return period conditions shows similar variation in the surge response

motion with the 20-Year conditions. For the 10 m/s wind speed conditions, the surge responses of the STLP and hybrid STLP-WEC have minimal variation for any return periods.

Fig. 6.8(a-e) shows the sway motion response for different wind speed conditions of 2-D EC model developed for 1-Year, 10-Year, 20-Year, 50-Year, and 100-Year return periods. Like the surge motion response, the sway motion response also increases with the increase in wind speed. For the 1-Year (Fig. 6.8a) and 10-Year (Fig. 6.8b) return period conditions, the sway responses are minimum for the STLP floating platform compared to the other hybrid configurations. For other higher return periods, the STLP+2WECs are observed to have higher sway motion response for 35 m/s wind speed conditions (Fig. 6.8c,d,e) compared to the single STLP floater. Further, the variation in the sway motion is minimum for the hybrid concepts which may be due to the wave motion in the positive x-direction. Minimum sway motion is observed for STLP+8WECs configuration. The STLP+8WECs are observed to have minimum translational motion compared to other hybrid concepts. Reducing lateral movements to a minimum keeps the wind turbine's orientation steady in relation to the direction of the wind, improving aerodynamic efficiency and energy output.

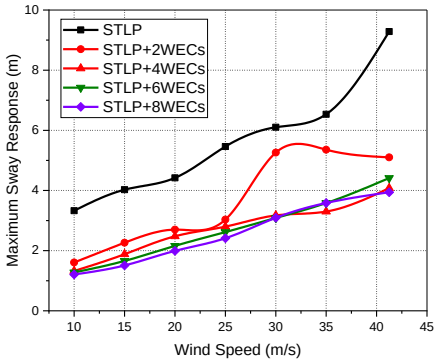


(a)

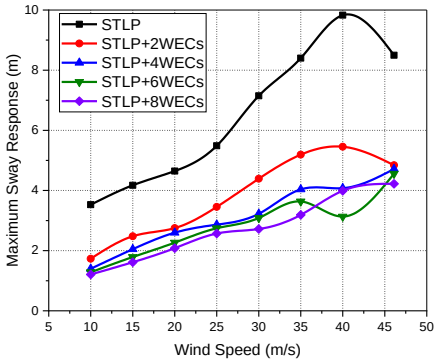


(b)

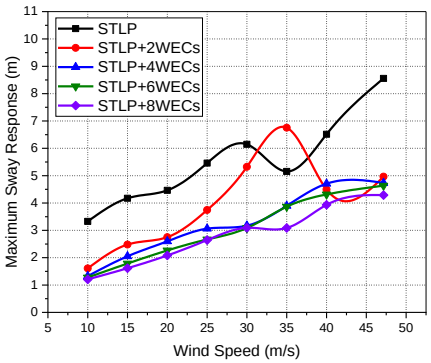


(c)

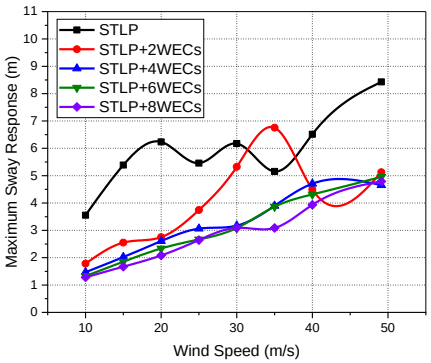


(d)

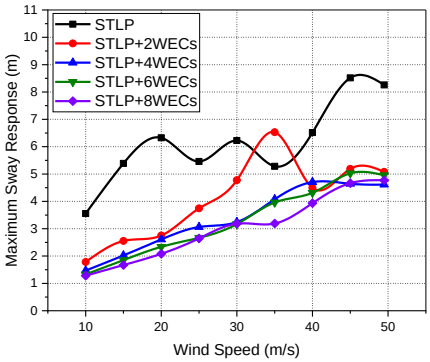


(e)

Fig. 6.8: Extreme sway response of STLP-WEC hybrid system for (a) 1-Year, (b) 10-Year, (c) 20-Year, (d) 50-year, and (e) 100-Year return period.

Fig. 6.9(a-e) shows the yaw motion response for the STLP and hybrid STLP-WEC platforms for waves of different return periods. Similar to surge and sway motion, the yaw motion responses increases with the increase in the wind speed condition. Also, it is observed that the yaw motion responses are reduced with the addition of the WECs with the STLP. This may be due to the additional stiffness the WECs offer to the single STLP. Further, WEC kept in line with the MSL may provide additional resistance to the wave load developing on the platform. Fig. 6.9(a) shows the yaw motion response for different wind speed conditions of the EC developed for the 1-Year return period. A steep increase in the yaw response is observed for the increase in the wind speed conditions. A variation in the sway motion responses is observed for the parked conditions of the wind turbine for the waves of the 10-Year return period (Fig. 6.9b). The STLP and STLP+2WECs are observed to have similar yaw motion responses for the parked wind speed condition. For STLP, STLP+2WECs, and STLP+6WECs, the sway motion tends to decrease for extreme wind speed conditions.

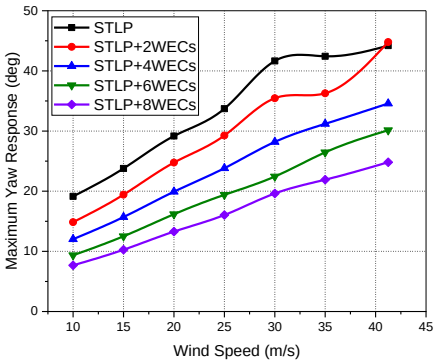


(a)

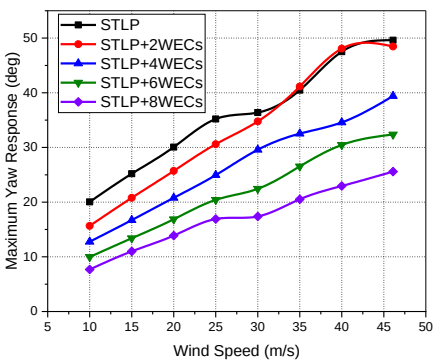


(b)

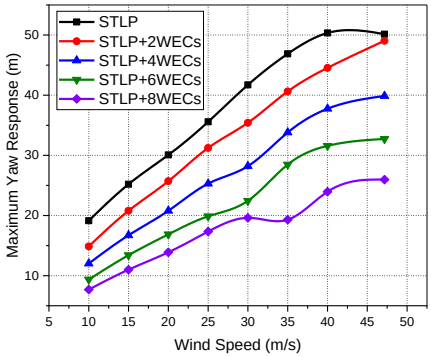


(c)

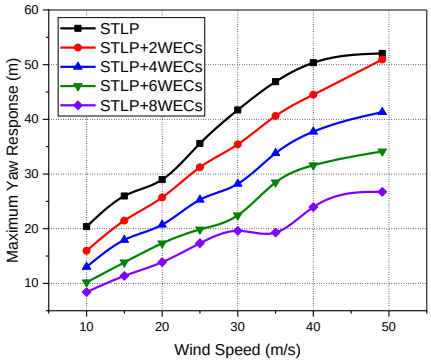


(d)

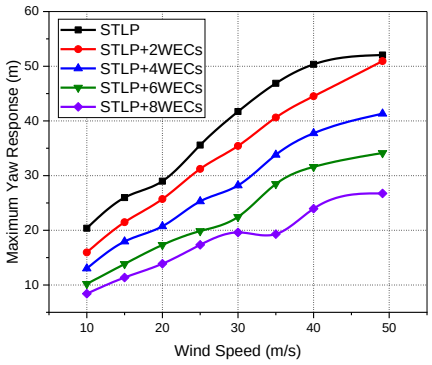


(e)

Fig. 6.9: Extreme yaw response of STLP-WEC hybrid system for (a) 1-Year, (b) 10-Year, (c) 20-Year, (d) 50-year, and (e) 100-Year return period.

The reduced sway motion for the extreme condition reduces dynamic load for the parked condition of the 5 MW wind turbine. Fig. 6.9(c) shows the yaw motion response for the 20-Year return period comparing different configurations of STLP and hybrid STLP-WEC.The yaw motion responses are observed to increase steeply with the increase in wind speed. Similar variation in yaw response is observed for the 50-Year (Fig. 6.9d) and 100-Year (Fig. 6.9e) models.

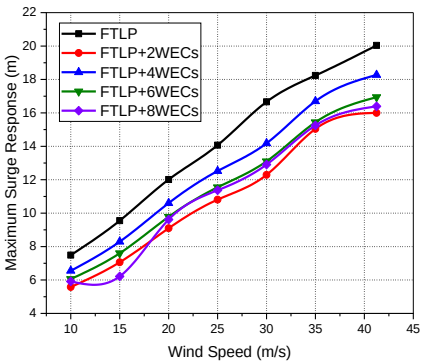


(a)

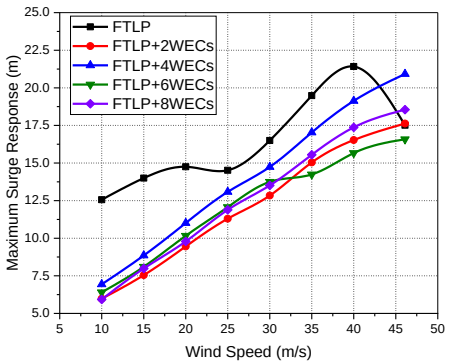


(b)

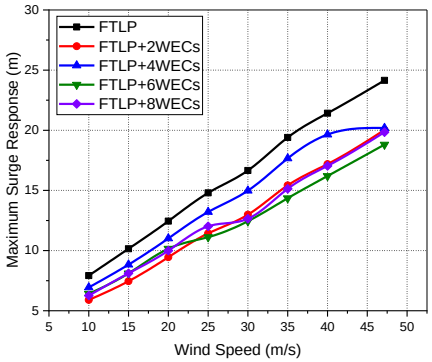


(c)

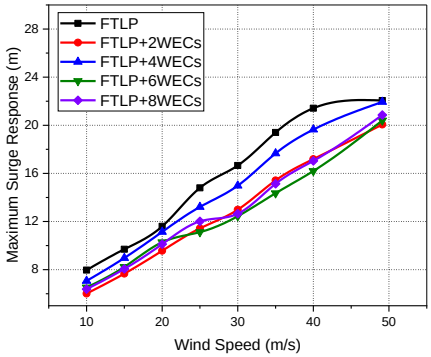


(d)

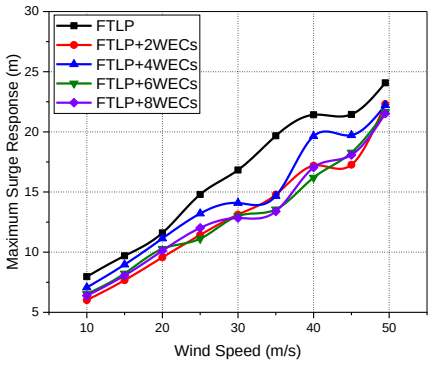


(e)

Fig. 6.10: Extreme surge response of FTLP-WEC hybrid system for (a) 1-Year, (b) 10-Year, (c) 20-Year, (d) 50-year, and (e) 100-Year return period.

Turbulence and uneven wind flow effects on the wind turbine could be considerably severe by yaw motion. The wind turbine may operate under more stable and predictable wind conditions by reducing yawing, which improves overall performance. Fig. 6.10(a-e) shows the extreme surge motion response of FTLP and hybrid FTLP-WEC developed from the EC models of 1-Year, 10-Year, 20-Year, 50-Year, and 100-Year return periods. The variation in the surge motion response with the addition of the WECs is observed to be minimal. The cone-cylinder WECs can dampen waves by absorbing some energy. The damping effect reduces motions brought on by waves, particularly surge motions. Adding WECs can result in more consistent surge motion responses by lessening the effect of waves on the platform. Fig. 6.10(a) shows the extreme surge motion response for the 1-Year return period waves. The responses are observed to increase with the change in the environmental variables (increase in the wind speed and wave height). The FTLP+2WECs are observed to have minimum surge motion response, though the variation in the surge motion response between FTLP+6WECs and FTLP+8WECs is minimal. Fig. 6.10(b) shows the extreme surge motion response for the 10-Year return period

waves. The variation is observed to be higher for the FTLP platform for the 10-Year. The hybrid concepts were observed to have minimum variation in the surge motion for the increase in the wind speed condition. The FTLP+2WECs are observed to have minimum surge motion response for the operational conditions. For the parked wind speed condition, the FTLP+6WECs are observed to have minimum surge motion response. Fig. 6.10(c) shows the extreme surge motion response for a 20-Year return period. The STLP+2WECs are observed to have minimum surge response for wind speed conditions below 25 m/s. For further wind speed conditions, the surge motion responses are minimum for FTLP+6WECs configuration. Also, FTLP+8WECs are observed to have reduced surge motion response for wind speed conditions above 24 m/s. Similar variation in the surge motion is observed for the 50-Year return period waves (Fig. 6.10d). The comparatively higher variation in surge response is observed for the hybrid concepts for the parked wind speed conditions of a 5 MW wind turbine (above 30 m/s). The FTLP+2WECs are observed to have minimum surge motion response for the operational wind speed conditions. But for the parked condition, the translational motion response is minimal for FTLP+6WECs and FTLP+8WECs. The hydrodynamic characteristics of the platform can change in the presence of cone-cylinder WECs, affecting its pitch and heave responses. Since pitch and heave motions can cause surge motions in certain wave circumstances, the decreased pitch and heave motions help to provide more stable surge motion behaviour.

Fig. 6.11(a-e) shows the yaw motion response for the different wind speed conditions for 1-Year, 10-Year, 20-Year, 50-Year, and 100-Year 2-D EC models. The sway responses are observed to be minimum for the hybrid FTLP-WEC compared to the single FTLP concept apart from the FTLP+2WECs configuration. Fig. 6.11(a) shows the sway response motion for the 1-Year EC model. Higher sway motions are observed for the FTLP and FTLP+2WECs. The responses are observed to reduce for the four, six and eight WECs configuration. This may be because, for the STLP+2WECs configuration, the restoring force may be minimum as no WECs are provided in the lateral direction with waves travelling along the positive x-direction. Similar variation in sway response is observed for other return period models. FTLP+4WECs, FTLP+6WECs and FTLP+8WECs are observed to have minimal variation in the sway motion response for the 1-Year return period waves. Fig. 6.11(b) shows the surge motion response for the 10-Year return period waves. A higher variation in surge motion is observed for the FTLP, FTLP+2WECs and FTLP+6WECs. The FTLP is observed to have a higher sway motion response for wind speed below 25 m/s, and it is observed to reduce for the higher wind speed

conditions. For FTLP+2WECs and FTLP+6WECs, the sway motion increases for wind speed above 25 m/s, reaches a maximum of 35 m/s and then reduces for higher wind speed conditions.

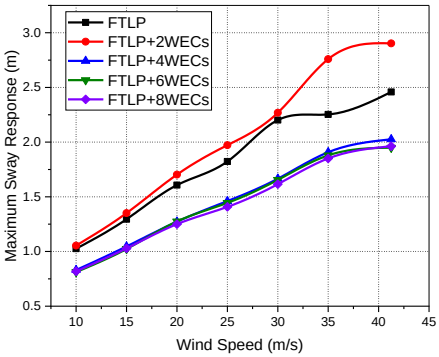


(a)

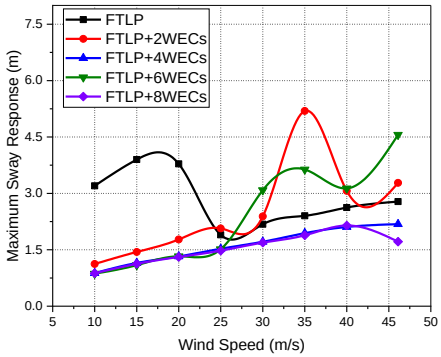


(b)

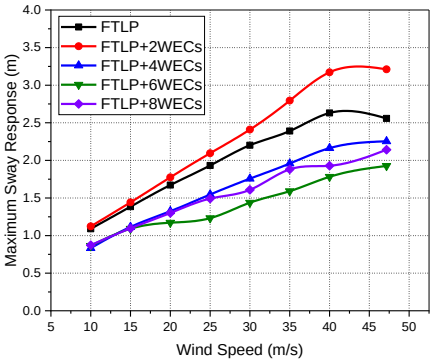


(c)

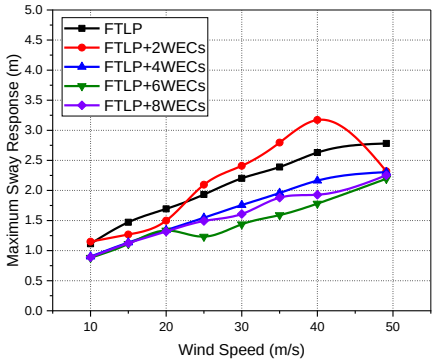


(d)

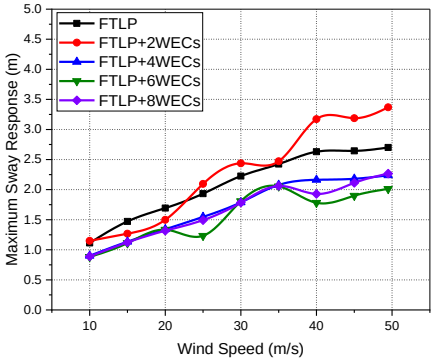


(e)

Fig. 6.11: Extreme sway response of FTLP-WEC hybrid system for (a) 1-Year, (b) 10-Year, (c) 20-Year, (d) 50-year, and (e) 100-Year return period.

The FTLP+4WECs and FTLP+8WECs are observed to have minimum sway motion for waves of a 10-Year return period. Fig. 6.11(c) shows the sway motion response for the 20-Year return period EC model. The variation in the sway responses is minimal for the 20-year return period waves, with maximum responses for the FTLP+2WECs and minimum for the FTLP+8WECs.

For the 50-Year (Fig. 6.11d) and 100-Year (Fig. 6.11e) 2-D EC model, the variation is similar for the operational wind speed conditions. But for the survival and parked conditions of the wind turbine, the sway responses of the FTLP+2WECs are higher for the 50-Year return period and are reduced for the 100-Year return period waves. Minimal sway responses are observed for the FTLP+6WECs configuration. The efficient conversion of wind energy into electricity is aided by stable sway motions. Reduced sway motion increases the wind turbine's ability to gather energy and provide more electricity overall, lessening the hybrid platform's environmental effect.

Fig. 6.12(a-e) shows the Yaw motion responses for the FTLP and hybrid FTLP-WEC for different wind speed conditions of 1-Year, 10-Year, 20-Year, 50-Year, and 100-Year return period 2-D EC models. The addition of the WECs is observed to have a stronger influence on the yaw motion response of the FTLP platform. The yaw motions responses are reduced by adding the WECs to the FTLP platform. Apart from the 10-Year EC model, the FTLP has minimal yaw motion for the operating wind speed conditions and is observed to increase for the wind speed conditions above 25 m/s (parked condition). Fig. 6.12(a) shows the variation in the yaw motion responses for the different wind speed conditions of the 1-Year 2-D EC model. The yaw motion responses have minimal variation for the operational wind speed conditions. Further, for the parked conditions of the wind turbine, a higher variation is observed for the FTLP+2WECs and FTLP+4WECs. The FTLP+8WECs are observed to have minimum sway motion response. However, for the 10-Year EC model, the variation in the sway motion responses is higher for the parked condition of the hybrid FTLP-WECs (Fig. 6.12b). The sway motion response for the FTLP+2WECs increases for the two WECs configuration of FTLP. Yaw motion for the 20-Year return period model varies for the parked conditions (Fig. 6.12c).

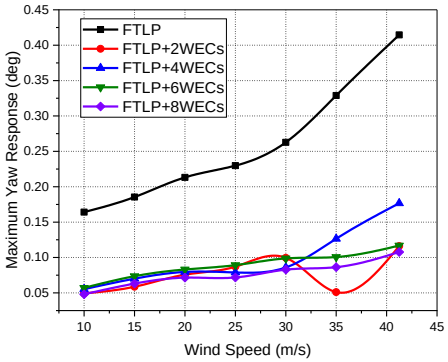


(a)

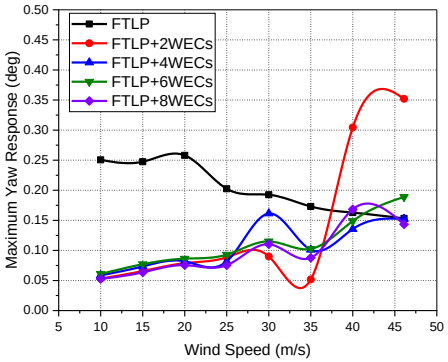


(b)

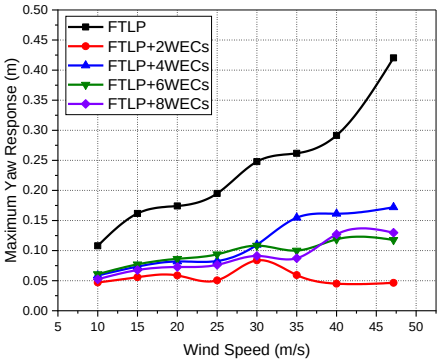


(c)

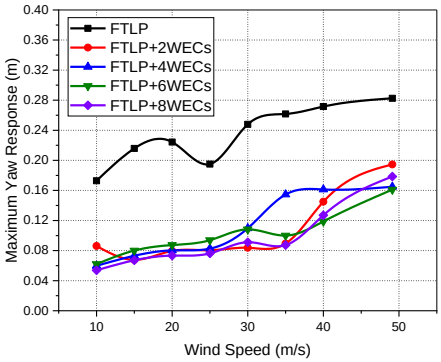


(d)

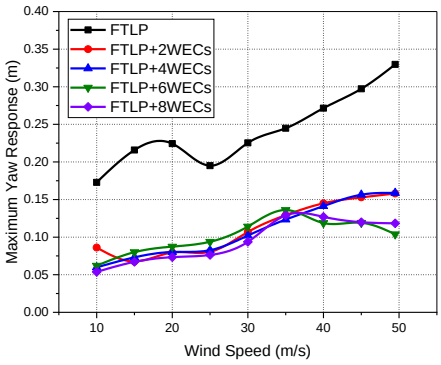


(e)

Fig. 6.12: Extreme Yaw response of FTLP-WEC hybrid system for (a) 1-Year, (b) 10-Year, (c) 20-Year, (d) 50-year, and (e) 100-Year return period.

The responses were observed to increase for the 30 m/s wind speed conditions for the hybrid FTLP-WECs. Further, the yaw motion responses reduce for the FTLP+2WECs configuration for higher wind speed conditions. For the FTLP+4WECs, FTLP+6WECs and FTLP+8WECs, the responses increase for wind speed conditions above 40 m/s. Similar variations in yaw responses are observed for the 50-Year (Fig. 6.12d) and 100-Year (Fig. 6.12e) return period models. The yaw motion responses of the hybrid platforms have higher variation for the wind speed above 30 m/s wind speed conditions. The responses are observed to increase for the 50-Year return period model. The FTLP++WECs and FTLP+8WECs have reduced yaw motion response for wind speed above 40 m/s for the 100-year return period model.

For offshore floating wind turbine platforms to be secure, dependable, and function most effectively, analysing the probability of exceeding extreme responses is essential. It makes it possible to take well-informed decisions, evaluate risks, and comply with rules, which helps offshore wind energy projects continue to expand and be successful. The probability of

exceedance of surge, sway, and yaw motion responses of the STLP and FTLP, along with the hybrid concepts, are studied for 1-Year, 10-Year, 20-Year, and 50-Year return period waves.

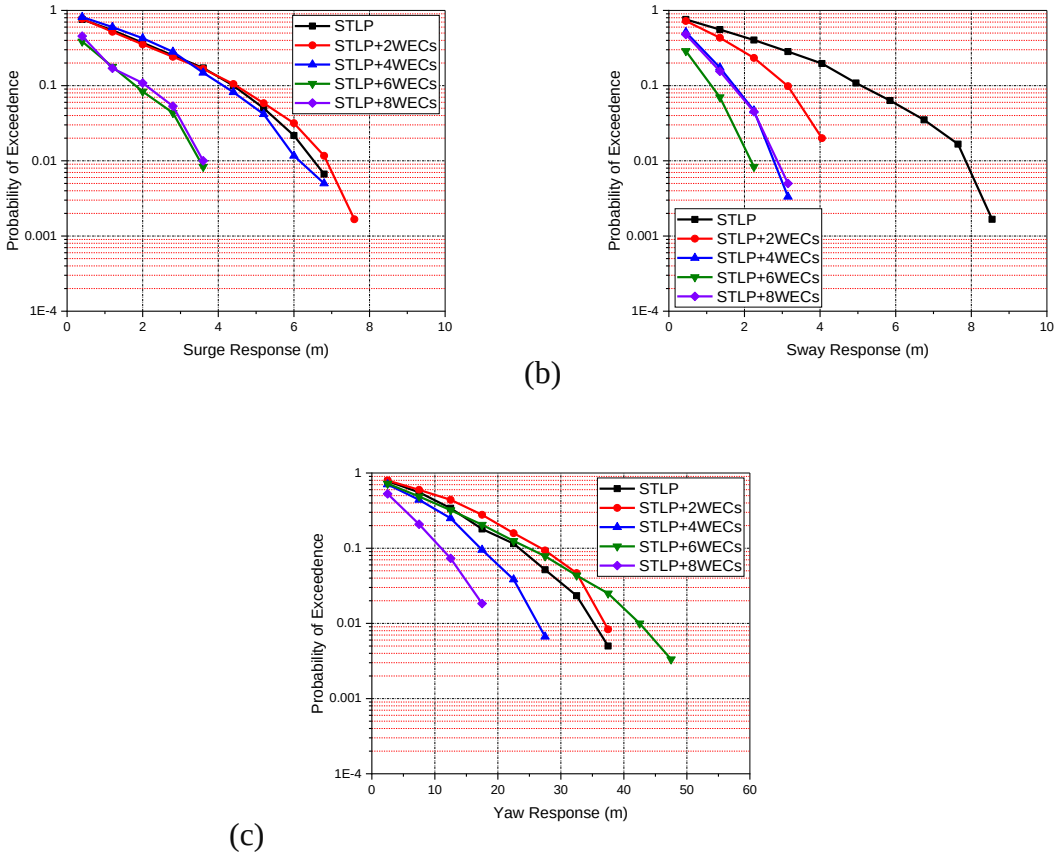


Fig. 6.13: Probability of exceedance of (a) Surge, (b) Sway, and (c) Yaw response for a 1-Year Return Period.

The extreme response study for both the TLP-type structures shows minimal variation in the responses for the 50-Year and 100-year return period waves. Fig. 6.13(a-c) shows the probability of exceedance of surge, sway, and yaw motion responses of the STLP and hybrid STLP-WEC platforms for the 1-Year return period. Higher surge motion responses (Fig. 6.13a) are observed for the STLP+2WECs configuration with minimum probability of occurrence. The variation in the surge response for the extreme wind speed condition is minimal for the STLP+6WECs and STLP+8WECs. The sway motion responses (Fig. 6.13b) are observed to have higher variation for the STLP platform. Adding the WECs is observed to have a higher influence on the sway motion response. The study observed a more than 50% reduction in the sway motion response with the addition of WECs. The STLP+6WECs are observed to have minimal sway motion variation. The STLP+4WECs and STLP+8WECs are observed to have similar sway motion responses. The addition of the WECs has increased the yaw motion

responses for the STLP+2WECs and STLP+6WECs (Fig. 6.13c). The variations are minimum for the lower probabilistic region, and the variation is observed to increase for higher yaw motion values at the lower occurrence region. The STLP+8WECs are observed to have the minimum yaw motion response, further having reduced dynamic loads at the mooring point junctions.

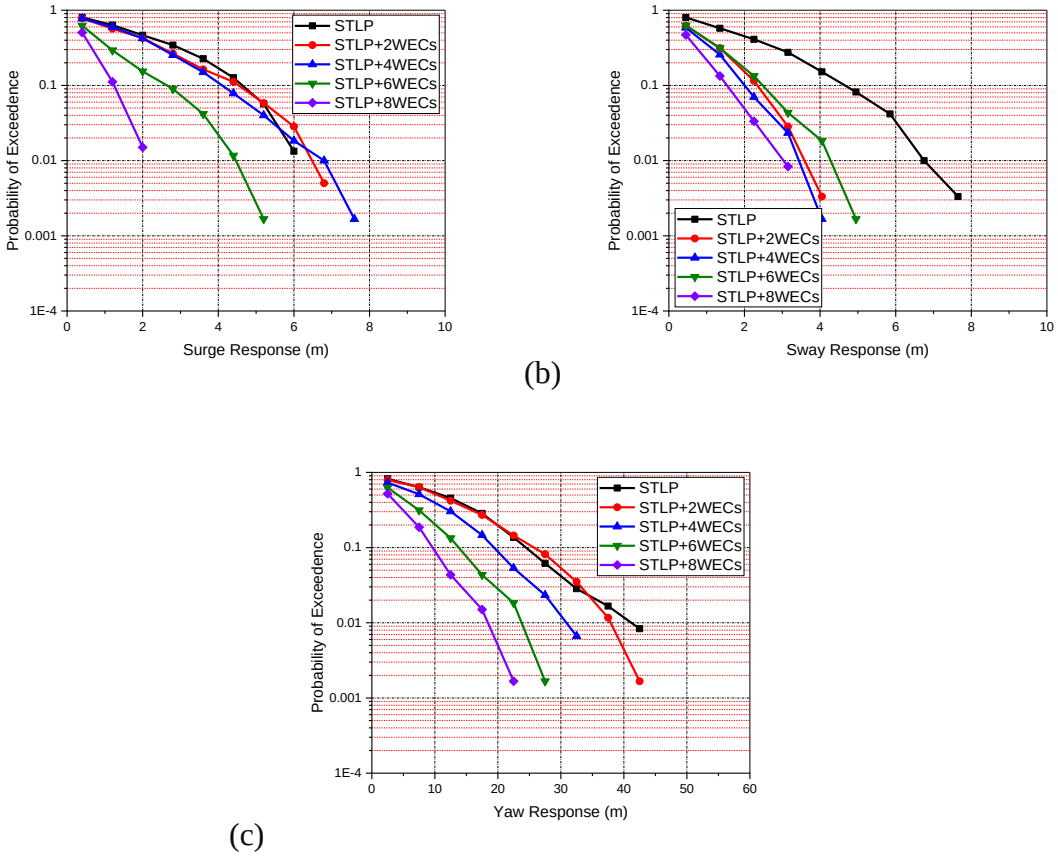


Fig. 6.14: Probability of exceedance of (a) Surge, (b) Sway, and (c) Yaw response for a 10-Year Return Period.

Fig. 6.14(a-c) shows the Probability of exceedance of surge, sway, and yaw motion responses of the STLP and hybrid STLP-WEC for a 10-Year return period. The variation in the surge, sway and yaw motion responses are higher for the waves of the 10-Year return period. The WECs have minimal influence on the surge motion of STLP+2WECs and STLP+4WECs, as the response values are observed to be much closer to the surge motion responses of the STLP (Fig. 6.14a). The STLP+6WECs have a higher surge response with a lesser probability of occurrence. The WECs have a higher influence on the sway motion response of the hybrid system (Fig. 6.14b). The variation in the surge and sway motion responses is almost similar for the STLP+6WECs, though the STLP+2WECs and STLP+4WECs have reduced sway motion

compared to the surge motion of the hybrid systems. The STLP+8WECs have the minimum surge and sway motion response for the 10-Year return period waves. Fig. 6.14(c) shows the variation in the yaw motion responses of the STLP and hybrid STLP-WECs for the 10-Year return period EC. The yaw motion response is slightly higher for the 10-Year return period waves. The higher variation in the surge, sway and yaw motion responses of the 10-Year return period waves may be because a wider range of wave frequencies can frequently be found in waves with longer return periods. The presence of varying wave frequencies can lead to higher responses of the floating platform. The waves with higher wave periods have steeper wave crests and deeper wave troughs. The steepness of the wave influences the responses of the platform, as the steepness affects how the platform interacts with the waves.

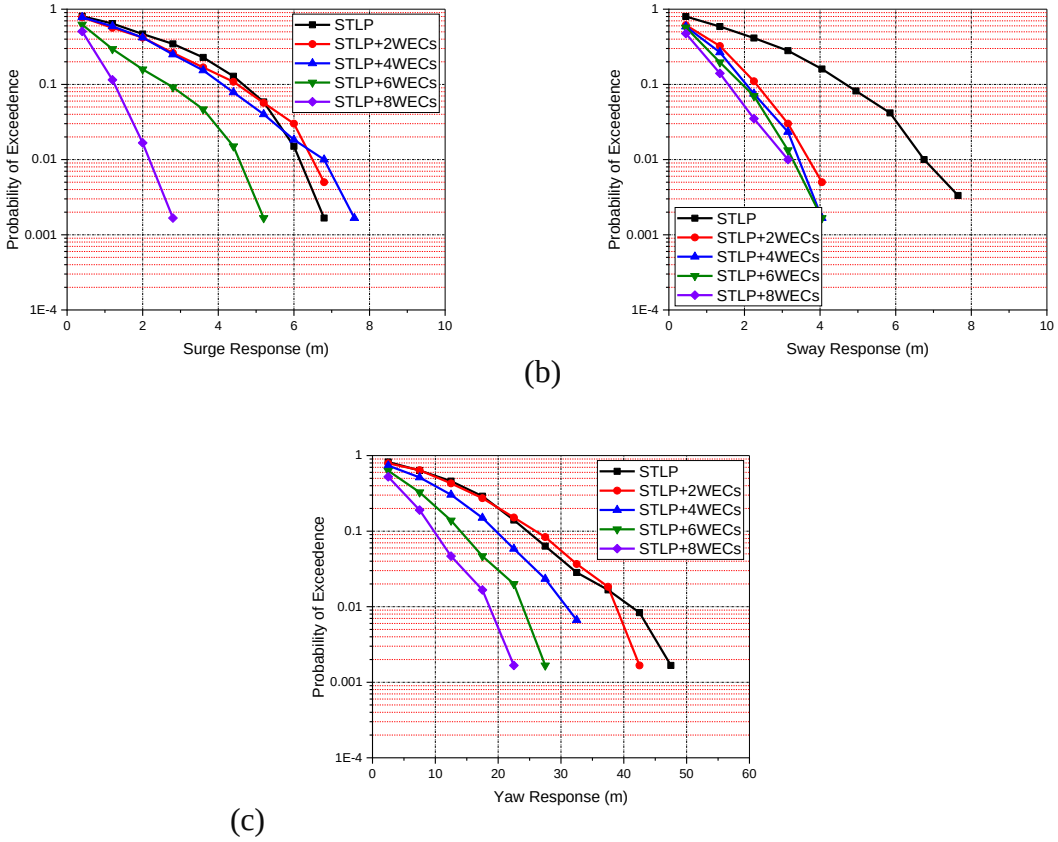


Fig. 6.15: Probability of exceedance of (a) Surge, (b) Sway, and (c) Yaw response for a 20-Year Return Period.

Fig. 6.15(a-c) shows the probability of exceedance of the surge, sway, and yaw motion responses of the STLP and hybrid STLP-WEC for the 20-Year return period EC model. The variation of the responses is observed to increase for the 20-Year return period waves. Minimum surge, sway, and yaw motion responses are observed for STLP+8WECs. The surge motion response for the STLP, STLP+2WECs, and STLP+4WECs are almost similar (Fig.

6.15a) for the 20-Year return period waves, with slightly higher surge response for the STLP+4WECs. Similar to the 10-Year return period waves, the STLP+6WECs have higher response values with a lower probability of occurrence. The minimum variation in sway response (Fig. 6.15b) is observed for the hybrid concepts of STLP for the 20-Year return period waves. The STLP+2WECs are observed to have higher surge and sway response motion compared to other hybrid concepts. The variation in sway response may be attributed to the spacing of the WECs. The WECs can interact with each other and with the platform leading to additional coupling loads causing higher lateral motion of the platform. The variation of the yaw motion (Fig. 6.15c) response is higher than the translational motions. The STLP+2WECs are observed to have higher yaw motion. This may be due to the complex flow pattern with the influence of the WECs in the direction of the wave.

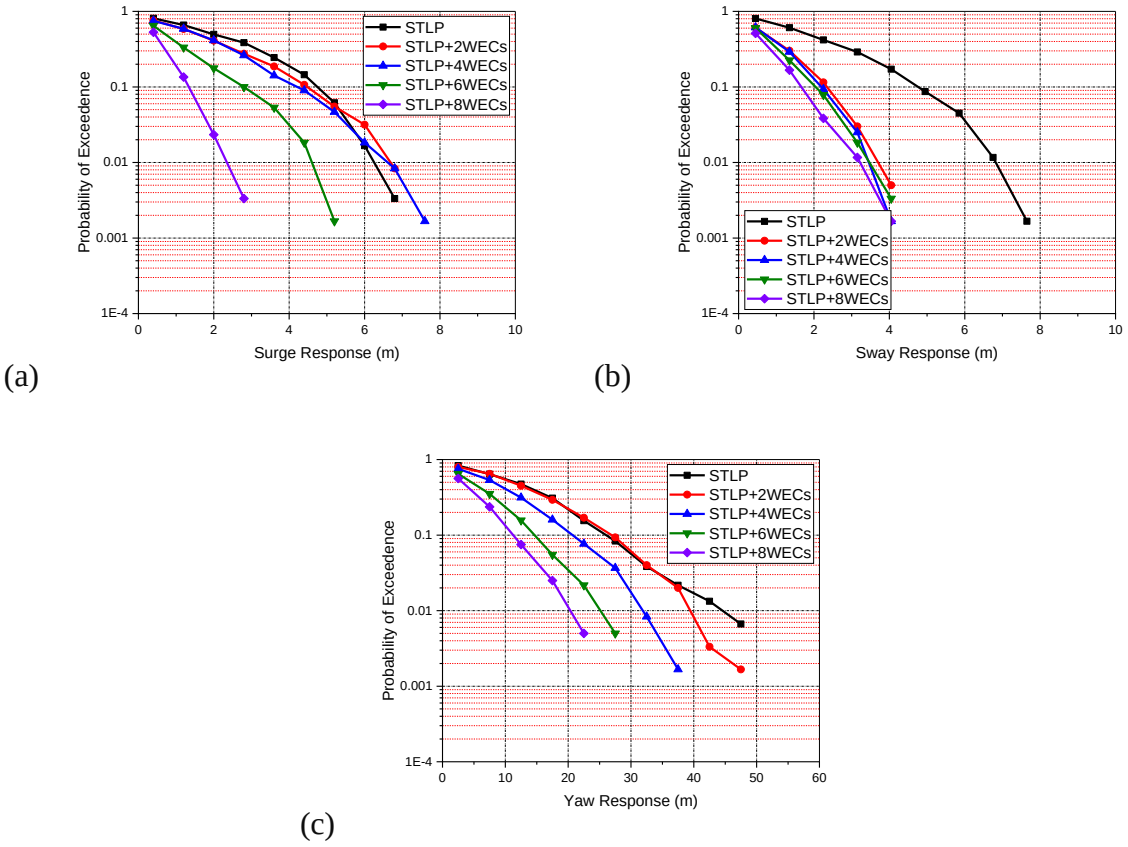


Fig. 6.16: Probability of exceedance of (a) Surge, (b) Sway, and (c) Yaw response for a 50-Year Return Period.

Fig. 6.16(a-c) shows the probability of exceedance of surge, sway, and yaw motion responses for the 50-Year 2-D EC model. The variation of the extreme responses for the 50-Year EC model is much like a 20-Year EC model. The surge responses are higher for the STLP+2WECs

compared to single STLP and are minimum for the STLP+8WECs (Fig. 6.16a). Higher surge motion responses with a lower probability of occurrence are observed for the STLP+4WECs configuration. The sway motion responses are higher for the single STLP, and the hybrid STLP-WECs have reduced sway motion responses (Fig. 6.16b) with a lower probability of occurrence. The yaw motion responses are also reduced for the hybrid STLP-WECs, STLP+8WECs having minimum yaw motion response, as seen in Fig. 6.16(c). The reduced surge, sway, and yaw motion response for the STLP+6WECs for any 2-D model ensure the reduced effect of turbulence and uneven wind flow onto the 5 MW reference wind turbine. Thus, the wind turbine can operate in more stable and predictable wind conditions, improving the overall performance. The reduced motion also ensures efficient maintenance operation of the platform.

Fig. 6.17(a-e) shows the probability of exceedance of surge, sway, and yaw motion responses of FTLP and hybrid FTLP-WEC for a 1-Year return period 2-D EC model. The addition of the WECs has minimum influence on the translational and rotation motions of the platform. This may be because the added mass of the WECs provided to the FTLP is not significant compared to the added mass of the FTLP platform. However, there is a reduction in the responses of the platform with the addition of the WECs. Fig. 6.17(a) shows the variation in the extreme surge motion response of the FTLP and hybrid FTLP-WEC for the waves of a 1-Year return period. The surge motion responses are minimal for the FTLP+8WEC configuration. Further, only minimum variation in the surge response is observed for the two, four and six WEC configurations of FTLP. The sway response value for the FTLP and hybrid FTLP-WECs is much lower than the surge response (Fig. 6.17b). This may be because, with the larger diameter below the mean sea level, the centre of buoyancy of the FTLP is lowered, which provides increased stability against sway motion. The buoyant forces act more effectively in resisting sway motions, leading to reduced sway responses. The probability of occurrence of higher sway response motions is higher for FTLP+2WECs and is minimum for FTLP+6WECs. The FTLP+4WECs and FTLP+8WECs are also observed to have minimal sway motion response for the extreme wind speed condition of the 1-Year model. The yaw motion responses of the FTLP (Fig. 6.17c) have a higher influence with the addition of WECs. The yaw motion responses are reduced for two, six and eight WEC configurations of FTLP and are increased for FTLP+4WECs. This may be because the WECs at specific locations on the FTLP can create coupling effects between the WECs and the platform's yaw motion. These coupling effects can amplify yaw motion under certain wave conditions.

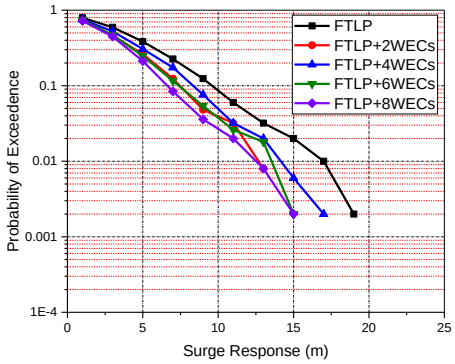


(a)

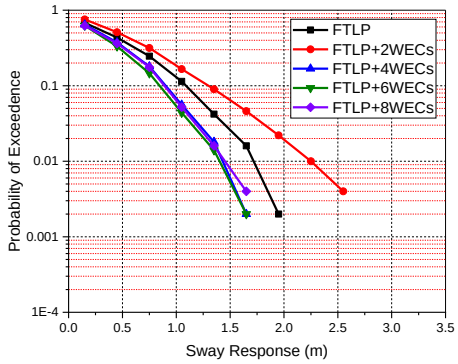


(b)

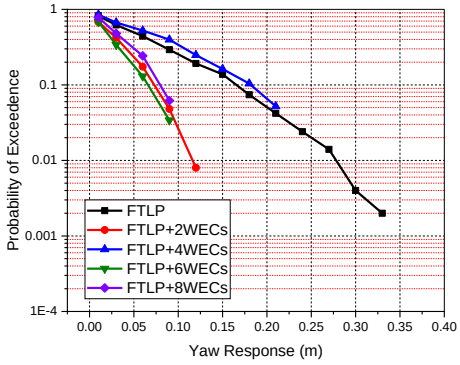


(c)

Fig. 6.17: Probability of exceedance of (a) Surge, (b) Sway, and (c) Yaw response for a 1-Year Return Period.

Fig. 6.18(a-c) shows the probability of exceedance of the surge, sway, and yaw motion responses of the FTLP and hybrid FTLP-WEC for 10-Year return period waves. The responses are slightly higher for the 10-Year return period waves. Similar to the 1-Year 2-D EC model, the surge motion response for the extreme conditions has minimal variation for the FTLP and hybrid FTLP-WEC (Fig. 6.18a). The surge responses are minimum for the FTLP+8WEC configuration.

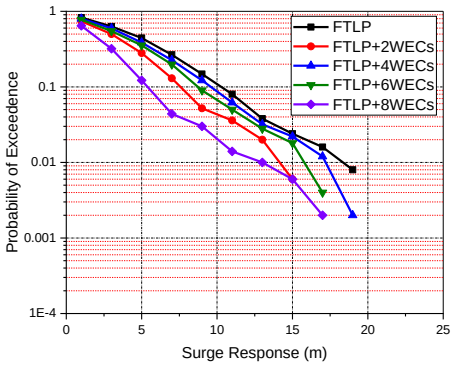


(a)

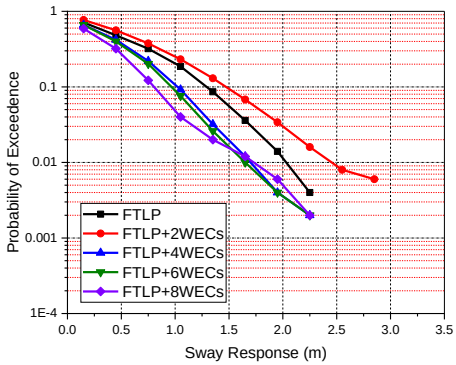


(b)

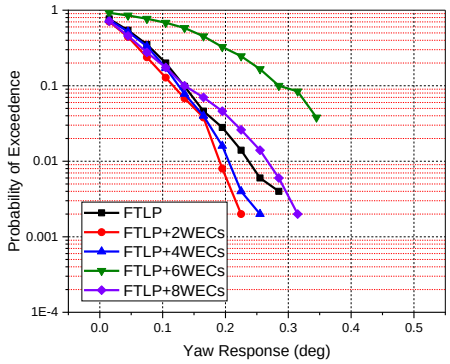


(c)

Fig. 6.18: Probability of exceedance of (a) Surge, (b) Sway, and (c) Yaw response for a 10-Year Return Period.

The sway motion responses are higher for the FTLP+2WECs and are minimum for the FTLP+8WECs (Fig. 6.18b). A higher variation in yaw response is observed for the hybrid FTLP+6WECs (Fig. 6.18c). The WECs attached to the outer pontoons may introduce asymmetry in the buoyancy distribution and hydrodynamic forces acting on the FTLP, resulting in uneven forces which can induce yawing moments on the platform, causing increased yaw motion.

Fig. 6.19(a-c) shows the variation in the surge, sway, and yaw motion responses of the FTLP and hybrid FTLP-WEC for the 20-Year EC 2-D model. The surge and the sway motion responses show similar variations with higher response values (Fig. 6.19(a,b)). The waves having higher return periods exhibits stronger wave grouping effects resulting in larger wave impacts on the hybrid platform, causing higher translation motions as the platform interacts with multiple wave crests and troughs within a short time span. Also, waves with higher wave height and longer spans have a significant influence on the added mass effect accounting for the inertia of the displaced water around the floating platform. Fig. 6.19(c) shows the variation in the yaw motion response of the FTLP and hybrid FTLP-WEC. For the waves of the 20-Year return period, the yaw motion responses are observed to increase with the addition of the WECs. The cone-cylinder point absorber WECs are designed to harness wave energy, and their motion in response to waves generates yawing moments on the hybrid FTLP. The wave-induced yawing moments can increase the yaw moments of the hybrid system. Also, the frequency characteristics of the heaving WECs and the natural frequency of the FTLP may coincide, leading to resonance, further amplifying the yaw motions. Minimum yaw motion is observed for the FTLP+6WECs, and higher yaw motion is observed for the FTLP+8WECs.

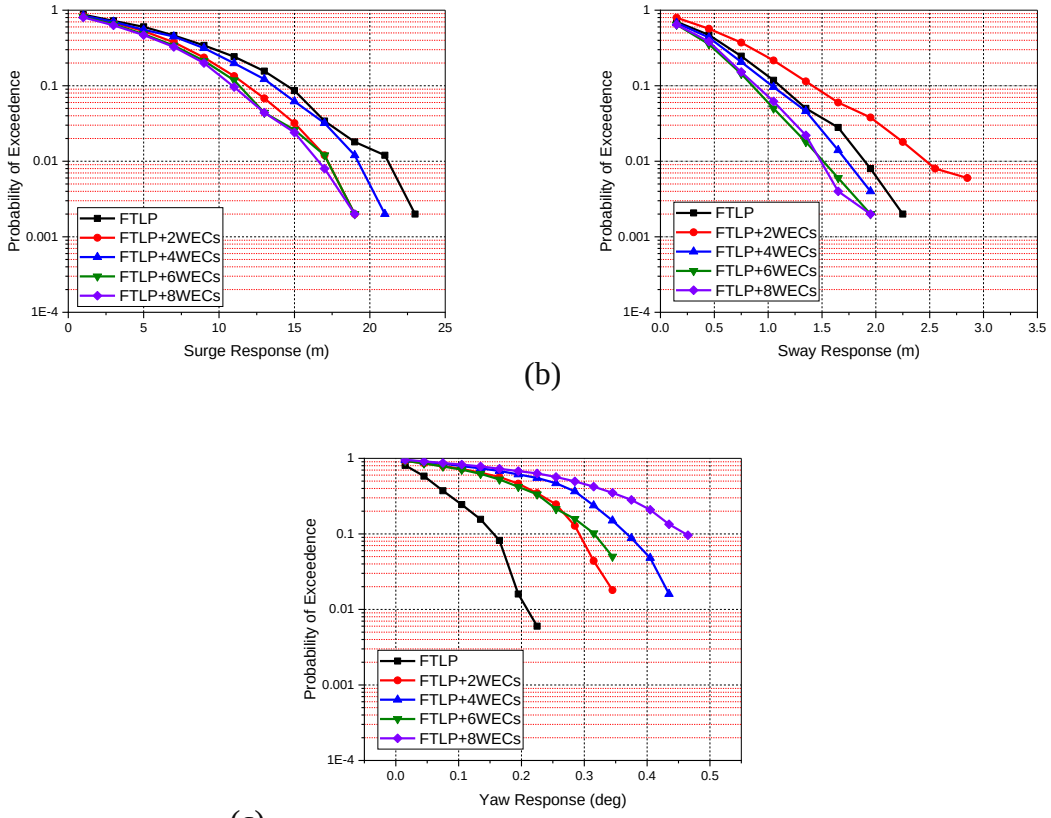


Fig. 6.19: Probability of exceedance of (a) Surge, (b) Sway, and (c) Yaw response for a 20-Year Return Period.

Fig. 6.20(a-c) shows the surge, sway, and yaw motion response of the FTLP and hybrid FTLP-WEC for the 50-Year 2-D EC model. The variation of the surge (Fig. 6.20a) and sway (Fig. 6.20b) response is almost similar to the 20-Year 2-D EC model. However, the surge and sway motion response have lower response values for the extreme wind speed condition than the 20-Year EC model. The varied wave duration may change the platform's dynamic response characteristics. The 50-Year return period waves may cause higher damping for longer-period waves, resulting in lower motion amplitudes. The 50-Year return waves may have a more favourable direction of incidence, leading to reduced motion amplitudes. The mooring system's stiffness and damping properties can also affect the motion response differently for different wave periods. Fig. 6.20(c) shows the yaw motion response of the 50-Year EC model for the FTLP and hybrid FTLP-WEC platforms. Like the 20-Year return model, the yaw motion response increases for the FTLP+6WECs and FTLP+8WECs. However, the yaw motion response is reduced for the FTLP+2WECs configuration compared to a single FTLP. The study of STLP and FTLP hybrid concepts shows the importance of WECs in reducing the motion responses of the platform, except for some extreme wind speed conditions.

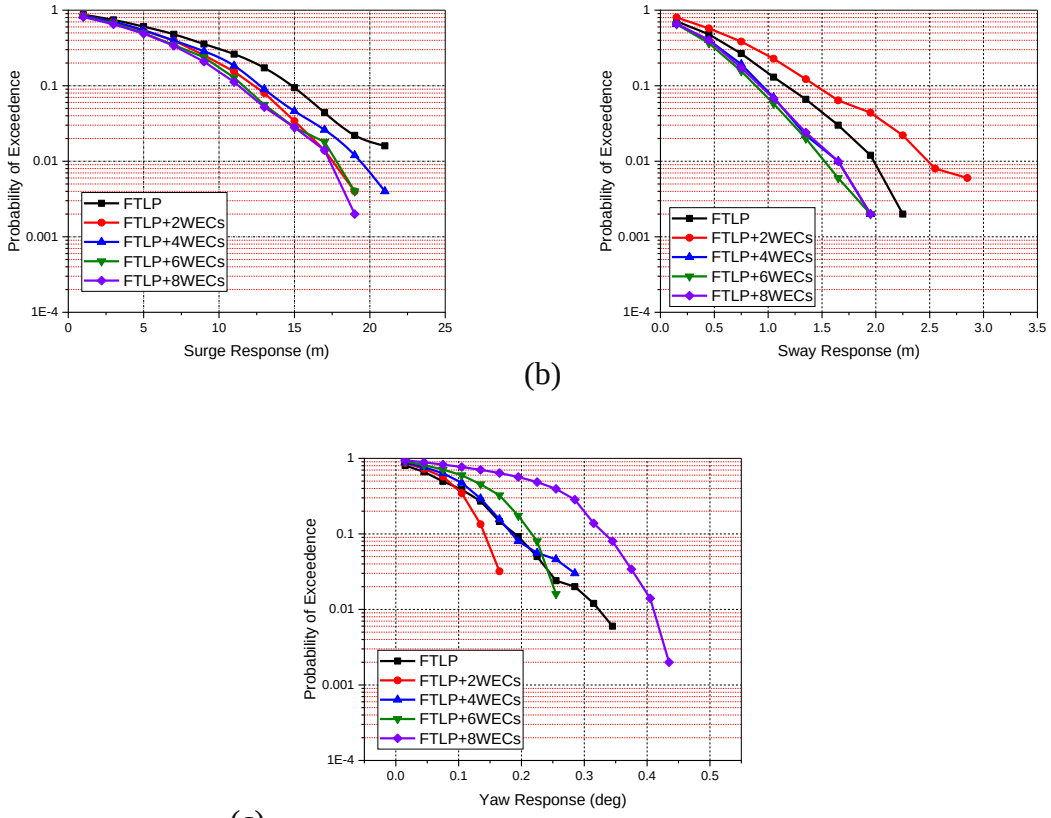


Fig. 6.20: Probability of exceedance of (a) Surge, (b) Sway, and (c) Yaw response for a 50-Year Return Period.

### 6.4.3 Variation of Tower Base Bending Moments with Mean Wind Speed

The dynamic interaction of the platform, supporting wind turbine and the environmental forces (wind, waves, and currents) results in developing the lateral loads, further resulting in the fore-aft bending moment, side-to-side bending moments and yaw moments developing at the base of the wind turbine tower. The waves moving in the positive x-direction develops horizontal forces in the platform, developing forward force on the platform. The forward force may result in developing the fore-aft bending moments at the base of the turbine tower. The surge, heave, and pitch motion also have a significant influence on developing the fore-aft bending moments. The rolling and pitching motion of the platform causes the platform to sway side-to-side and may develop side-to-side bending moments. The mass and inertia of the supporting wind turbine have an influence on how the platform reacts to external forces. The dynamic behaviour of the wind turbine tower and nacelle can induce additional side-to-side bending moments. The fore-aft and side-to-side bending moment for extreme wind speed conditions is studied for the hybrid STLP and FTLP for different return period waves.

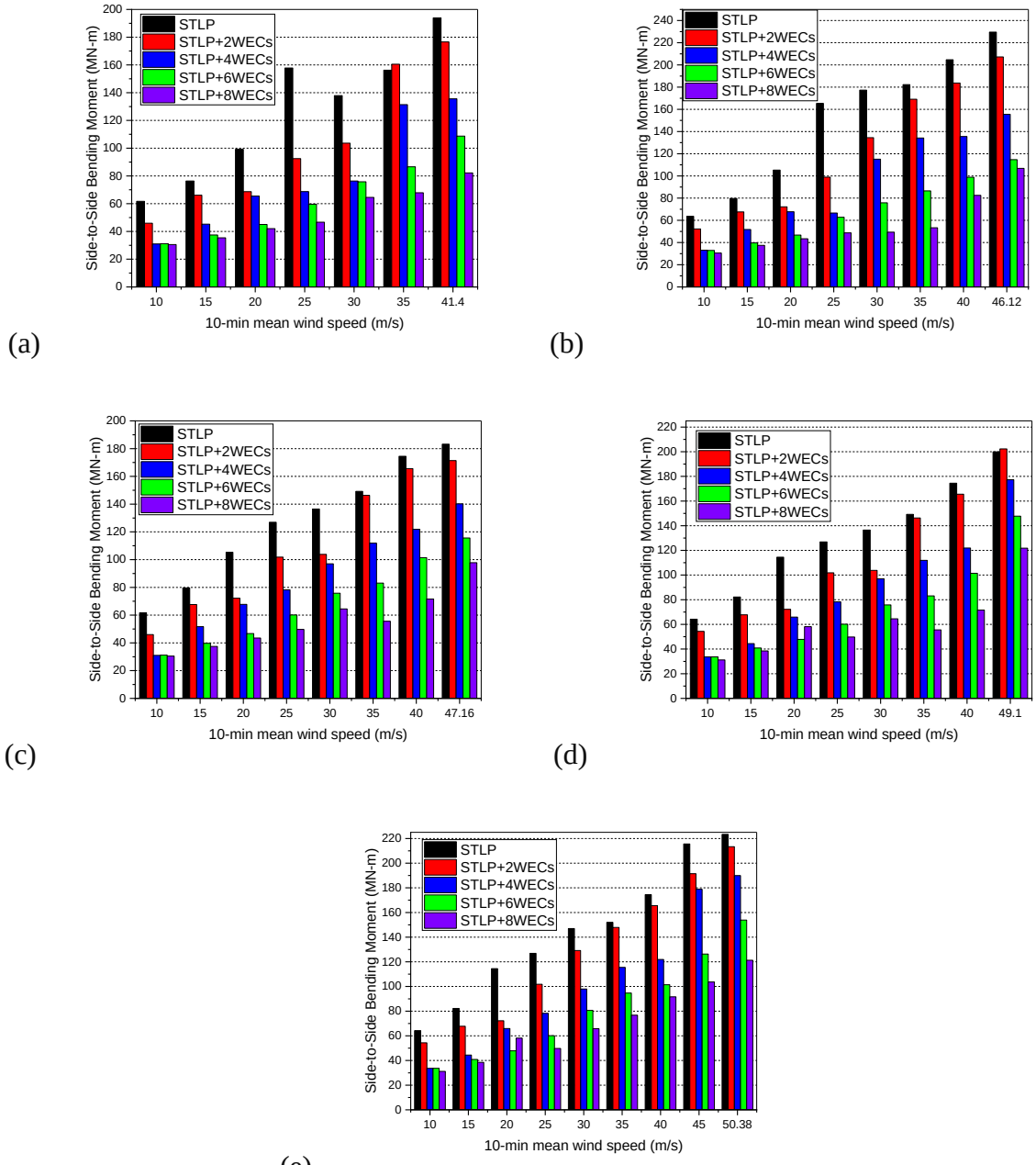


Fig. 6.21: Extreme Side-to-Side Bending Moments of STLP-WEC hybrid system for (a) 1-Year, (b) 10-Year, (c) 20-Year, (d) 50-year, and (e) 100-Year return period.

Fig. 6.21(a-e) shows the extreme values of side-to-side bending moments developed for the STLP and hybrid STLP-WEC for different wind speeds of 1-Year, 10-Year, 20-Year, 50-year, and 100-Year return periods. With the addition of the WECs, the side-to-side bending moment is observed to reduce for most wind speed conditions of different return periods. For the 35 m/s wind speed condition of a 1-Year return period, waves have slightly higher side-to-side bending moment for the STLP+2WECs than a single STLP, as seen in Fig. 6.21(a). A minimum value

for the side-to-side bending moment is observed for STLP+8WECs. The minimum side-to-side bending moment for the STLP+8WECs may be due to the minimum roll and pitch motion of the hybrid floating system. The minimum side-to-side bending moment ensures minimum lateral loads on the turbine blades, improving the efficiency of the wind power absorption. Fig. 6.21(b) shows the side-to-side bending moment developed for the 10-Year return period waves. The bending moment values are slightly higher for the 10-Year return period wave condition. This may be due to the resonance effect of the platform, as the wave frequency may coincide with the natural frequency of the floating platform. Similar variations in the side-to-side bending moments are observed for the 20-Year, 50-Year, and 100-Year return period wave condition (Fig. 6.21(c,d,e)). For any wind speed condition, minimum side-to-side bending moments are observed for the STLP+8WECs configuration except for the 25 m/s wind speed condition of the 50-Year and 100-Year EC model, for which the STLP+6WECs have reduced side-to-side bending moments. Also, the variation in the side-to-side bending moments for the hybrid STLP-WEC is minimal for the operational wind speed conditions of a 5 MW wind turbine. With the wind speed condition above 30 m/s, the variation in the side-to-side bending moments for the hybrid concepts is higher.

Fig. 6.22(a-e) shows the extreme side-to-side bending moments developed on the FTLP and hybrid FTLP-WEC platforms for 1-Year, 10-Year, 20-Year, 50-year, and 100-Year return periods. The side-to-side bending moments are much higher for the FTLP and hybrid FTLP-WEC platforms than for STLP and hybrid STLP-WEC platforms. This may be because, with the larger frontal area of the FTLP, the hydrodynamic forces acting on the platform in the side-to-side direction will be higher, resulting in higher side-to-side bending moments. Also, with a larger frontal area for the wave action, the added mass will be higher, resulting in increased wave-induced side-to-side moments. Fig. 6.22(a) shows the side-to-side bending moments for the 1-Year return period waves.

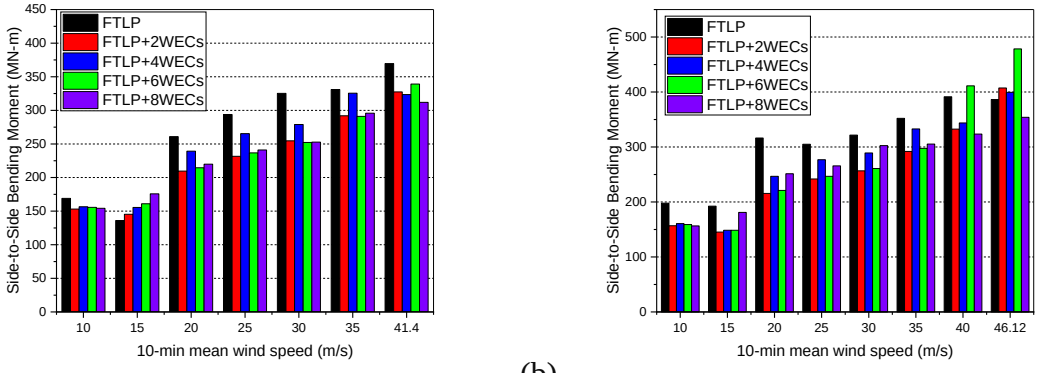


(a) (b)

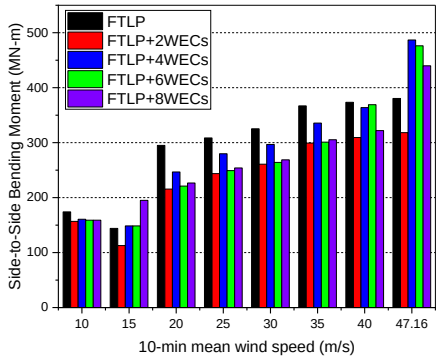


(c)

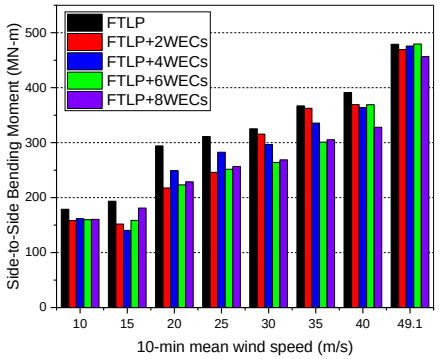


(d)

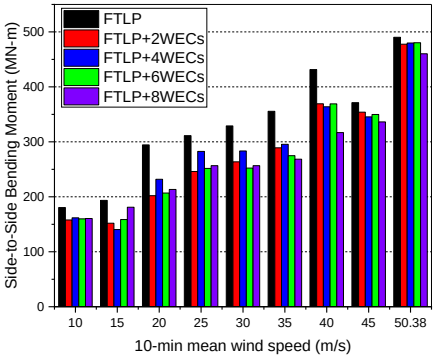


(e)

Fig. 6.22: Extreme Side-to-side Bending Moments of FTLP-WEC hybrid system for (a) 1-Year, (b) 10-Year, (c) 20-Year, (d) 50-year, and (e) 100-Year return period.

The bending moment is minimal for the 1-Year return period wave conditions, and the moments increase for higher return period waves. Apart from the 15 m/s wind speed condition, the moments are reduced by adding the WECs. For the 15 m/s condition, the resonance effect might increase the moments of the hybrid platforms. Fig. 6.22(b) shows the variation in extreme bending moment developed on the FTLP and hybrid FTLP-WEC for the 10-Year return period waves. For wind speed conditions below 35 m/s, adding WECs has reduced the bending moment developed for the FTLP. But for the extreme wind speed conditions, the moments are higher for FTLP+6WECs compared to single FTLP. Apart from the 15 m/s wind speed condition, the minimum moment is developed for the FTLP+8WECs hybrid platform. Fig. 6.22(c) shows the side-to-side bending moments for the 20-Year return period waves. Similar to the 10-Year return period waves, the 20-Year return period waves observe higher moments for the hybrid platforms for 15 m/s wind speed conditions. For other operation conditions of the wind turbine, the WECs have reduced the moment developed on the FTLP. Further, FTLP+4WECs have higher side-to-side bending moments for extreme wind speed conditions. The variation of side-to-side bending moments is similar for both 50-Year and 100-

Year return periods (Fig. 6.22(d,e)). For any wind speed conditions, adding WECs has reduced the side-to-side bending moments developed at the base of the turbine tower. For the operational conditions of the wind turbine, the FTLP+6WECs are observed to have lower side-to-side bending moments. For the survival conditions of the 5 MW wind turbine, the moments are minimum for the hybrid FTLP+8WECs configuration.

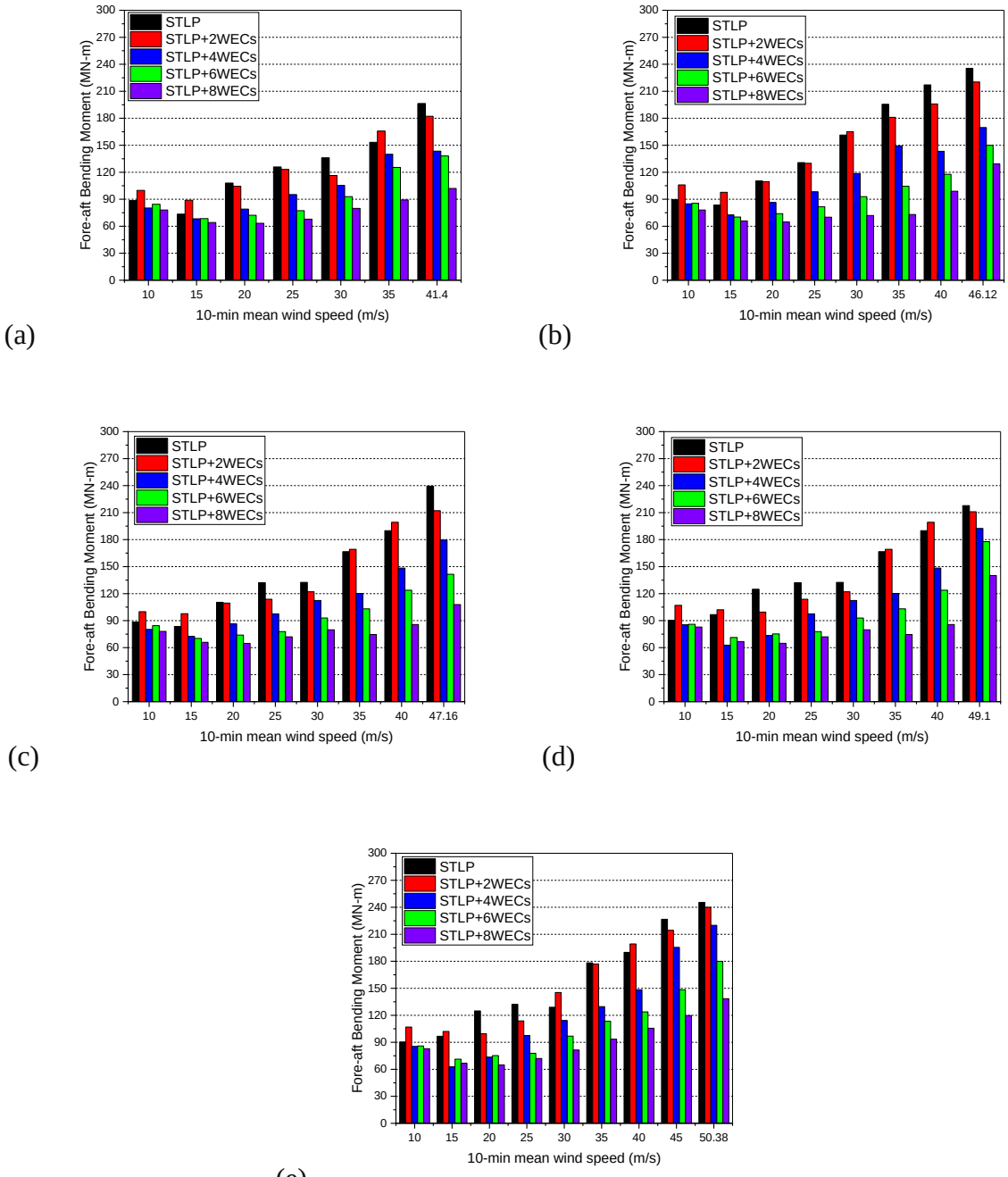


Fig. 6.23: Extreme Fore-aft Bending Moments of STLP-WEC hybrid system for (a) 1-Year, (b) 10-Year, (c) 20-Year, (d) 50-year, and (e) 100-Year return period.

Fig. 6.23(a-e) shows the fore-aft bending moment of STLP and hybrid STLP-WEC for 1-Year, 10-Year, 20-Year, 50-year, and 100-Year return periods. The fore-aft bending moments are higher for certain environmental conditions compared to the side-to-side bending moments. This may be because the platform may exhibit a higher sensitivity to forces acting in the fore-aft direction, developing higher fore-aft bending moments. Also, the combined effect of waves and wind acting from the same direction can develop higher fore-aft forces compared to the side-to-side forces. Similar to the case of the side-to-side bending moment, the variation in the hybrid concepts of STLP-WEC is uniform.

For most operational conditions of the platform, the STLP+8WECs are observed to have minimum fore-aft moment compared to other hybrid platforms. Also, for lower wind speed conditions (10 m/s and 15 m/s), the STLP+2WECs are observed to have higher moments compared to other hybrid concepts and single STLP. This may be due to the arrangement pattern of the WECs causing complex flow patterns, resulting in higher moments.

Fig. 6.24(a-e) shows the extreme Fore-aft bending moments developed at the base of the turbine tower for 1-Year, 10-Year, 20-Year, 50-year, and 100-Year return period EC model. The fore-aft bending moments developed for the FTLP and hybrid FTLP-WEC is lower compared to the STLP and hybrid STLP-WEC floating platforms. The variation in the fore-aft bending moments is minimum for the 1-Year return period waves (Fig. 6.24a) and is observed to increase for higher return period waves. For the 1-Year return period waves, the extreme wind speed condition is observed to have a higher fore-aft bending moment for the FTLP+8WECs configuration and is minimum for the FTLP+6WECs. For any wind speed condition of a 1-Year return period, the fore-aft bending moment is minimum for FTLP+6WECs. Fig. 6.24(b) shows the variation in the extreme fore-aft bending moments for 10-Year return period waves. For wind speed conditions below 25 m/s, the fore-aft bending moments are minimal for the hybrid FTLP-WEC compared to the single FTLP. However, a higher moment is observed for the FTLP+6WECs for 20 m/s wind speed. For wind speed above 40 m/s, the fore-aft moments are higher for the hybrid concept compared to a single FTLP. Fig. 6.24(c) shows the fore-aft moment for the 20-Year return period EC model. The moments developed on the base of the turbine tower for the hybrid concepts are observed to be higher for wind speeds above 10 m/s. This may be due to the resonance effect, when the natural frequency of the WECs may coincide with the natural frequency of the waves acting on the floating system. The FTLP+2WECs configuration is observed to have a minimum value of fore-aft bending moment compared to other hybrid concepts. Fig. 6.24(d) shows the fore-aft

bending moment for the 50-Year EC model. The hybrid FTLP+6WECs are observed to have higher variation for 15 m/s and 35 m/s wind speed conditions. For other operational conditions of the wind turbine, the hybrid concepts have reduced moment compared to a single FTLP. Fig. 6.24(e) shows the variations in the fore-aft bending moment of FTLP and hybrid FTLP-WEC for the 100-Year 2-D EC model.

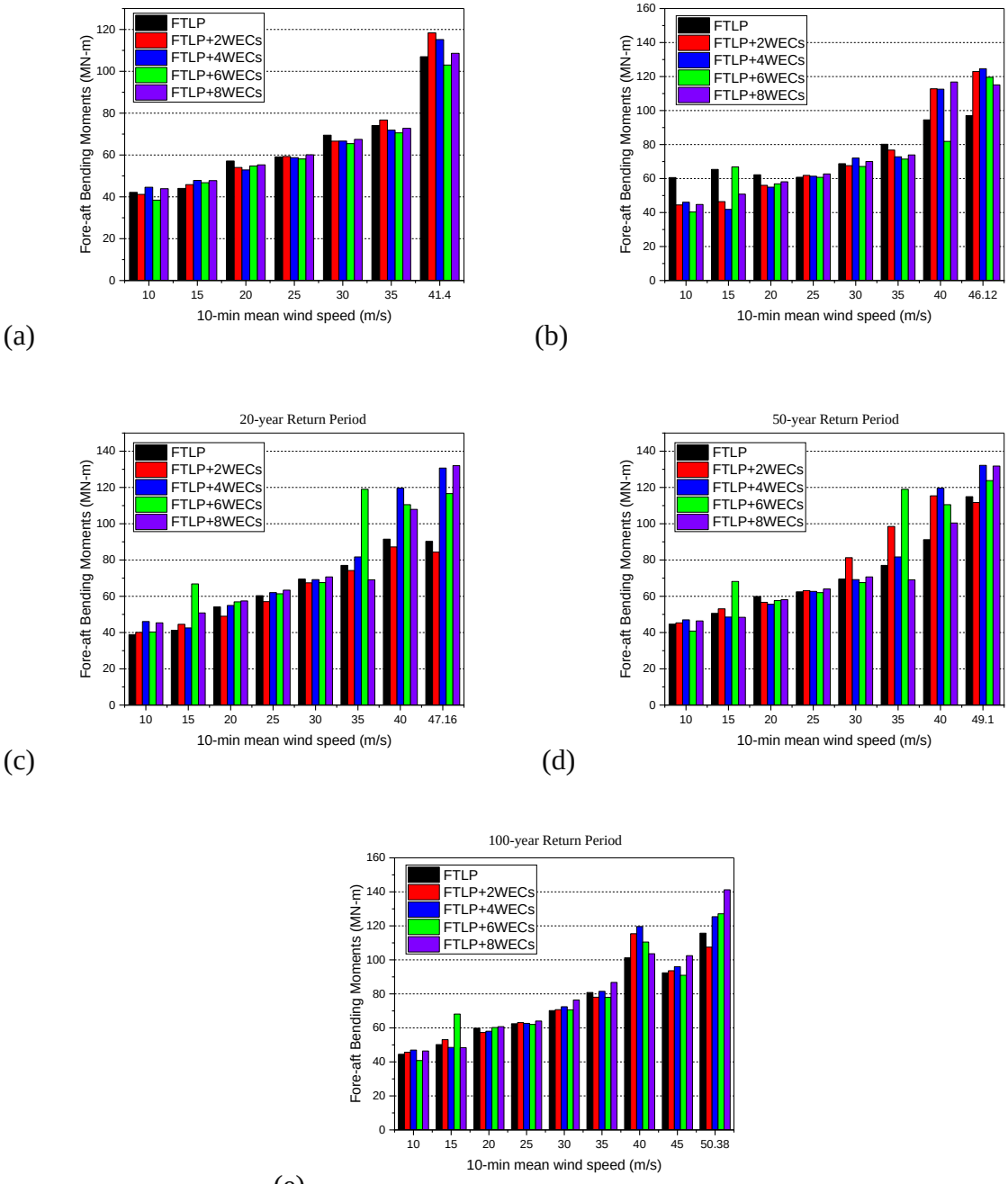


Fig. 6.24: Extreme Fore-aft Bending Moments of FTLP-WEC hybrid system for (a) 1-Year, (b) 10-Year, (c) 20-Year, (d) 50-year, and (e) 100-Year return period.

The variation is much similar to the 50-Year EC model apart from the 35 m/s. The fore-aft bending moment for the FTLP+6WECs is reduced for this environmental condition. Further, FTLP+4WECs are observed to have higher fore-aft bending moments for parked conditions of the wind turbine. The study of the fore-aft bending moment for hybrid STLP and FTLP showed different characteristics of the platform. The hybrid STLP platforms had uniformity in the variation of the moments, with STLP+8WECs having reduced fore-aft bending moments for any operational or parked conditions. But for the hybrid FTLP-WEC platforms, fore-aft bending moments vary for different return period waves. For most operational conditions, the fore-aft moment is reduced for FTLP with the addition of WECs.

Fig. 6.25(a,b) shows the extreme fore-aft and side-to-side bending moment developed on the STLP and hybrid STLP-WEC configurations for extreme wind speed conditions. The addition of the WECs has reduced the moments developed on the hybrid configuration, as discussed earlier. Minimum fore-aft and side-to-side bending moments are observed for the STLP+8WECs hybrid platform for the extreme wind speed conditions of waves of different wave periods. The variation in the fore-aft bending moment developed is similar for both STLP+6WECs and STLP+8WECs (Fig. 6.25a). Lower fore-aft bending moment values are observed for the 1-Year return period, and higher fore-aft bending moments are observed for both the 50-Year and 100-Year return periods for both the hybrid floating platforms. But for the STLP, STLP+2WECs and STLP+4WECs show higher fore-aft bending for the 100-Year return period waves than the 50-Year return period waves.

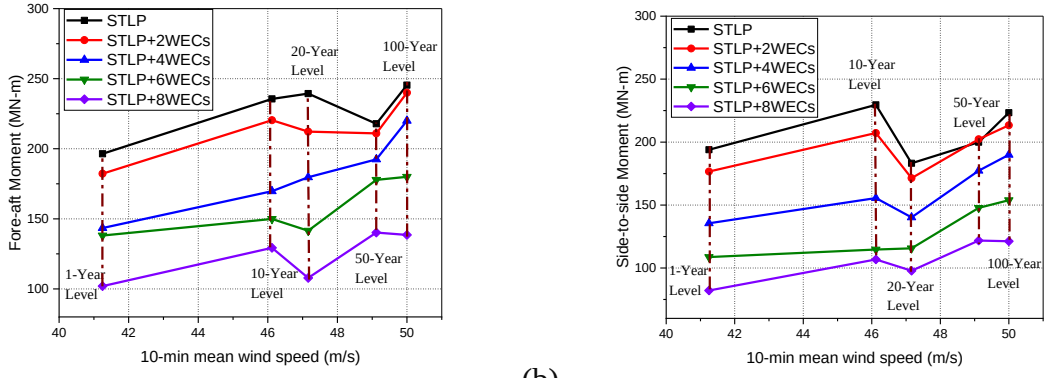


(a) (b)

Fig. 6.25: Extreme (a) Fore-aft Bending and (b) Side-to-Side Moments of STLP-WEC hybrid system for various extreme wind speed conditions.

This may be due to the arrangement pattern of the WECs, leading to a complex flow pattern for the waves around the STLP, causing the variation in the moments developed. The side-to-

side bending moment is slightly higher than the fore-aft moment, as seen in Fig. 6.25(b). The variation in the side-to-side moment developed is similar for all hybrid concepts except the STLP+6WECs. For the hybrid STLP+6WECs, the side-to-side moments are almost similar for 1-Year, 10-Year, and 20-Year return period waves. Further higher side-to-side bending moments are developed for the 50-Year and 100-Year return periods. For the other hybrid STLP-WEC platforms, minimum moments are observed for the waves of the 1-Year return period and higher moments are developed for the 100-Year return period waves.

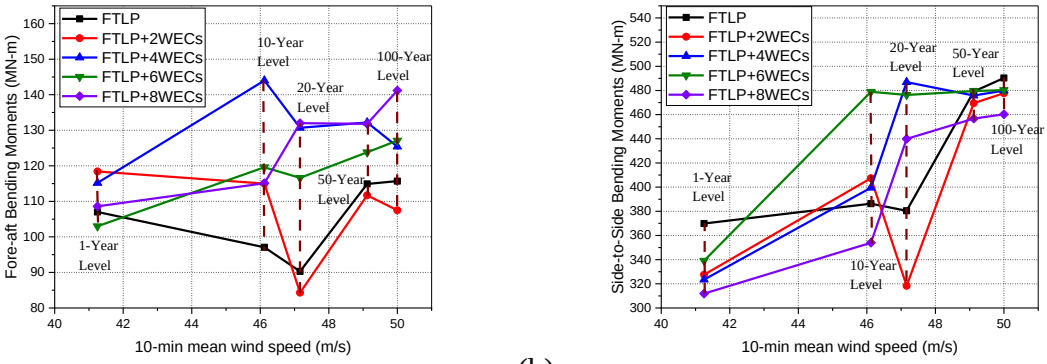


(a) (b)

Fig. 6.26: Extreme (a) Fore-aft Bending and (b) Side-to-Side Moments of FTLP-WEC hybrid system for various extreme wind speed conditions.

Fig. 6.26(a,b) shows the extreme fore-aft and side-to-side bending moments developed on the FTLP and FTLP-WEC hybrid platforms for extreme wind speed conditions. Fig. 6.26(a) shows the extreme fore-aft bending moment developed at the base of the turbine tower for different return period waves. For the FTLP and FTLP+2WECs, the extreme fore-aft moments are minimum for the 20-Year return period waves. The spectrum of incoming waves, including the direction, height and period, have a significant role in the fore-aft bending moments developed at the base of the turbine tower. Different wave conditions can result in varying fore-aft bending moment responses. Further, the higher frequency waves develop smaller dynamic motions in the platform, reducing fore-aft bending moments. Further, for the hybrid FTLP+4WECs, FTLP+6WECs and FTLP+8WECs, the lower fore-aft moments are developed for the 1-Year return period wave conditions and higher fore-aft bending moments are developed for the 100-Year return period waves. The side-to-side bending moments are higher compared to the fore-aft moments for the FTLP and hybrid FTLP-WEC (Fig. 6.26b). The higher side-to-side moments are due to the higher surge and pitch motion of the platform, causing the dynamic loads to act on the turbine tower. The FTLP+2WECs have similar variations for the side-to-side bending moments. For the single FTLP, 1-Year, 10-Year and 20-Year return period waves

have slightly similar variations but have higher moments developed for the 50-Year and 100-Year return period waves. There is a minimum variation in the side-to-side bending moments developed on the hybrid FTLP+6WECs for 10-Year, 20-Year, 50-year, and 100-Year return period waves. The minimum variation for different wave conditions ensures higher wind power absorption.

### 6.4.4 Mooring Tension for Extreme Wind Conditions

The mooring cables serve as tethers, giving the floating platform vertical support and limiting its ability to move excessively in reaction to waves, currents, and wind. The platform is kept in the desired position with respect to the seabed through the pre-tensioned cables, which are designed to maintain a particular tension level. This moderate tension reduces the platform's vertical movements and aids in maintaining stability. Careful consideration must be given to variables including sea depth, environmental circumstances (such as wave, current, and wind loads), the weight of the wind turbine and platform, material qualities, and the expected operational life of the offshore platform when choosing and designing mooring cables. The Fig. 6.27(a,b) shows the pictorial representation of the STLP and FTLP supported using the tensioned mooring cables where the wave is assumed to move towards the positive x-direction. Four tensioned mooring cables for provided the STLP (S_MC) on the four outer pontoons and six mooring cables are provided for the FTLP (F_MC) as shown in Fig. 6.27(a) and Fig. 6.27(b). The properties of the mooring cables used to support the floating platforms are detailed in Chapter 1. The position of the mooring cables remain same for the hybrid floating platform considered for the present study.

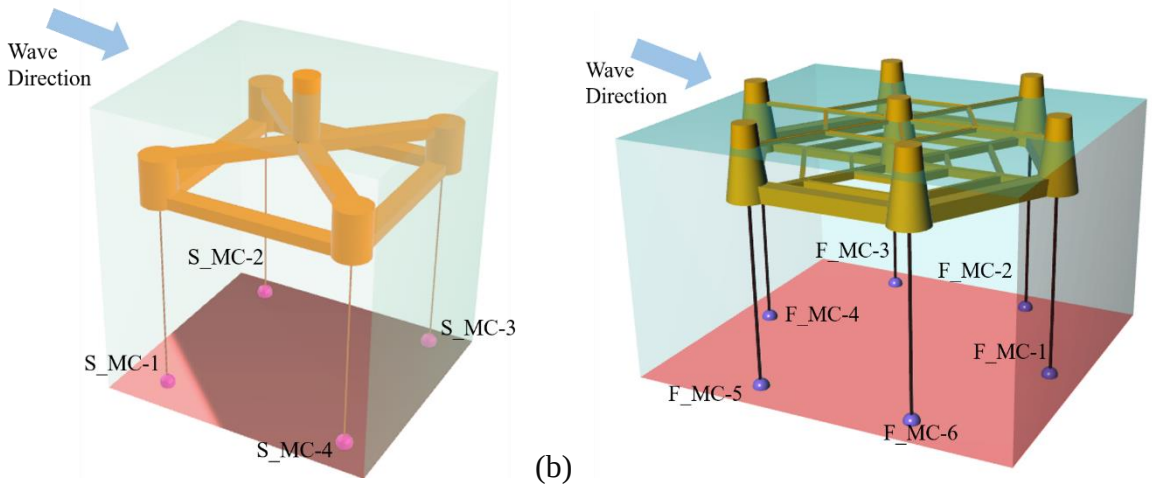


(a) (b)

Fig. 6.27: Geometric representation of (a) STLP, and (b) FTLP supported by mooring cables

Fig. 6.28(a-d) shows the maximum values of mooring tension developed on the four different mooring cables of the STLP and hybrid STLP-WEC. The S_MC-1 and S_MC-2 are provided on the seaward side of the platform, and the S_MC-3 and S_MC-4 are provided on the leeward side of the platform. The S_MC-1 experiences higher tension (145.2 MN) for the single STLP for different wind speed conditions (Fig. 6.28a). With the addition of the WECs, the tension developed on the S_MC-1 is reduced. With the increase in the wind speed, the tension developed on the S_MC-1 decreases. The hybrid STLP+8WECs have minimum tension (42.9 MN) value for the S_MC-1. Further, the minimum tension on the S_MC-1 for the STLP+6WECs is 43.4 MN for 49.1 m/s. Fig. 6.28(b) shows the tension developed on the S_MC-2 for the STLP and hybrid STLP-WEC.

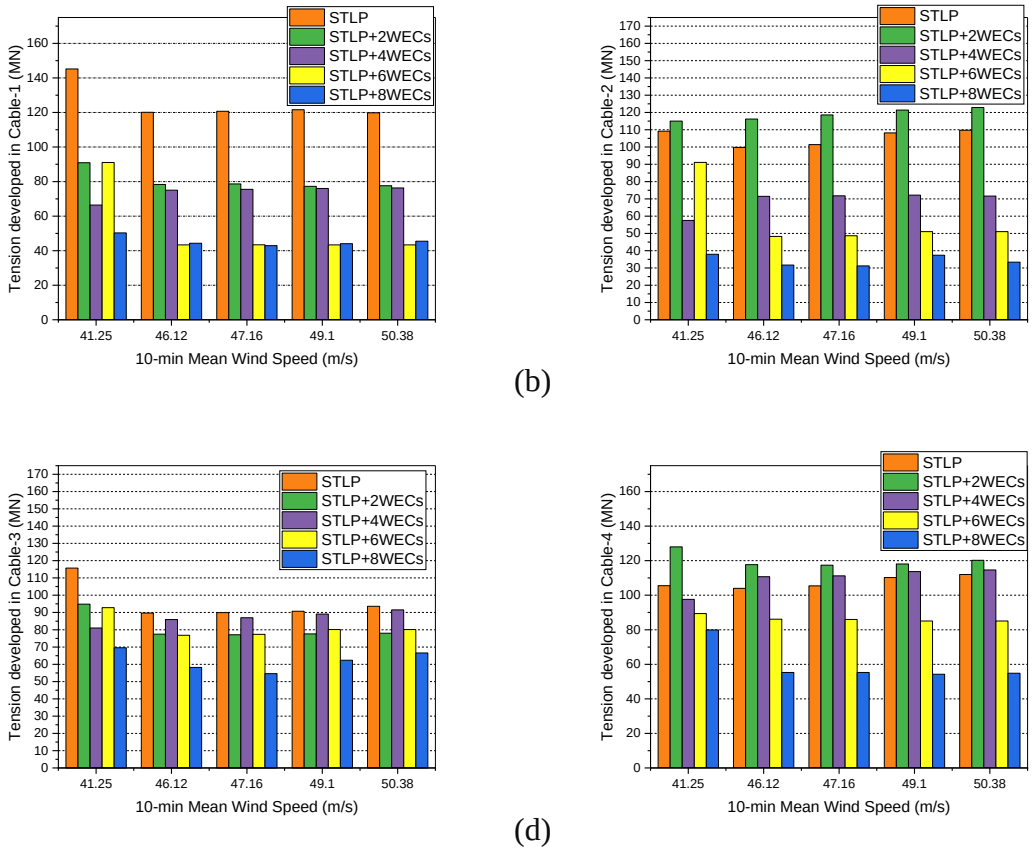


Fig. 6.28: Maximum tension developed on (a) S_MC-1, (b) S_MC-2, (c) S_MC-3 and (d) S_MC-4 of STLP-WEC hybrid systems for various extreme wind speed conditions.

Higher mooring tension (109.7 MN) is observed for STLP+2WECs. This may be because of the arrangement pattern of the two WECs in the direction of the wave providing minimum restoring forces. Further, with the increase in the WECs around STLP, the tension developed on the S_MC-2 is reduced. The hybrid STLP+8WECs are observed to have the minimum mooring tension developed (31.2 MN). The S_MC-3 has higher tension developed for the

single STLP and is reduced by adding WECs to the STLP (Fig. 6.28c). Further, the STLP+4WECs have higher tension (91.51 MN) for the mooring cables than other hybrid STLP-WEC platforms. Like other mooring cables, the S_MC-3 has minimum tension (54.6 MN) for the STLP+8WECs hybrid platform. Similar to the S_MC-2, the S_MC-4 on the leeward side of the platform has higher tension (128.2 MN) developed for the STLP+2WECs (Fig. 6.28d). Also, the tension developed on the S_MC-4 of the STLP+4WECs is higher (114.6 MN) than that of a single STLP.

Fig. 6.29(a-f) shows the extreme tension developed on the mooring cables of the FTLP and hybrid FTLP-WEC floating platforms. For any mooring cable, the FTLP+4WECs have higher tension developed on the mooring cable for the 20-Year return period waves. This may be because of the resonance effect where the natural frequency of the platform matches the natural frequency of the wave. So sufficient stiffness should be provided to counter the same. Further, the tension developed on the mooring cables supporting the FTLP is less compared to the STLP configurations. This may be because of the higher restoring force developed by the part of the FTLP platform lying above the MSL. Further, the tension developed on the Mooring cables of the FTLP and hybrid FTLP-WEC is almost observed to be similar for any conditions of the wave.

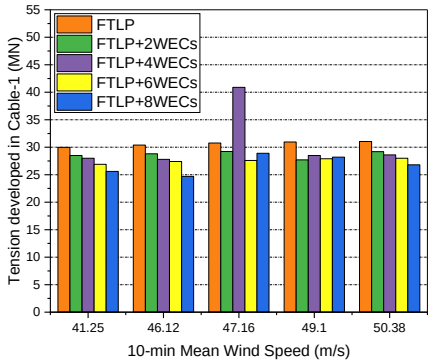


(a)

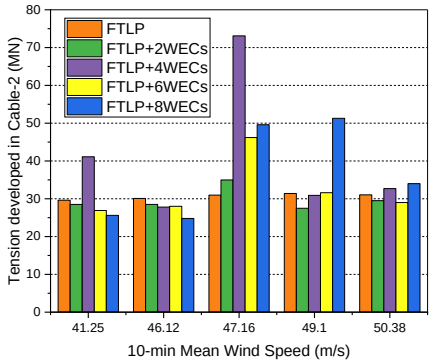


(b)

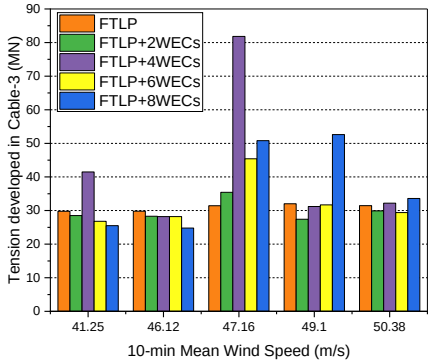


(c)

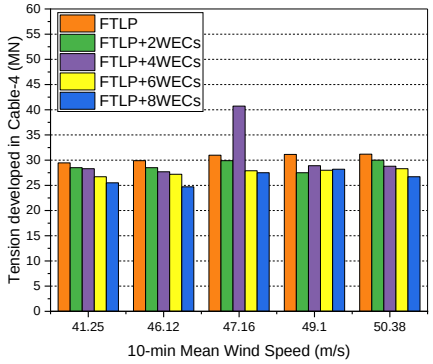


(d)

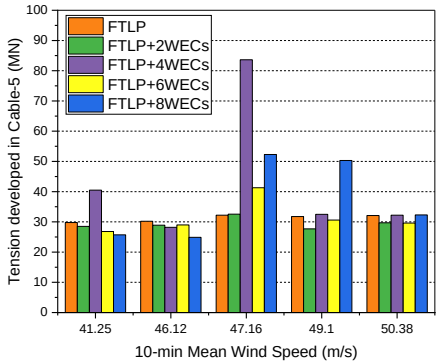


(e)

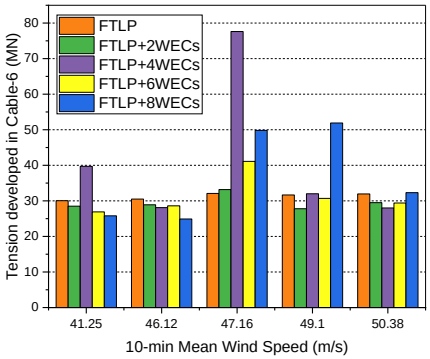


(f)

Fig. 6.29: Maximum tension developed on (a) F_MC-1, (b) F_MC-2, (c) F_MC-3, (d) F_MC-4, (e) F_MC-5 and (f) F_MC-6 of FTLP-WEC hybrid systems for various extreme wind speed conditions.

The addition of the WECs has reduced the tension developed on the F_MC-1 provided on the leeward side (Fig. 6.29a). For the F_MC-3 and F_MC-6 provided on the leeward side, near the central column has higher tension developed for the 20-Year and 50-Year return period waves (Fig. 6.29(b,f)). The FTLP+8WECs hybrid system experiences a higher tension (49.8 MN) other than the FTLP+4WECs. Also, for any wave conditions, the FTLP+6WECs (24.9 MN) are observed to have the minimum tension developed on the mooring cable for extreme wind speed conditions. The F_MC-3 of the hybrid FTLP+6WECs experiences higher tension (45.4 MN) for the 47.16 m/s wind speed condition (Fig. 6.29c). Similar variation is observed for the F_MC-3 and F_MC-5 kept on the seaward side, near to the central column (Fig. 6.29(c,e)). The Mooring cables on the seaward side experience higher tension than those on the leeward side. The tension developed on the mooring cables (F_MC-3 and F_MC-5) are higher (52.3 MN) for the FTLP+8WECs compared to other hybrid concepts for the 20-Year and 50-Year return period waves.

## 6.5 CLOSURE

The reliability analysis of the hybrid TLP-WEC FOWT is conducted to examine the design loads based on the EC method to understand the extreme responses. The study considers STLP and FTLP FOWT and the hybrid concepts combining the platform with the cone-cylinder-shaped point absorber WECs. The 1-D and 2-D EC models are developed to understand the extreme environmental conditions for a particular target return period. Further, the extreme environmental conditions for the 1-D and 2-D EC models are used to analyse the extreme response of the hybrid platforms. The NREL FAST simulation tool was employed to simulate

the same. The turbulence intensity and the wind properties for the FAST simulation were done using the TURBSIM simulator. Th observations made from the study are as follows:

- The extreme responses for the hybrid STLP-WEC and FTLP-WEC are observed for the 50-Year target return period. But for certain return periods, the extreme responses vary with the arrangement pattern of the WECs.
- The yaw motion responses for the STLP and hybrid STLP-WEC concepts are 73% (average) higher compared to the FTLP and hybrid FTLP-WEC concepts.
- The extreme fore-aft and side-to-side bending moments are almost similar for the STLP and hybrid STLP-WEC. Further, the variation is higher for the moments developed for the FTLP and the hybrid FTLP-WEC concepts.

# CHAPTER 7
# CONCLUSIONS AND FUTURE WORK

## 7.1 SUMMARY OF RESEARCH WORK

The exploitation of the combined wave and wind energy device is an emerging research topic with a limited number of studies performed on hybrid offshore wind and wave energy devices. Most of the studies carried out on the combined concepts are to enhance industrial and scientific collaboration to develop sustainable energy. Thus, with limited research on the combined wind and WEC concept, a hybrid platform of wind and WEC is a less exploited area. So, the present study considers two different TLP-type FOWT (STLP and FTLP) platforms integrated with multiple cone-cylinder-shaped WECs for the numerical analysis. The time-domain coupled dynamic analysis for different arrangements of WECs around the STLP and FTLP system in a circular pattern is conducted to understand the response behaviour of the system under various wind and wave load conditions. The estimated responses for different environmental conditions are compared for the different configurations of WECs around the platform. Further, the hydrodynamic performance of various arrays of heaving cone-cylinder point absorber-type WECs around STLP and FTLP floating wind turbines in circular and concentric patterns are examined. The North Sea wave data is considered to analyse the power absorption for various configurations of WECs surrounding the floating wind turbine platform. For various circular and concentric arrays of WECs, the hydrodynamic coefficient, time average wave power, the mean interaction factor and the capture width ratio are studied. Further, the study predicts the long-term extreme responses of the hybrid floating platforms using integration and reliability techniques.

### 7.1.1 Rigid Body Analysis of Hybrid Floating Wind Turbine Platforms

The aero-servo-hydro-elastic simulation of hybrid STLP-WEC and FTLP-WEC are performed for several operational wind speed conditions of 5MW wind turbine. The conclusions drawn from the study are detailed below:

- The RAOs of the hybrid system are observed to increase with the increase in wind speed and wave height, and the variation is observed to be minimum (2.1% average increase

with the increase in wind speed) once the wind speed crosses the rated wind speed of a 5 MW NREL wind turbine.

- The STLP+6WECs configuration is more stable as the hybrid system is observed to have lower surge and pitch response amplitudes for the North Sea environmental conditions. Average 45% reduction in surge motion and 16% reduction in pitch motion is observed for STLP+6WECs compared to single STLP.
- The surge, sway and yaw motion are more dominant for the tension leg floater. The surge and sway motions have minimal variation for all wave periods, but the yaw motion is observed to be higher for waves having wave periods above 15s.
- The effect of wind and waves on the forces and moments developed at the tower's base is high for waves of wave periods higher than 15s. The variation in the tower base forces and the moment is observed to be minimal (9.3% increase) with the increase in wind speed.
- The forces and moments developed in the for-aft direction are highest for the STLP+6WECs with zero-degree wave heading angle for the regular wave condition.
- The STLP+8WECs have the minimum mooring tension developed for the operational wind speed conditions. The 11.2 m/s wind speed conditions developed the maximum tension on the mooring cables. A 78% increase in tension is observed for the 11.2 m/s condition for the hybrid STLP+8WECs compared to a single STLP.
- The natural heave, roll and pitch frequencies for FTLP and STLP are observed to be closer compared to the surge, sway and yaw natural frequencies. Further, The FTLP with six mooring lines has minimum platform motions compared to the STLP floater with four mooring lines.
- The heave, roll and pitch motion amplitudes are minimal for all hybrid FTLP-WEC compared to the surge, sway and yaw motions.
- Minimum surge and pitch motion amplitude are observed for FTLP+8WECs for every wind speed condition, further having better wind power absorption than other FTLP-WEC configurations. Average 21% reduction in surge motion and 7% reduction in pitch motion is observed for FTLP+8WECs compared to single FTLP for wind speed conditions above the rated wind speed.
- The reduction in tension developed on the cables is observed with the addition of WECs. The FTLP+8WECs have a minimum value of tension developed on the cables.

An 81% reduction in tension developed is observed for the FTLP+8WECs compared to single FTLP apart for the 11.2 m/s wind speed condition.

- The forces and moments for the FTLP and hybrid FTLP-WEC are mostly wave-induced for different operational conditions of the wind turbine. The forces developed in the fore-aft direction are observed to be higher compared to the other two directions and have higher side-to-side moments.

### 7.1.2 Multi-body Analysis of Hybrid Floating Wind Turbine Platforms

The hydrodynamic performance of the circular and concentric arrangement of cone-cylinder point absorber WECs around STLP and FTLP is studied for the North Sea. The conclusions drawn from the study are detailed below:

- The effect of STLP and other WECs on the added mass and damping is minimal for both circular and concentric arrangement of two and six WEC configurations ($C_1$, $C_3$ and $C_4$ configurations) compared to other configurations as the ratio of the hydrodynamic coefficient is observed to be close to 1.0 for the lower wave periods $(T_P \leq 10)$. The minimal influence on added mass ensures a better sheltering effect of the platform and WECs.
- The effect of STLP and WECs on the added mass and radiation damping is minimal for both circular and concentric arrangements of eight WECs ($C_5$ and $C_6$ configurations) around the platform compared to other configurations for higher wave periods $(T_P > 10)$. The reduced damping for the WECs ensures higher absorption of wave power.
- The effect of STLP and WEC on added mass and damping is more significant in the lower wave period region for all the arrangements of WECs. The higher variation can be due to the influence of the incident and the reflected waves from the STLP and WEC.
- The total time average wave power absorbed is highest for a concentric pattern of twelve WECs around the STLP floating hybrid system ($C_7$ configuration). However, the park effect is positive for the $C_7$ configuration for all wave frequencies.
- The maximum power is absorbed by a single WEC when the point absorber-type WECs of eight numbers are arranged in a concentric pattern around the STLP ($C_6$ configuration). The maximum power absorption is due to the direct impact of waves on

the WEC without sheltering the platform or other WECs. Further, the influence of reflected waves is noted from the platform and other WECs.

- The reactive damping control or the spring-damping control is observed to absorb higher wave power than the linear damping control for the hydraulic PTO. Further, for most configurations, the highest wave power absorption for the reactive damping control is observed for the second sea state condition.
- The circular and concentric arrangement of eight numbers of WECs around STLP ($C_5$ and $C_6$ configurations) have a negligible influence on WECs as the mean interaction factor is close to 1.0 for waves of higher significant wave height. Further, it is observed that the q-factor improves with the increase of wave heading angle from 0° to 60°, which can be due to the destructive interference at corresponding incoming wave interaction.
- A minimum impact on added mass is observed for FTLP with six WECs in a circular pattern ($FW_3$). A higher impact on the added mass is observed for the eight WEC configurations ($FW_4$ and $FW_5$) when arranged in circular and concentric patterns. This may be due to sufficient space available for wave reflection.
- Negative damping is observed for the initial wave period and is close to zero, which shows the impact of the FTLP and other WECs in reducing the radiation damping. The negative damping may lead to a higher heave response of the WEC, further enhancing every possibility of structural damage to the system in a short period.
- The instantaneous wave power absorption is higher for the eight WECs in the concentric array ($FW_5$) for a zero-degree wave heading angle. Further, an average 12% increase in wave power absorption is observed for the $FW_5$ configuration as the wave direction changes from 0° to 60°.
- The maximum wave power absorption with RD-control strategy is higher for $FW_3$ and is almost like the wave power absorption pattern of $FW_6$, having twelve WECs in a concentric pattern. This may be due to the influence of the reflected waves with sufficient clearance between the FTLP and WECs. Further, only 4% reduction in wave power absorption is observed when the wave direction changes to a 60° wave heading angle.
- The mean interaction factor is almost similar for most configurations. The park effect is positive $(q\text{-factor} > 1)$ for the lower wave heights of the WEC with RD-control PTO

system. The higher power absorption in the lower wave period region may be due to the resonance conditions.

- The variation in power absorbed by the WECs in the hybrid system is higher with the increase in the WECs. The capture width ratio study concluded that the minimum variation in power absorption is for $FW_1$, $FW_2$ and $FW_3$. Also, the variation in power absorption is higher for wave heights above 2.0m. The wave crest utilisation is higher for $FW_6$ for any wave heading direction.

### 7.1.3 Mooring Analysis of Hybrid Floating Wind Turbine Platforms

The hybrid STLP+6WECs and FTLP+8WECs are analysed for different numbers of mooring lines. The motion responses, forces and moments at the base of the turbine tower and the tension developed on the mooring cables are analysed. The following conclusions drawn from the mooring analysis of hybrid FWT are as follows:

- The stiffness of the hybrid platform is observed to be higher in the vertical plane than in the horizontal plane for hybrid STLP-WEC. The natural frequency of FTLP and hybrid FTP-WEC is outside the frequency region 0.04-0.25 Hz, hence having higher structural integrity.
- Minimum variation in the natural frequency of STLP and FTLP is observed by adding WECs around the floater in a circular pattern.
- Minimum surge (45% reduced) and pitch (16% reduced) motion values are observed for the hybrid STLP+6WECs floater with a 4-Mooring layout, further having a better orientation of the wind turbine towards the wind direction, having higher efficiency for the wind power absorption.
- The chances for the occurance of resonance in surge and sway motion for the hybrid floater is higher for wind speeds below the rated wind speed of a 5MW reference wind turbine. The horizontal plane motions are 20% higher and vertical plane motions are 7% higher for the hybrid floater for any mooring configuration under regular wave conditions compared to random waves.
- The wave frequency for the STLP+6WECs, is above the natural frequency for the surge, sway, pitch and yaw motions and is below the natural frequency for the heave and pitch motion.
- The variation in roll motion is observed to be minimal for 4-Mooring and 5-Mooring configurations, further showing the higher stability of the floater.

- Tension developed in the mooring lines of the central column is 28% higher compared to other mooring cables for the 5-Mooring configuration and is 42% higher for 9-Mooring configuration of the hybrid STLP+6WECs floater. For wind velocities above rated wind speed conditions, higher values of mooring line tension are observed, implying a reduction in the restoration of responses for the hybrid floater system.
- The variation in forces developing at the turbine tower's base is minimal with the increase in mooring lines. The 4-Mooring configuration is observed to have a 32% reduction (average) for the forces developed at the base of the turbine tower .
- The standard deviation value for the moments is higher, showing the higher variation in moments developed at the turbine's base. The higher variation may be due to the influence of both wind and wave loads.
- The fore-aft shear force and the side-to-side bending moments are minimum for the 8-Mooring configuration for any wind load condition. The lowest shear force shows minimum wind load developing on the turbine, hence higher wind power absorption.
- FTLP+8WECs are observed to have the highest wind power absorption with the minimum surge (21% decrease) and pitch motion (7% decrease).
- Second-order wave excitations are observed in the case of roll and pitch motion response for the hybrid configurations of STLP and FTLP. This may be due to the non-alignment of frequencies of the wind-induced vibrations with the natural frequencies or the dominant wave frequencies.
- A 16% (average) decrease in surge motion and 22% (average) decrease in sway motion amplitudes are observed with the increasing number of mooring cables. However, a 69% (average) decrease in the yaw motion amplitudes are observed for the 7-Mooring layout supporting the hybrid FTLP+8WECs. The minimum sway motion of the platform ensures minimal lateral forces on the mooring cables.
- A 37% (average) increase in mooring tension is observed for the 11.2 m/s wind speed condition for the 6-Mooring layout. Further, the tension on the mooring cables is evenly distributed, ensuring a minimal risk of failure of the cables for the 7-Mooring, 12-Mooring and 13-Mooring layouts of FTLP+8WECs.
- The variation in the generator power for the FTLP+8WECs with the increase in the mooring cables is minimal for the 11.2 m/s and 14 m/s wind load conditions.

- The fore-aft bending moments are observed to be 18% (average) higher than the side-to-side moments for the hybrid FTLP+8WECs and are observed to decrease with the increase in the mooring cables. The wind and wave loads have minimum influence for the 12-Mooring and 13-Mooring configurations.
- The impact of the vertical mooring system on power generation is minimal for both regular and irregular wave conditions due to the minimum dynamic motion response to environmental loads for the hybrid system.

### 7.1.4 Long-Term Analysis of Hybrid Floating Wind Turbine Platforms

The long-term analysis is carried out for different circular arrays of cone-cylinder WECs around the STLP and FTLP system for different wave spectra models. The comparative study is conducted for different operational conditions of the wind turbine, and the conclusions drawn are as follows:

- A 63% (average) decrease in the long-term surge and 38% (average) decrease in long-term pitch values for operational wind speed conditions are observed for STLP+6WECs and FTLP+4WECs. The force and moments are observed to reduce with the addition of WECs and are observed minimum for STLP+6WECs, further having higher wind energy efficiency.
- The long-term response values for the translation and rotational motions are observed to be 28% (average) higher for 17 m/s wind speed and tend to be minimum for 14 m/s wind speed.
- The long-term surge and sway response is higher for STLP+8WECs for any wind speed condition. This may be because of the shift in the equilibrium position of the platform with the addition of the WECs. The minimum value for the long-term surge and sway response is observed for STLP+6WECs for any wind speed condition. This shows the minimum influence of WECs on the equilibrium position of the platform.
- The long-term response for roll motion at a $10^{-8}$ characteristic level for most hybrid systems is close to or less than 0.4 deg/m, having higher stability against overturning. The long-term response pitch motion for the hybrid STLP-WEC is observed to be minimum for 8 m/s wind speed and higher for 11.2 m/s wind speed. Thus, the need for ballasting the hybrid system will be higher for areas with wind speeds close to 11.2 m/s.

- Long-term response of tower base forces and moments concluded that the wind impact on the hybrid system is reduced for wind speeds less than the rated wind speed of the 5MW wind turbine.
- Forces and moments developed at the turbine's base during the turbine's lifetime are 53% (average) reduced for STLP+6WECs hybrid system for wind speeds below rated wind speed.
- The long-term surge, sway, and yaw motion response for the FTLP+8WECs are 6%, 9% and 29% higher than a single FTLP for 11.2 m/s wind speed conditions.
- The FTLP+6WECs have a 8% (average) higher surge motion response compared to other hybrid concepts. Other than for 11.2 m/s wind speed conditions, the variation of the surge response for the FTLP+6WECs is minimal than other hybrid FTLP-WECs. The FTLP+6WECs are observed to have minimum long-term pitch and yaw motion response at the characteristic level of $10^{-8}$.
- The long-term forces and moments are 65 % (average) higher for the FTLP+8WECs for the 8 m/s wind speed conditions. But for the higher operational wind speed conditions, the forces and the moments are minimum for the FTLP+8WECs.

### 7.1.5 Reliability Analysis of Hybrid Floating Wind Turbine Platforms

The reliability analysis of the hybrid TLP-WEC FOWT is conducted to examine the design loads based on the EC method to understand the extreme responses. The 1-D and 2-D 10-min mean wind speed-based EC models are developed to study the extreme responses of the hybrid platforms for a particular target return period. The conclusions from the study are as follows:

- The extreme responses (surge, sway, and yaw) of the floating hybrid system have minimal variation between the 1-D and 2-D EC models, and the responses increase with the increase in the wind speed. A 2.5% (average) increase in motion response values are observed for the 1-D models.
- The extreme surge response for the hybrid STLP+2WECs and STLP+8WECs is observed for the 1-year return period. But for the hybrid STLP+4WECs and STLP+6WECs, the extreme surge response is higher for a 50-year return period.
- The extreme sway and yaw responses for the hybrid FTLP-WEC are observed for the 50-year target return period. The extreme surge, sway and yaw motion responses are

minimal for the STLP+8WECs compared to the STLP+6WECs. Extreme surge, sway and yaw motion responses are 41%, 3.2% and 21.6 % reduced for the STLP+8WECs for the 50-Year return period waves.

- The minimum side-to-side bending moments are observed for the STLP+8WECs configuration except for the 25 m/s wind speed condition of the 50-year and 100-year EC model, for which the STLP+6WECs have reduced side-to-side bending moments.
- The hybrid STLP platforms had uniformity in the variation of the moments, with STLP+8WECs having 16% reduced fore-aft bending moments for operational or parked conditions.
- The extreme fore-aft moment reduces for the hybrid STLP-WEC with the increase in the WECs around STLP. The extreme fore-aft moments are minimal for the hybrid STLP+8WECs. An 22% (average) reduction in moments are observed for STLP+8WECs for the 50-Year return period.
- The extreme responses for the hybrid FTLP-WEC are observed for the 50-year target return period. However, for certain return periods, the extreme responses vary with the arrangement pattern of the WECs.
- The extreme surge response is observed to be 86% (average) higher compared to the sway motion. Minimum yaw motion is observed for FTLP and hybrid concepts compared to the conventional TLP-type platforms. A 99% (average) decrease in yaw motion responses are observed for the FTLP and hybrid FTLP-WEC concepts.
- The FTLP+6WECs are observed to have reduced surge motion response for most extreme conditions. The variation of sway and yaw motion is minimal for the hybrid concepts. The FTLP+8WECs are observed to have minimum sway (19% reduced) and yaw motion (34% reduced).
- Minimum fore-aft bending moments are observed for FTLP+6WECs, mostly for the operational wind speed conditions. Further, for the survival conditions, the fore-aft moments are 13% (average) lower for the FTLP+2WECs.
- The FTLP+8WECs have minimal side-to-side bending moment for the extreme operational conditions of a 5 MW wind turbine. For the survival conditions, the bending moments are 16% (average) lower for FTLP+2WECs.

- The mooring tension developed on the cables is minimal for the FTLP+6WECs for most extreme conditions. Minimum tension ensures reduced load developing on the cables.

## 7.2 SIGNIFICANT CONTRIBUTION FROM THE RESEARCH WORK

The study analyses the dynamic behaviour of hybrid STLP-WEC and FTLP-WEC supporting the 5MW wind turbine. The significant contributions to the hybrid floating platforms as detailed below:

- The surge, sway, and yaw motion RAOs are higher for the STLP and FTLP platforms than the heave, roll and pitch motion for the operational wind speed conditions of the 5MW NREL wind turbine.
- The addition of WECs to the STLP and FTLP platforms has minimum influence on the natural frequency of the platforms.
- The stiffness of the hybrid STLP-WEC platforms is higher in the vertical plane, as it has higher natural frequency values for the vertical plane motions. The structural integrity is higher for FTLP-WEC platforms, as the natural frequencies for the 6-DOFs are outside the 0.04-0.25Hz frequency range.
- The STLP+6WECs and FTLP+8WECs have minimum surge, sway, and pitch response for the operational conditions of the 5MW wind turbine. The minimal response ensures better orientation of the hybrid platforms towards the wind direction. The minimal sway motion ensures minimal lateral loads on the turbine tower.
- The eight WECs in circular and concentric patterns around STLP ($C_4$ and $C_5$) have minimum impedance to the motion of the WECs as the variation of the ratio of hydrodynamic coefficients (added mass and damping) from 1.0 is minimal. Also, the time average wave power absorption and the wave power absorption under RD-control are highest for the WEC placed in the $C_5$ configuration.
- The arrangement of six WECs around FTLP in a circular pattern ($FW_3$) is efficient, as the added mass and damping variation are minimal. In addition, the wave power absorption with an RD-control PTO system is higher than other arrangement patterns. Further, the wave energy absorbed from the array is higher than the isolated six WECs for the lower wave height region.

- The 5MW wind turbine supported on STLP+6WECs with 4-Mooring layout and FTLP+8WECs with 7-Mooring layout have a better orientation towards the wind direction.
- The long-term surge and pitch motion response is minimal for the STLP+6WECs and FTLP+4WECs. Further, the study suggests FTLP+6WECs, as the variation in the long-term surge response is minimal.
- The long-term wind load developing on the STLP+6WECs and FTLP+8WECs are minimal for any operational wind speed conditions. The variations in the extreme surge, sway and yaw motions responses are minimal for STLP+6WECs, FTLP+6WECs and FTLP+8WECs for any operational and parked conditions of the 5 MW wind turbine.

Table 7.1: Significant findings from the present study

| **Study performed** | **Platform** | **Significant findings** |
|---|---|---|
| Rigid-body analysis | STLP+6WECs | • Minimum surge (1.28 m/m), sway (0.27 m/m), and Pitch (0.0035deg/m) response.<br>• Minimum forces and moments in operational wind speed conditions. (Max Fore-aft force = 4127kN).<br>• Higher variation in tension developed on mooring cables. (Mean= 2.94E7 & STDV= 2.96E6).<br>• No significant change in the natural frequency of STLP with the addition of WECs. |
| | FTLP+8WECs | • Minimum surge (1.13 m/m), sway (0.23 m/m), and Pitch (.0033deg/m) response.<br>• Minimum forces and moments in operational wind speed conditions. (Max Fore-aft force = 8788 kN). |

| | | |
|---|---|---|
| | | • Minimum variation in tension developed on the mooring cables. (Mean= 8.97E7 & STDV= 7.43E6).<br>• No significant change in the natural frequency of STLP with the addition of WECs |
| Multi-body analysis | $C_5$ and $C_6$ (Eight WECs around STLP in Circular and Concentric array) | • Minimum impedance to the motion of the WECs (Ratio of hydrodynamic coefficients close to 1.0).<br>• Max wave power absorption with RD-control (273 kW and 278 kW)<br>• Minimum variation for q-factor. |
| | $FW_3$ (Six WECs around FTLP in circular array) | • Minimum impedance to the motion of the WECs (Ratio of hydrodynamic coefficients close to 1.0).<br>• Max wave power absorption with RD-control (287 kW).<br>• The variation in power absorption is minimal with the change in the wave direction |
| Mooring analysis | 4-Mooring Layout for STLP+6WECs | • Minimum values for the horizontal and vertical plane motions under irregular waves for all four load cases.<br>• Position of the mooring lines significantly influences the responses of the hybrid offshore floating platforms.<br>• Increase in mooring cables reduces tendon tension. |
| | 7-Mooring Layout for FTLP+8WECs | • Minimum surge, sway and yaw motions under irregular waves for all four load cases.<br>• The tension developed on the cables for any mooring layout is evenly distributed |

| | | |
|---|---|---|
| Long-term Analysis | STLP+6WECs | • Minimum long-term surge and pitch for wind speed conditions below 11.4 m/s. (37.4 m/m & 0.72deg/m).<br>• Minimum forces and moments. (Max Moment= 4.7E7) |
| | FTLP+8WECs | • Minimum long-term surge and pitch for wind speed conditions below 11.4 m/s. (276.2 m/m & 1.862 deg/m).<br>• Minimum variation for the forces and moments. (Max Moment= 1.75E7).<br>• Vertical forces are higher than the fore-aft force. |
| Reliability analysis | STLP+6WECs | • Reduced extreme surge, sway, and yaw motion response.<br>• Lower fore-aft bending moment for the 1-year, and 20-year return period, and higher fore-aft bending for the 50-year and 100-year return<br>• The side-to-side moments are almost similar for 1-year, 10-year, and 20-year return period waves. |
| | FTLP+6WECs<br>FTLP+8WECs | • FTLP+6WECs have reduced extreme surge motion response and bending moments for operational wind speed.<br>• FTLP+8WECs have minimal side-to-side bending moments for extreme operational conditions.<br>• Tension developed is minimum for FTLP+6WECs (20-year) |

## 7.3 FUTURE SCOPE OF RESEARCH

The future scope of research work in the dynamic analysis of the hybrid floating wind turbine are as follows:

- Physical model study can be carried out on wave tanks to simulate and evaluate the performance of hybrid configurations. The responses of the hybrid system and the tension on the mooring cables can be evaluated. Physical model studies on wave tanks for hybrid configurations provide a regulated and realistic environment to evaluate the functionality and operation of hybrid vessels in various sea states.
- The wave absorption of the WECs in the array can be studied considering the influence of the turbine tower and mooring system. Understanding the wave power absorption process within a WEC array is crucial for optimising its performance and overall efficiency. The mobility of the WEC units in response to wave forces can be influenced by dampening effects introduced by mooring lines and anchors. This dampening may impact the unit's ability to capture energy and respond to motion.
- The wave power absorption through different PTO systems can be studied considering different control parameters. The control parameters are crucial for maximising the PTO system's effectiveness and performance. Different iterative design methods can be implemented to study the wave power absorption.
- The levelized cost for the energy absorption using the hybrid STLP-WEC and FTLP-WEC can be studied. Sensitivity analysis is frequently used to determine the effects of changes in important factors on the LCOE, such as differences in capital costs, energy production, or discount rates that aids in determining which elements have the greatest impact on the WECs' economic viability.

# REFERENCES


Agarwal, P. and Manuel, L. (2009). Simulation of offshore wind turbine response for long-term extreme load prediction. *Engineering Structures*, 31, 2236-2246.

Alkarem, R.T. and Ozbahceci, B.O. (2021). A complemental analysis of wave irregularity effect on the hydrodynamic responses of offshore wind turbines with the semi-submersible platform. *Applied Ocean Research*, 113, 1-17.

Amare, G.D. and Ayele, Y.Z. (2018). Effect of negative damping on offshore structures. *Proceedings of 37th International Conference on Offshore Mechanics and Arctic Engineering*, 17th – 22nd June 2018, Madrid, Spain.

Ameachi, C.V., Odijile, A.C., Wang, F. and Ye, J. (2022). Numerical investigation on mooring line configurations of a Paired Column Semisubmersible for its global performance in deep water condition. *Ocean Engineering*. 250, 1-27.

Bachynski, E.E. and Moan, T. (2012). Design considerations for tension leg platform wind turbines. *Marine Structures*, 29, 89-114.

Bachynski, E.E. and Moan, T. (2013). Point absorber design for a combined wind and wave energy converter on a tension-leg support structure. *Proceedings of 32nd International Conference on Offshore Mechanics and Arctic Engineering*, 9th – 14th June 2013, Nantes, France.

Bagbanci, H., Karmakar, D. and Guedes Soares, C. (2015). Comparison of Spar and Semisubmersible floater concepts of offshore wind turbines using long term analysis. *Journal of Offshore Mechanics and Artic Engineering*, 137, 1-10.

Bae, Y.H., Kim, M.H. and Kim, H.C. (2017). Performance changes of a floating offshore wind turbine with broken mooring line. *Renewable Energy*, 101, 364-375.

Behrens, S., Hayward, J., Hemer, M. and Osman, P. (2012). Assessing the wave energy converter potential for Australian coastal regions. *Renewable Energy*, 43, 210-217.

Bellew, S. and Yde, A. (2014). Application of the aero-hydro-elastic model, HAWC2-wamit, to offshore data from floating power plants hybrid wind- and wave-energy test platform, P37. *Proceedings of 5th International Conference on Ocean Energy*, 4th -6th November 2014, Halifax, Canada.

Chandrasekaran, S. and Jain, A.K. (2002). Dynamic behaviour of square and triangular offshore tension leg platform under regular wave loads. *Ocean Engineering*, 29, 279-313.

Chandrasekaran, S., and Koshti, Y. (2013). Dynamic analysis of a tension leg platform under extreme waves. Journal of Naval Architecture and Marine Engineering, 10, 1-10.

Chen J., Hu Z., Liu G. and Wan, D. (2019). Coupled aero-hydro-servo-elastic methods for floating wind turbines. *Renewable Energy*, 130, 139-153.

Chen W., Gao F., Meng X., Chen B. and Ren A. (2016). W2P: A high-power integrated generation unit for offshore wind power and ocean wave energy. *Ocean Engineering*, 128, 41-47.

Cheng, P., Huang, Y. and Wan, D. (2019). A numerical model for fully coupled aero-hydrodynamic analysis of floating offshore wind turbine. *Ocean Engineering*, 173, 183-196.

Cheng, Z., Wen, T.R., Ong, M.C. and Wang, K. (2019). Power performance and dynamic responses of a combined floating vertical axis wind turbine and wave energy converter concept. *Energy*, 171, 190-204.

Child, B.F.M. and Venugopal, V. (2010). Optimal configurations of wave energy device arrays. *Ocean Engineering*, 37, 1402-1417.

Cho, I.H., Kim M.H. and Kewon, H.M. (2012). Wave energy converter uses relative heave motion between the buoy and inner dynamic system. *Ocean Systems Engineering*, 2, 297-314.

Christensen, C.F. and Nielsen, T.A. (2000). Return period for environmental loads-combination of wind and wave loads for offshore wind turbines, EFP 99.

Clement, C., Kosleck, S. and Lie, T. (2021). Investigation of viscous damping effect on the coupled dynamic response of a hybrid floating platform concept for offshore wind turbines. *Ocean Engineering*, 225, 1-12.

Collazo, C.P., Greaves, D. and Iglesias, G. (2015). A review of combined wave and offshore wind energy. *Renewable and Sustainable Energy Reviews*, 42, 141-153.

Cong, P., Teng, B., Bai, W., Ning, D. and Liu, Y. (2021). Wave power absorption by an oscillating water column (OWC) device of annular cross-section in a combined wind-wave energy system. *Applied Ocean Research*, 107, 1-18.

Couling, J.A., Goupee, J.A., Robertson, N.A., Jonkman, M. and Dagher, J.H. (2013). Validation of a FAST semi-submersible floating wind turbine numerical model with DeepCwind test data. *Journal of Renewable and Sustainable Energy*, 5, 1-29.

Crudu L, Obreja D.C. and Marcu O, (2016). Moored offshore structures-evaluation of forces in elastic mooring lines. *Materials Science and Engineering*, 147, 1-12.

da Silva, L., Sergiienko, N., Cazzolato, B. and Ding, B. (2022). Dynamics of hybrid offshore renewable energy platforms: Heaving point absorbers connected to a semi-submersible floating offshore wind turbine. *Renewable Energy*, 199, 1424-1439.

Ding, H., Han, Y., Le, C. and Zhang, P. (2017). Dynamic analysis of a floating wind turbine in wet tows based on multi-body dynamics. *Journal of Renewable and Sustainable Energy*, 9, 1-14.

Drew, B., Plummer, A.R. and Sahinkaya, M.N. (2009). A review of wave energy converter technology. *Journal of Power and Energy*, 223, 887-902.

Falnes, J. (2007). A review of wave-energy extraction. *Marine Structures*, 20, 185-201.

Fukuda, J. (1967). Theoretical determination of design wave bending moments. *Japan Ship Building and Marine Engineering*, 2, 13-22.

Gao, Z., Moan, T., Wan, L. and Michailides, C. (2016). Comparative numerical and experimental study of two combined wind and wave energy concepts. *Journal of Ocean Engineering and Science*, 1, 36-51.

Gaspar, J.F., Kamarlouei, M., Thiebaut, C. and C. Guedes Soares. (2021). Compensation of a hybrid platform dynamics using wave energy converters in different sea state conditions. *Renewable Energy*, 177, 871-883.

Gaspar, J.F., Calvario, M., Kamarlouei, M. and Guedes Soares, C. (2016). Power take-off concept for wave energy converters based on oil-hydraulic transformer units. *Renewable Energy*, 86, 1232-1246.

Ghafari, R.H., Neisi, A., Ghassemi, H. and Iranmanesh, M. (2021). Power production of the hybrid Wavestar point absorber mounted around the Hywind spar platform and its dynamic response. *Journal of Renewable and Sustainable Energy*, 13, 1-15.

Ghafari, R.H., Ghassemi, H., Abbasi A., Vakilabadi, K.A., Yazdi, H. and He, G. (2022). Novel concept of hybrid wavestar- floating offshore wind turbine system with rectilinear arrays of WECs. *Ocean Engineering*, 262, 1-21.

Guedes Soares C., Fonseca N., Pascoal R., Clauss G.F., Schmittner C.E. and Hennig J. (2004). Analysis of wave induced loads on FPSO due to abnormal waves. *Journal of Offshore Mechanics and Arctic Engineering*, 128, 241-247.

Guedes Soares, C. and Moan, T. (1991). Model uncertainty in long term distribution of waves induced bending moments for fatigue design of ship structures. *Marine Structures*, 4, 294-315.

Guedes Soares, C. (1993). Long term distribution of non-linear wave induced vertical bending moments. *Marine Structures*, 6, 475-483.

Hall, M. and Goupee, A. (2015). Validation of a lumped-mass mooring line model with deepcwind semisubmersible model test data. *Ocean Engineering*, 104, 590-603.

Hals, J., Falnes, J. and Moan, T. (2011). Constrained optimal control of a heaving buoy Wave-Energy Converter. *Journal of Offshore Mechanics and Arctic Engineering*, 133, 1-15.

Han, Y., Le, C., Ding, H., Cheng, Z. and Zhang, P. (2017). Stability and dynamic response analysis of a submerged tension leg platform for offshore wind turbines. *Ocean Engineering*, 129, 68-82.

Han, Z., Zhao, Y., Su, J., He, Y., Xu, Y., Wu, F., and Jiang, Z. (2022). On the hydrodynamic responses of a multi-column TLP floating offshore wind turbine model. *Ocean Engineering*, 253, 1-9.

Hansen, R.H. (2013). Design and control of the power take-off system for a wave energy converter with multiple absorbers, Ph.D. Thesis, Department of Energy Technology, Aalborg University.

Haver, S. and Winterstein, S.R. (1999). Environmental contour lines: a method for estimating long term extremes by a short-term analysis. *Transactions - Society of Naval Architects and Marine Engineers*, 116, 116-127.

Howey, B., Keri, M.C., Hann, M., Iglesias, G., Gomes, R.P.F., Henriques, J.C.C., Gato, L. M.C. and Greaves, D. (2021). Compact floating wave energy converter arrays: Inter-device mooring connectivity and performance. *Applied Ocean Research*, 115, 1-15.

Hu, J., Zhou, B., Vogel, C., Liu, P., Wilden, R., Sun, K., Zang, J., Geng, J., Jin, P., Cui, L., Jiang, B., Collu, M. (2020). Optimal design and performance analysis of a hybrid system combing a floating wind platform and wave energy converters. *Applied Energy*, 269, 2-16.

Hu, R., Le, C., Zang, P. and Ding, H. (2022). Hydrodynamic modelling effect analysis of a fully submerged tension leg concept integrating the DTU 10 MW offshore wind turbine. *Marine Structures*, 83, 1-17.

Jamalkia, A., Ettefagh, M.M. and Mojtahedi, A. (2016). Damage detection of TLP and spar floating wind turbine using dynamic response of the structure. *Ocean Engineering*, 125, 191-202.

Jeon, S.H., Cho. Y.U., Kimball, R.W., Seo, M.W. and Jeong, W.B. (2013). Dynamic response of floating substructure of spar type offshore wind turbine with catenary mooring cables. *Ocean Engineering*, 72, 356-364.

Jiang, X., Day, S. and Clelland, D. (2018). Hydrodynamic responses and power efficiency analyses of an oscillating wave surge converter under different simulated PTO strategies. *Ocean Engineering*, 170, 286-297.

Jin, R., Gou, Y., Geng, B., Zhang, H. and Liu, Y. (2020). Coupled dynamic analysis for wave action on a tension leg-type submerged floating tunnel in time domain. *Ocean Engineering*, 212, 1-14.

Johannessesn, K., Meling, T.S. and Hayer, S. (2001). Joint distribution for wind and waves in the Northern North Sea. *Proceedings of 11th International Conference on Offshore and Polar Engineering*, 17th – 22nd June 2001, Stavanger, Norway.

Jonkman, J.M. (2007). Dynamic modelling and loads analysis of an offshore floating wind turbine. National Renewable Energy Laboratory, Golden, CO, Technical Report No. NREL/TLP-500-41958.

Jonkman, J. M. (2009). Definition of the Floating System for Phase IV of OC3. National Renewable Energy Laboratory, Technical Report No. NREL/TP-500-47535.

Jonkman, J.M. and Matha, D. (2011). Dynamics of offshore floating wind turbine-analysis of three concepts. *Wind Energy*, 14, 557-569.

Kamarlouei, M., Gaspar, J.F., Calvario, M., Hallak, T.S., Mendes, M.J.G.C., Thiebaut, F., Guedes Soares, C. (2020). Experimental analysis of wave energy converters concentrically attached on a floating offshore platform. *Renewable Energy*, 152, 1171-1185.

Kamarlouei, M., Gaspar, J.F., Guedes Soares, C. (2022). Optimal design of an axisymmetric two-body wave energy converter with translational hydraulic power take-off system. *Renewable Energy*, 183, 586-600.

Karimi, M., Buckham, B. and Crawford, C. (2019). A fully coupled frequency domain model for floating offshore wind turbines. *Journal of Ocean Engineering and Marine Energy*, 5, 135-158.

Karimirad, M. and Koushan, K. (2016). WindWEC: Combining wind and wave energy inspired by Hywind and Wavestar. *Proceedings of 5th International Conference on Renewable Energy Research and Applications*, 20-23 November 2016, Birmingham, UK.

Karimirad, M. and Michailides, C. (2018). Effect of misaligned wave and wind action on the response of the combined concept wind WEC. *Proceedings of 37th International Conference on Ocean, Offshore and Arctic Engineering*, 17th – 22nd June 2018, Madrid, Spain.

Karmakar, D. and Guedes Soares, C. (2015). Extreme response prediction of offshore wind turbine using inverse reliability technique. *Proceedings of 34th International Conference on Ocean, Offshore and Arctic Engineering*, 31st May - 5th June 2015, Newfoundland, Canada.

Karmakar, D. and Guedes Soares, C. (2014). Reliability based design loads of an offshore semi-submersible floating wind turbine. *Developments in Maritime Transportation and Exploitation of Sea Resources*, Guedes Soares, C. and FL Pena, (Eds)., Taylor & Francis Group, London, 919-926.

Karmakar, D., Bagbanci, H. and Guedes Soares, C. (2016). Long-term extreme load prediction of spar and semisubmersible floating wind turbines using the environmental contour method. *Journal of Offshore Mechanics and Arctic Engineering*, 138, 1-9.

Katsidoniotaki, E., Göteman, M. (2022). Numerical modeling of extreme wave interaction with point-absorber using OpenFOAM. *Ocean Engineering*, 245, 1-11.

Katsidoniotaki, E., Nilsson, E., Rutgersson, A., Engström, J. and Göteman, M. (2021). Response of point-absorbing wave energy conversion system in 50-years return period extreme focused waves. *Journal of Marine Science and Engineering*, 9, 1-29.

Kim, S., Lee, J., Kang, D. and Lee, S. (2019). Motion characteristics of a floating wave energy converter with wave activating body type. *International Journal of Naval Architecture and Ocean Engineering*, 11, 244-255.

Kim, S.J., Koo, W. and Shin, M.J. (2019). Numerical and experimental study on a hemispheric point-absorber-type wave energy converter with a hydraulic power take-off system. *Renewable Energy*, 135, 1260-1269.

Kobayashi, M., Shimada, K., Fujihira, T. (1987). Study on dynamic response of a TLP in waves. *Journal of Offshore Mechanics and Artic Engineering*, 109, 61-66.

Kolios, A., Maio, L.F.D., Wang L., Cui, L. and Sheng, Q. (2018). Reliability assessment of point-absorber wave energy converters. *Ocean Engineering*, 163, 40-50.

Koniospoliatis D.N., Mavrakos, S.A. (2016). Hydrodynamic analysis of an array of interacting free-floating oscillating water column (OWC's) devices. *Ocean Engineering*, 111, 179-197.

Konispoliatis, D, N., Katsaounis, G.M., Manolas, D.I., Soukissian, T.H., Polyzos, S., Mazarakos, T,P., Voutsinas,S, G. and Mavrakos, S, A. (2021). REFOS: A Renewable Energy Multi-Purpose Floating Offshore System. *Energies*, 14, 1-28.

Koo, B.J., Goupee, A.J., Kimball, R.W. and Lambrakos, K.F. (2014). Model tests for a floating wind turbine on three different floaters. *Journal of Offshore Mechanics and Arctic Engineering*, 136, 1-11.

Le, C., Jian, Z., Hongyan, D., Puyang, Z. and Guilan, W. (2020). Preliminary design of a submerged support structure for floating wind turbines. *Journal of Ocean University China*, 19, 1265-1282.

Lee, C.F., Tryfonidis, C. and Ong, M.C. (2023). Power Performance and Response Analysis of a Semi-Submersible Wind Turbine Combined With Flap-Type and Torus Wave Energy Converters. *Journal of Offshore Mechanics and Arctic Engineering*, 145, 1-12.

Lee, C.H. (1995). WAMIT Theory Manual, Massachusetts Institute of Technology, Department of Ocean Engineering, Cambridge.

Lee, H., Bae, Y.H., and Cho, H. (2016). One-way coupled response analysis between floating wind-wave hybrid platform and wave energy converters. *Journal of Ocean Engineering and Technology*, 30, 84-90.

Li, L., Gao, Y., Yuan, Z., Day, S., and Hu, Z. (2018). Dynamic response and power production of a floating integrated wind, wave and tidal energy system. *Renewable energy*, 116, 412-422.

Li, L., Gao, Z. and Moan, T. (2015). Joint distribution of environmental conditions at five European offshore sites for design of combined wind and wave energy devices. *Journal of Offshore Mechanics and Arctic Engineering*, 137, 1-16.

Li., L. and Liu, Y. (2021). Short-crestedness effect on the dynamic response of offshore floating wind turbines. *Ships and Offshore Structures*, 16, 1-10.

Liu, J., Thomas, E., Goyal, A., and Manuel, L. (2019). Design loads for a large wind turbine supported by a semi-submersible floating platform. *Renewable Energy*, 138, 923-936.

Low, Y.M. and Huang, X. (2017). Long-term extreme response analysis of offshore structures by combining importance sampling with subset simulation. *Structural Safety*, 69, 79-95.

Luan, C., Michailides, C., Gao, Z. and Moan, T. (2014). Modeling and analysis of a 5 MW semi-submersible wind turbine combined with three flap-type wave energy converters. *Proceedings of 33rd International Conference on Ocean, Offshore and Arctic Engineering*, 8-13 June 2014, California, USA.

Ma, J., Zhou, D., Han, Z., Zhang, K., Bao, Y. and Dong, L. (2019). Fluctuating wind and wave simulations and its application in structural analysis of a semi-submersible offshore platform. *International Journal of Naval Architecture and Ocean Engineering*, 11, 624-637.

Martin, D., Li, X., Chen, C. A., Thiagarajan, K., Ngo, K., Parker, R. and Zuo, L. (2020). Numerical analysis and wave tank validation on the optimal design of a two-body wave energy converter. *Renewable Energy*, 145, 632-641.

Matha, D. and Jonkman, J. (2009). Model Development and Loads Analysis of an Offshore Wind Turbine on a Tension Leg Platform, with a Comparison to Other Floating Turbine Concepts. National Renewable Energy Laboratory, Technical Report No. NREL/SR-500-45891.

Mavrakos, S.A. (1991). Hydrodynamic coefficients for groups of interacting vertical axisymmetric bodies, *Ocean Engineering*, 18, 485-515.

Muliawan, M.J., Karimirad, M. and Moan, T. (2013). Dynamic response and power performance of a combined spar-type floating wind turbine and coaxial floating wave energy converter. *Renewable Energy*, 50, 47-57.

Muliawan, M.J., Karimirad, M., Gao, Z. and Moan, T. (2013). Extreme responses of a combined spar-type floating wind turbine and floating wave energy converter (STC) system with survival modes. *Ocean Engineering*, 65, 71-82.

Naess, A. and Moan, T. (2013). Stochastic dynamics of marine structures. Cambridge University Press.

Negahdari, M., Dalayeli, H. and Moghadas, M.H. (2018). Design of two-body wave energy converter by incorporating the effect of hydraulic power take-off parameter. *Journal of Marine Science and Technology*, 26, 496-507.

Niranjan, R. and Ramisetti, S.B. (2022). Insights from detailed numerical investigation of 15 MW offshore semi-submersible wind turbine using aero-hydro-servo-elastic code. *Ocean Engineering*, 251, 1-25.

Ozkop, E. and Altas, I.H. (2017). Control, power and electrical components in wave energy conversion systems: A review of the technologies. *Renewable and Sustainable Energy Reviews*, 67, 106-115.

Perez-Collazo, C., Greaves, D. and Iglesias G. (2018). Hydrodynamic response of the WEC sub-system of a novel hybrid wind-wave energy converter. *Energy Conversion and Management*, 171, 307-325.

Perez-Collazo, C., Pemberton, R., Greaves, D. and Iglesias, G. (2019). Monopile-mounted wave energy converter for a hybrid wind-wave system. *Energy Conversion and Management*, 199, 1-13.

Perveen, R., Kishor, N. and Mohanty, S.R. (2014). Offshore wind farm development: present status and challenges. *Renewable Sustainable Energy*, 29, 780-792.

Philippe, M., Babarit, A. and Ferrant, P. (2011). Comparison of time and frequency domain simulation of an offshore floating wind turbine. *Proceedings of 30th International Conference on Ocean, Offshore and Artic Engineering*, 19th – 24th June 2011, Rotterdam, Netherlands.

Quio, D., Ou, J. and Wu, F. (2012). Design selection analysis for mooring positioning system of deepwater semi-submersible platform. *Proceedings of 22nd International Offshore and Polar Engineering Conference*, 17th – 22nd June 2012, Rhodes, Greece.

Raed, K., Karmakar, D. and Guedes Soares, C. (2016). Long-term assessment of the wave load acting on semi-submersible wind turbine support structure. *Proceedings of 3rd International Conference on Maritime Technology and Engineering*, Lisbon, Portugal.

Raed, K., Teixeira, A.P. and Guedes Soares, C. (2019). Assessment of long-term extreme response of a floating support structure using the environmental contour method. *Advances in Renewable Energies Offshore*, 685-692.

Ren, N., Ma, Z., Shan, B., Ning, D. and Ou, J. (2020). Experimental and numerical study of dynamic responses of a new combined TLP type floating wind turbine and a wave energy converter under operational conditions. *Renewable Energy*, 151, 966-974.

Roy, S., Ghosh, V., Dey, S., Vimmadi, S. and Banil, A.K. (2017). A coupled analysis of motion and structural responses for an offshore spar platform in irregular waves. *Ships and Offshore Structures*, 12, 296-304.

Ruehl, K., Forbush, D.D., Yu, Y.H. and Tom, N. (2020). Experimental and numerical comparisons of a dual-flap floating oscillating surge wave energy converter in regular waves. *Ocean Engineering*, 196, 1-17.

Sakaris, S.C., Yang, Y., Bashir, M., Michailides, C., Wang, J., Sakellariou, S. J. and Chun, Li. (2021). Structural health monitoring of tendons in a multibody floating offshore wind turbine under varying environmental and operating conditions. *Renewable Energy*, 179, 1897-1914.

Saranyasoontorn, K. and Manuel, L. (2004). Efficient models for wind turbine extreme loads using inverse reliability. *Journal of Wind. Engineering and Industrial Aerodynamics*, 92, 789–804.

Saranyasoontorn, K. and Manuel, L. (2005). On assessing the accuracy of offshore wind turbine reliability-based design loads from environmental contour method. *Journal of Offshore and Polar Engineering*, 15, 1-9.

Saranyasoontorn, K. and Manuel, L. (2006). Design loads for wind turbines using environmental contour method. *Journal of Solar Energy Engineering*, 128, 554-561.

Setiyawan., Salim, H., Lukman, R.T., Hadi, S. and Hadihardaja, I.K. (2013). Spectral representation in Pacitan and Meulaboh coast. *International Journal of Civil & Environmental Engineering*, 13, 29-34.

Shen, M., Hu, Z. and Liu, G. (2016). Dynamic response and viscous effect analysis of a TLP-type floating wind turbine using a coupled aero-hydro-mooring dynamic code. *Renewable Energy*, 99, 800-812.

Sheng, W. (2019). Wave energy conversion and hydrodynamics modelling technologies: A review. *Renewable and Sustainable Energy Reviews*, 109, 482-498.

Sheng, W., Tapoglou, E., Ma, X., Yatlor, C.J., Dorrell, R., Parsons, D.R. and Aggidis, G. (2022). Time-Domain Implementation and Analyses of Multi-Motion Modes of Floating Structures. *Journal of Marine Science and Engineering*, 10, 1-24.

Si, Y., Chen, Z., Zeng, W., Sun, J., Zhang, D., Ma, X. and Qian, P. (2021). The influence of power-take-off control on the dynamic response and power output of combined semi-submersible floating wind turbine and point-absorber wave energy converters. *Ocean Engineering*, 227, 1-23.

Sinha, A., Karmakar, D. and Guedes Soares, C. (2016). Performance of optimally tuned arrays of heaving point absorbers. *Renewable Energy*, 92, 517-531.

Sinha, A., Karmakar, D., Guedes Soares, C. (2015). Numerical modelling of an array of heaving point absorbers. *Renewable Energies Offshore*, 383-391.

Sultania, A. and Manuel, L. (2018). Reliability analysis for a spar-supported floating offshore wind turbine. *Wind Engineering*, 42, 51–65.

Sun, T. and Zhang, Z. (2022). Optimal control and performance evaluation of an inverter-based point absorber wave energy converter. *Ocean Engineering*, 259, 1-17.

Tabeshpour, M.R., Ahmadi, A. and Malayjerdi, E. (2018). Investigation of TLP behaviour under tendon damage. *Ocean Engineering*, 156, 580-595.

Tabeshpour, M.R. and Abbasian, S.M.R.S. (2021). The optimum mooring configuration with minimum sensitivity to remove a mooring line for a semi-submersible platform. *Applied Ocean Research*, 114, 1-10.

Vantorre, M., Banasiak, R., Verhoeven, R. (2004). Modelling of hydraulic performance and wave energy extraction by a point absorber in heave. *Applied Ocean Research*, 26, 61-72.

Vardaroglu, M., Gao, Z., Avossa, A.M. and Ricciardelli, F. (2022). Validation of a TLP wind turbine numerical model against model-scale tests under regular and irregular waves. *Ocean Engineering*, 256, 1-13.

Vijay, K. G., Koley, S., Trivedi, K. and Nishad, C.S. (2022). Hydrodynamic coefficients of a floater near a partially reflecting seawall in the presence of an array of caisson blocks. *Journal of Offshore Mechanics and Arctic Engineering*, 144, 1-16.

Vijay, K.G., Karmakar, D. and Guedes Soares, C. (2020). Long-term response analysis of TLP type offshore wind turbine. *ISH Journal of Hydraulic Engineering*, 26, 31-43.

Wan, L., Gao, Z. and Moan, T. (2015). Experimental and numerical study of hydrodynamic responses of a combined wind and wave energy converter concept in survival modes. *Coastal Engineering*, 104, 151-169.

Wan, L., Gao, Z., Moan, T. and Lugni, C. (2016). Comparative experimental study of the survivability of a combined wind and wave energy converter in two testing facilities. *Ocean Engineering*, 111, 82-94.

Wan, L., Greco, M., Lugni, C., Gao, Z. and Moan, T. (2017). A combined wind and wave energy-converter concept in survival mode: Numerical and experimental study in regular waves with a focus on water entry and exit. *Applied Ocean Research*, 63, 200–216.

Wan, L., Ren, N. and Zhang, P. (2020). Numerical investigation on the dynamic responses of three integrated concepts of offshore wind and wave energy converter. *Ocean Engineering*, 217, 1-13.

Wan, L., Ren, N. and Tay, Z. (2019). Dynamic response of three combined offshore wind and wave energy conversion concepts applied in varied water depth. *Proceedings of 29th International Ocean and Polar Engineering Conference*, 16th – 21st June 2019, Hawaii, USA.

Wandji, W. N., Natarajan, A. and Dimitrov, N. (2016). Development and design of a semi-floater substructure for multi-megawatt wind turbines at 50m water depths. *Ocean Engineering*, 125, 226-237.

Wang, K., Ji, C., Xue, H. and Tang, W. (2016). Frequency domain approach for the coupled analysis of floating wind turbine system. *Ships and Offshore Structures*, 12, 767-774.

Wayman, E. N., Sclavouns, P. D., Butterfield, S., Jonkman, J. and Musial, W. (2006). Coupled dynamic modelling of floating wind turbine systems. *Proceedings of Offshore Technology Conference*, 1st – 4th May 2006, Houston, Texas, USA.

Weiss, C. V., Guanche, R., Ondiviela, B., Castellanos, O.F. and Juanes, J. (2018). Marine renewable energy potential: A global perspective for offshore wind and wave exploitation. *Energy Conversion and Management*, 177, 43-54.

Windt, C., Davidson, J., Faedo, N., Penalba, M. and Ringwood, J.V. (2022). On the Importance of High–Fidelity Numerical Modelling of Ocean Wave Energy Converters under Controlled Conditions. *Floating Offshore Energy Devices*, 20, 31-38.

Windt, C., Davidson, J., Ransley, E.J., Greaves, D., Jakobsen, M., Kramer, M. and Ringwood, J.V. (2020). Validation of a CFD-based numerical wave tank model for the power production assessment of the wavestar ocean wave energy converter. *Renewable Energy*, 146, 2499-2516.

Winterstein, S.R. and Engebretsen, K. (1998). Reliability based prediction of design loads and responses for floating ocean structures. *Proceedings of 17th International Conference on Offshore Mechanics and Arctic Engineering*, 5th – 6th July, 1998, Lisbon, Portugal.

Winterstein, S.R., Ude, T.C., Cornell, C.A., Bjerager, P. and Haver, S. (1993). Environmental contours for extreme response: inverse form with omission factors, *Proceedings of the*

*International Conference on Structural Safety and Reliability*, 9th – 13th August 1993, Innsbruck, Australia.

Xiang, S., Cheng, B., Tang, M. and Zhang, S. (2022). Hydrodynamic characteristics of deep-water floating foundations with different mooring systems. *Ocean Engineering*, 257, 1-16.

Yang, S.H., Ringsberg, J.W., Johnson, E. and Hu, Z. (2020). Experimental and numerical investigation of a taut-moored wave energy converter: a validation of simulated mooring line forces. *Ships and Offshore Structures*, 15, S55-S69.

Yang, Y., Bashir, M., Michailides, C., Mei, X., Wang, J. and Li, C. (2021). Coupled analysis of a 10MW multi-body floating offshore wind turbine subjected to tendon failure. *Renewable Energy*, 176, 89-105.

Yongsheng Z., Jianmin, Y., Yanping, H. and Mintong G. (2016). Dynamic Response Analysis of a Multi-Column Tension-Leg-Type Floating Wind Turbine Under Combined Wind and Wave Loading. *Journal of Shanghai Jiaotong University (Science)*, 21, 103-111.

Young-Bok Kim, B.S. (2003). Dynamic Analysis of Multiple-Body Floating Platforms Coupled with Mooring Lines and Risers, Ph.D. Thesis, Texas A&M University, Texas.

Yu, J., Hao, S., Yu, Y., Chen, B., Cheng, S. and Wu, J. (2019). Mooring analysis for a whole TLP with TTRs under tendon one-time failure and progressive failure. *Ocean Engineering*, 182, 360-385.

Zabihi, M., Mazaheri, S. and Namin, M.M. (2021). Experimental hydrodynamic investigation of a fixed offshore Oscillating Water Column device. *Applied Ocean Research*, 85, 20-33.

Zhang, L., Shi, W., Karimirad, M., Michailides, C. and Jiang, Z. (2020). Second-order hydrodynamic effects on the response of three semisubmersible floating offshore wind turbines. *Ocean Engineering*, 207, 1-22.

Zhang, Y., Zhao, Y., Sun, W. and Li, J. (2021). Ocean wave energy converters: Technical principle, device realization, and performance evaluation. Renewable and Sustainable Energy Reviews, 141, 110764.

Zhao, Y., Jianmin, Yang, J., He, Y. and Gu, M. (2016). Dynamic response analysis of a multi-column Tension-leg-type floating wind turbine under combined wind and wave loading. *Journal of Shanghai Jiaotong University*, 21, 103-111.

Zhao, Z., Shi, W., Wang, W., Qi, S. and Li, X. (2021). Dynamic analysis of a novel semi-submersible platform for a 10 MW wind turbine in intermediate water depth. *Ocean Engineering*, 237, 1-17.

Zheng, S. and Zhang, Y. (2018). Theoretical modelling of a new hybrid wave energy converter in regular waves. *Renewable Energy*, 128, 125-141.

Zhou, C.L.S., Shan, B., Hu, G., Song, X., Liu, Y., Hu, Y. and Yiqing, X. (2021). Dynamics of a Y-shaped semi-submersible floating wind turbine: a comparison of concrete and steel support structures. *Ships and Offshore Structures*. 17, 1-22.

Zhou, M., Pan, Y., Ren, N. and Zhu, Y. (2017). Operational Performance of a Combined TLP-type Floating Wind Turbine and Heave-type Floating Wave Energy Converter System. *Advances in Engineering Research*, 94, 1-5.

Zhou, Y., Ning, D., Shi, W., Johanning, L. and Liang, D. (2020). Hydrodynamic investigation on an OWC wave energy converter integrated into an offshore wind turbine monopile. *Coastal Engineering*, 162, 1-13.

# AUTHOR'S RESUME

**Rony J. S**
Ph.D. Research Scholar
Department of Water Resources and Ocean Engineering
National Institute of Technology Karnataka, Surathkal
Mangalore – 57502, Karnataka
Contact No: +91-8848078067
Email ID: ronyjs17@gmail.com

The author was born on 3rd October 1993 in Trivandrum District, Kerala, India. Having passed the All India Secondary School Examination from St. Mary's Central School, Trivandrum, Kerala, in 2009 he completed Intermediate in 2011 from St. Mary's Central School, Trivandrum. He graduated with Bachelor's in Civil Engineering from the Mar Baselios College of Engineering and Technology (MBCET), Kerala University, Trivandrum, in 2015. Thereafter, he obtained Master's in Marine Structures from the National Institute of Technology Karnataka, Surathkal, Mangalore, in 2018. After completing his Master's degree, he joined the Doctoral research program in the Department of Water Resources and Ocean Engineering, National Institute of Technology, Karnataka, Surathkal, in 2019. The author's interest lies in the problems related to wind and wave energy absorption through hybrid offshore floating platforms. He communicated and published his work in reputed international Journals and Conference proceedings during his research. The detailed list of publications is presented below:

**(a) List of Publications in Journals:**

1. **Rony, J.S**., Karmakar, D. and C. Guedes Soares. (2021). Coupled dynamic analysis of spar-type floating wind turbine under different wind and wave loading. *Marine Systems and Ocean Technology*, 16, 169-198. DOI: 10.1007/s40868-021-00106-7
2. **Rony, J.S**., and Karmakar, D. (2022). Coupled dynamic analysis of hybrid offshore wind turbine and wave energy converter. *Journal of Offshore Mechanics and Artic Engineering*, 144, 1-13. DOI: 10.1115/1.4052936
3. **Rony, J. S**., and Karmakar, D. (2023). Performance of a hybrid TLP floating wind turbine combined with arrays of heaving point absorbers. *Ocean Engineering*, 282, 1-17. DOI: 10.1177/147509022211127.
4. **Rony, J. S**., and Karmakar, D. (2023). Dynamic analysis of frustum TLP-type wind turbine multi-purpose floating platform. *Ships and Offshore Structures*, 1-15. DOI: 10.1016/j.oceaneng.2023.114939
5. **Rony, J. S**., and Karmakar, D. (2023). Coupled dynamic analysis of hybrid STLP-WEC offshore floating wind turbine with different mooring configurations. *Journal of Ocean Engineering and Marine Energy*, 1-29. DOI: 10.1007/s40722-023-00287-w

6. **Rony, J.S**., Chaitanya Sai, K., and Karmakar, D. (2023). Numerical investigation of offshore wind turbine combined with Wave Energy Converter. *Marine Systems and Ocean Technology*, 18, 14-44. DOI: 10.1007/s40868-023-00127-4
7. **Rony, J.S**. and Karmakar, D. (2023). Hydrodynamic response analysis of a hybrid TLP and heaving-buoy wave energy converter with PTO damping. *Renewable Energy*, 226, 1-17. DOI: 10.1016/j.renene.2024.120380
8. **Rony, J.S.** and Karmakar, D. (2023). Long-term response analysis of hybrid STLP-WEC offshore floating wind turbine. *Ships and Offshore Structures*. (Under Review).
9. **Rony, J.S.** and Karmakar, D. (2023). Extreme response analysis of hybrid Tension Leg-type offshore wind turbine platform using inverse reliability method. *Wind Engineering*, (Submitted).
10. **Rony, J.S.** and Karmakar, D. (2023). Reliability based design loads of hybrid Submerged Tension Leg-type offshore wind turbine platform, *Journal of Ocean Engineering and Marine Energy*. (Submitted).

**(b) List of Publications in Book Chapters:**

11. **Rony J.S**., Karmakar, D. and C. Guedes Soares. (2021). Dynamic analysis of submerged Tension-Leg-Platform combined with heaving wave energy converter, *Developments in Marine Technology and Engineering, (Eds. C. Guedes Soares and T.A. Santos), CRC Press*, Vol-2, pp. 639-646. DOI: 10.1201/9781003216599
12. **Rony J.S**., Karmakar, D. and C. Guedes Soares. (2021). Dynamic response analysis of a combined wave and wind energy platform under different mooring configuration, *Trends in Maritime Technology and Engineering, (Eds. C. Guedes Soares and T.A. Santos), CRC Press*, Vol-2, pp. 477-487. DOI: 10.1201/9781003320289
13. Sreebhadra, M.N., **Rony J.S**., Karmakar, D. and C. Guedes Soares. (2021). Extreme response analysis for TLP-type floating wind turbine using Environmental Contour Method, *Trends in Maritime Technology and Engineering, (Eds. C. Guedes Soares and T.A. Santos), CRC Press*, Vol-2, pp. 315-324. DOI: 10.1201/9781003320289
14. **Rony, J. S**. and Karmakar, D. (2023). Dynamic analysis of submerged tension leg platform combined with wave energy converters for different mooring configurations. *AIP Conference Proceedings*, Vol. 2584, 1-8. DOI: 10.1063/5.0127786

**(c) List of Publications in Conference Proceedings:**

15. **Rony J. S**. and D. Karmakar. (2019). Long-term response analysis of different configurations of spar-type floating wind turbine. *International Conference on Trending Moments and Steer Forces – Civil Engineering Today (TMSF)*, 20th October – 1st November 2019, Fatorda, Goa.

16. **Rony J.S**. and D. Karmakar. (2019), Response analysis of combined wave and wind energy spar type platform, *International Conference on Hydraulics, Water Resource and Coastal Engineering (HYDRO)*, 18th – 20th December 2019, University College of Engineering, Osmania University, Hyderabad.

17. K. Kalyan Kumar, **Rony J.S**. and D. Karmakar. (2020), Response analysis of spar type platform with different mooring line configuration, *International Conference on Recent Advances on Renewable Energy (RARE-2020)*, 7th – 9th February 2020, NITK Surathkal, Mangalore, India.

18. **Rony J. S.** and D. Karmakar. (2020). Coupled dynamic analysis of Submerged Tension-Leg-Platform combined with heaving wave energy converter, *1st Online International Conference on Recent Advances in Computational and Experimental Mechanics*, 4th – 6th September 2020, Indian Institute of Technology Kharagpur, India.

19. **Rony J. S.** and D. Karmakar. (2021). Hydrodynamic performance of array of heaving point absorbers combined with STLP-type floating wind turbine, *International Conference on Hydraulics, Water Resource and Coastal Engineering (HYDRO)*, 26th – 28th March 2021, National Institute of Technology Rourkela, Odisha, India.

20. **Rony J. S.** and D. Karmakar. (2022). Dynamic Response of Combined Tension Leg-Platform Floating Wind Turbine and Point Absorber Wave Energy Converter, *International Conference on Hydraulics, Water Resource and Coastal Engineering (HYDRO)*, 22nd – 24th December 2022, Punjab Engineering College, Chandigarh, India.

**(d) <u>List of Patent Submitted:</u>**

21. **Rony, J.S**., and Karmakar, D. (2021). Frustum Tension-leg platform for floating wind turbine. Indian Patent No. 202141018525, Filed Application No. TEMP/E-1/19819/2021-CHE.